

SOCIETÀ ITALIANA DI FISICA

PROCEEDINGS
OF THE
INTERNATIONAL SCHOOL OF PHYSICS
«ENRICO FERMI»

COURSE CLXXVIII

*From the Big Bang
to the Nucleosynthesis*



SOCIETÀ ITALIANA DI FISICA BOLOGNA-ITALY

SOCIETÀ ITALIANA DI FISICA

RENDICONTI
DELLA
SCUOLA INTERNAZIONALE DI FISICA
“ENRICO FERMI”

CLXXVIII CORSO

a cura di A. BRACCO e E. NAPPI

Direttori del Corso

VARENNA SUL LAGO DI COMO

VILLA MONASTERO

19 – 24 Luglio 2010

*Dal Big Bang
alla nucleosintesi*

2011



SOCIETÀ ITALIANA DI FISICA
BOLOGNA-ITALY

This page intentionally left blank

ITALIAN PHYSICAL SOCIETY

PROCEEDINGS
OF THE
INTERNATIONAL SCHOOL OF PHYSICS
“ENRICO FERMI”

COURSE CLXXVIII

edited by A. BRACCO and E. NAPPI

Directors of the Course

VARENNA ON LAKE COMO

VILLA MONASTERO

19 – 24 July 2010

*From the Big Bang
to the Nucleosynthesis*

2011

IOS
Press

AMSTERDAM, OXFORD, TOKIO, WASHINGTON DC

Copyright © 2011 by Società Italiana di Fisica

All rights reserved. No part of this publication may be reproduced, stored in a retrieval system, or transmitted, in any form or any means, electronic, mechanical, photocopying, recording or otherwise, without the prior permission of the copyright owner.

ISSN 0074-784X (print)

ISSN 1879-8195 (online)

ISBN 978-1-60750-973-8 (print) (IOS Press)

ISBN 978-1-60750-974-5 (online) (IOS Press)

ISBN 978-88-7438-066-4 (SIF)

LCCN 2011941636

Production Manager
A. OLEANDRI

Copy Editor
M. MISSIROLI

jointly published and distributed by:

IOS PRESS

Nieuwe Hemweg 6B
1013 BG Amsterdam
The Netherlands
fax: +31 20 687 0019
info@iopress.nl

SOCIETÀ ITALIANA DI FISICA
Via Saragozza 12
40123 Bologna
Italy
fax: +39 051 581340
order@sif.it

Distributor in the USA and Canada

IOS Press, Inc.
4502 Rachael Manor Drive
Fairfax, VA 22032
USA
fax: +1 703 323 3668
sales@iospress.com

Proprietà Letteraria Riservata
Printed in Italy

Supported by

Istituto Nazionale di Fisica Nucleare (INFN)

Camera di Commercio di Lecco

INFN, Sezione di Milano

INFN, Sezione di Bari

This page intentionally left blank

INDICE

A. BRACCO and E. NAPPI – Preface pag.XVII

Gruppo fotografico dei partecipanti al Corso » XX

SUPERNOVAE AND NEUTRON STARS

K. LANGANKE – Stellar evolution: From hydrostatic burning to core collapse » 3

1. Introduction	»	3
2. Astrophysical nuclear reaction rates	»	4
3. Hydrostatic burning stages	»	7
3'1. Hydrogen burning	»	8
3'2. Solar neutrinos	»	12
3'3. Helium burning	»	15
3'4. Carbon, neon, oxygen, silicon burning	»	16
4. Core collapse supernovae	»	17
4'1. Electron captures in core-collapse supernovae —the general picture	»	19
4'2. Weak-interaction rates and presupernova evolution	»	24
4'3. The role of electron capture during collapse	»	25
5. Making heavy elements in explosive nucleosynthesis	»	27
5'1. The νp process	»	27
5'2. The r-process	»	28
5'3. Neutrino nucleosynthesis	»	29
6. The Facility for Antiproton and Ion Research (FAIR)	»	29

M. BALDO – The theory of Neutron Stars and the role of Nuclear Physics . » 35

1. Introduction	»	36
2. Overall structure of a Neutron Star	»	37
2'1. The outer crust	»	39
2'2. The inner crust	»	42
2'3. The outer core	»	43
2'4. The inner core	»	44
3. The free Fermi gas of nucleons	»	45
3'1. The Equation of State	»	45
3'2. The compressibility	»	47
3'3. Momentum distribution	»	48

3'4.	The symmetry energy	pag.	48
3'5.	The single particle density of states	»	49
3'6.	The Pauli paramagnetism	»	49
3'7.	Other microscopic physical quantities	»	50
4.	Introducing the interaction	»	50
4'1.	Sketch of the nucleon-nucleon interaction	»	51
4'2.	Theoretical many-body methods	»	57
4'2.1.	The Brueckner-Bethe-Goldstone expansion	»	57
4'2.2.	The variational method	»	59
4'2.3.	The relativistic approach	»	60
4'2.4.	The V_{low} approach	»	64
4'2.5.	Trying a link to QCD: the chiral symmetry approach	»	66
5.	Neutron matter at very low density. An exercise in many-body theory	»	67
5'1.	A single G -matrix problem	»	67
5'2.	The “exact” EoS	»	69
6.	Going to nuclear structure	»	70
6'1.	The Thomas-Fermi approximation and implementations	»	71
6'2.	The density functional method	»	72
7.	Nuclear Physics and Neutron Star structure	»	77
7'1.	The Neutron Star inner crust	»	77
7'2.	The Neutron Star core and mass-radius relationship	»	82
8.	Conclusions and outlook	»	89

M. N. HARAKEH –	Spin-isospin modes: Implications for astrophysics	»	95
1.	Introduction	»	96
2.	The compression modes and incompressibility of nuclear matter	»	98
3.	Spin-isospin excitations	»	103
4.	GT strength in fp -shell nuclei	»	105
5.	Determination of GT [−] strength	»	106
6.	Determination of GT ⁺ strength and its astrophysical implications	»	112
7.	Conclusions and outlook	»	123

NUCLEAR STRUCTURE AND NUCLEAR ASTROPHYSICS WITH RADIOACTIVE BEAMS

T. AUMANN –	Nuclear-astrophysics experiments with relativistic radioactive beams	»	127
1.	Introduction	»	127
2.	Experiments with high-energy radioactive beams at GSI	»	133
2'1.	Mass measurements	»	133
2'2.	The dipole response of exotic nuclei	»	135
3.	Future perspectives—NuSTAR at FAIR	»	139
3'1.	The FAIR facility	»	139
3'2.	The radioactive beam facility	»	141
3'3.	Experiments with slowed-down and stopped beams	»	144

3'3.1.	The low-energy branch	pag. 144
3'3.2.	High-resolution in-flight spectroscopy (HISPEC)	» 144
3'3.3.	Decay spectroscopy (DESPEC)	» 146
3'3.4.	The advanced trapping system MATS	» 146
3'3.5.	The laser-spectroscopy experiment LASPEC	» 147
3'4.	Reactions with Relativistic Radioactive Beams (R^3B)	» 147
3'5.	Experiments with stored and cooled beams	» 149
3'5.1.	Isomeric beams, lifetimes, and masses (ILIMA)	» 149
3'5.2.	Reactions at internal targets in the NESR (EXL)	» 150
3'5.3.	Electron scattering with short-lived nuclei (ELISe)	» 152
3'5.4.	The Antiproton-Ion-Collider AIC	» 154
4.	Conclusion	» 154
 T. MOTOBAYASHI – Nuclear structure studies at RIKEN: New measurements with in-flight fast radioactive beams		» 157
1.	Introduction	» 157
2.	RIBF new facility	» 158
3.	Frontiers in the nuclear chart	» 160
3'1.	Nuclear chart	» 160
3'2.	Toward the <i>r</i> -process path	» 161
3'3.	Super-heavy nuclei	» 162
4.	Fate of magic numbers	» 163
4'1.	Disappearance of the $N = 20$ magic number	» 163
5.	Neutron-proton asymmetry: “egg” structure in ^{16}C	» 166
6.	Challenges at RIBF	» 167
6'1.	SHARAQ	» 167
6'2.	SAMURAI	» 168
6'3.	SCRIT	» 169
6'4.	SLOWRI	» 170
6'5.	Rare RI-ring	» 170
7.	Conclusions	» 171
 P. A. BUTLER – ISOL techniques to reach radioactive nuclei: From birth to EURISOL		» 173
1.	Introduction	» 173
2.	History of ISOL	» 174
3.	Targets and ion sources	» 174
	Surface ion source	» 175
	Plasma ion source	» 176
	Laser ion source	» 176
4.	Accelerated radioactive beam facilities	» 177
	Louvain-la-Neuve	» 177
	Holifield Radioactive Ion Beam Facility	» 178
	SPIRAL	» 178
	REX-ISOLDE	» 178
	ISAC	» 180

Other ISOL RIB facilities	pag.	180
5. Other ISOL techniques: IGISOL, Gas catchers and FRIB	»	181
Ion guide	»	181
Gas catcher	»	183
FRIB	»	183
6. Second-generation facilities in Europe	»	184
SPES	»	184
HIE-ISOLDE	»	184
7. EURISOL	»	185
8. Final words	»	188

M. LEWITOWICZ on behalf of the SPIRAL2 PROJECT GROUP and PHYSICS COLLABORATIONS – Low-energy reactions, moments and beta-decays with radioactive beams for nuclear structure and astrophysics problems. Results and perspectives with SPIRAL2

M. LEWITOWICZ on behalf of the SPIRAL2 PROJECT GROUP and PHYSICS COLLABORATIONS – Low-energy reactions, moments and beta-decays with radioactive beams for nuclear structure and astrophysics problems. Results and perspectives with SPIRAL2	»	191
1. Introduction	»	191
2. Goals and new avenues for physics with Radioactive Ion Beams	»	192
3. GANIL, SPIRAL and SPIRAL2 facilities	»	195
3'1. SPIRAL 2 Facility	»	197
3'1.1. SPIRAL 2 Driver Accelerator	»	198
3'1.2. Superconducting LINAC	»	198
3'1.3. Production of Radioactive Ion Beams at SPIRAL 2	»	199
3'1.4. Simultaneous operation of the GANIL/SPIRAL1/SPIRAL2 facility	»	201
3'1.5. The civil construction of the SPIRAL2 facility	»	202
4. Experiments with high-intensity stable-ion beams	»	202
4'1. S3	»	203
4'1.1. Final focal-plane detectors	»	204
4'1.2. Low-energy branch of S3	»	204
4'1.3. In-flight experiments with S3	»	205
4'1.4. Very-heavy nuclei and Superheavy elements (SHE)	»	206
4'1.5. Neutron-deficient nuclei	»	207
4'1.6. Neutron-rich nuclei with transfer and deep inelastic reactions	»	207
5. Experiments with low energy radioactive ion beams	»	207
5'1. DESIR	»	207
5'1.1. Physics case of DESIR	»	209
5'1.2. Beta-decay measurements of astrophysical interest	»	210
6. Experiments with post-accelerated RIB	»	212
6'1. EXOGAM 2	»	213
6'2. AGATA	»	216
6'3. PARIS	»	216
6'4. NEDA	»	218
6'5. GASPARD	»	218
6'6. FAZIA	»	221
6'7. ACTAR	»	222
6'8. HELIOS	»	223
7. Conclusions and outlook	»	223

THE QUARK-GLUON PLASMA AND BEYOND

F. ANTINORI and U. A. WIEDEMANN – Heavy-ion collisions—Selected topics	pag.	229
1. Preamble	»	229
2. Introduction	»	230
3. Kinematic variables	»	231
4. Invariant cross-sections	»	232
5. Multiplicity distributions	»	233
5'1. Glauber theory	»	234
5'1.1. Nucleon-nucleus (n-A) collisions	»	235
5'1.2. Nucleus-nucleus (A-B) collisions	»	236
5'2. Characterizing the collisions geometry by multiplicity distributions	»	238
5'3. Slicing-up multiplicity distributions	»	240
5'4. Constraining dynamical models by multiplicity distributions	»	242
6. Particle production with respect to the reaction plane	»	244
6'1. The cumulant method for n -th-order flow	»	245
6'2. Elliptic flow at RHIC and at the LHC	»	247
7. Hydrodynamic modeling of heavy-ion collisions	»	248
7'1. Tensor decomposition of $T^{\mu\nu}$	»	248
7'2. Equations of motion for a perfect fluid	»	250
7'3. Bjorken boost-invariant ideal fluid	»	252
7'4. Simulating a Bjorken boost-invariant perfect fluid	»	254
7'5. Dissipative corrections to perfect-fluid dynamics	»	257
7'6. Numerical results for dissipative hydrodynamics	»	259
8. Hard probes	»	261
8'1. High- p_T single inclusive hadron spectra in nucleus-nucleus collisions	»	261
8'2. Scattering of highly energetic partons in nuclear matter	»	264
8'3. Gluon radiation off quarks produced in the medium	»	268
8'4. Comparing parton energy loss calculations to data on R_{AA}	»	271
8'5. From single inclusive hadron suppression to reconstructed jet quenching	»	274
 C. BIANCHIN for the ALICE COLLABORATION – Open-charm analysis for energy loss studies with ALICE at LHC	»	279
1. Introduction	»	279
2. ALICE performance	»	280
2'1. Expected performance for $D^0 \rightarrow K\pi$ analysis in p-p	»	281
3. Status of the analysis of p-p collisions at $\sqrt{s} = 7$ TeV	»	282
4. Conclusions	»	284
 A. MASIERO – Dark matter: A window to New Physics at the electroweak scale	»	285
1. Introduction	»	285
2. The Standard Model of particle physics	»	289
2'1. The Higgs mechanism and vector boson masses	»	291
2'2. Fermion masses	»	292

2'3. Successes and difficulties of the SM	pag. 293
3. The dark matter problem: experimental evidence	» 293
4. Lepton number violation and neutrinos as HDM candidates	» 295
4'1. Neutrino masses in the SM and beyond	» 295
4'2. Thermal history of neutrinos	» 296
4'3. HDM and structure formation	» 298
5. Low-energy SUSY and DM	» 298
5'1. Neutralinos as the LSP in SUSY models	» 298
5'2. Neutralinos in the Minimal Supersymmetric Standard Model	» 300
5'3. Thermal history of neutralinos and Ω_{CDM}	» 301
6. Changing the expansion rate in the past	» 302
6'1. GR as a fixed point	» 304
7. Implications for dark matter in the CMSSM	» 305
8. Conclusion	» 306
 L. GARCÍA, J. TEJEIRO and L. CASTAÑEDA – Primordial nucleosynthesis in the presence of sterile neutrinos	 » 309
1. Introduction	» 309
2. Sterile neutrinos	» 310
3. Hubble factor and cosmological time	» 311
4. Computed abundances with sterile neutrinos	» 314
5. Conclusions	» 316
 LOW-ENERGY REACTIONS FOR ASTROPHYSICS	
 A. GUGLIELMETTI for the LUNA COLLABORATION – The LUNA experiment at LNGS	 » 319
1. Introduction	» 319
2. Why underground: the LUNA project	» 320
3. Results	» 321
4. On-going measurements	» 327
5. The future: LUNA MV project	» 330
 C. SPITALERI – Nuclear astrophysics results with the Trojan Horse Method	 » 333
1. Introduction	» 333
2. Basic theory	» 335
2'1. Energy prescriptions	» 337
2'2. PWIA: applicability conditions	» 338
2'3. Experimental momentum distribution	» 338
2'3.1. PWIA	» 338
2'3.2. DWBA	» 341
3. Data analysis	» 343
3'1. Selection of the Trojan horse nucleus	» 343
3'2. QF data selection: study of momentum distribution in angular correlation	» 344

3.3. Extraction of the two-body cross-section from the measured three-body reaction	pag. 345
4. Validity tests of pole approximation	» 346
4.1. Comparison of excitation functions	» 347
4.1.1. A1) $\sigma(E)$ above the Coulomb barrier	» 347
4.1.2. A2) $\sigma(E)$ below the Coulomb barrier	» 347
4.1.3. A3) above and below the Coulomb barrier	» 347
4.2. Comparison of the angular distributions: above and below the Coulomb barrier	» 348
5. Results	» 348
6. Astrophysics applications: The light element depletion problem	» 349
6.1. The ${}^7\text{Li}(p, \alpha){}^4\text{He}$ reaction	» 350
6.2. The ${}^6\text{Li}(p, \alpha){}^3\text{He}$ reaction	» 350
6.3. The ${}^6\text{Li}(d, \alpha){}^4\text{He}$ reaction	» 352
7. Conclusions	» 353

P. M. MILAZZO – Neutron capture measurements at the CERN neutron time-of-flight facility: Nuclear astrophysics aspects	» 355
1. Introduction	» 356
2. The n_TOF facility	» 357
3. The experimental setup	» 358
4. The neutron capture measurements	» 360
5. Measurements of astrophysical interest	» 361
5.1. The ${}^{90,91,92,93,94,96}\text{Zr}(n, \gamma), {}^{139}\text{La}$ reactions	» 361
5.2. The ${}^{151}\text{Sm}$ reaction	» 362
5.3. The ${}^{186,187,188}\text{Os}(n, \gamma)$ reactions	» 362
6. Conclusions	» 363

NUCLEAR STRUCTURE FOR ASTROPHYSICS

G. BENZONI – Isomeric states in neutron-rich lead isotopes populated by fragmentation of ${}^{238}\text{U}$ at 1 GeV A	» 367
1. Introduction	» 367
2. Experimental details	» 368
3. Identification of nuclear species	» 369
4. Isomeric decay	» 372
5. Conclusion and perspectives	» 374

JENNY LEE and M. B. TSANG – Neutron spectroscopic factors	» 377
1. Introduction	» 378
2. Extraction of spectroscopic factors from transfer reactions	» 378
3. Survey of spectroscopic factors from transfer reactions for stable nuclei	» 380
4. Transfer reaction measurements for exotic Ar isotopes	» 384
5. Conclusions	» 387

A. CORSI, A. BRACCO, F. CAMERA, F. C. L. CRESPI, A. GIAZ, S. LEONI, R. NICOLINI, V. VANDONE, O. WIELAND, G. BENZONI, N. BLASI, S. BRAMBILLA, B. MILLION, S. BARLINI, L. BARDELLI, M. BINI, G. CASINI, A. NANNINI, G. PASQUALI, G. POGGI, V. L. KRAVCHUK, M. CINAUSERO, M. DEGERLIER, F. GRAMEGNA, T. MARCHI, D. MONTANARI, G. BAIOCCHI, M. BRUNO, M. D'AGOSTINO, L. MORELLI, G. VANNINI, M. CIEMALA, M. KMIECICKI, A. MAJ, K. MAZUREK, W. MECZYNSKI and S. MYALSKI – Measurement of isospin mixing in hot ^{80}Zr compound nucleus..	pag. 391
1. Isospin mixing in nuclei	» 392
2. Measurement of isospin symmetry via Giant Dipole Resonance	» 394
3. Description of the experiment	» 395
4. Data analysis	» 396
4'1. Data reduction	» 396
4'2. Statistical model analysis	» 396
5. Results and conclusions	» 398
 POSTERS	
F. BARILE on behalf of the ALICE COLLABORATION – Identification of hadrons at high momentum with the HMPID detector in the ALICE experiment at the LHC	» 403
1. Introduction	» 403
2. The ALICE-HMPID detector	» 404
3. Analysis and results	» 405
4. Conclusion	» 405
A. GIAZ, A. CORSI, F. CAMERA, A. BRACCO, F. C. L. CRESPI, S. LEONI, R. NICOLINI, V. VANDONE, G. BENZONI, N. BLASI, S. BRAMBILLA, B. MILLION, O. WIELAND, T. MARCHI, V. L. KRAVCHUK, M. CINAUSERO, M. DEGERLIER, F. GRAMEGNA, V. RIZZI, P. BEDNARCYK, M. CIEMALA, M. KMIECICKI, A. MAJ, K. MAZUREK, W. MECZYNSKI, G. BAIOCCHI, M. BRUNO, M. D'AGOSTINO, L. MORELLI, G. VANNINI, S. BARLINI, L. BARDELLI, M. BINI, S. CARBONI, G. CASINI, M. CHIARI, A. NANNINI, G. PASQUALI, S. PIANTELLI, G. POGGI, A. ORDINE, R. ALBA, C. MAIOLINO, D. SANTONOCITO, M. COLONNA, M. DI TORO, C. RIZZO and D. MONTANARI – New studies of the dynamical dipole in asymmetric heavy-ion reactions: A probe of the nuclear equation of state.....	» 407
1. Introduction	» 408
2. Experimental setup	» 409
3. Preliminary results	» 410
L. GUERRO – A pair spectrometer for E0 transitions measurements	» 413
1. E0 transitions.....	» 413
1'1. Pair creation by internal conversion	» 414

2. The pair spectrometer	pag.	414
2.1. Monte Carlo simulation of the detector performances	»	415
3. Conclusions	»	416
R. NICOLINI, A. BRACCO, S. LEONI, F. CAMERA, F. BIROCCHI, A. CORSI, F. C. L. CRESPI, A. GIAZ, L. PELLEGRI, S. RIBOLDI, V. VANDONE, A. CAMPLANI, G. BENZONI, N. BLASI, C. BOIANO, S. BRAMBILLA, B. MILLION, O. WIELAND, D. BAZZACCO, E. FARNEA, A. GOTTARDO, C. MICHELAGNOLI, D. MONTANARI, C. UR, D. MENGONI, G. DE ANGE- LIS, P. MOLINI, D. R. NAPOLI, F. RECCHIA, E. SAHIN, J. J. VALIENTE- DOBON, A. GADEA, A. MAJ, M. CIEMALA, M. KMIECIK, R. KEMPLEY, A. BÜRGER and P. REITER – Study of high-lying states in ^{208}Pb with the AGATA Demonstrator		
	»	417
1. Introduction	»	418
2. Experimental setup and data analysis	»	418
3. Conclusions	»	421
L. PELLEGRI, F. BIROCCHI, A. BRACCO, F. CAMERA, A. CORSI, F. C. L. CRESPI, A. GIAZ, S. LEONI, R. NICOLINI, S. RIBOLDI, V. VANDONE, G. BENZONI, N. BLASI, S. BRAMBILLA, C. BOIANO, B. MILLION, O. WIELAND and D. MONTANARI – Recent developments in gamma-ray spec- troscopy with new scintillators, $\text{LaBr}_3(\text{Ce})$, to investigate nuclear structure at high excitation and far from stability		
	»	423
1. Introduction	»	424
2. Methods	»	424
3. Application	»	424
V. VANDONE, S. LEONI, A. BRACCO, S. BOTTONI, F. CAMERA, A. CORSI, F. C. L. CRESPI, A. GIAZ, R. NICOLINI, G. BENZONI, N. BLASI, C. BOIANO, S. BRAMBILLA, B. MILLION, O. WIELAND, D. BORTOLATO, E. CALORE, A. GOTTARDO, D. R. NAPOLI, E. SAHIN, J. J. VALIENTE DOBON, D. BAZZACCO, M. BELLATO, E. FARNEA, S. LUNARDI, D. MEN- GONI, C. MICHELAGNOLI, D. MONTANARI, F. RECCHIA, C. A. UR, A. GADEA, T. HÜYÜK, N. CIEPLICKA, A. MAJ, M. KMIECIK, A. ATAC, S. AKKOYUN, A. KASKAS, S. KETENCI, J. NYBERG and P. A. SÖDERSTRÖM – Order-to-chaos transition in warm rotating ^{174}W nuclei		
	»	427
1. Introduction	»	428
2. The experiment	»	429
Elenco dei partecipanti		
	»	431

This page intentionally left blank

Preface

The CLXXVIII Course of the International School of Physics “Enrico Fermi”, entitled “From the Big Bang to the Nucleosynthesis”, held in Varenna from July 19 to 24, 2010, was devoted to the present understanding of the primordial universe and of the origin of the elements as achieved by studying nuclei and their constituents in extreme regimes of energy and composition. In the quest to work out a comprehensive theory of the appearance and evolution of nuclear matter, physicists have so far made a great effort in reproducing in laboratory the conditions which characterized the Big Bang and the various nucleosynthesis mechanisms occurring in the stars. In particular, by colliding heavy ions at ultrarelativistic energies, one tries to recreate the predicted primordial state of high-energy density matter in which quarks and gluons are effectively deconfined, the so-called Quark Gluon Plasma (QGP), whereas the knowledge of the present-day abundances of heavy elements requires the exploration of the structure and reaction properties of very unstable nuclei as carried out by experiments with radioactive beams.

The actual high-energy frontier of relativistic heavy-ion physics has moved in the last few years from RHIC at BNL to the LHC at CERN, where ALICE is the experiment specifically designed to provide unambiguous evidence of the QGP formation and to characterize its properties. The physics programme underlying this experiment was illustrated by the two world-recognized experts in the field: F. Antinori and U. Wiedemann.

Nuclei far from stability are presently studied in various laboratories and new facilities featuring high-intensity beams are either just completed, under construction or in the planning stage. The main objective is to move further away from stability thus producing, in the most effective way, the relevant unstable nuclei involved in the nucleosynthesis stages and to understand how a many-body nuclear system can be described in conditions very much different from those we find on Earth. The different techniques needed to produce exotic nuclei and to study their degrees of freedom from the ground state and the properties of the excited states have been presented and pedagogically discussed in several lectures by renowned physicists, namely T. Aumann, P. Butler, M. Lewitowicz, T. Motobayashi. In connection with these lectures they gave very focused overviews of the major facilities (GSI-FAIR, CERN-ISOLDE and EURISOL, GANIL-SPIRAL2, RIKEN-RIBF) and their planned experimental programmes.

The complex but appealing theory describing the supernovae explosion and neutron stars was presented by the experts M. Baldo and K. Langanke, who clearly showed that, in addition to the very important role played by the radioactive beams, one also needs precise measurements of the Gamow-Teller strength in stable nuclei and exclusive measurements carried out in heavy-ion collisions around the Fermi energy. These experiments and their associated techniques were the subject of the lectures of M. Harakeh and W. Lynch, pioneers in this field and of the seminar of B. Tsang. The theoretical description of neutron stars as presented in this school pointed out the need of the combined information from ALICE and exotic-nuclei experiments. In addition, exciting lectures on dark energy and matter were given by A. Masiero.

The main lectures were complemented by seminars on issues of current interest and on their future prospect. These concerned the Big Bang nucleosynthesis and energy and solar neutrino production (A. Guglielmetti and C. Spitaleri) and the nuclear cosmochronology (P. Milazzo), which are among the most interesting topics in nuclear astrophysics addressed at the INFN LNS and LNGS laboratories and at CERN by the n_TOF experiment. Beta and gamma decay relevant for nucleosynthesis of heavy nuclei was also presented (G. Benzoni).

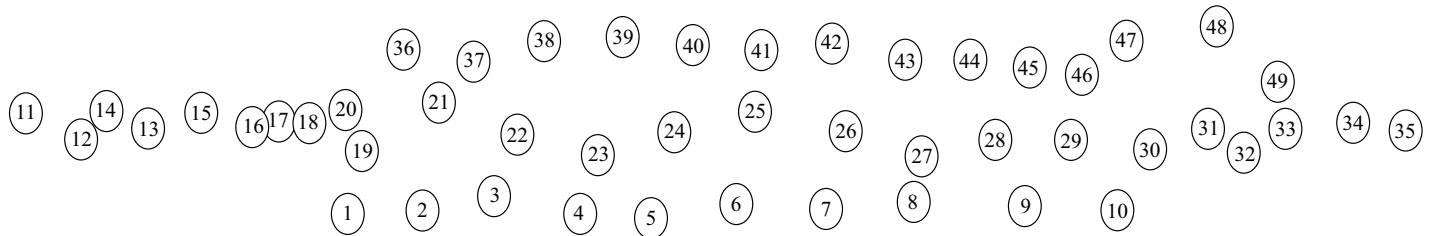
The students had the opportunity to compete in a poster session devoted to their activities, the authors of the best posters were selected to illustrate their main achievements in dedicated talks. The atmosphere of the conference was very pleasant and all the participants enjoyed of the presence, for the entire Course, of Prof. R. A. Ricci (honorary President of SIF), who provided a warm welcome and an appreciated concluding talk. The President of CNR, Prof. L. Maiani, honored us with a short visit in which he shared with all the participants his thoughts about the future of nuclear and particle physics. The Course also benefited from the unexpected visit of the former student, Prof. Uri Haber-Schaim, who attended the second course directed by Prof. G. Puppi, 56 years ago.

We are particularly indebted to Prof. L. Cifarelli, President of SIF, for having given us the opportunity to organize such an inspiring Course, and to all the lecturers, who greatly contributed to the scientific programme. We gratefully acknowledge the financial support of the Istituto Nazionale di Fisica Nucleare (INFN) and the technical support of INFN-CNAF, which allowed the lectures to be broadcasted via web. We express our heartfelt gratitude to Ms B. Alzani, Ms G. Bianchi Bazzi and Dr. A. Di Giuseppe for their very professional and efficient help before and during the School. A special thank to Dr. B. Million, scientific secretary of the Course, who played a key role towards the success of this Course. The continuous and invaluable support provided by the Varenna School staff together with the enthusiastic and active participation of the attendees have made this Course an unforgettable experience for us on both scientific and human aspects.

This page intentionally left blank

Società Italiana di Fisica
SCUOLA INTERNAZIONALE DI FISICA «E. FERMI»
CLXXVIII CORSO - VARENNA SUL LAGO DI COMO
VILLA MONASTERO 19 - 24 Luglio 2010





- | | | | | | |
|------------------------|-------------------------|---------------------------|-----------------------|----------------------|-------------------------|
| 1) Antonio Masiero | 10) Karlheinz Langanke | 19) Uzma Tabassam | 28) Fay Filmer | 35) Roberta Spartà | 43) Alina Movsesyan |
| 2) Angela Bracco | 11) Marta Pigazzini | 20) Caterina Michelagnoli | 29) Luz Angela Garcia | 36) Roberto Nicolini | 44) Fiorella Maria |
| 3) William Lynch | 12) Laura Strolin | 21) Stefano Carboni | Peñaloza | 37) Leonardo Guerro | Celeste Fionda |
| 4) Eugenio Nappi | 13) Ramona Brigatti | 22) Luna Pellegrini | 30) Chiara Bianchin | 38) Francesco Barile | 45) Cristina Terrevoli |
| 5) Renato Angelo Ricci | 14) Stefano Meneghini | 23) Agnese Giaz | 31) Francesca Bellini | 39) Livio Bianchi | 46) Susanna Bertelli |
| 6) Urs Wiedemann | 15) Fabio Bisi | 24) Valeria Vandone | 32) Giovanna Benzoni | 40) Liam Gaffney | 47) Daniele De Gruttola |
| 7) Muhsin N. Harakeh | 16) Luigi Vannucci | 25) Daniele Madaffari | 33) Jasna Krivicic | 41) Mihai Straticiuc | 48) Andrea Agostinelli |
| 8) Thomas Aumann | 17) Bénédicte Million | 26) Anna Corsi | 34) Oscar Trippella | 42) Ion Burducea | 49) Tommaso Marchi |
| 9) Marcello Baldo | 18) Farnaz Ghazi Moradi | 27) Jitka Brabcová | | | |

This page intentionally left blank

SUPERNOVAE AND NEUTRON STARS

This page intentionally left blank

Proceedings of the International School of Physics “Enrico Fermi”
Course CLXXVIII “From the Big Bang to the Nucleosynthesis”, edited by A. Bracco and E. Nappi
(IOS, Amsterdam; SIF, Bologna)
DOI 10.3254/978-1-60750-974-5-3

Stellar evolution: From hydrostatic burning to core collapse

K. LANGANKE

GSI Helmholtzzentrum für Schwerionenforschung - Darmstadt, Germany

Institut für Kernphysik, Technische Universität Darmstadt - Darmstadt, Germany

Frankfurt Institute for Advanced Studies - Frankfurt, Germany

Summary. — These lectures discuss selected topics in nuclear astrophysics. They include hydrogen burning, solar neutrinos, advanced stellar burning stages, the final fate of massive stars as core-collapse supernovae and the associated explosive nucleosynthesis. The emphasis is on the nuclear ingredients, which determine the evolution and dynamics of the astrophysical objects.

1. – Introduction

Nuclear astrophysics has developed in the last twenty years into one of the most important subfields of “applied” nuclear physics. It is a truly interdisciplinary field, concentrating on primordial and stellar nucleosynthesis, stellar evolution, and the interpretation of cataclysmic stellar events like novae and supernovae.

The field has been tremendously stimulated by recent developments in the laboratory and observational techniques. In the laboratory the development of radioactive ion beam facilities as well as low-energy underground facilities have allowed to remove some of the most crucial ambiguities in nuclear astrophysics arising from nuclear physics input parameters. This work has been accompanied by significant progress in nuclear theory

which makes it now possible to derive some of the input at stellar conditions based on microscopic models. Nevertheless, much of the required nuclear input is still insufficiently known. Here, decisive progress is expected once radioactive ion beam facilities of the next generation, like FAIR (Facility for Antiproton and Ion Research), are operational. The nuclear progress goes hand-in-hand with tremendous advances in observational data arising from satellite observations of intense galactic gamma-sources, from observation and analysis of isotopic and elemental abundances in deep convective Red Giant and Asymptotic Giant Branch stars, and abundance and dynamical studies of nova ejecta and supernova remnants. Recent breakthroughs have also been obtained for measuring the solar neutrino flux, giving clear evidence for neutrino oscillations and confirming the solar models. Also, the latest developments in modeling stars, novae, X-ray bursts, type I supernovae, and the identification of the neutrino wind-driven shock in type II supernovae as a possible site for the r-process allow now much better predictions from nucleosynthesis calculations to be compared with the observational data.

It is impossible to cover the large width of this truly interdisciplinary field in two lectures. Hence I have made a biased choice and concentrate only on the nuclear aspects of stellar evolution. After a brief introduction about some general ideas concerning stellar nuclear reactions, the next sections discuss the nuclear reactions occurring during the long lifetime of stars when these generate their energy in a sequence of nuclear burning stages in hydrostatic equilibrium. The fourth section is focussed on recent progress with respect to nuclear aspect of the collapse of the inner core of massive stars and the star's explosion as a type II supernova. In a short section we then briefly discuss the explosive nucleosynthesis occurring during this explosion which leads to the production of heavy elements by the rapid neutron capture process and potentially also by the recently discovered νp process.

2. – Astrophysical nuclear reaction rates

During the hydrostatic burning stages of a star, charged-particle reactions most frequently occur at energies far below the Coulomb barrier, and are possible only via the *tunnel effect*, the quantum-mechanical possibility of penetrating through a barrier at a classically forbidden energy. At these low energies, the cross-section $\sigma(E)$ is dominated by the penetration factor, which for point-like particles and in the absence of a centrifugal barrier (*s*-wave) is well approximated by [1]

$$(1) \quad P(E) = \exp \left[-\frac{2\pi Z_1 Z_2 e^2}{\hbar v} \right] \equiv \exp [-2\pi\eta(E)],$$

where $\eta(E)$ is often called the Sommerfeld parameter. In numerical units,

$$(2) \quad 2\pi\eta(E) = 31.29 Z_1 Z_2 \sqrt{\frac{\mu}{E}},$$

where the energy E is defined in keV.

It is convenient and customary to redefine the cross-section in terms of the astrophysical S -factor by factoring out the known energy dependences of the penetration factor and the de Broglie factor, in the *model-independent* way,

$$(3) \quad S(E) = \sigma(E)(E) \exp[2\pi\eta(E)].$$

For low-energy, nonresonant reactions, the astrophysical S -factor should have only a weak energy dependence that reflects effects arising from the strong interaction, as from antisymmetrization, and from small contributions from partial waves with $l > 0$ and for the finite size of the nuclei. The validity of this approach has been justified in numerous (nonresonant) nuclear reactions for which the experimentally determined S -factors show only weak E -dependences at low energies.

The reaction rate of two nuclear species x, y with number densities N_x and N_y , respectively, is given by

$$(4) \quad R_{xy} = \frac{1}{1 + \delta_{xy}} N_x N_y \langle \sigma(v)v \rangle,$$

where one has to account for the velocity distributions of target and projectile in the astrophysical environment. As these are given by Maxwell-Boltzmann distributions, one has ($E = \frac{\mu}{2}v^2$)

$$(5) \quad \langle \sigma(v)v \rangle = \left(\frac{8}{\pi\mu} \right)^{1/2} \left(\frac{1}{kT} \right)^{3/2} \int_0^\infty \sigma(E) E \exp \left[-\frac{E}{kT} \right] dE,$$

$$(6) \quad = \left(\frac{8}{\pi\mu} \right)^{1/2} \left(\frac{1}{kT} \right)^{3/2} \int_0^\infty S(E) \exp \left[-\frac{E}{kT} - 2\pi\eta(E) \right] dE.$$

For typical applications in hydrostatic stellar burning, the product of the two exponentials forms a peak (“Gamow-peak”) which may be well approximated by a Gaussian,

$$(7) \quad \exp \left[-\frac{E}{kT} - 2\pi\eta(E) \right] \cong I_{\max} \exp \left[-\left(\frac{E - E_0}{\Delta/2} \right)^2 \right]$$

with [1]

$$(8) \quad E_0 = 1.22(Z_1^2 Z_2^2 \mu T_6^2)^{1/3} \quad (\text{keV}),$$

$$(9) \quad \Delta = \frac{4}{\sqrt{3}} \sqrt{E_0 kT} \\ = 0.749(Z_1^2 Z_2^2 \mu T_6^5)^{1/6} \quad (\text{keV}),$$

$$(10) \quad I_{\max} = \exp \left[-\frac{3E_0}{kT} \right];$$

TABLE I. – *Values for E_0 , Δ , and I_{\max} at solar core temperature ($T_6 = 15.6$) [1].*

Reaction	E_0 (keV)	$\Delta/2$ (keV)	I_{\max}
$p + p$	5.9	3.2	1.1×10^{-6}
$^3\text{He} + ^3\text{He}$	22.0	6.3	4.5×10^{-23}
$^3\text{He} + ^4\text{He}$	23.0	6.4	5.5×10^{-23}
$p + ^7\text{Be}$	18.4	5.8	1.6×10^{-18}
$p + ^{14}\text{N}$	26.5	6.8	1.8×10^{-27}
$\alpha + ^{12}\text{C}$	56.0	9.8	3.0×10^{-57}
$^{16}\text{O} + ^{16}\text{O}$	237.0	20.2	6.2×10^{-239}

T_6 measures the temperature in units of 10^6 K. Examples of E_0 , Δ and I_{\max} , evaluated for some nuclear reactions at the solar core temperature ($T_6 \approx 15.6$), are summarized in table I.

We can draw a few interesting conclusions from table I. At first, reactions operate in relatively narrow energy windows around the astrophysically most effective energy E_0 . Secondly, the penetration factor dominates the reaction rates at astrophysical energies which is also true if one accounts for the different strengths of the fundamental interactions. Hence stellar burning will start with the fusion of those nuclei with the smallest product of charges, *i.e.* the smallest Coulomb barrier. As neutrons are not available when stars form this will be hydrogen burning, as we will discuss in the next section. It becomes also clear from inspecting the different I_{\max} values that reactions of nuclei with large charge numbers effectively cannot occur in the sun as, for these reactions, even the solar core is far too cold.

However, it usually turns out that the astrophysically most effective energy E_0 is smaller than the energies at which the reaction cross-section can be measured directly in the laboratory. Thus for astrophysical applications, an extrapolation of the measured cross-section to stellar energies is usually necessary, often over many orders of magnitude. In the case of nonresonant reactions, the extrapolation can be safely performed in terms of the astrophysical S -factor, because of its rather weak energy dependence.

We finally have to mention that the nuclear reaction rates are enhanced in stellar environments as the repulsive Coulomb barrier is somewhat shielded by other plasma particles [2]. Such shielding effects are also encountered in laboratory measurements of nuclear cross-sections at low energies as the electrons present in the target (and perhaps also in the projectile) effectively reduce the Coulomb barrier [3]. We stress, however, that laboratory and plasma screening are different. Hence, the first has to be removed from the data to determine the cross-sections for bare nuclei which then, in astrophysical applications, has to be modified due to plasma effects.

TABLE II. – *Evolutionary stages of a $25 M_{\odot}$ star (from [4]).*

Evolutionary stage	Temperature (keV)	Density (g/cm ³)	Time scale
Hydrogen burning	5	5	7×10^6 y
Helium burning	20	700	5×10^5 y
Carbon burning	80	2×10^5	600 y
Neon burning	150	4×10^6	1 y
Oxygen burning	200	10^7	6 mo
Silicon burning	350	3×10^7	1 d
Core collapse	700	3×10^9	seconds
Core bounce	15000	4×10^{14}	10 ms
Explosion	100–500	10^5 – 10^9	0.01 to 0.1 s

3. – Hydrostatic burning stages

When the temperature and density in a star’s interior rises as a result of gravitational contraction, it will be the lightest charged nuclides that can react first and supply the energy and pressure to stop the gravitational collapse of the gaseous cloud. Thus it is hydrogen burning (the fusion of four protons into a ${}^4\text{He}$ nucleus) in the stellar core that stabilizes the star first and for the longest time. However, because of the larger charge ($Z = 2$), helium, the ashes of hydrogen burning, cannot effectively react at the temperature and pressure present during hydrogen burning in the stellar core. After exhaustion of the core hydrogen, the resulting helium core will gravitationally contract, thereby raising the temperature and density in the core until the temperature and density are sufficient to ignite helium burning, starting with the triple-alpha reaction, the fusion of three ${}^4\text{He}$ nuclei to ${}^{12}\text{C}$. In massive stars, this sequence of contraction of the core nuclear ashes continues until ignition of these nuclei in the next burning stage repeats itself several times. After helium burning, the massive star goes through periods of carbon, neon, oxygen, and silicon burning in its central core. As the binding energy per nucleon is a maximum near iron (the end-product of silicon burning), freeing nucleons from nuclei in and above the iron peak by charged-particle reactions, to build still heavier nuclei, requires more energy than is released when these nucleons are captured by the nuclei present. Therefore, the procession of nuclear burning stages ceases. This results in a collapse of the stellar core and an explosion of the star as a type II supernova. As an example, table II shows the timescales and conditions for the various hydrostatic burning stages of a $25 M_{\odot}$ star. One observes that stars spend most of their lifetime ($\sim 90\%$) during hydrogen burning (then the stars will be found on the main sequence in the Hertzsprung-Russell diagram). The rest is basically spent during core helium burning. During this evolutionary stage, the star expands dramatically and becomes a Red Giant.

Stellar evolution depends very strongly on the mass of the star. On general grounds, the more massive a star the higher the temperatures in the core at which the various burning stages are ignited. Moreover, as the nuclear reactions depend very sensitively

TABLE III. – *Hydrogen burning timescales τ_H as function of stellar mass (from [4]).*

$M (M_\odot)$	τ_H (y)
0.40	2×10^{11}
0.80	1.4×10^{10}
1.00	1×10^{10}
1.10	9×10^9
1.70	2.7×10^9
2.25	5×10^8
3.00	2.2×10^8
5.00	6×10^7
9.00	2×10^7
16.00	1×10^7
25.00	7×10^6
40.00	1×10^6

on temperature, the nuclear fuel is faster exhausted the larger the mass of the star (or the core temperature). This is quantitatively demonstrated in table III which shows the timescales for core hydrogen burning as a function of the main-sequence mass of the star. One observes that stars with masses less than $\sim 0.5M_\odot$ burn hydrogen for times which are significantly longer than the age of the Universe (about 13 billion years). Thus such low-mass stars have not completed one lifecycle and did also not contribute to the elemental abundances in the Universe. A star like our Sun has a life-expectation due to core hydrogen burning of about 10^{10} y, which is about double its current age ($\sim 4.55 \times 10^9$ y).

As the temperatures and densities required for the higher burning stages increase successively, stars need a minimum mass to ignite such burning phases. For example, a core mass slightly larger than $1M_\odot$ is required to ignite carbon burning. One also has to consider that stars, mainly during core helium burning, have mass losses due to flashes or stellar winds. In summary, as a rule-of-thumb, stars with main-sequence masses $\leq 8M_\odot$ end their lives as White Dwarfs. These are stars which are dense enough so that their electrons are highly degenerate and which are stabilized by the electron degeneracy pressure. There exists an upper limit for the mass of a star which can be stabilized by electron degeneracy. This is the Chandrasekhar mass of $\sim 1.4M_\odot$. Stars with masses of $\geq 13M_\odot$ go through the full cycle of hydrostatic burning stages and end with a collapse of their internal iron core. If the mass of the star is less than a certain limit, $M \sim 30M_\odot$, the star becomes a supernova leaving a compact remnant behind after the explosion; this is a neutron star. More massive stars might collapse directly into black holes.

3.1. Hydrogen burning. – In low-mass stars, like our Sun, hydrogen burning proceeds mainly via the *pp* chains (see fig. 1), with small contributions from the CNO cycle. The latter becomes the dominant energy source in hydrogen-burning stars, if the temperature

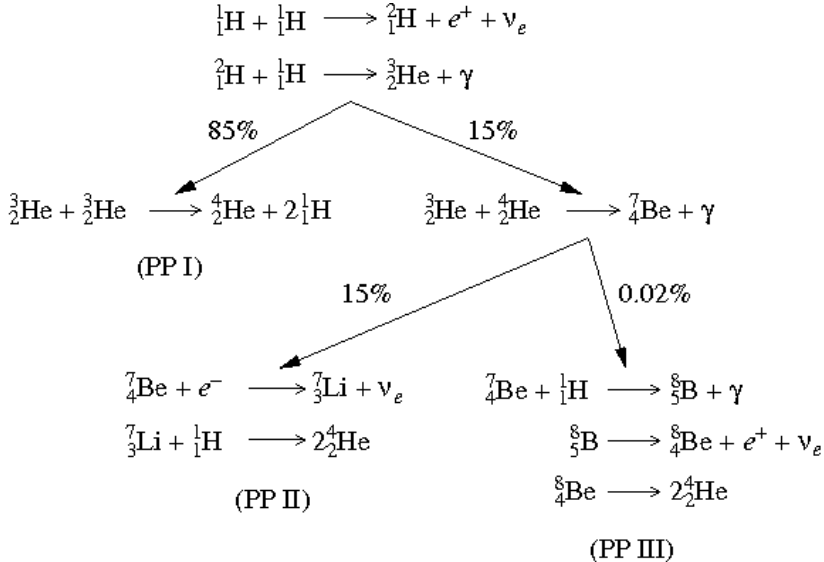


Fig. 1. – The reactions of the solar *pp* chains.

in the stellar core exceeds about 20 million degrees (the temperature in the solar core is 15.6×10^6 K).

The *pp* chains start with the fusion of two proton nuclei to the only bound state of the two-nucleon system, the deuteron. This reaction is mediated by the weak interaction, as a proton has to be converted into a neutron. Correspondingly, the cross-section for this reaction is very small and no experimental data at low proton energies exist. Although the reaction rate at solar energies is based purely on theory, the calculations are generally considered to be under control and the uncertainty of the solar $p + p$ rate is estimated to be better than a few percent [5]. The next reaction ($p + d \rightarrow {}^3\text{He}$) is mediated by the electromagnetic interaction. It is therefore much faster than the $p + p$ fusion with the consequence that deuterons in the solar core are immediately transformed to ${}^3\text{He}$ nuclides and no significant abundance of deuterons is present in the core (there is about 1 deuteron per 10^{18} protons in equilibrium under solar core conditions). As no deuterons are available and ${}^4\text{Li}$ (the endproduct of $p + {}^3\text{He}$) is not stable, the reaction chain has to continue with the fusion of two ${}^3\text{He}$ nuclei via ${}^3\text{He} + {}^3\text{He} \rightarrow 2{}^4\text{He}$. This reaction terminates the *ppI* chain where in summary four protons are fused to one ${}^4\text{He}$ nucleus with an energy gain of 26.2 MeV; the rest of the mass difference is spent to produce two positrons and is radiated away by the neutrinos produced in the initial $p + p$ fusion reaction. Once ${}^4\text{He}$ is produced in sufficient abundance, the *pp* chain can be completed by two other routes. At first ${}^3\text{He}$ and ${}^4\text{He}$ fuse to ${}^7\text{Be}$ which then either captures a proton (producing ${}^8\text{B}$) or, more likely, an electron (producing ${}^7\text{Li}$). The two chains are then terminated by the weak decay of ${}^8\text{B}$ to an excited state in ${}^8\text{Be}$, which subsequently decays into two ${}^4\text{He}$ nuclei, and by the ${}^7\text{Li}(p, {}^4\text{He})$ reaction. In summary, both routes

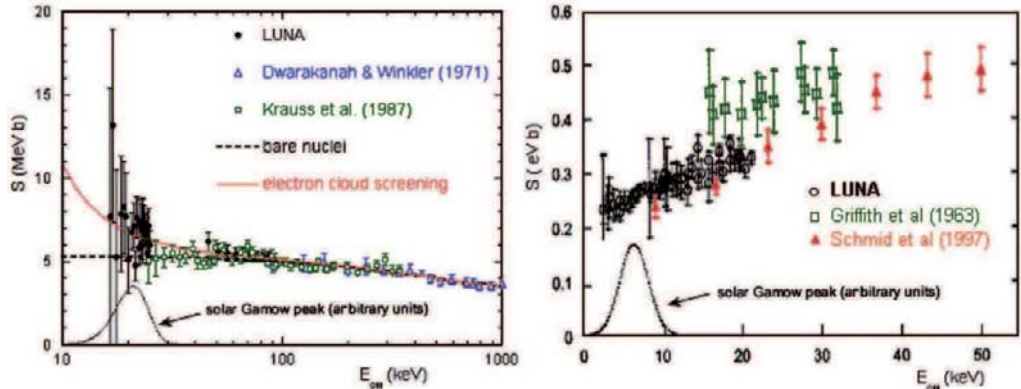


Fig. 2. – S -factors for the low-energy ${}^3\text{He} + {}^3\text{He}$ and $d + p$ fusion reactions. The data have been taken at the Gran Sasso Underground Laboratory by the LUNA Collaboration. For the first time, it has been possible to measure nuclear cross-sections at the astrophysically most effective energies covering the regime of the Gamow peak. The ${}^3\text{He} + {}^3\text{He}$ data include electron screening effects which have been removed to obtain the cross section for bare nuclei (from [7]).

fuse 4 protons into one ${}^4\text{He}$ nucleus. The energy gain of these two branches of the pp chains is slightly smaller than in the dominating ppI chain, as neutrinos with somewhat larger energies are produced en route [6].

All of the pp chain reactions are non-resonant at low energies such that the extrapolation of data taken in the laboratory to stellar (solar) energies is quite reliable [5]. For two reactions (${}^3\text{He} + {}^3\text{He} \rightarrow {}^4\text{He} + 2p$ and $p + d \rightarrow {}^3\text{He}$) the cross sections have been measured at the solar Gamow energies, thus making extrapolations of data unnecessary (see fig. 2). These important measurements have been performed by the LUNA group at the Gran Sasso Laboratory [7] far underground to effectively remove background events due to the shielding by the rocks above the experimental hall. For many years the $p + {}^7\text{Be}$ fusion reaction has been considered the most uncertain nuclear cross-sections in solar models. However, impressive progress has been achieved in determining this reaction rate in recent years and it appears that the goal of knowing the solar reaction rate for this reaction better than the limit of 5%, as desired for solar models, has been reached [8].

Despite this impressive progress extrapolations of S -factors determined in the laboratory to the lower energies relevant for solar hydrogen burning are still needed. Obviously such extrapolations should be performed based on the most reliable theoretical model at hand. Recently Neff [9, 10] has presented calculations of the ${}^3\text{He}({}^4\text{He}, \gamma){}^7\text{Be}$ S -factors at low energies based on the Fermionic Molecular Dynamics (FMD) model by Hans Feldmeier [11]. This microscopic many-body model combines several virtues. It consistently describes bound states, resonances and continuum states of a many-nucleon system within the same model space taking the relevant degrees of freedom of the system into account. Furthermore the many-body Hamiltonian contains a realistic effective interaction which has been derived from the Argonne-V18 interaction by treating explicitly short-range

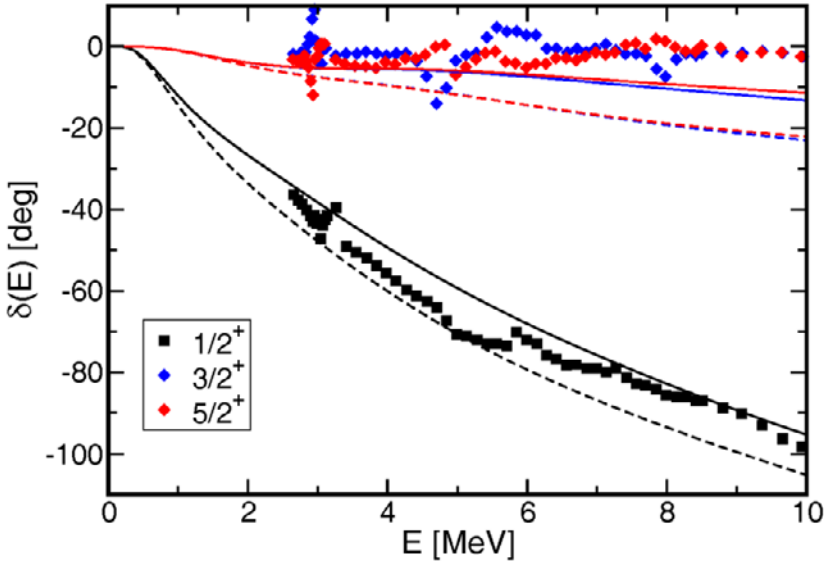


Fig. 3. – Comparison of ${}^3\text{He} + {}^4\text{He}$ phase shifts calculated in the FMD with experimental data (from [10]).

central and tensor correlations. Neff and Feldmeier succeeded to simultaneously describe the bound state spectrum in ${}^7\text{Be}$ and the ${}^3\text{He} + {}^4\text{He}$ phase shifts (fig. 3). Employing the ${}^3\text{He} + {}^4\text{He}$ continuum and ${}^7\text{Be}$ bound-state wave functions astrophysical ${}^3\text{He}({}^4\text{He}, \gamma){}^7\text{Be}$ S -factors have been derived (fig. 4). The calculation reproduces the recent data remarkably well in absolute magnitude and in the measured energy dependence. In particular, the FMD S -factors also reproduce the rise in the S -factors experimentally observed for energies above $E = 1$ MeV. This rise was missed in previous microscopic calculations based on schematic effective interactions and less sophisticated many-body model spaces (*e.g.*, [12-14]). There has also been recent progress based on indirect theoretical approaches to constrain S -factors of hydrogen-burning reactions at solar energies using Variational Monte-Carlo [15] or the No-Core Shell Model [16] to calculate asymptotic normalization coefficients from many-body bound-state wave functions.

Also in the CNO cycle four protons are fused to one ${}^4\text{He}$ nucleus. However, this reaction chain requires the presence of ${}^{12}\text{C}$ as catalyst. It then proceeds through the following sequence of reactions:



The slowest step is the $p + {}^{14}\text{N}$ reaction. There has been decisive experimental progress in determining this reaction rate in the last years by the LUNA and LENA Collaborations which both showed that the reaction rate is actually smaller by a factor 2 than previously believed [17, 18]. As a consequence the CNO cycle contributes less than 1% of the

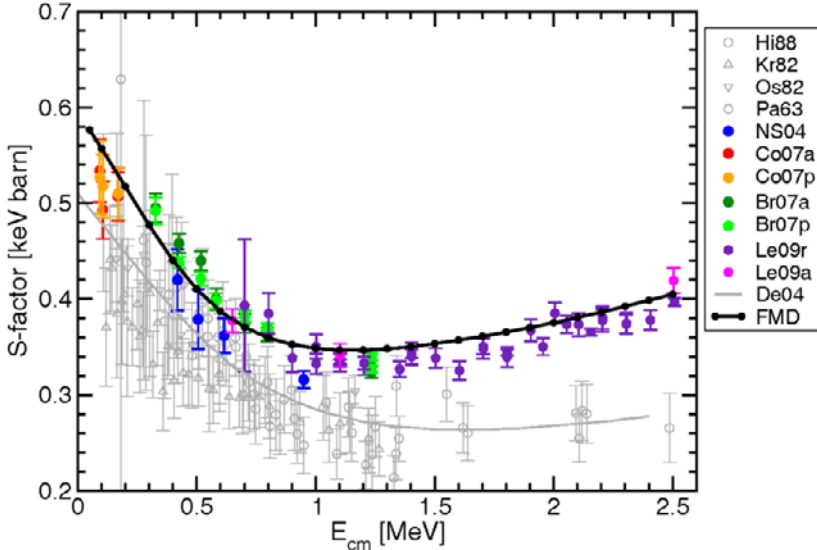


Fig. 4. – Comparison of astrophysical S -factors for the low-energy ${}^3\text{He}({}^4\text{He}, \gamma){}^7\text{Be}$ reaction calculated in the FMD with experimental data (from [10]).

total energy generation in the SUN. The new $p + {}^{14}\text{N}$ reaction rate has also interesting consequences for the age determination of globular clusters [19].

A recent compilation and critical discussion of solar reaction cross-sections is given by Adelberger *et al.* [20].

3.2. Solar neutrinos. – Every second more than 100 billion neutrinos, which are produced by hydrogen burning in the interior of the Sun, pass through every square-centimeter of the Earth surface (fig. 5). As the neutrino-matter interaction is extremely small, most of these neutrinos go unnoticed. However, a few of them are detected by large, dedicated detectors and indeed have proven that the Sun generates its energy by nuclear burning. Nevertheless, the event rate of detected solar neutrinos turned out to be less than predicted by the solar models (fig. 6); this constituted the famous “solar neutrino problem” [6] which could only be solved recently. The solution to the problem are neutrino oscillations. Within the solar pp chains only ν_e neutrinos are produced. Enhanced by matter effects some of these neutrinos are transformed into ν_μ or ν_τ neutrinos on their way out of the Sun. As the original solar neutrino detectors can only observe ν_e neutrinos (with energies larger than a certain threshold which depends on the mass difference of the target nucleus and its daughter, see fig. 5), the observed neutrino flux in these detectors is smaller than the total neutrino flux generated in the Sun. This picture was confirmed by the SNO Collaboration in the recent years [21]. The SNO detector has the capability to observe neutral current events induced by neutrinos (the neutrino dissociation of deuterons into protons and neutrons in heavy water). As the neutral

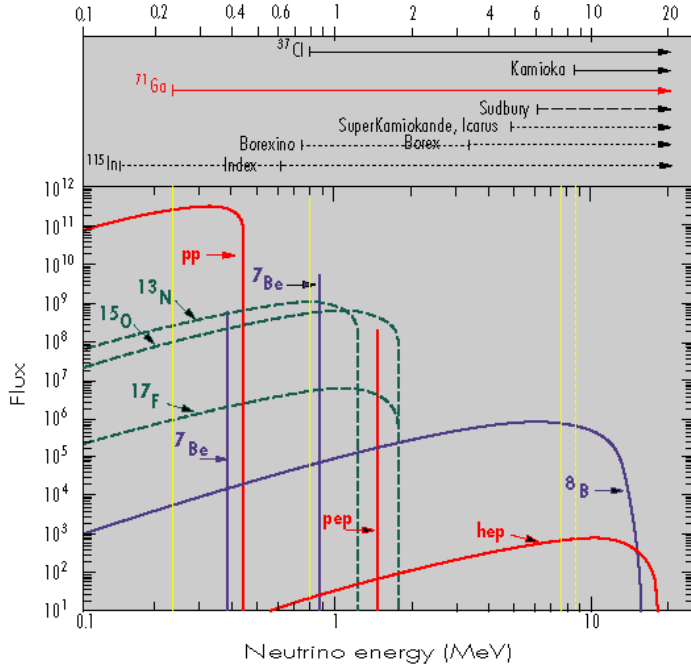


Fig. 5. – Solar neutrino flux per second and cm^2 on the Earth surface, as expected from the various hydrogen-burning reactions. The arrows show the energy range for which various detectors can observe solar neutrinos (courtesy J. N. Bahcall).

current events can be induced by all neutrino families such signal determines the total solar neutrino flux. It is found that it is larger than the ν_e flux and agrees nicely with the predictions of the solar models. It is also important to stress that the Superkamiokande detector, with its sensitivity to the direction of the incoming neutrino, has unequivocally proven that the detected neutrinos are indeed coming from the Sun!

The important SNO result is shown in fig. 7. At first, charged-current reactions can only be mediated by ν_e neutrinos via $\nu_e + d \rightarrow p + p + e^-$; a potential flux of other neutrino species (ν_μ and ν_τ produced by oscillations) cannot be detected. Hence such charged-current events are presented by a band with fixed ν_e , but unspecified $\nu_\mu + \nu_\tau$ flux in the neutrino flux diagram shown in fig. 6. On the other hand, the neutral-current reactions $\nu + d \rightarrow p + n + \nu$ can be induced by all three neutrino species. Thus, its observed event rate constrains the sum of ν_e and $\nu_\mu + \nu_\tau$ fluxes and corresponds to the “diagonal” band in the flux diagram. The diagram contains additionally results from the Superkamiokande detector where solar neutrinos can be detected by scattering off electrons. Such a process is possible for all 3 neutrino species; however, the cross-section is larger by about a factor 7 for ν_e neutrinos than for the other two due to a charged-current contribution which is only possible for ν_e neutrinos. The results from electron scattering thus correspond to

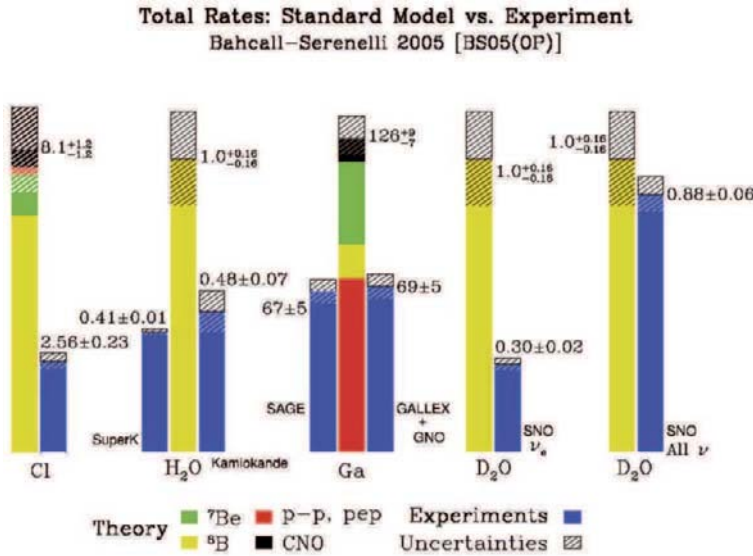


Fig. 6. – Comparison of detected neutrino rates (or fluxes) with the predictions of the solar model (from [23]).

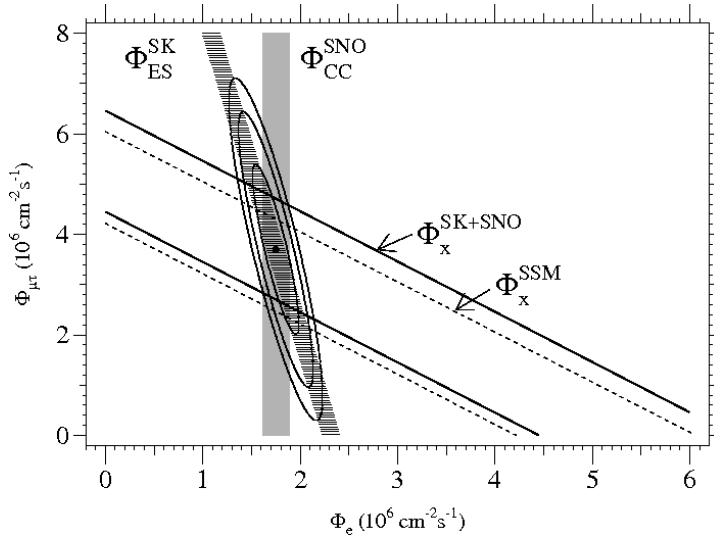


Fig. 7. – Constraints of the solar ν_e and $\nu_\mu + \nu_\tau$ fluxes from the observations of charged-current and neutral-current events at SNO and of electron-scattering events at Superkamiokande. The observed total solar neutrino flux agrees with the predictions from the solar model (from [21]).

the slightly tilted band shown in the flux diagram. Importantly the three independent experimental constraints have a common overlap corresponding to a non-vanishing $\nu_\mu + \nu_\tau$ flux. As ν_μ , ν_τ neutrinos are not generated by solar hydrogen burning, they must be produced by oscillations of solar ν_e neutrinos. As such oscillations are only possible if not all neutrinos are massless, the solution of the solar neutrino problem also opens the door to physics beyond the standard model of particle physics.

3.3. Helium burning. – No stable nuclei with mass numbers $A = 5$ and $A = 8$ exist. Thus, fusion reactions of $p + {}^4\text{He}$ and ${}^4\text{He} + {}^4\text{He}$ lead to unstable resonant states in ${}^5\text{Li}$ and ${}^8\text{Be}$ which decay extremely fast. However, the lifetime of the ${}^8\text{Be}$ ground-state resonance ($\sim 10^{-16}$ s) is long enough to establish a small ${}^8\text{Be}$ equilibrium abundance under helium burning conditions ($T \sim 10^6$ K, $\rho \sim 10^5$ g/cm 3), which amounts to about $\sim 5 \times 10^{-10}$ of the equilibrium ${}^4\text{He}$ abundance. As pointed out by Salpeter [22], this small ${}^8\text{Be}$ equilibrium abundance allows the capture of another ${}^4\text{He}$ nucleus to form the stable ${}^{12}\text{C}$ nucleus. The second step of the triple-alpha fusion reaction is highly enlarged by the presence of an s -wave resonance in ${}^{12}\text{C}$ at a resonance energy of 287 keV (the Hoyle state). To derive the triple-alpha reaction rate under helium-burning conditions, it is sufficient to know the properties of this resonance (its γ -width and its α -width). These quantities have been determined experimentally and it is generally assumed that the triple-alpha rate is known with an accuracy of about 15% for helium burning in Red Giants. A current estimate for the uncertainty of the triple- α rate is given in ref. [24] which discusses also the influence of the rate on some aspects of subsequent stellar evolution. An improved triple- α rate for temperatures higher than in Red Giant helium burning is given in [25].

The second step in helium burning, the ${}^{12}\text{C}(\alpha, \gamma){}^{16}\text{O}$ reaction, is the crucial reaction in stellar models of massive stars. Its rate determines the relative importance of the subsequent carbon- and oxygen-burning stages, including the abundances of the elements produced in these stages. The ${}^{12}\text{C}(\alpha, \gamma){}^{16}\text{O}$ reaction determines also the relative abundance of ${}^{12}\text{C}$ and ${}^{16}\text{O}$, the two bricks for the formation of life, in the Universe. Stellar models are very sensitive to this rate and its determination at the most effective energy in helium burning ($E = 300$ keV) with an accuracy of better than 20% is asked for. Despite enormous experimental efforts in the last 3 decades, this goal has not been achieved yet, as the low-energy ${}^{12}\text{C}(\alpha, \gamma){}^{16}\text{O}$ reaction cross-section is tremendously tricky. Data have been taken down to energies of about $E = 1$ MeV, requiring an extrapolation of the S -factor to $E = 300$ keV. The data are dominated by a $J = 1^-$ resonance at $E = 2.418$ MeV. Unfortunately there is another $J = 1^-$ level at $E = -45$ keV, just below the $\alpha + {}^{12}\text{C}$ threshold. These two states interfere. In the data the broad resonance at $E = 2.418$ MeV dominates, while at stellar burning energies it is likely to be the other way round. It turns out to be quite difficult to determine the properties of the particle-bound states, although a major step forward has been achieved using indirect means by studying the β -decay of the ${}^{16}\text{N}$ ground state to states in ${}^{16}\text{O}$ above the α -threshold and their subsequent decay into the $\alpha + {}^{12}\text{C}$ channel [26]. The γ -decay of the $J = 1^-$ states to the ${}^{16}\text{O}$ ground state is of dipole ($E1$) nature. If isospin were a good quantum number, this transition would be exactly forbidden, as all involved nuclei (${}^4\text{He}$, ${}^{12}\text{C}$, ${}^{16}\text{O}$)

have isospin quantum numbers $T = 0$. The observed dipole transition must then come from small isospin-symmetry-breaking admixtures. The data, indeed, suggest that the transitions are suppressed by about 4 orders of magnitude compared to “normal” $E1$ transitions. Such a large suppression makes it possible that $E2$ (quadrupole) transitions can compete with the dipole contributions. This is confirmed by measurements of the $^{12}\text{C}(\alpha, \gamma)^{16}\text{O}$ angular distributions at low energies which are mixtures of dipole and quadrupole contributions. While both, dipole and quadrupole, cross-sections can thus be determined from the data (although the measurement of angular distributions is much more challenging than the determination of the total cross-section), the extrapolation of the $E2$ data to stellar energies at $E = 300\text{ keV}$ is strongly hampered by the fact that the stellar cross-section is dominated by the tail of a particle-bound $J = 2^+$ state at $E = -245\text{ keV}$, which, however, is much weaker in the data taken at higher energies. Recent results for the $^{12}\text{C}(\alpha, \gamma)^{16}\text{O}$ S -factor are presented in [27], [28] and in [29].

The $^{16}\text{O}(\alpha, \gamma)^{20}\text{Ne}$ is non-resonant at stellar energies and hence very slow, compared to the $\alpha + ^{12}\text{C}$ reaction. Thus, helium burning finishes with the $^{12}\text{C}(\alpha, \gamma)^{16}\text{O}$ reaction.

3.4. Carbon, neon, oxygen, silicon burning. – In the fusion of two ^{12}C nuclei, the α and proton-channels have positive Q -values ($Q = 4.62\text{ MeV}$ and $Q = 2.24\text{ MeV}$). Thus, the fusion produces nuclides with smaller charge numbers, which can then interact with other carbon nuclei or produced elements. The main reactions in carbon burning are: $^{12}\text{C}(^{12}\text{C}, \alpha)^{20}\text{Ne}$, $^{12}\text{C}(^{12}\text{C}, p)^{23}\text{Na}$, $^{23}\text{Na}(p, \alpha)^{20}\text{Ne}$, $^{23}\text{Na}(p, \gamma)^{24}\text{Mg}$, $^{12}\text{C}(\alpha, \gamma)^{16}\text{O}$, which determine the basic energy generation. However, many other reactions can occur, even producing elements beyond ^{24}Mg like ^{26}Mg and ^{27}Al .

Neon burning occurs at temperatures just above $T = 10^9\text{ K}$. At these conditions the presence of high-energy photons is sufficient to photodissociate ^{20}Ne via the $^{20}\text{Ne}(\gamma, \alpha)^{16}\text{O}$ reaction which has a Q -value of -4.73 MeV . This reaction liberates α -particles which react then very fast with other ^{20}Ne nuclei leading to the production of ^{28}Si via the chain $^{20}\text{Ne}(\alpha, \gamma)^{24}\text{Mg}(\alpha, \gamma)^{28}\text{Si}$. Again, many other reactions induced by protons, ^4He and also neutrons, which are produced within the occurring reaction chains, occur.

In the fusion of two ^{16}O nuclei, the α and proton-channels have positive Q -values ($Q = 9.59\text{ MeV}$ and $Q = 7.68\text{ MeV}$). Like in carbon burning, the liberated protons and ^4He nuclei react with other ^{16}O nuclei. Among the many nuclides produced during oxygen burning are ^{33}Si and ^{35}Cl . These have quite low Q -values against electron captures making it energetically favorable to capture electrons from the degenerate electron sea (the Fermi energies of electrons during core oxygen burning is of order 1 MeV) via the $^{33}\text{Si}(e^- \nu)^{33}\text{P}$ and $^{35}\text{Cl}(e^- \nu)^{35}\text{S}$ reactions. The emitted neutrinos carry energy away, thus cooling the star. As we will see in the next section, electron captures play a decisive role in core-collapse supernovae.

The nuclear reaction network during silicon burning is initiated by the photodissociation of ^{28}Si , producing protons, neutrons and α -particles. These particles react again with ^{28}Si or the nuclides produced. During silicon burning, the temperature is already quite high ($T \sim 3\text{--}4 \times 10^9\text{ K}$). This makes the nuclear reactions mediated by the strong

and electromagnetic force quite fast and a chemical equilibrium between reactions and their inverse processes establishes. Under such conditions, the abundance distributions of the nuclides present in the network becomes independent of the reaction rates, establishing the Nuclear Statistical Equilibrium (NSE) (see [30, 31]). Then the abundance of a nuclide with proton and neutron numbers Z and N can be expressed in terms of the abundance of free protons and neutrons by

$$(11) \quad Y_{Z,N} = G_{Z,N}(\rho N_A)^{(A-1)} \frac{A^{3/2}}{2^A} \left(\frac{2\pi\hbar^2}{m_u kT} \right)^{3/2(A-1)} \exp \left[\frac{B_{Z,N}}{kT} \right] Y_n^N Y_p^Z,$$

where $G_{Z,N}$ is the nuclear partition function (at temperature T), $B_{Z,N}$ the binding excess of the nucleus, m_u the unit nuclear mass and Y_p , Y_n are the abundances of free protons and neutrons. The NSE distribution is subject to the mass and charge conservation, which can be formulated as

$$(12) \quad \sum_i A_i Y_i = 1; \quad \sum_i Z_i Y_i = Y_e,$$

where Y_e is the electron-to-nucleon ratio and the sum runs over all nuclides. Until the onset of oxygen burning, one has $Y_e = 0.5$ (nuclei like ^{12}C have identical proton and neutron numbers, while the number of electrons equals the proton number). Once electron capture processes start, the Y_e value is reduced (protons are changed into neutrons, while the total number of nucleons is preserved).

We finally note that, during silicon burning, not a full NSE is established. However, the nuclear chart breaks into several regions in which NSE equilibrium is established. The different regions are not yet in equilibrium, as the nuclear reactions connecting them are yet not fast enough. One uses the term “Quasi-NSE” for these conditions.

4. – Core collapse supernovae

Massive stars end their lives as type II supernovae, triggered by a collapse of their central iron core with a mass of more than $1M_\odot$. The general picture of a core collapse supernova is probably well understood and has been confirmed by various observations from supernova 1987A. It can be briefly summarized as follows:

At the end of its hydrostatic burning stages (fig. 8), a massive star has an onion-like structure with various shells where nuclear burning still proceeds (hydrogen, helium, carbon, neon, oxygen and silicon shell burning). As nuclei in the iron/nickel range have the highest binding energy per nucleon, the iron core in the star’s center has no nuclear energy source to support itself against gravitational collapse. As mass is added to the core, its density and temperature raises, finally enabling the core to reduce its free energy by electron captures of the protons in the nuclei [32]. This reduces the electron degeneracy pressure and the core temperature as the neutrinos produced by the capture can initially leave the star unhindered. Both effects accelerate the collapse of the star. With increasing density, neutrino interactions with matter become decisively important

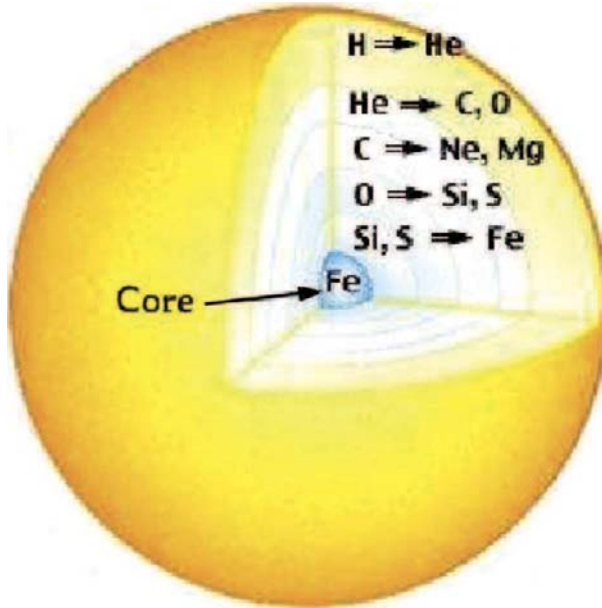


Fig. 8. – At the end of hydrostatic burning a star has an onion-like structure with nuclear burning occurring in various shells.

and neutrinos have to be treated by Boltzmann transport. Nevertheless the collapse proceeds until the core composition is transformed into neutron-rich nuclear matter. Its finite compressibility brings the collapse to a halt, a shock wave is created which traverses outwards through the infalling matter of the core's envelope. This matter is strongly heated and dissociated into free nucleons. Due to current models the shock has not sufficient energy to explode the star directly. It stalls, but is shortly after revived by energy transfer from the neutrinos which are produced by the cooling of the neutron star born in the center of the core. The neutrinos carry away most of the energy generated by the gravitational collapse and a fraction of the neutrinos are absorbed by the free nucleons behind the stalled shock. The revived shock can then explode the star and the stellar matter outside of a certain mass cut is ejected into the Interstellar Medium. A brief sketch of the various supernova phases is given in fig. 9. Due to the high temperatures associated with the shock's passage, nuclear reactions can proceed rather fast giving rise to explosive nucleosynthesis which is particularly important in the deepest layers of the ejected matter. Reviews on core-collapse supernovae can be found in [33-35].

Nevertheless, the most sophisticated spherical supernova simulations, including detailed neutrino transport [36-38], currently fail to explode indicating that improved input or numerical treatment is required. Among these microscopic inputs are nuclear processes mediated by the weak interaction, where recent progress has been made possible by improved many-body models and better computational facilities, as is summarized

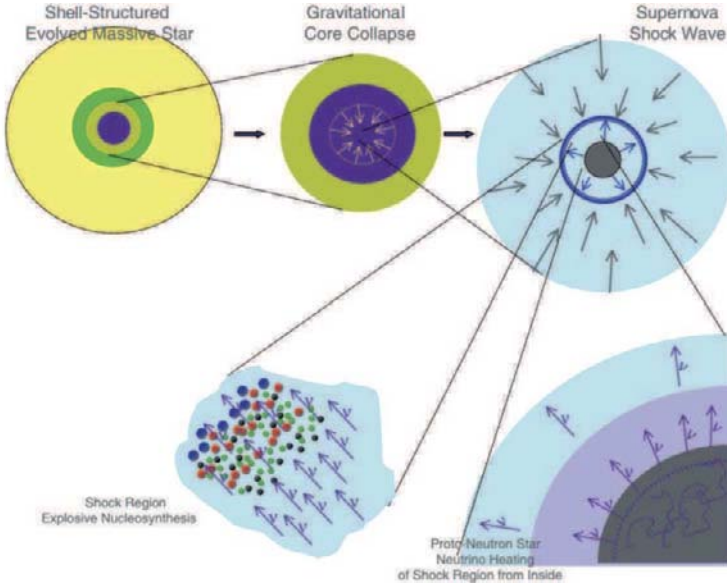


Fig. 9. – Schematic stages of the collapse of a massive star and a supernova explosion (courtesy of Roland Diehl).

in [39]. Here we focus on the electron capture on nuclei, which strongly influences the dynamics of the collapse and produces the neutrinos present during the collapse, and on recent developments in explosive nucleosynthesis, where again neutrino-induced reactions are essential. Recent two-dimensional simulations stress also the importance of plasma instabilities, which in fact initiated successful numerical explosions [40, 41].

4.1. Electron captures in core-collapse supernovae —the general picture. – Late-stage stellar evolution is described in two steps. In the presupernova models the evolution is studied through the various hydrostatic core and shell-burning phases until the central core density reaches values up to 10^{10} g/cm^3 . The models consider a large nuclear reaction network. However, the densities involved are small enough to treat neutrinos solely as an energy loss source. For even higher densities this is no longer true as neutrino-matter interactions become increasingly important. In modern core-collapse codes neutrino transport is described self-consistently by multigroup Boltzmann simulations [36-38]. While this is computationally very challenging, collapse models have the advantage that the matter composition can be derived from Nuclear Statistical Equilibrium (NSE) as the core temperature and density are high enough to keep reactions mediated by the strong and electromagnetic interactions in equilibrium. This means that for sufficiently low entropies, the matter composition is dominated by the nuclei with the highest binding energies for a given Y_e . The presupernova models are the input for the collapse simulations which follow the evolution through trapping, bounce and hopefully explosion.

The collapse is a competition of the two weakest forces in nature: gravity versus weak interaction, where electron captures on nuclei and protons and, during a period of silicon burning, also β -decay play the crucial roles [42]. The weak-interaction processes become important when nuclei with masses $A \sim 55\text{--}60$ (pf -shell nuclei) are most abundant in the core (although capture on sd shell nuclei has to be considered as well). As weak interactions changes Y_e and electron capture dominates, the Y_e value is successively reduced from its initial value ~ 0.5 . As a consequence, the abundant nuclei become more neutron rich and heavier, as nuclei with decreasing Z/A ratios are more bound in heavier nuclei. Two further general remarks are useful. There are many nuclei with appreciable abundances in the cores of massive stars during their final evolution. Neither the nucleus with the largest capture rate nor the most abundant one are necessarily the most relevant for the dynamical evolution: What makes a nucleus relevant is the product of rate times abundance.

For densities $\rho < 10^{11}$ g/cm³, stellar weak-interaction processes are dominated by Gamow-Teller (GT) and, if applicable, by Fermi transitions. At higher densities forbidden transitions have to be included as well. To understand the requirements for the nuclear models to describe these processes (mainly electron capture), it is quite useful to recognize that electron capture is governed by two energy scales: the electron chemical potential μ_e , which grows like $\rho^{1/3}$, and the nuclear Q -value. Further, μ_e grows much faster than the Q values of the abundant nuclei. We can conclude that at low densities, where one has $\mu_e \sim Q$ (*i.e.* at presupernova conditions), the capture rates will be very sensitive to the phase space and require an accurate as possible description of the detailed GT₊ distribution of the nuclei involved. Furthermore, the finite temperature in the star requires the implicit consideration of capture on excited nuclear states, for which the GT distribution can be different than for the ground state. It has been demonstrated [43, 44] that modern shell model calculations are capable to describe nuclear properties relevant to derive stellar electron capture rates (spectra and GT₊ distributions) rather well (an example is shown in fig. 10) and are therefore the appropriate tool to calculate the weak-interaction rates for those nuclei ($A \sim 50\text{--}65$) which are relevant at such densities. At higher densities, when μ_e is sufficiently larger than the respective nuclear Q values, the capture rate becomes less sensitive to the detailed GT₊ distribution and is mainly only dependent on the total GT strength. Thus, less sophisticated nuclear models might be sufficient. However, one is facing a nuclear structure problem which has been overcome only very recently. Once the matter has become sufficiently neutron rich, nuclei with proton numbers $Z < 40$ and neutron numbers $N > 40$ will be quite abundant in the core. For such nuclei, Gamow-Teller transitions would be Pauli forbidden (GT₊ transitions change a proton into a neutron in the same harmonic oscillator shell) were it not for nuclear correlation and finite temperature effects which move nucleons from the pf shell into the gds shell (fig. 11). To describe such effects in an appropriately large model space (*e.g.*, the complete $fpgds$ shell) is currently only possible by means of the Shell Model Monte Carlo approach (SMMC) [45-47]. In [48] SMMC-based electron capture rates have been calculated for many nuclei which are present during the collapse phase.

Recently the GT₊ strength for ^{76}Se (with $Z = 34$ and $N = 42$) has been measured [49]. Indeed it is experimentally observed that cross-shell correlations induce

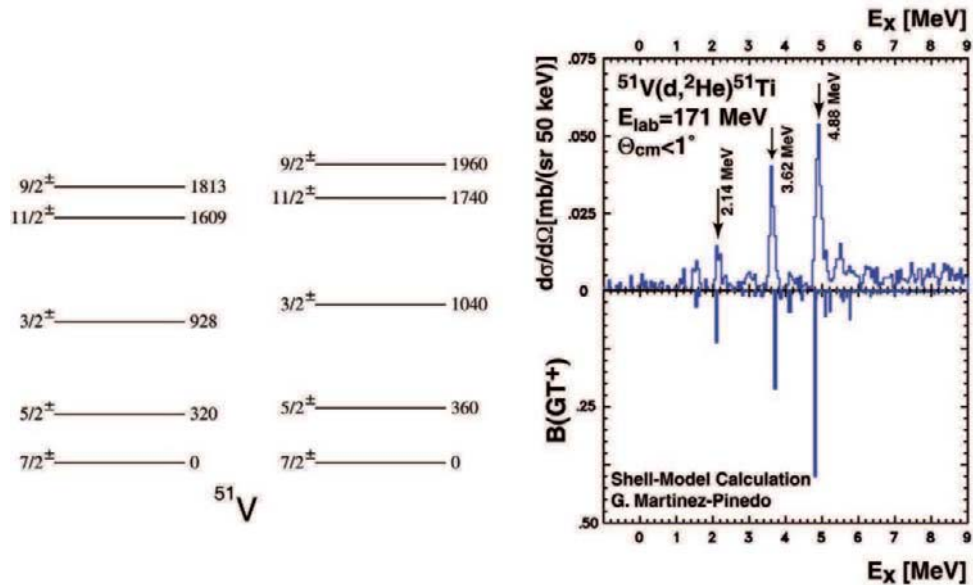


Fig. 10. – Comparison of the measured spectrum (left) and $^{51}\text{V}(d, ^2\text{He})^{51}\text{Ti}$ cross section (right) at forward angles (which is proportional to the GT_+ strength) with the shell model spectrum and GT distribution in ^{51}V (partially from [55]).

a non-vanishing GT_+ strength which is well reproduced by shell model calculations [50]. These studies consider the (pf) orbitals for protons and the $(p, f_{5/2}, g_{9/2})$ orbitals for neutrons. The calculations also reproduce the experimentally determined orbital occupation numbers [51], predicting about 3.5 neutron holes in the (pf) shell which make

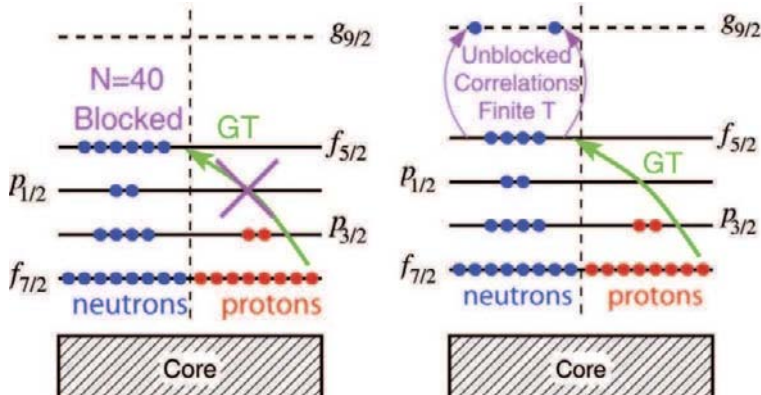


Fig. 11. – In the independent particle model GT transitions are blocked at neutron number $N = 40$.

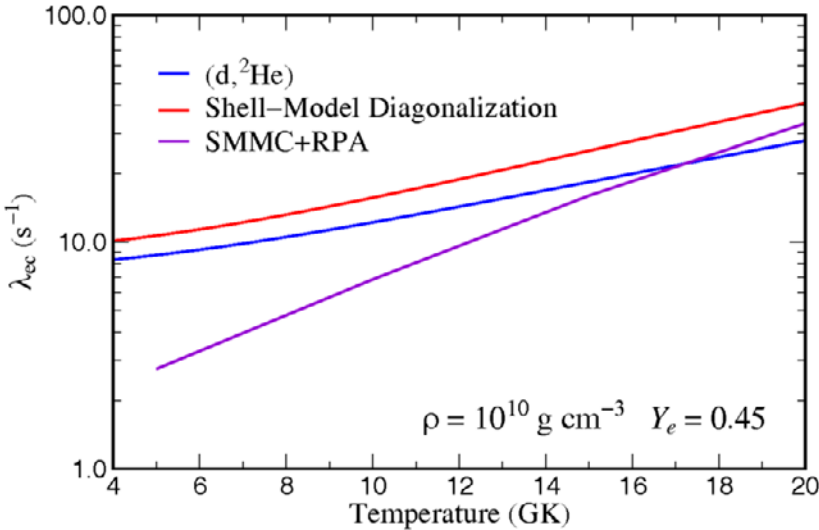


Fig. 12. – Electron capture rates on ^{76}Se as function of temperature (in units of 10^9 K) derived from the experimental [49] and shell model [50] GT₊ strength distributions. A density of 10^{10} g/cm^3 and an electron-to-nucleon ratio $Y_e = 0.45$ are assumed. For comparison also the SMMC/RPA rates are shown.

GT₊ transitions possible. Figure 12 compares the electron capture rates determined from the shell model and experimental GT ground state distributions. These rates do not include contributions from thermally excited nuclear states and hence correspond to stellar capture rates at finite temperatures only if one assumes that the GT₊ distributions are the same for all parent states (often called Brink's hypothesis). For comparison also the SMMC/RPA capture rates are shown. These rates are smaller than the others at smaller temperatures indicating that the model is not completely capable to resolve the strength distribution at low excitation energies. The agreement gets significantly improved at the larger temperatures (and densities) at which the SMMC/RPA model is used to predict stellar capture rates.

The shell model results for fd shell nuclei [44] and the SMMC/RPA results for heavier nuclei [48] have been combined for a compilation of electron capture rates which covers the composition during the early collapse phase well (until densities to a few 10^{10} g/cm^3). However, at even higher densities the continuous electron capture drives the matter composition to more neutron-rich and heavier nuclei than considered in [48]. The neglect of these nuclei could lead to a systematic overestimate of the capture rates as the neglected nuclei have larger Q values and enhanced Pauli blocking due to increased neutron excess than the nuclei considered. Unfortunately an SMMC evaluation of the several thousands of nuclei present in the matter composition during the late phase of collapse before neutrino trapping is numerically not feasible. Hence a simpler approach has to be adopted. This is based on the observation that the single-particle occupation numbers obtained in

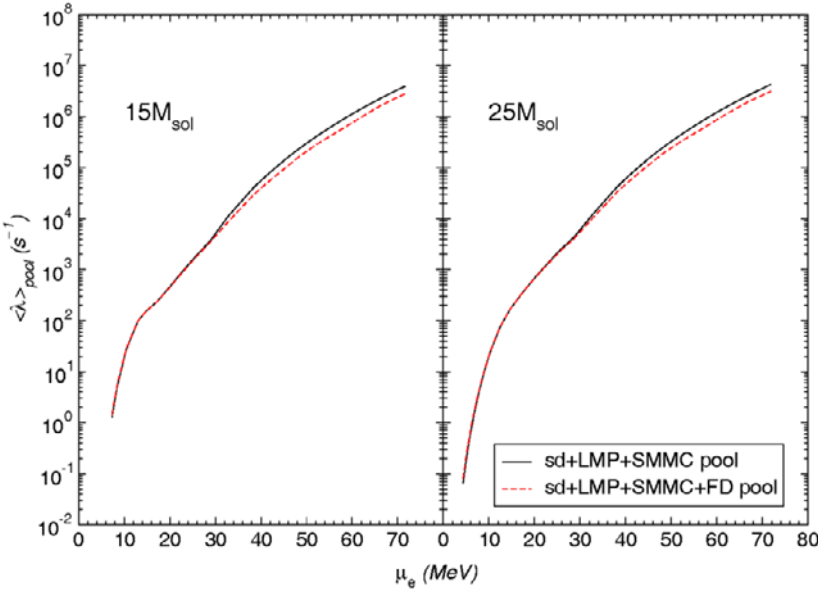


Fig. 13. – Comparison of NSE-averaged electron capture rates calculated for about 3000 individual nuclei (solid, see text) with those obtained for the restricted set of nuclei (dashed) considered in [48] (from [52]).

the SMMC calculations can be well approximated by a parametrized Fermi-Dirac distribution. By adjusting the parameters of this distribution to the SMMC results for about 250 nuclei, occupation numbers were derived for nearly 3000 nuclei and the respective individual rates have been calculated within an RPA calculation based on these partial occupations. It is found that this simplified approach reproduces the SMMC results quite well at electron chemical potential $\mu_e > 15$ MeV [52]. This corresponds to the density regime where the previously neglected nuclei become abundant in the matter composition. At smaller electron chemical potentials (*i.e.* at lower densities) details of the GT distribution are important which are not recovered by the simple parametrized approach. However, at these conditions electron capture is dominated by nuclei for which individual shell model rates exist.

Figure 13 compares the capture rate derived for the pool of more than 3000 nuclei (*i.e.* combining the rates from shell model diagonalization, SMMC, and from the parametrized approach) with those obtained purely on the basis of the shell model results. While the agreement is excellent at small electron chemical potentials (here the shell model rates dominate), the rates for the large pool are slightly smaller at higher μ_e values due the presence of neutron-rich heavy nuclei with smaller individual rates. Furthermore the new rates also include plasma screening effects which lead to an increase of the effective Q values and a reduction of the electron chemical potential, which both reduce the electron capture rates. The effect is rather mild and does not alter the conclusion that electron capture on nuclei dominates over capture on protons during the collapse.

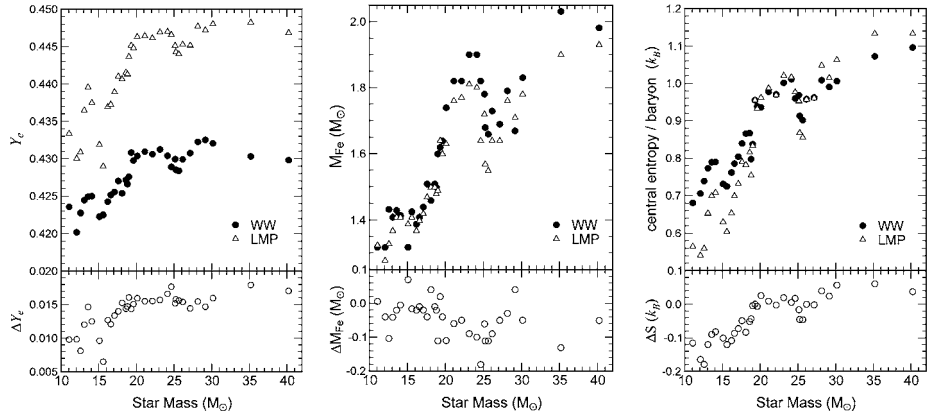


Fig. 14. – Comparison of the center values of Y_e (left), the iron core sizes (middle) and the central entropy (right) for 11 – $40 M_{\odot}$ stars between the WW models, which used the FFN rates, and the ones using the shell model weak interaction rates (LMP) (from [53]).

4.2. Weak-interaction rates and presupernova evolution. – Up to densities of a few 10^{10} g/cm^3 electron capture is still dominated by capture on nuclei in the $A \sim 45$ – 65 mass range, for which capture rates have been derived on the basis of large-scale shell model diagonalization studies. Importantly, the shell model rates are noticeably smaller than those derived previously on the basis of the independent particle model [44]. To study the influence of these slower shell model rates on presupernova models Heger *et al.* [42, 53] have repeated the calculations of Weaver and Woosley [54] keeping the stellar physics, except for the weak rates, as close to the original studies as possible. Figure 14 exemplifies the consequences of the shell model weak interaction rates for presupernova models in terms of the three decisive quantities: the central Y_e value and entropy and the iron core mass. The central values of Y_e at the onset of core collapse increased by 0.01–0.015 for the new rates. This is a significant effect. We note that the new models also result in lower core entropies for stars with $M \leq 20 M_{\odot}$, while for $M \geq 20 M_{\odot}$, the new models actually have a slightly larger entropy. The iron core masses are generally smaller in the new models where the effect is larger for more massive stars ($M \geq 20 M_{\odot}$), while for the most common supernovae ($M \leq 20 M_{\odot}$) the reduction is by about $0.05 M_{\odot}$.

Electron capture dominates the weak-interaction processes during presupernova evolution. However, during silicon burning, β -decay (which increases Y_e) can compete and adds to the further cooling of the star. With increasing densities, β -decays are hindered as the increasing Fermi energy of the electrons blocks the available phase space for the decay. Thus, during collapse β -decays can be neglected.

We note that the shell model weak-interaction rates predict the presupernova evolution to proceed along a temperature-density- Y_e trajectory where the weak processes are dominated by nuclei rather close to stability. Thus it will be possible, after radioactive ion-beam facilities become operational, to further constrain the shell model

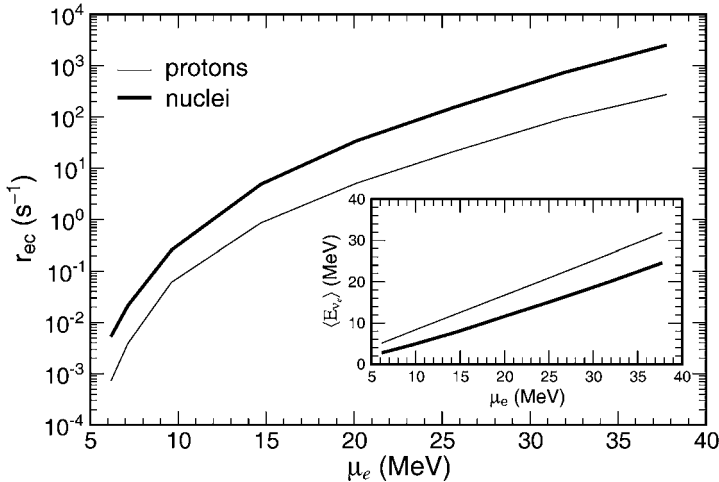


Fig. 15. – The reaction rates for electron capture on protons (thin line) and nuclei (thick line) are compared as a function of electron chemical potential along a stellar collapse trajectory. The insert shows the related average energy of the neutrinos emitted by capture on nuclei and protons. The results for nuclei are averaged over the full nuclear composition (see text, from [48]).

calculations by measuring relevant beta decays and GT distributions for unstable nuclei. References [42, 53] identify those nuclei which dominate (defined by the product of abundance times rate) the electron capture and beta decay during various stages of the final evolution of a $15M_{\odot}$, $25M_{\odot}$ and $40M_{\odot}$ star.

4.3. The role of electron capture during collapse. – Until recently core-collapse simulations assumed that electron capture on nuclei are prohibited by the Pauli blocking mechanism [56]. However, based on the SMMC calculations it has been shown in [48] that capture on nuclei dominates over capture on free protons (the later was evaluated in [57] and has been included in the simulations). This is demonstrated in fig. 15 which compares the two capture rates. The figure also shows that neutrinos from captures on nuclei have a mean energy 40–60% less than those produced by capture on protons. Although capture on nuclei under stellar conditions involves excited states in the parent and daughter nuclei, it is mainly the larger $|Q|$ -value which significantly shifts the energies of the emitted neutrinos to smaller values. These differences in the neutrino spectra strongly influence neutrino-matter interactions, which scale with the square of the neutrino energy and are essential for collapse simulations [38, 37].

The effects of this more realistic implementation of electron capture on heavy nuclei have been evaluated in independent self-consistent neutrino radiation hydrodynamics simulations by the Oak Ridge and Garching Collaborations [48, 58]. The changes compared to the previous simulations, which basically ignored electron capture on nuclei, are significant: In denser regions, the additional electron capture on heavy nuclei results in

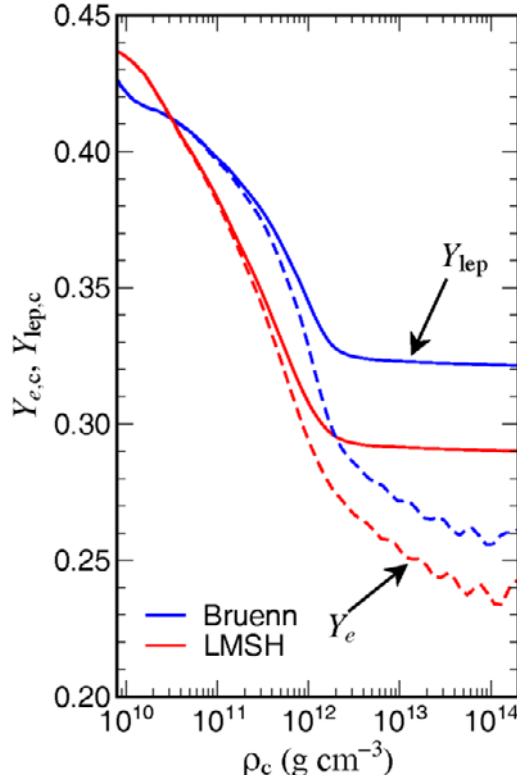


Fig. 16. – The electron and lepton fraction in the center during the collapse phase. The thin line is a simulation using the Bruenn parameterization [57], while the thick line is for a simulation using the shell model rates (courtesy of Hans-Thomas Janka).

more electron capture in the new models. In lower density regions, where nuclei with $A < 65$ dominate, the shell model rates [44] result in less electron capture. The results of these competing effects can be seen in fig. 16, which shows the center value of Y_e and Y_{lep} (the lepton-to-baryon ratio) during the collapse. At densities above 10^{12} g/cm^3 , Y_{lep} is (nearly) constant indicating that the neutrinos are trapped and a Fermi sea of neutrinos is being built up. Weak-interaction processes are now in equilibrium with their inverse. The changes in electron captures strongly reduce the temperatures and entropies in the inner core and hence affect its composition. They also strongly influence the shock. The combination of increased electron capture in the interior with reduced electron capture in the outer regions causes the shock to form with 16% less mass interior to it and a 10% smaller velocity difference across the shock (see fig. 17). In spite of this mass reduction, the radius from which the shock is launched is actually displaced slightly outwards to 15.7 km from 14.8 km in the old models. Also the altered gradients in density and lepton fraction play an important role in the behavior of the shock. Though also the new models fail to produce explosions in the spherically symmetric limit, the altered gradients allow

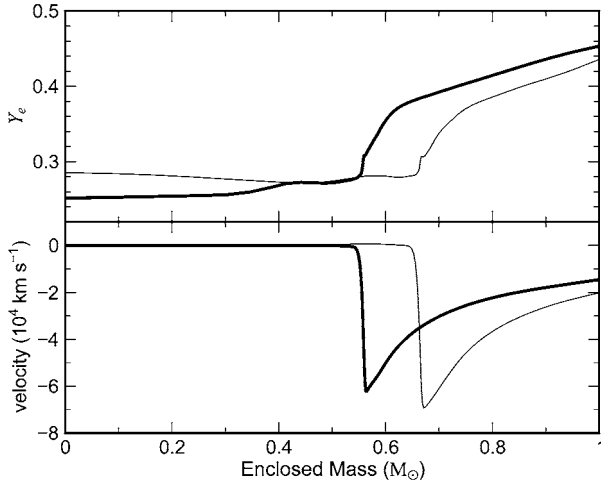


Fig. 17. – The electron fraction and velocity as functions of the enclosed mass at bounce for a $15 M_{\odot}$ model [42]. The thin line is a simulation using the Bruenn parameterization [57], while the thick line is for a simulation using the shell model rates.

the shock in the case with improved capture rates to reach 205 km, which is about 10 km further out than in the old models.

Astrophysics simulations have demonstrated that electron capture rates on nuclei have a strong impact on the core collapse trajectory and the properties of the core at bounce. The evaluation of the rates has to rely on theory as a direct experimental determination of the rates for the relevant stellar conditions (*i.e.* rather high temperatures) is currently impossible. Nevertheless it is important to experimentally explore the configuration mixing between *pf* and *sdg* shell in extremely neutron-rich nuclei as such understanding will guide and severely constrain nuclear models. Such guidance is expected from future radioactive ion-beam facilities like FAIR.

5. – Making heavy elements in explosive nucleosynthesis

In a successful explosion the shock heats the matter it traverses, inducing an explosive nuclear burning on short time-scales. This explosive nucleosynthesis can alter the elemental abundance distributions in the inner (silicon, oxygen) shells. Recently explosive nucleosynthesis has been investigated consistently within supernova simulations. These studies found that in the early phase after the bounce the ejected matter is proton rich [59, 60], giving rise to a novel nucleosynthesis process (the νp -process [61]). In later stages, the matter becomes presumably neutron rich [62] allowing for the r-process to occur.

5.1. The νp process. – The freeze-out of proton-rich matter favors the production of α nuclei (${}^4\text{He}$, ${}^{56}\text{Ni}$, ${}^{64}\text{Ge}$, etc.), with some free protons left. In the supernova environment

this freeze-out matter is subjected to extreme neutrino fluences. The neutrino energies are too small ($\langle E_{\nu_e} \rangle \approx 11 \text{ MeV}$, $\langle E_{\bar{\nu}_e} \rangle \approx 15 \text{ MeV}$) to induce sizable reaction rates on nucleons bound in nuclei. However, this is different for the free protons, which by anti-neutrino captures, can be converted to neutrons. This way a supply of free neutrons exists at rather late times during the nucleosynthesis process when heavy α -nuclei like ^{56}Ni or ^{64}Ge are quite abundant. These nuclei have rather long lifetimes against weak decays and proton captures and would stop the matter-flow to even heavier nuclei. Due to the presence of free neutrons this is circumvented by (n, p) reactions, which act like fast β decays, and allow for the production of nuclides in the mass range $A \sim 80\text{--}100$ in the νp process, including the light p -isotopes $^{92,94}\text{Mo}$ and $^{96,98}\text{Ru}$.

5.2. The r-process. – About half of the elements heavier than mass number $A \sim 60$ are made within the *r*-process, a sequence of rapid neutron captures and β -decays [63, 64]. The process occurs in environments with extremely high neutron densities [65]. Then neutron captures are much faster than the competing decays and the r-process path runs through very neutron-rich, unstable nuclei. Once the neutron source ceases, the process stops and the produced nuclides decay towards stability producing the neutron-rich heavier elements.

Despite many promising attempts the actual site of the r-process has not been identified yet. However, parameter studies have given clear evidence that the observed r-process abundances cannot be reproduced at one site with constant temperature and neutron density [66]. Thus the abundances require a superposition of several (at least three) r-process components. This likely implies a dynamical r-process in an environment in which the conditions change during the duration of the process. The currently favored r-process sites (type II supernovae [67] and neutron-star mergers [68]) offer such dynamical scenarios. However, recent meteoritic clues might even point to more than one distinct site for our solar r-process abundance [69]. The same conclusion can be derived from the observation of r-process abundances in low-metallicity stars [70], a milestone of r-process research.

The r-process path runs through such extremely neutron-rich nuclei that most of their properties (*i.e.* mass, lifetime, neutron capture cross sections and fission rates and yields) are experimentally unknown and have to be modelled, based on experimental guidance. The most important nuclear ingredient in r-process simulations are the nuclear masses as they determine the flow-path. They are traditionally modelled by empirical mass formulae parametrized to the known masses [71, 72]. A new era has been opened recently, as for the first time, nuclear mass tables have been derived on the basis of nuclear many-body theory (Hartree-Fock-Bogoliobov model) [73, 74] rather than by parameter fit to data.

The nuclear half-lives strongly influence the relative r-process abundances. In a simple β -flow equilibrium picture the elemental abundance is proportional to the half-life, with some corrections for β -delayed neutron emission [75, 76]. As r-process half-lives are longest for the magic nuclei, these waiting point nuclei determine the minimal r-process duration time; *i.e.* the time needed to build up the r-process peak around $A \sim 200$. We

note, however, that this time depends also crucially on the r-process path and can be as short as a few 100 milliseconds if the r-process path runs close to the neutron dripline.

There are a few milestone half-life measurements including the $N = 50$ waiting point nuclei ^{80}Zn , ^{79}Cu , ^{78}Ni and the $N = 82$ waiting point nuclei ^{130}Cd and ^{129}Ag [77-79]. Although no half-lives for $N = 126$ waiting points have yet been determined, there has been decisive progress towards this goal recently [80]. These data play crucial roles in constraining and testing nuclear models which are still necessary to predict the bulk of half-lives required in r-process simulations. It is generally assumed that the half-lives are dominated by allowed Gamow-Teller (GT) transitions, with forbidden transitions contributing noticeably for the heavier r-process nuclei [81, 80].

If the r-process occurs in strong neutrino fluences, different neutrino-induced charged-current (*e.g.* (ν_e, e^-)) and neutral-current (*e.g.* (ν, ν')) reactions, which are often accompanied by the emission of one or several neutrons [82-84], have to be modelled and included as well. Recently neutrino-induced fission has been suggested to explain the robust r-process pattern observed in old, metalpoor stars [85]. Respective fission rates and yield distributions have been calculated on the basis of the RPA model [86, 87].

5.3. Neutrino nucleosynthesis. – When neutrinos, produced in the hot supernova core, pass through the outer shells of the star, they can induce nuclear reactions and in this way contribute to the elementsynthesis (the ν -process, [89]). For example, the nuclides ^{11}B and ^{19}F are produced by $(\nu, \nu'n)$ and $(\nu, \nu'p)$ reactions on the quite abundant nuclei ^{12}C and ^{20}Ne . These reactions are dominantly induced by ν_μ and ν_τ neutrinos and their antiparticles (combined called ν_x neutrinos) which have larger average energies (about 20 MeV) than ν_e and $\bar{\nu}_e$ neutrinos. As found in detailed stellar evolution studies [90] the rare odd-odd nuclides ^{138}La and ^{180}Ta are mainly made by the charged-current reaction $^{138}\text{Ba}(\nu_e, e^-)^{138}\text{La}$ and $^{180}\text{Hf}(\nu_e, e^-)^{180}\text{Ta}$. Hence, the ν -process is potentially sensitive to the spectra and luminosity of ν_e and ν_x neutrinos, which are the neutrino types not observed from SN1987a. Both charged-current cross-sections are dominated by the low-energy tail of the GT₋ strength distribution which is notoriously difficult to simulate. As large-scale shell model calculations are yet not possible for ^{138}Ba or ^{180}Hf , the charged-current cross-sections had been evaluated within the random phase approximation [90]. As a major improvement it has been possible recently to measure the GT₋ strengths on ^{138}Ba and ^{180}Hf below the particle thresholds and to convert these data into the relevant (ν_e, e^-) cross-sections [91]. It is found that the new cross-sections are somewhat larger than the RPA predictions. Upon using these results in stellar evolution models, slightly larger ^{138}La and ^{180}Hf abundances are found, which agree reasonably well with observation [91].

6. – The Facility for Antiproton and Ion Research (FAIR)

FAIR is the next generation facility for fundamental and applied research with antiproton and ion beams [92]. It will provide worldwide unique accelerator and experimental facilities, allowing for a large variety of unprecedented fore-front research in physics and

applied sciences. FAIR is an international project with 16 partner countries and more than 2500 scientists and engineers involved in the planning and construction of the accelerators and associated experiments. FAIR will be realized in a stepwise approach. The Modularized Start Version, comprising the Heavy-Ion Synchrotron SIS100, the antiproton facility, the Superconducting Fragment Separator and experimental areas and novel detectors for atomic, hadron, heavy-ion, nuclear, and plasma physics and applications in material sciences and biophysics, is expected to be operational in 2016. Completion of FAIR, including the synchrotron SIS300, to follow soon after.

The main thrust of FAIR research focuses on the structure and evolution of matter on both a microscopic and on a cosmic scale—bringing our Universe into one laboratory. The basis for the realization of the wide-spread and pathbreaking research activities are worldwide unique accelerator and experimental facilities. FAIR will allow, in comparison to the existing GSI facilities, to increase the beam intensities by factors 100 to 10000 and the beam energies by factors 15–20. Moreover, the use of beam cooling techniques enables the production of antiproton and ion beams of highest quality, *i.e.* with very precise energy and extremely fine profile. Upon completion, the FAIR accelerator complex can support up to 5 experimental programs simultaneously with beams of different ion species in genuine parallel operation. This unique feature is made possible by an optimal balance of the usage of the various accumulator, collector and experimental storage rings.

In this paper we have discussed some of the outstanding research opportunities at FAIR, concentrating on forefront questions relevant to supernova dynamics and nucleosynthesis, as they are part of the program of the NuSTAR collaboration. This gives only a restricted glimpse on the research program at FAIR, omitting important aspects. For example,

- the CBM/HADES experiment will explore the phase diagram of Quantumchromodynamics (QCD) in the region of very high baryon densities and moderate temperatures, supplementing related programs at the Relativistic Hadron Collider and the Large Hadron Collider, which probe the phase diagram at high temperatures and almost zero net baryon densities. The aim of CBM/HADES is to study the nuclear matter equation of state with strong relevance for supernova dynamics and neutron star structure, to search for the predicted first order phase transition between hadronic and partonic matter, and to search for the QCD critical point and the chiral phase transition.
- The highest-quality antiproton beams and the extreme energy resolution of the PANDA detector allow to produce and unravel the structure of exotic hadronic states made of quarks and gluons testing the predictions of QCD and bringing forward our understanding of the generation of mass in the world of the strong interaction. The PANDA experiment will also extend the nuclear chart into the third dimension of strangeness by producing many new hypernuclei. This will also include $\Lambda\Lambda$ hypernuclei opening here the possibility to experimentally study the interaction of two Λ particles and the $N\Lambda\Lambda$ interaction which both are important requirements for the study of neutron star structure.

- The experimental program of the FLAIR Collaboration with low-energy antiprotons focuses on the production of novel configurations of antimatter like anti-hydrogen atoms and molecules and anti-helium ultimately using these physical systems for tests of matter-antimatter symmetry.
- For plasma physics the availability of high-energy, high-intensity ion-beams enables the investigation of High-Energy Dense Matter in regimes of temperature, density and pressure, as they exist insides of stars and large planets, but which have not been experimentally accessible so far.
- Experiments by the APPA Collaboration with stored relativistic heavy ions, like uranium, which are stripped of most of their electrons and have a helium- or lithium-like configuration will study electron correlations in extreme electromagnetic fields comparable to those on the surface of neutron stars and perform test of the fundamental symmetries of QED.
- The study of the biological effectiveness of high-energy and high-intensity beams is a prerequisite to estimate the expected radiation damage induced by cosmic rays on Moon and Mars missions and to solve related protection issues.

* * *

The work presented here has benefitted from a close and intensive collaboration with G. MARTINEZ-PINEDO during more than one decade. I also would like to thank I. BORZOV, D. DEAN, H. FELDMEIER, C. FRÖHLICH, A. HEGER, R. HIX, T. JANKA, A. JUODAGALVIS, A. KELIC, M. LIEBENDÖRFER, T. MEZZACAPPA, B. MESER, T. NEFF, P. VON NEUMANN-COSEL, A. RICHTER, J. SAMPAIO, K.-H. SCHMIDT, F.-K. THIELEMANN and S. WOOSLEY for many discussions and fruitful collaborations. The work has been supported by the Helmholtz International Center for FAIR, the Helmholtz Alliance EMMI and the SFB 634 of the Deutsche Forschungsgemeinschaft.

REFERENCES

- [1] ROLFS C. E. and RODNEY W.S., *Cauldrons in the Cosmos* (Chicago Press, Chicago) 1988.
- [2] SALPETER E. E., *Austr. J. Phys.*, **7** (1954) 373.
- [3] ASSENBAUM H.J., LANGANKE K. and ROLFS C. E., *Z. Phys. A*, **327** (1987) 461.
- [4] WOOSLEY S. E. in *Proceedings of the Accelerated Radioactive Beam Workshop*, edited by BUCHMANN L. and D'AURIA J. M. (TRIUMF, Canada) 1985.
- [5] ADELBERGER E. *et al.*, *Rev. Mod. Phys.*, **70** (1998) 1265.
- [6] BAHCALL J. N., *Neutrino Astrophysics* (Cambridge University Press, Cambridge) 1989.
- [7] BONETTI R. *et al.*, *Phys. Rev. Lett.*, **82** (1999) 5205.
- [8] JUNGHANS A. R. *et al.*, *Phys. Rev. C*, **68** (2003) 065803.
- [9] NEFF T., *Phys. Rev. Lett.*, **106** (2011) 042502.
- [10] NEFF T., FELDMEIER H. and LANGANKE K., *Prog. Part. Nucl. Phys.*, **66** (2011) 341.
- [11] FELDMEIER H. and SCHNACK J., *Rev. Mod. Phys.*, **72** (2000) 655.

- [12] KAJINO T., *Nucl. Phys. A*, **460** (1986) 559.
- [13] LANGANKE K., *Nucl. Phys. A*, **457** (1986) 351.
- [14] DESCOUVEMONT P. and BAYE D., *Nucl. Phys. A*, **567** (1994) 341.
- [15] NOLLETT K. M., *Phys. Rev. C*, **63** (2001) 054002.
- [16] NAVRATIL P., BERTULANI C. A. and CAURIER E., *Phys. Rev. C*, **73** (2006) 065801.
- [17] IMBRIANI G. *et al.*, *Eur. Phys. J. A*, **25** (2005) 455.
- [18] RUNKLE R. C. *et al.*, *Phys. Rev. Lett.*, **94** (2005) 082503.
- [19] DEGL'INNOCENTI S. *et al.*, *Phys. Lett. B*, **590** (2004) 13.
- [20] ADELBERGER E. *et al.*, *Rev. Mod. Phys.*, **83** (2011) 195.
- [21] AHMED S. N. *et al.*, *Phys. Rev. Lett.*, **87** (2001) 071301; **89** (2002) 011301.
- [22] SALPETER E. E., *Phys. Rev.*, **88** (1952) 547; **107** (1957) 516.
- [23] BAHCALL J. N., BASU S. and SERENELLI A. M., *Astrophys. J.*, **631** (2005) 1281.
- [24] AUSTIN S. M., *Nucl. Phys. A*, **758** (2005) 375.
- [25] FYNBO H. *et al.*, *Nature*, **433** (2005) 135.
- [26] BUCHMANN L. *et al.*, *Phys. Rev. Lett.*, **70** (1993) 726.
- [27] KUNZ R., JAEGER M., MAYER A., HAMMER J. W., STAUDT G., HARISOPoulos S. and PARADELLIS T., *Phys. Rev. Lett.*, **86** (2001) 3244.
- [28] TISCHHAUSER P. *et al.*, *Phys. Rev. Lett.*, **88** (2002) 072501.
- [29] BUCHMANN L. and BARNES C. A., *Nucl. Phys. A*, **777** (2006) 254.
- [30] SHAPIRO S. L. and TEUKOLSKY S. A., *Black Holes, White Dwarfs and Neutron Stars* (Wiley-Interscience, New York) 1983.
- [31] MEYER B. S. and WALSH J. H., *Nuclear Physics in the Universe*, edited by GUIDRY M. W. and STRAYER M. R. (Institute of Physics, Bristol) 1993.
- [32] BETHE H. A., BROWN G. E., APPLEGATE J. and LATIMER J. M., *Nucl. Phys. A*, **324** (1979) 487.
- [33] BETHE H. A., *Rev. Mod. Phys.*, **62** (1990) 801.
- [34] JANKA H.-TH., KIFONIDIS K. and RAMPP M., *Lect. Notes Phys.*, **578** (2001) 333.
- [35] JANKA H.-TH. *et al.*, *Phys. Rep.*, **442** (2007) 38.
- [36] BURAS R., RAMPP M., JANKA H.-TH. and KIFONIDIS K., *Phys. Rev. Lett.*, **90** (2003) 241101.
- [37] JANKA H. TH. and RAMPP M., *Astrophys. J.*, **539** (2000) L33.
- [38] MEZZACAPPA A. *et al.*, *Phys. Rev. Lett.*, **86** (2001) 1935.
- [39] LANGANKE K. and MARTINEZ-PINEDO G., *Rev. Mod. Phys.*, **75** (2003) 819.
- [40] BURROWS A. *et al.*, *Ap. J.*, **640** (2006) 878.
- [41] MAREK A. and JANKA H.-TH., *Astrophys. J.*, **694** (2009) 664.
- [42] HEGER A., LANGANKE K., MARTINEZ-PINEDO G. and WOOSLEY S. E., *Phys. Rev. Lett.*, **86** (2001) 1678.
- [43] CAURIER E., LANGANKE K., MARTÍNEZ-PINEDO G. and NOWACKI F., *Nucl. Phys. A*, **653** (1999) 439.
- [44] LANGANKE K. and MARTÍNEZ-PINEDO G., *Nucl. Phys. A*, **673** (2000) 481.
- [45] JOHNSON C. W., KOONIN S. E., LANG G. H. and ORMAND W. E., *Phys. Rev. Lett.*, **69** (1992) 3157.
- [46] LANGANKE K. *et al.*, *Phys. Rev. C*, **52** (1995) 718.
- [47] KOONIN S. E., DEAN D. J. and LANGANKE K., *Phys. Rep.*, **278** (1997) 2.
- [48] LANGANKE K. *et al.*, *Phys. Rev. Lett.*, **90** (2003) 241102.
- [49] GREWE E. W. *et al.*, *Phys. Rev. C*, **78** (2008) 044301.
- [50] ZHI Q. *et al.*, *Nucl. Phys. A*, **859** (2011) 172.
- [51] KAY B. P. *et al.*, *Phys. Rev. C*, **79** (2009) 021301.
- [52] JUODAGALVIS A. *et al.*, *Nucl. Phys. A*, **848** (2011) 014308.

- [53] HEGER A., WOOSLEY S. E., MARTINEZ-PINEDO G. and LANGANKE K., *Astrophys. J.*, **560** (2001) 307.
- [54] WOOSLEY S. E. and WEAVER T. A., *Astrophys. J. Suppl.*, **101** (1995) 181.
- [55] BÄUMER C. *et al.*, *Phys. Rev. C*, **68** (2003) 031303(R).
- [56] FULLER G. M., *Astrophys. J.*, **252** (1982) 741.
- [57] BRUENN S. W., *Astrophys. J. Suppl.*, **58** (1985) 771; MEZZACAPPA A. and BRUENN S. W., *Astrophys. J.*, **405** (1993) 637; **410** (1993) 740.
- [58] HIX R. W. *et al.*, *Phys. Rev. Lett.*, **91** (2003) 210102.
- [59] PRUET J. *et al.*, *Astrophys. J.*, **623** (2005) 1.
- [60] FRÖHLICH C. *et al.*, *Astrophys. J.*, **637** (2006) 415.
- [61] FRÖHLICH C. *et al.*, *Phys. Rev. Lett.*, **96** (2006) 142502.
- [62] WANAJI S., *Astrophys. J.*, **647** (2006) 1323.
- [63] BURBIDGE E. M., BURBIDGE G. R., FOWLER W. A. and HOYLE F., *Rev. Mod. Phys.*, **29** (1957) 547.
- [64] CAMERON A. G. W., Chalk River Report CRL-41 (1957).
- [65] COWAN J. J., THIELEMANN F.-K. and TRURAN J. W., *Phys. Rep.*, **208** (1991) 267.
- [66] KRATZ K. L. *et al.*, *Astrophys. J.*, **402** (1993) 216.
- [67] WOOSLEY S. E. *et al.*, *Astrophys. J.*, **399** (1994) 229.
- [68] FREIBURGHAUS C., ROSSWOG S. and THIELEMANN F.-K., *Astrophys. J.*, **525** (1999) L121.
- [69] WASSERBURG G. J., BUSSO M., GALLINO R. and NOLLETT K. M., *Nucl. Phys. A*, **777** (2006) 5.
- [70] SNEDEN C. *et al.*, *Astrophys. J.*, **591** (2003) 936.
- [71] MÖLLER P., NIX J. R. and KRATZ K. L., *At. Data Nucl. Data Tables*, **66** (1997) 131.
- [72] BORSOV I. N., GORIELY S. and PEARSON J. M., *Nucl. Phys. A*, **621** (1997) 307c.
- [73] GORIELY S., SAMYN M., PEARSON J. M. and ONSI M., *Nucl. Phys. A*, **750** (2005) 425.
- [74] STONE J. R., *J. Phys. G*, **31** (2005) 211.
- [75] KRATZ K. L. *et al.*, *J. Phys. G*, **24** (1988).
- [76] MARTINEZ-PINEDO G. and LANGANKE K., *Phys. Rev. Lett.*, **83** (1999) 4502.
- [77] KRATZ K. L. *et al.*, *Z. Phys. A*, **325** (1986) 489.
- [78] HOSMER P. T. *et al.*, *Phys. Rev. Lett.*, **94** (2005) 112501.
- [79] LETTRY J. *et al.*, *Rev. Sci. Instrum.*, **69** (1998) 761.
- [80] KURTUKIAN-NIETO T. *et al.*, *Nucl. Phys. A*, **829** (2009) 587c: submitted to *Phys. Lett.*
- [81] BORZOV I. N., *Phys. Rev. C*, **67** (2003) 025802.
- [82] FULLER G. M. and MEYER B. S., *Astrophys. J.*, **453** (1995) 792.
- [83] QIAN Y.-Z., HAXTON W. C., LANGANKE K. and VOGEL P., *Phys. Rev. C*, **55** (1997) 1532.
- [84] HAXTON W. C., LANGANKE K., QIAN Y.-Z. and VOGEL P., *Phys. Rev. Lett.*, **78** (1997) 2694.
- [85] QIAN Y.-Z., *Astrophys. J.*, **569** (2002) L103.
- [86] KOLBE E., LANGANKE K. and FULLER G. M., *Phys. Rev. Lett.*, **92** (2004) 111101.
- [87] KELIC A. *et al.*, *Phys. Lett. B*, **616** (2006) 48.
- [88] BENLIURE J. *et al.*, *Nucl. Phys. A*, **628** (1998) 458.
- [89] WOOSLEY S. E. *et al.*, *Astrophys. J.*, **356** (1990) 272.
- [90] HEGER A. *et al.*, *Phys. Lett. B*, **606** (2005) 258.
- [91] BYELIKOV A. *et al.*, *Phys. Rev. Lett.*, **98** (2007) 082501.
- [92] HENNING W. F. *et al.*, *The International Accelerator Facility for Beams of Ions and Antiprotons* (GSI publication, November 2001).

This page intentionally left blank

Proceedings of the International School of Physics "Enrico Fermi"
Course CLXXVIII "From the Big Bang to the Nucleosynthesis", edited by A. Bracco and E. Nappi
(IOS, Amsterdam; SIF, Bologna)
DOI 10.3254/978-1-60750-974-5-35

The theory of Neutron Stars and the role of Nuclear Physics

M. BALDO

INFN, Sezione di Catania - Via S. Sofia 64, 95123 Catania, Italy

Summary. — In the three lectures that I delivered at the School I tried to introduce some of the main topics in the theory of Neutron Stars where Nuclear Physics plays a major role. In the first part of these lecture notes the structure of (isolated) Neutron Stars is described briefly. The physics of the crust is first developed at basic level, with a short discussion about the properties of the Coulomb lattice of nuclei that is present both in the outer and in the inner crust. The relevance of very asymmetric nuclei is stressed, in relation with the facilities that are developing and planned throughout the world to study exotic nuclei. The many-body theory of nuclear matter is then developed, including the comparison among the different methods. Special attention is payed to neutron matter at low density, as it is present in the outer crust of Neutron Stars. Applications are developed to the theory of nuclei, by means of the energy density functional method with a microscopic basis. The many-body theory is then systematically applied to the structure of Neutron Stars. The structure of nuclei present in the lattice that forms the crust is illustrated in some detail, and a discussion is devoted to the degree of uncertainty that is present in the theory of (non-homogeneous) low density asymmetric nuclear matter. The nuclear matter EoS at higher density is discussed in relation not only to the astrophysical observations, but also to the data on heavy ion collisions at intermediate energy. The complementarity of the laboratory experiments and astrophysical observations is especially emphasized and the fruitful link between the two fields is illustrated.

The problem of the maximum mass of Neutron Stars and the transition to quark matter is then introduced, and the latest observational data and their fundamental relevance are briefly discussed. It is shown that it is likely that transition to quark matter occurs at the center of massive Neutron Stars, but the overall content of quark matter is quite uncertain and model dependent. Despite these difficulties, from the latest observations it seems to emerge clearly that the quark matter EoS is more repulsive than in the simplest versions of the quark matter models usually employed to describe the high density deconfined phase. The presentation is kept at the basic level, while the more advanced developments are illustrated with specific examples. The researches that are at the frontier of the theory of Neutron Star structure are sketched, leaving to the references the detail of the theoretical developments. Unfortunately, due to the lack of time (and space) some issues, like superfluidity, are not even touched. Despite that, I hope that the present notes can stimulate the interest on these research lines and be of help to the beginners, entering this wide research field, that is promising new discoveries both at phenomenological and fundamental levels.

1. – Introduction

The continuous and vivid interest on the properties of what one can call “nuclear medium”, the particular state of matter composed of nucleons, is due to the extremely wide body of phenomena and physical systems, on the Earth and in the Universe, where it plays a central role. Although, since the discovery of nuclei one century ago, the experiments in laboratory and nuclear theory have developed towards a deep knowledge of these many-nucleon systems, several questions are still open. In the meanwhile the discovery of pulsars and associated neutron stars has widened enormously the possibility of probing the nuclear medium under different and extreme physical conditions. Compact astrophysical objects, notably supernovae and neutron stars, are the main places in the Universe where nuclear matter is present at large asymmetry, not reachable in laboratory, and compressed to a baryon density several times the value present in nuclei. The baryon density reached in neutron stars is probably the highest in the Universe and at the same time the gravitational field is the largest possible in an object that is not a black hole. Many other phenomena, static and dynamic, occur in neutron stars that are connected, directly or indirectly, with the properties of the nuclear matter at low or high density. One can mention the glitches and the cooling process, where, *e.g.* the superfluidity plays a central role, or the emission of gravitational waves, directly connected with the theory of gravity, whose detection would be a fundamental achievement.

In these lectures I will sketch first what is a Neutron Star and its structure, to show the relevance of the theory of nuclear matter and nuclei in the extreme wide range of density and physical conditions they are expected to be present in its interior. The second part will be devoted to the many-body theory of nuclear matter and nuclei, up to the

present frontiers where it has been developed. In the last part I will try to present some of the applications to the theory of neutron star structure, starting from the crust and going down to the inner core, with an increase of density of many orders of magnitude.

The presentation, following the spirit of the school, is pedagogical, but I will also report on some of the most recent theoretical results and observational analysis. For a more detailed study of the many-body theory, I can mention the books of refs. [1, 2], where part of the material included in the second part can be found. On Neutron Stars I can recommend the recent book of ref. [3] and the classical textbook of ref. [4]. An overview of the history and structure of Neutron Stars can be found in the book of ref. [3].

2. – Overall structure of a Neutron Star

Neutron Stars (NS) are dense remnants of a supernova explosions of type II. These supernovae are the final stage of the slow evolution of massive stars, presently believed to be the ones with a mass approximately between 10 and $100M_{\odot}$ (solar mass). As the nuclear burning which occurs in these stars proceeds, heavier elements are produced and the stars undergoes a series of contractions and warming processes. In this way the star reaches an (approximate) onion structure where the heavier elements correspond to deeper layers inside the star. The burning becomes more and more accelerate, until iron is formed at the inner core. At this point nucleosynthesis of heavier elements stops, because the isotope ^{56}Fe is the nuclide with the highest binding energy in nature. The size of the iron core then starts to increase rapidly, until it reaches a critical mass, the Chandrasekhar mass [3], above which the core and the entire star becomes unstable towards a collapse. The collapse cannot be stopped until the nuclei in the central part start to fuse and form homogeneous nuclear matter. Then the density reached in the core becomes so high that the compressed nuclear matter develops such a large pressure to undergo a bounce and a shock wave. Through a complex series of processes an explosion is produced, the supernova, and at the same time a dense remnant is formed at the center. This is the protoneutron star, that, after the cooling process, originates the Neutron Star (NS). The rest of the star is expelled and originates what is called a nebula. The whole collapse can end in a black hole instead of a Neutron Star, mainly if the original star is more massive. The collapse is a very complex process, and its discussion is well outside the scope of these lectures. It turns out that in numerical simulations it is quite difficult to obtain an explosive event, and only recently [5, 6] fully 3-dimensional simulations seem to be able to describe a release of energy large enough to justify an explosion. It has to be stressed that the energy released, mainly by neutrino emission, is of gravitational origin. Here general relativity is in full action, since the gravitational energy is a substantial fraction of the entire mass of the star. Accordingly, the gravitational binding of a Neutron Star is a substantial fraction of the star mass. Typically a NS is an object with a radius of about $10\text{--}12$ km and a mass of $1\text{--}2M_{\odot}$. It readily follows that the average density is few times the nuclear saturation density, 0.16 fm^{-3} nucleons per unit volume. Furthermore, a compact object is characterized by the so-called compression ratio $\xi = R/R_S$ between the radius and the Schwarzschild radius $R_S = GM/2c^2$, where G is the gravitational

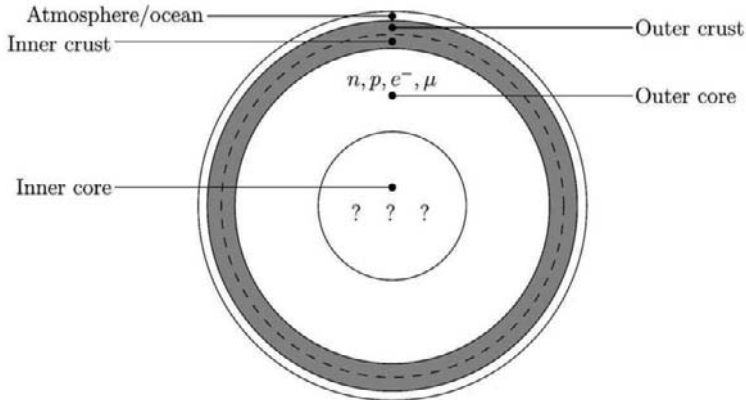


Fig. 1. – Schematic representation of the structure of a NS. The sizes of the different regions are only indicative and are not realistic. The shaded area corresponds to the crust, where a solid lattice of nuclei is present. The core is homogeneous and fluid.

constant, M the mass and c the velocity of light. Its value characterizes the relevance of the gravitational field and how close the object is to the gravitational collapse. For the Sun $\xi \approx 10^{-6}$, for a white dwarf $\xi \approx 10^{-4}$, and finally for a NS $\xi \approx 10^{-1}$. Notice that a white dwarf has a smaller ξ only for the much larger radius, while the mass is comparable with the one of a NS. Accordingly, for a black hole $\xi \approx 1$ or larger. This shows that NS are the astrophysical objects closer to a gravitational collapse.

As any object bound by gravity, the density of a NS increases going from the surface to the center. Furthermore, a NS has an onion structure, as schematically depicted in fig. 1. One can distinguish few zones, each one characterized by a different structure. Going from the surface to the inner part they can be described as follows.

- 1) The “atmosphere”, a dense gaseous region, whose composition varies from NS to NS.
- 2) The “ocean”, a liquid region, again with a composition characterizing each NS.
- 3) The “outer crust”, a solid region, whose composition is mainly determined by the chemical equilibrium between a gas of electrons and a lattice of nuclei.
- 4) The “inner crust”, where besides electrons and nuclei a gas of neutrons in chemical equilibrium is present. The neutrons drip from nuclei because they are so asymmetric that the neutron chemical potential is positive.
- 5) The “outer core”, a homogeneous quantum liquid of nucleons, composed of neutrons, protons, electrons and muons, mainly at supra-saturation density. Its exact composition is determined by the nuclear matter Equation of State (EoS) at high density.

- 6) The “inner core”. Here the density can be so high that exotic compositions can take place. Hyperons, kaons, pions or quark matter can appear. This is the most unknown region, but unfortunately it is essential for some of the NS physical parameters like the mass or the radius.

The stratification that appears in the regions 1-3 is due to the properties of a plasma. At low enough temperature and large enough density the plasma undergoes a phase transition to a liquid metal state and, at increasing density, to a Coulomb lattice. While atomic and molecular physics in a strong magnetic field is necessary to describe the gaseous and liquid envelope, in the crust nuclear physics plays an essential role. In the following we will consider the NS structure starting from the crust down to the inner core.

2.1. The outer crust. – The outer crust composition, *i.e.* the atomic number that dominates at each density, or equivalently at each depth, is determined just by the chemical equilibrium with the electrons. It is important to realize that the ions in the whole crust are fully ionized, and therefore the electrons form a quantum liquid, approximately uniform. That the electrons are delocalized can be realized by considering the radius r_Z of the most internal orbits in an ion of atomic number Z . If the average distance between electrons r_e is smaller than r_Z , then the electrons tend to be delocalized and the ions fully ionized. The radius r_Z is approximately a_0/Z , where a_0 is the Bohr radius, while r_e is related to the electron density n_e

$$(1) \quad a_0 = \frac{\hbar^2}{m_e e^2} \approx 0.53 \times 10^{-8} \text{ cm}; \quad n_e = \frac{3}{4\pi r_e^3}.$$

Equating r_Z to r_e one finds the minimal density ρ_c above which electrons form a quantum liquid

$$(2) \quad \rho_c \approx 2.7 A Z^2 \text{ g cm}^{-3},$$

where we have introduced the typical astrophysical unit for the density. In the crust the density is several orders of magnitude larger than the critical density, even for iron, for which $\rho_c \approx 10^5 \text{ g cm}^{-3}$. Furthermore, electrons at this density are essentially ultrarelativistic, as we will check in the next section. The chemical equilibrium can be therefore calculated by the relation among the chemical potential of neutrons μ_n , protons μ_p and electrons μ_e

$$(3) \quad \mu_n = \mu_p + \mu_e$$

corresponding to the beta decay and electron capture of the nuclei in the crust. Here μ_e is calculated for a free ultrarelativistic electron gas and neutrinos are escaping from the star, so that their chemical potential is zero. The nucleons chemical potentials can be extracted from the nuclear mass table. However this does not yet fix the actual value of the atomic number of the nuclei in the lattice, but we have still to minimize the energy,

or more generally, the free energy per particle. To see all that we have to state clearly the number of free physical parameters of the problem. To each nucleus of the lattice we can assign an occupied volume, *i.e.* the volume V of the unit cell in the lattice. Then the physical parameters that fix completely the configuration of the system at a given average density of the crust are

Physical parameters

A = mass number inside the cell

Z = atomic number (proton number)

($N = A - Z$ = neutron number)

V = volume of the cell

N_e = electron number

that are a total of 4.

To these 4 physical parameters we have to impose the following physical conditions:

Physical conditions

Charge neutrality: $N_e = Z$

Fixing the (average) baryon density $\rho = A/V$

that are a total of 2. The remaining 2 physical parameters must be obtained by minimizing the (free) energy (at a fixed average density). Let us take N and Z as the independent parameters to minimize the free energy

$$(4) \quad F_{\text{WS}} = F_{\text{WS}}(N, Z, N_e, R),$$

with $N = A - Z$, $N_e = Z$ and $R = R(A, \rho)$. At the minimum the derivative along any direction in the (N, Z) -plane must vanish (N and Z are taken as continuous). In particular, if we take a fixed cell volume and then a fixed value of the mass number A , we must have

$$(5) \quad \left(\frac{\partial F}{\partial Z} \right)_{A, Z, R} = - \left(\frac{\partial F}{\partial N} \right)_{A, Z, R} + \left(\frac{\partial F}{\partial Z} \right)_{N, N_e, R} + \left(\frac{\partial F}{\partial N_e} \right)_{N, Z, R} = 0,$$

where the derivatives are just the chemical potentials for neutrons (μ_n), protons (μ_p) and electrons (μ_e), so we get the already introduced eq. (3) on the basis of physical considerations. This is a particular case of a general result of Statistical Thermodynamics for coupled systems that can exchange particles: at the minimum the relations among chemical potentials that correspond to the possible reactions must hold.

The free energy can be decomposed into three contributions, the nuclear, electron and lattice contributions

$$(6) \quad F = F_{\text{nuc}}(N, Z) + F_e(Z, R) + W_L(Z, R).$$

If we neglect the lattice contribution, the chemical potential of electrons can be calculated from the expression of an ultra-relativistic electron gas. This turns out to be a good approximation.

Once the optimal value of Z has been found, at a given mass number A and cell volume V , the absolute minimum of the free energy can be obtained varying another independent physical parameter, *e.g.* the number of neutron N . As N varies, also the volume and the mass number change, keeping the density $\rho = A/V$ constant. The minimum along this line of minima is of course the absolute minimum. Then the optimal values of all physical parameters are fixed, $A, Z, N, N_e = Z, V$, at a given density. The procedure fixes the structure of the crust at each given density.

Of course, any other two-dimensional minimization method is equally well suited. Few comments are in order to complete the introduction to the physics of the outer crust. Let us first check that electrons are ultra-relativistic. As a reminder, the Fermi momentum of electrons is related to their density by

$$(7) \quad k_F^e = (3\pi^2 \rho^e)^{1/3}.$$

If we take

$$(8) \quad \rho^e = 10^8 \text{ g/cm}^3 \approx 6.022 \times 10^{-8} \text{ particles/fm}^3$$

that is a typical density of the crust, then we have $k_F^e = 1.213 \times 10^{-2} \text{ fm}^{-1}$ and the electron Fermi energy $E_F^e = \sqrt{(\hbar c k_F^e)^2 + (m_e c^2)^2} = 2.4473 \text{ MeV} \gg m_e c^2$, $m_e c^2 = 0.51 \text{ MeV}$. As a second comment, let us mention that the lattice energy W_L is just the whole energy of the electron-ion and ion-ion Coulomb interaction. It can be divided into the contribution coming from inside each cell, that is simply the electron-ion electrostatic interaction, and the intra-cell contribution (Madelung sum). The latter depends on the lattice geometrical structure. The lattice energy differences among the possible lattice structures are small with respect to all the others involved in the minimization. However, it is just this small additional energy variation that fixes which Coulomb lattice structure is preferred. It turns out that the cubic body-centered lattice is the lowest in energy at these densities, even if the difference with respect to other possible structures is minuscule.

The actual minimization of the energy can be done by using the mass table, where possible. To have an idea of what is the effect of the electron gas on the nuclei in the outer crust we can use the Liquid Drop Model (LDM) for the binding of nuclei. Let us take the simplest version of the LDM, following the presentation of ref. [7]

$$(9) \quad M(N, Z) = m_n N + m_p Z - a_v A + a_s A^{2/3} + a_c \frac{Z^2}{A^{1/3}} + a_a \frac{(N - Z)^2}{A},$$

where

$a_v \approx 16 \text{ MeV}$, volume term

$a_s \approx 18 \text{ MeV}$, surface term

$a_c \approx 0.71 \text{ MeV}$, Coulomb term

$a_a \approx 23.4 \text{ MeV}$, symmetry energy term.

Then the difference between neutron and proton chemical potential is given by

$$(10) \quad \begin{aligned} \mu_n - \mu_p &= m_n - m_p - \frac{1}{3} a_c \frac{Z}{A^{4/3}} + 4a_a \frac{(N-Z)}{A} \\ &= m_n - m_p - \frac{1}{3} a_c \frac{x_p}{A^{1/3}} + 4a_a (1 - 2x_p), \end{aligned}$$

where $x_p = Z/A$ is the proton fraction. For isolated nuclei, the condition of minimal energy for a given mass number A , that is the condition $\mu_n \approx \mu_p$, gives the position of the bottom along the stability valley. As a function of A one then gets the nuclear binding curve.

Inside the electron gas the condition $\mu_n = \mu_p + \mu_e$ shifts the value of Z or x_p . One can see from the previous expression that in order to increase the difference $\mu_n - \mu_p$ the only possibility is to decrease x_p . In this case, in fact, the negative Coulomb term decreases and the positive symmetry term increases. This means that as we proceed inside the outer crust, the asymmetry of nuclei should increase, at least on the average, with respect to the bottom of the stability valley. The LDM does not include shell effects, so that fluctuations around this trend are possible. In any case, at a certain density the asymmetry can be so large that the nuclei are in the region of exotic nuclei or even in the region where the mass table cannot be experimentally reached. This is the case also if we use, instead of the LDM, the experimental mass table to get the nuclear binding as a function of Z and N . This was done a long ago in ref. [8], where in the unknown region of the mass table the Moller mass formula was used. Refinements of this procedure were presented more recently in the literature [9], where in the unknown region different Skyrme functionals were employed to calculate the nuclear binding. These calculations have shown that the results at the highest density of the outer crust, near the drip point, can depend on the functional employed. This is of course not surprising, since the Skyrme functionals are tuned to reproduce the experimental data on nuclei close to the stability valley and possibly some exotic region, and one has to extrapolate them to reach the unknown region relevant for the outer crust. As expected, much less sensitivity appears in the region well before the drip point, where only normal nuclei are present, that are supposed to be well described by Skyrme functionals. All these results show that very exotic nuclei should be present in the higher density part of the outer crust, which is a challenge for the microscopic many-body theory of nuclei.

2.2. The inner crust. – When we proceed further inside the star, since the asymmetry has an increasing trend, the neutron chemical potential also increase, until it becomes positive, *i.e.* the neutrons can escape freely from nuclei. This is the drip point, and below this point, at higher density, the NS matter is composed also of delocalized neutrons. This is schematically illustrated in fig. 2, where an arrow indicate the position of the neutron chemical potential with respect to nuclear potential. The Coulomb lattice is still present, and in first approximation one can imagine that the system contains nuclei, electrons (and possibly muons) and a neutron gas. However a sharp separation between nuclei and neutron gas is not possible, and one should treat the crystal within the formalism

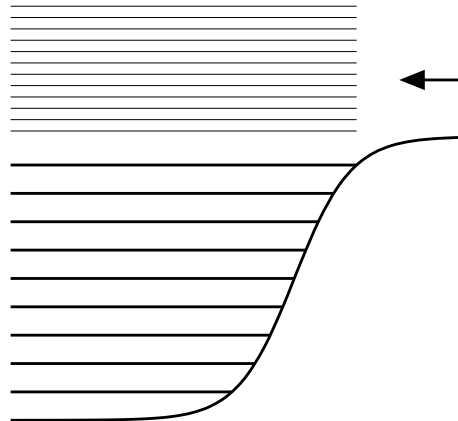


Fig. 2. – Schematic representation of the position of the neutron chemical potential (arrow) with respect to the nuclear potential well of the central nucleus inside the Wigner-Seitz cell of the lattice in the NS crust.

of Bloch wave functions, as in solid-state physics [10], and the nuclear problem for the ground state is considered within the unit cell with proper boundary conditions. A strong simplification is the Wigner-Seitz approximation, also used in solid state [10], where each cell is approximated by a spherical region and independent of the other cells. In this way the problem is reduced to search for the ground state of a piece of NS matter inside a sphere. The boundary conditions to be fixed at the surface of the sphere are then a little arbitrary. This point will be discussed later. Notice the strong difference with the inner crust, where indeed the cells could be treated as independent, except of course for the lattice energy. However, the physical parameters to be fixed by the energy minimization are exactly the same, and the considerations we have done on this point for the inner crust are still valid. In particular the parameters in the minimization procedure are the same. The nuclear physics part can be approached within various schemes of approximations. After the lecture on the microscopic theory of nuclear matter this item will be considered in detail.

2.3. The outer core. – As the density increases going inside the NS, the Coulomb lattice spacing becomes smaller and the cells are more closely packed. Accordingly the neutron gas density increases and becomes a substantial fraction of the saturation density, that is essentially the value at the center of each cell where a “nucleus” is present. Actually one can say only that a “blob” of nuclear matter is apparent at the center of the cell, with a shallow surface going at the border of the cell. At a certain density the state of minimal energy is the one with uniform matter, and this marks the transition from the crust to homogeneous nuclear matter inside the NS, that is the outer core. This happens also within the Wigner-Seitz approximation. However it is likely that this transition is not so simple but it is characterized by a region of density where matter neither has a regular lattice structure nor it is homogeneous, but rather a disordered inhomogeneous

structure, similar to the amorphous materials in solid state. The description of this state, that is expected to be present in a narrow interval of density, is quite difficult. It is also possible that unusual regular configurations can take place, like slabs, rods, voids, again immersed in a neutron gas [11]. Because also narrow structures similar to “spaghetti” could be present, this phase is often called “pasta phase”. This matter state will not be discussed here, because the determination of its actual configuration is only marginally a nuclear physics problem.

Once homogeneous matter sets in, other questions must be answered. Among many others we can mention the following ones.

- 1) How large is the proton fractions as a function of density?
- 2) Which is the equation of state of this very asymmetric nuclear matter?
- 3) Are there observational data that can constrain the EoS in this region?
- 4) Can we relate the EoS at high density in NS with the EoS relevant for heavy ion reactions, where also nuclear matter at supra-saturation density can be produced?

Question 1 is essential to establish at which density the so-called Urca process can occur. This process is the neutrino emission from the beta decay



and the corresponding inverse reaction (neutrino emission). This is a very efficient cooling process for an old NS, that is at a temperature lower than 100–200 keV. However it can occur only if the proton fraction is higher than about 14% [4], and this depends of course on the behavior of the nuclear symmetry energy at high density. It turns out that the symmetry energy is a quantity most sensitive to the many-body theory adopted for the nuclear matter, as it will be discussed later.

The compressibility at high density of the NS matter, that also depends on the symmetry energy, is the key quantity that fixes the EoS and the mass-radius relation of a NS, provided only nucleons are present.

The other questions will be discussed after the microscopic many-body theory will be presented.

2.4. The inner core. – As already mentioned, this region of a NS is the most unknown one. The internal high density part presents the challenge of predicting not only the nucleonic EoS, for which one needs to extrapolate the nuclear forces to momenta where they have not been tested, but also the possible onset of exotic components of the matter. Possible exotic components are hyperons, pions, kaons and quarks. Hyperons are likely to appear because of the large difference between neutron and proton chemical potential due to the large asymmetry. This difference can overcome the in-medium mass difference between, *e.g.*, the Σ^- and the nucleon.

Quark matter can also appear, since at high enough density a transition to the deconfined phase is expected to occur. If one calculate the average radius r_n of the volume

available to each neutron for a neutron gas at a density ρ that is ten times saturation density, one finds

$$(12) \quad r_n = (3/4\pi\rho)^{1/3} \approx 0.53 \text{ fm}$$

that is essentially the proton core radius. This means that the neutrons are deeply in contact with each other and it is hard to believe that they still keep their identity. It is likely that even at lower density the transition to quark matter could occur. Unfortunately QCD lattice calculations are not yet feasible, and we do not know yet where exactly inside the NS the possible transition to quark matter can occur, even if it is likely that it should occur in the most massive NS.

Also this item will be considered in more detail after the EoS is discussed on the basis of the microscopic many-body theory

3. – The free Fermi gas of nucleons

Before going to the microscopic many-body theory of nuclear matter, I remind the elementary properties of a free Fermi gas of nucleons. This will serve as a starting point when the nuclear interaction is introduced and at the same time as a reference for comparison with the realistic treatment and results.

3.1. The Equation of State. – If we assume that no interaction takes place between the N nucleons, we have the simplest model of nuclear matter, the free fermion gas. This is not at all a realistic model, but it can be useful to establish on elementary basis the relevance of the main correlation among nucleons, the Pauli principle. The ground state is obtained by filling the lowest N levels, since this will be the state with the lowest energy. Let us suppose, for the moment, that neutrons and protons are in equal number. Then

$$(13) \quad N = \sum_k 1 = \sum_{\mathbf{k}, \xi} 1 = g \sum_{\mathbf{k}} 1,$$

g being the degeneracy of each level, $g = 4$ in our case (summation over spin and isospin degrees of freedom). The summation over k is extended up to the highest (in energy) occupied levels. One can easily check that for infinitely large volume V , one has the identity

$$(14) \quad \frac{1}{V} \sum_{\mathbf{k}} = \frac{1}{(2\pi)^3} \int d^3k$$

since, for instance

$$(15) \quad \frac{1}{L_x} \sum_{k_x} = \frac{1}{(2\pi)} \sum_{k_x} \left(\frac{2\pi}{L_x} \right) = \frac{1}{(2\pi)} \sum_{k_x} (\Delta k_x) \implies \frac{1}{(2\pi)} \int dk_x,$$

where L_x is the linear box size. Therefore, from eq. (13) one gets

$$(16) \quad \frac{N}{V} = \rho = \frac{g}{(2\pi)^3} \int d^3k = \frac{g}{6\pi^2} k_F^3 = \frac{2}{3\pi^2} k_F^3.$$

Here periodic boundary conditions are assumed, but the results will not depend on this particular choice. Equation (16) establishes the connection between the number density ρ and the modulus of the highest occupied wave vector k_F . The corresponding momentum $p_F = \hbar k_F$ is the Fermi momentum.

The total energy E of the system is the sum over the single particle energies

$$(17) \quad E = \sum_k \frac{\hbar^2 \mathbf{k}^2}{2m} = g \sum_{\mathbf{k}} \frac{\hbar^2 \mathbf{k}^2}{2m} = \frac{gV\hbar^2}{2m} \int_{|\mathbf{k}| < k_F} \frac{\mathbf{k}^2 d^3k}{(2\pi)^3},$$

and the energy per particle e is given by

$$(18) \quad e = \frac{E}{N} = \frac{g\hbar^2}{2m\rho} \int_{|\mathbf{k}| < k_F} \frac{\mathbf{k}^2 d^3k}{(2\pi)^3} = \left(\frac{3\hbar^2 k_F^2}{10m} \right) = \frac{3}{5} E_F.$$

In eq. (18) we have used eq. (17) and introduced the Fermi energy $E_F = \hbar^2 k_F^2 / 2m$, the energy of the highest occupied level. From eqs.(18) and (16), one gets

$$(19) \quad e = \frac{3}{5} \frac{\hbar^2}{2m} \left(\frac{3\pi^2}{2} \right)^{2/3} \rho^{2/3},$$

which relates the energy per particle e to the density ρ , and therefore it is the EoS (the simplest one) for a free symmetric nucleon gas at zero temperature. If one measures the energy in MeV, the length in femtometers (fm) (otherwise also called “fermi”), and adopts for the nucleon mass $mc^2 = 938.9$ MeV, an average value between neutron and proton masses, for simplicity, then $\hbar^2/2m = 20.74$, and

$$(20) \quad e = 75.03 \rho^{2/3} \text{ MeV}.$$

This well-known result indicates that the energy of a free fermion gas increases monotonically with the density. If nuclear matter must be stable in mechanical equilibrium at a density $\rho = \rho_0 \approx 0.16 \text{ fm}^{-3}$, the so-called saturation density, a net attractive potential energy must be present around this density. This attraction, coming from the nucleon-nucleon interaction, must produce a minimum in the EoS, namely in the curve $e = e(\rho)$, at $\rho = \rho_0$. This requirement originates from the phenomenological observation that the central density of medium and heavy nuclei (as extracted from, *e.g.*, electron scattering data) is pretty constant along the nuclear mass table and close to the above-mentioned value of ρ_0 . This is interpreted as being the mechanical equilibrium density of nuclear matter and it is the starting point for the development of the empirical mass formula in its different versions. Before introducing the interaction, some considerations on the free gas model and some of its applications will be discussed.

3.2. The compressibility. – Another way of presenting the free gas EoS is to consider the pressure

$$(21) \quad p = - \left(\frac{dE}{dV} \right)_N = \frac{\rho^2}{N} \left(\frac{dE}{d\rho} \right)_N = \rho^2 \left(\frac{de}{d\rho} \right) = \\ = \frac{2}{5} \frac{\hbar^2}{2m} \left(\frac{3\pi^2}{2} \right)^{2/3} \rho^{5/3} \approx 50.02 \rho^{5/3} \text{ MeV fm}^{-3},$$

which can be considered the “Pauli pressure”, namely the pressure due to the exclusion principle, a typical quantal effect. From the pressure, the compressibility K_0 can be derived according to the usual definition

$$(22) \quad K_0 = -V \left(\frac{dp}{dV} \right) = \rho \left(\frac{dp}{d\rho} \right) = \\ = \frac{2}{3} \frac{\hbar^2}{2m} \left(\frac{3\pi^2}{2} \right)^{2/3} \rho^{5/3} \approx 83.36 \rho^{5/3}.$$

The definition of eq. (22) is in agreement with the usual one adopted in textbooks on basic mechanics and thermodynamics. For practical reasons, it is more customary among nuclear physicists to use the alternative definition

$$(23) \quad K = k_F^2 \left(\frac{d^2 e}{dk_F^2} \right),$$

which has the dimension of an energy. The following relationship can be easily checked:

$$(24) \quad K_0 = \frac{4}{3}p + \frac{1}{9}\rho K.$$

Equation (24) is not restricted to the free-gas model, but it is valid in general. At saturation $p = 0$, and the two definitions have a very simple connection. If one drops the first term on the right-hand side of eq. (24) and adopts for K_0 the free-gas value given by eq. (22), one gets

$$(25) \quad K = 6E_F \approx 221 \text{ MeV},$$

where eq. (16) has been used and the numerical value is taken at $\rho \approx \rho_0$. This value is close to the values obtained in several phenomenological analysis of the data on the monopole frequency in heavy nuclei. It is appreciably lower than the value of 240 MeV obtained in ref. [12] on the basis of a Skyrme force fit to the properties of a wide set of medium-heavy nuclei. This approximate agreement must be considered essentially fortuitous. In fact, the monopole frequency is determined by the mechanical incompressibility K_0 , but for the free Fermi gas the pressure term $4/3p$ of eq. (24) is quite large at $\rho = \rho_0$. Therefore, the procedure we followed to extract K is clearly inconsistent. The agreement is the result of some “compensation of errors”. Of course, one can always define the compressibility as $K' = 9K_0/\rho$ instead of eq. (23) for all densities, in which

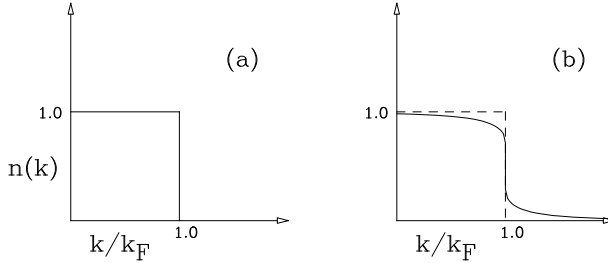


Fig. 3. – Schematic representation of the momentum distributions in a free fermion gas (a) and in an interacting fermion gas (b).

case for a free Fermi gas indeed $K' = 6E_F$. Anyhow, the connection between monopole frequency and incompressibility is less obvious than at first sight [13].

3.3. Momentum distribution. – The ground state of the free fermion gas is characterized by the filling of the lowest single-particle levels, *i.e.* the occupation number of the states k is one below the Fermi momentum k_F and zero above, as indicated in fig. 3a. This picture is expected to be modified by the nucleon-nucleon interaction, as shown in fig. 3b. Here the discontinuity at the Fermi energy is assumed to persist despite the nucleon-nucleon correlations. The Fermi liquids that have this property are called “normal” Fermi liquid. The deviation of the discontinuity from one is a measure of the strength of the correlations. The persistency of the discontinuity at k_F is the basis of the Landau theory of Fermi liquid and of the concept of quasi-particle [14]. If nuclear matter is superfluid, as it appears to be in a range of density, the discontinuity disappears. Apart from the possible onset of superfluidity, which affects only weakly the gross properties of the EoS, nuclear matter appears to be a normal Fermi liquid. Superfluidity changes of course dramatically the transport properties of nuclear matter.

3.4. The symmetry energy. – If the proton number N_p is different from the neutron number N_n , with $N = N_n + N_p$, then the neutron and proton Fermi momenta are different, since the neutron and proton densities are different, see eq. (16). Accordingly, the EoS of eq. (19) has to be generalized. Defining

$$(26) \quad \beta = \frac{N_n - N_p}{N_n + N_p} = \frac{\rho_n - \rho_p}{\rho}$$

as the “asymmetry” parameter, one easily gets

$$(27) \quad \begin{aligned} E &= E_n + E_p = N_p \frac{3}{5} E_F(p) + N_n \frac{3}{5} E_F(n) \\ e &= \frac{E}{N} = \frac{3}{10} \frac{\hbar^2}{2m} \left(\frac{3\pi^2}{2} \right)^{\frac{2}{3}} \rho^{\frac{2}{3}} \left[(1 + \beta)^{\frac{5}{3}} + (1 - \beta)^{\frac{5}{3}} \right] \\ &\approx e(\beta = 0) + a_{sy} \beta^2 + \dots, \\ a_{sy} &= \frac{1}{3} E_F. \end{aligned}$$

Thus, for a fixed value of the total density ρ , the energy per particle e has a minimum at $\beta = 0$. The coefficient a_{sy} is called the symmetry energy. At $\rho \approx \rho_0$, one finds $a_{sy} \approx 12 \text{ MeV}$. From the systematics on the asymmetry dependence of the binding energy of medium-heavy nuclei, a_{sy} turns out to be more than twice larger than this value. Here the interaction must play a major role. The density dependence of a_{sy} is one of the most relevant issues in nuclear astrophysics, but also in nuclear structure.

3·5. The single particle density of states. – For many physical phenomena the single-particle density of states at the Fermi energy is a relevant quantity. For the free-gas model one can readily get an explicit expression

$$(28) \quad D(E_F) = \sum_k \delta \left(E_F - \frac{\hbar^2 \mathbf{k}^2}{2m} \right) = \frac{V \cdot g}{(2\pi)^3} \int d^3 k \delta \left(E_F - \frac{\hbar^2 \mathbf{k}^2}{2m} \right) = \\ = \frac{N}{\rho} \frac{g}{(2\pi)^3} 4\pi \frac{m}{\hbar^2} k_F = \frac{3N}{2E_F} \approx \frac{N}{23} \text{ MeV}^{-1},$$

where the last equality holds at $\rho \approx \rho_0$. This elementary result is expected to be modified by the presence of the interaction [15]. The effect of the nucleon-nucleon correlations on $D(E_F)$ can be introduced by substituting the free nucleon mass with the so called nucleon “effective mass”, which will be shortly discussed in the section on Landau theory. Another related useful quantity is the single-particle level density per unit volume, that for symmetric matter can be written as

$$(29) \quad d(E_F) = D(E_F)/V = \frac{2m}{\pi^2 \hbar^2} k_F.$$

It depends only on the nuclear matter density.

3·6. The Pauli paramagnetism. – If a free gas of neutron is subject to a magnetic field \mathbf{H} , the state k with the spin parallel and anti-parallel to the direction of the magnetic field splits into two different levels, with an energy difference equal to $\Delta E = 2\mu_n H$. Here μ_n is the neutron magnetic moment. Since μ_n is negative, states with spin anti-parallel to \mathbf{H} are lower in energy. Then the Fermi momenta for neutrons with spin parallel is different from the ones with spin anti-parallel, a situation analogous to the case discussed in point c) for the asymmetry energy. If we indicate by δ the “magnetization” parameter

$$(30) \quad \delta = \frac{N_n^+ - N_n^-}{N_n},$$

then, following eq. (27), one gets for the increase of the gas energy per particle due to the different population of the spin states

$$(31) \quad e_g = e(\delta = 0) + \frac{1}{3} E_F \delta^2 + \dots .$$

The total energy is obtained by adding the magnetic energy

$$(32) \quad e_t = e(H=0) - 2\mu H \delta + \frac{1}{3} E_F \delta^2 + \dots$$

The actual magnetization is obtained by minimizing the total energy. For small δ one gets

$$(33) \quad \delta = \frac{3\mu H}{E_F} = \chi_M H,$$

where χ_M is the Pauli magnetic susceptibility. The nucleon-nucleon interaction can strongly affect such a simple estimate, both by changing the Fermi energy E_F and because of the spin dependence of the interaction. These considerations are of no relevance for nuclei, since it is not possible to produce in practice magnetic fields strong enough to have any effect on the nucleon spin, and anyhow nuclear structure dominates the magnetic properties of nuclei. However, the response of a free fermion gas to a static magnetic field is of some relevance for the outer crust of neutron stars, where a low density neutron gas is present, which is indeed under the influence of an exceedingly large magnetic field.

3.7. Other microscopic physical quantities. – In order to characterize the properties of nuclear matter other quantities are necessary, noticeably the ones that are involved in transport phenomena. Bulk and shear viscosity are essential to describe the dynamics of Neutron Stars, but they are dominated by the nucleon-nucleon interaction, and therefore they will be discussed after the correlations among nucleons are introduced and discussed. In finite nuclei viscosity must to be treated in a different scheme than in nuclear matter, since the presence of the nuclear surface plays a major role. This issue is relevant for many macroscopic phenomena in NS and is closely linked to the many-body structure of nuclear matter, but, for lack of space (and time) will not be discussed in these notes.

4. – Introducing the interaction

The properties of nuclear matter are determined or strongly affected microscopically by the features of the nucleon-nucleon (NN) interaction. In particular, one of the main characteristics of the NN interaction is the presence of a hard repulsive core, whose relevance can be hardly overlooked. Furthermore, any realistic NN potential must include a complex structure of operators involving spin, isospin and orbital angular momentum. This non-trivial structure is one of the main reasons that renders the microscopic many-body theory of nuclear matter and nuclei so hard to be handled. Another characteristics of the NN interaction is the presence of a quasi-bound state (1S_0 channel) and a bound state (3S_1 - 3D_1 channel) in the s -wave. This peculiar feature is probably unique in nature and strongly affects the structure of low density nuclear matter. At increasing density the effect of the bound and quasi-bound states tends to be reduced and this indicates that the many properties of the nuclear medium should change strongly with density.

Furthermore at very low density we know that nuclear matter at not too high temperature must form clusters, *i.e.* light nuclei, and this has a decisive role for the Neutron Star or proto-neutron star crust, as well for heavy ion collision processes. In order to illustrate these fundamental features of nuclear matter as a many-fermion system, in this Section the NN interaction is introduced on the basis of the meson-nucleon model of the strong interaction in the baryon sector and the many-body theory of nuclear matter is then schematically developed following the most established methods. Each microscopic many-body theory has a particular scheme to treat the hard repulsive core, that, implicitly or explicitly, introduces an effective NN interaction, more manageable than the original NN interaction.

4.1. Sketch of the nucleon-nucleon interaction. – The nucleon-nucleon interaction was intensively studied when Nuclear Physics started developing. Along the years the phenomenological analysis has been more and more refined. Presently the phase shifts in different two-body channels are known with high precision up to an energy of about 300 MeV in the laboratory, even if discrepancies between the results of different groups still persist [16]. For future reference in the paper we remind very briefly the connection between the two-body interaction and the cross-section, the quantity which is actually measured. If one assumes that the interaction can be described by a static non-relativistic potential v , the scattering process at the energy E can be described by the T -matrix. It can be calculated solving the integral equation

$$(34) \quad T(E) = v + v \frac{P}{E - H_0} T(E),$$

where H_0 is the free kinetic energy Hamiltonian and P indicates the principal value for the integral, which fixes the stationary wave boundary conditions. With these boundary conditions the T -matrix is often called R -matrix. For a central potential, the phase shift in a given channel l is given by

$$(35) \quad \tan \delta_l = -q\mu(q|T(E)|q),$$

where q is the relative momentum and μ the reduced mass. The differential cross-section is given by

$$(36) \quad \frac{d\sigma}{d\Omega} = \frac{1}{q^2} |\Sigma_l(2l+1)(e^{2i\delta_l} - 1)P_l(\theta)|^2.$$

The nucleon-nucleon interaction, as we will see, contains not only central interaction but also more complex operators, and the summation is extended to single and coupled channels α , characterized by the total angular momentum J , total spin S , total isospin T and the orbital angular momenta l, l' ($l = l'$ for single channel). Fitting the data on the cross-sections at different energy, the phase shifts δ_α for each channel can be extracted. For the NN interaction a particular form is assumed, as suggested by the meson-nucleon

theory of strong interaction, that contains several parameters that are fitted to reproduce the phase shifts. In this way one can fix the nucleon-nucleon potential, which however partly remains model dependent. For details, see, *e.g.*, ref. [17]. Here we sketch the main ideas of the meson theory of the nucleon-nucleon interaction. For simplicity we use a non-relativistic treatment, as a first schematic introduction to the theory of nuclear forces. Of course, the correct framework is the relativistic field theory of the meson-nucleon system. Let us consider the simplest possible case, the coupling of nucleons with a spinless neutral meson. If we indicate by b^\dagger_q (b_q) the creation (annihilation) operator of a meson with momentum q , the simplest coupling term is the scalar one

$$(37) \quad H_c = G_s \int d^3x \psi^\dagger(x) \psi(x) \phi(x)$$

$$= G_s \frac{1}{\sqrt{V}} \sum_{kq} \sqrt{\frac{\hbar}{2\omega(q)}} (a^\dagger_k a_{k+q} b^\dagger_q + a^\dagger_k a_{k-q} b_q),$$

which describes the processes of emission and absorption of a meson. The two processes are included together, with the same weight, as required by the hermiticity of the interaction H_c and of the scalar field $\phi(x)$. The momentum conservation has been explicitly worked out and the constant G_s is the meson-nucleon coupling constant. In eq. (37) $\omega(q)$ is the meson energy and the factor in front, $1/\sqrt{2\omega}$, comes from the usual quantization of the boson (meson) field in a set of harmonic oscillators [18]. The creation and annihilation meson operators satisfy the usual boson commutation relations

$$[b_{k'}, b^\dagger_k]_- = -[b^\dagger_{k'}, b_{k'}]_- \equiv b_{k'} b^\dagger_k - b^\dagger_{k'} b_{k'} = \delta_K(k - k').$$

In eq. (37) the product $a^\dagger a$ includes a scalar product in the spin component, $a^\dagger a \equiv \sum_\sigma a^\dagger_\sigma a_\sigma$. The total Hamiltonian will include, besides the free nucleon Hamiltonian, also the free meson part

$$h_0 = \sum_q \omega(q) b^\dagger_q b_{-q}$$

and we can take the relativistic expression $\omega(q) = \sqrt{(mc^2)^2 + q^2c^2}$ since the meson mass m is usually much smaller than the nucleon mass, and therefore its kinematics is surely relativistic. We will indicate by H_0 the non-interacting part of the Hamiltonian. The inclusion of the coupling term of eq. (37) in a non-relativistic framework is somehow problematic. In fact, since it involves the creation or annihilation of a particle, the center-of-mass energy in such a process cannot be conserved and therefore Galilei invariance is manifestly broken. The breaking is proportional to the ratio between the meson and the nucleon masses, and therefore it vanishes in the limit of infinitely heavy nucleons. This is indeed the limit in which the concept of a static nucleon-nucleon potential has a meaning. Perturbation theory in H_c of different physical quantities can easily be developed and the different terms can be represented by diagrams. For our purposes only the lowest

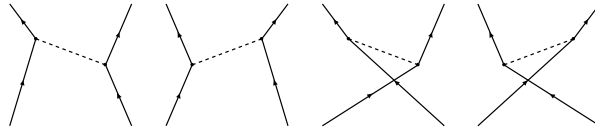


Fig. 4. – The four possible meson exchange processes. Dashed lines indicate mesons, full lines nucleons.

order has to be considered. In the framework of the meson-nucleon theory, the effective nucleon-nucleon interaction can be identified with the irreducible part of the two-nucleon scattering matrix $T^{(2)}$. By “irreducible” here we mean the set of (connected) diagrams which cannot be separated into two distinct parts by cutting two nucleon lines at any given level along the diagram. The general perturbation theory for $T^{(2)}$ can be obtained from the usual expansion for the scattering matrix

$$(38) \quad \begin{aligned} T^{(2)}(E) &= H_c + H_c \frac{1}{E - H_0} T^{(2)} \\ &= H_c + H_c \frac{1}{E - H_0} H_c + H_c \left(\frac{1}{E - H_0} H_c \right)^2 \dots \end{aligned}$$

In this expansion we have to select the processes which indeed correspond to the scattering of two nucleons and are irreducible. The lowest order which can contribute is the second order, since to first order the coupling term H_c can describe only emission or absorption of a meson. Let us denote by $|kk'\rangle$ the free (antisymmetrized) state $a_k^\dagger a_{k'}^\dagger |0\rangle$ of two nucleons with momenta k and k' . The amplitude for the scattering from the state $|k_0 k'_0\rangle$ to the state $|k_1 k'_1\rangle$ can be extracted from the second-order term of $T^{(2)}$,

$$\langle k_1 k'_1 | T^{(2)} | k_0 k'_0 \rangle \approx \langle k_1 k'_1 | H_c \frac{1}{E - H_0} H_c | k k' \rangle.$$

If we insert the expression of eq. (37) for H_c , since by definition H_0 is diagonal in the free-state representation, we can use Wick’s theorem for the vacuum state in a straightforward way. For the meson operators this is trivial (they commute with the nucleon operators). The four contractions which can contribute can be depicted as in fig. 4 which give four distinct contributions. The corresponding analytical expressions for the two-body scattering matrix is given by

$$(39) \quad \begin{aligned} \langle k_1 k'_1 | T^{(2)} | k_0 k'_0 \rangle &= \sum_q \frac{\hbar}{V} \frac{G_s^2}{2\omega_q} \delta_K(k_0 + k'_0 - k_1 - k'_1) \\ &\times \left\{ (\delta_K(q - k_0 + k_1) - \delta_K(q - k_0 - k'_1)) \frac{1}{E_0 - E + E_{k_0 - q} - E_{k_0} + \omega_q} \right. \\ &\quad \left. + (\delta_K(q - k'_1 + k_0) - \delta_K(q - k_1 - k_0)) \frac{1}{E_0 - E + E_{k_0' - q} - E_{k_0'} + \omega_q} \right\}, \end{aligned}$$

where $E_0 = E_{k_0} + E_{k'_0}$ is the initial energy. If we interpret this matrix element as the matrix element of a two-body potential v between nucleons, this potential is clearly non-local and energy dependent. It is convenient to introduce the relative and total momenta of the initial and final two nucleon states

$$(40) \quad \begin{aligned} Q &= \frac{1}{2}(k'_0 - k_0); & P &= k'_0 + k_0, \\ Q' &= \frac{1}{2}(k'_1 - k_1); & P' &= k'_1 + k_1. \end{aligned}$$

Putting $E = E_0$, the matrix element of v can be written as

$$(41) \quad \langle k_1 k'_1 | v | k_0 k'_0 \rangle = \frac{1}{2} \frac{\hbar}{V} G_s^2 \delta_K(P - P') \times \left(-\frac{1}{\omega_{Q-Q'}} \left(\frac{1}{E_{Q'_+} - E_{Q_+} + \omega_{Q-Q'}} + \frac{1}{E_{Q'_-} - E_{Q_-} + \omega_{Q-Q'}} \right) + \frac{1}{\omega_{Q+Q'}} \left(\frac{1}{E_{Q'_-} - E_{Q_+} + \omega_{Q+Q'}} + \frac{1}{E_{Q'_+} - E_{Q_-} + \omega_{Q+Q'}} \right) \right),$$

where $Q_{\pm} = \pm Q + P/2$. The fact that a dependence on the total momentum is still present is a consequence of the already mentioned breaking of Galilei invariance. In the limit of large nucleon mass, the terms corresponding to the nucleon recoil can be neglected, which is equivalent to put $E_k \approx M$ everywhere in the expression. In this approximation a very simple form is obtained

$$(42) \quad \langle k_1 k'_1 | v | k_0 k'_0 \rangle = \frac{\hbar}{V} G_s^2 \delta_K(P - P') \left(-\frac{1}{\omega_{Q-Q'}^2} + \frac{1}{\omega_{Q+Q'}^2} \right) = \frac{\hbar}{V} G_s^2 \delta_K(P - P') \left(-\frac{1}{(Q-Q)^2 c^2 + (mc^2)^2} + \frac{1}{(Q+Q')^2 c^2 + (mc^2)^2} \right),$$

where the explicit form for $\omega(q)$ has been used. The expression is now Galilei invariant, since it depends only on the relative momenta Q and Q' . The expression of eq. (42) can be interpreted as the direct and exchange matrix elements of a local potential. In agreement with the scalar nature of the exchanged meson, the interaction is independent of the spins of the nucleons. The form of such a potential in coordinate representation is the celebrated Yukawa potential

$$(43) \quad v(r) = -G_s^2 \frac{\hbar}{V} \sum_q \frac{1}{q^2 c^2 + (mc^2)^2} e^{i\mathbf{q} \cdot \mathbf{r}/\hbar} = -\frac{G_s^2}{4\pi\hbar^2 c^3} (mc^2) \frac{e^{-\mu r}}{\mu r}.$$

The range $a = 1/\mu = \hbar/mc$ of this potential is the Compton wavelength of the meson. This means that heavier mesons produce shorter potential range. The limit of large nucleon mass is equivalent to neglect the recoil energy of the nucleons involved in the

interaction. It is also equivalent to consider the exchange of the meson as instantaneous, and therefore the approximation is usually referred to as the static approximation. It is only in this limit that the very concept of potential can be introduced. For the validity of such an approximation it is essential that the ratio between meson and nucleon masses be small. Unfortunately not all the possible mesons which can be considered involved in the nucleon-nucleon interaction processes have indeed a mass small compared to the nucleon one. The potentials derived from heavier meson exchange processes have therefore to be considered as effective ones, and the corresponding parameters as effective ones. The latter can therefore differ from the phenomenological ones extracted from meson nucleon scattering. Equation (37) is schematic, since mesons and nucleons are not point-like particles, and therefore a more refined treatment must introduce vertex corrections in the interaction processes. Usually these corrections are described by phenomenological vertex form factors which multiply the expressions of the type of eq. (42) for the NN potentials. The corresponding form in coordinate representation is modified accordingly. From the above results it turns out that the local potential mediated by a scalar meson is attractive. This is the case of the so-called σ meson, which is commonly believed to be responsible for the intermediate range attraction characteristic of the two-nucleon interaction. The lightest known (strongly interacting) meson, the π meson, is known to be a pseudoscalar meson, *i.e.* a meson with negative internal parity, which is therefore described by a field which changes sign under the parity operation. For the π meson the scalar coupling of eq. (37) cannot be used, since the Hamiltonian of strong interaction must be parity invariant. In the non-relativistic limit the only possibility in this case is a pseudo-vector coupling. Furthermore the π meson has three charge states and it is therefore a vector in isospin space. The simplest non-relativistic coupling is of the form

$$(44) \quad H_c = G_{pv} \frac{1}{\sqrt{V}} \sum_{kq} \sqrt{\frac{\hbar}{2\omega(q)}} (a^\dagger_k (\boldsymbol{\sigma} \cdot \mathbf{q}) \boldsymbol{\tau} a_{k+q} b^\dagger_q + a^\dagger_k (\boldsymbol{\sigma} \cdot \mathbf{q}) \boldsymbol{\tau} a_{k-q} b_q),$$

where now the b and b^\dagger operators refer to the π meson. The quantities $\boldsymbol{\sigma} \equiv \sigma_x, \sigma_y, \sigma_z$ are the usual Pauli matrices which act on the spin variables of the nucleon creation and annihilation operators. The particular form ensures rotational invariance. Since the Pauli matrices form a pseudo-vector, the expression for H_c is indeed a scalar. The matrices $\boldsymbol{\tau} \equiv \tau_x, \tau_y, \tau_z$ are the Pauli matrices in isospin spaces and as such they act on the isospin variables of the nucleon operators. The expression includes a scalar product of these three Pauli matrices, which form a three-vector, with the isospin variables of the meson operator, namely $\boldsymbol{\tau}b \equiv \sum_i \tau_i b_i$ (and analogously for b^\dagger), where i labels the three possible isospin (charge) states of the π meson. The scalar product ensures that H_c is scalar in isospin space, and this is dictated by the charge independence of the nuclear forces, which is phenomenologically observed to a very high degree of accuracy. Following the same procedure as in the case of a scalar meson, one gets the following expression for the direct matrix element of the interaction in the static limit, with $k = Q - Q'$:

$$(45) \quad \langle Q'P'|v|QP\rangle = -G_{pv}^2 \frac{\hbar}{V} \delta_K(P - P') \frac{(\boldsymbol{\sigma}_1 \cdot \mathbf{k})(\boldsymbol{\sigma}_2 \cdot \mathbf{k})}{k^2 c^2 + (mc^2)^2} (\boldsymbol{\tau}_1 \cdot \boldsymbol{\tau}_2),$$

where the matrix elements between spin-isospin states of the corresponding Pauli matrices have to be taken, *i.e.* the expression has to be considered still an operator in spin-isospin space. It is customary to introduce the tensor operator

$$(46) \quad S_{12} = 3(\boldsymbol{\sigma}_1 \cdot \mathbf{k})(\boldsymbol{\sigma}_2 \cdot \mathbf{k}) - \boldsymbol{\sigma}_1 \cdot \boldsymbol{\sigma}_2 k^2$$

and the expression can be written

$$(47) \quad \langle Q'P'|v|QP\rangle = -\frac{1}{12}G_{pv}^2 \frac{\hbar}{V} \delta_K(P - P') \\ \cdot \left[\frac{S_{12}}{k^2 c^2 + (mc^2)^2} - \boldsymbol{\sigma}_1 \cdot \boldsymbol{\sigma}_2 \frac{m^2 c^2}{k^2 c^2 + (mc^2)^2} + \boldsymbol{\sigma}_1 \cdot \boldsymbol{\sigma}_2 \right] \boldsymbol{\tau}_1 \cdot \boldsymbol{\tau}_2.$$

A pseudoscalar meson gives rise to a tensor-isospin interaction plus a spin-isospin interaction. The last term is a contact interaction (a delta-function in coordinate space). A more complete treatment should include the vertex form factors also in this case. It has to be noticed that the coupling constant has a different definition here than in the relativistic treatment. More complex couplings are possible, and they naturally arise in a relativistic treatment, which is the framework in which the theory of nuclear forces has ultimately to be formulated. The interaction is attractive or repulsive according to the quantum numbers of the interacting nucleons, namely on the two-body channel (including isospin). It turns out that the tensor part is attractive in the s -wave channels. The π meson is responsible of the long-range attractive part of the NN interaction. Another important case is the exchange of a vector meson, namely a meson of spin one. The treatment of this case is more complex and requires a full relativistic treatment. It turns out that a vector meson produces mainly a repulsive interaction. Therefore, at least a part of the repulsive core, characteristic of the NN interaction, can be described by the exchange of spin-one mesons, like the ω meson. However, at distances smaller than the typical core size (~ 0.4 fm) the structure of the nucleons, as described by QCD, starts to play a role and the meson picture cannot be any more maintained. The meson theory in this range can be regarded as an effective model for more complex processes and the corresponding coupling constants and cut-off have to be considered as parameters to be adjusted to fit the experimental data on NN scattering.

In all these considerations, one assumes that only one meson is exchanged at a time, so that the NN interaction is fully determined by the set of known mesons and by their couplings with nucleons. This is the so-called one boson exchange potential (OBEP). It turns out, however, that the intermediate-range attraction cannot be obtained in this way. As already mentioned, it is customary then to introduce a fictitious scalar meson, the σ meson, with suitable mass and coupling to reproduce the phenomenological intermediate-range attraction. It is usually believed that the hypothetical σ meson simulates the simultaneous exchange of two pions both correlated and uncorrelated. The phenomenology on pion-pion scattering gives only a broad structure in the s -wave channel, and therefore a fully satisfactory theoretical basis for the introduction of the σ meson is still lacking. For a historical account of the OBEP theory, see ref. [17].

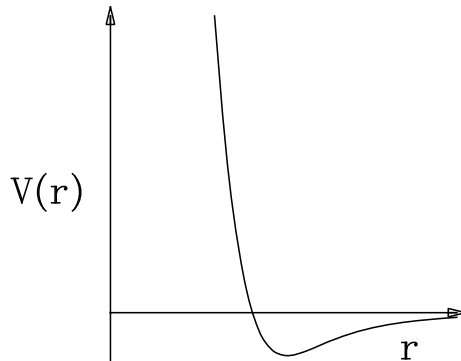


Fig. 5. – Schematic representation of the nucleon-nucleon interaction potential.

The main features of the NN interaction, derived from the meson-nucleon model and the phenomenological analysis, can be summarized schematically as in fig. 5. At large distance, $r \geq 1$ fm, the interaction is attractive with an exponential tail. At intermediate distance, $0.4 \leq r \leq 1$ fm, a stronger attraction is present, at least once an average is made over the different partial waves and quantum numbers (*i.e.* channels). At short distance, $r \leq 0.4$ fm, a strong repulsive core is in any case present. The repulsion is so strong that in the early versions of the NN potential an infinite impenetrable barrier was assumed to exist below about 0.4 fm. In the more modern versions the repulsive core is taken finite but very large with respect to the usual nuclear physics energy scale. The details of the interaction depend on the specific model for NN forces, but the schematic picture of fig. 5 is in any case valid and the nuclear matter EoS is strongly influenced by these simple properties.

4.2. Theoretical many-body methods. – Once the interaction between two nucleons is established, one can try to solve the many-body problem for the nuclear matter. However, it is not obvious that the nuclear Hamiltonian includes only two-body forces. Since we know that the nucleon is not an elementary particle, we can expect that the interaction in a system of nucleons is not fully additive, namely it is not simply the sum of the interactions between pairs of nucleons, but also three or more nucleon forces must be considered. This important issue is discussed later. For the moment we restrict the treatment to the case of two-body forces, which are expected anyhow to be dominant around saturation or slightly above.

4.2.1. The Brueckner-Bethe-Goldstone expansion. The Brueckner-Bethe-Goldstone (BBG) many-body theory is based on the re-summation of the perturbation expansion of the ground-state energy. The original bare NN interaction is systematically replaced by an effective interaction that describes the in-medium scattering processes. The in-vacuum T -matrix of the general equation (34) is replaced by the so-called G -matrix, that takes into account the effect of the Pauli principle on the scattered particles and the

in-medium potential $U(k)$ felt by each nucleon. The corresponding integral equation for the G -matrix can be written as

$$(48) \quad \langle k_1 k_2 | G(\omega) | k_3 k_4 \rangle = \langle k_1 k_2 | v | k_3 k_4 \rangle + \sum_{k'_3 k'_4} \langle k_1 k_2 | v | k'_3 k'_4 \rangle \frac{(1 - \Theta_F(k'_3))(1 - \Theta_F(k'_4))}{\omega - e_{k'_3} + e_{k'_4}} \langle k'_3 k'_4 | G(\omega) | k_3 k_4 \rangle,$$

where the two factors $1 - \Theta_F(k)$ force the intermediate momenta to be above the Fermi momentum (“particle states”), the single-particle energy $e_k = \hbar^2 k^2 / 2m + U(k)$ and the summation includes spin-isospin variables. The G -matrix has not any more the hard core of the original bare NN interaction and it is defined even for bare interaction with an infinite hard core. In this way the perturbation expansion is more manageable. The introduction and choice of the single-particle potential are essential to make the resummed expansion convergent. In order to incorporate as much as possible higher-order correlations the single-particle potential is calculated self-consistently with the G -matrix itself

$$(49) \quad U(k) = \sum_{k' < k_F} \langle k k' | G(e_{k_1} + e_{k_2}) | k k' \rangle.$$

An account on the diagrammatic method, the degree of convergence of the BBG expansion and a summary of the results can be found in refs. [19, 1]. Here we restrict to indicate the expression of the correlation energy at the so-called Brueckner level (“two hole-line” approximation)

$$(50) \quad \Delta E_2 = \frac{1}{2} \sum_{k_1, k_2 < k_F} \langle k_1 k_2 | G(e_{k_1} + e_{k_2}) | k_3 k_4 \rangle_A,$$

where $|k_1 k_2\rangle_A = |k_1 k_2\rangle - |k_2 k_1\rangle$. At this level of approximation, that mainly includes two-body correlations, one can find that the corresponding ground-state wave function Ψ can be written consistently as

$$(51) \quad |\Psi\rangle = e^{\hat{S}_2} |\Phi\rangle,$$

where Φ is the unperturbed free-particle ground state and \hat{S}_2 is the two-particle correlator

$$(52) \quad \hat{S}_2 = \sum_{k_1 k_2, k'_1 k'_2} \frac{1}{4} \langle k'_1 k'_2 | S_n | k_1 k_2 \rangle a^\dagger(k'_1) a^\dagger(k'_2) a(k_2) a(k_1),$$

where the k 's are hole momenta, *i.e.* inside the Fermi sphere, and the k' 's are particle momenta, *i.e.* outside the Fermi sphere. The function \hat{S}_2 is the so-called “defect function”. It can be written in terms of the G -matrix and it is just the difference between the in-medium interacting and non-interacting two-body wave functions [19, 1]. A recent

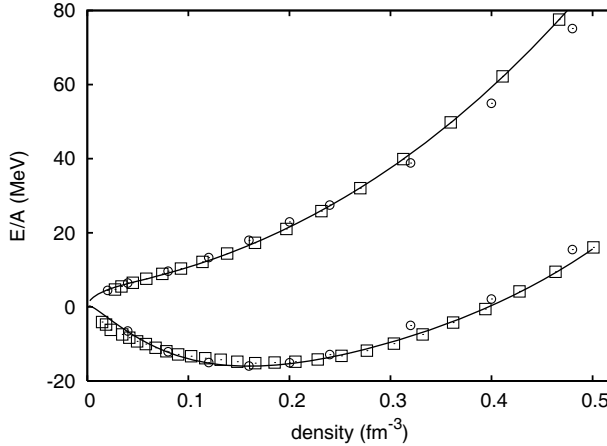


Fig. 6. – Symmetric and pure neutron matter EoS from BHF scheme including TBF (squares). The full lines is a fit to the points. The circles indicate the EoS from ref. [22].

systematic study of the dependence of the resulting EoS on the NN interaction can be found in ref. [20].

One of the well-known results of all these studies, that lasted for about half a century, is the need of three-body forces (TBF) in order to get the correct saturation point in symmetric nuclear matter. Once the TBF are introduced, the resulting EoS, for symmetric matter and pure neutron matter, is reported in fig. 6 for the two-body interaction Av_{18} . The TBF produce a shift in energy of about +1 MeV in energy and of about -0.01 fm^{-3} in density. This adjustment is obtained by tuning the two parameters contained in the TBF [21] and was performed to get an optimal saturation point (the minimum). For comparison is also reported the variational EoS of ref. [22], that will be discussed in the next Section. The connection between two-body and three-body forces within the meson-nucleon theory of nuclear interaction is discussed and worked out in refs. [23-25]. The possible interplay between two-body interaction and TBF for the resulting EoS is discussed in ref. [26].

4.2.2. The variational method. In the variational method one assumes that the ground-state wave function Ψ can be written in a form as in eq. (51), *i.e.*

$$(53) \quad \Psi(r_1, r_2, \dots) = \Pi_{i < j} f(r_{ij}) \Phi(r_1, r_2, \dots),$$

where Φ is the unperturbed ground-state wave function, properly antisymmetrized, and the product runs over all possible distinct pairs of particles. The correlation factor is here determined by the variational principle, *i.e.* by imposing that the mean value of the Hamiltonian gets a minimum (or in general stationary point)

$$(54) \quad \frac{\delta}{\delta f} \frac{\langle \Psi | H | \Psi \rangle}{\langle \Psi | \Psi \rangle} = 0.$$

In principle this is a functional equation for the correlation function f , which however can be written explicitly in a closed form only if additional suitable approximations are introduced. The function $f(r_{ij})$ is assumed to converge to 1 at large distance and to go rapidly to zero as $r_{ij} \rightarrow 0$, to take into account the repulsive hard core of the NN interaction. Furthermore, at a distance just above the core radius a possible increase of the correlation function beyond the value 1 is possible.

For nuclear matter it is necessary to introduce a channel-dependent correlation factor, which is equivalent to assume that f is actually a two-body operator \hat{F}_{ij} . One then assumes that \hat{F} can be expanded in the same spin-isospin, spin-orbit and tensor operators appearing in the NN interaction. Momentum-dependent operators, like spin-orbit, are usually treated separately. The product in eq. (53) must be then symmetrized since the different terms do not commute anymore.

If the two-body NN interaction is local and central, its mean value is directly related to the pair distribution function $g(\mathbf{r})$

$$(55) \quad \langle V \rangle = \frac{1}{2} \rho \int d^3 r v(r) g(\mathbf{r}),$$

where

$$(56) \quad g(\mathbf{r}_1 - \mathbf{r}_2) = \frac{\int \Pi_{i>2} d^3 r_i |\Psi(r_1, r_2 \dots)|^2}{\int \Pi_i d^3 r_i |\Psi(r_1, r_2 \dots)|^2}.$$

The main job in the variational method is to relate the pair distribution function to the correlation factors F . Again, in nuclear matter also the pair distribution function must be considered channel dependent and the relation with the correlation factor becomes more complex. In general this relation cannot be worked out exactly, and one has to rely on some suitable expansion. Furthermore, three-body or higher correlation function must in general be introduced, which will depend on three or more particle coordinates and describe higher-order correlations in the medium. Many excellent review papers exist in the literature on the variational method and its extensive use for the determination of nuclear matter EoS [27, 2]. The best known and most used variational nuclear matter EoS is the one of ref. [22], and it is reported in fig. 6. A detailed discussion on the connection between variational method and BBG expansion can be found in ref. [19].

4.2.3. The relativistic approach. One of the deficiencies of the Hamiltonian considered in the previous sections is the use of the non-relativistic limit. The relativistic framework is of course the framework where the nuclear EoS should be ultimately based. The best relativistic treatment developed so far is the Dirac-Brueckner approach. Excellent review papers on the method can be found in the literature [28] and in textbooks [29]. Here we restrict the presentation to the main basic elements of the theory.

In the relativistic context the only NN potentials which have been developed are the ones of OBE (one boson exchange) type. The starting point is the Lagrangian for the

nucleon-mesons coupling

$$(57) \quad \mathcal{L}_{pv} = -\frac{f_{ps}}{m_{ps}} \bar{\psi} \gamma^5 \gamma^\mu \psi \partial_\mu \varphi^{(ps)},$$

$$(58) \quad \mathcal{L}_s = +g_s \bar{\psi} \psi \varphi^{(s)},$$

$$(59) \quad \mathcal{L}_v = -g_v \bar{\psi} \gamma^\mu \psi \varphi_\mu^{(v)} - \frac{f_v}{4M} \bar{\psi} \sigma^{\mu\nu} \psi \left(\partial_\mu \varphi_\nu^{(v)} - \partial_\nu \varphi_\mu^{(v)} \right),$$

with ψ the nucleon and $\varphi_{(\mu)}^{(\alpha)}$ the meson fields, where α indicates the type of meson and μ the Lorentz component in the case of vector mesons. For isospin 1 mesons, $\varphi^{(\alpha)}$ is to be replaced by $\boldsymbol{\tau} \cdot \boldsymbol{\varphi}^{(\alpha)}$, with τ^l ($l = 1, 2, 3$) the usual Pauli matrices. The labels ps , pv , s , and v denote pseudoscalar, pseudovector, scalar, and vector coupling/field, respectively.

The one-boson-exchange potential (OBEP) is defined as a sum of one-particle-exchange amplitudes of certain bosons with given mass and coupling. The main difference with respect to the non-relativistic case is the introduction of the Dirac-spinor amplitudes. The six non-strange bosons with masses below $1 \text{ GeV}/c^2$ are used. Thus,

$$(60) \quad V_{\text{OBEP}} = \sum_{\alpha=\pi,\eta,\rho,\omega,\delta,\sigma} V_\alpha^{\text{OBE}}$$

with π and η pseudoscalar, σ and δ scalar, and ρ and ω vector particles. The contributions from the isovector bosons π, δ and ρ contain a factor $\boldsymbol{\tau}_1 \cdot \boldsymbol{\tau}_2$. In the so-called static limit, *i.e.* treating the nucleons as infinitely heavy (their energy equals the mass) the usual denominator of the interaction amplitude in momentum space, coming from the meson propagator, is exactly the same as in the non-relativistic case (since in both cases meson kinematics is relativistic). This limit is not taken in the relativistic version, noticeably in the series of Bonn potentials, and the full expression of the amplitude with the nucleon relativistic (on-shell) energies is included. As an example, let us consider one pion exchange. In the non-relativistic and static limit the corresponding local potential is reported in eq. (45). This has to be compared with the complete expression of the matrix element between nucleonic (positive energy) states [16]. In the center-of-mass frame it reads

$$V_\pi^{\text{full}} = -\frac{g_\pi^2}{4M^2} \frac{(E' + M)(E + M)}{k^2 c^2 + (mc^2)^2} \left(\frac{\boldsymbol{\sigma}_1 \cdot \mathbf{q}'}{E' + M} - \frac{\boldsymbol{\sigma}_1 \cdot \mathbf{q}}{E + M} \right) \times \left(\frac{\boldsymbol{\sigma}_2 \cdot \mathbf{q}'}{E' + M} - \frac{\boldsymbol{\sigma}_2 \cdot \mathbf{q}}{E + M} \right),$$

where E, E' are the initial and final nucleon energies. One can see that in this case some non-locality is present, since the matrix element depends separately on \mathbf{q} and \mathbf{q}' . Putting $E = E' = M$, one gets again the local version. Notice that in any case the two versions coincide on-shell ($E = E'$), and therefore the non-locality modifies only the off-shell behaviour of the potential. The matrix elements are further implemented by form factors at the NN-meson vertices to regularize the potential and to take into account the finite size of the nucleons and the mesons. In applications of the DBHF method usually one version of the relativistic OBE potential is used, which therefore implies that

a certain degree of non-locality is present. The fully relativistic analogue of the two-body scattering matrix is the covariant Bethe-Salpeter (BS) equation. In place of the NN non-relativistic potential the sum \mathcal{V} of all connected two-particle irreducible diagrams has to be used, together with the relativistic single-particle propagators. Explicitly, the BS equation for the covariant scattering matrix \mathcal{T} in an arbitrary frame can be written as

$$(61) \quad \mathcal{T}(q', q|P) = \mathcal{V}(q', q|P) + \int d^4k \mathcal{V}(q', k|P) \mathcal{G}(k|P) \mathcal{T}(k, q|P),$$

with

$$(62) \quad \mathcal{G}(k|P) = \frac{i}{(2\pi)^4} \frac{1}{(\frac{1}{2}P + \not{k} - M + i\epsilon)^{(1)}} \frac{1}{(\frac{1}{2}P - \not{k} - M + i\epsilon)^{(2)}}$$

$$(63) \quad = \frac{i}{(2\pi)^4} \left[\frac{\frac{1}{2}P + \not{k} + M}{(\frac{1}{2}P + k)^2 - M^2 + i\epsilon} \right]^{(1)} \left[\frac{\frac{1}{2}P - \not{k} + M}{(\frac{1}{2}P - k)^2 - M^2 + i\epsilon} \right]^{(2)},$$

where q , k , and q' are the initial, intermediate, and final relative four-momenta, respectively (with, *e.g.*, $k = (k_0, \mathbf{k})$), and $P = (P_0, \mathbf{P})$ is the total four-momentum; $\not{k} = \gamma^\mu k_\mu$. The superscripts refer to particle (1) and (2). Of course all quantities are appropriate matrices in spin (or helicity) and isospin indices. The use of the OBE potential as the kernel \mathcal{V} is equivalent to the so-called ladder approximation, where one-meson exchanges occur in disjoint time intervals with respect to each other, *i.e.* at any time only one-meson is present. Unfortunately, even in the ladder approximation the BS equation is difficult to solve since \mathcal{V} is in general non-local in time, or equivalently energy dependent, which means that the integral equation is four-dimensional. It is even not sure in general if it admits solutions. It is then customary to reduce the four-dimensional integral equation to a three-dimensional one by approximating properly the energy dependence of the kernel. In most methods the energy exchange k_0 is fixed to zero and the resulting reduced BS equation is similar to its non-relativistic counterpart. In the Thompson reduction scheme this equation for matrix elements between positive-energy spinors (c.m. frame) reads

$$(64) \quad \mathcal{T}(\mathbf{q}', \mathbf{q}) = V(\mathbf{q}', \mathbf{q}) + \int \frac{d^3k}{(2\pi)^3} V(\mathbf{q}', \mathbf{k}) \frac{M^2}{E_{\mathbf{k}}^2} \frac{1}{2E_{\mathbf{q}} - 2E_{\mathbf{k}} + i\epsilon} \mathcal{T}(\mathbf{k}, \mathbf{q}|P)$$

where both $V(\mathbf{q}', \mathbf{q})$ and \mathcal{T} have to be considered as matrices acting on the two-particle helicity (or spin) space, and $E_{\mathbf{k}} = \sqrt{\mathbf{k}^2 + M^2}$ is the relativistic particle energy. In the alternative Blankenbecler-Sugar [16] reduction scheme some different relativistic kinematical factors appear in the kernel. This shows that the reduction is not unique. The partial wave expansion of the \mathcal{T} -matrix can then be performed starting from the helicity representation. The corresponding amplitudes include single as well as coupled channels, with the same classification in quantum numbers JLS as in the non relativistic case and therefore their connection with phase shifts is the same. In the intermediate states of momentum \mathbf{k} only the positive energy states are usually considered (by the proper Dirac

projection operator). As in the case of the OBEP potential, again the main difference with respect to the non-relativistic case is the use of the Dirac spinors.

The DBHF method can be developed in analogy with the non-relativistic case. The two-body correlations are described by introducing the in-medium relativistic G -matrix. The DBHF scheme can be formulated as a self-consistent problem between the single-particle self-energy Σ and the G -matrix. Schematically, the equations can be written

$$(65) \quad \begin{aligned} G &= V + i \int V Q g g G, \\ \Sigma &= -i \int_F (\text{Tr}[gG] - gG), \end{aligned}$$

where Q is the Pauli operator which projects the intermediate two-particle momenta outside the Fermi sphere, as in the BHF G -matrix equation, and g is the single-particle Green's function. The self-consistency is entailed by the Dyson equation

$$g = g_0 + g_0 \Sigma g,$$

where g_0 is the (relativistic) single-particle Green's function for a free gas of nucleons. The self-energy is a matrix in spinor indices, and therefore in general it can be expanded in the covariant form

$$(66) \quad \Sigma(k, k_F) = \Sigma_s(k, k_F) - \gamma_0 \Sigma_0(k, k_F) + \boldsymbol{\gamma} \cdot \mathbf{k} \Sigma_v,$$

where γ_μ are the Dirac gamma matrices and the coefficients of the expansion are scalar functions, which in general depend on the modulus $|\mathbf{k}|$ of the three-momentum and on the energy k_0 . Of course they also depend on the density, *i.e.* on the Fermi momentum k_F . The free single-particle eigenstates, which determine the spectral representation of the free Green's function, are solutions of the Dirac equation

$$[\gamma_\mu k^\mu - M] u(k) = 0,$$

where u is the Dirac spinor at four-momentum k . For the full single-particle Green's function g the corresponding eigenstates satisfy

$$[\gamma_\mu k^\mu - M + \Sigma] u(k)^* = 0.$$

Inserting the above general expression for Σ , after a little manipulation, one gets

$$[\gamma_\mu k^{\mu*} - M^*] u(k)^* = 0,$$

with

$$(67) \quad k^{0*} = \frac{k^0 + \Sigma_0}{1 + \Sigma_v}; \quad k^{i*} = k^i; \quad M^* = \frac{M + \Sigma_s}{1 + \Sigma_v}.$$

This is the Dirac equation for a single particle in the medium, and the corresponding solution is the spinor

$$(68) \quad u^*(\mathbf{k}, s) = \sqrt{\frac{E_{\mathbf{k}}^* + M^*}{2M^*}} \begin{pmatrix} 1 \\ \frac{\sigma \cdot \mathbf{k}}{E_{\mathbf{k}}^* + M^*} \end{pmatrix} \chi_s; \quad E_{\mathbf{k}}^* = \sqrt{\mathbf{k}^2 + M^{*2}}.$$

In line with the Brueckner scheme, within the BBG expansion, in the self-energy of eq. (65) only the contribution of the single-particle Green's function pole is considered (with strength equal one). Furthermore, negative energy states are neglected and one gets the usual self-consistent condition between self-energy and scattering G -matrix. The functions to be determined are in this case the three scalar functions appearing in eq. (66). However, to simplify the calculations these functions are often replaced by their value at the Fermi momentum.

In any case, the medium effect on the spinor of eq. (68) is to replace the vacuum value of the nucleon mass and three-momentum with the in-medium values of eq. (67). This means that the in-medium Dirac spinor is “rotated” with respect to the corresponding one in vacuum, and a positive (particle) energy state in the medium has some non-zero component on the negative (anti-particle) energy state in vacuum. In terms of vacuum single nucleon states, the nuclear medium produces automatically anti-nucleon states which contribute to the self-energy and to the total energy of the system. It has been shown in ref. [30] that this relativistic effect is equivalent to the introduction of well defined TBF at the non-relativistic level. These TBF turn out to be repulsive and consequently produce a saturating effect. The DBHF gives indeed in general a better saturation point than BHF. Of course one can wonder why these particular TBF should be selected, but anyhow a definite link between DBHF and BHF + TBF is, in this way, established. Indeed, including in BHF only these particular TBF one gets results close to DBHF calculations, see, *e.g.*, [20].

Despite the DBHF is similar to the non-relativistic BHF, some features of this method are still controversial. The results depend strongly on the method used to determine the covariant structure of the in-medium G -matrix, which is not unique since only the positive energy states must be included. It has to be stressed that, in general, the self-energy is better calculated in the matter reference frame, while the G -matrix is more naturally calculated in the center of mass of the two interacting nucleons. This implies that the G -matrix has to be Lorentz transformed from one reference frame to the other, and its covariant structure is then crucial. Formally, the most accurate method appears to be the subtraction scheme of ref. [31]. Generally speaking, the EoS calculated within the DBHF method turn out to be stiffer above saturation than the ones calculated from the BHF + TBF method.

4.2.4. The V_{low} approach. The main effect of the hard core in the NN interaction is to produce scattering to high momenta of the interacting particles. It is possible to soften the hard core of the NN interaction from the start by integrating out all the momenta larger than a certain cutoff Λ and “renormalize” the interaction to an effective interaction

V_{low} in such a way that it is equivalent to the original interaction for momenta $q < \Lambda$. By construction V_{low} must give the same half of the energy shell scattering T -matrix or R -matrix $(q'|R(E_q)|q)$ as the original interaction, where E_q is the energy of the initial state at relative momentum q . This can be done in a variety of methods, among which one can mention the Renormalization Group, the low momenta Effective Theory and the Lee-Suzuky scheme. It is surely outside the scope of the present report to describe these methods and we refer to recent review and papers where they are extensively discussed and applied [32, 33]. All these possible V_{low} interactions are of course much softer, since no high momentum components are present. The short-range repulsion is replaced by the non-local structure of the interaction. It has to be kept in mind that any V_{low} is a legitimate realistic NN interaction. In fact, due to the mentioned equivalence, they fit exactly the same phase shifts up to an energy corresponding to the cutoff. The latter is taken above 300 MeV in the laboratory, corresponding to the relative momentum $q \approx 2.1 \text{ fm}^{-1}$, that is the largest energy where the data are established. This means that the data and the NN interaction are not sensitive to the details of the hard-core behavior. Indeed, for the same reason, all the V_{low} , at least their diagonal matrix elements, are almost identical up to the cutoff, provided it is not taken too large above 2.1 fm^{-1} . The fact that V_{low} is soft has the advantage to be much more manageable than a hard-core interaction, in particular it can be used in perturbative expansion and in nuclear structure calculations in a more efficient way. Again, at purely phenomenological level, a non-local interaction at short distance is perfectly legitimate as a hard-core, since the behavior of the potential at short distance is not experimentally accessible. In principle, it is only a question of representation. However, as strongly stressed in ref. [32], the required equivalence implies that, even starting from a local two-body interaction, the renormalization procedure introduces necessarily three-body forces, which has to be handled in many-body calculations. This is more apparent if V_{low} is constructed directly in the medium, in which case the procedure has some similarities with the Brueckner G -matrix construction.

If for the in-vacuum V_{low} one takes only the two-body component, one finds that nuclear matter does not saturate and actually seems to collapse towards infinite negative energy. This can be ascribed to the missing three-body forces, which should provide saturation. According to ref. [32] the off-shell effects are not the main responsible for the saturation mechanism present in the BHF theory. This is probably partly true, but one has to keep in mind that a BHF procedure without the single-particle potential, which is responsible for the presence of an off-shell energy, would dramatically overestimate the binding energy in nuclear matter.

In any case, up to now the consistent three-body force in V_{low} has not been used in nuclear matter calculations or in nuclear structure. Furthermore the renormalization procedure for a possible three-body force has not yet been worked out. Up to now the two-body part of V_{low} has been used in nuclear matter in conjunction with TBF fitted separately in three- and four-nucleon systems. If the TBF are averaged over the quantum numbers of one of the three particles, this approximate scheme seems to produce a reasonable saturation point. This is line with the fact that in BHF the repulsive part of

the same TBF has to be drastically reduced to get the correct saturation point, since the two-body interaction gives a saturation point not too far from the empirical one. If the saturation property of V_{low} and its good performance in few-body nuclear systems survive to a more consistent treatment of the renormalization procedure and the corresponding TBF, this will open a new route to the microscopic many-body theory of the nuclear medium. This point needs still to be clarified.

4.2.5. Trying a link to QCD: the chiral symmetry approach. One of the main ambitions of nuclear physics is to connect the low energy nuclear-physics phenomena with the underlying more fundamental theory of strong interaction, *i.e.* QCD and the standard model, based on quark and gluons degrees of freedom, together with the Weinberg-Salam-Glashow theory of weak interaction. This is quite difficult because the whole hadron sector is in the non-perturbative regime, due to confinement. A possible strategy is the systematic use of the symmetries embodied in the hadronic QCD structure. The main symmetry that still remains visible in the confined matter is the chiral symmetry, the symmetry that QCD possesses if the bare quark masses are put equal to zero. The symmetry is spontaneously broken in the confined phase, *i.e.* in hadronic matter, but, according to the general theorem by Goldstone, a zero-mass boson should be present. This is indeed the π meson, that in the limit of zero quark mass should have also zero mass. This is the main signature of the underlying chiral symmetry. For non-strange matter, only u and d quarks are relevant, and they indeed are expected to have a mass of few MeV. This small explicit breaking of chiral symmetry results in the physical mass of the pion, that is the lightest meson, even if it is not small at the energy scale of many nuclear phenomena. All that suggests to treat the pion degrees of freedom explicitly and to describe the short-range part by structureless contact terms. Along this line Weinberg [34-36] proposed a scheme for the expansion of the NN interaction in the ratio Q/M between the relative momenta and the nucleon mass. The pion exchange term is still treated explicitly, and is considered the lowest-order (LO) term of the expansion. Then contact terms are added and a power counting scheme is introduced. These terms can be considered as expansion of the nucleonic loops, that are the ones that give the largest contributions. At the same time the contact terms can be considered as counterterms to regularize and renormalize the divergences coming from the loop integrals appearing as the order of the expansion increase. This procedure of renormalization is common in quantum field theory, like Quantum Electrodynamics (QED). In renormalizable field theory the number of counterterms are finite and their strengths are fixed by demanding that some quantities have their physical values. In QED they are fixed by imposing the physical values of the electron charge and mass. Then the perturbation expansion terms are all finite. In the case of nuclear physics one demands that the phase shifts in some channels and specific energies are reproduced correctly. However in this case at any order new counterterms must be introduced. This renormalized expansion, the Chiral Perturbation Expansion (ChPE), can be used to construct NN interactions that are of reasonably good quality [33,37] in reproducing the two-body data. They contain a set of parameters, and therefore they are still models, whose connection with QCD is still a little

loose. To tighten the QCD link a non-perturbative regularization and renormalization has been tried, where the results are shown numerically to be independent of the single cut-off used in the renormalization procedure. This property assures a clear-cut separation between the long-range pion exchange processes and the unresolved short-range part of the interaction. Along this line progress has been made recently [38], but still a reasonable realistic interaction has not been constructed.

To summarize, the ambitious program of connecting the NN interaction with the underlying QCD theory is still a work in progress, but the connection is becoming stronger and solid. It requires the development of a quite complex formalism, that is hoped will be able to shed light on the origin of the NN interaction, including few-body interactions.

5. – Neutron matter at very low density. An exercise in many-body theory

The low density region of pure neutron matter, as present in the inner crust of Neutron Stars, is less trivial than one could expect at a first sight since the neutron-neutron scattering length is extremely large, about -18 fm , due to the well-known virtual state in the 1S_0 channel, and therefore even at very low density one cannot assume the neutrons to be uncorrelated. These considerations have also stimulated a great interest in the so-called unitary limit, *i.e.* the limit of infinite (negative) scattering length of a gas of fermions at vanishing small density. A series of works [39-41] have been presented in the literature based on various approximations and a recent Monte Carlo calculation [42] on a related physical system has shown that the unitary limit can present a quite complex structure, involving both fermionic and bosonic effective degrees of freedom, which has still to be elucidated. Variational [43] and finite-volume Green's function Monte Carlo calculations [44] for neutron matter at relatively low density have shown that the EoS, in a definite density range, can be written as the free-gas EoS multiplied by a factor ξ , which turns out to be close to 0.5. This is actually what one could expect in the unitary limit regime, since no scale exists in this case, except the Fermi momentum. Monte Carlo calculations [39-41] with schematic forces in a regime close to the unitary limit have found a factor $\xi \approx 0.44$. The connection between the variational results and the unitary limit has been studied in ref. [45] by means of effective theory methods.

5.1. A single G-matrix problem. – Since the scattering length a and effective range r_0 in the 1S_0 channel of the neutron-neutron interaction differ by about a factor 6, there is no density interval where the unitary limit can be considered strictly valid. However, in the range $r_0 < d < |a|$, where d is the average inter-particle distance, the physical situation should be the “closest” possible to the unitary limit. This range corresponds to Fermi momentum range $0.4 \text{ fm}^{-1} < k_F < 0.8 \text{ fm}^{-1}$, which corresponds to densities between about 1/50 and 1/5 of the saturation density. Let us choose as realistic nucleon-nucleon potential the Argonne v₁₈ interaction [46]. The first finding is that the three-body forces of the Urbana model, adjusted to reproduce the correct saturation point [47], give a contribution which is less than 0.01 MeV, and therefore we can neglect three-body forces to a good approximation. The second finding is that the single-particle potential is very

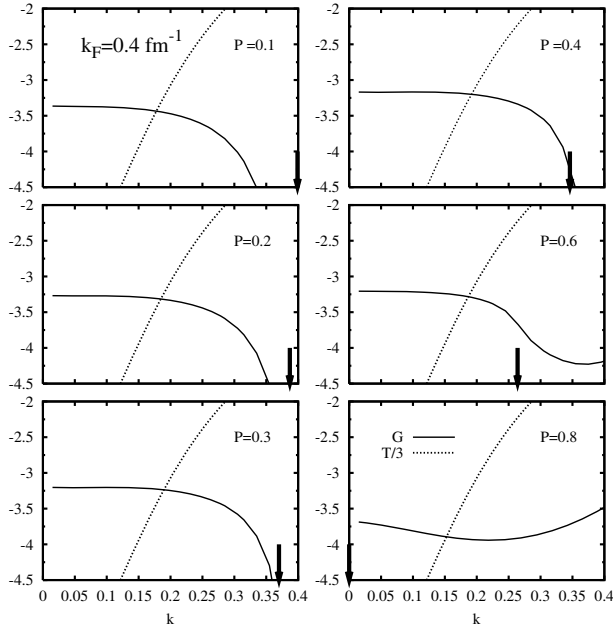


Fig. 7. – Plots of the free K -matrix (T), divided by 3 for convenience, in comparison with the in-medium K -matrix (G), at the indicated Fermi momentum, for different total momentum p , as a function of the relative momentum k . All the momenta are in fm^{-1} . The results are for the 1S_0 channel in pure neutron matter. The arrow indicates the maximum momentum needed in the calculation of the EoS. See ref. [48] for details.

small in this density range, and its effect can be neglected. It affects the energy per particle less than 0.1 MeV.

It is enlightening to compare the in-medium G -matrix with the free T -matrix in the 1S_0 channel, reported in fig. 7, taken from ref. [48], at selected values of the relative momentum k and total momentum P (in fm^{-1}) at the Fermi momentum $k_F = 0.4 \text{ fm}^{-1}$. For sake of comparison the free T -matrix has been divided by 3. Due to Galilei invariance, the free K -matrix is independent of P . Despite the Fermi momentum is quite small, a drastic difference between the two scattering matrices is apparent, not only in shape but also in absolute value. The Pauli operator effect is enhanced in this particular channel since the virtual state is suppressed in the medium. This illustrates the dramatic difference that can exist between the in-medium effective interaction and the free bare interaction. The large enhancement at the Fermi momentum and for small total momentum P is due to the pairing singularity. The BBG expansion relies on the basic idea that the contributions of the diagrams of the expansion decrease with increasing number of hole-lines which are included. Although the BBG scheme is essentially a low density expansion, it has been found [49, 50] that the convergence is valid up to densities as high as few times saturation density in symmetric nuclear matter and even better in neutron

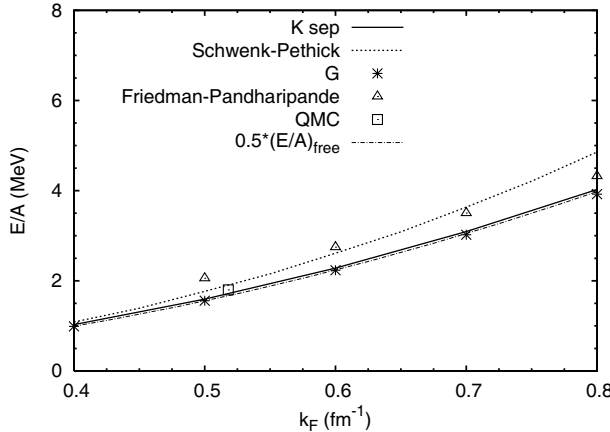


Fig. 8. – Neutron matter EoS calculated within the BBG method (label G), within the variational method of ref. [43] (triangles), according to the estimate of ref. [45] (dotted line) and with the separable representation of the G -matrix (label K sep). The dash-dotted line is one half of the free-gas EoS. The square represents the result of the quantum Monte Carlo calculation of ref. [51].

matter. It is then likely that at the low densities we are considering this convergence should be even faster. This is indeed confirmed by explicit numerical calculations [48], and indeed the third finding is that the three hole-line contribution is at most 0.15 MeV at the highest density considered and rapidly decreasing to vanishingly small values as the density decreases. Finally, the fourth finding is that higher partial waves give a negligible contribution both at the two hole-lines (Brueckner) and three hole lines level. These four findings, all together, point out that the many-body problem of neutron matter at low density is reduced to a single G -matrix problem, *i.e.* to the calculation of the 1S_0 G -matrix.

5.2. The “exact” EoS. – The two EoS, one calculated within the full BBG expansion up to the three hole-lines contributions and the other calculated with the single 1S_0 G -matrix, are compared in fig. 8, taken from ref. [48]. They are mainly indistinguishable. The energy per particle is very close to $1/2$ of the kinetic energy. It turns out that the G -matrix is fully determined by the scattering length and effective range. One can construct a rank-one separable interaction [48]

$$(69) \quad (k'|v|k) = \lambda \phi(k')\phi(k),$$

with a simple form factor

$$(70) \quad \phi(k) = 1/(k^2 + b^2),$$

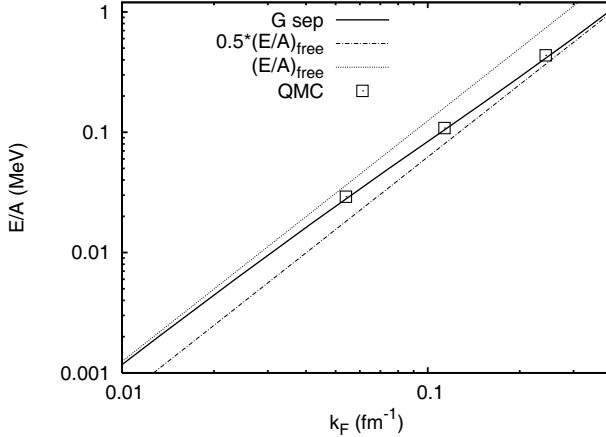


Fig. 9. – Neutron matter EoS calculated with the separable representation of the G -matrix, in comparison with the free Fermi gas EoS and one half of it. The squares represent the results of the quantum Monte Carlo calculation of ref. [51].

where the parameters λ and β are determined by imposing that the scattering length and effective range are reproduced. Then the G -matrix can be obtained analytically and the corresponding EoS by simple numerical integration. The procedure is equivalent to an effective theory with smooth cut-off and its accuracy is shown in fig. 8. The calculation can be extended to very small density, as reported in fig. 9, where one can see that the EoS approaches the one for a free gas, as it must be for $k_F < 1/|a|$. In both figs. 8, 9 the squares indicate the results of the Monte Carlo calculations of ref. [51]. They agree fairly well with the BBG results up to the density where the Monte Carlo calculation can be performed.

What is missing in the BBG calculations is the pairing correlations. The contribution to the EoS of pairing is not expected to be relevant, but it is important to know the value of the gap for many phenomena in Neutron Stars and as an indication for finite nuclei.

6. – Going to nuclear structure

One of the basic questions that was posed since the first developments of nuclear physics is to what extent the properties of the bulk nuclear medium can be transferred to finite nuclei or to what extent they influence the general trends that are observed in nuclear structure studies. Otherwise stated, is there a link between the nuclear medium properties and the structure of finite nuclei? The simplest scheme where this link is exploited is the liquid drop model. As already illustrated, in this semi-classical model the assumed constant saturation energy per particle is corrected by the surface and Coulomb energy to explain the binding energy of finite nuclei. In more sophisticated variants of the model other terms are introduced, but in any case a set of parameters are introduced which cannot be derived from the theory. Furthermore, quantal characteristics like shell

effects are not included. We will briefly describe some of the methods that have been used and developed to understand more deeply this possible link and, at the same time, to devise practical and general theoretical scheme for nuclear structure.

6·1. The Thomas-Fermi approximation and implementations. – Historically, the first method to relate the properties of finite quantal systems to the corresponding homogeneous system was the semi-classical Thomas-Fermi scheme. It was devised to calculate the ground-state properties of large atoms and molecules in the case of independent particle limit. In fact, even in this limit, the quantal calculations can become quite complex. The original form of the scheme is equivalent to take the zero-order term in the expansion in \hbar of the density matrix for the independent particle wave function, but it can be easily derived by assuming that the system is locally equivalent to a free Fermi gas at the local density and local potential. We remind here some features of the approximation that are useful for the development of the presentation. In its simplest version it can be formulated within the density functional method, *i.e.* assuming that the energy of the system can be written as a functional of the density $\rho(\mathbf{r})$

$$(71) \quad E_{TF} = T_F(\{\rho\}) + V_c(\{\rho\}) + V_{pp}(\{\rho\}),$$

where T_F is the kinetic energy contribution, V_c the external potential and V_{pp} the particle-particle interaction. In case of atoms, V_c is the energy due to the central Coulomb potential and V_{pp} is the electron-electron Coulomb interaction energy

$$(72) \quad \begin{aligned} T_F(\{\rho\}) &= \frac{3}{5} \int d^3r E_F(\rho(\mathbf{r})) \rho(\mathbf{r}); \\ V_c(\{\rho\}) &= -Z \int d^3r' v(r) \rho(\mathbf{r}'), \\ V_{pp}(\{\rho\}) &= \int d^3r \int d^3r' v(|\mathbf{r} - \mathbf{r}'|) \rho(\mathbf{r}) \rho(\mathbf{r}'), \end{aligned}$$

with Z the charge of the nucleus, $v = 4\pi e^2/r$ the Coulomb potential between two electrons (of charge e) and E_F the Fermi energy for a free gas at the density $\rho(\mathbf{r})$. The Euler-Lagrange equation corresponding to the minimization of this functional with the constraint of a fixed number of particles is

$$(73) \quad E_F(\rho(\mathbf{r})) - Zv(r) + \int d^3r' v(|\mathbf{r} - \mathbf{r}'|) \rho(\mathbf{r}') = \mu,$$

where μ is the Lagrange multiplier, that has the meaning of chemical potential. Notice that μ is a constant, independent of the position. The solution of this equation gives the density and then the energy of the ground state. A way of solving this equation is to apply the Laplacian differential operator and use the Poisson equation $\Delta V_C = -4\pi e^2 \rho(\mathbf{r})$, where V_C is the last term at the left-hand side of eq. (73), that is the potential produced by all electrons at \mathbf{r} . This gives the familiar differential equation for the

density of the Thomas-Fermi scheme in its simplest form. We will not discuss the many refinements of the approximation that have been developed, to include, *e.g.*, the exchange interaction, but rather we consider the Thomas-Fermi approximation in the nuclear case. The physical situation is rather different. There is no central interaction, and the binding must come from the NN interaction. The latter is not long range, like the Coulomb potential, but it is short range, even zero range if we adopt a Skyrme effective interaction. Then eq. (73) has no solution, except in the trivial case of a homogeneous system. To get any sensible result for a nucleus one has to go to the next order in the expansion in \hbar of the kinetic energy term in the functional. This introduces gradient terms [52]. To order \hbar only one term contributes, proportional to $(\nabla\rho)^2$. With the inclusion of this term, a surface can develop and the nuclear Thomas-Fermi approximation can describe the density profile of a nucleus.

This discussion makes clear that in the nuclear case the kinetic term must be treated at a different order in the expansion in \hbar and at a different level of approximation. The full quantal treatment of the kinetic term must be considered to construct any accurate nuclear energy functional.

Despite that, the Thomas-Fermi approximation, or more advanced expansions in \hbar can be useful. In fact the Thomas Fermi approximation and its implementations are expected to describe the smooth part, *e.g.*, of the density of states, leaving outside of their possibility the description of the shell effects, that are a pure quantal effect. Indeed the expansion in \hbar of many quantities is actually asymptotic, and the quantal effects depend non-analytically on \hbar . This property of the \hbar expansions can be used to evaluate the shell effects in the so-called microscopic-macroscopic approach. The difference between the exact quantal calculations and the results of the expansion is taken as an estimate of the shell effects. Implicitly, it is assumed that shell effects are essentially the same in the independent particle model as in the fully correlated system. The smooth part, obtained from the liquid drop or droplet models, are expected to include in an effective way the correlation contribution. Along these lines, recently in ref. [53] the Kirkwood \hbar expansion to fourth order has been used to estimate the shell effect by comparing the results with the quantal calculations. This method, as similar ones based on \hbar expansions, are methods alternative to the Strutinski smoothing method [54].

A step further along these lines is the construction of general effective energy density functionals that are devised to include all the correlations in an effective way and without any \hbar expansion. Although they are necessarily in part phenomenological, *i.e.* they contain a certain number of parameters, the ambition is to relate their characteristics in terms of the properties of the nuclear medium. On the other hand, if they are treated at purely phenomenological level, they turn out to be extremely accurate. These items will be discussed in the next section.

6.2. The density functional method. – A fully quantal microscopic method to connect the nuclear medium properties and the structure of finite nuclei is to introduce an effective NN force, whose parameters are fitted, on the one hand, to reproduce the nuclear matter EoS, as derived phenomenologically and microscopically, and, on the other hand, to

reproduce binding energy and radii of a representative set of nuclei. This is the scheme of the Skyrme forces. These effective forces have been developed along the years with increasing success and have been widely used in nuclear structure and spectroscopic studies. It is surely not possible to review the enormous literature on the subject, and we limit here to sketch the main features of the method. The simplest Skyrme force can be written, for symmetric system as

$$(74) \quad V = t_0 \rho(\mathbf{r}) \delta(\mathbf{r} - \mathbf{r}') + t_3 \rho(\mathbf{r})^2 \delta(\mathbf{r} - \mathbf{r}') \delta(\mathbf{r}' - \mathbf{r}''),$$

where ρ is the nucleon number density at the point \mathbf{r} and the parameters t_0 (negative) and t_3 (positive) are adjusted to reproduce the saturation point of nuclear matter, where the force depends only on the constant total density. They correspond to effective two-body and three-body interactions, respectively. Besides these parameters, an effective mass m^* is also usually introduced in the kinetic part, so that the total Hamiltonian can be written as

$$(75) \quad H = T + V, \quad T = -\frac{\hbar^2}{2m^*} \nabla \delta(\mathbf{r} - \mathbf{r}') \nabla.$$

Then the force is used to calculate the ground state of nuclei in the Hartree-Fock (mean field) approximation, thus establishing an indirect link between nuclear matter and finite nuclei. Much more elaborated forces have been developed, in which density gradient terms and asymmetry-dependent terms are introduced. Then the number of parameters increases, but the precision of the fit on the overall mass table can be really impressive, see, *e.g.*, refs. [55, 56]. More elaborated terms involving higher degrees of the density derivatives can be still introduced, and the accuracy of the fit can be astonishingly good [57, 58]. However, along this line, the connection with NN bare forces and nuclear matter EoS is gradually lost, since the additional terms have a form loosely connected with the NN interaction and are all vanishing in uniform matter.

Another method that tries to keep more closely the connection with the properties of the bulk nuclear medium is based on the Kohn and Sham (KS) [59-65] approach, first devised for atomic, molecular and solid systems and developed also for nuclear system. Let us consider the microscopic bulk EoS, as reported in fig. 6, extended to asymmetric nuclear matter. This can be taken as the bulk contribution to the Energy Density Functionals (EDF). For numerical applications it can be written in a polynomial form. The functional must be then implemented mainly by three additional contributions. The first one is the Coulomb energy, that can be calculated with different degrees of sophistication, *e.g.*, by including the exchange and short-range parts. The second one must take into account the presence of the surface, that in nuclei is sharply localized, within a length of the order of 1 fm, and therefore cannot be described only by the bulk part. The additional contribution has to be localized at the surface, and the simplest way to do so is to introduce density gradient terms or non-local short-range convolution terms. The surface terms are connected to the surface tension of nuclear matter, because, in the macroscopic limit, they modify the surface energy of the system. Finally, it is mandatory

to add a spin-orbit term, since it strongly affects the single-particle level scheme and it is mandatory in order to reproduce the shell sequence (*i.e.* the “magic numbers”). The spin-orbit interaction is roughly proportional to the gradient of the single-particle potential, and therefore it is also localized at the surface. The strength of this term is severely constrained by phenomenology, but it has still some degree of uncertainty. It is desirable to keep the number of surface and spin-orbit terms to a minimum, since they introduce additional phenomenological parameters. It is one of the ambitions of the energy density functional method to get these parameters from microscopic many-body theory, but in order to get a high-precision fit to the wide set of nuclear binding and radii throughout the mass table they must be fine tuned beyond the possibility in accuracy of any microscopic theory. The possibility still remains to have a guidance to their values within a reasonable accuracy and to get a deeper understanding of their microscopic origin. This program has still to be developed.

Following the above considerations, the EDF can be written

$$(76) \quad E = T_0 + E^{s.o.} + E_{\text{int}}^{\infty} + E_{\text{int}}^{FR} + E_C.$$

For the surface term, following ref. [66], one can take a simple finite-range term

$$(77) \quad E_{\text{int}}^{FR}[\rho_n, \rho_p] = \frac{1}{2} \sum_{t,t'} \int \int d^3r d^3r' \rho_t(\mathbf{r}) v_{t,t'}(\mathbf{r} - \mathbf{r}') \rho_{t'}(\mathbf{r}') \\ - \frac{1}{2} \sum_{t,t'} \gamma_{t,t'} \int d^3r \rho_t(\mathbf{r}) \rho_{t'}(\mathbf{r}),$$

with $t = \text{proton/neutron}$ and $\gamma_{t,t'}$ the volume integral of $v_{t,t'}(r)$. The subtraction in (77) is made in order not to contaminate the bulk part, determined from the microscopic infinite matter calculation E_{int}^{∞} . Finite-range terms have been used in, *e.g.*, [67-69], generalizing usual Skyrme functionals. In refs. [66, 70], for the finite-range form factor $v_{t,t'}(r)$ a simple Gaussian ansatz: $v_{t,t'}(r) = V_{t,t'} e^{-r^2/r_0^2}$ was taken, so that a minimum of three open parameters was introduced: $V_{p,p} = V_{n,n} = V_L$, $V_{n,p} = V_{p,n} = V_U$, and r_0 .

In eq. (76), E_{int}^{FR} and E_C are the spin-orbit and Coulomb parts, respectively. More details on their determination can be found in refs. [66, 70]. The first piece T_0 in eq. (76) corresponds to the uncorrelated part of the kinetic energy and within the KS method it is written as

$$(78) \quad T_0 = \frac{\hbar^2}{2m} \sum_{i,s,t} \int d^3r |\nabla \psi_i(\mathbf{r}, s, t)|^2,$$

where the functions $\psi_i(\mathbf{r})$ form an auxiliary set of A orthonormal single-particle wave functions, A being the number of particles, and the density is assumed to be given by

$$(79) \quad \rho(\mathbf{r}) = \sum_{i,s,t} |\psi_i(\mathbf{r}, s, t)|^2,$$

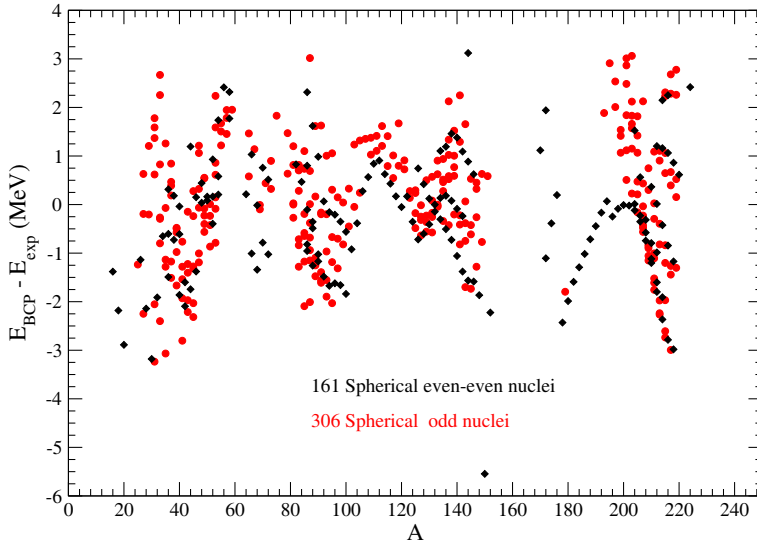


Fig. 10. – Energy differences as a function of mass number for a set of 161 spherical nuclei (black diamonds) and 306 spherical odd nuclei (red full circles).

where s and t stand for spin and iso-spin indices. At each point \mathbf{r} the bulk term equals the nuclear matter EoS at the corresponding local density (and asymmetry). Then, upon variation to minimize the EDF, one gets a closed set of A Hartree-like equations with an effective potential, the functional derivative of the interaction part with respect to the local density $\rho(\mathbf{r})$. Since the latter depends on the density, and therefore on the ψ_i 's, a self-consistent procedure is necessary. The equations are exact if the exact EDF would be known. The existence of the latter is proved by the Hohenberg-Kohn (HK) theorem [71], which states that for a Fermi system, with a non-degenerate ground state, the total energy can be expressed as a functional of the density $\rho(\mathbf{r})$ only. Such a functional reaches its variational minimum when evaluated with the exact ground-state density. In practice of course a reliable approximation must be found for the otherwise unknown density functional, taking inspiration from physical considerations and microscopic input, as discussed above. It has to be stressed that in the KS formalism the exact ground-state wave function is actually not known, the density being the basic quantity. It has also to be noticed that in the standard KS scheme, the kinetic energy term includes the bare nucleon mass, but variants with an effective mass are possible (to incorporate the correlated part of the kinetic energy).

As an illustration of the method, in fig. 10, taken from ref. [70], is reported the difference in total binding energy between the calculated and the experimental values for a wide set of spherical nuclei. The parameters of the functional have been fixed by fitting a set of deformed nuclei, both normal and super-heavy (functional BCP). The choice of fitting first deformed nuclei is suggested by the consideration that these nuclei

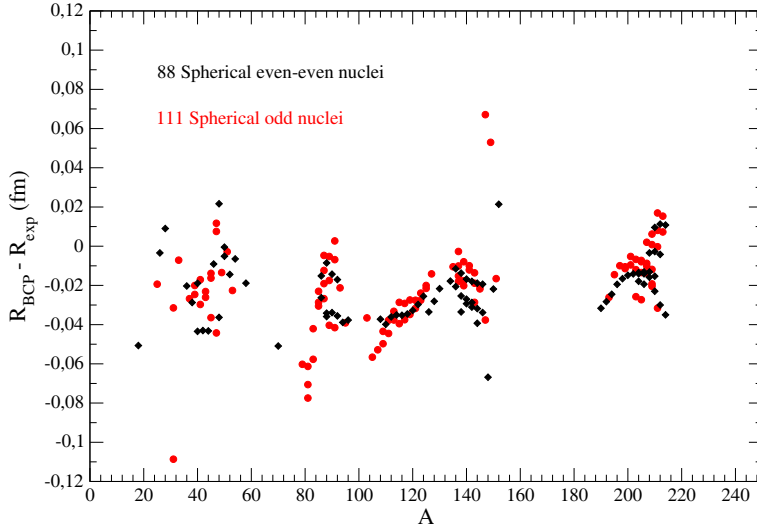


Fig. 11. – Differences of radii are shown as a function of mass number for a set of 88 spherical nuclei (black diamonds) and 111 spherical odd nuclei (red full circles).

should be better described by mean field, while spherical nuclei need corrections due to zero-point motion in the ground state, *e.g.*, RPA correlations in the ground state. The mean error in binding energy in the fit of deformed nuclei is about $\sigma_E = 0.52$ MeV, while the discrepancy for the spherical nuclei, where the functional was fixed and no fit was any more performed, is about $\sigma_E = 1.2$ MeV. In fig. 11 the corresponding deviations for the root mean square radii are reported for the spherical nuclei.

The performance is comparable with the best Skyrme forces, like the Gogny D1S [72], but of lower quality than the one from HFB calculations of, *e.g.*, refs. [55, 56]. It must be stressed again that the functional of eq. (76) has been developed by introducing a minimal set of finite-size terms, *i.e.* surface and spin-orbit terms, in addition to the bulk part fixed once for ever from microscopic nuclear matter EoS. In this way one can clearly separate the bulk and surface contribution to the binding and the radius in finite nuclei and establish a link between the properties of the nuclear medium (EoS and the bulk symmetry energy) and the structure of finite nuclei. It would be interesting to further analyze this link on the basis of an extended set of results.

Finally it is worth mentioning that an additional term in the functional should be included, the so-called “Wigner term” [55], that introduces an additional binding for symmetric nuclei, but rapidly vanishes as the nucleus becomes asymmetric. In a purely phenomenological approach it has a parametrical form of the type [55]

$$(80) \quad E_W = V_W \exp \left[-\lambda \left(\frac{N-Z}{A} \right)^2 \right] + V'_W |N-Z| \exp \left[- \left(\frac{A}{A_0} \right)^2 \right]$$

and it can be ascribed to neutron-proton correlation/pairing, that indeed tends to disappear as soon as neutrons and protons occupy different shells. This is expected to produce a strong improvement in the overall quality of the fit. Again, it is an ambition of the microscopic approach to calculate, at least approximately, the values of the parameters appearing in this expression, following their physical interpretation [55, 56].

7. – Nuclear Physics and Neutron Star structure

In this section the structure of NS will be examined on the basis of the microscopic many-body theory of homogeneous matter and of nuclei that has been developed up to now. I will proceed again starting from the external low density part down to the inner core. I will try to stress the role of nuclear physics as well the possible observational data that can possibly check the predictions of the theory.

The outer crust has been already discussed in some detail, and therefore I will begin with the inner crust.

7.1. The Neutron Star inner crust. – We have seen that the crust of Neutron Stars is the place in the Universe where the most asymmetric nuclei are present in a stable manner. The reason is of course the existence of the electron gas that is surrounding the nuclei and prevents their beta decay due to the Pauli blocking. In the inner crust also a neutron gas exists, but at not too high density it is possible to separate out, at least approximately, the nucleus at the center of the lattice cell. In this way one can picture the inner crust as a lattice of nuclei surrounded by a neutron gas (besides the electron gas). These nuclei are therefore unstable even with respect to the strong interaction (neutrons are “dripping” from them), but they are in equilibrium with the surrounding neutron gas. To illustrate this point, in fig. 12 are reported the results of the calculations in ref. [73], where the neutron density profile in the WS cell is compared, at different density, with the corresponding profile of a nucleus with the same atomic number and a mass number equal to the number of nucleons inside the radius of the “blob” (approximately estimated). They are evaluated with the same functional, and are stable with respect to strong interaction. One observes the formation of the neutron gas outside the “nucleus” at the center of the WS cell as the density increases. Of course these nuclei would be strongly unstable with respect to the weak interaction. Beyond the reported maximum density, it is not possible any more to find finite nuclei corresponding to the “blob” at the center of the WS cell, because they are unstable even with respect to strong interaction. Then it is not any more possible to distinguish the “blob” as a nucleus separated from the surrounding neutron gas.

The structure of all these WS cells can be studied solely on the basis of a strong extrapolation of the theoretical methods, in particular of the various EDF, developed and checked along the available mass table. Unfortunately, despite all EDF must agree, within a certain accuracy, for the nuclei that can be produced in the laboratory, their predictions on the nuclei of such a large asymmetry are often diverging. This indicates that we are still far from having under control the microscopic theory of the asymmetry dependence

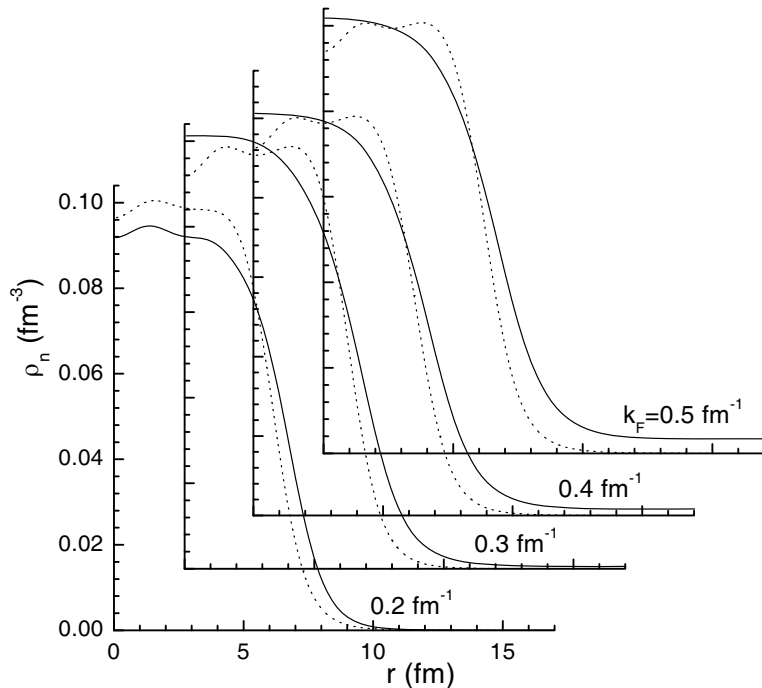


Fig. 12. – Neutron density profile of the nuclei at the upper edge of the inner crust of a neutron star. The dotted lines indicate the corresponding neutron density profile of a nucleus with the same atomic and mass numbers of the “cluster” of matter at the center of the Wigner-Seitz cell.

of the nuclear medium properties. This uncertainty reflects into the uncertainty of the Neutron Star crust, and the discrepancy extends to the region of higher density, where it is not possible to separate any more a definite nucleus at the center of the cell, until the transition to homogeneous matter occurs. As illustration in table I are reported the

TABLE I. – *Atomic number Z and radius R_c of the WS cell as a function of density. For the meaning of the different columns, see the text.*

k_F (fm $^{-1}$)	Z				R_c (fm)		
	P1	P2	P3	NV	P1	P2	P3
0.6	58	56	56	50	37.51	36.85	36.92
0.7	52	46	46	50	32.02	30.31	30.27
0.8	42	40	40	50	26.90	25.97	25.97
0.9	24	20	20	40	20.26	18.34	18.39
1.0	20	20	20	40	16.69	16.56	16.56
1.1	20	20	20	40	14.99	15.05	15.05
1.2	20	20	20	40	13.68	13.73	13.74

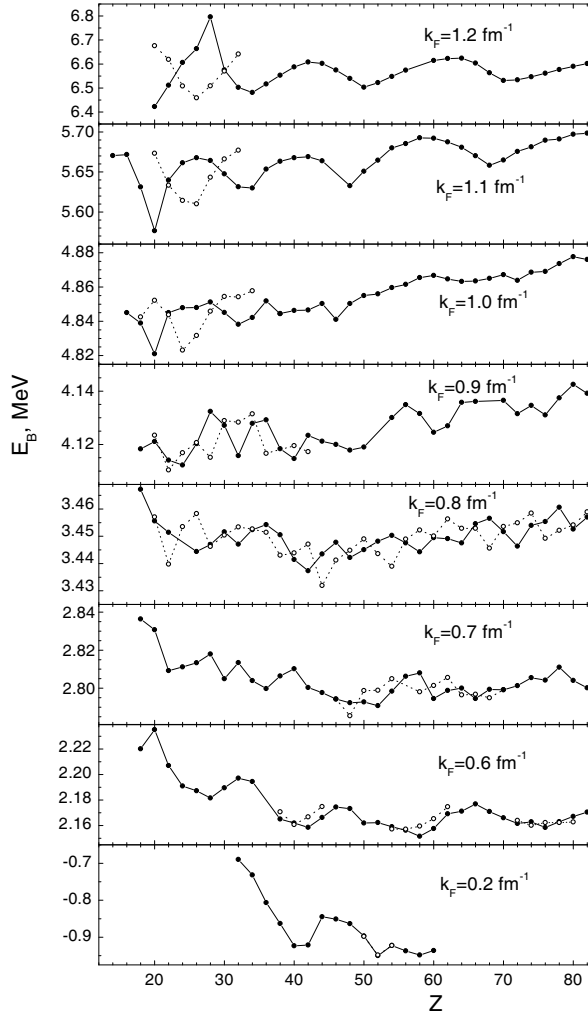


Fig. 13. – Energy per particle as a function of the atomic number in the Wigner-Seitz cell. The minimum corresponds to the actual configuration of the crust at the given density. The dotted lines indicate the results for a different choice of the boundary conditions at the edge of the cell, see ref. [75]. The discrepancy between the full and dotted lines is a measure of the uncertainty in the Wigner-Seitz approximation.

values of the atomic numbers of nuclei in the inner crust calculated in the seminal paper by Negele and Vautherin [74] and with a different functional [75]. The latter includes also the pairing correlations with three different strengths (P1, P2 and P3). The reason of these type of discrepancies remain to be clarified, but it has to be stressed that the position of the minimum in the energy as a function of the atomic number is quite delicate because it can often happen that different local minima are competing among

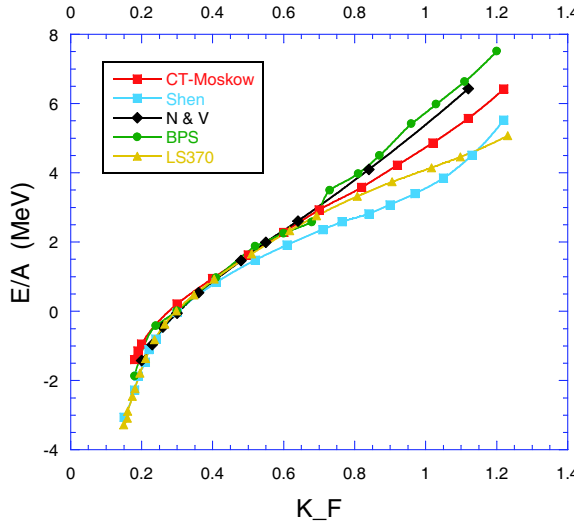


Fig. 14. – The inner crust EoS in different models. The one labeled CT-Moskow is from ref. [75], that is discussed in the text. The label LS370 indicates the Lattimer and Swesty EoS [76] with a particular value of the incompressibility. The other EoS are specified in the text.

each other. In the table are reported also the values of the Wigner-Seitz cell radius, that turns out to be a less sensitive quantity. It must be pointed out that these discrepancies persist at lower density, down to the drip point and slightly below, as systematically explored in ref. [9] for a wide set of Skyrme forces and relativistic mean-field functionals. To illustrate the difficulty and uncertainty in these calculations, in fig. 13 are reported typical energy curves for the WS cell as a function of the atomic number [75]. Besides the apparent competition among different anergy minima, it has to be noticed the tiny variation of the binding energy. The accuracy needed to predict the absolute minimum is of the order of 5–10 keV per particle, which is at the limit of the performance of the best EDF, and surely the extrapolation to so asymmetric matter is not yet under control.

In fig. 14 is reported the equation of state of the inner crust starting from the drip density up to the density where the transition to homogeneous matter is expected to occur. For comparison, the corresponding EoS obtained with other methods are also reported. The Lattimer and Swesty scheme [76] is based on the liquid drop model, the Shen EoS [77] is obtained within a relativistic mean-field functional and finally the EoS from seminal paper of ref. [74] is based on a non-relativistic Skyrme force. The results indicate a spread of results at the higher density, where however the system probably enters inside the “pasta phase”. It has to be stressed that the contribution of the nuclear medium to the EoS is increasing at increasing density, and become dominant at the lower edge of the inner crust.

To illustrate the relevance of the shell effects in fig. 15 we show the sequence of (Z, N) values in the crust values obtained with the BCP functional discussed in subsect. 6.2

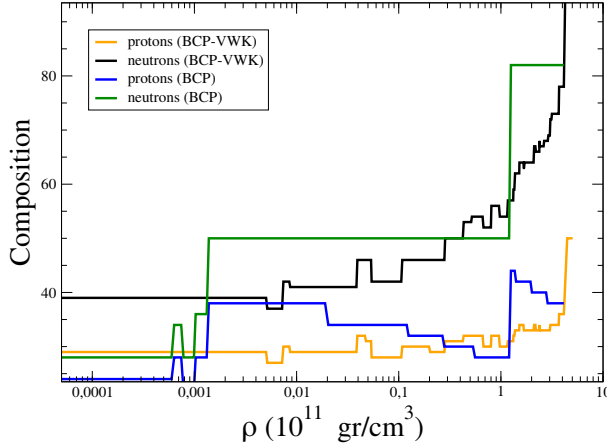


Fig. 15. – The total neutron and proton composition of the Wigner-Seitz cell in the inner crust of NS. The lines labeled VWK correspond to Thomas-Fermi approximation with \hbar^2 corrections.

in the fully quantal calculation and in the semi-classical approximation (Thomas-Fermi with \hbar^2 corrections). In any case, since the structure of these nuclei cannot be studied in laboratory, one has to look for observational data on Neutron Stars that are sensitive to their properties. The main physical parameters of the crust is the values of the atomic number of the nuclei in the lattice as a function of density and the lattice spacing. Other quantities, like the shear modulus or the compressibility are functions of these

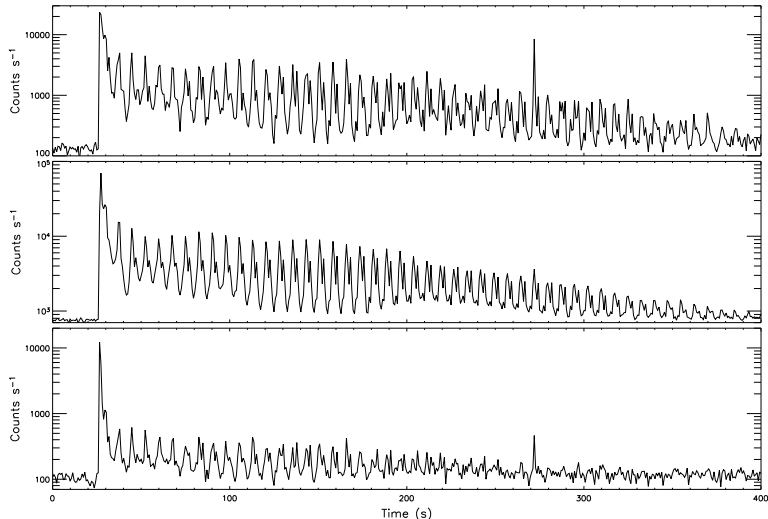


Fig. 16. – Light curves in the tail of a hyperflare from the SGR 1806-20. Observations and analysis of ref. [81].

parameters on the basis of well known properties of Coulomb lattices. In fact, even in the inner crust, the effect of the neutron gas on these quantities is negligible. The observation of NS oscillations during flares of X-ray or gamma ray emission in accreting process or in magnetar quakes can be a possibility of studying the structure of the crust. These observations are now numerous [78-81]. If in the oscillations the crust is decoupled from the core, the spectral analysis of these data can be used to constrain the shear modulus and, consequently, the density dependence of the symmetry energy [82]. These types of analysis are partly model dependent, but they open a window on the possibility of studying, even if in a very indirect way, the nuclear medium for very high asymmetry at and below saturation density. As illustration we report in fig. 16 the luminosity oscillations discovered in ref. [81] in the tail of a hyperflare of SGR 1806-20. Within the sequence of rotational pulses one can notice the modulations due to the NS oscillations. The three panels correspond to three different bands of the radiation frequency.

7.2. The Neutron Star core and mass-radius relationship. – In the outer core the composition of matter is determined by the nuclear matter EoS, more precisely by the density dependence of the symmetry energy, because beta equilibrium must be imposed to neutrons, protons, electrons and muons. This requires the chemical potential to satisfy relation (3), plus the equality between electron and muon chemical potentials. In the core the muons can have some relevance, especially at the higher density, while in the crust they can be neglected. At the same time incompressibility of symmetric matter fixes the stiffness of the EoS. It is the interplay between the symmetric matter incompressibility and the rise of the symmetry energy with density that finally determines the NS matter EoS, *e.g.*, if it is stiff or soft. This EoS must be then joined with EoS of the crust. The density profile of the NS is obtained from this overall EoS. In fact, a NS is bound by gravity, and it is kept in hydrostatic equilibrium only by the pressure produced by the compressed nuclear matter. It is then apparent that the nuclear matter EoS is the main medium property that is relevant in this case, as can be seen in the celebrated Tolman-Openheimer-Volkoff [83,84] equations, valid for spherically symmetric NS

$$(81) \quad \begin{aligned} \frac{dP}{dr} &= -G \frac{\varepsilon m}{r^2} \left(1 + \frac{P}{\varepsilon}\right) \left(1 + \frac{4\pi P r^3}{m}\right) \left(1 - \frac{2Gm}{r}\right)^{-1}, \\ \frac{dm}{dr} &= 4\pi r^2 \varepsilon, \end{aligned}$$

where G is the gravitational constant, P the pressure, ε the energy density, and r the (relativistic) radius coordinate. To close the equations we need the relation between pressure and density, $P = P(\varepsilon)$, *i.e.* just the EoS. In the Newtonian limit the energy density is just the mass density and in each parenthesis the second term is neglected, and we get the equations of hydrostatic equilibrium in non-relativistic mechanics. The use of General Relativity (GR) is demanded by the high gravitational field. Integrating numerically these equations starting from the center, one gets the mass and radius of the star for each central density for a given EoS. In this way the mass as a function of the central density

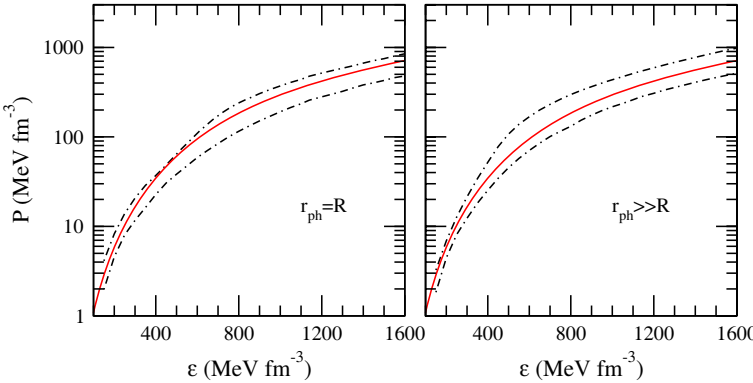


Fig. 17. – Comparison of the phenomenological allowed region (within the dot-dashed lines) for the Neutron Star matter EoS with the corresponding microscopic EoS from the BHF method (full line). Phenomenological data are from ref. [87].

or of the radius is obtained. These relationships are therefore characteristic of each EoS. Equations (81) were first derived independently by Tolman [84] and Oppenheimer and Volkoff [83]. The latter work presents also the first numerical calculations along the lines just described. They used for the nuclear EoS the one corresponding to a free neutron gas. The results showed that NS mass cannot exceed a definite maximum mass. With that EoS the maximum mass is about $0.7M_{\odot}$, with a corresponding radius of about 10 km. This first finding already indicates the extremely high density of the object. Many years later, it was possible to measure with high precision the masses of a neutron star binary system. In this system the companion of the pulsar B1913+16 has a mass of $1.44M_{\odot}$. This can be considered the first case in which astrophysical observations could exclude a high density nuclear EoS. The data tell us that the EoS of a free neutron gas is too soft, additional repulsion is needed. This is not surprising, since we know that the NN interaction is mainly repulsive at short distance, which means that at high density the EoS should be stiffer than for a free gas. In this way we have a first connection between the astrophysical observations on NS and the laboratory nuclear physics experiments.

In general it turns out that the mass of the NS has a maximum value as a function of radius (or central density), above which the star is unstable against collapse to a black hole. The value of the maximum mass depends on the nuclear EoS, so that the observation of a mass higher than the maximum one allowed by a given EoS simply rules out that EoS. Up to now the best microscopic EoS are compatible with the largest observed masses, that are close to 1.7 solar mass [85]. It would be of course desirable to have some phenomenological data also on the radius of NS. Unfortunately this is quite difficult, but some tentative analysis looks promising [86]. In particular a recent analysis of the data on six NS based on Bayesian statistical framework [87] has led to a tentative constraint on the nuclear EoS. Depending on the hypothesis made on the structure of the NS, the results are slightly different. The overall allowed region where the EoS should

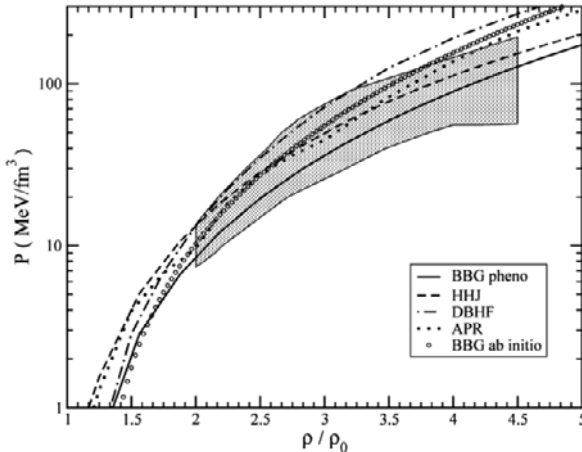


Fig. 18. – Different EoS in comparison with the phenomenological constraint extracted by Danielewicz *et al.* [88] (shaded area), where $\rho_0 = 0.16 \text{ fm}^{-3}$. Full line: EoS from the BBG method with phenomenological TBF [90]. Dashed line: modified variational EoS of Heiselberg and Hjorth-Jensen [91]. Dotted line: variational EoS of Akmal *et al.* [22]. Open circle: EoS from the BBG method with *ab initio* TBF [90]. Dash-dotted line: EoS from Dirac-Brueckner method (by van Dalen *et al.* [92]).

lie is reported in fig. 17, where the theoretical EoS from the BHF calculations is also reported. The theoretical EoS appears to be compatible with the extracted observational constraints. It turns out that other microscopic EoS do not show the same agreement, in particular the EoS of ref. [22] looks too repulsive at high density [87]. These boundaries obtained from astrophysical data are complementary to the ones obtained from heavy ion reactions. In ref. [88] the phenomenological data were summarized by plotting the region where any reasonable EoS should pass through in the pressure *vs.* density plane. The pressure was taken at the center of the interaction zone at the moment of maximal density during the collision, using all the simulations with different EoS compatible with different data and including the uncertainties. The plot is reproduced in fig. 18, as taken from ref. [19], in comparison with some microscopic calculations, in particular the same BHF theory used in fig. 17. It has to be stressed that the EoS employed in such a construction have compressibility that ranges from $K = 167 \text{ MeV}$ to $K = 380 \text{ MeV}$. Only the densities above twice the saturation density were included, since this guarantees that quasi-equilibrium in the participant zone was reached. This shows that only the EoS at high density can be studied in heavy ion collisions. The values of the incompressibility do not characterize completely the EoS, since it is actually density dependent, but in any case the analysis indicates the broad constraints on the EoS that can be obtained from heavy ion collisions. Despite they are somehow a little loose, they are able to exclude some of the phenomenological EoS [89]. It is quite relevant to compare the same theory with both astrophysical and laboratory analysis of data. In fact, in heavy ion the matter

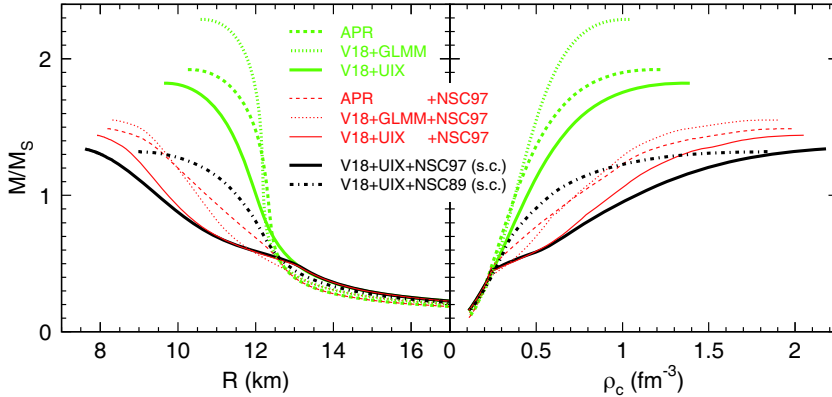


Fig. 19. – The NS mass as a function of radius (left panel) and central density (right panel) for various EoS. The upper group of lines corresponds to nucleonic EoS, the lower group to EoS that include also hyperons. For details and specifications of the EoS see ref. [93].

tested is essentially symmetric, while in NS the matter is highly asymmetric. Considered together, the two types of constraints probe the density dependence of the symmetry energy.

Unfortunately the theoretical situation for the EoS in NS and for the maximum mass is actually much more complicated. In fact, in NS weak processes have time to develop and, if energetically convenient, they can produce strange particles like hyperons, and then change the composition of the nuclear medium. This is clearly at variance with what can happen in heavy ion reactions, where the collision time is short and the multiplicity of strange particle is so small that a bulk strange matter cannot be formed. On the contrary in NS, at least above a certain density, the difference of the neutron and proton chemical potentials is so high to overcome the mass difference between hyperons and neutrons. This is indeed the case, according to microscopic calculations [93]. Above 2-3 times saturation density Σ^- or Λ hyperons appear. This softens so much the EoS that the maximum mass becomes smaller than the most established NS mass observed [94,85], that is around $1.44M_\odot$. In fig. 19, taken from ref. [93], is reported the NS mass as a function of central density and radius for different choices of the nucleon-nucleon and nucleon-hyperon interactions, in comparison with the case without hyperons. The softening of the EoS is apparent from the lowering of the maximum mass from a value around $2M_\odot$ down to values not exceeding $1.4\text{--}1.5M_\odot$. Notice that the EoS labeled GLMM includes three-body forces so repulsive that, in the case of nucleons only, it becomes super-luminal at the center of the massive NS, *i.e.* the speed of sound exceeds the velocity of light. It should be therefore corrected to avoid such a drawback. The conclusion that, with the presence of hyperons, the resulting maximum mass is too small, seems to be quite robust and not dependent on the not so well-known hyperon-nucleon or hyperon-hyperon interaction [95]. The only way out seems to be, up to now, a possible phase transition to quark matter. Indeed, calculations [96-100] on the basis of simple models can result in a maximum mass

that is (marginally) compatible with the observed largest mass. Of course it could also be that the quark matter EoS is stiffer than assumed in simple models [101, 102], but in any case it seems that we are close to test our knowledge on the QCD deconfined phase at high density. All that makes clear that the NS physics connected with the central high density core is quite different with the ones in heavy ions, where at ultra-relativistic collisions at LHC the deconfined QCD phase is tested at zero baryon density and high temperature. However it is a basic challenge for the theory to be able to connect the transition to quark matter in these two extreme different physical situations. Advances both in phenomenological observations and theoretical methods are needed.

The maximum mass problem clearly can lead far from traditional nuclear physics. However the distinction between traditional nuclear physics and QCD physics is partly artificial, and they should be considered as the two complementary aspects of the same physical realm.

Finally one has to observe that an observation of a maximum mass of 2 solar masses or higher would be a real breakthrough of our knowledge on high density nuclear medium, since it would question the simple models of quark matter. Recent observations [103] on the pulsar of the binary system PSR J1614-2230 seems to indicate such a possibility, and as anticipated in ref. [96], it would imply the necessity of a repulsive interaction in quark matter [104].

To illustrate this point we consider some standard models for the description of the quark matter and show that in their simpler form they lead to NS masses not larger than $1.7\text{--}1.8M_{\odot}$. Let us start with the MIT bag model [105]. In this model one assumes that the confining interaction among quarks can be described by a potential well, inside which quarks are essentially free. This model has suggested to describe hadrons as “bag” of quarks [106]. In a gas of nucleons, *i.e.* in nuclear matter, if the phase transition to the deconfined phase takes place, quarks behave as free particles, but with an additional constant energy density and pressure that are necessary in order to take into account the transition from the real non-perturbative vacuum to the perturbative vacuum. This additional pressure is the “bag constant”, that is mainly a parameter of the model. The energy density T_q of a free Fermi gas of massless quarks has a very simple expression, valid for ultra-relativistic particles

$$(82) \quad T_q = \frac{3}{4\pi^2} \frac{\mu_q^4}{(\hbar c)^3},$$

where μ_q is the chemical potential of the quarks of flavor q and the spin and color degeneracies have been included. To this kinetic energy term one has to add the bag constant B , and the total energy \mathcal{E}_q is then

$$(83) \quad \mathcal{E}_q = \frac{3}{4\pi^2} \frac{\mu_q^4}{(\hbar c)^3} + B$$

and the partial pressure P_q can be derived from the grand-canonical potential

$$(84) \quad P_q = -\Omega_q/V = -(\mathcal{E}_q - \mu_q n_q) = \frac{1}{4\pi^2} \frac{\mu_q^4}{(\hbar c)^3} - B,$$

where n_q is the quark density. Perturbative corrections in the (running) QCD coupling constant α_s can also be introduced. At the one gluon exchange level one gets a correction [107] proportional to α_s

$$(85) \quad P_q = \frac{1}{4\pi^2} \frac{\mu_q^4}{(\hbar c)^3} \left(1 - \frac{2\alpha_s}{\pi} \right) - B.$$

However, for small but non-zero quark mass it is necessary to renormalize the expansion, because it contains logarithmic terms that are large in the small mass limit. Then a renormalization point must be chosen and the expression for the energy and the pressure is slightly more involved. For details see refs. [107, 97]. The total energy and pressure is obtained by summing over the flavor q .

The MIT bag model, as most of the models, is not able to describe confinement and the corresponding hadronic phase. However we can consider that the hadronic EoS is known up to a relatively large density. If the phase transition is first order, then one has to look at the crossing of the hadronic and quark EoS in the pressure chemical potential plane. In fact, at the transition the two phases must be in mechanical and chemical equilibrium inside the NS. However, we must impose the equality of both proton and neutron chemical potentials

$$(86) \quad \mu_n = 2\mu_d + \mu_u; \quad \mu_p = 2\mu_u + \mu_d,$$

where μ_u and μ_d are the chemical potentials of the u and d quarks, respectively, in the deconfined quark phase. If hyperons are also present in the hadronic phase, other relations among chemical potentials must be imposed, with the inclusion of the strange quark s in the quark phase [97]. In any case, one can easily verify that the number of relations to be imposed exceeds by one unit the number of physical quantities to be fixed. It is then necessary to introduce the so-called “mixed phase”, where a mixture of hadronic and quark phase is present. The fraction of each phase is an additional unknown parameter to be fixed, thus equating the number of equations to the number of unknowns. In this case the transition from hadronic matter to quark matter is smooth, and the corresponding construction is called, within the context of NS physics, the “Glendenning construction” [108]. In this procedure, the overall charge neutrality is imposed, leaving the possibility of the hadronic and quark phase to be charged. The extension of the region where the mixed phase is present inside the NS depends mainly on the surface tension between the hadronic and the quark phase [109]. To simplify the procedure one can just impose at the transition the equality only of the neutron chemical potential, releasing the equation for the proton chemical potential, since the neutron component is

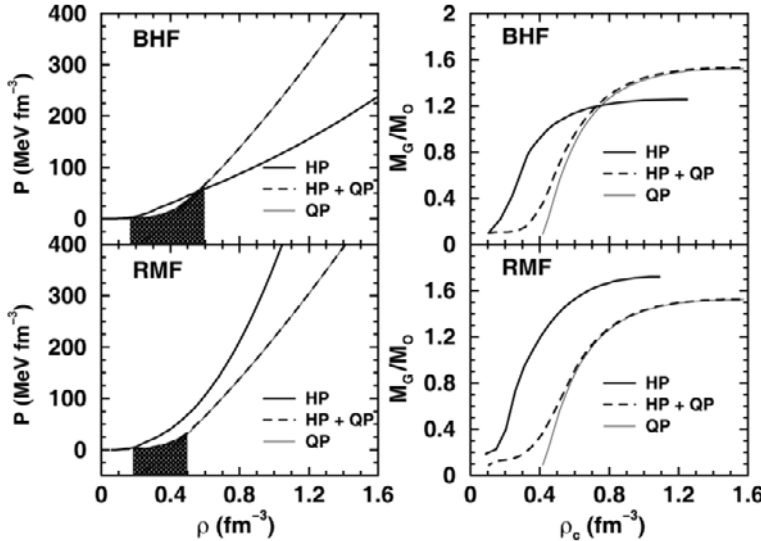


Fig. 20. – In the left panel is shown the EoS for neutron star matter (dashed lines labeled by HP+QP) for a density-independent value of the bag constant $B = 90 \text{ MeV fm}^{-3}$, with BHF and RMF (relativistic mean field) hadronic equations of state. The shaded areas indicate the mixed phase region. The corresponding masses *vs.* central densities are shown on the right panels. In all cases the thin and thick lines correspond to the results obtained for a pure quark and a pure hadron EoS, respectively.

dominant. It turns out that this approximation leaves most of the conclusions on the NS properties almost unchanged [109, 97].

In fig. 20, taken from ref. [97], are reported the results for the EoS and the NS mass if the transition to quark matter is allowed. In this calculation the value $B = 90 \text{ MeV fm}^{-3}$ has been chosen. The shaded area in the EoS plot corresponds to the region of the mixed phase. One can notice that the transition to quark matter hardens the EoS with respect to the hadronic case (that includes hyperons) and increases appreciably the maximum mass. Notice that the crossing between the two EoS has not a particular meaning since it occurs in the pressure-density plane. On the right panel for comparison the plot of the NS mass is reported also for the pure quark EoS. One can notice that the maximum mass is determined mainly by the quark EoS. In the lower panels an example of calculation with the relativistic mean-field EoS is reported. In this case the original hadronic EoS is harder, since a repulsive nucleon-hyperon interaction has been introduced, but the transition to quark matter softens the EoS and the final result is very similar. This is again because the quark matter is the same as in the BHF calculation (upper panels).

A higher maximum mass can be obtained by lowering the value of the bag constant, but below $B \approx 50 \text{ MeV fm}^{-3}$ one finds that the symmetric quark matter, *i.e.* with equal number of u and d quarks, at saturation density is lower in energy than the nucleonic

symmetric matter. This low value of the bag constant is therefore not physically acceptable. Within this simple version of the bag model the observed largest NS masses, that is at least $1.7M_{\odot}$ cannot be explained, even if the first perturbative correction in α_s is included [97]. Additional repulsion in the quark sector is needed. This repulsion can be introduced in several schemes, in particular following the method used in ref. [101]. The additional repulsion can shift the transition to quark matter at higher density, and possibly no quark matter can any more be present in the NS.

Other models for the quark sector have been considered, but the results [96-100] still indicate that the maximum mass does not exceed $1.7M_{\odot}$. The main difference among the models is the extension of the region where quark matter is present, either inside the mixed phase or as a single component. In particular with the Nambu-Jona Lasinio model the NS can at most contain a mixed phase in the central core, but no pure quark matter can be present, while in the MIT bag model a large fraction of the star is filled by quark matter. As already mentioned, the recent observation of the $2M_{\odot}$ NS could shed new insight and put challenging questions on the problem of the maximum mass of NS, on the high density EoS and on the appearance of quark matter inside NS.

Besides the gravitational mass and the radius, other NS physical characteristics and several phenomena that can occur in NS could probe their internal structure, but their discussion is beyond the scope of the present lectures or they would require, like the superfluid properties of NS matter, an additional dedicated series of lectures.

8. – Conclusions and outlook

Since the first observation of a pulsar in 1967 [110], an intense theoretical activity on the structure of Neutron Stars has developed, with a strong and fruitful connection with the continuously growing body of astrophysical observations. It has been more and more evident that Nuclear Physics is deeply involved in the development of a coherent theory of NS structure. At the same time a stronger and stronger link was established between the observational data and the laboratory experiments on heavy ion collisions and exotic nuclei. This cross fertilizing connection between the two fields of research has started to give the first fruitful results, in particular in constraining the nuclear EoS at high density and high asymmetry. On the other hand, in the crust of NS a set of very asymmetric nuclei are expected to be present and observational data on, *e.g.*, NS oscillations could allow to study exotic nuclei that cannot be produced in the laboratory. In this way the prospects of Nuclear Physics in the region of large asymmetry is enormously extended. The possibility of phase transition from hadron to quark matter in the core of NS is likely to occur, since the density that is expected to be reached is such that nucleons start to be in close contact, *i.e.* their hard cores are in touch among each other. The properties of this transition and of the EoS in general under these conditions are still to be explored, since the connection with the observational data is quite indirect, but relevant progresses are expected from additional data and theoretical developments. Also in this field the confrontation with experimental data on ultra-relativistic heavy ion collisions is a challenge for the theories that are able to relate the transition to deconfined quark matter at zero baryon den-

sity and high temperature, typical of experiments at LHC, with the one at high baryon density and zero temperature, that should occur at the center of massive Neutron Stars.

In these lectures I tried to give an overview of the developments that are occurring in the theory of NS, the role played by Nuclear Physics and the connection between laboratory experiments and observational data.

Other properties of nuclear matter and nuclei, like superfluidity, have a decisive relevance for the physics of NS, but unfortunately I could not touch for lack of time.

Finally, I would like to schematize with a simple list the lines of research that are at the frontier in the physics of NS in general and of the fundamental issues that are expected to receive decisive contributions from the physics of NS. The list is of course biased by my personal view and limitations.

- 1) Development of an accurate density Functional for nuclei and the crust.
- 2) Neutrino emissivity, heat capacity of nuclear matter and cooling of NS.
- 3) Quantal treatment of the “pasta phase”.
- 4) Superfluidity of nucleonic matter and vortices dynamics.
- 5) Consistent treatment of viscosity and gravitational wave emission.
- 6) Hyperonic matter and the EoS.
- 7) The onset of quark matter and the EoS.
- 8) Theory of gravity. Physics of strong gravitational field and alternative theories.

Each one of these items is connected with astrophysical observations, where rapid developments are occurring. New discoveries and surprises can be expected, both at phenomenological and fundamental level.

* * *

I would like to thank all my collaborators with whom I shared along the years our efforts to develop the nuclear astrophysics of Neutron Stars, Dr. G. F. BURGIO, Dr. H.-J. SCHULZE, Prof. U. LOMBARDO, Dr. C. MAIERON, Dr. C. DUCOIN, Prof. E. E. SAPERSTEIN, Prof. M. ZVEREV, Dr. S. PANKRATOV, Dr. S. V. TOLOKONNIKOV, Prof. P. SCHUCK, Prof. X. VINAS. To them I want to express my gratitude and friendship. Prof. X. VINAS is kindly acknowledged for providing figs. 10, 11 and 15, Dr. G. F. BURGIO for fig. 17. I would like also to thank Prof. A. BRACCO and Prof. E. NAPPI for their kind hospitality during the whole period of the School. The support of COMPSTAR, a research and training program of the European Science Foundation, is kindly acknowledged.

REFERENCES

- [1] BALDO M. (Editor), *Nuclear Methods and the Nuclear Equation of State, International Review of Nuclear Physics*, Vol. **8** (World Scientific) 1999.
- [2] FABROCINI A., FANTONI S. and KROTSCHECK E. (Editors), *Introduction to the Modern Methods of Quantum Many-Body Theory and Their Applications, Series on Advances*, in *Quantum Many-Body Theory*, Vol. **7** (World Scientific) 2002.
- [3] HAENSEL P., POTEKHIN A. Y. and YAKOVLEV D. G., *Neutron Stars*, Vol. **1** (Springer) 2007.
- [4] SHAPIRO S. L. and TEUKOLSKY S. A., *Black Holes, White Dwarfs and Neutron Stars* (John Wiley and Sons, New York) 1983.
- [5] NORDHAUS J., BURROWS A., ALMGREN A. and BELL J., arXiv:1006.3792 [astro-ph.SR].
- [6] HAMMER N. J., JANKA H.-TH. and MÜLLER E., *Astrophys. J.*, **714** (2010) 1371.
- [7] ROCA-MAZA X. and PIEKAREWICZ J., *Phys. Rev. C*, **78** (2008) 025807.
- [8] BAYM G., PETHICK C. and SUTHERLAND P., *Astrophys. J.*, **170** (1971) 199.
- [9] RÜSTER S. B., HEMPEL M. and SCHAFFNER-BIELICH J., *Phys. Rev. C*, **73** (2006) 035804.
- [10] ASHCROFT N. W. and MERMIN N. D., *Solid State Physics* (Thomson Learning, Inc.) 1976.
- [11] PETHICK C. J. and RAVENHALL D. G., *Annu. Rev. Nucl. Sci.*, **45** (1995) 429.
- [12] MYERS W. D. and SWIATECKY W. J., *Nucl. Phys. A*, **601** (1996) 141.
- [13] BLAIZOT J. P., *Phys. Rep.*, **64** (1980) 171.
- [14] MIGDAL A. B., *Theory of Finite Fermi Systems and Application to Atomic Nuclei* (Wiley Interscience, New York) 1967.
- [15] BOHR A. and MOTTELSON B. R., *Nuclear Structure*, Vol. **I** (1974) and Vol. **II** (1975) (Benjamin, New York).
- [16] MACHLEIDT R., *Phys. Rev. C*, **63** (2001) 024001.
- [17] MACHLEIDT R. and SLAUS I., *J. Phys. G: Nucl. Part. Phys.*, **27** (2001) R69.
- [18] MANDL F. and SHAW G., *Quantum Field Theory* (John Wiley and Sons) 1995.
- [19] BALDO M. and MAIERON C., *J. Phys. G: Nucl. Part. Phys.*, **34** (2007) R1.
- [20] LI Z. H., LOMBARDO U., SCHULZE H.-J., ZUO W., CHEN L. W. and MA H. R., *Phys. Rev. C*, **74** (2006) 047304.
- [21] ZHOU X. R., BURGIO G. F., LOMBARDO U., SCHULZE H.-J. and ZUO W., *Phys. Rev. C*, **69** (2004) 018801.
- [22] AKMAL A., PANDHARIPANDE V. R. and RAVENHALL D. G., *Phys. Rev. C*, **58** (1998) 1804.
- [23] GRANGE' P., LEUJEUNE A., MARTZOLFF M. and MATHIOT J.-F., *Phys. Rev. C*, **40** (1989) 1040.
- [24] ZUO W., LEUJEUNE A., LOMBARDO U. and MATHIOT J.-F., *Nucl. Phys. A*, **706** (2002) 418.
- [25] ZUO W., LEUJEUNE A., LOMBARDO U. and MATHIOT J.-F., *Eur. Phys. J. A*, **14** (2002) 469.
- [26] BALDO M. and SHABAN ALAA ELDEEN, *Phys. Lett. B*, **661** (2008) 373.
- [27] PANDHARIPANDE V. R. and WIRINGA R. B., *Rev. Mod. Phys.*, **51** (1979) 821.
- [28] MACHLEIDT R., *Advances in Nuclear Physics*, Vol. **19** (Plenum Press) 1989.
- [29] BROCKMANN R. and MACHLEIDT R., *Nuclear Methods and the Nuclear Equation of State, International Review of Nuclear Physics*, edited by BALDO M., Vol. **8** (World Scientific) 1999.
- [30] BROWN G. E., WEISE W., BAYM G. and SPETH J., *Commun. Nucl. Part. Phys.*, **17** (1987) 39.
- [31] GROSS-BOELTING T., FUCHS CH. and FAESSLER A., *Nucl. Phys. A*, **648** (1999) 105.

- [32] BOGNER S. K., FURNSTALL R. J. and SCHWENK A., *Prog. Part. Nucl. Phys.*, **65** (2010) 94.
- [33] ENTEM D. R. and MACHELEIDT R., *Phys. Lett. B*, **524** (2003) 93.
- [34] WEINBERG S., *Phys. Lett. B*, **251** (1990) 288.
- [35] WEINBERG S., *Nucl. Phys. B*, **363** (1991) 3.
- [36] WEINBERG S., *Phys. Lett. B*, **295** (1992) 114.
- [37] HOLT J. W., KAISER N. and WEISE W., *Phys. Rev. C*, **81** (2010) 024002.
- [38] MACHELEIDT R., LIU P., ENTEM D. R. and RUIZ ARRIOLA E., *Phys. Rev. C*, **81** (2010) 024001.
- [39] CARLSON J., CHANG S.-Y., PANDHARIPANDE V. R. and SCHMIDT K. E., *Phys. Rev. Lett.*, **91** (2003) 050401.
- [40] ASTRAKHARCHIK G. E., BORONAT J., CASULLERAS J. and GIORGINI S., *Phys. Rev. Lett.*, **93** (2004) 200404.
- [41] BULGAC A., DRUT J. E. and MAGIERSKI P., *Phys. Rev. Lett.*, **96** (2006) 090404.
- [42] BULGAC A., DRUT J. E. and MAGIERSKI P., *Phys. Rev. Lett.*, **99** (2007) 120401.
- [43] FRIEDMAN B. and PANDHARIPANDE V. R., *Nucl. Phys. A*, **361** (1981) 501.
- [44] CARLSON J., MORALES J., PANDHARIPANDE V. R. and RAVENHALL D. G., *Phys. Rev. C*, **68** (2003) 025802.
- [45] SCHWENK A. and PETHICK C. J., *Phys. Rev. Lett.*, **95** (2005) 160401.
- [46] WIRINGA R. B., STOKS V. G. J. and SCHIAVILLA R., *Phys. Rev. C*, **51** (1995) 38.
- [47] BALDO M., BOMBACI I. and BURGIO G. F., *Astron. Astrophys.*, **328** (1997) 274.
- [48] BALDO M. and MAIERON C., *Phys. Rev. C*, **77** (2008) 015801.
- [49] BALDO M., GIANSIRACUSA G., LOMBARDO U. and SONG H. Q., *Phys. Lett. B*, **473** (2000) 1.
- [50] BALDO M., FIASCONARO A., GIANSIRACUSA G., LOMBARDO U. and SONG H. Q., *Phys. Rev. C*, **65** (2001) 017303.
- [51] GEZERLIS A. and CARLSON J., *Phys. Rev. C*, **77** (2008) 032801.
- [52] RING P. and SCHUCK P., *The Nuclear Many-Body Problem* (Springer Verlag, Berlin) 1980.
- [53] BHAGWAT A., VINAS X., CENTELLES M., SCHUCK P. and WYSS R., arXiv: 0911.4648 [nucl-th].
- [54] STRUTINSKY V. M., *Nucl. Phys. A*, **95** (1967) 420; **122** (1968) 1; **218** (1974) 169.
- [55] CHAMEL N., GORIELY S. and PEARSON J. M., *Nucl. Phys. A*, **812** (2008) 72.
- [56] CHAMEL N., GORIELY S. and PEARSON J. M., *Phys. Rev. C*, **80** (2009) 065804.
- [57] CARLSON B. G., DOBACZWESKI J., MIZUYAMA K. and TOIVANEN J., *Phys. Rev. C*, **77** (2008) 064307.
- [58] DOBACZWESKI J., arXiv:1009.0899 [nucl-th].
- [59] KOHN W. and SHAM L. J., *Phys. Rev. A*, **140** (1965) 1133.
- [60] JONES R. O. and GUNNARSSON O., *Rev. Mod. Phys.*, **61** (1989) 689.
- [61] ESCHRIG H., *The Fundamentals of Density Functional Theory* (B. G. Teubner, Stuttgart) 1996.
- [62] MATTSSON A. E., *Science*, **298** (2002) 759.
- [63] PERDEW J. P. and SCHMIDT K., *Density Functional Theory and Its Applications to Material*, edited by VAN DOREN V. et al., (American Institute of Physics, Melville, NY) 2001.
- [64] TAO JIANMIN, PERDEW J. P., STAROVEROV V. N. and SCUSERIA G. F., *Phys. Rev. Lett.*, **91** (2003) 146401.
- [65] TAO JIANMIN and PERDEW J. P., *Phys. Rev. Lett.*, **95** (2005) 196403.
- [66] BALDO M., SCHUCK P. and VINAS X., *Phys. Lett. B*, **663** (2008) 390.
- [67] BONCHE P., KOONIN S. and NEGELE J. W., *Phys. Rev. C*, **13** (1976) 1226.

- [68] UMAR A. S., STRAYER M. R., REINHARD P.-G., DAVIES K. T. R. and LEE J.-S., *Phys. Rev. C*, **40** (1989) 706.
- [69] FAYANS S. A. *et al.*, *Nucl. Phys.*, **676** (2000) 49.
- [70] BALDO M., ROBLEDO L., SCHUCK P. and VINAS X., *J. Phys. G.: Nucl. Part. Phys.*, **37** (2010) 064015.
- [71] HOHENBERG P. and KOHN W., *Phys. Rev.*, **136** (1964) 864.
- [72] BERGER J. F., GIROD M. and GOGNY D., *Comput. Phys. Commun.*, **63** (1991) 365; *Nucl. Phys. A*, **502** (1989) 85c.
- [73] BALDO M., SAPERSTEIN E. E. and TOLOKONNIKOV S. V., *Phys. Rev. C*, **76** (2007) 025803.
- [74] NEGELE J. and VAUTHERIN D., *Nucl. Phys. A*, **207** (1973) 298.
- [75] BALDO M., SAPERSTEIN E. E. and TOLOKONNIKOV S. V., *Eur. Phys. J. A*, **32** (2007) 97.
- [76] LATTIMER J. and SWESTY F. D., *Nucl. Phys. A*, **535** (1991) 331.
- [77] SHEN H., *Phys. Rev. C*, **65** (2002) 035802.
- [78] ISRAEL G. L., BELLONI T., STELLA L., REPHAELI Y., GRUBER D. E., CASELLA P., DALL' OSSO S., REA N., PERSIC M. and ROTHSCHILD R. E., *Astrophys. J.*, **628** (2005) L53.
- [79] ALTAMIRANO D., LINARES M., PATRUNO A., DEGENAAR N., WIJNANDS R., KLEIN-WOLT M., VAN DER KLIS M., MARKWARDT C. and SWANK J., arXiv:0908.4039 [astro-ph.HE].
- [80] ALTAMIRANO D., WATTS A., LINARES M., MARKWARDT C. B., STROHMEYER T. and PATRUNO A., arXiv:1005.5299 [astro-ph.HE].
- [81] WATTS A. L. and STROHMEYER T. E., *Astrophys. J.*, **637** (2006) L117.
- [82] STEINER A. W. and WATTS A. L., *Phys. Rev. Lett.*, **103** (2009) 181101.
- [83] OPPENHEIMER J. R. and VOLKOFF G. M., *Phys. Rev.*, **55** (1939) 374.
- [84] TOLMAN R. C., *Phys. Rev.*, **55** (1939) 364.
- [85] YAKOVLEV D. G., *Exotic States of Nuclear Matter*, edited by LOMBARDO U., BALDO M., BURGIO F. and SCHULZE H.-J. (World Scientific) 2008.
- [86] ÖZEL F., BAYM G. and GÜVER T., arXiv:1002.3153 [astro-ph.HE].
- [87] STEINER A. W., LATTIMER J. M. and BROWN E. F., arXiv:1005.0811 [astro-ph.HE].
- [88] DANIELEWICZ P., LACEY R. and LINCH W., *Science*, **298** (2002) 1592.
- [89] KLÄHN T., BLASCHKE D., SANDIN F., FUCHS CH., FAESSLER A., GRIGORIAN H., ROPKE G. and TRÜMPER J., arXiv:nucl-th/0609067.
- [90] LI A., BURGIO G. F., LOMBARDO U. and ZUO W., *Phys. Rev. C*, **74** (2006) 055801.
- [91] HEISELBERG H. and HJORTH-JENSEN M., *Astrophys. J.*, **525** (1999) L45.
- [92] VAN DALEN E. N. E., FUCHS CH. and FAESSLER A., *Phys. Rev. C*, **72** (2005) 065803.
- [93] SCHULZE H.-J., POLL S. A., RAMOS A. and VIDANA I., *Phys. Rev. C*, **73** (2006) 058801.
- [94] HULSE R. A. and TAYLOR J. H., *Astrophys. J.*, **195** (1975) L51.
- [95] VIDANA I., LAGOTETA D., PROVISENCIA C., POLL S. A. and BOMBACI I., arXiv:1006.5660 [nucl-th].
- [96] BALDO M., BURGIO G. F., SAHU P., SANTRA A. B. and SCHULZE H.-J., *Phys. Lett. B*, **526** (2002) 19.
- [97] BALDO M., BURGIO G. F., SAHU P. and SCHULZE H.-J., *Phys. Rev. C*, **66** (2002) 025802.
- [98] BALDO M., BUBALLA M., BURGIO G. F., NEUMANN F., OERTEL M. and SCHULZE H.-J., *Phys. Lett. B*, **562** (2003) 153.
- [99] MAIERON C., BALDO M., BURGIO G. F. and SCHULZE H.-J., *Phys. Rev. D*, **70** (2004) 043010.
- [100] BALDO M., BURGIO G. F., CASTORINA P., PLUMARI S. and ZAPPALÀ D., *Phys. Rev. D*, **78** (2008) 063009.

- [101] ALFORD M., BRABY M., PARIS M. and REDDY S., *Astrophys. J.*, **629** (2005) 969.
- [102] ALFORD M., BLASCHKE D., DRAGO A., KLAHN T., PAGLIARA G. and SCHAFFNER-BIELICH J., *Nature*, **445** (2007) E7.
- [103] DEMOREST P. B., PENNUCCI T., RANSOM S. M., ROBERTS M. S. E. and HESSELS J. W. T., *Nature*, **467** (2010) 1081.
- [104] ÖZEL F., PSALTIS D., RANSOM S., DEMOREST P. and ALFORD M., arXiv:1010.5790 [astro-ph.HE].
- [105] CHODOS A., JAFFE R. L., JOHNSON K., THORN C. B. and WEISSKOPF V. F., *Phys. Rev. D*, **9** (1974) 3471.
- [106] BHADURI R. K., *Models of the Nucleon* (Addison-Wesley Publishing Company, Inc.) 1988.
- [107] FARHI E. and JAFFE R. L., *Phys. Rev. D*, **30** (1984) 2379.
- [108] GLENDEENING N. K., *Phys. Rev. D*, **46** (1992) 1274.
- [109] MARUYAMA T., CHIBA S., SCHULZE H.-J. and TATSUMI T., *Phys. Rev. D*, **76** (2007) 123015.
- [110] HEWISH A., BELL S. J., PILKINGTON J. D. H., SCOTT P. F. and COLLINS R. A., *Nature*, **217** (1968) 709.

Proceedings of the International School of Physics “Enrico Fermi”
Course CLXXVIII “From the Big Bang to the Nucleosynthesis”, edited by A. Bracco and E. Nappi
(IOS, Amsterdam; SIF, Bologna)
DOI 10.3254/978-1-60750-974-5-95

Spin-isospin modes: Implications for astrophysics

M. N. HARAKEH

GSI Helmholtzzentrum für Schwerionenforschung - D-64291 Darmstadt, Germany

Kernfysisch Versneller Instituut, University of Groningen

Zernikelaan 25, NL-9747 AA, Groningen, The Netherlands

Summary. — The study of giant resonances has been very fruitful in understanding the structure of these modes of excitation of the nucleus and also in helping to shed light onto certain astrophysical phenomena. For example, the compression modes, the isoscalar giant monopole (ISGMR) and dipole (ISGDR) resonances, were extensively studied because of their importance for the determination of the nuclear matter incompressibility and consequently their implications for the equation of state (EoS) of nuclear matter. Gamow-Teller (GT) transitions, on the other hand, play very important roles in various phenomena in nature. In nucleosynthesis, the β -decay of nuclei in the s- and r-processes determines the paths that these processes follow and the abundances of the elements synthesized. In supernova collisions, GT transitions are of paramount importance in the pre-supernova phase where electron capture occurs on neutron-rich fp -shell nuclei at the high temperatures reached in giant stars. Electron capture, which is mediated by GT transitions, removes the electron pressure that keeps the star from collapsing precipitating a cataclysmic implosion followed by a huge explosion throwing much of the star material into space leaving a neutron star or black hole behind.

1. – Introduction

After the discovery of the isovector giant dipole resonance (IVGDR) by Bothe and Gentner [1] and later by Migdal, Baldwin, and Klaiber [2, 3] and the interpretation by Goldhaber and Teller [4] and Steinwedel and Jensen [5], systematic studies were performed in the following decades. These employed electron accelerators to produce bremsstrahlung that in turn was used to study the resonant γ absorption in nuclei. In addition, experiments with quasi-monochromatic photons could be performed by using a tagged-photon beam or e^+e^- annihilation in flight; see ref. [6] and references therein.

In addition to the IVGDR, there exist other types of giant resonances that can be described in a hydrodynamical model as the oscillations of a liquid drop composed of four different types of fluids: protons and neutrons with spins up and down. The giant resonances can therefore be characterized by their multipolarity, spin and isospin. An isoscalar mode corresponds to protons and neutrons oscillating in phase whereas an isovector mode corresponds to protons and neutrons oscillating out of phase. Similarly, a scalar (electric) mode corresponds to nucleons with spin-up and spin-down oscillating in phase and a vector (magnetic) mode corresponds to nucleons with spin-up and spin-down oscillating out of phase. In fig. 1, a schematic representation is given for the lowest three multipoles: $\Delta L = 0$ (monopole), $\Delta L = 1$ (dipole) and $\Delta L = 2$ (quadrupole) and for isoscalar electric, isovector electric, isoscalar magnetic and isovector magnetic, respectively. The representation for the isoscalar giant dipole resonance (ISGDR) is missing because in first order it corresponds to a spurious center-of-mass (c.o.m.) motion, *i.e.* translational motion of the nucleus as a whole without intrinsic excitation of it. In higher order, the ISGDR exists as will be discussed below.

The study of giant resonances including the IVGDR has been very intensive in the last six decades. This started with the discovery of the isoscalar giant quadrupole resonance (ISGQR) in electron scattering in 1971 [7] and isoscalar giant monopole resonance (ISGMR) in inelastic α scattering in 1977 [8, 9]. Other modes were discovered and investigated extensively. Among these, the ISGMR and ISGDR are of special interest because they are compression modes and their excitation energies are dependent on the compression modulus of the nucleus. Charge-exchange modes are also very important because of the role they play in nucleosynthesis and other astrophysical phenomena as we will discuss in more detail below.

In microscopic models, a giant resonance can be described as a coherent superposition of one-particle-one-hole excitations that are induced by the operation of one-body operators on the ground state of a nucleus:

$$(1) \quad |\Psi^{\lambda\sigma\tau}\rangle = O^{\lambda\sigma\tau}|\Psi_{\text{g.s.}}\rangle,$$

where λ refers to the multipolarity of the giant resonance, and σ and τ to its spin and isospin structure, respectively. The multipole operators are obtained from the first-order terms in the expansion of the spherical Bessel function $j_\lambda(qr)$ of order (multipolarity) λ ;

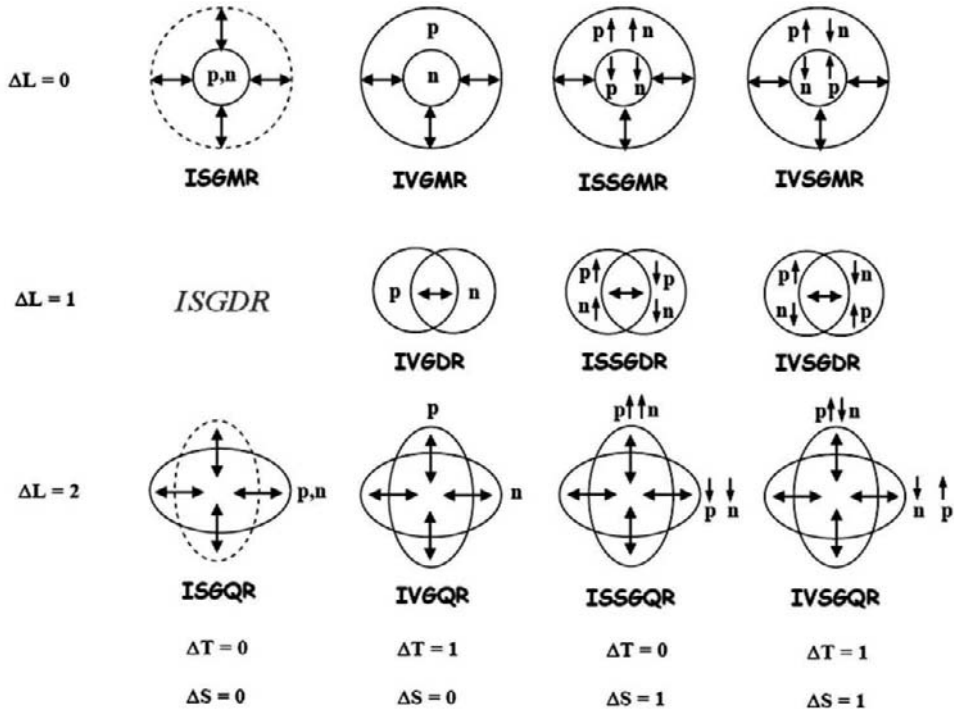


Fig. 1. – Schematic representation of giant resonances for the monopole, dipole and quadrupole modes. Isoscalar and isovector modes correspond to neutrons and protons moving in phase and out of phase, respectively. Similarly, electric (scalar) and magnetic (vector) spin modes correspond to nucleons with spin-up and spin-down moving in phase and out of phase, respectively. The notation used is self-explanatory.

here, q is the momentum transfer and r is the spherical radial coordinate. This is true except for the isoscalar monopole and dipole operators.

The transition operators for the isoscalar monopole and dipole excitations can be obtained from the expansion of the Bessel function of order $\lambda = 0$ and $\lambda = 1$, respectively. For the monopole, the first-order term is a constant that does not induce any excitations. The second-order term in the expansion is proportional to r^2 and thus can lead to $2\hbar\omega$ monopole excitations. For the dipole, the first-order term is proportional to the center-of-mass (c.o.m.) coordinate and corresponds to the spurious c.o.m. motion.

$$(2) \quad O^{L=1} = \sum_i r_i Y_0^1 + \sum_i r_i^3 Y_0^1 + \dots$$

Intrinsic isoscalar dipole excitations can be induced by the second-order term in the expansion which is proportional to r^3 and thus can lead to $1\hbar\omega$ and $3\hbar\omega$ excitations. The isoscalar dipole resonance is associated with the $3\hbar\omega$ excitation.

TABLE I. – *Multipole operators for the first four multipolarities ($\Delta L = 0, 1, 2$ and 3) isoscalar and isovector electric modes and isovector magnetic modes. Note the absence of the operators for the isoscalar magnetic modes, since these have not been observed experimentally. The operators for the IAS (Fermi) transition and Gamow-Teller resonance (GTR) are also given and do not involve a radial part.*

	$\Delta S = 0,$ $\Delta T = 0$	$\Delta S = 0,$ $\Delta T = 1$	$\Delta S = 0,$ $\Delta T = 1$	$\Delta S = 1,$ $\Delta T = 1$	$\Delta S = 1,$ $\Delta T = 1$
$\Delta L = 0:$ Monopole	ISGMR $r^2 Y_0$	IAS $\tau_{\pm} Y_0$	IVGMR $\tau r^2 Y_0$	GTR $\tau_{\pm} \sigma Y_0$	IVSGMR $\tau \sigma r^2 Y_0$
$\Delta L = 1:$ Dipole	ISGDR $r^3 Y_1$		IVGDR $\tau r Y_1$		IVSGDR $\tau \sigma r Y_1$
$\Delta L = 2:$ Quadrupole	ISGQR $r^2 Y_2$		IVGQR $\tau r^2 Y_2$		IVSGQR $\tau \sigma r^2 Y_2$
$\Delta L = 3:$ Octupole	LEOR, HEOR (ISGOR) $r^3 Y_3$				

In table I, multipole operators for the first four multipolarities: monopole, dipole, quadrupole and octupole are given for both isoscalar and isovector modes, and electric and magnetic modes. The operators for the isoscalar magnetic modes are not shown since these modes have not been observed experimentally. The operator for the isobaric analog state (IAS) is given and it consists of an isospin lowering or raising operator that changes a neutron to a proton or a proton to neutron, respectively, without changing the other quantum numbers, *i.e.* the radial, orbital and spin wave functions remain the same. The operator for the Gamow-Teller (GT) excitation involves in addition the spin-operator and therefore it will induce a spin flip in addition to the isospin flip. It induces thus transitions of neutrons to protons (lowering) or protons to neutrons (raising) without changing the radial and orbital wave functions; however, the spin wave function may change. Thus, transitions between spin-orbit partners are also allowed.

2. – The compression modes and incompressibility of nuclear matter

As stated above, the compression modes, ISGMR and ISGDR, provide the possibility to determine the nuclear matter incompressibility experimentally because of the relation between their excitation energies and the incompressibility of nuclei. These two compression modes are depicted in fig. 2. The ISGMR (also called breathing mode) shows a volume oscillation around an equilibrium shape, thereby moving between rarefied and denser situations. The ISGDR (also called squeezing mode) displays oscillations wherein the density increases on one side of the nucleus and decreases on the other keeping the c.o.m. fixed. For comparison the normal ISGQR is also depicted in fig. 2. It displays a quadrupole oscillation without a change in density.

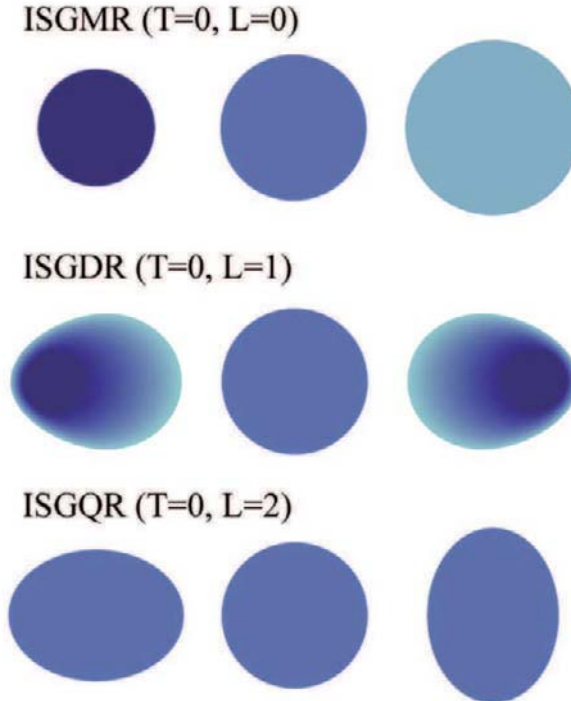


Fig. 2. – Oscillation of the nucleus about an equilibrium shape shown for ISGMR (top), ISGDR (middle) and ISGQR (bottom). The ISGMR (breathing mode) and the ISGDR (squeezing mode) display density variations and therefore are denoted as compression modes. The ISGQR displays no density variations.

The incompressibility of nuclear matter is an important ingredient of the equation of state (EoS) of nuclear matter. The EoS is more complex than for infinite neutral liquids because the nuclear fluid has protons and neutrons with different interactions; in particular the long-range Coulomb interaction for protons becomes very important for large volumes. The EoS governs: i) the collapse and explosion of giant stars (supernovae explosions), ii) the formation of neutron stars (mass, radius and crust) and iii) the collisions of heavy ions. The incompressibility is an important ingredient of the nuclear forces that determine the properties of nuclei. For a definition of the incompressibility of nuclear matter, one notes that for the EoS of nuclear matter at saturation nuclear density [10]:

$$(3) \quad \left[\frac{d(E/A)}{d\rho} \right]_{\rho=\rho_0} = 0.$$

Here, E/A is the binding energy per nucleon, ρ is the nuclear density and ρ_0 is the nuclear density at saturation. The incompressibility of nuclear matter can then be

derived as the second derivative with respect to the nuclear density:

$$(4) \quad K_{nm} = \left[9\rho^2 \frac{d^2(E/A)}{d\rho^2} \right]_{\rho=\rho_0}.$$

The excitation energies of the ISGMR and ISGDR are given in the constrained and scaling models as [10]:

$$(4) \quad E_{\text{ISGMR}} = \hbar \sqrt{\frac{K_A}{m\langle r^2 \rangle}}, \quad E_{\text{ISGDR}} = \hbar \sqrt{\frac{7}{3} \frac{K_A + \frac{27}{25}\varepsilon_F}{m\langle r^2 \rangle}},$$

where m is the nucleon mass, $\langle r^2 \rangle$ is the mean-square radius, ε_F is the Fermi energy and the nucleus incompressibility K_A is given by

$$(5) \quad K_A = [r^2(d^2(E/A)/dr^2)]_{r=R_0}.$$

In the scaling model the nucleus compressibility can be expanded (Leptodermous expansion) into several terms, as follows:

$$(6) \quad K_A = K_{\text{vol}} + K_{\text{surf}} A^{-1/3} + K_{\text{sym}} ((N - Z)/A)^2 + K_{\text{Coul}} Z^2 A^{-4/3}.$$

In principle, one can obtain the various terms through a fit to K_A values obtained for many nuclei. In this way, K_{vol} and K_{sym} can be determined. K_{vol} can be associated with the incompressibility of nuclear matter, $K_{nm} \equiv K_\infty$. This is, however, not what is done because using the Leptodermous expansion is not considered a reliable method to determine the parameters. Instead, it is considered more correct and reliable to determine the excitation energies of the compression modes through non-relativistic or relativistic calculations with different types of nucleon-nucleon (NN) interactions. The incompressibility of nuclear matter is then taken from the NN interaction that leads to the best reproduction of the isoscalar giant monopole and dipole resonances.

We will not go here into details of how the excitation energies of the ISGMR and ISGDR are determined. The most important experimental and analysis steps are discussed briefly in the following. The best reaction to study these isoscalar compression modes is inelastic α scattering at incident energies of ~ 160 MeV or higher and at very forward angles including 0° . At these angles and bombarding energies the angular distributions are characteristic of the different multipolarities. However, for measuring at and near 0° the use of a magnetic spectrometer is imperative to separate the beam from inelastically scattered α -particles. Inelastic α -scattering spectra for different scattering angles are generated by software division of the angular bins. Special techniques have to be used to remove the experimental background. Once the experimental background is removed, a multipole decomposition analysis (MDA) is performed on the spectra for the different angular bins. This results in spectra for the strength distributions of the different multipoles as a function of excitation energy.

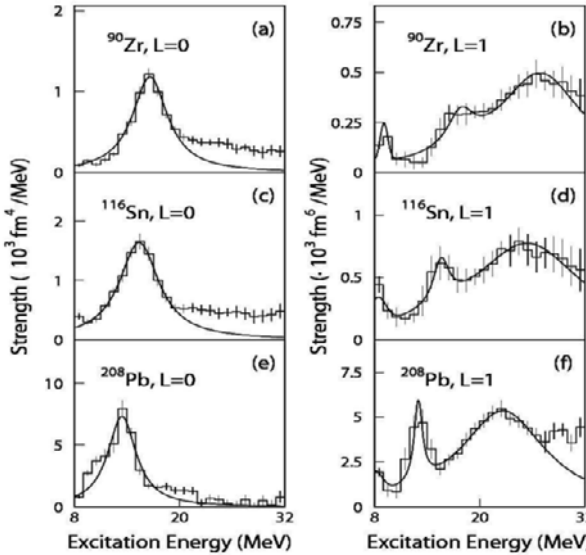


Fig. 3. – Strength distributions of the ISGMR and the ISGDR in ^{90}Zr , ^{116}Sn , and ^{208}Pb determined from MDA of experimental spectra obtained [11] in inelastic α scattering at incident energy of 386 MeV. The results of fitting the ISGMR with a Breit-Wigner function are indicated. For the ISGDR, the results of fitting with two Breit-Wigner functions for the region of $E_x > 10$ MeV are shown.

In fig. 3, the results of such an analysis for the strength distributions of the ISGMR and the ISGDR in ^{90}Zr , ^{116}Sn , and ^{208}Pb are shown. The experimental spectra have been obtained in inelastic α scattering at incident energy of 386 MeV [11]. The results of fits with Breit-Wigner functions are shown. From the ISGMR data on ^{90}Zr and ^{208}Pb , the incompressibility of nuclear matter is determined [12] to be $K_\infty = 240 \pm 10$ MeV. This value seems to be consistent with both ISGMR and ISGDR data and with non-relativistic and relativistic calculations.

To determine the coefficient of the symmetry term of the incompressibility, inelastic α scattering at 400 MeV was studied on all stable even-A Sn isotopes [13]. Isoscalar monopole strength as a function of excitation energy was determined via MDA. These are shown in fig. 4 together with fits with Lorentzian functions. The energies of the ISGMR obtained from these fits are within the uncertainties in good agreement with the values obtained also from the moment ratio $\sqrt{m_1/m_{-1}}$, where the k -th moment of the strength distribution is defined as

$$(7) \quad m_k = \int E_x^k S(E_x) dE_x,$$

where the integration was performed in the excitation energy interval 10.5–20.5 MeV.

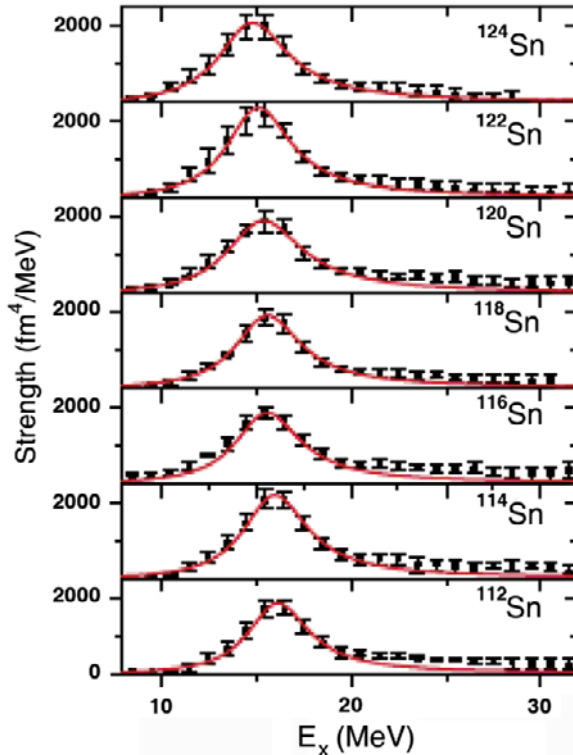


Fig. 4. – Strength distributions of the ISGMR for all even- A Sn isotopes obtained [13] from inelastic α scattering at incident energy of 400 MeV. The results of fitting the ISGMR strength distributions with a Lorentzian function are shown.

Equation (6) for the nucleus incompressibility can be rewritten:

$$K_A - K_{\text{Coul}} Z^2 A^{-4/3} \sim K_{\text{vol}}(1 + cA^{-1/3}) + K_\tau[(N - Z)/A]^2.$$

Here, $c \approx -1$ [14] and K_{Coul} is essentially model independent allowing to calculate the Coulomb term for each of the isotopes. Hence, the difference $K_A - K_{\text{Coul}} Z^2 A^{-4/3}$ for an isotopic chain can be approximated to be a quadratic function of $(N - Z)/A$, with K_τ as a coefficient. In fig. 5, the difference $K_A - K_{\text{Coul}} Z^2 A^{-4/3}$ is plotted for all the even Sn isotopes, for which the moment ratio $\sqrt{m_1/m_{-1}}$ was determined as discussed above, as a function of the asymmetry parameter, $(N - Z)/A$. The values of K_A were determined using the moment ratios $\sqrt{m_1/m_{-1}}$ for E_{ISGMR} in eq. (4). The data were fitted with quadratic function. This is shown as a solid line in fig. 5. The fit gives $K_\tau = 550 \pm 40$ MeV; the error is only due to the fitting procedure. Considering all other uncertainties that arise from different sources, a value $K_\tau = 550 \pm 100$ MeV is obtained.

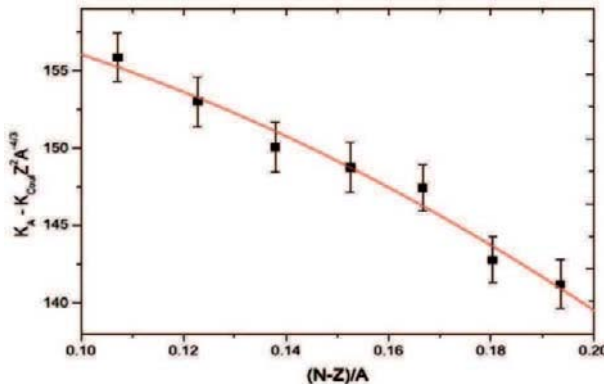


Fig. 5. – Systematics of the difference $K_A - K_{\text{Coul}} Z^2 A^{-4/3}$ determined for the Sn isotopes as discussed in the text as a function of $(N-Z)/A$ [13]; $K_{\text{Coul}} = -5.2 \text{ MeV}$ [15]. The line represents a least-squares quadratic fit to the data.

3. – Spin-isospin excitations

Neutrino scattering from nuclei can proceed via neutral currents, *i.e.* elastic and inelastic scattering (ν, ν') and charged currents, *i.e.* (ν_e, e^-) , $(\bar{\nu}_e, e^+)$. Neutrino scattering proceeds largely through spin-flip and isospin-flip transitions (in charged-current transitions isospin-flip occurs by nature of reaction). These types of transitions are important in various phenomena some of which will be discussed below and are mediated by the weak interaction. Neutral-current transitions of spin-flip and isospin-flip character, in short spin-isospin excitations, can be studied also with inelastic electron scattering and/or inelastic proton scattering at intermediate energies. In this way, the important transition matrix elements, such as for M0, M1 and M2 transitions, can be determined. Charged-current transitions can be studied with charge-exchange reactions such as (p, n) and $(^3\text{He}, t)$ which induce transitions analogous to β^- decay, *i.e.* isospin-lowering transition $\Delta T_z = -1$, or as (n, p) , $(d, ^2\text{He})$ and $(t, ^3\text{He})$ which induce transitions analogous to β^+ decay, *i.e.* isospin-raising transition $\Delta T_z = +1$. These charge-exchange reactions induce excitations of GTR, IVSGMR, IVSGDR, etc. These excitation modes play important roles in nuclear astrophysics, neutrino physics, double-beta decay, determination of neutron-skin thickness, etc. In order to study spin-isospin modes with charge-exchange reactions a few points have to be considered. For example, if one wants to study spin-flip transitions one has to choose an incident energy where the $V_{\sigma\tau}$ spin-isospin part of the nucleon-nucleon (NN) interaction dominates over the V_τ isospin part. This is illustrated in fig. 6 where the various central parts of the NN interaction are plotted *versus* incident energy [16]. In the region between 100 and 500 MeV incident energy, $V_{\sigma\tau}$ dominates strongly over V_τ . In this region, also the dominant V_0 part of the NN interaction has a broad minimum. In the $(^3\text{He}, t)$ studies that were performed at RCNP, Osaka a bombarding energy of $\sim 150 \text{ MeV/u}$ has been used, where the ratio of $V_{\sigma\tau}/V_\tau \geq 3$ resulting in a ratio of cross-sections of ~ 10 .

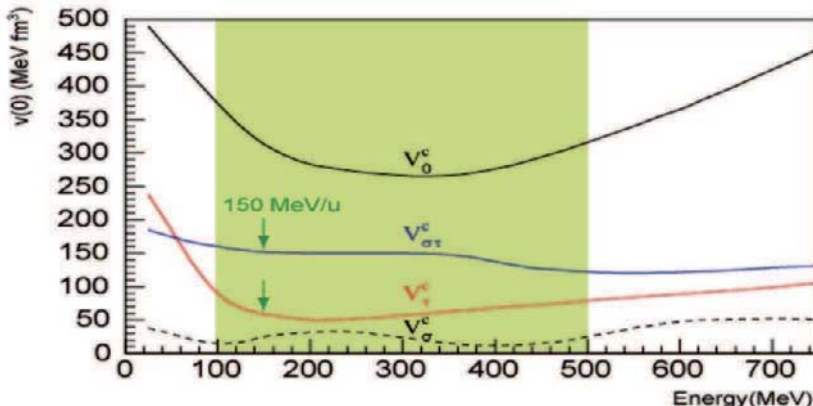


Fig. 6. – Volume integrals of the central components of the NN interaction are plotted as a function of the incident energy [16]. “c” denotes central. Note that, whereas $V_{\sigma\tau}$ varies slightly in the energy range 100–500 MeV, V_τ goes through a minimum.

Other considerations that come into play are the complexity of the reaction mechanism and the experimental conditions. The first favors light projectiles with no bound states at intermediate incident energies, *i.e.* in the region where the V_0 part of the NN interaction has its broad minimum. The second favors certain reactions over others. For example, the (p, n) reaction has a simpler reaction mechanism than the $(^3\text{He}, t)$ reaction, but it is more difficult to get high energy resolution because this would require very long flight paths with the time-of-flight method. Long flight paths imply loss of geometrical efficiency. In the case of the $(^3\text{He}, t)$ reaction, very high energy resolution can be obtained with the use of a magnetic spectrometer with a detection efficiency approaching 100%. For the (n, p) -type reactions, all of the light-ion reactions (n, p) , $(d, ^2\text{He})$ and $(t, ^3\text{He})$ present experimental problems. The first and third reactions require secondary beams which result in low beam intensities and very low energy resolutions, which is worse for neutron beams than for triton beams. In principle, one can use primary triton beams with very high energy resolution, but this presents other problems with radio protection. The $(d, ^2\text{He})$ reaction can be performed with primary beams of high energy resolution but the ${}^2\text{He}$ ejectile is not bound and the two protons have to be detected with high energy and angular resolutions in order to reconstruct the ${}^2\text{He}$ in its singlet S state with high resolution.

In fig. 7, the relative dependence of $V_{\sigma\tau}$ and V_τ as a function of proton incident energy is demonstrated making use of the ${}^{14}\text{C}(p, n){}^{14}\text{N}$ reaction at 0° . The ground and first-excited states of ${}^{14}\text{N}$ have spin-parity of 1^+ and 0^+ , respectively. Transitions from the 0^+ ground state of ${}^{14}\text{C}$ to the 1^+ and 0^+ levels in ${}^{14}\text{N}$ are mediated by the $V_{\sigma\tau}$ and V_τ parts of the NN interaction, respectively. The displayed spectra have been measured for proton incident energies ranging from 60 MeV to about 650 MeV. The height of the peak of the 1^+ level has been arbitrarily normalized to be a constant as a function of

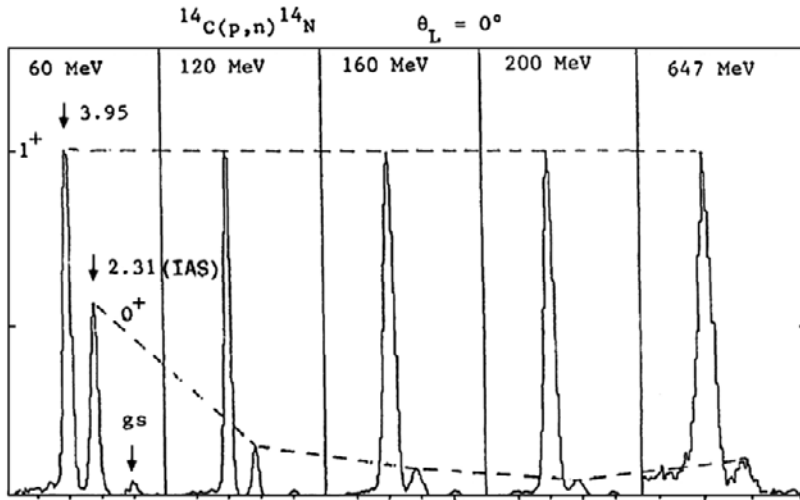


Fig. 7. – The spectra show the yields for the 1^+ and 0^+ states of ^{14}N populated by the $^{14}\text{C}(p,n)^{14}\text{N}$ reaction at 0° and the indicated bombarding energies. The spectra have been arbitrarily normalized so that the height of the 1^+ peak is constant as a function of bombarding energy. See refs. [17, 18].

bombarding energy similar to the dependence of $V_{\sigma\tau}$ in fig. 6. Interestingly, the height of the peak of the 0^+ level follows the same energy dependence as that of the V_τ in fig. 6.

Therefore, to study GT transitions ($\Delta L = 0$, $\Delta S = 1$, $\Delta T = 1$) in nuclei it is important to measure at and near 0° using a bombarding energy between 100 and 500 MeV/u where strong excitation of GT levels is expected. For GT^- transitions, the (p,n) and $(^3\text{He},t)$ reactions can be used. If the target ground state has isospin T_0 , then three components of the GTR can be populated with: $T_0 - 1$, T_0 , and $T_0 + 1$. For GT^+ transitions, the (n,p) , $(d, ^2\text{He})$ and $(t, ^3\text{He})$ reactions can be used. If the target ground state has isospin T_0 , then in this case only one component of the GTR can be populated with $T_0 + 1$.

4. – GT strength in fp -shell nuclei

Bethe *et al.* [19] and Fuller, Fowler and Newman (FFN) [20] recognized that (GT) transitions in fp -shell nuclei play an important role in the calculation of the weak-interaction rates of processes taking place during the last few days of a heavy star in its pre-supernova stage. This led to renewed interest in determination of the GT strength distributions in fp -shell nuclei, and there were many studies, both experimentally and theoretically, of the GT strength in fp -shell nuclei in the last two to three decades. This is important for a number of reasons. The core of a heavy star with a mass of 10 solar masses and heavier is composed of fp -shell nuclei after having burnt its fuel and reached the pre-supernova stage. These fp -shell nuclei can capture electrons at the

high temperatures in which the stars find themselves thus reducing the electron pressure that counteracts gravitational collapse precipitating the collapse that is followed by a cataclysmic supernova explosion. Furthermore, neutrino absorption cross-sections by *fp*-shell nuclei are essential for understanding of nuclear synthesis in supernova explosions. The matrix elements that govern electron capture and neutrino absorption are difficult to calculate in the shell model because of the open shell structure of *fp*-shell nuclei though there has been much progress recently with large-basis shell-model calculations. Therefore, it is of the utmost importance to measure spin-isospin responses of *fp*-shell nuclei to gauge theoretical calculations.

For GT^- transitions, the (p, n) and $(^3\text{He}, t)$ reactions can be used, and for GT^+ transitions, the (n, p) , $(d, ^2\text{He})$ and $(t, ^3\text{He})$ reactions can be used. The cross-section can be written at momentum transfer $q = 0$ as [21, 22]

$$(8) \quad \frac{d\sigma}{d\Omega}(q = 0) = \frac{\mu_i \mu_f}{(\pi \hbar^2)^2} \left(\frac{k_f}{k_i} \right) (N_D^\tau |J_\tau|^2 B(\text{F}) + N_D^{\sigma\tau} |J_{\sigma\tau}|^2 B(\text{GT})).$$

Here, μ_i and μ_f are the reduced masses in the initial and final channels, and k_i and k_f the momenta of the incoming and outgoing particles, respectively. N_D is the distortion factor for Fermi (τ) or GT ($\sigma\tau$) transitions, J_τ and $J_{\sigma\tau}$ are the volume integrals of the isospin and spin-isospin components of the central part of the NN interaction and $B(\text{F})$ and $B(\text{GT})$ are the transition strengths for the Fermi and GT parts of the transition. Note the similarity between this cross-section of the (p, n) and $(^3\text{He}, t)$ reactions at $q = 0$ and the neutrino absorption cross-section given by

$$(9) \quad \sigma = \frac{1}{\pi \hbar^4 C^3} [G_V^2 B(\text{F}) + G_A^2 B(\text{GT})] \times F(Z, E_e) p_e E_e.$$

Here, G_V and G_A are the vector and axial-vector coupling constants. This similarity indicates the importance of charge-exchange reactions at intermediate energies for determining $B(\text{GT})$ values. In the case of pure GT transition, eq. (8) simplifies to

$$(10) \quad \frac{d\sigma}{d\Omega}(q = 0) = \frac{\mu_i \mu_f}{(\pi \hbar^2)^2} \left(\frac{k_f}{k_i} \right) N_D^{\sigma\tau} |J_{\sigma\tau}|^2 B(\text{GT}).$$

In principle, one can determine the $B(\text{GT})$ value directly from measuring the cross-section at 0° and extrapolating it to $q = 0$ and calculating N_D and $J_{\sigma\tau}$. However, after these steps are taken usually the value is normalized to a calibrated $B(\text{GT})$ value for known transitions from β -decay. In this way, a unit cross-section for $B(\text{GT})$ transitions could be defined.

5. – Determination of GT^- strength

In order to demonstrate the power of intermediate energy charge-exchange reactions, we show in the following the results of the $^{176}\text{Yb}(^3\text{He}, t)^{176}\text{Lu}$ reaction [23]. Because of

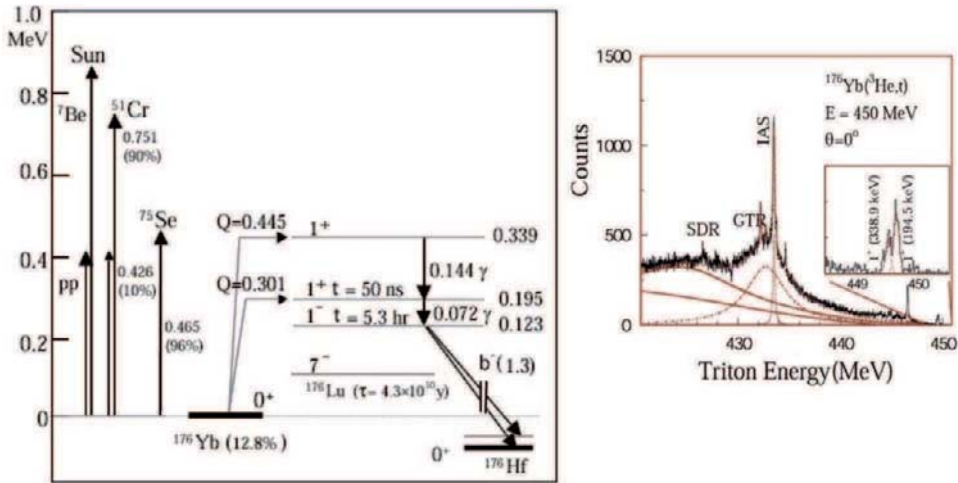


Fig. 8. – Left panel: level scheme and γ -ray tags for solar-neutrino detection by ^{176}Yb (12.8% natural abundance). All energies are in MeV. Right panel: triton energy spectrum from the $^{176}\text{Yb}(^3\text{He}, t)^{176}\text{Lu}$ reaction taken at 0° and incident energy $150 \text{ MeV}/u$. In addition, to structures observed at high excitation energies the two 1^+ states at low excitation energy are observed and resolved as displayed in the expanded inset; see ref. [23] for details.

the low-lying GT transitions from ^{176}Yb to ^{176}Lu , ^{176}Yb has been considered as a solar neutrino detector to resolve the discrepancy between the observed neutrino flux from the Sun [24, 25] in comparison with the predicted neutrino flux by the Standard Solar Model [26]. The dominant part of the neutrino flux from the Sun is due to the $pp \rightarrow de^+\nu$ with a maximum energy of the neutrinos of 420 keV, which nicely matches with the energy needed for the GT transition to the lowest 1^+ level in ^{176}Lu . The GT transition to the second 1^+ level requires neutrinos with energies above 445 keV which is beyond the maximum energy of the pp neutrinos; see left panel of fig. 8, which shows the maximum neutrino energies from the different sources as arrows and gives the low-lying levels of ^{176}Lu .

In a (p, n) experiment [27] performed in parallel, the two levels at 195 keV and 339 keV could not be resolved and a summed $B(\text{GT})$ value of 0.32 ± 0.04 was reported. Since the pp neutrinos can only excite the 195 keV level, it was imperative to resolve these two levels. An experiment was performed [23] with the high-resolution Grand Raiden Spectrometer [28] at RCNP, Osaka with ^3He beam at energy of $150 \text{ MeV}/u$. The two low-lying 1^+ levels could be resolved as can be seen in the inset of the right panel of fig. 8. Their $B(\text{GT})$ could be calibrated with the known ^{164}Dy weak matrix element. The obtained $B(\text{GT})$ values are listed in table II. The $B(\text{GT})$ of the higher level is found to be about half of that of the lower level, but their sum is in excellent agreement with the result obtained from (p, n) experiment [27].

Almost an order of magnitude improvement with the resolution of detected scattered particles was obtained when the West-South (WS) beam line was constructed at RCNP,

TABLE II. – *Gamow-Teller B(GT) of the levels observed in the $^{176}\text{Yb}({}^3\text{He}, t)^{176}\text{Lu}$ [23].*

E_x (MeV)	$0.195 + 0.339 (p, n)$	0.195	$0.339 ({}^3\text{He}, t)$
$B(\text{GT})$	0.32 ± 0.04	0.20 ± 0.04	0.11 ± 0.02

Osaka [29]. This allowed unprecedented high-resolution measurements at a ${}^3\text{He}$ energy of ~ 450 MeV using the momentum-dispersion technique. Beams from the Ring Cyclotron are transported to the target through the high-dispersive WS beam line; see fig. 9. After charge-exchange reactions with target nuclei the ejectile tritons are measured with Grand Raiden applying dispersion matching. A high resolution of around 30 keV has been achieved with thin targets. This provides excellent new opportunities to study GT strength in fp -shell nuclei in great details.

To illustrate the great potential of this facility we present here the study of the $^{58}\text{Ni}({}^3\text{He}, t)^{58}\text{Cu}$ reaction with the aim to study the structure of the GTR in ${}^{58}\text{Cu}$ and decompose its isospin components. Starting from ${}^{58}\text{Ni}$ ground state with isospin $T_0 = 1$, one can, in principle, separate the isospin components by comparison among the spectra obtained by (n, p) , (p, p') and (p, n) reactions on ${}^{58}\text{Ni}$. This is, however, very difficult in practice because of the high level density for populated states with different isospin.

Grand-Raiden Spectrometer

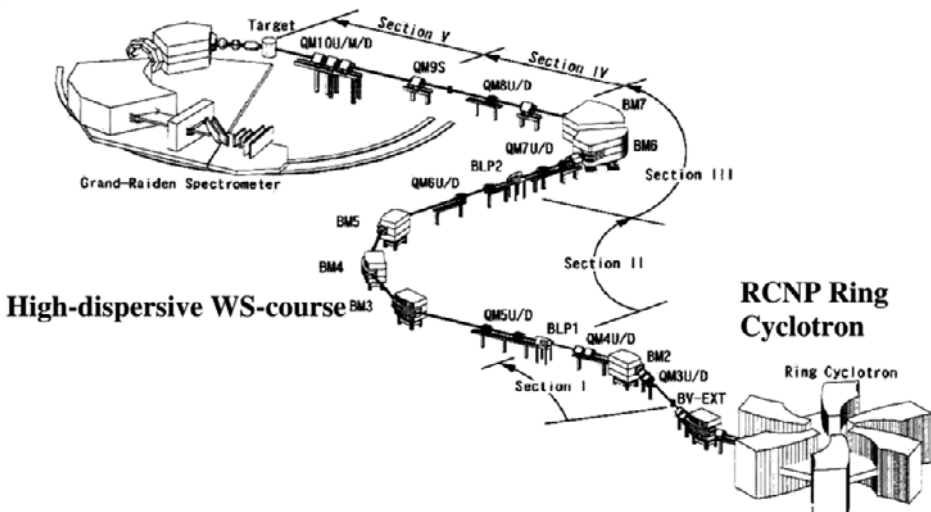


Fig. 9. – Schematic layout of the experimental setup at RCNP allowing high-resolution measurements making use of dispersion-matching technique. Beams from the Ring Cyclotron are transported to the scattering chamber of the Grand-Raiden spectrometer through the high-dispersive WS beam line [29].

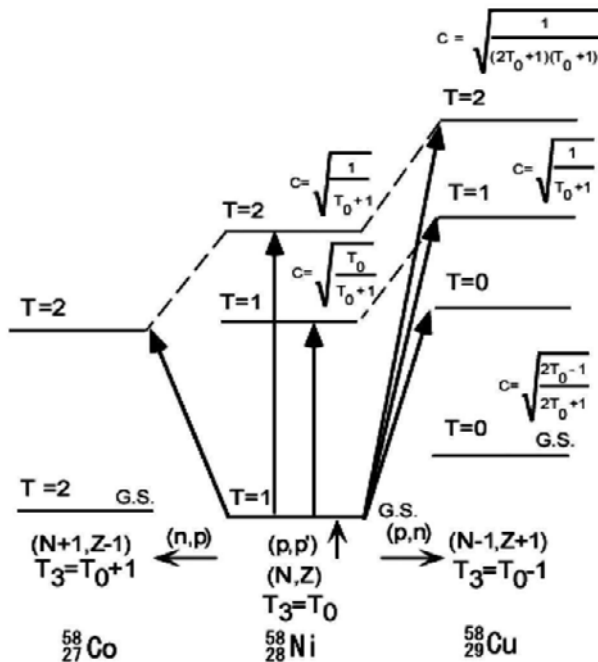


Fig. 10. – Schematic representation of population of various isospin components of 1^+ levels in (n,p) [GTR], (p,p') [M1 resonance] and (p,n) [GTR] reactions starting from a target nucleus with isospin quantum number $T = T_3 = T_0$. Dashed lines connect analog levels in the parent and daughter nuclei. Isospin Clebsch-Gordan (CG) coefficients that determine the relative excitation of the different components are shown. For ^{58}Ni $T_0 = 1$.

High-energy resolution experiments are therefore necessary to be able to perform this decomposition. A successful attempt to decompose the isospin components of the GTR in ^{58}Cu was performed by Fujita *et al.* [30].

The $^{58}\text{Ni}(^3\text{He}, t)$ reaction at 0° strongly excites $J^\pi = 1^+$ states with $T = 0, 1$ and 2 in ^{58}Cu because of the $\Delta T = 1$ transfer. In (p,p') and (e,e') , excited 1^+ ($M1$) states with $T = 1$ or 2 are observed as analog states in ^{58}Ni . In fig. 10, the various isospin components that can be populated in the (n,p) , (p,p') and (p,n) reactions and their analog relationships and isospin CG coupling coefficients are shown. Since ^{58}Ni ground state has isospin $T_0 = 1$, the square of the CG coefficient of isospin coupling leads to a transition strength ratio of $\sigma_{T=0} : \sigma_{T=1} : \sigma_{T=2} = 2 : 3 : 1$ for the $T_0 - 1$, T_0 and $T_0 + 1$ components, respectively; see fig. 10. Because of the nuclear structure of ^{58}Ni , which corresponds to a large extent to 2 neutrons outside a ^{56}Ni core of 28 protons and 28 neutrons filling all shells up to and including $1f_{7/2}$ one can show that in this simple model the expected $J^\pi = 1^+$ $B(\text{GT})$ strength of 19.7 in ^{58}Cu is distributed among the three isospin components $T_0 - 1$, T_0 and $T_0 + 1$ with the ratio of 47%, 41% and 12%, respectively [30].

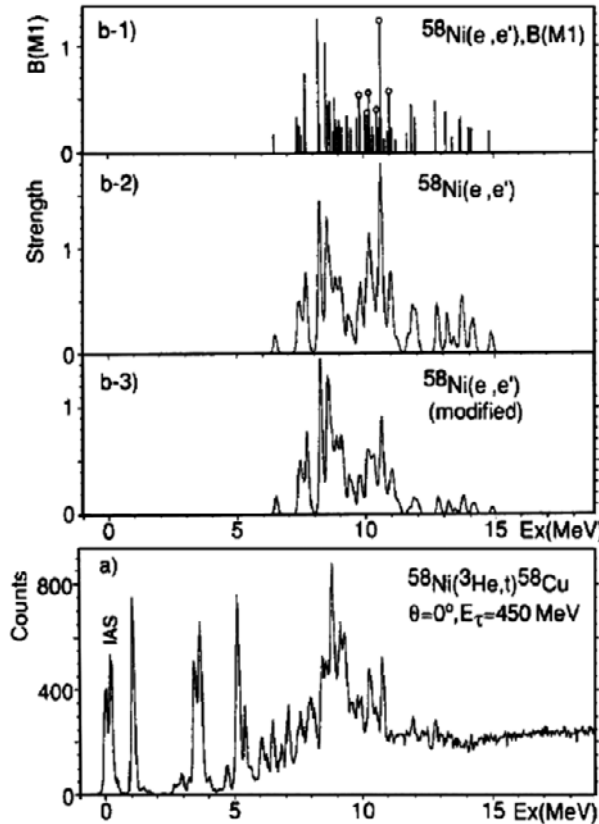


Fig. 11. – Comparison between the 0° $^{58}\text{Ni}(^3\text{He},t)$ spectrum (a), which is mainly GT strength, and the MI strength distribution obtained in the $^{58}\text{Ni}(e,e')$ experiment [31]. (b-1) The $B(\text{M}1)$ distribution deduced in the $^{58}\text{Ni}(e,e')$ experiment. (b-2) The reconstructed $^{58}\text{Ni}(e,e')$ spectrum after convoluting with the experimental energy resolution of the $(^3\text{He},t)$ experiment. (b-3) The same as (b-2), but $T = 2$ strength scaled down by a factor of three. Since the IAS of the ^{58}Ni ground state is observed at 0.20 MeV in ^{58}C , the excitation energy in ^{58}Ni is shifted with 0.20 MeV relative to ^{58}Cu . This figure is from ref. [30].

In fig. 11(a), the 0° spectrum of the $^{58}\text{Ni}(^3\text{He},t)^{58}\text{Cu}$ reaction obtained at a bombarding energy of 450 MeV is shown [30]. The energy resolution was 140 keV that was achieved before the WS beam line was constructed. Because of the strong excitation of $\Delta L = 0$ transitions at 0° and this high bombarding energy, mainly 1^+ levels are excited in addition to the isobaric analog state (IAS) at 0.20 MeV excitation energy in ^{58}Cu . This spectrum should be compared to the 1^+ levels observed in $^{58}\text{Ni}(e,e')$. In fig. 11(b-1), the $B(\text{M}1)$ strength distribution deduced from inelastic electron scattering measurement [31], in which an energy resolution of 30 keV was achieved, is shown. In order to compare with the spectrum obtained in the $^{58}\text{Ni}(^3\text{He},t)^{58}\text{Cu}$ reaction the $B(\text{M}1)$ strength distribution was convoluted with the experimental energy resolution of the $(^3\text{He},t)$ experiment; see

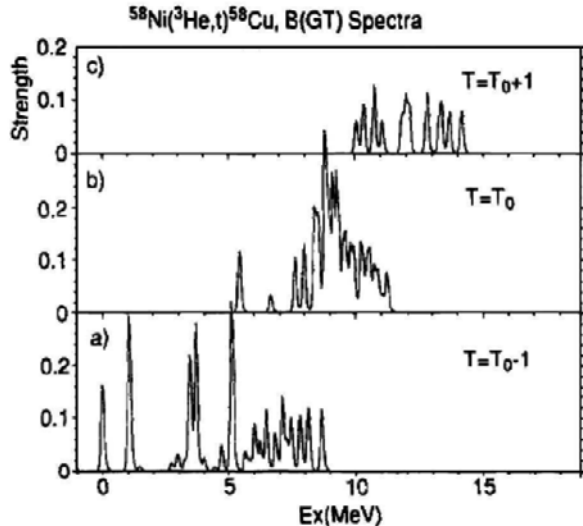


Fig. 12. – The $B(\text{GT})$ strength distributions for the three isospin components as could be deduced from comparison of various probes as discussed in detail in the text [30].

fig. 11(b-2). Before the final comparison is made, one notes that the relative excitation of the T_0 and $T_0 + 1$ components in ^{58}Cu is $\sigma_{T=1} : \sigma_{T=2} = 3 : 1$, whereas in ^{58}Ni it is $\sigma_{T=1} : \sigma_{T=2} = 1 : 1$; see fig. 10. Therefore, one has to identify the $T = 2$ levels in ^{58}Ni and reduce their relative excitation by a factor 3 before the final comparison is made. This was done by comparing to the results of a $^{58}\text{Ni}(t, {}^3\text{He})^{58}\text{Co}$ measurement performed at 25 MeV bombarding energy [32] and a recent $^{58}\text{Ni}(n, p)^{58}\text{Co}$ measurement at 198 MeV bombarding energy [33], which populates only $T = 2$ levels. In the $(t, {}^3\text{He})$ measurement, six 1^+ GT levels were identified and consequently their analogs in ^{58}Ni were identified. These are marked with the small circles in fig. 11(b-1). The (n, p) measurement did not have sufficient energy resolution to resolve discrete levels. However, the $T = 2$ GT strength was found to exist continuously between 1 MeV and 5 MeV excitation energy. This corresponds in ^{58}Ni to the excitation-energy region above 11.5 MeV. Therefore, the relative strength of the six 1^+ states and the region above 11.5 MeV were scaled down by factor of 3. The resulting spectrum is shown in fig. 11(b-3).

By comparing fig. 11(a) and fig. 11(b-3) and knowing the $T = 2$ GT distribution from the $(t, {}^3\text{He})$ and (n, p) measurements, Fujita *et al.* were able to determine the $B(\text{GT})$ strength distributions for all three isospin components. These are shown in fig. 12 after convoluting with the experimental energy resolution of the $({}^3\text{He}, t)$ experiment. It can be observed that the observed $B(\text{GT})$ strength is fragmented for all isospin components. Furthermore, the integrated strengths for the three isospin components are in better agreement with the predictions of the simplified shell-model calculations than with the predictions purely on basis of the CG coefficients.

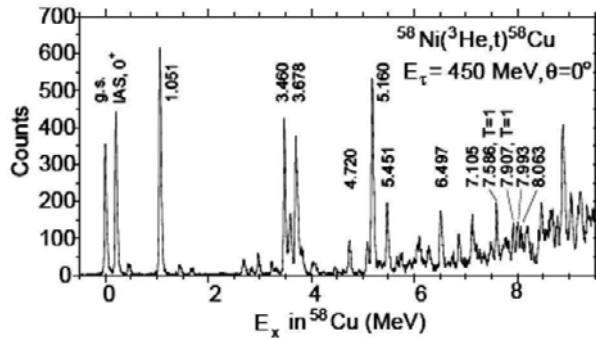


Fig. 13. – A $^{58}\text{Ni}(^3\text{He}, t)^{58}\text{Cu}$ spectrum taken at 0° and 450 MeV incident energy is shown; the energy resolution achieved is about 50 keV. States with $L = 0$ character are indicated by their excitation energies [30].

With the construction of the WS beam line at Osaka, it became possible to achieve much better energy resolution through use of the dispersion-matching technique. In fig. 13, a 0° spectrum of the $^{58}\text{Ni}(^3\text{He}, t)^{58}\text{Cu}$ reaction taken at a bombarding energy of 450 MeV is shown. A high resolution of 50 keV was achieved. By comparing this spectrum with that of fig. 11(a), one can observe the great improvement in resolving the low-lying levels and the fine structure of the GTR. With this achieved high-resolution, the ($^3\text{He}, t$) reaction becomes a powerful tool to study spin-isospin modes and, in particular, the GT strength in great detail. It has indeed been used very effectively in the last decade in studies of the spin-isospin modes with the facility at RCNP, Osaka. Many nuclei in the sd and fp shells have been studied in this period allowing the extraction of the $B(\text{GT}^-)$ distributions in the final nuclei with very high energy resolution of about 35 keV full width at half maximum [34].

6. – Determination of GT^+ strength and its astrophysical implications

In a heavy star that initially is formed of hydrogen gas but with a mass larger than 10 solar masses ($M > M_\odot$), the collapse due to gravitational pressure increases the temperature in the star interior to $\sim 10^7$ – 10^8 K initiating thus a fusion of hydrogen through the weak process: $pp \rightarrow de^+\nu$. The thermal pressure keeps the star from further collapsing while all the hydrogen in the star interior is converted to ^4He through different reaction paths essentially converting: $4p \rightarrow ^4\text{He} 2e^+ 2\nu + 26.7 \text{ MeV}$. After about 10^6 – 10^7 years, hydrogen burning ends in the core of the star. The star starts contracting again under gravitational pressure and the temperature increases to 2×10^8 K resulting in a red giant wherein He-burning occurs in the core while hydrogen burning starts in the surrounding region at temperatures appreciably exceeding 10^7 K. After about 5×10^5 years, the processes of burning heavier elements at higher temperatures occur resulting in an onion-shell structure of the star with a core constituted mainly of Fe and Ni isotopes

at a mass of around $1.4 M_{\odot}$ surrounded by shells filled consecutively with Si, O, C, He and H. At this stage, gravitational pressure increases but is balanced by the pressure due to a degenerate electron gas which keeps the star from completely collapsing up to the Chandrasekhar limit which is about $1.4 M_{\odot}$. Above this limit the electron gas pressure cannot keep the star from collapsing. The collapse starts when the temperature reaches $T = 10^9$ K and a density $\rho = 3 \times 10^7$ g/cm³. This is accelerated by the neutronization (de-leptonization) of the core of the star through electron capture processes on nuclei of Fe and Ni isotopes. The reduction of Y_e the electron-to-baryon ratio through the electron capture process leads to a reduction in the pressure of the degenerate gas and to accelerated collapse followed by a re-bounce from the star core resulting in a supernova explosion.

The electron-capture (EC) process on *fp*-shell and, in particular, Fe and Ni nuclei plays a dominant role during the last few days of the life (pre-supernova stage) of a heavy star [19]. The rate for EC is governed by the GT⁺ strength distributions at low excitation energy; which are not accessible to β -decay. First estimates of EC rates in stellar environments were made in the early eighties by FFN using simple single-particle model [20]. In the late nineties, shell-model codes were developed and new computer hardware became available that allowed to perform large-basis shell-model calculations [35]. This made it possible to calculate relevant GT strength distributions in *fp*-shell nuclei using a very large number of configurations. The results obtained in these large-scale shell-model calculations [35, 36] marked deviations from FFN EC rates and indicated that the EC rates are in general smaller than was calculated by FFN [20]. These conclusions have led to revisiting pre-supernova models [37]. The new evaluations resulted in a smaller mass of the iron core of the pre-supernova star and a larger value for the electron-to-baryon ratio Y_e as compared to calculations by FFN.

It became evident that stellar weak reaction rates should be determined with improved reliability compared to FFN. Large-scale shell model calculations provided the possibility to improve the prediction of EC rates by tuning these to reproduce GT⁺ strength measured in, *e.g.*, (*n, p*) reaction. Calculations of the EC rates relied on (*n, p*) data from TRIUMF, which have a rather poor energy resolution [33, 38]. The calculations showed nice agreement with the data after folding with the energy resolution of 1 MeV for the (*n, p*) reaction; see fig. 14.

At low temperatures, the EC rates depend sensitively on the discrete structure of the low-lying GT strength. Therefore, it is important to resolve the low-lying GT states. To test this a case study was made to determine the low-lying GT levels of ^{58}Ni in a reaction with which a much better energy resolution can be obtained compared to the (*n, p*) reaction [39]. For this reason, the (*d, ^2He*) reaction was chosen which in addition to a better energy resolution offers other advantages; see fig. 15. In this figure, a schematic representation of the charge-exchange (*d, ^2He*) reaction is shown. The deuteron ground state is a 3S_1 state ($S = 1$) with isospin $T = 0$. The unbound di-proton system (isospin $T = 1$) is referred to as ^2He , if the two protons are in a relative 1S_0 state. The 1S_0 state dominates if the relative 2-proton kinetic energy $\varepsilon < 1$ MeV. Experimentally, an almost pure 1S_0 state can be selected by limiting the relative energy of the di-proton system to

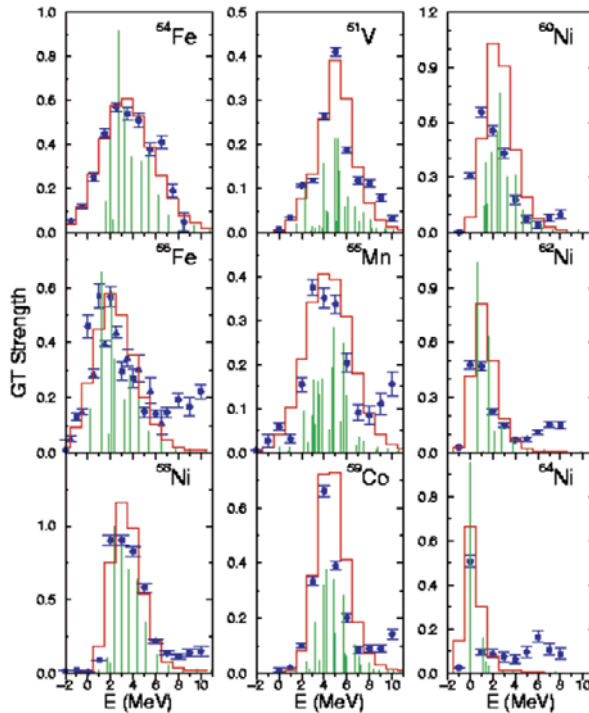


Fig. 14. – Comparison of GT^+ data obtained with the (n, p) reaction on several nuclei in the fp -shell [33, 38] with calculated strength distributions making use of large-scale shell-model calculations [35]. The theoretical predictions are shown by discrete lines which are folded with the experimental energy resolution to obtain the plotted histograms; figure obtained from ref. [35].

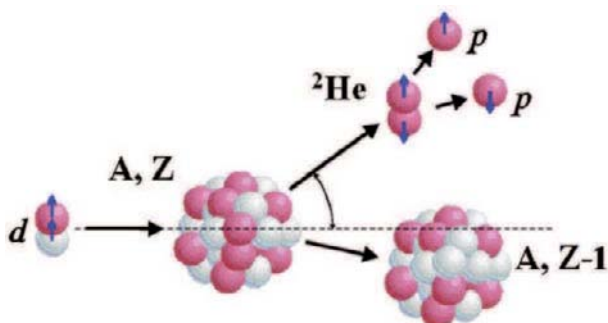


Fig. 15. – Schematic representation of the $(d, {}^2\text{He})$ charge-exchange reaction on a nucleus A with atomic number Z . The deuteron has $S = 1$, $T = 0$, and the unbound ${}^2\text{He}$ has $S = 0$, $T = 1$.

less than 1 MeV, as in this case the contribution of higher-order partial waves is of the order of a few percent only. Furthermore, the reaction mechanism forces a spin-flip and isospin-flip transition ($\Delta S = \Delta T = 1$). Therefore, the $(d, {}^2\text{He})$ reaction is an (n, p) -type probe with exclusive $\Delta S = 1$ character and at small momentum transfers, mainly probes the GT^+ transition strengths. However, a disadvantage of this reaction near 0° is the tremendous background originating from d -breakup.

The ${}^{58}\text{Ni}(d, {}^2\text{He})$ reaction was studied at KVI using the Big-Bite Spectrometer [40] and the EuroSuperNova (ESN) focal-plane detection system [41]. The focal-plane detection system consists of two vertical-draft chambers (VDC), with the capability to determine the position of incidence of a scattered particle in two dimensions, and a scintillation detector for particle identification and timing purposes. The angle of incidence can be determined from the positions of incidence on the two VDCs, and this can be converted to the scattering angle of the particle through ray-tracing techniques. Because of the large background due to d -breakup the VDCs need to have fast readout which is realized with pipeline TDCs and decoding using imaging techniques. Furthermore, the VDCs need to have good double-tracking capability which is essential for detecting the two protons from ${}^2\text{He}$ down to very small separation distances at the focal plane. Using the VDC information obtained in this way, good phase-space coverage for small relative proton energies is assured making it possible to select the 1S_0 state of the two coincident protons.

In the ${}^{58}\text{Ni}(d, {}^2\text{He})$ experiment, a 170 MeV deuteron beam was used to bombard a self-supporting ${}^{58}\text{Ni}$ target. The experimental details can be found in ref. [39]. Using the dispersion-matching technique, an energy resolution of 130 keV was achieved, which is an order of magnitude better than has been achieved in the (n, p) experiments [33, 38]. The experimental method and data-reduction techniques have been described in [42]. In fig. 16, the double-differential cross-section up to $E_x = 10$ MeV is shown and compared to data from the ${}^{58}\text{Ni}(n, p)$ reaction obtained with 1 MeV energy resolution [33]. The superiority of the spectrum obtained with the $(d, {}^2\text{He})$ is evident.

In order to determine the $B(\text{GT})$ distribution, the double-differential cross-sections have to be determined as a function of scattering angle. The cross-section due to $\Delta L = 0$ transfer has to be determined through a DWBA analysis in order to subtract any $\Delta L = 2$ contribution which could be mediated by the tensor part of the NN interaction. The cross-section is then extrapolated to $q = 0$ transfer (see eq. (10)) and then the $B(\text{GT})$ value is determined.

For the region $E_x < 4.1$ MeV, the experimental angular distributions were obtained for all the peaks indicated with numbers in fig. 16 by fitting the spectra with peaks at 6 angular bins in the range between $\theta = 0^\circ$ and 6.5° [39]. Peaks with $\Delta L = 0$ strength corresponding to $J^\pi = 1^+$ states can be identified based on their enhanced cross-sections near a scattering angle of 0° as compared to more backward scattering angles (*i.e.*, $\theta_{\text{c.m.}} = 4^\circ$).

As discussed earlier, the $B(\text{GT})$ values have to be normalized to a $B(\text{GT})$ value known, *e.g.*, from β -decay. This was performed for the $(d, {}^2\text{He})$ charge-exchange reaction using the GT transitions to low-lying states in ${}^{12}\text{B}$ and ${}^{24}\text{Na}$ [42]. This is illustrated in

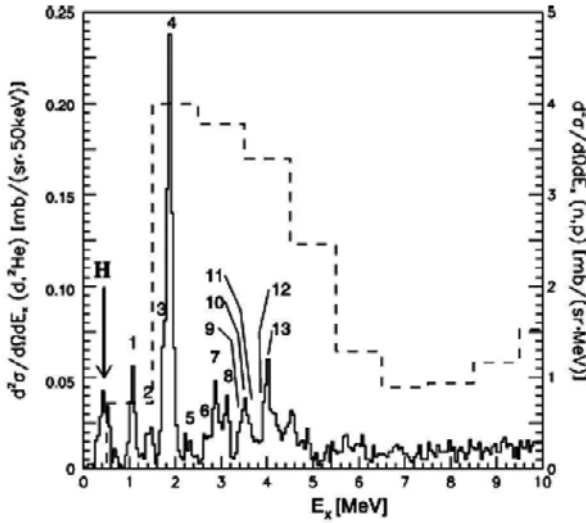


Fig. 16. – A spectrum obtained with the $^{58}\text{Ni}(d, ^2\text{He})$ charge-exchange reaction in the angular range $\theta = 0^\circ - 1^\circ$. The peak caused by contamination of the target with hydrogen is indicated by “H”. The dashed histogram represents the spectrum from the (n, p) reaction at $\theta = 0^\circ$ [33].

fig. 17 for ^{24}Na . In this figure, the $^{24}\text{Mg}(d, ^2\text{He})$ spectrum [42] obtained at $\theta = 0.4^\circ$ and 170 MeV incident energy (fig. 17a) is compared to the $^{24}\text{Mg}(p, n)$ spectrum [43] obtained at $\theta = 0.2^\circ$ and 135 MeV incident energy (fig. 17b). These two reactions lead to mirror nuclei and therefore mirror transitions will have the same $B(\text{GT})$ values. Since the $B(\text{GT})$ values determined from (p, n) have been calibrated making use of several $B(\text{GT})$ values deduced from β -decay in even-even sd -shell nuclei, they could be used to calibrate the ones determined from the $^{24}\text{Mg}(d, ^2\text{He})$ reaction. In fig. 17c, the $B(\text{GT})$ values determined from the $^{24}\text{Mg}(p, n)$ reaction for several levels in ^{24}Al are plotted *versus* the differential cross-sections extrapolated to $q = 0$ for the mirror levels in ^{24}Na determined in the $^{24}\text{Mg}(d, ^2\text{He})$ reaction. There is a linear proportionality relationship between the two quantities indicating that extracting the $B(\text{GT})$ values for ^{58}Co as described above will be reliable.

In fig. 18, a comparison is made between the $B(\text{GT}^+)$ strength obtained from the $^{58}\text{Ni}(d, ^2\text{He})$ experiment [39] with those obtained from the (n, p) experiment [33]. The dots in the upper panel represent the $B(\text{GT}^+)$ values determined for the numbered peaks as obtained from the fitting procedure. The gray histogram represents the $B(\text{GT}^+)$ values as obtained from MDA taking 1 MeV energy bins. Up to an excitation energy of 4 MeV, the integrated $B_{\text{exp}}(\text{GT}^+)$ strength obtained through the two different methods is consistent. Taking into account systematic errors, the integrated $B_{\text{exp}}(\text{GT}^+)$ strength up to $E_x = 4$ MeV of 2.1 ± 0.4 from $^{58}\text{Ni}(d, ^2\text{He})$ is in agreement with the integrated $B_{\text{exp}}(\text{GT}^+)$ strength of 2.7 ± 0.3 deduced from the (n, p) reaction. However, the two distributions differ significantly in shape. In the lower panel of fig. 18, the results of

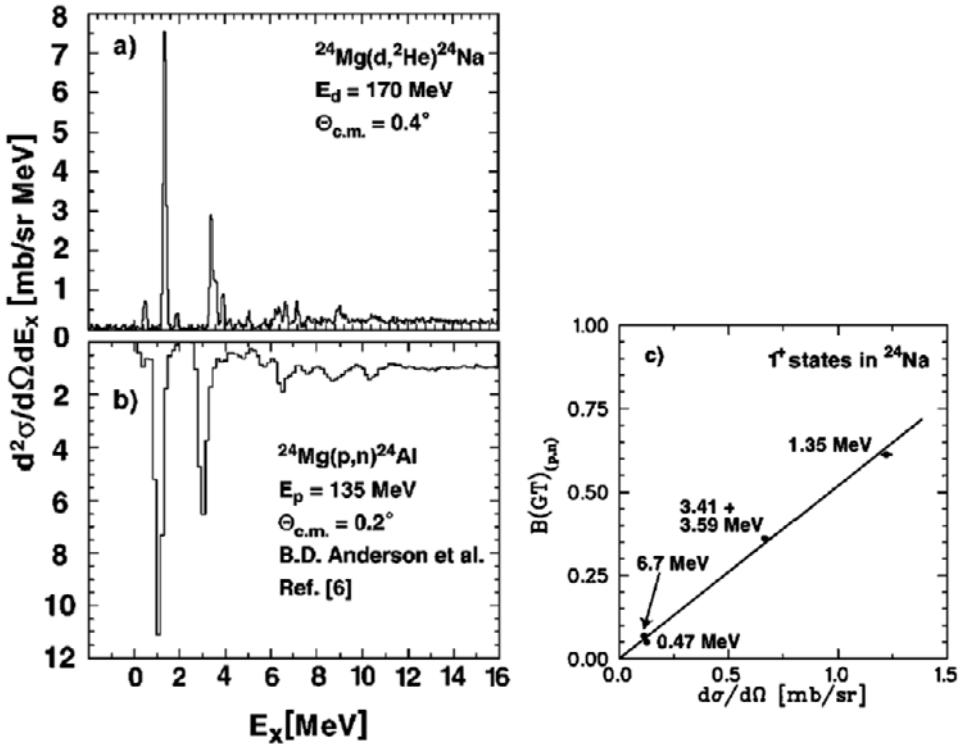


Fig. 17. – a) $^{24}\text{Mg}(d, ^2\text{He})$ spectrum [42] obtained at $\theta = 0.4^\circ$ and 170 MeV incident energy. b) $^{24}\text{Mg}(p, n)$ spectrum [43] obtained at $\theta = 0.2^\circ$ and 135 MeV incident energy. c) The $B(\text{GT})$ values determined from the $^{24}\text{Mg}(p, n)$ reaction for several levels in ^{24}Al are plotted *vs.* the differential cross-sections extrapolated to $q = 0$ for the mirror levels in ^{24}Na determined in the $^{24}\text{Mg}(d, ^2\text{He})$ reaction.

large-scale shell-model calculations for the GT strength distribution are presented. The open squares show the results of the calculations performed by Honma *et al.* [44] which have been obtained using the GXPF1 effective interaction. The results displayed as dots have been obtained using the KB3G effective interaction [36]. It should be noted that the theoretical results have been calculated using a quenching factor of 0.74 for the GT operator. Both calculations reproduce fairly well the GT strength distribution obtained from the $(d, ^2\text{He})$ reaction. However, the enhancement of the GT strength in the region around 1.9 MeV is only reproduced using the KB3G interaction. The results from the earlier calculations [35] (not shown here) do not reproduce as well the GT strength distribution obtained from the $(d, ^2\text{He})$ reaction.

The experimental data shown in fig. 18 were used to check whether the new results have an impact on the electron-capture rates in the stellar environment. The method to calculate electron-capture (EC) rates follows the formalism derived by FFN [20]. The

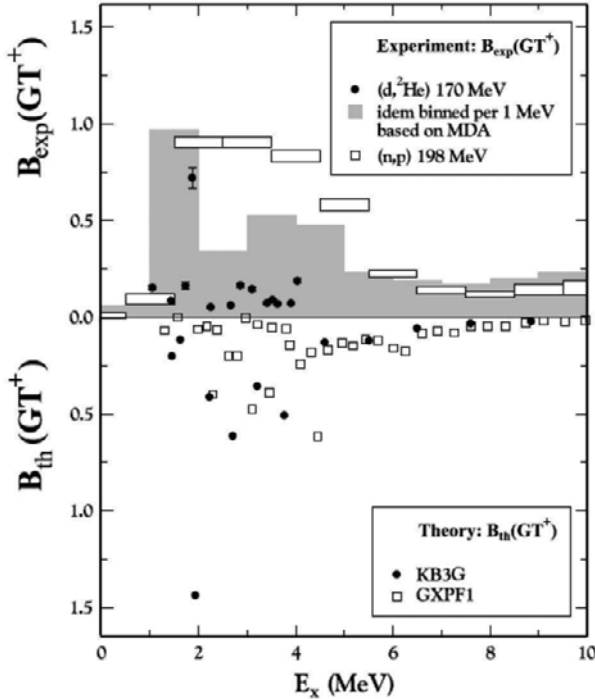


Fig. 18. – Upper panel: the experimental GT^+ strength distribution displayed per peak (dots) and per bin of 1 MeV (gray histogram) and the results from the (n, p) reaction [33] displayed per bin of 1 MeV. Lower panel: the results from calculations using the KB3G interaction [39] and those using the GXPF1 interaction [44].

formula for determining the EC rate is

$$(11) \quad \lambda_{ee} \approx \sum_i B_i(\text{GT}) \int_{\omega_1}^{\infty} \omega p(Q_i + \omega)^2 F(Z, \omega) S_e(\omega, T) d\omega.$$

Here, $B_i(\text{GT})$ is the Gamow-Teller strength distribution as determined from experiment or theory, ω and p are the energy and momentum of electrons, respectively, $F(Z, \omega)$ is the relativistic Coulomb barrier factor and $S_e(\omega, T)$ is the Fermi-Dirac distribution for an electron gas at temperature T . As representative values for the temperature, density and Y_e the conditions following silicon depletion are taken for the model labeled LMP listed in table 2 of ref. [37], *i.e.* $T_9 = 4.05$ where T_9 measures temperatures in units of 10^9 K, $\rho = 3.18 \times 10^7 \text{ g cm}^{-3}$, and $Y_e = 0.48$. This corresponds to the evolution of the core of a $25 M_\odot$ star using the weak-interaction rates of ref. [36].

At finite temperatures, there is a finite probability that nuclei are found in their excited states as well. In such a case, EC occurs not only through the ground state of a nucleus but also through the populated excited states. At the conditions present in

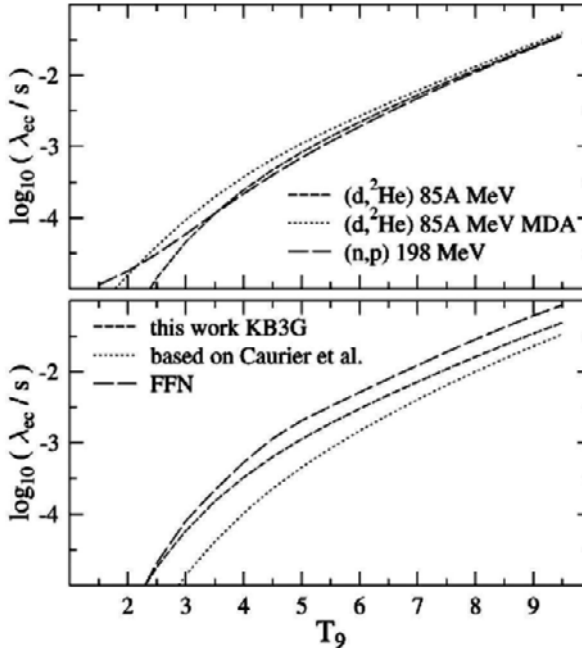


Fig. 19. – Upper panel: EC rates based on $B(\text{GT})$ distributions from the (n, p) measurement [33] and the $(d, ^2\text{He})$ measurement [39]. Lower panel: obtained from the shell-model calculations using the KB3G interaction [36, 39], the earlier works of FFN [20] and Caurier *et al.* [35]; see text for more details.

a hot heavy star, the contribution of transitions starting from excited nuclear states is thus non-negligible. For the particular conditions mentioned above, the shell-model calculations predict that the rate for EC through excited states of ^{58}Ni is 50% the rate as calculated using only the ground-state contribution [36]. This contribution was fixed and added to the EC capture rate through the ground state of ^{58}Ni . The latter contribution was recomputed using the GT-strength distribution measured in the (n, p) and $(d, ^2\text{He})$ reactions or computed using the various available theoretical calculations including the one with KB3G interaction. The results of the rates are displayed in fig. 19 as a function of temperature and for the values of density and Y_e mentioned above. Because of the high sensitivity to the Q -value for EC at low temperatures, the calculated theoretical rates use experimental excitation energies for the first two 1^+ states in ^{58}Co . The details of the GT-strength distribution (excitation energies and $B(\text{GT})$ -values) have a strong impact on the electron-capture rate. This can be seen in fig. 19, where the rates calculated applying the results from the MDA (see fig. 18) are substantially larger than the rates using the high-resolution data. They also differ especially at the low temperatures from the rates based on the (n, p) data [33]. Also, the rates calculated with the large-scale shell-model calculations with the KB3G interaction [39] differ substantially from the earlier ones by Caurier *et al.* [35] and the ones based on the results of FFN [20].

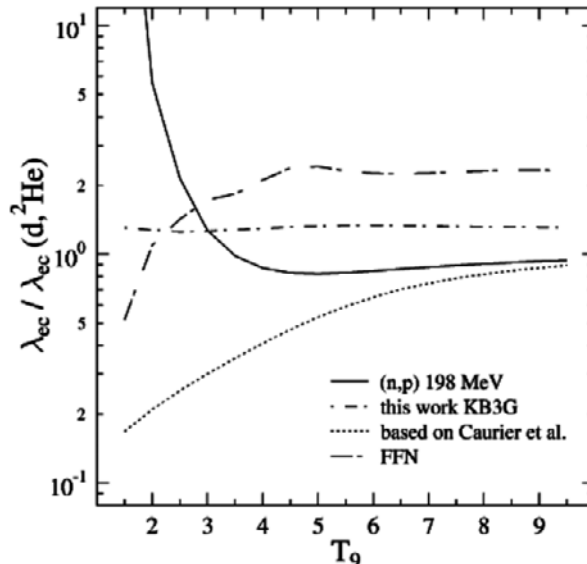


Fig. 20. – Electron-capture rates relative to the rate obtained from the $^{58}\text{Ni}(d, ^2\text{He})$ data; for the details on the various curves representing experimental and theoretical EC rates, see also caption of fig. 19.

The electron-capture rates in fig. 19 are shown in fig. 20 relative to the ones computed using the $(d, ^2\text{He})$ data for the ground-state contribution. It can be seen that the rates based on the large-scale shell-model calculations with the KB3G interaction reproduce the rates based on the $(d, ^2\text{He})$ data rather well over the whole temperature range only exceeding them by a constant factor of about 30%. These rates based on the KB3G interaction are also in good agreement with those based on the (n, p) data in the relevant temperature range ($3 < T_9 < 4$). The rate based on the calculations of Caurier *et al.* [35] deviates by a factor 3 or more for the lowest temperatures. For the relevant temperature range, the FFN rate deviates by about a factor 2. It should be noted that this FFN rate [20] does not include any quenching factor. If such a factor is taken into account, it will cause the rates to become smaller. It is clear from fig. 20, that high-resolution experimental information can provide opportunities to decide between different effective interactions used in large-scale shell-model calculations at zero temperature. This gives, of course, more confidence in these calculations at higher temperatures when they reproduce the data at $T = 0$.

It is important to note that there are many nuclei which contribute to the electron-capture rate in the pre-supernova stage. It is therefore quite important to check the shell-model predictions for other nuclei. In particular, the difference between the FFN [20] and the large-scale shell-model calculations calls for high-resolution determination of GT strength distributions relevant to the pre-supernova evolution using the $(d, ^2\text{He})$ reaction to test both calculations.

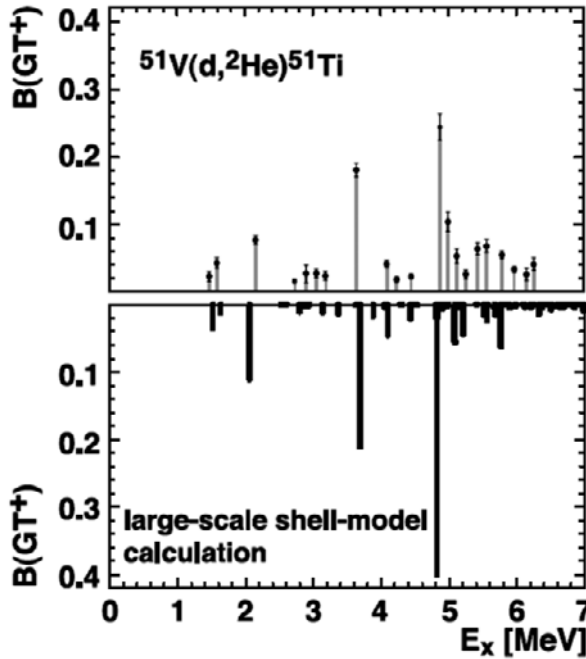


Fig. 21. – Comparison between the $B(\text{GT}^+)$ distribution deduced from the $(\text{d},^2\text{He})$ reaction (top) and the results from the large-scale shell-model calculation (bottom) [36, 45]. The error bars in the top figure are statistical only.

At KVI several experiments have been performed to provide such tests and a few of the results have been published: $^{51}\text{V}(\text{d},^2\text{He})^{51}\text{Ti}$ [45], $^{50}\text{V}(\text{d},^2\text{He})^{50}\text{Ti}$ [46] and $^{64}\text{Ni}(\text{d},^2\text{He})^{64}\text{Co}$ [47]. Several other target nuclei of importance for the EC process in the pre-supernova stage have also been investigated with the $(\text{d},^2\text{He})$ reaction such as: ^{56}Fe , ^{57}Fe , ^{61}Ni and ^{67}Zn [48]. The latter studies have not been published as separate journal articles, but summarized in a talk by Frekers [48]. As an example, we show in fig. 21 a comparison between the spectrum of extracted $B(\text{GT}^+)$ strength obtained in the $^{51}\text{V}(\text{d},^2\text{He})^{51}\text{Ti}$ reaction and the results from large-scale shell-model calculations.

The ground state of the initial (*i*) nucleus ^{51}V has $J_i^\pi = 7/2^-$, which allows GT transitions to $J_f^\pi = 5/2^-, 7/2^-$, and $9/2^-$ in the final (*f*) nucleus ^{51}Ti . The shell-model calculation was performed in the complete *fp* shell employing the KB3G interaction [36, 45]. It should be noted that the shell-model calculations show little strength above 6 MeV in agreement with the experimental results. Furthermore, the data and the calculations are in excellent agreement as far as the distribution of $B(\text{GT}^+)$ strength is concerned, both in magnitude and excitation energy of the fragmented strength. Similar observations could be made with respect to the other nuclei studied.

In order to have a feeling of how the results of the FFN and the large-scale shell-model calculations compare to the experimentally deduced GT^+ strength distribution,

TABLE III. – Comparison of the centroids (given in MeV) of the GT^+ strength distributions obtained from FFN [20], from large-scale shell-model calculations (SM) [36] and from the $(d, {}^2\text{He})$ reaction on the various nuclei: ${}^{51}\text{V}$ [45], ${}^{50}\text{V}$ [46] and all others [48] (Exp.).

	Nucleus	FFN	SM	Exp.
Even-Even	${}^{56}\text{Fe}$	3.8	2.2	1.9
	${}^{58}\text{Ni}$	3.8	3.6	3.4
Odd A-Odd Z	${}^{51}\text{V}$	3.8	4.7	4.1
Odd A-Odd N	${}^{57}\text{Fe}$	5.3	4.1	2.9
	${}^{61}\text{Ni}$	3.5	4.6	4.2
	${}^{67}\text{Zn}$	4.4	–	3.4
Odd-Odd	${}^{50}\text{V}$	9.7	8.5	8.8

the centroids of these distributions are compared in table III for several nuclei that play a very important role in the final steps of the pre-supernova stage preceding the star collapse. Several observations can be made:

- 1) The centroids predicted by the shell-model calculations are in general lower than those predicted by FFN except for the odd- A nuclei ${}^{51}\text{V}$ and ${}^{61}\text{Ni}$.
- 2) The centroids predicted by the shell-model calculations are all in better agreement with the ones deduced from experiments except possibly for ${}^{51}\text{V}$, where the FFN result seems to reproduce the experimental result slightly better.
- 3) Since a lower centroid energy implies enhanced EC rates, then one would expect that the EC rates predicted by the shell model will be higher thereby lowering the value of Y_e except in the cases of ${}^{51}\text{V}$ and ${}^{61}\text{Ni}$. This is, however, not the full story since the GT strength in FFN is not quenched whereas in the shell model distribution a quenching factor of $(0.74)^2$ is included.

One can conclude from the above comparison and the comparison of the experimental and shell-model GT^+ strength distributions of the different nuclei, case by case, that the large-scale shell-model calculations with the KB3G interaction reproduces these experimental distributions very well. Therefore, it is important to take the large-scale shell-model calculations and use them to calculate the EC rates in stellar scenarios at finite temperatures. These can be then used in large nuclear networks of pre-supernova models to determine the course that the star follows until the moment of collapse.

The collapse models describe the final collapse and the explosion phase. At the resulting high temperature, all reactions mediated by the strong and electromagnetic interactions are in equilibrium. The star collapse continues until the central density becomes substantially larger than the nuclear density. Then nuclear pressure slows down the collapse and finally stops it before it rebounds and a shock starts. The equation of state (EoS) plays a decisive role in this stage of the collapse. The important parameters of the EoS are the incompressibility of infinite nuclear matter and the coefficient of the

symmetry term of the incompressibility, both of which could be determined from studies of the compression modes: the ISGMR and ISGDR.

7. – Conclusions and outlook

Pre-supernova models depend sensitively on electron-capture (EC) rates on *fp*-shell nuclei. In turn, GT⁺ strength distributions in *fp*-shell nuclei play a decisive role in determining EC rates and thus provide input into modeling of explosion dynamics of massive stars. In principle, these GT⁺ strength distributions can be determined experimentally through the high-resolution (*d*,²He) reaction at intermediate energies. However, these new high-resolution (*d*,²He) experiments should be considered as providing essential tests for the shell-model calculations at zero temperature. For finite temperatures as exist in heavy stars, it is important to perform large-scale shell-model calculations. This can yield the EC rates as a function of *T*. These large-scale shell-model calculations lead to smaller EC rates than FFN as a result of the interplay between centroids and quenching of GT⁺ strength and thus they lead to larger *Y_e* (electron-to-baryon ratio) and smaller iron core mass.

In addition, the use of radioactive-ion beams to study the GT strength distribution is of importance, especially for nuclei with $(N - Z)/A > 0.1$, where the GT strength moves to even lower excitation energy. At the moment, radioactive ion beams at intermediate energies where it is possible to study GT transitions are available at RIKEN and GSI, and they will become available at NSCL, FAIR, and EURISOL in the future. This will allow to determine GT[±] strength in unstable *sd* and *fp* shell nuclei. This will provide excellent opportunities to determine electron-capture rates and neutrino-capture rates on key radioactive nuclei. Such a key nucleus is ⁶⁰Co, since in the FFN model, the most important EC rate is caused by the ⁶⁰Co(*e*[−], *ν*)⁶⁰Fe reaction for a huge range of temperatures and densities during the pre-supernova evolution. This rate is greatly reduced in the shell-model calculations [36]. Future high-resolution (*d*,²He) data taken in inverse kinematics could provide an accurate determination of the EC rate on ⁶⁰Co.

REFERENCES

- [1] BOTHE W. and GENTNER W., *Z. Phys.*, **71** (1937) 236.
- [2] MIGDAL A. B., *J. Phys. (USSR)*, **8** (1944) 331.
- [3] BALDWIN G. C. and KLAIBER G. S., *Phys. Rev.*, **71** (1947) 3.
- [4] GOLDHABER M. and TELLER E., *Phys. Rev.*, **74** (1948) 1046.
- [5] STEINWEDEL H. and JENSEN J. H. D., *Phys. Rev.*, **79** (1950) 1019.
- [6] HARAKEH M. N. and VAN DER WOUDE A., *Giant Resonances: Fundamental High-Frequency Modes of Nuclear Excitations* (Oxford University Press, New York) 2001, and references therein.
- [7] PITTHAN R. and WALCHER TH., *Phys. Lett. B*, **36** (1971) 563.
- [8] HARAKEH M. N. et al., *Phys. Rev. Lett.*, **38** (1977) 676; *Nucl. Phys. A*, **327** (1979) 373.
- [9] YOUNGBLOOD D. et al., *Phys. Rev. Lett.*, **39** (1977) 1188.
- [10] BLAIZOT J. P., *Phys. Rep.*, **64** (1980) 171.

- [11] UCHIDA M. *et al.*, *Phys. Rev. C*, **69** (2004) 051301.
- [12] COLÒ G. *et al.*, *Phys. Rev. C*, **70** (2004) 024307.
- [13] LI T. *et al.*, *Phys. Rev. Lett.*, **99** (2007) 162503; *Phys. Rev. C*, **81** (2010) 034309.
- [14] PATRA S. K. *et al.*, *Phys. Rev. C*, **65** (2002) 044304.
- [15] SAGAWA H. *et al.*, *Phys. Rev. C*, **76** (2007) 034327.
- [16] PETROVICH F. and LOVE W. G., *Nucl. Phys. A*, **354** (1981) 499c.
- [17] GAARDE C., in *Proceedings of Niels Bohr Centennial Conference, Copenhagen*, edited by BROGLIA R., HAGEMAN G. and HERSKIND B. (North-Holland, Amsterdam) 1985.
- [18] RAPAPORT J. and SUGARBAKER E., *Annu. Rev. Nucl. Part. Sci.*, **44** (1994) 109, and references therein.
- [19] BETHE H. A. *et al.*, *Nucl. Phys. A*, **324** (1979) 487.
- [20] FULLER G. M., FOWLER W. A., NEWMAN M. J., *Astrophys. J. Suppl. Ser.*, **42** (1980) 447; **48** (1982) 279; *Astrophys. J.*, **252** (1982) 715; **293** (1985) 1.
- [21] TADDEUCCI T. N. *et al.*, *Nucl. Phys. A*, **469** (1987) 125.
- [22] BERGQVIST I. *et al.*, *Nucl. Phys. A*, **469** (1987) 648.
- [23] FUJIWARA M. *et al.*, *Phys. Rev. Lett.*, **85** (2000) 4442.
- [24] KIRSTEN T. A., *Nucl. Phys. B*, **77** (1999) 26.
- [25] GAVRIN V. N., *Nucl. Phys. B*, **77** (1999) 20.
- [26] BAHCALL J. N., *Nucl. Phys. B*, **77** (1999) 64.
- [27] BHATTACHARYA M. *et al.*, *Phys. Rev. Lett.*, **85** (2000) 4446.
- [28] FUJIWARA M. *et al.*, *Nucl. Instrum. Methods Phys. Res. A*, **422** (1999) 484.
- [29] WAKASA T. *et al.*, *Nucl. Instrum. Methods Phys. Res. A*, **482** (2002) 79.
- [30] FUJITA Y. *et al.*, *Phys. Lett. B*, **365** (1996) 29; *Eur. Phys. J. A*, **13** (2002) 411.
- [31] METTNER W. *et al.*, *Nucl. Phys. A*, **473** (1987) 160.
- [32] AJZENHERG-SELOVE F. *et al.*, *Phys. Rev. C*, **30** (1984) 1850; **31** (1985) 777.
- [33] EL-KATEB S. *et al.*, *Phys. Rev. C*, **49** (1994) 3128.
- [34] FUJITA Y. *et al.*, *Phys. Rev. C*, **67** (2003) 064312; *Phys. Rev. Lett.*, **92** (2004) 062502; FUJITA Y., *Nucl. Phys. A*, **805** (2008) 408c, and references therein.
- [35] CAURIER E. *et al.*, *Nucl. Phys. A*, **653** (1999) 439, and references therein.
- [36] LANGANKE K. and MARTÍNEZ-PINEDO G., *Nucl. Phys. A*, **673** (2000) 481; *At. Data Nucl. Data Tables*, **79** (2001) 1; *Rev. Mod. Phys.*, **75** (2003) 819; POVES A. *et al.*, *Nucl. Phys. A*, **694** (2001) 157.
- [37] HEGER A. *et al.*, *Phys. Rev. Lett.*, **86** (2001) 1678; *Astrophys. J.*, **560** (2001) 307.
- [38] ALFORD W. P. *et al.*, *Nucl. Phys. A*, **514** (1990) 49; VETTERLI M. C. *et al.*, *Phys. Rev. C*, **40** (1989) 559; ALFORD W. P. *et al.*, *Phys. Rev. C*, **48** (1993) 2818; WILLIAMS A. L. *et al.*, *Phys. Rev. C*, **51** (1995) 1144.
- [39] HAGEMANN M. *et al.*, *Phys. Lett. B*, **579** (2004) 251; *Phys. Rev. C*, **71** (2005) 014606.
- [40] VAN DEN BERG A. M., *Nucl. Instrum. Methods Phys. Res. B*, **99** (1995) 637.
- [41] RAKERS S. *et al.*, *Nucl. Instrum. Methods Phys. Res. A*, **481** (2002) 253; HAGEMANN M. *et al.*, *Nucl. Instrum. Methods Phys. Res. A*, **437** (1999) 459; HANNEN V. M. *et al.*, *Nucl. Instrum. Methods Phys. Res. A*, **500** (2003) 68.
- [42] RAKERS S. *et al.*, *Phys. Rev. C*, **65** (2002) 044323.
- [43] ANDERSON B. D. *et al.*, *Phys. Rev. C*, **43** (1991) 50.
- [44] HONMA M. *et al.*, *Phys. Rev. C*, **69** (2004) 034335.
- [45] BÄUMER C. *et al.*, *Phys. Rev. C*, **68** (2003) 031303(R).
- [46] BÄUMER C. *et al.*, *Phys. Rev. C*, **71** (2005) 024603.
- [47] POPESCU L. *et al.*, *Phys. Rev. C*, **75** (2007) 054312.
- [48] FREKERS D., *Prog. Part. Nucl. Phys.*, **57** (2006) 217.

NUCLEAR STRUCTURE AND NUCLEAR ASTROPHYSICS WITH RADIOACTIVE BEAMS

This page intentionally left blank

Proceedings of the International School of Physics “Enrico Fermi”
Course CLXXVIII “From the Big Bang to the Nucleosynthesis”, edited by A. Bracco and E. Nappi
(IOS, Amsterdam; SIF, Bologna)
DOI 10.3254/978-1-60750-974-5-127

Nuclear-astrophysics experiments with relativistic radioactive beams

T. AUMANN(*)

*Institut für Kernphysik, Technische Universität Darmstadt
Schlossgartenstraße 9, 64 289 Darmstadt, Germany*

Summary. — Experiments with high-energy radioactive beams for nuclear astrophysics are discussed. Emphasis is paid to measurements of masses of exotic nuclei relevant for nucleosynthesis processes and the determination of dipole strength functions for neutron-rich nuclei relevant for both the r-process nucleosynthesis and neutron-star matter. Finally, an outlook is given on the experimental program planned at the radioactive-beam facility NuSTAR at the accelerator facility for anti-proton and ion research FAIR.

1. – Introduction

A central question of nuclear astrophysics is how are the elements synthesized in the universe. Only the lightest elements up to Li were created in the earliest stage of cosmic evolution within 1000 seconds after the Big Bang. All heavier elements have been and are still being synthesized through sequences of nuclear reactions taking place in a variety of stellar environments. In particular the elements heavier than iron are to a large

(*) E-mail: t.aumann@gsi.de

fraction being created in explosive nucleosynthesis processes such as the r-process (rapid neutron capture) and rp-process (rapid proton capture). Such processes involve unstable nuclei, in case of the rp-process on the neutron-deficient side, and on the neutron-rich side of the valley of stability in case for the r-process, as indicated in fig. 1. Basis for the theoretical understanding and modelling of such processes is the knowledge of properties of the exotic nuclei involved and their reactions. Examples of such properties are masses, lifetimes, radii, shell structure, level densities, dipole-strength functions, Gamov-Teller strength distributions, reaction rates, and others. Here, radioactive beams play a fundamental role in the determination of such properties. Although reactions in astrophysical environments happen often at relatively low energies below 1 MeV, high-energy radioactive beams play a central role in the determination of the above-mentioned properties due to several reasons. One is the fact that beams of very exotic nuclei are most efficiently produced in high-energy fragmentation or fission reactions with subsequent separation in flight. In particular, for the heavier elements beam energies in the order of 1 GeV/nucleon are needed in order to ensure a proper separation and identification of fragments by magnetic spectrometers. Another reason lies in the experimental approaches which have to be applied for short-lived nuclei. For such nuclei, reactions can only be studied in inverse kinematics using the nuclei of interest as the beam. It turns out that most of the reactions are preferentially being performed at high beam energies, although the experimental effort becomes sometimes immense due to the high resolution required. We will discuss the example of the measurement of the dipole strength later, which is related to the r-process nucleosynthesis as well as to properties of neutron-rich matter relevant for the understanding of properties of neutron stars. Another example is the technique of high-energy storage rings, which offers unique possibilities to study properties and reactions of stored radioactive nuclei. The example of mass measurements in the storage ring ESR at GSI will be discussed. Other astrophysical relevant measurements will be mentioned in sect. 3, where the planned experimental program at the future FAIR facility with radioactive beams will be briefly reviewed.

The rapid-neutron capture nucleosynthesis process involves heavy neutron-rich nuclei. A possible pathway of this process is indicated in fig. 1 as orange area on the neutron-rich side with respect to nuclei in the valley of stability indicated by the black squares. In this process, which takes place in an explosive event generating a huge neutron flux, elements are created via a chain of neutron captures and subsequent β decays. After a few seconds, the process ends and the unstable nuclei decay until stable isotopes are formed. The abundance of the produced elements in the solar system shows a particular pattern, which is related to the process and the properties of the nuclei involved. Figure 2 shows a nuclear chart and the measured r-process solar abundances as an inset. The apparent maxima are related to the neutron-shell closures at $N = 50, 82$, and 126 [2,3]. The capture processes are slowed down at the “waiting point” nuclei, where the binding energy of the next neutron to be captured becomes comparatively small. There, the nuclei have to “wait” for decay to reach a nucleus with higher neutron binding energy. This effect, being most pronounced at the magic neutron numbers $N = 82$ and 126 , leads to strong maxima in the mass abundance (see fig. 2) at the corresponding neutron

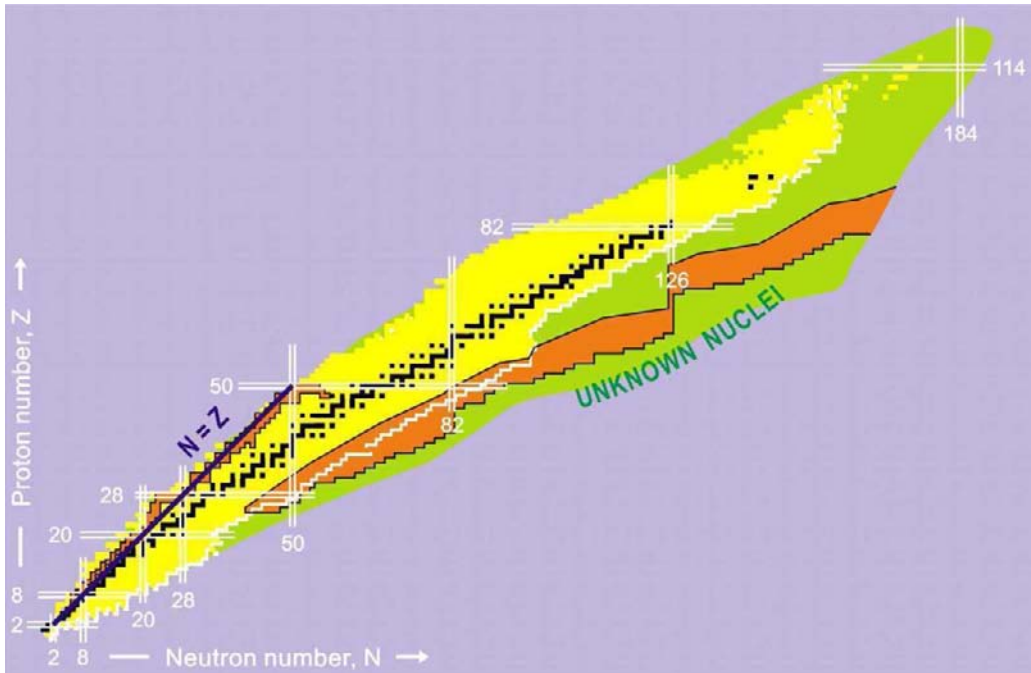


Fig. 1. – Chart of nuclei. Stable nuclei are marked by black squares. The yellow area covers unstable nuclei already observed in the laboratory, while the green area marks the unknown region where it is believed that nuclei are bound. The orange areas cover the regions of the stellar nucleosynthesis pathways of the rp-process on the neutron-deficient side, and of the r-process on the neutron-rich side. Closed shells known for stable nuclei are labelled with the respective neutron and proton numbers. The figure is taken from ref. [1].

shell closures. The nucleosynthesis via the r-process is modelled by detailed network calculations. The data most urgently needed for such calculations are nuclear masses which govern the r-process pathway itself, and β -decay half-lives which determine the accumulated abundance pattern along this path. Such mass measurements for neutron-rich nuclei can be provided very efficiently by using a storage ring where the circulation frequency of cooled stored radioactive isotopes is measured, as will be discussed in the next section.

During the time period of the r-process when radiative neutron-capture reactions and photodissociation reactions fall out of equilibrium, details of the strength distribution of the involved nuclei will play a role and influence the abundance pattern. It has been pointed out by Goriely [4] that the particular dipole response of neutron-rich nuclei, such as the appearance of low-lying “Pygmy” dipole strength, may have large impact on the r-process abundances. A systematic change of the dipole response of nuclei when moving from stable to neutron-proton asymmetric nuclei is expected, and experimental evidence for the appearance of low-lying strength has been accumulated, as will be discussed in the next section. A detailed analysis of how neutron-capture rates are influenced by the

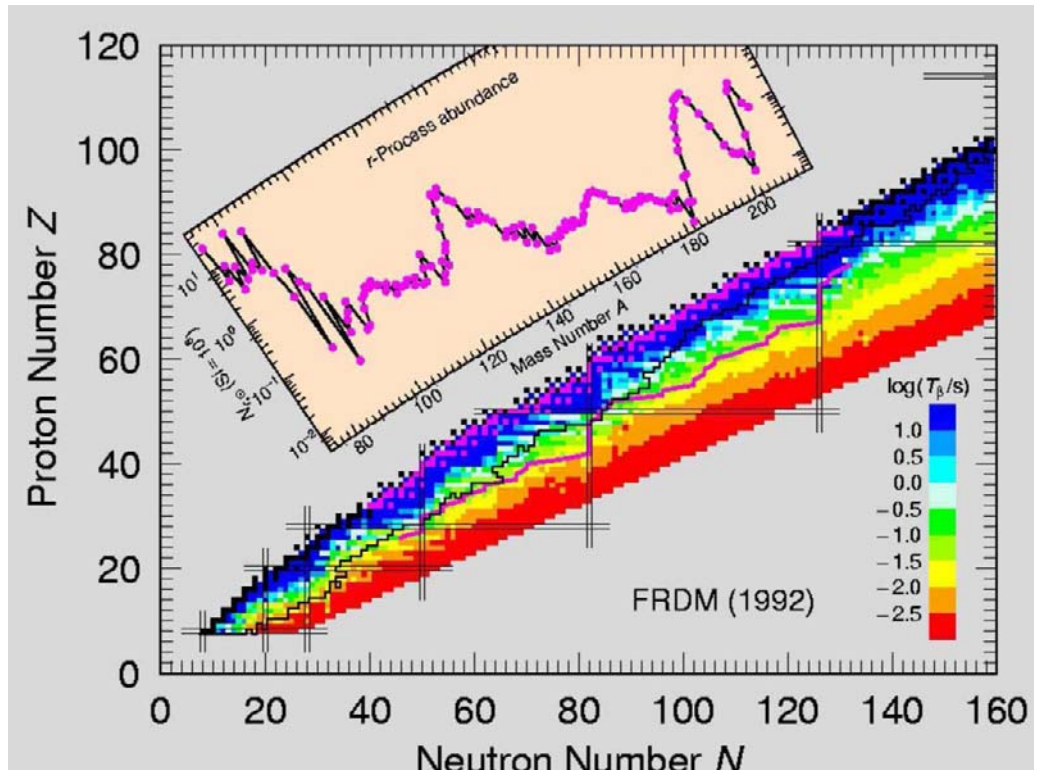


Fig. 2. – Chart of nuclides color coded according to half-lives as calculated in the framework of the finite-range droplet model [3]. A likely pathway of the r-process is indicated by the purple line. The inset shows the measured solar abundances of nuclei produced via the r-process. The pronounced maxima are related to closed neutron shells, indicated by black bars (see also fig. 1). The figure is taken from the Conceptual Design Report for FAIR [1].

change of the dipole strength function has been carried out by Litvinova *et al.* [5]. The results are shown in fig. 3. The upper panels show γ strength functions for tin isotopes as calculated by Litvinova *et al.* [5] microscopically within the Relativistic Quasiparticle Time Blocking Approximation (RQTBA) approach (solid; model A) [6] and the Quasiparticle Random Phase Approximation (QRPA) model of Goriely and Khan [7] (dashed; model D). The dotted and dash-dotted curves represent empirical Lorentzian parameterizations of the strength as they are commonly used in r-process network calculations. The strong deviations of the microscopic calculations from the Lorentzian parametrization close to the threshold (indicated by the horizontal lines) for the neutron-rich nuclei are due to the Pygmy resonance strength predicted by the microscopic models. The lower panels show the neutron-capture cross-sections calculated within the Hauser-Feshbach approach and using the above strength functions as an input. The huge difference in capture cross-sections for the Lorentzian parametrization and the microscopical derived

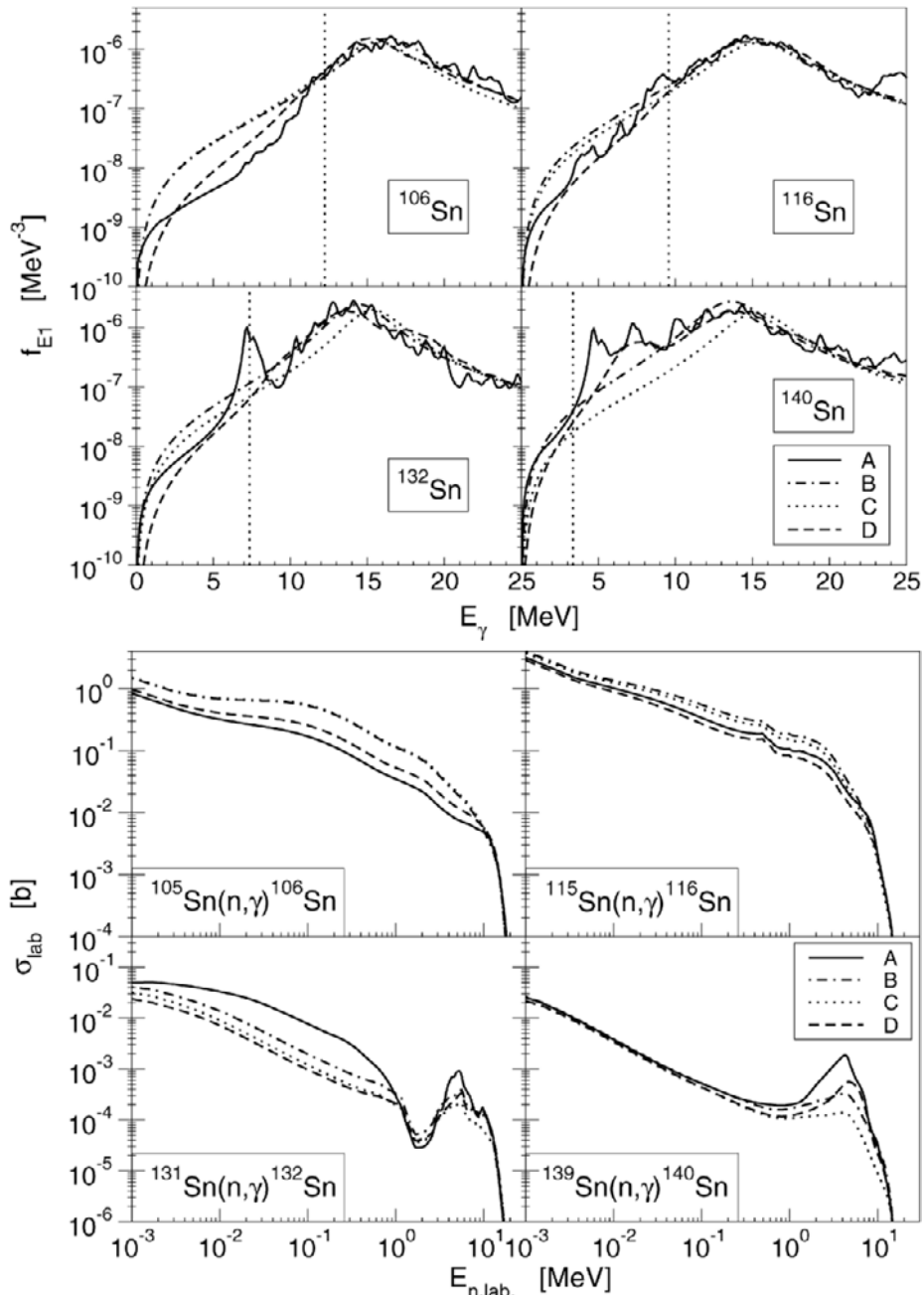


Fig. 3. – Theoretical calculations of neutron-capture cross-sections for tin isotopes (lower panel) using different γ strength functions as input (see upper panel). Models A and D are based on the RQTBA and QRPA microscopic models, respectively, while the models B and C are based on Lorentzian parametrizations of the strength functions. The figure is taken from Litvinova *et al.* [5].

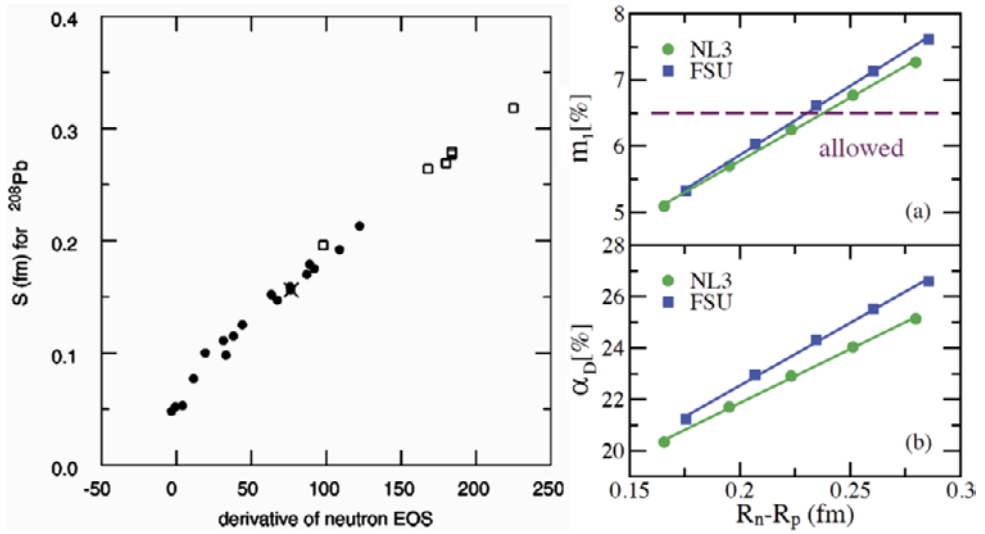


Fig. 4. – Left panel: the derivative of the neutron equation of state at a density of 0.1 neutrons/fm³ *vs.* the calculated neutron-skin thickness in ^{208}Pb for various Skyrme and relativistic mean-fiel models, from Typel and Brown [8]. Right panel: percentage of the energy weighted sum rule (a) and dipole polarizability (b) exhausted by the Pygmy dipole resonance in ^{68}Ni as a function of the neutron-skin thickness of ^{208}Pb as calculated within the relativistic random phase approximation by Piekarewicz [11]. The figures are taken from refs. [8,11].

strength function for neutron capture on ^{131}Sn in the astrophysical relevant energy range up to 1 MeV is related to the Pygmy dipole resonance in ^{132}Sn close to the threshold. Besides the strength function the level densities play a crucial role. For nuclei at closed shells, as for the ^{132}Sn case, or for neutron-rich nuclei with low neutron-separation thresholds, the level density becomes small and the direct transitions may dominate. Here, the Pygmy resonance located at the threshold in the RQTBA calculations is the reason for the much larger capture cross-sections on ^{131}Sn up to a neutron energy of around 1 MeV. So far, experimental information on the dipole strength function of neutron-rich nuclei including the Pygmy dipole resonance is still scarce, see next section. From the experimental point of view, it is of utmost importance to deduce the dipole strength as complete as possible, including measurements above and below the neutron separation threshold, as well as including direct γ and cascade decays.

The second important subject related to astrophysics and the dipole strength in nuclei is the equation of state (EoS) of neutron-rich matter, which is a fundamental input to any calculation modelling the properties of neutron stars. It has been pointed out by several authors, see refs. [8] and [9] for examples, that a measurement of the neutron-skin thickness in heavy nuclei may give important constraints on the density-dependence of the symmetry energy describing the isospin-dependent part of the EoS. More recently, Piekarewicz [10] pointed out that the low-lying dipole strength in neutron-rich nuclei may as well give a constraint on this quantity. The left panel of fig. 4 shows the correlation

of the density-dependence of the neutron EoS at a density of 0.1 neutrons/fm³ with the calculated neutron-skin thickness in ²⁰⁸Pb for various Skyrme and relativistic mean-field models as derived by Typel and Brown [8]. A clear linear dependence is observed. The right panel shows the result of a calculation within a relativistic random phase model by Piekarewicz [11]. A clear correlation of the calculated neutron-skin thickness in ²⁰⁸Pb and the predicted low-lying Pygmy dipole strength is found [11] implying a strong sensitivity of the Pygmy strength in neutron-rich nuclei to the density dependence of the symmetry energy. Thus both, the measurement of neutron-skin thickness as well as the dipole strength, give important constraint on the isospin-dependent part of the EoS. The experimental determination of the neutron-skin thickness remains a challenge. The Lead Radius experiment (PREx) aims to determine the neutron radius of ²⁰⁸Pb model independently using parity-violating electron scattering at the electron accelerator at Jefferson Laboratory [12, 13]. The advantage of performing neutron-skin measurements with neutron-rich nuclei would be that the effect is much bigger and that systematic studies along isotopic chains can be performed. Several methods have been proposed for such studies including reaction cross-section measurements, determination of charge radii by charge-changing cross-sections, laser spectroscopy, and electron scattering, the measurement of spin-dipole and giant dipole resonance strength, proton-elastic scattering, as well as anti-proton scattering, to name a few. All of those methods will be available at the future NuSTAR facility at FAIR, see sect. 3. The strategy with radioactive beams will be to use different experimental methods in order to understand possible systematic model dependences inherent to the different methods and to arrive at a consistent description. The fact that the change of the neutron-skin thickness along an isotopic chain can be determined will in addition eliminate model dependences. The measurement of the low-lying dipole strength of neutron-rich nuclei is one of the particularly appealing methods, first results will be discussed in the next section. Quite a few open questions, however, have to be clarified experimentally in the future, as will be discussed in the next section.

2. – Experiments with high-energy radioactive beams at GSI

2.1. Mass measurements. – As discussed in the previous section, masses of exotic nuclei are fundamental input to any network calculation modelling nucleosynthesis processes such as the r-process. The masses determine the pathway of the nucleosynthesis process. The challenge for mass measurements of very neutron-rich nuclei as those created during the r-process is the low production rate. Very sensitive experiments are thus required. Two methods have been developed at GSI employing the storage ring ESR: The Schottky Mass Spectrometry (SMS) for cooled beams of longer-lived isotopes, and Isochronous Mass Spectrometry (IMS) for uncooled beams of short-lived fragments. Both methods rely on the precise measurement of the circulation frequency of the ions in the storage ring. In case of the Schottky method, the radioactive ions produced at the Fragment Separator FRS are injected into the ESR and electron cooled. By elastic collisions the average velocity of the heavy ions approaches that of the cooler electrons, and the velocity

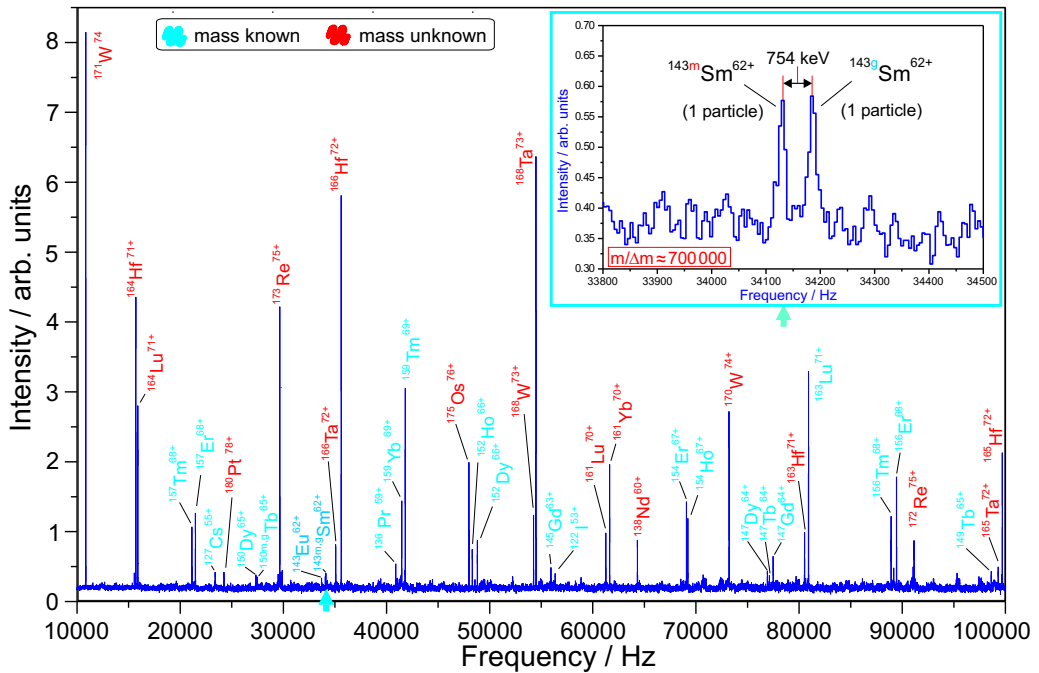


Fig. 5. – Schottky frequency spectrum of cooled ions circulating in the storage ring ESR stemming from fragmentation of a bismuth beam. Ions with previously known and unknown masses are shown in red and blue, respectively. The inset shows a Schottky frequency spectrum obtained from only two bare ^{143}Sm ions, one in the ground state, the other one in the isomeric state. The data are from ref. [14]. The figure is taken from the Conceptual Design Report for FAIR [1].

spread of the ions is decreased drastically. The revolution frequencies of the stored ions are obtained by a Fourier transformation of their signals induced in pick-up probes at each turn in the ring. Figure 5 shows a Schottky frequency spectrum obtained after injection and cooling of ions produced in fragmentation reactions of a bismuth beam [14]. Isotopes with previously known and unknown masses are marked in the spectrum by the blue and red colors, respectively. This figure demonstrates the power of the method. Since many isotopes are circulating in the storage ring simultaneously, many masses can be determined very efficiently in one experiment. The fact that also many ions with known masses are visible at the same time allows for an accurate calibration and mass determination. The inset shows a zoom where the signals induced by two single ^{143}Sm ions are visible, one in its ground state, the other in its isomeric state. This demonstrates the ultimate sensitivity of this method, as well as the resolving power. At the present GSI facility, most of the nuclei on the r-process path cannot be reached due to the limited intensity as well as due to the low injection efficiency into the storage ring. At the future FAIR facility, a combination of an accumulator ring with fast stochastic pre-cooling and

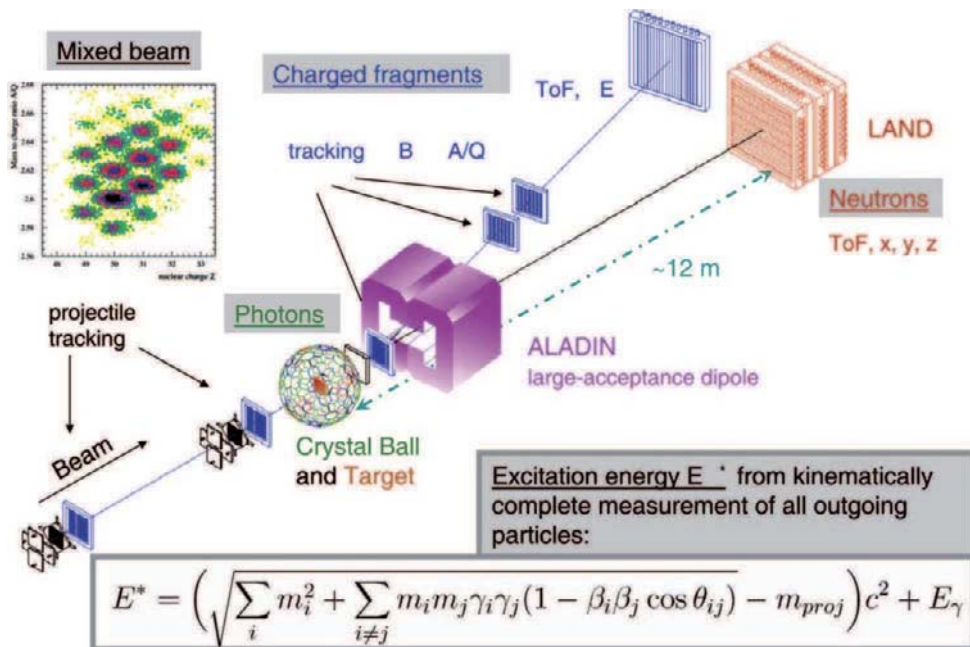


Fig. 6. – Schematic view of the R3B-LAND setup for kinematically complete measurements of reactions with relativistic radioactive beams.

an experimental storage ring equipped with electron cooling will provide a much higher injection efficiency. This together with the higher radioactive beam intensities will allow covering a large fraction of r-process nuclei, see sect. 3.

2.2. The dipole response of exotic nuclei. – The dipole strength function of short-lived nuclei is most effectively measured by heavy-ion-induced electromagnetic excitation. The projectile nuclei are thereby excited by absorption of virtual photons induced by the rapidly varying electromagnetic field of a heavy target nucleus seen by the projectile. The spectrum of virtual photons is continuous and depends strongly on the beam energy. In order to reach photon energies and thus excitation energies over the full energy range of interest which includes the giant dipole resonance, beam energies of several hundred MeV/nucleon are required. The excited nuclei decay by particle and γ emission in flight. Due to the high beam velocities of typically 70% speed of light, emitted nucleons appear in the laboratory frame in a narrow cone around the beam axis. By measuring precisely the momenta of all outgoing particles and photons, the excitation energy prior to decay can be reconstructed using the invariant-mass method. Figure 6 shows a schematic drawing of the R3B-LAND setup at GSI, which is used for such kinematically complete measurements of reactions with relativistic radioactive beams (R3B). The incoming radioactive beam is tracked by position-sensitive detectors. By means of energy-loss and time-of-flight measurements, the ions are identified on an event-by-event

basis. The upper left inset shows an example of a mixed secondary beam produced by uranium fission and optimized for the transmission of ^{132}Sn . For electromagnetic excitation of the projectiles, a lead target is used which is surrounded by the 4π photon calorimeter Crystal Ball, which consists of 160 individual NaI crystals. The granularity of the detector is used to Doppler correct the photon energy into the rest-frame of the projectile. Heavy fragments emerging after the reactions are deflected by the large-acceptance dipole ALADIN. Their trajectories through the dipole field are determined by position measurements before and behind the magnet. In front of the magnet, typically position-sensitive PIN diodes are used, which provide a position resolution of about 0.1 mm rms for ions in the mass region of tin isotopes. Behind the magnet, large-area scintillating fibres are used with an active area of $50 \times 50 \text{ cm}^2$ and a pitch width of 1 mm. The tracking through the dipole field serves to determine the magnetic rigidity, which yields together with an energy-loss and time-of-flight measurement the fragment charge and mass, similarly to the identification of the incoming ions. Neutrons which are emitted from the projectile in flight are kinematically focussed to forward direction and detected by the Large-Area-Neutron-Detector LAND placed typically 12 m downstream from the target. Typical neutron energies in the rest frame of the projectile are in the MeV range. Up to a kinetic energy of 5 MeV in the rest frame, the acceptance of 80 mrad of LAND for neutrons corresponds to a 4π measurement. The time-of-flight of the neutrons and the position on LAND is measured with a resolution of 250 psec and 3 cm rms, respectively. This resolution contributes to the resolution in excitation energy of about 0.2 to 2 MeV depending on the excitation energy. The formula for calculating the excitation energy from the measured quantities is displayed in fig. 6 as well.

The R3B-LAND setup has been used to measure dipole excitations of neutron-rich nuclei for light halo and skin nuclei, as well as for neutron-rich nuclei around ^{132}Sn , see ref. [15] for an overview. The experimental results [16] for the tin isotopes ^{130}Sn and ^{132}Sn are shown in the upper right panel of fig. 7. The two left frames of the upper right panel display the measured cross-section for electromagnetic excitation on a lead target at a beam energy of 500 MeV/nucleon. The two right frames show the same data but converted into photo-neutron cross-sections. Below the giant dipole resonance region, a peak-like structure is visible around 10 MeV excitation energy corresponding to the Pygmy dipole resonance. The left frames show the extracted $B(E1)$ distributions of several neutron-rich nuclei around ^{132}Sn after subtracting the contribution from the giant dipole resonance [17]. All nuclei exhibit additional strength close to the neutron-separation threshold. The origin of the observed odd-even staggering of the centroid of the additional low-lying Pygmy strength is not clear. It might be related to the fact that the experiment was sensitive to the strength above the threshold only, and that part of the strength is missing for even nuclei because it is located below the threshold. Clearly, the next-generation experiments have to be sensitive to the full strength function independent of the neutron threshold in order to solve this issue. The lower right panel shows a result obtained by the RISING collaboration at GSI [18]. Here, the γ decay has been measured after electromagnetic excitation of ^{68}Ni projectiles [18]. A peak-like structure at around 10 to 11 MeV is visible in the γ spectrum which is attributed

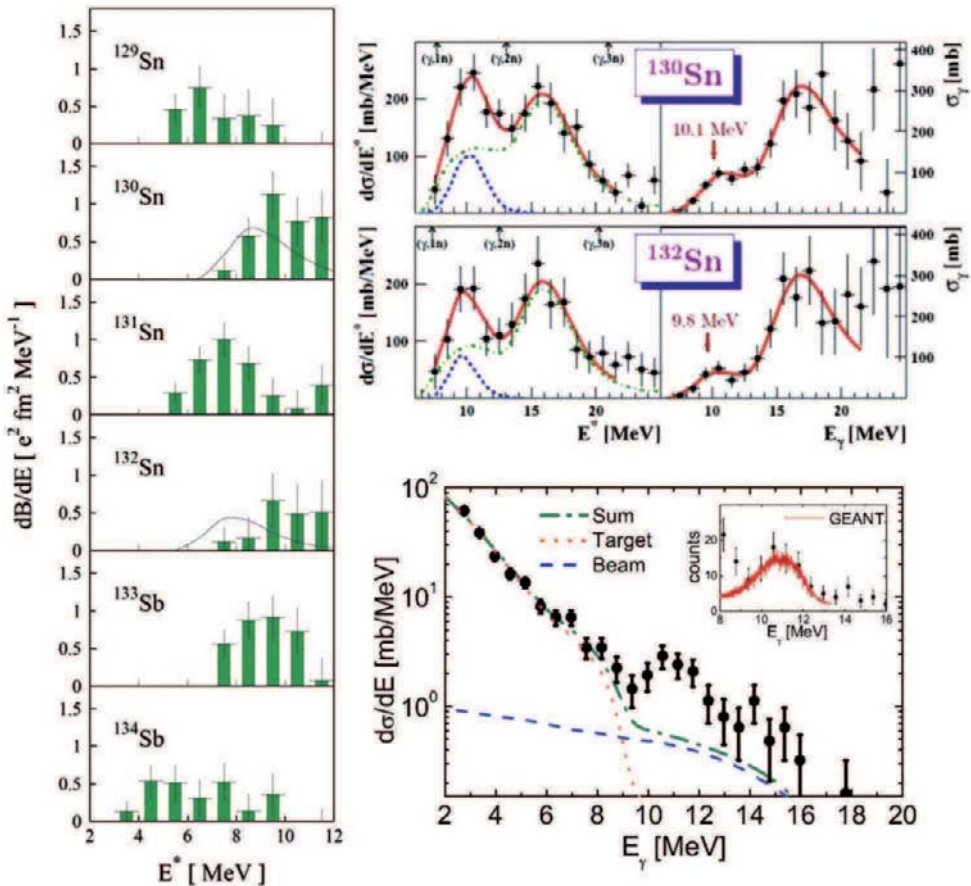


Fig. 7. – Dipole strength of neutron-rich nuclei derived from measurements of heavy-ion-induced electromagnetic excitation at relativistic energies. The upper right panels show results for the isotopes ^{130}Sn and ^{132}Sn [16]. The two left frames of the upper right panel display the measured cross-section for electromagnetic excitation on a lead target at a beam energy of 500 MeV/nucleon. The two right frames show the same data but converted into photo-neutron cross-sections. The left panel shows extracted $B(E1)$ distributions for neutron-rich nuclei around ^{132}Sn after subtracting the contribution from the giant dipole resonance [17]. The lower right panel shows the γ -decay spectrum after electromagnetic excitation of ^{68}Ni projectiles [18].

to the Pygmy dipole resonance. This virtual-photon scattering experiment is sensitive also to the strength below the threshold, which is covered, however, by a rather large background. It is interesting to note, that the peak is observed at an excitation energy above the threshold. The measured cross-section is thus a product of excitation cross-section and a γ -branching ratio. By assuming a statistical decay and level densities, the authors have estimated a direct γ -decay branch of 4%. With this value, the cross-section corresponds to a sum-rule exhaustion of 5%, similar as observed for the tin isotopes.

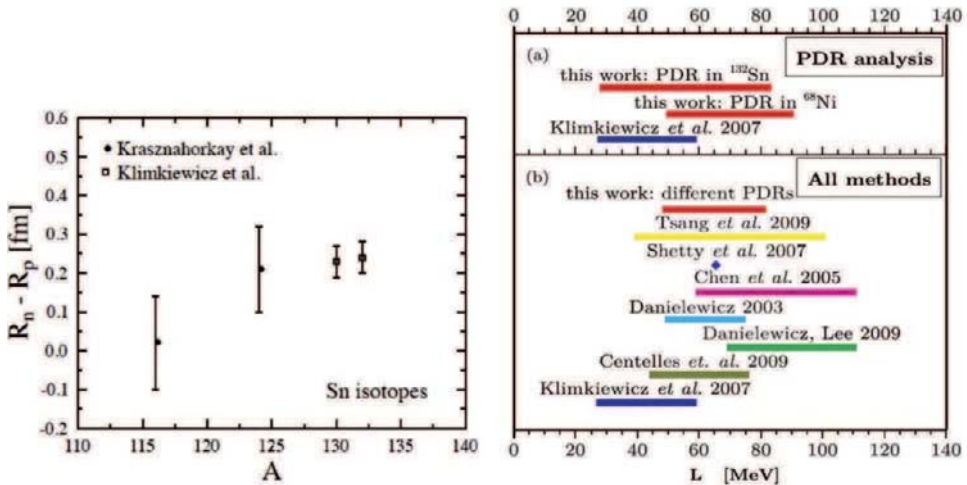


Fig. 8. – The left panel shows the experimentally derived neutron-skin thickness for tin isotopes. For the stable isotopes, the excitation cross-section of the giant dipole resonance with an isoscalar probe utilizing alpha scattering has been applied [19]. The values for the neutron-rich isotopes have been derived from the low-lying Pygmy dipole strength observed in heavy-ion-induced electromagnetic excitation [17]. Right panel: Density dependence L of the symmetry energy compiled by Carbone *et al.* [20] as derived from different experimental methods (see refs. in [20]). The values obtained from the Pygmy dipole analysis are shown in the upper frame.

It should be noted, however, that this heavily relies on the assumptions on the level densities. In turn, a determination of the total strength by including a measurement of the neutron decay could provide interesting information on the level densities in exotic nuclei and the structure of the Pygmy dipole resonance.

As discussed in the introductory section, the low-lying dipole strength may provide important constraint on the density-dependence of the symmetry energy and on the neutron-skin thickness in heavy nuclei. Klimkiewicz *et al.* [17] have extracted values for p_0 and a_4 from the Pygmy dipole strength observed in neutron-rich tin isotopes, as well as the related neutron-skin thicknesses. Values of 0.24 ± 0.04 fm for ^{132}Sn and of 0.18 ± 0.035 fm for ^{208}Pb have been derived. The values for the tin isotopes are compared in fig. 8 to the values obtained for stable isotopes by Krasznahorkay *et al.* [19] from cross-section measurements for exciting the isovector giant dipole resonance with an isoscalar probe utilizing α inelastic scattering. The right panel of the figure shows the compilation of values for the density dependence L of the symmetry energy at saturation density from the work of Carbone *et al.* [20]. The combination of the result for the Sn isotopes and the result for ^{68}Ni (under the above-mentioned assumptions on the decay branching ratio) is shown in the upper frame of the figure. The analysis is based on a theoretical framework using the RPA approach and different Skyrme effective forces. The result is consistent with the values extracted from completely different analysis of

other experimental observables. It is also interesting to note that, by comparing the result derived by Klimkiewicz for the neutron skin thickness in ^{208}Pb of 0.18 ± 0.035 fm with the relativistic RPA approach of Piekarewicz [11] discussed in the introduction, a L value of about 53 MeV is derived (see Table II in ref. [11]) consistent with the analysis of Carbone *et al.* [20].

Clearly, the measurement of dipole strength functions for neutron-rich nuclei using heavy-ion-induced electromagnetic excitation at high beam energies looks very promising for deriving the necessary information for the understanding of the neutron-capture nucleosynthesis processes as well as for constraining the EoS for neutron-star matter. The experimental situation concerning the pygmy dipole response of exotic and even stable nuclei is, however, far from being clear. It is mandatory that measurements of exotic nuclei are performed which are sensitive to the full strength function below and above the threshold including a measurement of the γ branching ratios. In addition, the quality of the data in terms of statistics and experimental response will be improved in the future. But even for stable nuclei, the situation is not clear. Low-lying dipole strength has been observed in stable nuclei below the threshold. The experimental method, however, was sensitive only to direct γ decays back to the ground state. An important part of the strength decaying by cascades is thus missing. First experimental evidence that indeed a substantial part of the strength particularly close to the threshold is missing has been obtained [21, 22] recently.

3. – Future perspectives—NuSTAR at FAIR

3.1. The FAIR facility. – The new facility for antiproton and ion research (FAIR) which is being built at GSI will provide high-intensity primary and secondary beams for a variety of different experiments enabling a broad range of physics goals to be addressed. The science areas covered include i) the structure of nuclei far from stability and astrophysics, ii) hadron spectroscopy and hadronic matter, iii) compressed nuclear matter, iv) high energy density in bulk matter, v) quantum electrodynamics, strong fields, and ion-matter interactions. The science cases as well as the facility concept and layout have been worked out by a large international community and is described in detail in the Conceptual Design Report (CDR) [1] of the facility. The concept is based on a double-ring synchrotron structure SIS100/300, which utilizes the existing UNILAC/SIS18 accelerators as an injector. Beams of all ions from hydrogen to uranium, as well as antiprotons with a large energy range from rest up to 35 GeV/ u will be provided by FAIR. A schematic layout of the facility is displayed in fig. 9, showing in addition several storage rings and experimental areas.

Two aspects of the concept are most important to overcome the present intensity limit given by the fact that the space-charge limit is reached in the synchrotron SIS18: i) First, a faster cycling of the synchrotron of 3 Hz compared to the present situation of 0.3 Hz yields an order of magnitude increase in average intensity, and ii) the acceleration of uranium ions with charge state 28^+ instead of 73^+ will increase the space-charge limit by one order of magnitude. In order to reach the same beam energy (1.5 to 2 GeV/ u) while

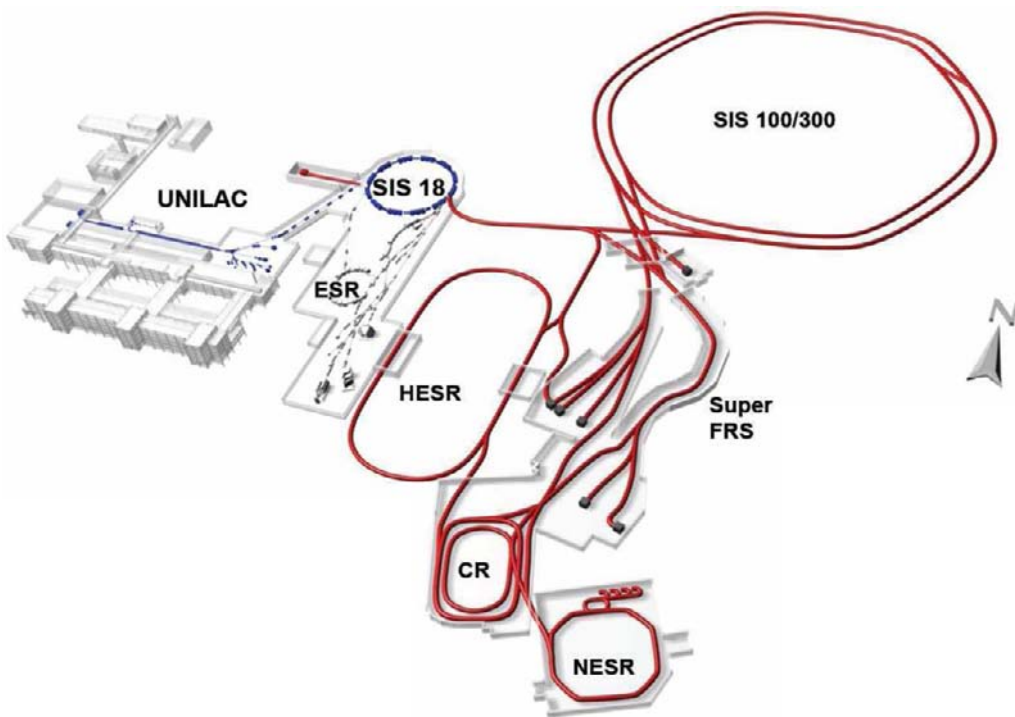


Fig. 9. – Schematic layout of the FAIR facility. The existing GSI accelerators UNILAC and SIS-18 serve as an injector for the two large synchrotron rings SIS-100/300. The beams are distributed to various experimental areas or to the production targets for the anti-proton or radioactive-isotope beam facilities. For beam storage and manipulation several rings are foreseen including the high-energy storage ring HESR for anti-protons, the collector ring CR, and the experimental storage ring NESR. The storage-ring complex provides possibilities of beam cooling as well as target areas for scattering experiments. The superconducting fragment separator Super-FRS for preparation of rare-isotope beams is indicated as well.

accelerating a lower charge-state, a synchrotron with higher magnetic rigidity (100 Tm) is needed, which is provided by the SIS100 ring. An average intensity of more than 10^{11} ions/s will be reached, *e.g.*, for uranium beams at 1.5 GeV/u. The second ring, SIS300, serves either as a stretcher ring to provide slow extracted high-duty cycle beams, *e.g.*, for experiments with short-lived nuclei. Alternatively, the two synchrotrons may be used to accelerate ions with higher charge state to higher beam energies (with lower intensity) up to about 30 GeV/u as required, *e.g.*, for the nucleus-nucleus collisions programme. The rigidity of 100 Tm does also allow accelerating protons up to 30 GeV, which is optimum for anti-proton production. The experiments utilizing high-energy anti-proton beams are placed around an internal target in the High-Energy Storage Ring HESR, where the antiprotons are circulating and cooled by an electron-cooling system. The system can provide both pulsed beams, *e.g.*, for injection into storage rings or the

plasma physics experiments, as well as continuous high-duty cycle beams as required for external target experiments like the Compressed-Barionic Matter (CBM) experiment or several other experiments utilizing secondary beams of short-lived nuclei. A recent collection of articles on the FAIR physics program including a status report can be found in ref. [23].

A high degree of parallel operation of different research programs was an important aspect considered in the design of FAIR. The scheme of multiple synchrotron and storage rings and the resulting possibilities for in-ring experimentation offers itself for a truly parallel and multiple use. For other recent overviews on the FAIR project see refs. [24,25].

The construction of FAIR is planned in a modularized start version. The first stage comprising modules 0 to 3 will comprise the heavy-ion synchrotron SIS100, the superconducting fragment separator Super-FRS for production of rare-isotope beams, the CR and HESR storage rings and experimental areas. Already with completion of this start version, the radioactive-beam physics program can be started and will benefit from much higher secondary beam intensities than available presently at GSI, which are provided due to the increased SIS-18 ramping rate, the acceleration of low charge-state ions in SIS18 and SIS100, and the large phase-space acceptance of the Super-FRS. The buildings are planned being ready for installations in 2017.

This section is focussing on the part of the facility dealing with unstable nuclei. As discussed in the previous sections, the astrophysical processes, *e.g.*, the nucleosynthesis via rapid-neutron capture (*r*-process), involves heavy very neutron-rich nuclei that will be accessible for experiments for the first time at the future next-generation radioactive-beam facility NuSTAR (Nuclear Structure, Astrophysics and Reactions) at FAIR.

A brief overview on the NuSTAR facility is given in the next subsection. The individual experimental approaches are then discussed in the subsequent subsections. The physics program can be grouped essentially into two categories, one concerned with nuclear ground state and decay properties, one devoted to nuclear structure studies by reactions with various probes. The physics program and the experimental equipment has been proposed and elaborated by a large international collaboration, the NuSTAR Collaboration (about 700 scientists), and published as a collection of Letters of Intent, see ref. [26]. Apart from the fact that new regions of the nuclear chart will be in reach due to the higher beam intensities, emphasis has been put to further develop the experimental approaches to substantially increase their potential and quality, as well as to develop new advanced techniques providing access to methods not available so far for radioactive beams. In addition to the physics program, a detailed technical description of the experimental approaches and proposed instrumentation has been presented in individual Technical Proposals of NuSTAR, which have been evaluated by international expert committees. The project proposals of the recommended NuSTAR experiments are published as a separate volume of the Baseline Technical Report (July 2006) [27] of the FAIR facility.

3.2. The radioactive beam facility. – A schematic view of the layout of the NuSTAR facility is shown in fig. 10. The key requirements for the production of secondary beams

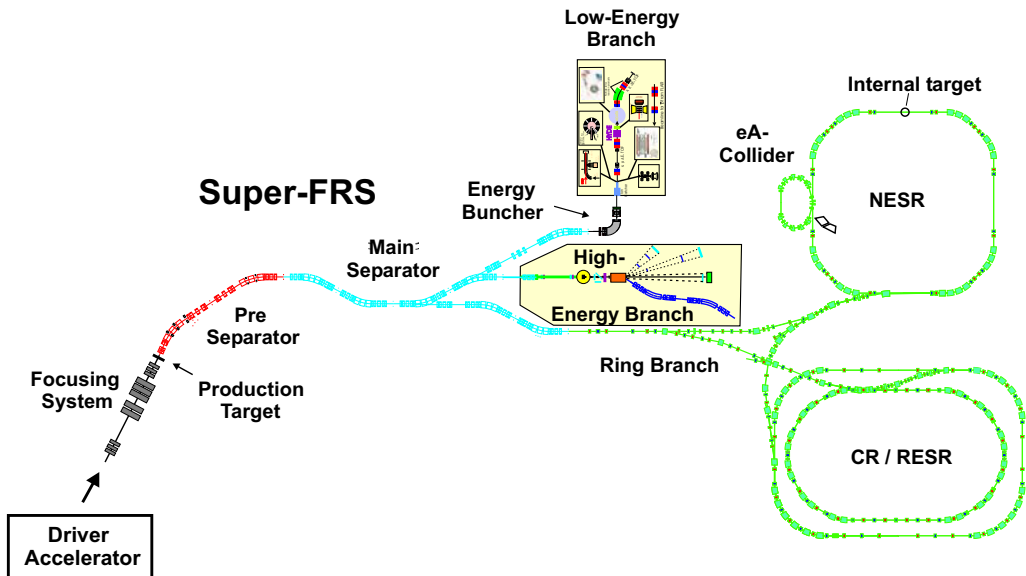


Fig. 10. – Schematic drawing of the two-stage large-acceptance superconducting fragment separator Super-FRS consisting of a pre-separator and a main separator. The Super-FRS serves three experimental areas, the low-energy branch, high-energy branch, and the storage ring complex comprising a large-acceptance collector ring (CR), an accumulator ring (RESR), and the experimental storage ring NESR including an internal target and the electron-ion (eA) collider. The building for the low-energy branch as well as the storarage rings RESR and NESR are not part of the start version. The figure is taken from ref. [1].

of short-lived nuclei by fragmentation and fission are high primary-beam intensities and beam energies of up to $1.5 \text{ GeV}/u$. The latter is important due to several reasons: Firstly, an efficient transport of the secondary beams, in particular those produced by uranium fission, is achievable with reasonable sized magnetic separators only by making use of the kinematic forward focussing due to the high beam energy. Secondly, the $B\rho - \Delta E - B\rho$ separation method allows clean isotopic separation and identification only for one ionic charge state, *i.e.*, fully ionized fragments, which can be reached for heavy ions ($Z \approx 80$) only for energies above one GeV/u . Besides the requirements due to the production and separation method, high energies of the secondary beams are also advantageous due to experimental and physics reasons, among those the possibility of using thick targets, high-acceptance measurements, and a clean separation of reaction mechanisms and spectroscopic information to be deduced.

Figure 10 shows a schematic layout of the rare-isotope facility including a superconducting fragment recoil separator Super-FRS [28] and three experimental areas, the low-energy branch, high-energy branch, and ring branch. The ring branch consists of several storage rings. First the collector ring CR, which has a large acceptance to allow efficient injection of secondary beams. Before injection into the new experimental storage

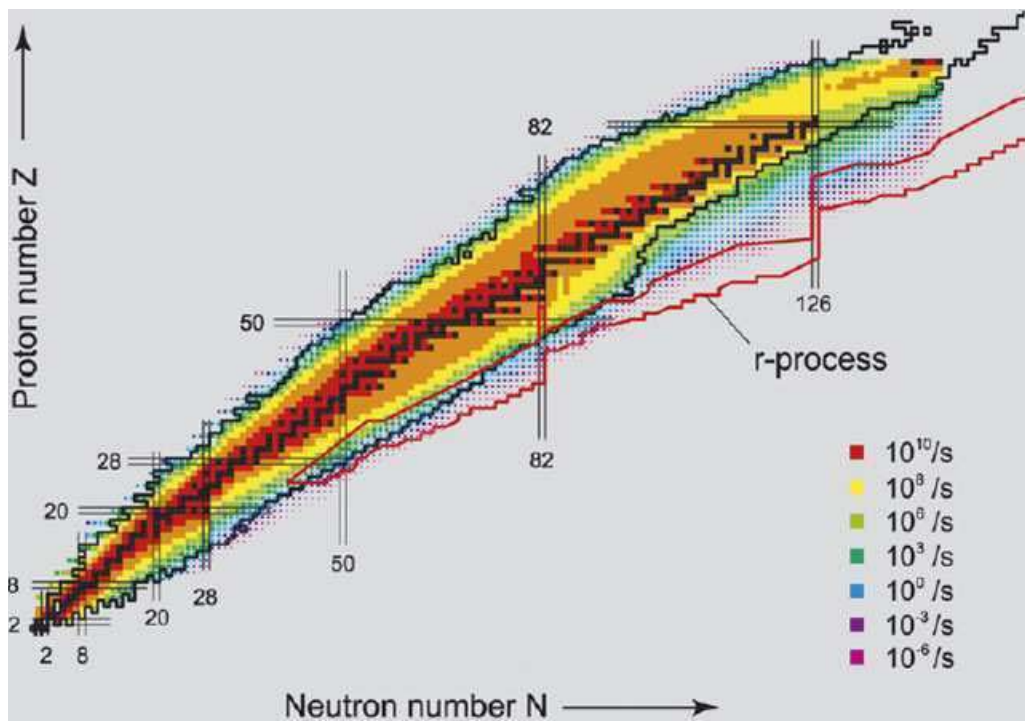


Fig. 11. – Estimated intensities for radioactive beams behind the Super-FRS. The region of the astrophysical r-process path is indicated by the red line. The black lines indicate the present limits of known nuclei. The figure is taken from ref. [1].

ring NESR, the beam is stochastically pre-cooled. Further electron cooling is provided in the NESR, which is equipped with an internal target for reaction studies. A smaller intersecting electron storage ring allows for the first time electron-scattering experiments off radioactive isotopes to be performed in a collider mode (eA-collider). An additional accumulator ring (RESR) is foreseen for fast deceleration with about 1 T/s ramping rate.

The Super-FRS is optimized for efficient transport of fission fragments implying a rather large acceptance of 5% in momentum and ± 40 mrad and ± 20 mrad angular acceptance in the horizontal and vertical planes, respectively. Although the acceptance is largely increased compared to the present FRS, an ion-optical resolving power of 1500 has been retained (for 40π mm mrad). Besides the resolution, an additional pre-separator ensures low background and clean isotopic separation of the beams of interest. The calculated transmission for beams of neutron-rich medium mass nuclei produced via fission of uranium with primary beam energy of $1.5 \text{ GeV}/u$ amounts to about 50%. The gain in transmission compared to the present separator is, as an example, a factor of 30 for the ^{78}Ni region. Together with the gain in primary beam intensity, intensities for separated rare-isotope beams will increase by significant more than three orders of magnitude. Estimated beam intensities are given in fig. 11. Substantially increased beam intensities are

achieved in particular for medium- heavy and heavy neutron-rich nuclei far extending into the region of hitherto unknown nuclei (the limits of known nuclei are indicated by the black line). Measurements of masses and decay properties of nuclei important for the understanding of nucleosynthesis of heavy elements in the cosmos by rapid neutron capture processes (r-process) will be possible as indicated in the figure.

In order to achieve a broad and at the same time in-depth insight into the structure of exotic nuclei, it is indispensable to utilize different experimental techniques to measure similar or related observables. Different probes and/or different beam energies are needed in order to optimize the sensitivity to particular nuclear structure observables. Three experimental areas are foreseen behind the Super-FRS, one housing a variety of experiments with low-energy and stopped beams, a high-energy reaction setup, and a storage and cooler ring complex including electron and antiproton colliders. In the following, a few aspects of the different branches will be briefly outlined. This discussion cannot be comprehensive, a more complete and detailed description of the proposed experiments can be found in the Letters of Intent of the NUSTAR Collaboration [26].

3·3. Experiments with slowed-down and stopped beams

3·3·1. The low-energy branch. For experiments requiring low-energy beams or implanted ions, the high-energy radioactive beams have to be slowed down. The key instrument for these experiments is an energy-focusing device [29], which reduces the energy spread of the secondary beams delivered by the Super-FRS. The principle is sketched in fig. 12.

It consists of a high-resolution dispersive separator stage in combination with a set of profiled energy degraders. After the monoenergetic degrader, the momentum spread is greatly reduced allowing, *e.g.*, the ions to be stopped in a 1 m long gas cell, from which they can be extracted for further manipulation and experiments. This method combines the advantages of in-flight separation (no limitations on lifetime and chemistry) with the ISOL type experimental methods. For gamma spectroscopy studies, beams can be slowed down also to intermediate energies (100 MeV/u) or even energies around the Coulomb barrier.

3·3·2. High-resolution in-flight spectroscopy (HISPEC). The core of the HISPEC experimental instrumentation is the AGATA 4π germanium γ -ray spectrometer. Due to its tracking capabilities, the first point of interaction and by that the emission angle of the photon can be determined. This allows to reconstruct the center-of-mass energy of the photons emitted in flight with high resolution even at rather large velocities, *e.g.*, with a resolution of about 0.5% at a velocity of 50% velocity of light. The AGATA array in combination with a magnetic analysis after the target and beam tracking detectors (see right-upper inset in fig. 12) will allow high-resolution γ spectroscopy experiments using the in-flight technique at medium beam energies (around 100 MeV/u). At higher beam energies, the γ energy in the laboratory frame becomes rather large due to the Doppler boost in forward direction. In that case, the interaction of the photons in the material are dominated by pair production limiting the tracking capabilities of the detector yielding

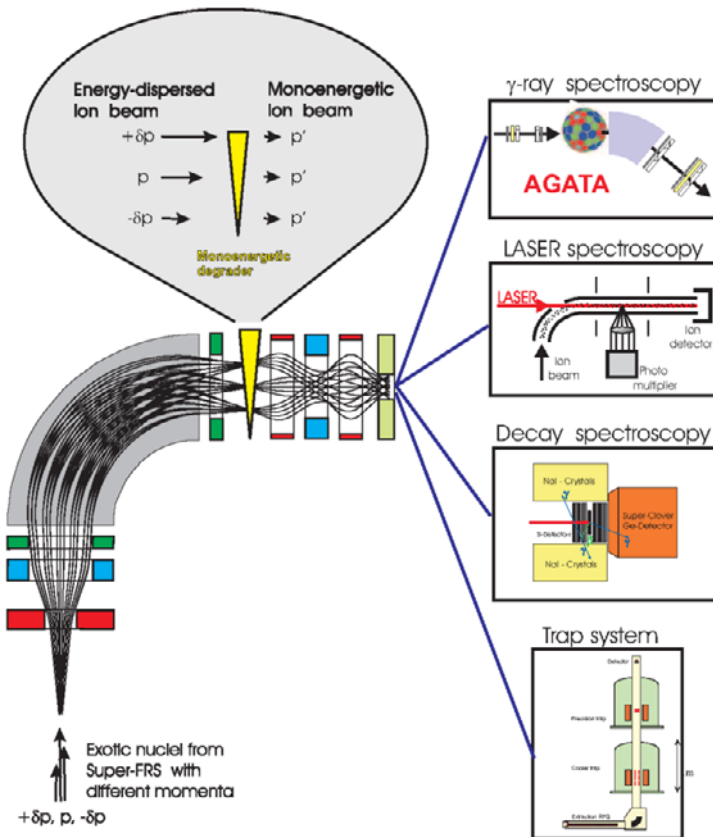


Fig. 12. – Schematic view of the experimental setup for experiments with low-energy and stopped radioactive beams. Beams from the Super-FRS with large momentum spread are analyzed in a dispersive dipole stage followed by a shaped energy degrader reducing the momentum spread of the slowed-down beam. The beams can be either stopped or directed directly to one of the experimental areas indicated as well. The figure is from ref. [1].

to larger Doppler broadening effects. For such high energies (at around $500 \text{ MeV}/u$), experiments will be performed more efficiently at the R^3B setup using a high-efficiency γ calorimeter with high granularity, see subsect. 3'4.

The physics program of HISPEC concentrates on the two energy domains around $50\text{--}100 \text{ MeV}/u$ and also around Coulomb barrier energies. At $50\text{--}100 \text{ MeV}/u$, the first 2^+ state can be excited very efficiently by electromagnetic excitation using heavy targets such as lead. The large cross-sections in combination with the good energy resolution of AGATA allows to determine $B(E2)$ values for short-lived nuclei even with low beam intensities. Shell structure and deformation of exotic nuclei can thus be studied in a wide range. In conjunction with proton inelastic scattering experiments performed at the EXL facility (see subsect. 3'5.2), deformations of the neutron and proton densities can be investigated.

Another important part of the experimental program is the γ spectroscopy after fragmentation reactions. Excited states are populated in few-nucleon removal reactions and the γ decays are measured with AGATA in coincidence with the identified fragments after the target. In these reactions, very neutron-rich nuclei can be reached by starting with a neutron-rich beam and observing the excited states in nuclei after few-proton removal reactions. Such reactions promise also access to medium-high spin states of exotic nuclei.

Beam energies reduced to that around the Coulomb barrier are also considered and would allow to access high-spin states by multiple Coulomb excitation or fusion-evaporation reactions.

3.3.3. Decay spectroscopy (DESPEC). The setup proposed by the DESPEC Collaboration consists of compact neutron and gamma-ray arrays of high granularity and auxiliary detectors arranged around the active stopper with which time and position signals from the implanted ion and the subsequent beta decay can be correlated. The range straggling due to the large momentum spread of the beam is largely reduced due to the use of the energy buncher.

From the measurement of the decay of stopped ions, half-lives, branching ratios, nuclear moments, as well as information on excited states can be determined. The study of isomeric states and exotic decays such as the two-proton decay are further topics of interest. An important characteristic of the decay spectroscopy experiments is its high sensitivity allowing to deduce nuclear-structure information like the lifetime with very low beam intensity, down to about 10^{-3} particles/sec. The half-lives of astrophysical relevant nuclei like the very neutron-rich r-process nuclei can thus be determined in a wide range, see fig. 11. This information together with the masses basically determines the complex path of nucleosynthesis as discussed in previous sections. An impressive example was recently reported by the MSU group. The half-life of the r-process waiting-point nucleus ^{78}Ni was determined to be 110_{-60}^{+100} ms [30] measuring a total number of 11 ^{78}Ni isotopes with a beam intensity of about 3×10^{-4} /s.

3.3.4. The advanced trapping system MATS. MATS stands for “Precision Measurements of very short-lived nuclei using an Advanced Trapping System for highly-charged ions”. Two techniques will be applied: high-accuracy mass measurements and in-trap spectroscopy of conversion-electron and alpha decays. A schematic view of the system is displayed in fig. 13. Radioactive ions from the Super-FRS are energy-bunched and stopped in a gas cell. Figure 13 indicates the manipulation steps from the extraction to the final storage in the precision Penning trap. The MATS Collaboration aims for relative mass precision of better than 10^{-8} even for nuclides with half-lives of 10 ms only.

The mass-measurement program of MATS is complementary to the ILIMA experiment at the storage rings, see subsubsect. 3.5.1. While the storage ring experiments are able to very effectively measure many masses of radioactive nuclei in a short time, MATS provides a superior resolution. The masses measured by MATS may also serve as calibration points for the survey measurements at the storage rings. Besides its importance

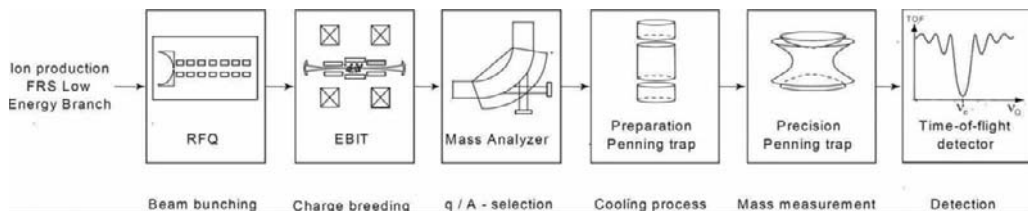


Fig. 13. – Schematic view of the experimental scheme for precision measurements with trapped ions. The figure is taken from the MATS LoI [26].

for nuclear structure and astrophysics, as discussed above, precise mass values are also needed for tests of the Standard Model, *i.e.* the unitarity test of the CKM matrix in weak decays. Here, the Q values enter and the masses of mother and daughter nuclei have to be known with a precision of about 1×10^{-8} , which will be reached with the MATS Penning-trap system.

3.3.5. The laser-spectroscopy experiment LASPEC. A multi-purpose laser-spectroscopy station is proposed by the LASPEC Collaboration. The setup will permit utilizing a variety of optical methods that have been developed and pioneered at ISOL facilities [31], such as fluorescence, resonance ionization and polarization based spectroscopy. These techniques are used to measure isotopic and isomeric nuclear spins, magnetic dipole moments, electric quadrupole moments and changes in mean square charge radii. The latter, *e.g.*, is accomplished by a precise measurement of the isotope shift in an atomic transition. A recent example for the application of this technique is the determination of the charge-radius change for the lithium isotopes ${}^9,{}^{11}\text{Li}$ [32]. The isotope shift in the $2s \rightarrow 3s$ two-photon transition was measured with an uncertainty $< 10^{-5}$ for ${}^{11}\text{Li}$ (half-life 8.5 ms) with a production rate of $\approx 10^4$ atoms/s only. Together with high-precision calculations for the mass shift, a charge radius of $2.467(37)$ fm was deduced. The difference in the two charge radii of ${}^9\text{Li}$ and ${}^{11}\text{Li}$ is related to the correlations among the neutrons in the halo.

The availability of the laser-spectroscopy instrumentation at the NuSTAR low-energy branch offers the unique opportunity of applying such techniques also to isotopes not accessible at ISOL facilities as the refractory elements.

3.4. Reactions with Relativistic Radioactive Beams (R^3B). – The instrumentation at the high-energy branch is designed for experiments using directly the high-energy secondary beams as delivered from the separator with magnetic rigidities up to 20 Tm, thus taking full advantage of the characteristics of radioactive beams produced by the in-flight separation method including the highest possible transmission to the target. The incoming ions are identified on an event-by-event basis and tracked onto the reaction target enabling a simultaneous use of beams composed out of many isotopes.

The R^3B [33] experimental configuration is based on a concept similar to the existing R3B-LAND reaction setup at GSI discussed in the previous section but introducing

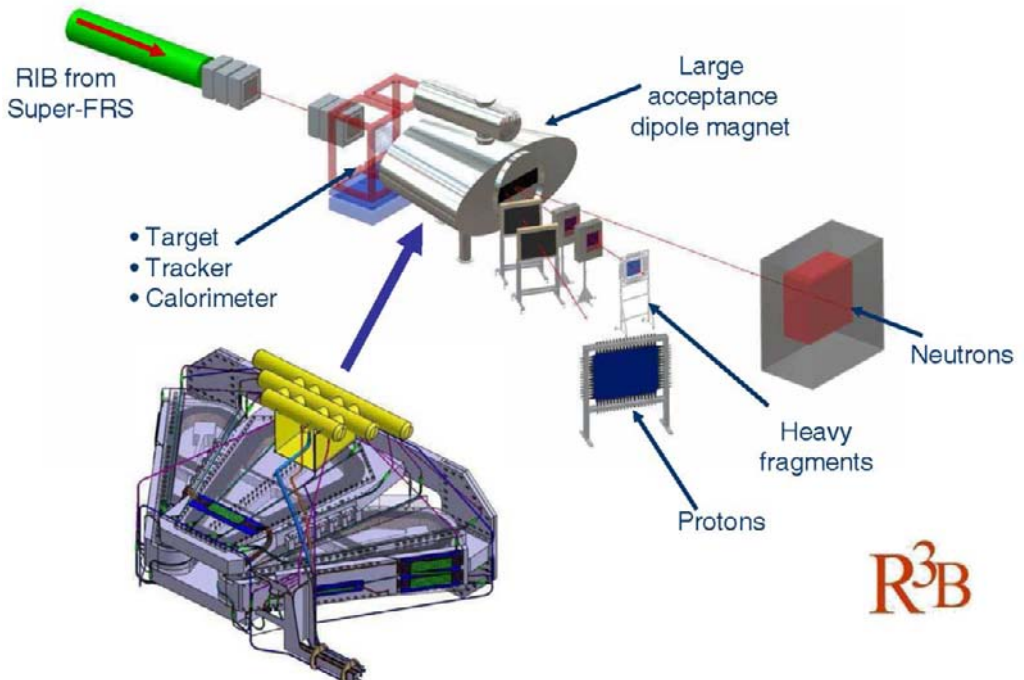


Fig. 14. – Schematic view of the experimental setup for scattering experiments with relativistic radioactive beams comprising γ -ray and target recoil detection, a large-acceptance dipole magnet, neutron and light-charged particle detectors, and a variety of heavy-ion detectors.

substantial improvement with respect to resolution and an extended detection scheme, which comprises the additional detection of light (target-like) recoil particles and a high-resolution fragment spectrometer. The start version of the setup without the spectrometer is schematically depicted in fig. 14. The complete version foresees two operation modes, one for large-acceptance measurements of heavy fragments and light charged particles (as shown in fig. 14), and alternatively for high-resolution momentum measurements ($\Delta p/p \approx 10^{-4}$) using a magnetic spectrometer (not shown in fig. 14). A large-acceptance superconducting dipole magnet, already under construction and in part funded by the European Commission, serves together with tracking detectors in the momentum analysis of the heavy fragments. The large gap of the dipole allows charged particles and neutrons of projectile rapidity emitted from excited fragments to be detected behind the magnet by drift chambers and a neutron detector at zero degree, respectively, which provide excellent position and time resolution. The target area, with the possibility of inserting a liquid- or frozen-hydrogen target, is surrounded by a silicon vertex tracker and a combined charged particle and gamma calorimeter.

The experimental configuration is suitable for kinematical complete measurements for a wide variety of scattering experiments, *i.e.* such as heavy-ion-induced electromagnetic

excitation, knockout and breakup reactions, or light-ion (in)elastic and quasi-free scattering in inverse kinematics, thus enabling a broad physics programme with rare-isotope beams to be performed. More details can be found in the Letter of Intent of the R³B Collaboration [33, 26].

The use of high beam energies around few hundred MeV/u for studies of nuclear structure and astrophysics is advantageous both from an experimental point of view as well as from theoretical considerations. The high beam energies result in short interaction times and small scattering angles, which allow the use of certain approximations and thus enable a quantitative description of the underlying reaction mechanisms. Experimental merits are the possibility of using relatively thick targets (in the order of g/cm²) and kinematical forward focusing, which makes full-acceptance measurements feasible with moderately sized detectors. Thus nuclear-structure investigations of very exotic nuclei at the driplines are possible even if such beams are produced with very low rates in the order of one ion per second.

The new setup will allow extending kinematical complete measurements towards the heaviest isotopes, *e.g.*, neutron-rich lead isotopes. As mentioned already earlier, beam energies in the order of 1 GeV/u are needed to ensure fully stripped ions in order to allow for a separation and identification of heavy fragments by a magnetic analysis. This implies rather demanding requirements on the design of the setup. The combination of the dipole with large field integral and thin high-resolution tracking detectors will enable identification of fragments up to the mass $A \approx 200$ region. In order to achieve a good invariant-mass resolution even at the high beam energies, the neutrons have to be detected with high resolution. The design of the new neutron detector NeuLAND foresees a time resolution of better than 100 psec rms, and a position resolution of about 1 cm rms. Together with the calorimeter with a high granularity of a few thousand crystals, precise Doppler correction will be possible, which is necessary at the high beam energies. For particular cases, the neutron detector may be placed at a distance of up to 30 m. In such cases, an invariant-mass resolution of about 20 keV can be reached, which is particularly interesting for high-resolution measurements close to the threshold in the astrophysical interesting energy window.

3·5. Experiments with stored and cooled beams

3·5·1. Isomeric beams, lifetimes, and masses (ILIMA). The third branch of the SuperFRS serves a storage- and cooler-ring complex. A schematic layout is shown in the right part of fig. 10. Fragment pulses as short as 50 ns are injected into a Collector Ring (CR) with large acceptance, where fast stochastic pre-cooling is applied. A momentum spread of $\Delta p/p \approx 10^{-4}$ is achieved within less than 500 ms. The CR may also be used for mass and lifetime measurements of short-lived nuclei applying ToF measurements in the isochronous mode [34] as proposed by the ILIMA Collaboration [26]. In the isochronous mode, the ring optics is tuned such that the differences in velocities are compressed by different trajectories. From the precise measurement of the revolution frequency, masses of short-lived nuclei down to the μ s range can be extracted. Nuclei with half-lives

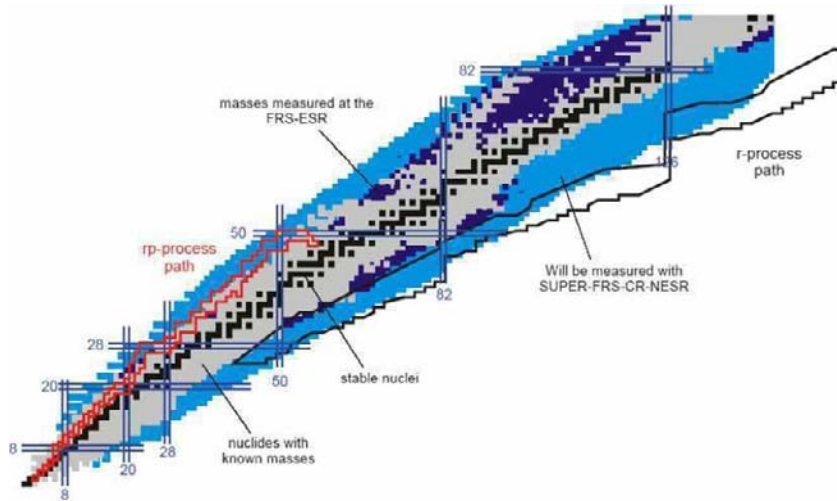


Fig. 15. – Overview on possible mass measurements at the storage rings at NuSTAR@FAIR. The region of the r-process is indicated in the figure showing that mass measurements will be possible for a major part of the r-process nuclei. The figure is taken from the Technical Proposal of the ILIMA Collaboration [27].

longer than about 1 s can be injected after stochastic pre-cooling in the CR into the New Experimental Storage Ring NESR, where electron cooling is applied. Here, the Schottky method [34] is applied to determine the revolution frequency and masses with a resolving power of about 10^6 . Both methods for mass- and lifetime measurements have been developed at GSI using the fragment separator FRS and the storage ring ESR at the present GSI facility, as discussed in the previous section. The installation at FAIR will benefit not only from the higher beam intensities and larger acceptance of the Super-FRS, but also from the significantly improved acceptance of the CR for hot fragment beams compared to the present storage ring ESR. This will allow mass measurements to be performed in a wide range of the nuclear chart as can be seen in fig. 15. The light-blue color indicates the region of accessible nuclei at the new facility. The importance of mass measurements for nuclear structure and astrophysics has been already discussed in previous sections. The new facility will make accessible almost the complete region of nuclei involved in the r-process nucleosynthesis. The expected region of the r-process path is indicated in fig. 15.

3.5.2. Reactions at internal targets in the NESR (EXL). The EXL project (EXotic nuclei studied in light-ion-induced reactions at the NESR storage ring) aims at investigating light-ion-induced direct reactions in inverse kinematics by using a universal detector system built around the internal target station at the NESR. For studies with the EXL apparatus, the FAIR storage rings are operated in the following scheme: secondary beams of unstable nuclei are produced by fragmentation or fission reactions, are separated in the

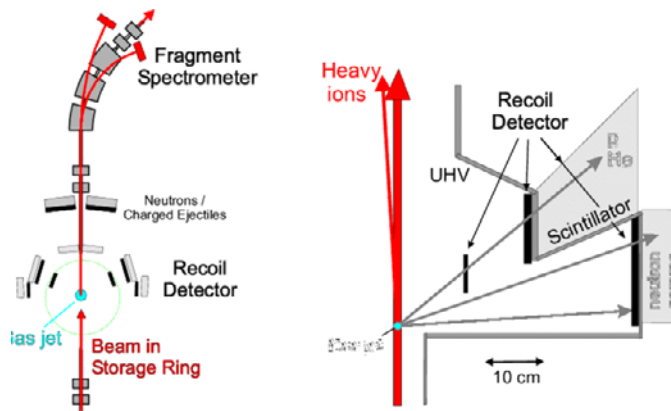


Fig. 16. – Detection scheme for reaction studies at the internal target in the NESR [1].

Super-FRS fragment separator, and then accumulated in the Collector Ring (CR). Bunch rotation and stochastic pre-cooling improves the beam quality to a level already sufficient for most of the envisaged measurements. If required, fast beam energy variation (down to tens of MeV per nucleon) is achieved in the RESR ring. Finally, the beam is transferred into the NESR ring where the measurement is performed. Continuous accumulation of the beam in the NESR can be provided by longitudinal stacking simultaneously to the measurement, and electron cooling compensates an emittance growth from beam-target interactions. In principle, the ions can be decelerated down to energies of a few MeV, the domain of beam energies for transfer and capture reactions, but at the expense of beam losses due to emittance growth.

A schematic layout of the setup is displayed in fig. 16. The cooled radioactive-ion beam passes a gas-jet target while circulating in the storage ring. Recoiling target ions, *e.g.*, protons or α -particles, are detected by the recoil detector surrounding the target. Particles are tracked by position-sensitive Si-strip detectors and their energy is measured in a scintillator (see right part of fig. 16). In forward direction, charged ejectiles and neutrons are measured by detectors placed at small angles around the beam pipe. Heavy fragments can be analyzed by using the first arc of the storage ring as a magnetic spectrometer. The experimental approach allows thus a kinematical complete measurement of the reaction products.

The experimental program at the EXL facility comprises elastic and inelastic scattering, knockout and transfer reactions, as well as charge-exchange reactions. The program has some overlap with the physics aims of the R^3B experiment discussed in subsect. 3.4. The experimental approach of EXL, however, is complementary to the R^3B one since it covers the low-momentum transfer part of the scattering processes, which cannot be measured efficiently at R^3B . The kinematics of the scattering process in inverse kinematics is illustrated in fig. 17.

The kinetic energy of the recoiling (target) nuclei is shown *versus* the scattering angle in the laboratory frame. An example is shown for inelastic scattering of α -particles off

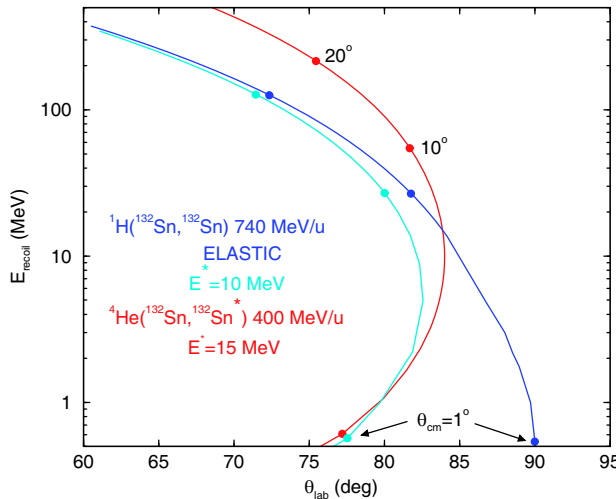


Fig. 17. – Kinetic energy *vs.* scattering angle in the laboratory frame of recoiling ^1H and ^4He target nuclei. Center-of-mass angles θ_{cm} are indicated at the curves. The figure is taken from ref. [1].

^{132}Sn nuclei at 400 MeV/ u , a typical reaction used to study isoscalar excitations such as the giant monopole resonance. The angular distribution, which is sensitive to the multipolarity, has to be measured down to low center-of-mass angles, for monopole transitions preferentially close to 0 degree. This means that recoiling particles will have very little kinetic energy as can be seen from fig. 17, implying the need of using thin targets. External target experiments would thus yield very low luminosities. The advantage of performing such experiments in a storage ring arises mainly from the fact that thin gas targets can be used while gaining luminosity by the revolution frequency of $\approx 10^6 \text{ s}^{-1}$ and by continued accumulation of the secondary beams. EXL will thus allow to extend the applicability of high-energy reactions towards the low-momentum transfer region not accessible so far, or only with rather low luminosity. Besides the nuclear-structure interest in such reactions, this is of particular importance for nuclear-astrophysics measurements. This includes the measurement of Gamow-Teller strength, as well as experiments for constraining the EoS of asymmetric nuclear matter. For the latter case, measurements of the giant monopole resonances in neutron-rich nuclei will provide information on the compressibility of asymmetric nuclear matter. Such measurements require alpha scattering at low momentum transfer which will be achievable with good luminosity only at the storage ring. Secondly, the elastic proton scattering will provide matter radii, which in combination with other measurements of the charge radii will provide neutron-skin thickness measurements for heavy nuclei, which is a key observable for determining the density dependence of the symmetry energy, as discussed in the previous sections.

3.5.3. Electron scattering with short-lived nuclei (ELISe). Electron scattering has been a very powerful tool for decades to extract charge densities and radii of nuclei as well

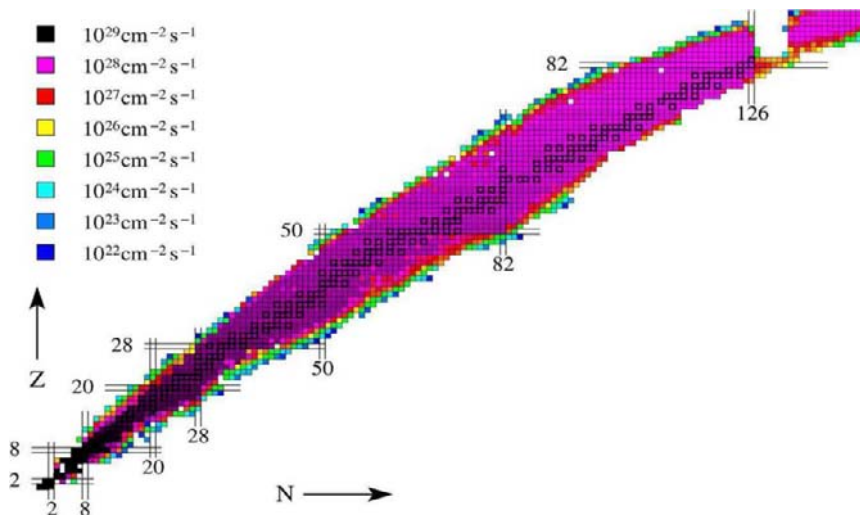


Fig. 18. – Estimated luminosities for electron-scattering experiments off radioactive nuclei. The figure is taken from the Technical Proposal of the ELISe Collaboration [27].

as to investigate collective states by means of inelastic scattering. In addition, electron-induced knockout reactions give access to the single-particle structure as well as nucleon-nucleon correlations in nuclei. The advantages of using electrons in nuclear-structure investigations essentially arise from the fact that electrons are point-like particles and that the electron-nucleus interaction is relatively weak and theoretically well described. Charge distributions and transition densities can thus be reliably deduced from measured cross-sections. Independent variation of energy- and momentum transfer allows selecting certain scattering processes.

So far, the application of the electron-scattering process to short-lived nuclei was impossible. The ELISe Collaboration proposes to utilize two intersecting storage rings, the NESR and a smaller storage ring for electrons, to scatter electrons in a collider mode off radioactive nuclei circulating in the NESR, see fig. 10 (E-A collider). The stored electrons with variable energies from 125 to 500 MeV are contra-propagating to heavy-ion bunches with energies typically between 200 and 740 MeV/u. Scattered electrons will be momentum analyzed by a large-acceptance spectrometer. The crucial quantity first of all is the reachable luminosity. The number of stored ions is apart from production limitations and short lifetimes limited by space-charge effects. A full simulation of expected luminosities including the production as well as transmission losses, nuclear and beam (storage) lifetime is shown in fig. 18. This has to be compared to the luminosity requirements of the different experiments. Giant resonance studies, for instance, can be performed with luminosities around $10^{28} \text{ cm}^{-2}/\text{s}$. Clearly, a large number of rare isotopes potentially become accessible for such studies, and even more for measurements of elastic scattering. As mentioned already in the previous section, the combination of precise charge-radius measurements with proton-elastic scattering data will allow for determining the neutron-skin thickness in heavy nuclei.

3.5.4. The Antiproton-Ion-Collider AIC. The AIC Collaboration proposes to use the electron storage ring, or a modified version of it, for storing antiprotons. This would allow to study antiproton-ion scattering in a collider mode similar to the eA collider. The total antiproton absorption cross-section is the interesting quantity from which the neutron-skin thickness of nuclei can be determined by measuring the individual cross-sections for annihilations on proton and neutrons. The antiproton will annihilate on an individual nucleon. The resulting A-1 fragments are circulating in the storage ring where they can be individually detected via the Schottky method. In head-on collisions with the unstable nuclei stored in the NESR, luminosities of $10^{23} \text{ cm}^{-2} \text{ s}^{-1}$ are estimated in case of 10^6 stored ions. Since antiproton absorption cross-sections are of the order of a barn, systematic studies over extended isotopic or isotonic chains are enabled.

4. – Conclusion

A major challenge of nuclear astrophysics is providing the nuclear input necessary for the understanding of nucleosynthesis processes, in particular the r-process involving heavy neutron-rich nuclei, and the properties of neutron-star matter. High-energy radioactive beams are particularly well suited for such studies. Examples discussed are the measurements of masses and lifetimes of r-process nuclei, which are fundamental input to a theoretical description of the astrophysical process by large network calculations. The calculation of neutron-capture rates needs the dipole strength function of very exotic nuclei exhibiting a dipole response very different compared to stable ones due to the neutron-proton asymmetry and the weaker binding of valence nucleons forming a neutron skin. The particular response of such nuclei including Pygmy dipole vibrations influences the capture rates and thus the r-process abundance of synthesized elements systematically. Heavy-ion-induced electromagnetic excitation at relativistic energies is an ideal tool to provide the strength function of very neutron-rich nuclei. The systematic study of low-lying dipole excitation modes related to the neutron skin will yield tight constraints on the density-dependence of the isospin-dependent part of the nuclear equation of state, which is fundamental for a theoretical description of neutron stars. In this context, innovative experimental methods being designed for the radioactive-beam facility NuSTAR at FAIR will provide profound knowledge on the properties of neutron-rich nuclei and neutron-rich matter.

The NuSTAR facility will allow the extraction of the basic properties of nuclei at the extremes of nuclear existence while at the same time allowing in-depth investigations of exotic nuclei closer to stability. Exploring nuclear structure and nuclear stability under extreme conditions is essential for a comprehensive understanding of the nuclear many-body system. It is also the basis for understanding the various aspects of nuclear astrophysics and for many applications of nuclear physics.

High beam intensities provided by the FAIR accelerators, effective radioactive-beam production and transportation by the Super-FRS, in combination with advanced experimental instrumentation of high sensitivity and efficiency are the most important ingredients for the next-generation rare-isotope beam facility. The NuSTAR facility will span

the full range of experimental techniques needed to pursue the intellectual challenges related to the many-body system nucleus, including novel experimental techniques not available at present for radioactive nuclei like, *e.g.*, light-ion and electron scattering off exotic nuclei.

REFERENCES

- [1] *An International Accelerator Facility for Beams of Ions and Antiprotons*, Conceptual Design Report, GSI (2001), <http://www.gsi.de/GSI-Future/cdr/>.
- [2] PFEIFFER B., KRATZ K.-L. and THIELEMANN F.-K., *Z. Phys. A*, **357** (1997) 235.
- [3] Courtesy: Peter Moeller.
- [4] GORIELY S., *Phys. Lett. B*, **436** (1998) 10.
- [5] LITVINNOVA E., LOENS H. P., LANGANKEA K., MARTINEZ-PINEDO G., RAUSCHER T., RING P., THIELEMANN F.-K. and TSELYAEV V., *Nucl. Phys. A*, **823** (2009) 26.
- [6] LITVINNOVA E., RING P. and TSELYAEV V., *Phys. Rev. C*, **78** (2008) 014312.
- [7] GORIELY S. and KHAN E., *Nucl. Phys. A*, **706** (2002) 217.
- [8] TYPEL S. and BROWN B. A., *Phys. Rev. C*, **64** (2001) 027302.
- [9] FURNSTAHL R. J., *Nucl. Phys. A*, **706** (2002) 85.
- [10] PIEKAREWICZ J., *Phys. Rev. C*, **73** (2006) 044325.
- [11] PIEKAREWICZ J., arXiv:submit/0160295 [nucl-th] 8 Dec 2010.
- [12] HOROWITZ C. J., POLLOCK S. J., SOUDER P. A. and MICHAELS R., *Phys. Rev. C*, **63** (2001) 025501.
- [13] KUMAR K., MICHAELS R., SOUDER P. A. and URCIUOLI G. M., (2005), URL <http://hallaweb.jlab.org/parity/prex>.
- [14] HAUSMANN M., ATTALLAH F., BECKERT K., BOSCH F., DOLINSKIY A., EICKHOFF H., FALCH M., FRANCZAK B., FRANZKE B., GEISSEL H., KERSCHER Th., KLEPPER O., KLUGE H.-J., KOZHUHAROV C., LÖBNER K. E. G., MÜNZENBERG G., NOLDEN F., NOVIKOV YU. N., RADON T., SCHATZ H., SCHEIDENBERGER C., STADLMANN J., STECK M., WINKLER T. and WOLNIK H., *Nucl. Instrum. Methods A*, **446** (2000) 569.
- [15] AUMANN T., *Eur. Phys. J. A*, **26** (2005) 441.
- [16] ADRICH P., KLIMKIEWICZ A., FALLOT M., BORETZKY K., AUMANN T., CORTINA-GIL D., DATTA PRAMANIK U., ELZE TH. W., EMLING H., GEISSEL H., HELLSTRÖM M., JONES K. L., KRATZ J. V., KULESSA R., LEIFELS Y., NOCIFORO C., PALIT R., SIMON H., SURÓWKA G., SÜMMERER K. and WALUS W., *Phys. Rev. Lett.*, **95** (2005) 132501.
- [17] KLIMKIEWICZ A., PAAR N., ADRICH P., FALLOT M., BORETZKY K., AUMANN T., CORTINA-GIL D., DATTA PRAMANIK U., ELZE TH. W., EMLING H., GEISSEL H., HELLSTRÖM M., JONES K. L., KRATZ J. V., KULESSA R., NOCIFORO C., PALIT R., SIMON H., SUROWKA G., SÜMMERER K., VRETERNAR D. and WALUS W. (LAND COLLABORATION), *Phys. Rev. C*, **76** (2007) 051603.
- [18] WIELAND O., BRACCO A., CAMERA F., BENZONI G., BLASI N., BRAMBILLA S., CRESPI F. C. L., LEONI S., MILLION B., NICOLINI R., MAJ A., BEDNARCZYK P., GREBOSZ J., KMIECIK M., MECZYNSKI W., STYCZEN J., AUMANN T., BANU A., BECK T., BECKER F., CACERES L., DOORRENBAL P., EMLING H., GERL J., GEISSEL H., GORSKA M., KAVATSYUK O., KAVATSYUK M., KOJOUHAROV I., KURZ N., LOZEGA R., SAITO N., SAITO T., SCHAFFNER H., WOLLERSHEIM H. J., JOLIE J., REITER P., WARR N., DEANGELIS G., GADEA A., NAPOLI D., LENZI S., LUNARDI S., BALABANSKI D., LOBIANCO G., PETRACHE C., SALTARELLI A., CASTOLDI M., ZUCCHIATTI A., WALKER J. and BÜRGER A., *Phys. Rev. Lett.*, **102** (2009) 092502.

- [19] KRASZNAHORKAY A., BACELAR J., BORDEWIJK J. A., BRANDENBURG S., BUDA A., VAN T HOF G., HOFSTEE M. A., KATO S., POELHEKKEN T. D., VAN DER WERF S. Y., VAN DER WOUDE A., HARAKEH M. N. and KALANTAR-NAYESTANAKI N., *Phys. Rev. Lett.*, **66** (1991) 1287.
- [20] CARBONE A., COLO G., ANGELA BRACCO, CAO LI-G., BORTIGNON P. F., CAMERA F. and WIELAND O., *Phys. Rev. C*, **81** (2010) 041301.
- [21] MAKINAGA A., SCHWENGNER R., RUSEV G., DÖNAU F., FRAUENDORF S., BEMMERER D., BEYER R., CRESPO P., ERHARD M., JUNGHANS A. R., KLUG J., KOSEV K., NAIR C., SCHILLING K. D. and WAGNER A., *Phys. Rev. C*, **82** (2010) 024314.
- [22] TONCHEV A. P., HAMMOND S. L., KELLEY J. H., KWAN E., LENSKE H., RUSEV G., TORNOW W. and TSONEVA N., *Phys. Rev. Lett.*, **104** (2010) 072501.
- [23] *Nuclear Physics News*, Vol. **16** (2006).
- [24] HENNING W. F., *Nucl. Phys. A*, **734** (2004) 654.
- [25] GUTBROD H. H., *Nucl. Phys. A*, **752** (2005) 457c.
- [26] Letters of Intent of the NUSTAR Collaboration at FAIR (April 2004), http://www.gsi.de/forschung/kp/kp2/nustar_e.html/.
- [27] *FAIR, An International Accelerator Facility for Beams of Ions and Antiprotons*, Baseline Technical Report, Vol. 4, July 2006, <http://www.gsi.de/fair/reports/btr.html>.
- [28] GEISSEL H., WEICK H., WINKLER M., MÜNZENBERG G., CHICHKINE V., YAVOR M., AUMANN T., BEHR K. H., BÖHMER M., BRÜNLE A., BURKARD K., BENLIJURE J., CORTINA-GIL D., CHULKOV L., DAEL A., DUCRET J.-E., EMLING H., FRANCZAK B., FRIESE J., GASTINEAU B., GERL J., GERNHÄUSER R., HELLSTRÖM M., JONSON B., KOJOUHAROVA J., KULESSA R., KINDLER B., KURZ N., LOMMEL B., MITTIG W., MORITZ G., MÜHLE C., NOLEN J. A., NYMAN G., ROUSSEL-CHOMAZ P., SCHEIDENBERGER C., SCHMIDT K.-H., SCHRIEDER G., SHERRILL B. M., SIMON H., SÜMMERER K., TAHIR N. A., VYSOTSKY V., WOLNIK H. and ZELLER A. F., *Nucl. Instrum. Methods B*, **204** (2003) 71.
- [29] SCHEIDENBERGER C., GEISSEL H., MAIER M., MÜNZENBERG G., PORTILLO M., SAVARD G., VAN DUPPEN P., WEICK H., WINKLER M., YAVOR M., ATTALLAH F., BEHR K.-H., CHICHKINE V., ELISEEV S., HAUSMANN M., HELLSTRÖM M., KAZA E., KINDLER B., LITVINOV Y., LOMMEL B., MARX G., MATOS M., NANKOV N., OHTSUBO T., SÜMMERER K., SUN Z.-Y. and ZHOU Z., *Nucl. Instrum. Methods B*, **204** (2003) 119.
- [30] HOSMER P. T., SCHATZ H., APRAHAMIAN A., ARNDT O., CLEMENT R. R. C., ESTRADE A., KRATZ K.-L., LIDDICK S. N., MANTICA P. F., MUELLER W. F., MONTES F., MORTON A. C., OUELLETTE M., PELLEGRINI E., PFEIFFER B., REEDER P., SANTI P., STEINER M., STOLZ A., TOMLIN B. E., WALTERS W. B. and WÖHR A., *Phys. Rev. Lett.*, **94** (2005) 112501.
- [31] OTTEN E. W., *Nuclear radii and moments of unstable isotopes*, in *Treatise on Heavy-Ion Science*, edited by BROMLEY D. A. (Springer) 1989, pp. 517-638.
- [32] SÁNCHEZ R., NÖRTERSHÄUSER W., EWALD G., ALBERS D., BEHR J., BRICAULT P., BUSHAW B. A., DAX A., DILLING J., DOMBSKY M., DRAKE G. W. F., GÖTTE S., KIRCHNER R., KLUGE H.-J., KÜHL TH., LASSEN J., LEVY C. D. P., PEARSON M. R., PRIME E. J., RYJKOV V., WOJTASZEK A., YAN Z.-C. and ZIMMERMANN C., *Phys. Rev. Lett.*, **96** (2006) 033002.
- [33] Reactions with Relativistic Radioactive Beams (R3B), <http://www-land.gsi.de/r3b/>.
- [34] GEISSEL H. and WOLNIK H., *Nucl. Phys. A*, **693** (2001) 19.

Proceedings of the International School of Physics “Enrico Fermi”
Course CLXXVIII “From the Big Bang to the Nucleosynthesis”, edited by A. Bracco and E. Nappi
(IOS, Amsterdam; SIF, Bologna)
DOI 10.3254/978-1-60750-974-5-157

Nuclear structure studies at RIKEN: New measurements with in-flight fast radioactive beams

T. MOTOBAYASHI

RIKEN Nishina Center - 2-1 Hirosawa, Wako, Saitama, 351-0198, Japan

Summary. — New facility of RIBF, Radioactive Isotope Beam Factory, at RIKEN started operation in 2007. It is designed to have capability of accessing 1000 more nuclei compared with the currently known 3000 isotopes by the projectile-fragmentation scheme. One of the advantages of the RIBF new facility, as well as of the old facility, is the availability of fast beams of nuclei far from the stability regardless of chemical property of the element of interest. Some recent studies with these fast beams and development of new devices to fully exploit the capability of the RIBF new facility are presented.

1. – Introduction

Recent development of nuclear structure studies owes largely to the increase of the number of nuclides available for experimental investigation. RI beams⁽¹⁾ at RIKEN have been produced by the projectile fragmentation scheme since 1990. Heavy-ion beams

⁽¹⁾ The word “RI beams” is the abbreviation of “Radioactive Isotopes beams”, and is equivalent to “radioactive ion beams” or beams with unstable nuclei.

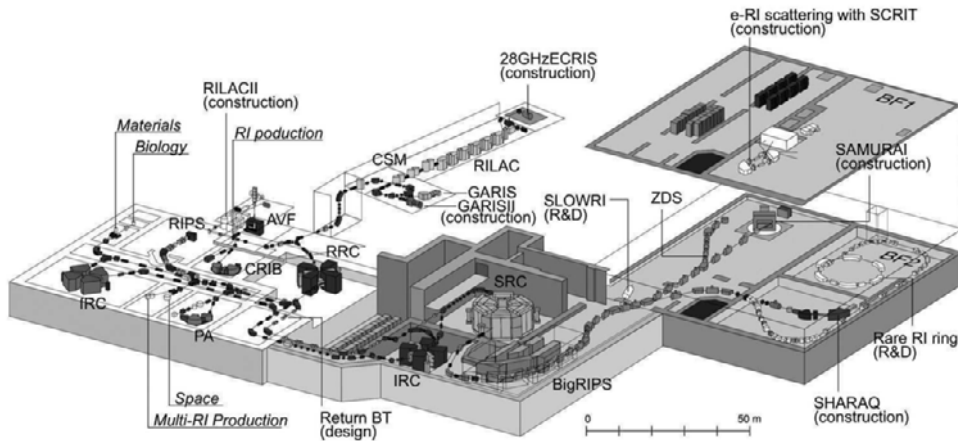


Fig. 1. – Schematic view of the RIKEN accelerator complex.

with intermediate energy (typically 100 MeV/nucleon) bombard a production target, and products of projectile fragmentation reactions are separated by a magnetic analyzer system and served as beams. Though the availability of the RI beam is limited to light nuclei, the world-highest-intensity RI beams are available for many neutron-rich nuclei, due to the high performance of the RIKEN Projectile fragment Separator (RIPS) [1]. Recently RIKEN constructed a new facility. It utilizes the existing and newly built accelerator complex, and provides the beams up to 345 MeV/nucleon for all chemical elements up to uranium. It is designed to provide world-strongest RI beams.

Nuclear structure studies with such fast RI beams are mostly categorized as: extention of the nuclear chart and nuclear spectroscopy with fast-beam-induced direct reactions or decay measurements of stopped beams. Recent developments at RIKEN are discussed in the following sections together with a brief introduction of the RIBF new facility.

2. – RIBF new facility

The new facility of RIBF provided its first beam in December 2006 after 10 years construction. A schematic view of the entire RIBF is shown in fig. 1. The new part of the accelerator complex consists of three cyclotrons, the fixed-frequency Ring Cyclotron (fRC) with $K = 570$ MeV, Intermediate stage Ring Cyclotron (IRC) with $K = 980$ MeV, and Superconducting Ring Cyclotron (SRC) with $K = 2600$ MeV, which successively boosts the beam energy up to 345 MeV/nucleon [2]. The 16 MV variable-frequency linear accelerator (RILAC) and four-sector ring cyclotron (RIKEN Ring Cyclotron, RRC) with $K = 540$ MeV, which have been in operation since 1987, are used as their injectors.

RI beams are produced via the projectile fragmentation of heavy ions or in-flight fission of uranium ions (see fig. 2) by a superconducting fragment separator BigRIPS [3], shown in fig. 3. It consists of fourteen magnets of superconducting quadrupole triplets

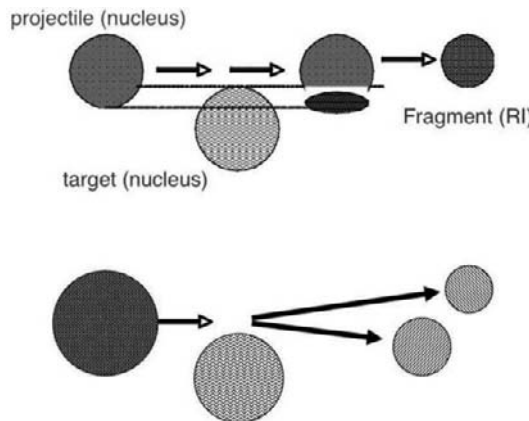


Fig. 2. – Two scheme of RI-beam production at RIBF: projectile fragmentation (top) and projectile fission (bottom).

and six room-temperature dipole magnets. Separation of reaction products is made by a two-stage separation scheme. The first stage serves to produce and separate RI beams with a wedge-shaped degrader inserted at the momentum-dispersive focus F1. The second-stage identifies RI beam species event-by-event and tags the secondary beam that still contains various different ions. The horizontal and vertical angular acceptances are designed respectively to 80 mrad and 100 mrad, while the momentum acceptance

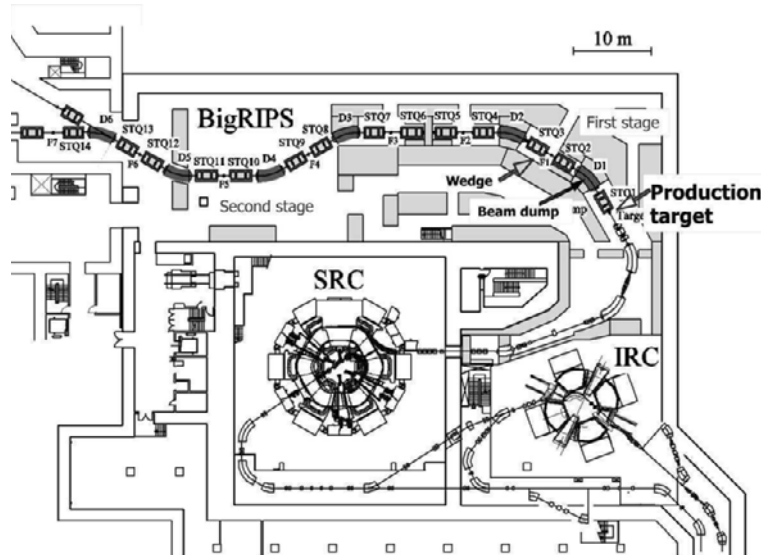


Fig. 3. – BigRIPS, superconducting RI separator at the new facility of RIKEN RIBF.

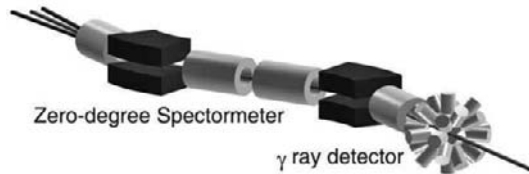


Fig. 4. – Setup for measurements of γ -rays from direct-reaction products with fast RI beams provided by RIBF.

is 6%. These angular and momentum acceptances enable one to collect about half of the fission fragments and most of the projectile fragments of interest produced by a 345 MeV/nucleon uranium beam.

The ZeroDegree spectrometer (ZDS), following the BigRIPS, analyzes secondary reaction products emitted in the beam direction. Its typical use is for γ -ray measurements in coincidence with fast-moving excited nuclei (see fig. 4) as in essentially the same way as for the ^{32}Mg experiment at RIPS discussed later. The ZDS is used to identify the reaction product. For other applications, such as β -decay measurements with stopped RIs, the ZDS is also useful.

The first extraction of the primary beam has been made by 345 MeV/nucleon $^{27}\text{Al}^{10+}$ on December 28 in 2006. After the accelerator tuning, ^{238}U ions were accelerated in Mar. 2007 and used for RI production.

The first secondary reaction experiments have been performed in December 2008 with intense ^{48}Ca beams. The current capability in producing nuclei far from the stability is exceeding the one of any other facilities in the world, and will even be enhanced to reach the level where about 1000 unknown isotopes can be created. Several new experimental installations are planned or being constructed.

3. – Frontiers in the nuclear chart

3.1. Nuclear chart. – Figure 5 shows a current nuclear chart. The solid squares represent stable isotopes, which are counted to about 300, and the nuclei experimentally known so far are about 3000 as shown by the open squares. Theoretical estimates give approximately 10000 isotopes that have lifetimes longer than micro seconds. They are stable against particle decay including proton- and neutron-emission and fission. Nuclear physicists have made continuous effort to extend the territory of known nuclei. About 500 nuclei were already known in 1940, and the number of known nuclei has increased steadily until now.

With the goal intensity of the primary beams, 1 p μ A for ions up to uranium, the RI beam yield is estimated by the code EPAX2 [4]. In fig. 5, the limit of RI beam intensity higher than one particle per day is indicated. The total number of isotopes expected to be produced in that condition is estimated to be about 4000, 1000 more than the currently known nuclides as mentioned. Most of the expected path of the r -process nucleosynthesis can be reached for the first time. This high capability encourages detailed studies of nuclei far from the stability valley.

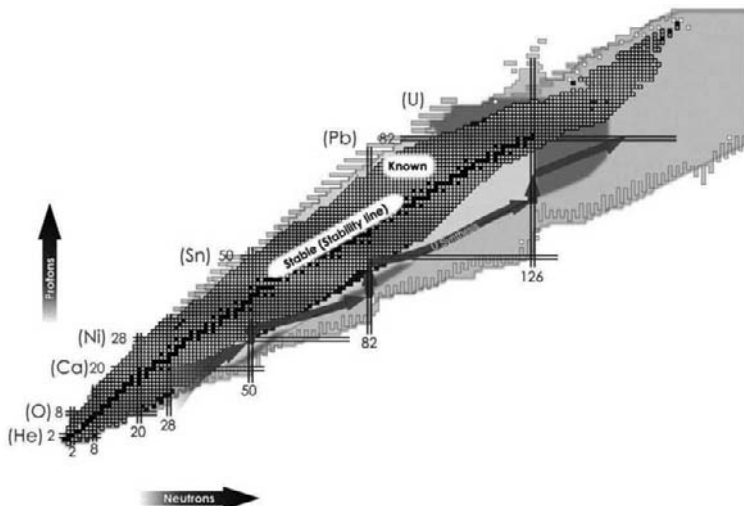


Fig. 5. – Nuclear chart. The expected *r*-process path is indicated by the lines with arrows. The thick solid curves indicate the limit of RI productions of 1 particle per day with 1 μA primary beam intensity at RIBF.

Nuclear physics research is not only to extend the territory in the nuclear chart. To understand the interaction and structure of atomic nuclei, a very important issue is to study properties of excited states of nuclei, which are less known for nuclei far from the stability line. It is also known that nuclear reactions play important roles in evolution of the Universe by creating energies in astrophysical objects and generating chemical elements. Reactions with unstable nuclei are important for explosive nuclear burning in stars and early Universe.

3.2. Toward the *r*-process path. – Experiments for new isotope production were performed in BigRIPS. By measuring the magnetic rigidity (trajectory measurement), stopping power (energy loss measurement) and velocity (time-of-flight measurement), particle identification was successfully made. As shown in fig. 6 for palladium, each isotope is separated from the one with a different charge state. In the first run in 2007 by the faint $^{238}\text{U}^{86+}$ beam of 4×10^7 particle/s on an average (about 10^{-5} of the goal), two new isotopes ^{125}Pd and ^{125}Pd were created [5]. The second run was performed in November 2008. Due to extensive accelerator improvements, the uranium beam intensity ($2 \times 10^9 \text{ s}^{-1}$) and stability were much increased, and 45 more new isotopes have been identified [6]. For example, hundred times more counts for ^{125}Pd and ^{126}Pd were obtained, and ^{127}Pd and ^{128}Pd were newly produced. These 2+45 new isotopes are located in the edge of the region of known isotopes as indicated in fig. 5.

It should be noted that the isotope ^{128}Pd is located in the classical waiting point of the *r*-process. The present result encourages to study nuclei of waiting points in near future with stronger uranium beams.

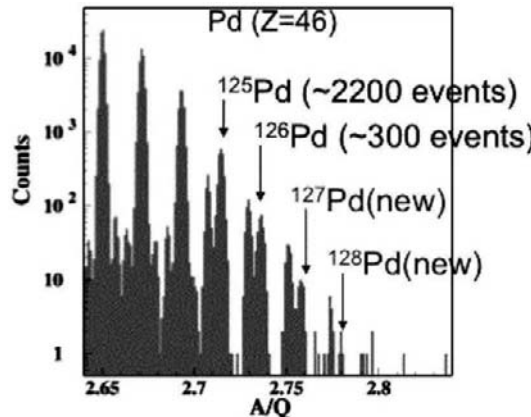


Fig. 6. – A/Q spectrum for Pd isotopes in the second run.

The first series of secondary reaction experiments have been performed with ^{48}Ca primary beams in Dec. 2008. Inelastic $^{32}\text{Ne} + ^{12}\text{C}$ scattering at 225 MeV/nucleon to determine the location of the first excited 2^+ state in ^{32}Ne [7] as will be discussed later. Inclusive Coulomb dissociation measurements for ^{22}C and ^{31}Ne provided candidates of new halo nuclei [8]. Interaction cross-section measurements for neutron-rich neon isotopes [9] were also performed. The ^{48}Ca intensity of around 100 pnA was achieved, and the gain more than 1000 was obtained for the secondary beam intensity compared with those in RIPS with lower energy primary beams. Since capability of RIPS is already in the world top level, the RI beam production rate at RIBF is far above the intensity in any other facility in the world. For example, the intensity of ^{30}Ne was about 300 cps, 1500 times higher than 0.2 cps obtained at RIPS. Our preliminary analysis on the production rate at 345 MeV/nucleon suggests higher production cross-sections for very neutron-rich nuclei compared with lower energy data taken at 63 MeV/nucleon with RIPS [10]. Though further investigation with a thin production target to avoid possible plural reactions in the target is necessary to draw more definite conclusions, this is also encouraging to go farther from the stability valley.

One of the important quantities of r -process nuclei is the β -decay lifetime. The first attempt was made in 2009 to access $A \approx 100$ region. Several new lifetimes are expected to be determined (see fig. 7). We expect to extend such β -decay studies to the region close to or in the r -process path.

3.3. Super-heavy nuclei. – Another frontier is the region of super-heavy nuclei. Thanks to several improvements for the injector RILAC of RIBF, intense ions at several MeV/nucleon energies became available at RILAC itself. Super-heavy element search has been performed by “cold” fusion reactions with these intense primary beams. In 2004, the first event indicating the production of the isotope $^{278}\text{113}$ by the $^{209}\text{Bi}(^{70}\text{Zn}, \text{n})$ fusion reaction has been observed [11], followed by the second event in 2005.

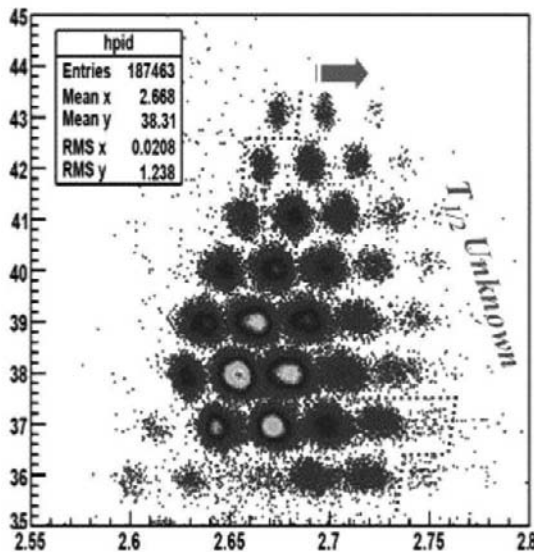


Fig. 7. – Two-dimensional plot for the neutron-rich products from Kr to Tc for lifetime measurements. The region where the lifetime is not known is indicated.

Recently, a new experiment was performed to strengthen the identification of the α -decay chains originating from the nucleus $^{278}\text{113}$. Plenty of α -decays from its grand-grand daughter, ^{266}Bh created by the $^{248}\text{Cm}(^{23}\text{Na}, 5\text{n})$ reaction, were observed and connection of the element 113 and known nuclei has been confirmed [12]. Figure 8 shows the alpha-decay chain from $^{278}\text{113}$ to ^{258}Lr through ^{266}Bh .

4. – Fate of magic numbers

4.1. Disappearance of the $N = 20$ magic number. – Disappearance of magic numbers is a subject of interest for unstable nuclei. The first Coulomb excitation experiment with fast RI beams has been performed at the old facility of RIKEN for the neutron-rich ^{32}Mg nucleus with the $N = 20$ magic number [13]. The extracted large $B(\text{E}2)$ value in contrast to heavier $N = 20$ nuclei (see fig. 9) indicates that the $N = 20$ shell closure disappears in ^{32}Mg . This phenomenon called “island of inversion”, which has been suggested much earlier by β -decay studies [14], was clearly confirmed by this experiment.

This experiment was the first application of a new method for studying properties of unstable nuclei. That is the measurement of γ -rays from fast-moving excited nuclei in coincidence with reaction products with particle identification. For such measurements, the detector array DALI was developed. As schematically shown in fig. 10, the emission angle of de-excitation γ -ray was determined by the scintillator location, and the Doppler shift was corrected to obtain the transition energy event-by-event. By identifying the reaction product as ^{32}Mg or specifying the reaction channel as inelastic scattering with

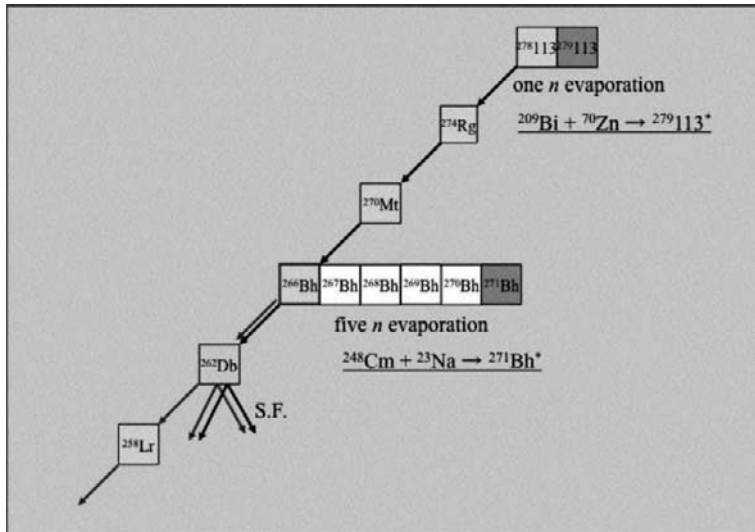


Fig. 8. – Alpha-decay chains of the super-heavy nucleus $^{278}113$. Decay chains from ^{266}Bh were newly measured to confirm the identification of $^{278}113$.

the ^{208}Pb target, yield for the Coulomb excitation for the $0^+ \rightarrow 2^+$ transition can be extracted. Since then, many experiments using this technique have been performed for nuclear spectroscopy of nuclei far from the stability valley. Similar phenomena, disappearance of magic numbers, have been studied around $N = 8$ and $N = 20$.

Recently DALI2 [15] (see fig. 11), new and improved version of DALI, has been built. Its high granularity and larger total volume of NaI(Tl) were designed for the RIBF new facility, where the secondary beam energy is higher (200–300 MeV/nucleon). The DALI2 array was already used in many RIPS experiments.

A recent highlight in the “old” facility is the proton inelastic scattering to study excited states other than 2^+ discussed above in ^{32}Mg [16]. A number of γ lines were observed in coincidence with ^{32}Mg nuclei scattered off by a liquid-hydrogen target. Thanks to the high beam-target luminosity by the reasonable intensity of ^{32}Mg beam (450s^{-1}) and the use of liquid-hydrogen as the target material, the high detection efficiency of DALI2, and a very large collection efficiency for ^{32}Mg detection due to the forward focusing in the reversed kinematics and the use of the newly built TOF spectrometer TOMBEE, γ - γ coincidence measurements could be made and several new levels were identified.

Another important result is for the second excited state. By analyzing the inelastic angular distribution with the help of distorted-wave calculation, this state at 2321 keV is identified as 4^+ as shown in fig. 12. The resultant 4^+ to 2^+ energy-ratio ($R_{2/4}$) of 2.6 indicates a transitional character of ^{32}Mg from spherical ($R_{2/4} = 2$) to well-deformed ($R_{2/4} = 3.33$) shapes. It should be noted that the ratio of 3.1 [17] for ^{34}Mg with two more neutrons is close to the rotational limit of 3.33.

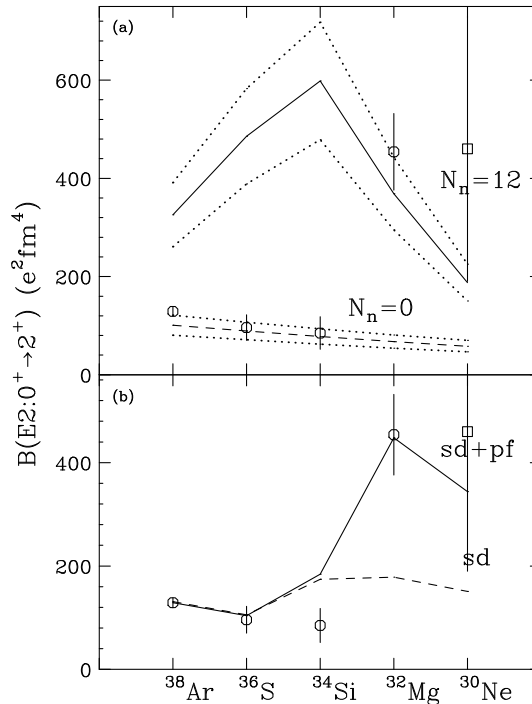


Fig. 9. – Reduced transition probability $B(E2)$ of $N = 20$ even-even nuclei.

In the $^{32}\text{Ne} + ^{12}\text{C}$ experiment [7] mentioned before, the DALI2 setup was also used. The secondary carbon target was set at the focus “F8” (see fig. 3), and forward-going reaction products were identified by the ZeroDegree spectrometer to specify the reaction channel as schematically shown in fig. 4. The DALI2 setup surrounded the target to measure γ -rays from the reaction products. The intensity of ^{32}Ne was about 5 cps, which was enough to find the $2^+ - 0^+$ γ peak in the seven hours run. This demonstrates

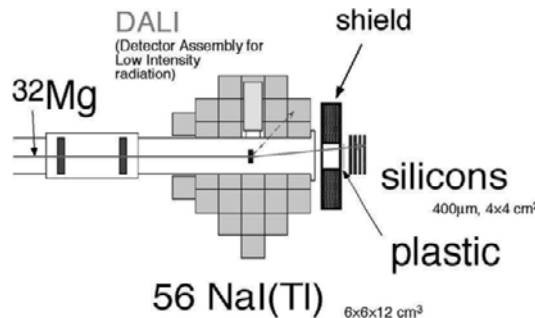


Fig. 10. – Setup with DALI for the ^{32}Mg Coulomb-excitation experiment at RIKEN.

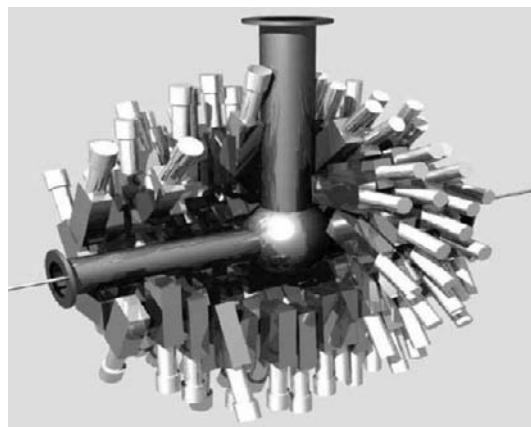


Fig. 11. – NaI(Tl) array DALI2.

the potential of RIBF together with efficient methods of experiment. The γ energy of 772(9) keV corresponds to the location of the 2^+ state, and clearly indicates that the nucleus ^{32}Ne is in the “island of inversion” found at around $N = 20$.

5. – Neutron-proton asymmetry: “egg” structure in ^{16}C

Recently, decoupling of protons and neutrons has been revealed in excitation of the ^{16}C nucleus to its 2^+ state by measuring the 2^+ lifetime [18,19], inelastic scattering with ^1H [20], and the one with ^{208}Pb [21]. Analysis of the interference between the nuclear and Coulomb excitation amplitudes in the angular distribution for the $^{16}\text{C} + ^{208}\text{Pb}$ inelastic

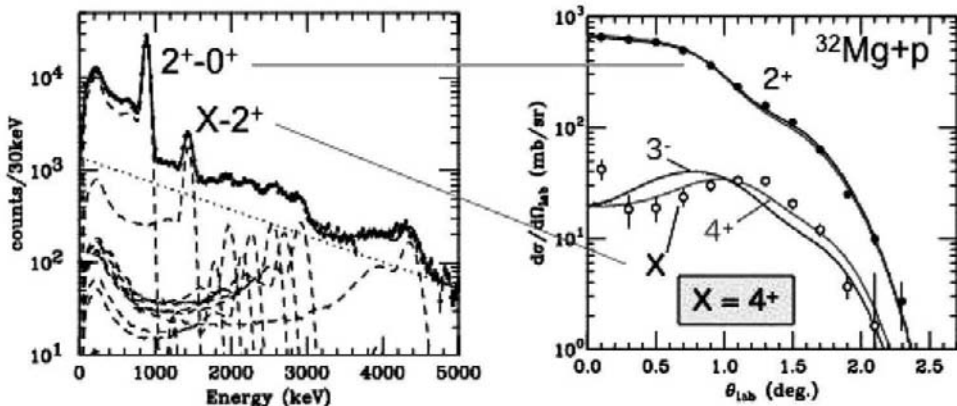


Fig. 12. – Energy spectrum of γ -rays associated with the proton inelastic scattering on ^{32}Mg (left) and angular distributions for excitation to the first excited 2^+ state and second state “X” at $E_x = 2321$ keV (right).

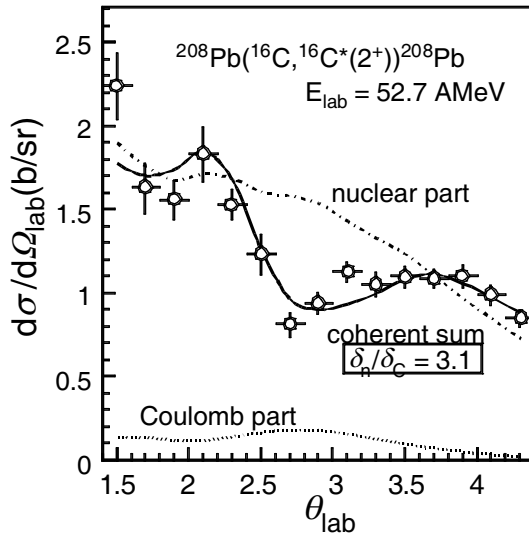


Fig. 13. – Angular distribution of the ${}^{16}\text{C} + \text{Pb}$ inelastic scattering feeding the first 2^+ state in ${}^{16}\text{C}$.

scattering (see fig. 13) could separate the proton and neutron contributions to the 2^+ state excitation. The separation is also possible by comparing the lifetime and proton inelastic data. Both the results indicate that neutrons strongly contribute to the 2^+ state excitation, while protons have little contribution.

The nuclear reactions used in these studies involve no mass transfer and match the fast RI beam, since their good kinematical matching persist even in the relevant energy range.

This decoupling picture might be related to the low electric quadrupole moments measured for ${}^{15}\text{B}$ and ${}^{17}\text{B}$ using the β -NMR technique [22].

6. – Challenges at RIBF

Various experimental programs at RIBF have been planned, and some new experimental installations are under construction or planned. Their locations are indicated in fig. 14.

6.1. SHARAQ. – The SHARAQ spectrometer [23] is of a QQ-D-Q-D configuration as shown in fig. 15, designed for high-resolution missing-mass measurements. By employing dispersion-matching optics with a specially designed beam line from the BigRIPS, the momentum resolution of 15000 will be achieved. Its construction was completed in 2008, and the first experiment, the charge-exchange ($t, {}^3\text{He}$) reaction, has been performed.

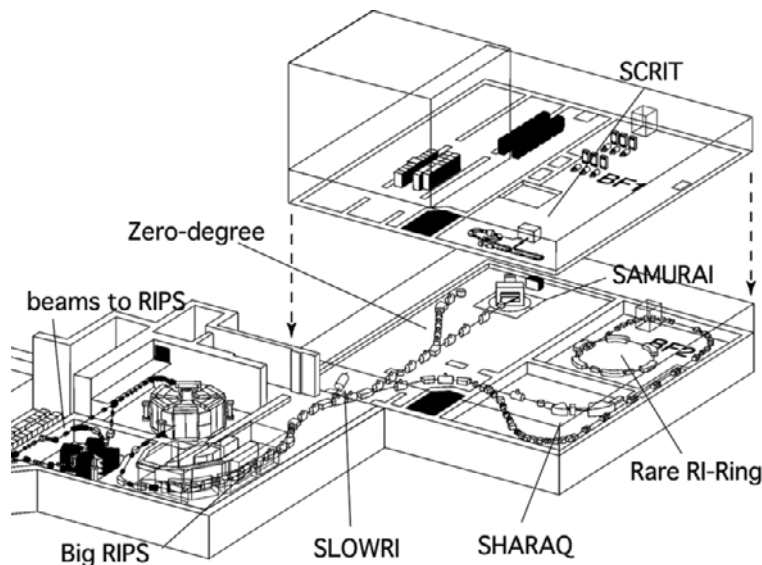


Fig. 14. – New equipment planned or being constructed at RIBF.

6.2. SAMURAI. – SAMURAI (see fig. 16) is a spectrometer with a large solid angle and a large momentum acceptance dedicated to particle-correlation studies. Its dipole magnet is a superconducting one with 6.7 Tm rigidity. The large gap of 80 cm is useful for measurements of projectile-rapidity neutrons. Its construction has been started, and the commissioning is foreseen in early 2012.

It is suitable for particle-correlation studies with high efficiency, and hence is useful, for example, for Coulomb dissociation experiments either for (p, γ) or (n, γ) processes.

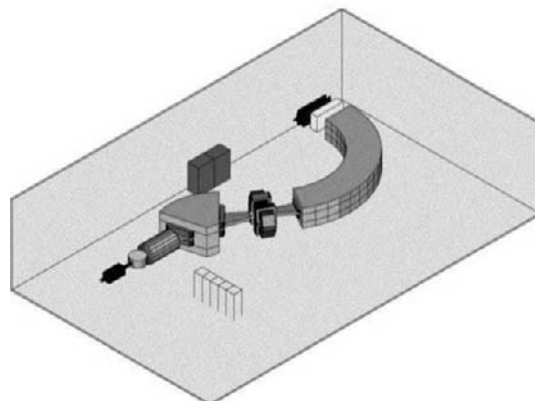


Fig. 15. – Schematic view of SHARAQ.

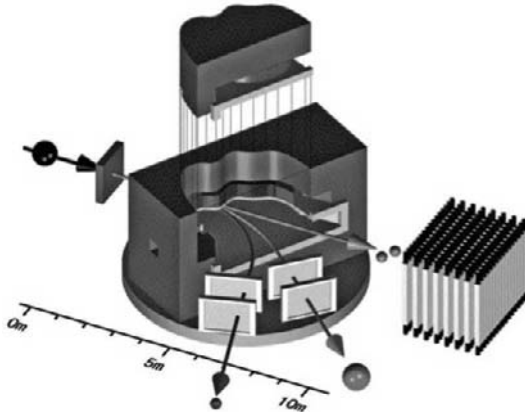


Fig. 16. – SAMURAI, superconducting spectrometer with a large solid angle and momentum acceptance, being built at RIKEN RIBF.

Several key processes for explosive hydrogen burning and explosive neutron captures including the r -process will be studied. Other applications are search and spectroscopy for halo nuclei, nucleon knockout reactions, multi-fragmentation for investigating asymmetric nuclear matter, and so on.

6.3. SCRIT. – In SCRIT (Self-Confining Radioactive Ion Target) [24], RI ions are transversely confined by the attractive force caused by the electron beam itself as shown in fig. 17. A mirror potential is applied externally to achieve longitudinal confinement. This confinement mechanism has been successfully confirmed at an existing electron ring [25], and electron scattering with trapped cesium ions was observed [26]. The entire equipment at RIKEN will consist of a 1 kW–150 MeV microtron and an electron storage ring accepting 300–700 MeV electron with intensity of 300 mA. The microtron serves as the injector to the ring and also the source of photon for fission. Construction with a SCRIT setup and a photo-fission ion source started in 2008, and first e-RI scattering experiments will be conducted by 2012.

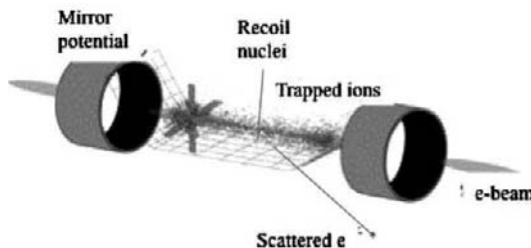


Fig. 17. – Schematic view of the Self-Confining Radioactive Ion Target (SCRIT).

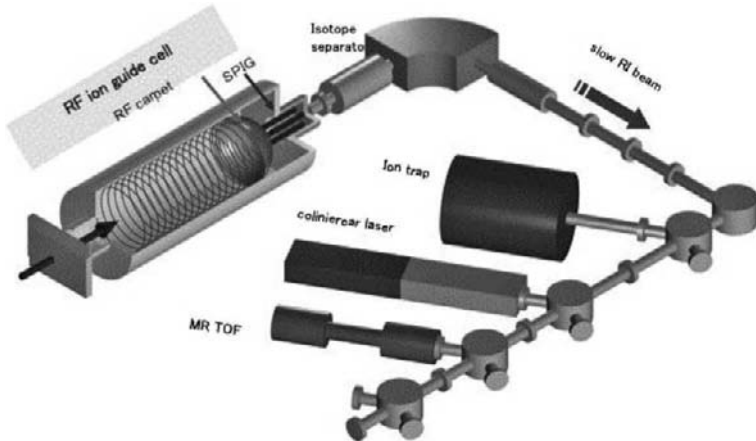


Fig. 18. – SLOWRI and various setups using slow RI beams.

6.4. SLOWRI. – The SLOWRI [27] aims at conducting various experiments using slow RI beams. Fast secondary beams from the Big RIPS will be efficiently stopped and extracted by a gas-catcher system with the RF ion-guide technique. The extracted slow beams are delivered to various setups as shown in fig. 18.

6.5. Rare RI-ring. – The rare RI mass ring [28] is to measure the mass of rarely produced (1 particle per day, for example) exotic nuclides in 10^{-6} accuracy. Each ion is injected individually to the ring by a trigger signal provided from a counter in the Big RIPS. The ring is tuned to achieve the isochronous condition, and a time-of-flight of the ion in the ring is measured (see fig. 19).

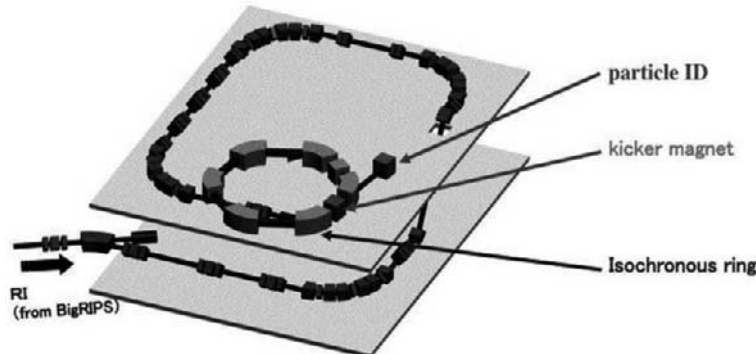


Fig. 19. – Ring for rarely produced ions.

7. – Conclusions

The RIKEN RI Beam Factory (RIBF), one of the new-generation facilities for beams of unstable nuclei, has started its operation. RI-beams are produced by the RIBF accelerator complex with three newly-built cyclotrons coupled with the superconducting RI beam separator Big RIPS. Their potential was already demonstrated by production of 47 new isotope by a ^{238}U primary beam with intensity more than three orders of magnitude weaker than the goal, 1 p μA . A few experiments of secondary reaction have been made since December 2008 with intense ^{48}Ca beams. New results on the halo structure and the islands of inversion have been obtained with neutron-rich RI beams with the intensities that could not be realized before. To fully exploit the capability of RIBF, further developments on new ideas are desirable. More inputs from the worldwide community is encouraged.

When the RIBF reaches its full performance, almost all nuclides along the r -process nuclear synthesis can be created and experimentally studied. Continuous attempts to improve the primary beam intensity together with construction of various experimental equipment will open a new domain of nuclear physics, and will create a new view on atomic nucleus as well as on the element genesis in the Universe, together with the world efforts for realizing RI-beam facilities being constructed or planned.

REFERENCES

- [1] KUBO T. *et al.*, *Nucl. Instrum. Methods B*, **70** (1992) 309.
- [2] YANO Y., *Nucl. Instrum. Methods B*, **261** (2007) 1009.
- [3] KUBO T. *et al.*, *IEEE Trans. Appl. Supercond.*, **17** (2007) 1069.
- [4] SUEMMERER K. and BLANK B., *Phys. Rev. C*, **61** (2000) 034607.
- [5] OHNISHI T. *et al.*, *J. Phys. Soc. Jpn.*, **77** (2008) 083201.
- [6] OHNISHI T. *et al.*, *J. Phys. Soc. Jpn.*, **79** (2010) 073201.
- [7] DOORNEBAL P. *et al.*, *Phys. Rev. Lett.*, **103** (2009) 032501.
- [8] NAKAMURA T. *et al.*, *Phys. Rev. Lett.*, **103** (2009) 262501.
- [9] TAKEUCHI M. *et al.*, *International Conference Nucleus Nucleus Collision*, August 16-21, 2009, Beijing, China, edited by H. ZHANG, S. ZHU, S. ZHAO, W. LIU, D. YUAN, Y. WNAG, *Nucl. Phys. A*, **834** (2010) 412c.
- [10] See <http://www.rarf.riken.jp/Eng/index.html>.
- [11] MORITA K. *et al.*, *J. Phys. Soc. Jpn.*, **73** (2004) 2593.
- [12] MORITA K. *et al.*, *J. Phys. Soc. Jpn.*, **78** (2009) 064201.
- [13] MOTOBAYASHI T. *et al.*, *Phys. Lett. B*, **346** (1995) 9.
- [14] DÉTRAZ C. *et al.*, *Phys. Rev. C*, **19** (1979) 164; GUILLEMAUD-MUELLER D. *et al.*, *Nucl. Phys. A*, **426** (1984) 37.
- [15] TAKEUCHI S. *et al.*, *RIKEN Accel. Prog. Rep.*, **36** (2003) 148.
- [16] TAKEUCHI S. *et al.*, *Phys. Rev. C*, **79** (2009) 054319.
- [17] YONEDA K. *et al.*, *Phys. Lett. B*, **499** (2001) 233.
- [18] IMAI N. *et al.*, *Phys. Rev. Lett.*, **92** (2004) 062501.
- [19] ONG H. J. *et al.*, *Phys. Rev. C*, **78** (2008) 014308.
- [20] ONG H. J. *et al.*, *Phys. Rev. C*, **73** (2006) 024610.
- [21] ELEKES Z. *et al.*, *Phys. Lett. B*, **686** (2004) 34.

- [22] UENO H. *et al.*, *Nucl. Phys. A*, **738** (2004) 211.
- [23] UESAKA T. *et al.*, *CNS Annual Report 2004* (2005) p. 42.
- [24] M. WAKASUGI *et al.*, *Nucl. Instrum. Methods A*, **532** (2004) 216.
- [25] WAKASUGI M. *et al.*, *Phys. Rev. Lett.*, **100** (2008) 164801.
- [26] SUDA T. *et al.*, *Phys. Rev. Lett.*, **102** (2009) 102501.
- [27] WADA M. *et al.*, *Nucl. Instrum. Methods A*, **532** (2004) 40.
- [28] YAMAGUCHI Y. *et al.*, *CNS Annual Report 2004* (2005) p. 83.

ISOL techniques to reach radioactive nuclei: From birth to EURISOL

P. A. BUTLER

Oliver Lodge Laboratory, University of Liverpool - Liverpool L69 7ZE, UK

Summary. — These lectures describe the key elements of ISOL technology and the production of accelerated radioactive ions beams (RIB). A brief history of the ISOL technique is given and current ISOL RIB facilities are described. New developments in ion guide and gas catcher technology are also presented. The second-generation ISOL facilities in Europe and the ultimate EURISOL facility are also described.

1. – Introduction

There are two types of radioactive ion beam (RIB) facilities: these are the ISOL and in-flight (or fragmentation) facilities. In the ISOL case, a beam of particles, which can be protons, neutrons, light ions or heavy ions from a so-called driver accelerator, impinges on a thick target in which the radioactive nuclei are produced at rest. They then diffuse out of the target and effuse into an ion source, where they are ionised, which allows them to be extracted and accelerated. These ions can then either be transported at very low energy towards an experimental area or be post-accelerated in order to induce nuclear reactions. In an in-flight facility, a high-energy primary beam is fragmented on a thin target, and the resulting fast radioactive nuclei are selected by a fragment-separator and transported to the experimental area. No post-acceleration is necessary. The main

advantages of an ISOL facility are very high secondary-beam intensities for many species (so long as their lifetime is not too short compared to the diffusion/effusion time) and beam qualities (resolution, purity and emittance), which are comparable with those of stable beams. Thus, they are well adapted to highly elaborate experimental approaches. The fragmentation technique is most interesting a) for very short-lived nuclei in the vicinity of the drip-lines and/or b) for RIB production at very high energies, for which the construction of a post-accelerator would become prohibitively costly. The emittance of beams produced in-flight is poor, but storing and cooling techniques can be applied which allow for highly efficient and highly sensitive experiments, at the expense once again of the intensities of very short-lived species. The two techniques are thus very complementary.

In these lectures I will present different ISOL technologies and how various facilities world-wide adopt these technologies in order to produce beams of accelerated radioactive ion beams.

2. – History of ISOL

At the beginning of the sixties European nuclear physicists and nuclear chemists started discussions about the feasibility of a general-purpose on-line project for the production of short-lived nuclei. An important driving force behind these discussions was a pilot experiment performed in 1951 at the Institute for Theoretical Physics at the University of Copenhagen (today The Niels Bohr Institute). In this experiment, an isotope separator was linked directly to the Copenhagen cyclotron. The great success of the Copenhagen experiments was that the production method was shown to work and a number of formerly unknown isotopes of the elements krypton and xenon were identified. When the European nuclear physics community discussed the best possible location for an on-line activity an obvious choice was the 600 MeV proton synchrocyclotron (SC) at CERN; the SC had at that time an in-house Nuclear Chemistry Group with an isotope separator built in 1961. Tests at the SC were performed and it was found that the production capacity of radioactive isotopes in an external beam was very high. This gave a firm basis for launching a dedicated project for the production of short-lived isotopes based on the on-line technique at CERN. The Director General, V. F. Weisskopf, approved the project and invited the groups to submit proposals for experiments at the end of 1964. The present ISOLDE facility employs 1.4 GeV protons from the Proton Synchrotron Booster at CERN. For further details see [1]. It should also be mentioned that pioneering work was also carried out using 24 GeV protons from the CERN Proton Synchrotron in the 1970's, see [2].

3. – Targets and ion sources

The heart of an on-line isotope separator is its target and ion source. The target should assure a fast liberation of the radioactive nuclei produced in a bulky target. The combination with the ion-source should be able to produce an ion beam which

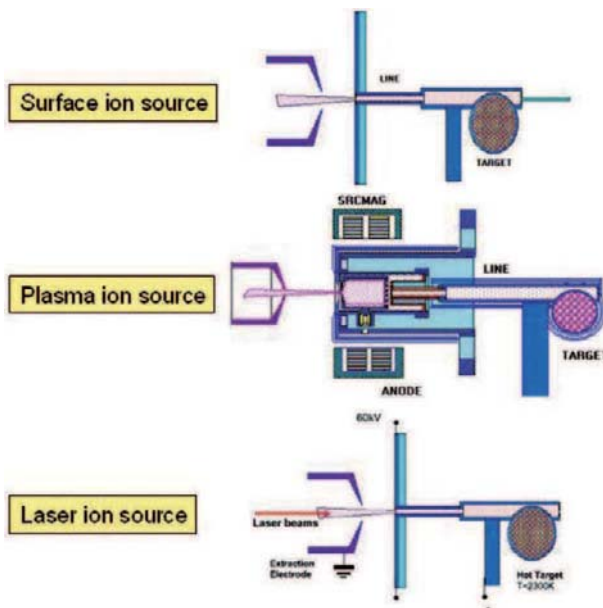


Fig. 1. – Schematic of the three types of ion sources that are commonly used at ISOL facilities.

preferably should only contain isotopes from one chemical element. The development of this experimental technique is a field of radiochemistry, which also involves metallurgy, high temperature chemistry and surface physics. ISOLDE has the most experience in this field, and has developed many different advanced target-ion-source combinations, which have allowed the users of the facility to study radioisotopes from more than 60 different elements.

Some of the targets used at ISOLDE consist of molten metals kept at temperatures from 700 °C and up to about 1400 °C. Such targets are characterized by a relatively long release time of the produced isotopes and a typical time constant of the release is about 30 seconds. Faster release times, in the order of one second or less, can be obtained, if target material in the form of refractory metal powder, metals or carbides is used at temperatures above 2000 °C. An expected decrease in the release time due to the “shock-wave” effect of the pulsed proton beam has been observed. Time constants down to some tenths of a second can be reached for the fastest targets.

There are three different types of ion sources commonly used, as shown in fig. 1 (see [3-6]):

Surface ion source. – The surface ion source is the simplest set-up for ionizing atoms produced in the target. The ionizer consists only of a metal tube (“line”), for example tantalum or tungsten, which has a higher work function than the atom that should be ionized. Depending on the line’s material it can be heated up to 2400 °C. Surface ion sources have been used in combination with most of the different target materials.

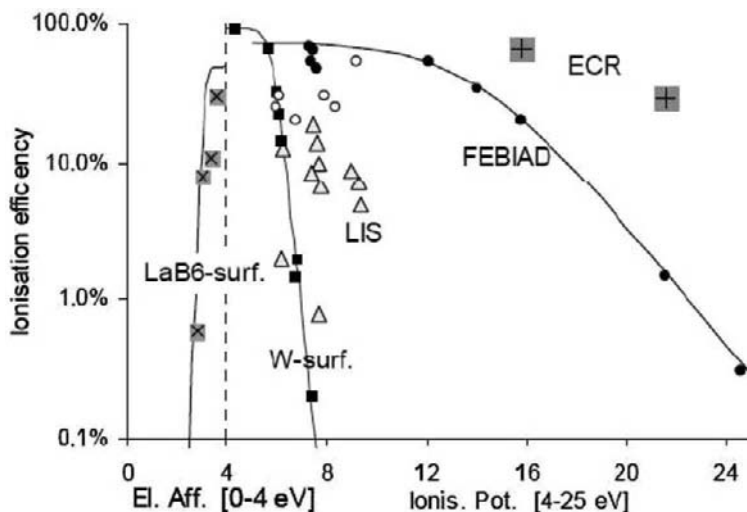


Fig. 2. – 1+ Ionization efficiencies measured with surface (black squares), plasma-FEBIAD (circles), laser (triangles) and ECR ion sources. Taken from ref. [7].

Plasma ion source. – The plasma ion source is used to ionize elements that cannot be surface-ionized (see fig. 2). The plasma is produced by a gas mixture (typical Ar and Xe) that is ionized by electrons being accelerated between the transfer line and the extraction electrode by supplying an anode voltage of about 100 V. For the optimization of this process an additional magnetic field is used. Plasma ion sources have been used in combination with most target materials.

For the production of noble gas isotopes the set-up has been modified in the way that the transfer line between target and gas plasma is cooled by a continuous water flow to suppress the transport of less volatile elements and reduce via this mechanism the isobaric contamination in the ISOLDE ion beams.

Laser ion source. – One of the main problems of ion sources used at on-line mass separators for radioactive beam production is to obtain chemically pure ion beams of the various elements. As a result of the thermal character of surface ionization or ionization in a gas-discharge plasma the ionization is in many cases non-selective with respect to the different chemical elements. Hence, the separated ion beams are contaminated by isobars, which significantly complicates, and in a number of cases renders impossible, the study of the nuclear properties of radioactive isotopes. The process of resonance laser ionization of atoms is of non-thermal nature. The atoms are ionized whenever the laser radiation frequencies coincide with the atomic transition frequencies. Since the atom of each element has its own specific energy level structure the ionization process has an exceptionally high chemical selectivity. It should be remarked that the efficiency of photo-ionization is also high so that the ion yield may reach tens of percent. This is also true for elements with a high ionization potential. When it is used as an ion source for

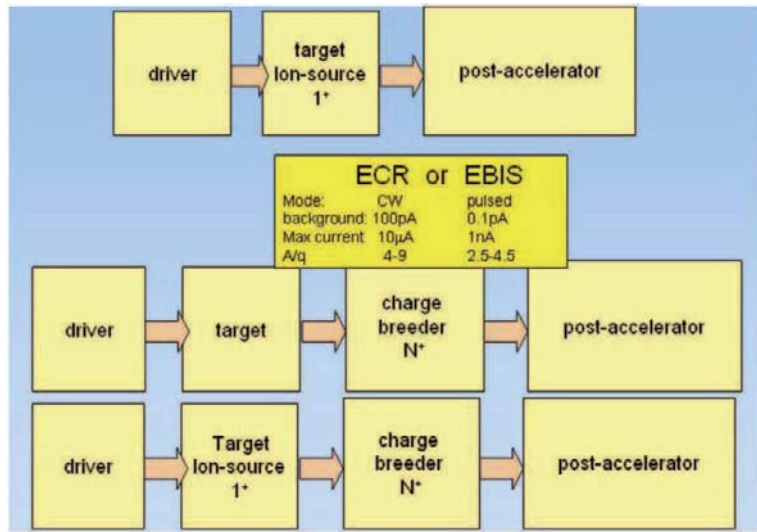


Fig. 3. – Methods by which radioactive ion beams are prepared for postacceleration. A comparison of the relative merits of the ECR and EBIS charge-breeder ion sources is also given.

a mass separator, it is necessary to substantially increase the overall ionization efficiency. For this purpose the method of resonance laser ionization of atoms in a hot cavity was developed. For further details see [8].

4. – Accelerated radioactive beam facilities

I present here a selection of facilities that have successfully produced accelerated radioactive beams. They use different methods to inject the radionuclides into the post-accelerator, *e.g.*, direct injection of singly charged ions followed by stripping in the accelerator, effusion of the radionuclides into a charge breeder prior to injection into the accelerator, or injection of singly charged ions into a charge breeder followed by post-acceleration. A summary of the different methods is given in fig. 3. The last technique is known as the 1^+ to N^+ scheme, and is employed almost universally by the next-generation facilities. The charge-breeder is usually ECR-type, or EBIS-type; for a comparison of these see [9].

Louvain-la-Neuve. – The Radioactive Ion Beam Project at Louvain-la-Neuve [10] started in 1987 as a collaboration between three Belgian universities. The project aimed at the production of an intense, energetic radioactive ion beam by coupling the two cyclotrons of Louvain-la-Neuve. In 1989 the first ^{13}N beam was accelerated. Since then the project has produced a variety of beams for numerous scientific experiments. At Louvain-la-Neuve the first cyclotron, CYCLONE 30, which is a 30 MeV proton accelerator, is used to produce the desired unstable element in suitable targets. Beam intensity up to 300 μA

(depending on target and desired charge state) is used to irradiate the production target. This resulting activity diffuses out of the hot target and is fed into the 6.4 GHz ECR ion source for ionization. The ion source is designed to produce low charge states but with a high efficiency. After a first magnetic separation in a low mass resolution dipole, the ions are injected in the second cyclotron, CYCLONE 110, for subsequent acceleration up to the desired energy. To remove any isobaric contamination from the beam, the cyclotron is tuned as a radiofrequency mass spectrometer. This is done by reducing the acceleration voltage in order to increase the number of turns in the machine. This allows the separation of beams with relative mass difference of $2 \cdot 10^{-4}$ (*e.g.*, ^{19}Ne and ^{19}F). This method results in an isobaric suppression factor of 10^{-6} while maintaining a transmission through the cyclotron (acceleration and separation) of 3 to 5%.

Holifield Radioactive Ion Beam Facility. – The HRIBF facility [11] at Oak Ridge uses two accelerators, the Oak Ridge Isochronous Cyclotron (ORIC) and the 25 URC Tandem Electrostatic Accelerator. ORIC is a high-intensity, light-ion accelerator which is used to produce radioactive ions in the target-ion source which is located on the RIB-injector platform. The ions diffuse out of the target and are ionized and extracted from the ion source. The beam of ions is mass analyzed and if needed, passed through a charge exchange cell to produce a 200 keV beam of negative ions. This beam is transmitted through a high-resolution isobar separator and injected into the tandem for acceleration and delivery to the experiment. The high-voltage tandem accelerator, located inside a 100-ft-high, 33-ft-diameter pressure vessel, has been built in a folded configuration with both low- and high-energy acceleration tubes contained within the same column structure. Reversal of ion direction in the high-voltage terminal is provided by a 180 deg magnet which also serves to prevent ions of unwanted charge state from being introduced into the high-energy acceleration tube. The insulating gas used for the tandem is pure SF₆.

SPIRAL. – The SPIRAL project [12] at GANIL was funded in December 1993. The primary light or heavy-ion beam accelerated by the GANIL cyclotrons bombard a production target (graphite), kept at high temperature (2300 K). The RIB produced by nuclear reactions are released from the target and pass through a transfer tube into a permanent magnet ECRIS. The radioactive atoms are then ionised up to charge states $q/m = 0.09$ to 0.40. After extraction from the ECRIS, the low-energy RIB are selected by a relatively low-resolution separator, and injected into the $K = 265$ compact cyclotron CIME. The corresponding energy range varies from 1.7 A MeV to 25 A MeV . After acceleration, the RIB is selected in magnetic rigidity by the modified alpha-shaped spectrometer and directed to the existing experimental areas. The separation between isobars is performed for the most part by the cyclotron, which is a good spectrometer for fast ions, with a resolution of $\Delta m/m$ of $5 \cdot 10^{-4}$.

REX-ISOLDE. – REX [13] makes use of the large variety of radionuclides that have been extracted from the on-line mass separator ISOLDE. In order to use these beams, significant developments in beam cooling and charge breeding were required, as whereas

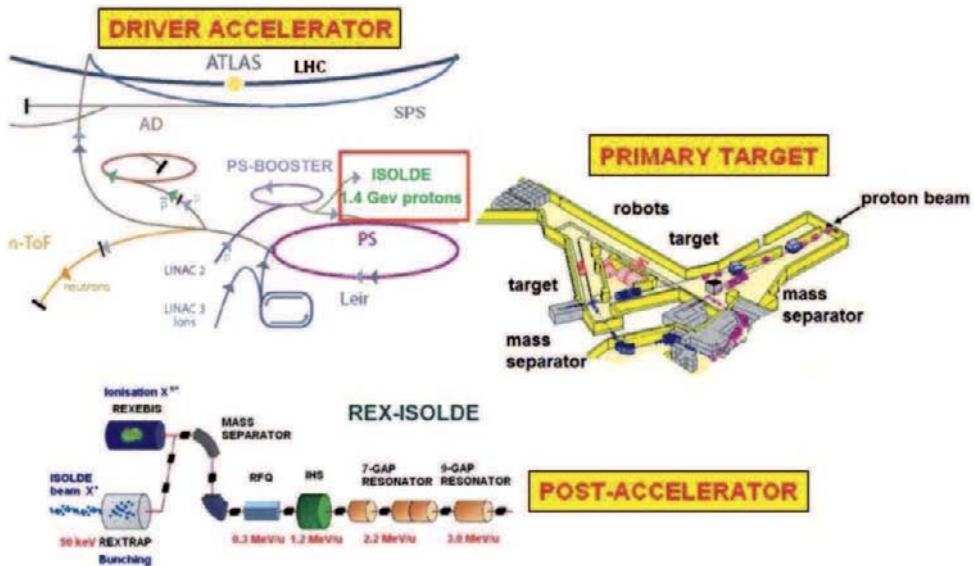


Fig. 4. – Layout of ISOLDE and REX-ISOLDE facility.

the output of the ISOLDE primary mass separator is a quasi-DC beam (the intensity varies between the 1.2 s primary proton pulses according to the release characteristics and the nuclide half-life) having charge state 1^+ , the low duty-factor post accelerator requires multiply charged ($A/q < 4.5$) pulsed beams. A schematic layout of the ISOLDE and REX-ISOLDE facility is shown in fig. 4.

The first stage of the preparation of the ISOLDE beam is to continuously inject the beam from the mass separator into REXTRAP [14] where it is cooled, accumulated and extracted as bunches. The accumulation and cooling is achieved by collisions with a buffer gas. In the collisions the loss of energy of the ion enables it to be trapped within a potential barrier. The barrier is reduced every 20 ms so that the accumulated ions are ejected as a 20 μ s pulse. The transverse emittance of the beam is also reduced by the cooling procedure. This is important because the next stage, REXEBIS (REX Electron Beam Ion Source) [15], has a small acceptance (3 mm mrad). REXEBIS employs a 500 mA 5 keV electron beam that is focussed to a high current density (250 A/cm^2) by a 2 T axial magnetic field. The ion beam is confined longitudinally by applied electric potentials and undergoes stepwise ionization via electron collisions until its mean charge state has the desired value. For $A < 50$ the breeding time in REXTRAP to reach $A/q = 3-4$ is around 20 ms. For ^{133}Cs ions the breeding time was 80 ms.

The yield of the radioactive isotopes from ISOLDE can be several orders of magnitude lower than the amount of residual gas ions from C, N, O and Ar coming out of the EBIS. Therefore, a mass separator is employed with a q/A -resolution of about 1/150 which is sufficient to select the highly charged rare radioactive ions from rest-gas contaminants.

In the first stage of the REX-ISOLDE linac the ions are accelerated from $5 \text{ keV}/u$ to $300 \text{ keV}/u$ by a 4-rod RFQ. In order to match the beam from the RFQ into the acceptance of the IH (Interdigital-H-type)-structure, a section consisting of two magnetic quadrupole triplet lenses and a rebuncher is required. A feature of the REX-ISOLDE-IH resonator is the possibility to vary the final energy between $0.8A$ and $1.2A$ MeV.

The next section ($0.8A$ – $2.2A$ MeV) of the linac consists of three 7-gap resonators. These spiral resonators are designed and optimised for synchronous velocities of $\beta = 5.4\%$, 6.0% and 6.6% . Each resonator has a single resonance structure, which consists of a copper half shell and three arms attached to both sides of the shell. All linac structures are operated at 101.28 MHz. Finally, an additional 9-gap IH structure, operating at a frequency of 202.56 MHz provides ions accelerated to $3.1A$ MeV.

ISAC. – In the ISAC-I facility [16] at TRIUMF, Vancouver, 500 MeV protons at up to $100 \mu\text{A}$ can be steered onto one of two production targets to produce radioactive isotopes. The isotopes pass through a heated tube to a source where they are ionized, accelerated off the source's high-voltage platform at up to 60 kV and sent through a mass separator to select the ion beam of choice. The beam is transported in the low-energy beam transport (LEBT) electrostatic beam line and sent via a switchyard to either the low-energy experimental area or to a series of room-temperature accelerating structures to the ISAC-I medium-energy experimental area. In ISAC-1, a 35 MHz CW RFQ accelerates isotopes with $q/A > 1/30$ from $2 \text{ keV}/u$ to $150 \text{ keV}/u$. Following the RFQ the beam is passed through a stripper and magnetic bend to select a charge state with $q/A = 1/6$ prior to rebunching and injection into a CW drift tube linac (DTL) operating at 105 MHz. The output beam, with energy continuously variable from 0.15 to $1.5A$ MeV, is transported to one of a number of experimental stations. For high-energy delivery, the drift tube linac (DTL) beam is deflected north along an S-bend transfer line to the ISAC-II superconducting linear accelerator (SC-linac) for acceleration above the Coulomb barrier (5 – $11A$ MeV).

Other ISOL RIB facilities. – There are many facilities world-wide that now produce a limited range of radioactive isotopes by post-acceleration following ISOL production. For example, the EXCYT facility [17] at the INFN-LNS laboratory, Catania, is based on a K-800 Superconducting Cyclotron, as a driver for stable heavy ion beams (up to $80A$ MeV, $1 \mu\text{A}$) onto a graphite direct target, and on a 15 MV Tandem for post-accelerating the radioactive ion beams. Proton-rich light ion beams like $^{8,9}\text{Li}$ and ^{21}Na are reaccelerated with intensities in the order of 10^4 – 10^5 pps. At the joint KEK-JAEA funded TRIAC facility [18], Tokai, Japan, radioactive nuclei have been produced through nuclear reactions with thick targets by impinging a 36 MeV $3 \mu\text{A}$ proton beam provided by a Tandem accelerator. The radioactive nuclei were extracted as singly positively charged ions, injected into an ECR-ion source for charge breeding, and accelerated in a linac to energies up to $1.1A$ MeV linacs (and eventually to $5A$ – $8A$ MeV).

A comparison of the range of radionuclides already provided to users by a selection of ISOL RIB facilities is given in fig. 5.

FACILITY	DRIVER	POWER	USER BEAMS ACCELERATED	MAX ENERGY
HRIBF Oak Ridge (USA) 1997	50-100 MeV p, d, α (-ve ion source)	1.5 kW	^{7-10}Be , $^{17-18}\text{F}$, ^{26}Al , $^{76-79}\text{Cu}$, $^{67,83-85}\text{Ga}$, $^{78,80,82-86}\text{Ge}$, ^{69}As , $^{83,84}\text{Se}$, ^{92}Sr , $^{117,118,120,122,124,126}\text{Ag}$, $^{126,128,130-136}\text{Sn}$, ^{129}Sb , $^{129,132,134,136}\text{Te}$ (44)	5-15 MeV/u tandem
ISAC TRIUMF (CANADA) 2000	500 MeV protons	50 kW	$^{6,9,11}\text{Li}$, $^{10,11}\text{Be}$, ^{18}F , $^{20,21,25,29}\text{Na}$, ^{23}Mg , ^{26}Al (12)	14 MeV/u linac
SPIRAL GANIL (FRANCE) 2001	100 MeV/u heavy ions	6 kW	$^{6,8}\text{He}$, $^{14,16,19-22}\text{O}$, ^{18}F , $^{17-19,23-26}\text{Ne}$, $^{33-35,44,46}\text{Ar}$, $^{74-77}\text{Kr}$ (25)	10-25 MeV/u cyclotron
REX ISOLDE (CERN) 2001	1.4 GeV protons	3 kW	$^{8,9,11}\text{Li}$, $^{10-12}\text{Be}$, ^{10}C , ^{17}F , $^{24-30}\text{Na}$, $^{28-32}\text{Mg}$, $^{61-63}\text{Mn}$, $^{61,62}\text{Fe}$, $^{66,68}\text{Ni}$, $^{67-71,73}\text{Cu}$, $^{74,76,78,80}\text{Zn}$, ^{70}Se , $^{88,92,94,96}\text{Kr}$, ^{96}Sr , ^{108}In , $^{105-110}\text{Sn}$, $^{100,102,104,122,124,126}\text{Cd}$, $^{138,140,142,144}\text{Xe}$, $^{140,142,148}\text{Ba}$, ^{148}Pm , ^{153}Sm , ^{156}Eu , $^{162,164,166,168}\text{Hg}$, ^{200}Po , $^{202,204}\text{Rn}$ (72)	3 MeV/u linac

Fig. 5. – For a selection of facilities, the table gives the range of radionuclides that have been post-accelerated for experiments.

5. – Other ISOL techniques: IGISOL, Gas catchers and FRIB

Usually the use of description “ISOL” refers to production of RIB by bombardment of a thick ($\approx 100 \text{ g/cm}^2$) target, in which the radionuclides have to diffuse through the material before being released for subsequent ionisation. The release efficiency and transport efficiency is therefore very chemistry dependent and half-lives of $< 1 \text{ s}$ cannot easily be extracted. A different approach is to produce the RIB in thin targets in the range 1 mg/cm^2 to 10 g/cm^2 so that the range of the radionuclides is larger than the target thickness. The radioactive atoms are then ionised and collected efficiently, in a manner that is chemistry independent and fast.

Ion guide. – The basic idea of the ion guide [19] is to slow down and thermalize initially energetic recoil ions from nuclear reactions in a gas, which is typically helium, but sometimes argon. Ions are transported by a gas flow out of the gas cell and injected through a differentially pumped electrode system to the high vacuum section of the isotope separator for further acceleration and separation by mass, see fig. 6. Thus, the technique is limited to thin targets with a thickness equal to the maximum range of a recoil ion in the target material, this being of the order of 1 mg/cm^2 for fusion evaporation residues and 15 mg/cm^2 for fission fragments.

When ions slow down in gas their charge state is constantly reset in charge exchange collisions defined by their velocity. The most important mechanisms for losses of ions are diffusion to the walls of the target chamber, the formation of molecular ions with

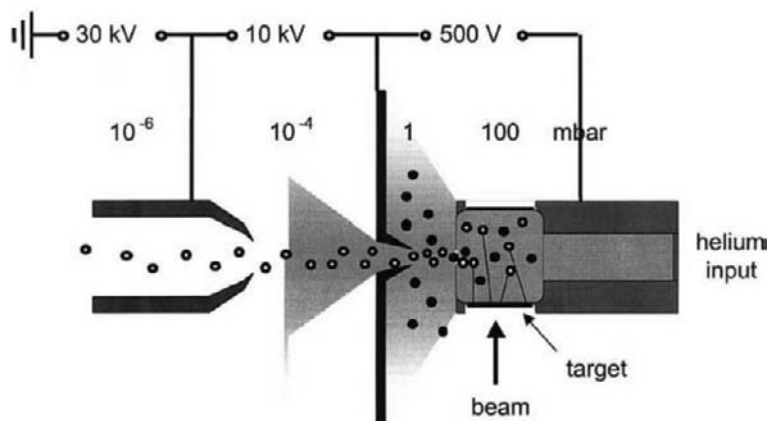


Fig. 6. – The principle of the ion guide. Primary reaction products are thermalized as the ions and are transported in gas flow and electric fields into the accelerating section of the mass separator.

impurities in the gas, as well as three-body recombination. The conditions in which ions are slowed down vary greatly for different reactions, and consequently no unique recipe is available to describe the characteristics of the ion guide.

The first ion guide systems were designed for reaction products from light-ion-induced fusion evaporation reactions. Typical efficiencies of the order of 1 to 10% could be achieved when separating ions that were thermalized in the gas cell. In the course of these studies it was also demonstrated that the technique could be used for submms activities. Recently it was shown with alpha-recoil ions that transport efficiencies above 50% could be easily reached.

Fission fragments emerging from the actinide targets following light-ion bombardment are emitted nearly isotropically in space. This allows separation of fission fragments from the primary beam, and removes all problems due to ionization by the intense primary beam. In the Jyväskylä design the 15 mg/cm^2 uranium target is tilted by 7 deg with respect to the beam direction, making the effective target thickness as high as 120 mg/cm^2 . Employing a 30 MeV proton beam the fission rate in the target is about $3.10^9 \text{ fissions/s}/\mu\text{C}$. A quantitative measurement of the yield for the $A = 112$ fission product ^{112}Rh gives a total efficiency of about 0.02% with a beam intensity of $10 \mu\text{A}$. This corresponds to a yield of the order of 10^5 ions/s . In fact, it has been observed that at higher beam intensities the yield does not scale linearly, but rather with the square root of the beam intensity. The reason for this is not fully understood, but it is obvious that the plasma effect generated by fission fragments themselves passing through the stopping gas volume is responsible for this effect.

An ion cooler can be used to improve the ion beam quality and bunch the beam for laser spectroscopy and for injection into a Penning trap. The Penning trap allows either high mass resolving power purification of the ion beams to be provided for nuclear

spectroscopy experiments, or very precise (down to $1 \text{ keV}/c^2$) mass measurement of the ions. A new development is resonant laser ionisation of atoms in the helium gas jet leaving the ion guide.

Gas catcher. – A new approach to the production of low energy radioactive beams involves the stopping of reaction products of fragmentation, in-flight fission or fusion-evaporation reactions into a gas cell or gas catcher where the reaction products are thermalized in a high-purity noble gas and extracted as singly charged ions for post-acceleration. This removes the limitation present in standard ISOL technique for species that are difficult to extract from the target/ion source assembly.

The Leuven group have developed a gas cell for thermalizing, storing and transporting radioactive ions and atoms. Two-step laser ionization has been used to produce ions of radioactive isotopes inside the cell, and the ions have been extracted using a sextupole ion guide. The performance of this device is described in detail in ref. [20].

The gas catcher approach has been implemented at the Argonne National Laboratory since 1998 to inject fusion evaporation products in an ion trap system [21]. Following a series of improvements since then, efficiencies can be reached for these devices of close to 50% with delay times below 10 ms. The Argonne gas catcher system used for stopping of fusion-evaporation products is filled with ultra-high purity helium gas fed by an all stainless-steel gas system. This catcher delivers the extracted ions into a three-section RFQ gas cooler where the flowing helium gas is pumped away in the first section by clean booster pumps backed by a Roots blower. The gas catcher has DC fields guiding the positive ions towards the extraction region where an RF-focusing cone focuses the ions on the 1.6 mm diameter extraction nozzle. The focusing force is essentially an RF wall which keeps the ions away from the cone. The repulsive force depends on the mobility of the ions in the gas and decreases with higher gas pressure.

At in-flight facilities, the fast ions are slowed down in solid degraders and stopped in a buffer gas in a stopping cell, presently linear in design. They have been successfully used for experiments with rare isotopes but they have beam-rate limitations due to space charge effects [22], and their extraction time will induce decay losses for short-lived isotopes. The overall efficiency of the system at GSI [23] was measured to be 2% and can be divided into a stopping efficiency of 5% and an extraction and transport efficiency of 40%. The overall efficiency is hence limited mostly by the stopping efficiency, which could be increased in the future by operating at higher gas cell pressures. From extraction time measurements of polyatomic ions formed in the gas cell extraction times of atomic ions of 20–50 ms were determined.

FRIB. – In the USA a Facility for Rare Isotope Beams (FRIB) [24] has been funded to provide intense beams of rare isotopes for a wide variety of studies in nuclear structure, nuclear astrophysics, and fundamental symmetries. This facility will use gas stopping in order to convert high-energy beams of rare isotopes produced by projectile fragmentation into low-energy beams. This will employ a new gas stopper concept [25], which avoids these limitations and fulfills the needs of next-generation rare isotope beam facilities. It

uses a gas-filled cyclotron magnet. The large volume, and a separation of the regions where the ions stop and where the maximum ionization is observed are the key to a higher beam-rate capability. The longer stopping path due to the magnetic field allows a lower pressure to be used, which decreases the extraction times. The driver accelerator of FRIB will be a superconducting-RF driver linear accelerator that provides 400 kW for all beams with uranium accelerated to 200 A MeV and lighter ions with increasing energy (protons at 600 MeV). The post-accelerator will also be superconducting, providing beams up to 12 A MeV (uranium) and higher energies for lighter beams (*e.g.*, 21 A MeV for ^{48}Cr).

6. – Second-generation facilities in Europe

The European community has expressed strong support already in 2004 for the construction of advanced in-flight and ISOL facilities, FAIR and EURISOL, respectively [26]. Because of the time-line for EURISOL, the community has recognised that new projects should be constructed that have a shorter time-scale. These are SPIRAL2, HIE-ISOLDE and SPES. These projects, that are now all under construction, will bridge the gap between now and the operation of EURISOL. Furthermore, the technical developments required for these intermediate projects are in many cases the ones required EURISOL. I will describe in more detail SPES and HIE-ISOLDE; SPIRAL-2 is described in the lectures of M. Lewitowicz.

SPES. – SPES [27] is an ISOL facility dedicated to the production of neutron-rich beams. It is an INFN project involving the two national laboratories, LNL and LNS and other INFN sites in Italy. The project consists of a proton driver, a 70 MeV cyclotron with two exit ports for a total current of 750 μA , an UC_x ISOL target and ion source, a beam transport system with a high-resolution mass selection and the superconducting PIAVE-ALPI accelerator complex in operation at LNL that will be used as radioactive beam re-accelerator. A 40 MeV 200 μA proton beam, delivered by the cyclotron, impinges on the uranium carbide target. The neutron-rich isotopes, produced as fission fragments with a rate of 10^{13} fission/s, are extracted by the ion source, mass separated and sent via beam lines to the PIAVE-ALPI re-accelerator. The re-acceleration stage with the superconductive linac ALPI will provide a final energy which is sufficient to perform nuclear reactions close to the Coulomb barrier between medium-heavy mass ions. The uranium carbide targets have been already developed and represent an innovation in terms of capability to sustain the primary beam power. The ions, extracted in a 1⁺ state with different ion sources, depending on the kind of isotope, will be transported in ALPI, with a benefit from the experience gained in LNS (Catania) with the EXCYT project, which will be taken as a reference for the optimization of the various magnetic elements and diagnostics. To fit the proper entrance parameters for beam reacceleration with the linac, an RFQ-cooler and a charge breeder are planned.

HIE-ISOLDE. – ISOLDE at CERN produces radioactive beams through fission, spallation and fragmentation reactions induced by 1.4 GeV protons from the PS booster. It

offers the largest variety of post-accelerated radioactive beams in the world today. In order to broaden the scientific opportunities far beyond the reach of the present facility the HIE-ISOLDE (High Intensity and Energy) project [28, 29] will provide major improvements in energy range, beam intensity and beam quality. A major element of the project will be an increase of the final energy of the post-accelerated beams to 10 A MeV throughout the periodic table. This will be achieved by replacing the current REX LINAC by superconducting cavities and will be implemented in a staged fashion. The first stage will boost the energy to 6 A MeV where the Coulomb excitation cross sections are strongly increased with respect to the current 3 A MeV and many transfer reaction channels will be opened. In the second stage additional cryo-modules will be added to bring the energy up to 10 A MeV for all nuclides with $A/Q = 4.5$ and up to 14 A MeV for $A/Q = 3$. This will offer ideal conditions for transfer reactions over the whole periodic table, particularly the heavy elements uniquely produced at ISOLDE. Moreover the provision of low-beta superconducting cavities allows for CW operation and the delivery of beams with energies down to 0.5 A MeV for astrophysics oriented measurements. The prototyping of these sputtered cavities is already ongoing. In addition the new CERN injector LINAC 4 will provide a major boost of the proton intensity onto the ISOLDE target. In the framework of HIE-ISOLDE the target areas and ion sources are also being respectively upgraded and optimized in order to make use of the more intense proton beams from LINAC4 and to improve the efficiency for ion extraction and charge breeding. This will enable up to an order of magnitude more RIB intensity to be delivered for many nuclides. Improved beam quality will arise from several technological advances: the already implemented solid-state lasers equipping the RILIS ion source and use of the recently commissioned RFQ cooler ISCOOL together with the construction of a new high-resolution mass separator. The possibility of providing polarized beams will also be investigated.

7. – EURISOL

It is recognised that the main limiting factors for ISOL facilities are threefold: i) the driver beam intensity, ii) the target and ion-source technology and safety related issues and iii) the energy of the post-accelerated beams. Major advances in these three areas will give access to new and unique research opportunities. In the period 2004-2009 detailed feasibility studies and technical preparatory work of the most challenging components for the ultimate EURISOL facility, was carried out in the framework of a Design Study funded within the European Union Sixth Framework programme [30, 31]. Twenty institutions and laboratories from 14 European countries became full participants in the project, contributing their expertise to the design of EURISOL and to build and test prototypes of the most challenging elements. In addition, another 20 laboratories from Europe, Asia and North America agreed to take part as contributors conveying their unique know-how on specific points. The full report of the Design Study can be downloaded from [32].

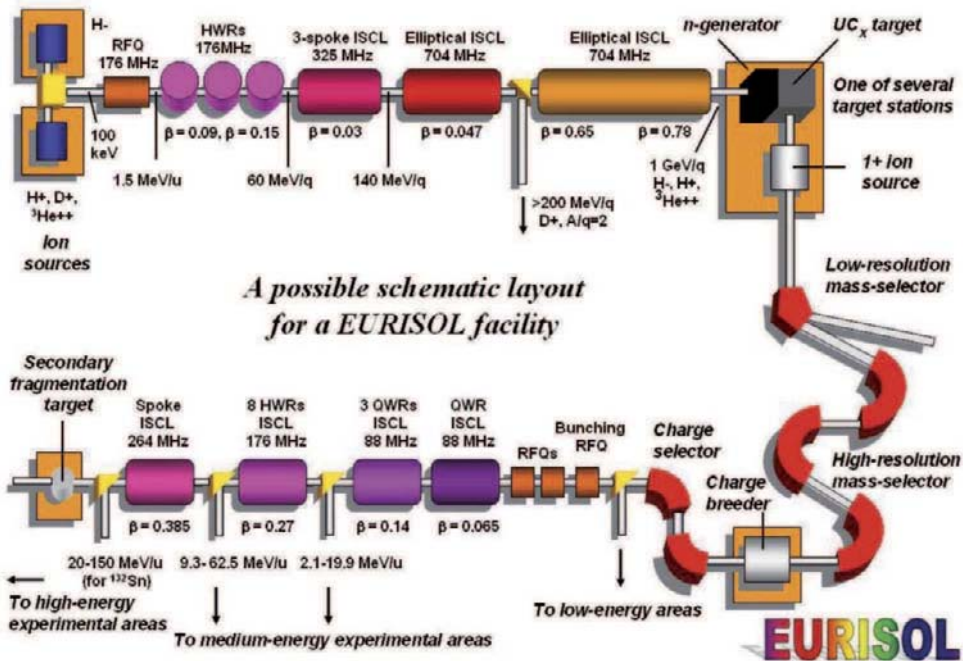


Fig. 7. – Schematic view of the EURISOL design.

A baseline concept for the next-generation ISOL facility has been devised and a schematic drawing of the concept is shown on fig. 7. The driver is a 1 GeV continuous wave superconducting LINAC which can accelerate a proton beam with an intensity of 5 mA corresponding to 5 MW power. Capability for accelerating ^3He , deuterons and $A/Q = 2$ ions, will be included.

At the Multi MegaWatt (MMW) target station, the proton beam will impinge on a liquid-Hg converter to produce a copious amount of neutrons in order to induce more than 10^{15} fissions per second in each of six UCX targets, enriched in ^{235}U . Two different designs for the Hg converter are envisaged, and represented on fig. 8. In the Coaxial Guided Stream (CGS) design [33], which is the baseline design, the mercury is kept under pressure and flows within a double-walled tube with a proton beam window at one end. The mercury flows towards the proton beam in the outer part of the tube and along the p-beam in the inner part making a u-turn at the window. The so-called Windowless Transverse Mercury Film (WTMF) target avoids the technical difficulties related to pressurized beam windows and is advantageous in terms of neutronics. Mercury flowing through the upper tube is guided into a vertical jet by sets of fins. Prototypes of the two systems have been built and are currently being tested at the IPUL laboratory in Latvia.

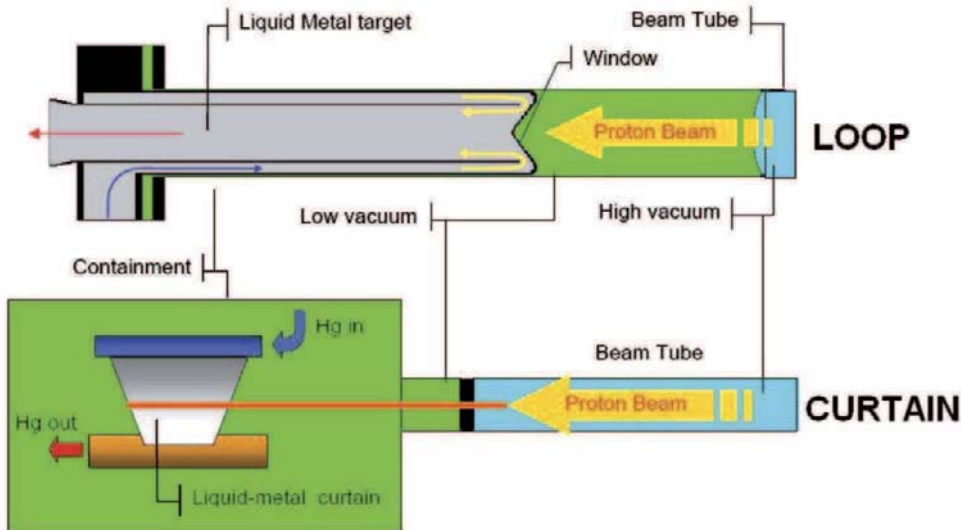


Fig. 8. – Two designs for the MMW converter (see text).

EURISOL targets are derived from the concept proposed by the PIAFE project at ILL in Grenoble and the MAAF project in Munich. Conceptually, a target filled with ^{235}U or other actinide is inserted, through a channel created in the shielding, close to the neutron source at the position of maximum neutron flux. Each target module can be inserted, replaced and serviced by means of remote handling.

Thanks to an original beam splitting system based on magnetic stripping [34], a small fraction of the primary beam (100 kW) will impinge directly on spallation targets. The beam from the target stations has to be prepared for the post acceleration with the merging, cooling, mass-separation and charge state multiplication of the six beams from the multi MW fission targets representing the biggest challenge. Preliminary studies have been performed of merging using a so-called arc ECRIS source [35] which has geometry suitable for injection of several beams into an ECR plasma from which a single beam later can be extracted. The transverse cooling will be done in a newly developed high-intensity RFQ cooler. The mass separation will be done with a classical dipole system consisting of up-to four independent dipoles. The charge breeding will be done in either an ECR source or in a new high-intensity CW EBIS source which is under development.

The beams will be reaccelerated by a superconducting LINAC with minimum beam losses. The design of the first stages of the LINAC is similar to that of the SPIRAL2 driver. The final energy of the RIB can be adjusted continuously from rest to 150 A MeV for ^{132}Sn . EURISOL is designed to provide a large energy range for a wide selection of isotopes which will allow physicists to combine an unprecedented variety of complementary probes for the study of exotic nuclei.

8. – Final words

In 2010 we are on the threshold of new prospects of research in nuclear structure and nuclear astrophysics that exploit a wide range of radioactive beams. In North America the FRIB facility will combine the advantages of in-flight production methods with those of ISOL facilities using innovative methods of gas-catching. The TRIUMF facility has great potential in its current ISAC facility, and there are new plans to build an intense photo-fission RIB factory using an electron linac driver. There are also plans to build an ambitious ISOL ultra-versatile facility in South Korea. An ultimate ISOL facility such as EURISOL holds broad scientific promise but represents a formidable technological challenge. A European roadmap has been established which includes building of 3 so-called “intermediate-generation” ISOL facilities: HIE-ISOLDE at CERN, SPES in Legnaro, Italy and SPIRAL2 at GANIL, Caen, France.

* * *

The original publication of this article is available at <http://www.sif.it/SIF/en/portal/journals>. Support from the UK STFC and the Società Italiana di Fisica is acknowledged.

REFERENCES

- [1] JONSON B. and RICHTER A., *Hyp. Int.*, **129** (2000) 1.
- [2] THIBAULT C. *et al.*, *Phys. Rev. C*, **12** (1975) 644.
- [3] <http://isodele.web.cern.ch/ISOLDE/>.
- [4] http://www.lng.infn.it/~spes/TDR2008/Chapter6_source.pdf
- [5] KÖSTER U. *et al.*, *Radiochim. Acta*, **89** (2001) 77777.
- [6] VAN DUPPEN P. *et al.*, *Rev. Sci. Instrum.*, **63** (1992) 2381.
- [7] LETTRY J., *Proceedings of the 1999 Particle Accelerator Conference, New York, 1999*.
- [8] MISHIN V. I. *et al.*, *Nucl. Instrum. Methods B*, **73** (1993) 550.
- [9] WENANDER F., *Nucl. Instrum. Methods B*, **266** (2008) 4346.
- [10] <http://www.cyc.ucl.ac.be/RIB/>.
- [11] <http://www.phy.ornl.gov/hribf/>.
- [12] <http://pro.ganil-spiral2.eu/laboratory/ganil-accelerators/spiral/introduction>.
- [13] HABS D. *et al.*, *Hyp. Int.*, **129** (2000) 43.
- [14] BOLLEN G. *et al.*, *Nucl. Instrum. Methods A*, **368** (1996) 675.
- [15] WOLF B. H. *et al.*, *Nucl. Instrum. Methods B*, **204** (2003) 428.
- [16] <http://www.triumf.ca/research/research-facilities/isac-facilities-for-rare-isotope-beams>.
- [17] CIAVOLA G. *et al.*, *Proceedings of EPAC 2000, Vienna, Austria*, edited by LACLARE J.-L. *et al.*, p. 2597; available at <http://accelconf.web.cern.ch/accelconf/e00/PAPERS/WEP5B01.pdf>.
- [18] <http://triac.kek.jp/en/>.
- [19] ÄYSTÖ J., *Nucl. Phys. A*, **693** (2001) 477.
- [20] KUDRYAVTSEV Y. *et al.*, *Nucl. Instrum. Methods B*, **179** (2001) 412.
- [21] SAVARD G. *et al.*, *Nucl. Instrum. Methods B*, **204** (2003) 582.

- [22] HUYSE M. *et al.*, *Nucl. Instrum. Methods B*, **187** (2002) 535.
- [23] PETRICK M. *et al.*, *Nucl. Instrum. Methods B*, **266** (2008) 4493.
- [24] <http://www.frib.msu.edu/>.
- [25] BOLLEN G. *et al.*, *Nucl. Instrum. Methods A*, **550** (2005) 27.
- [26] http://www.nupec.org/pub/lrp03/long_range_plan_2004.pdf.
- [27] <http://www.lngd.infn.it/~spes/>.
- [28] <http://hie-isolde.web.cern.ch/HIE-ISOLDE/>.
- [29] LINDROOS M. *et al.*, *Nucl. Instrum. Methods B*, **266** (2008) 4687.
- [30] <http://www.eurisol.org>.
- [31] BLUMENFELD Y. *et al.*, *Int. J. Mod. Phys. E*, **18** (2009) 1960.
- [32] http://www.eurisol.org/site02/doc_details.php?operation=download&docu=1075&type=25.
- [33] SAMEC K. *et al.*, *Nucl. Instrum. Methods A*, **606** (2009) 281.
- [34] FACCIO A. *et al.*, *Phys. Rev. ST Accel. Beams*, **10** (2007) 091001.
- [35] SUOMINEN P. and WENANDER F., *Rev. Sci. Instrum.*, **79** (2008) 02A305.

This page intentionally left blank

Proceedings of the International School of Physics “Enrico Fermi”
Course CLXXVIII “From the Big Bang to the Nucleosynthesis”, edited by A. Bracco and E. Nappi
(IOS, Amsterdam; SIF, Bologna)
DOI 10.3254/978-1-60750-974-5-191

Low-energy reactions, moments and beta-decays with radioactive beams for nuclear structure and astrophysics problems. Results and perspectives with SPIRAL2

M. LEWITOWICZ

on behalf of the SPIRAL2 PROJECT GROUP and PHYSICS COLLABORATIONS

Grand Accélérateur National d’Ions Lourds - GANIL, CEA/DSM-CNRS/IN2P3

BP 55027, 14076 Caen Cedex, France

Summary. — The SPIRAL 2 project, an important extension of the GANIL facility which has recently entered in the construction phase is shortly presented. The physics case of the facility based is on the use of high-intensity stable and radioactive beams. Expected performances and main technical parameters of the facility are introduced. Examples of physics topics and related measurements are discussed in the context of new experimental halls and devices to be constructed in order to fully explore the possibilities offered by this advanced Radioactive Ion Beam facility.

1. – Introduction

The lectures presented in the following are dealing with science of Radioactive (or Rare) Ion Beams (RIB) which became in the last decades the major new topic in nuclear physics and related areas. More particularly, using an example of the GANIL/SPIRAL2

and SPIRAL2 RIB facility it will be shown how new developments in accelerator and detector technologies are related to open questions in our understanding of nuclear structure and nuclear reactions. The lectures are aiming to introduce this vast field of nuclear science in the context of use of high-quality and high-intensity beams delivered by advanced Isotope Separation On-Line (ISOL) facilities.

2. – Goals and new avenues for physics with Radioactive Ion Beams

The creation of nuclear species and their observed abundances today reflect the diverse phases of the evolution of the Universe. They remain as evidence of its long history. While the lighter elements were produced in the first minutes after the Big Bang, the heavier elements were and still are synthesized in the cores of stars. It is not just nucleosynthesis but all energetic cosmic phenomena that bring nuclear forces into play. The understanding of our Universe, its origin and its evolution is thus intimately related to progress in our knowledge of nuclear physics.

The recent progress in studies of the nucleus and the interactions between its components is mainly linked to the synthesis of new nuclei, developments of experimental methods for investigating them as well as improvements in theoretical modeling of the nucleus. Because of their very unusual proton-to-neutron ratio, the exotic nuclei allow one to perform unprecedented studies underlying and amplifying the phenomena related to the isospin asymmetry in nuclei and nuclear matter. SPIRAL2 and other RIB facilities will give access to a whole range of experiments on exotic nuclei, which have been impossible up to now. In particular it will provide intense beams of neutron-rich, exotic nuclei whose properties are little explored at present.

In the studies of nuclear structure there are many questions still waiting for a full answer:

- What are the limits to nuclear existence?
- What is the influence of states in the continuum on nuclear structure and nuclear reactions close to drip-lines?
- Will new forms of collective motion be observed far from stability?
- What happens to the well-known shell structure seen in stable nuclei as we move away from stability?
- What will be the forms of nuclear matter at the extremes of stability? It is already known that some neutron-rich, light nuclei have a halo of neutrons, a pronounced neutron skin or they behave as nuclear molecules. How these phenomena evolve going to heavier nuclei?
- Do the dynamical symmetries seen in near-stable nuclei appear in exotic nuclei as well?

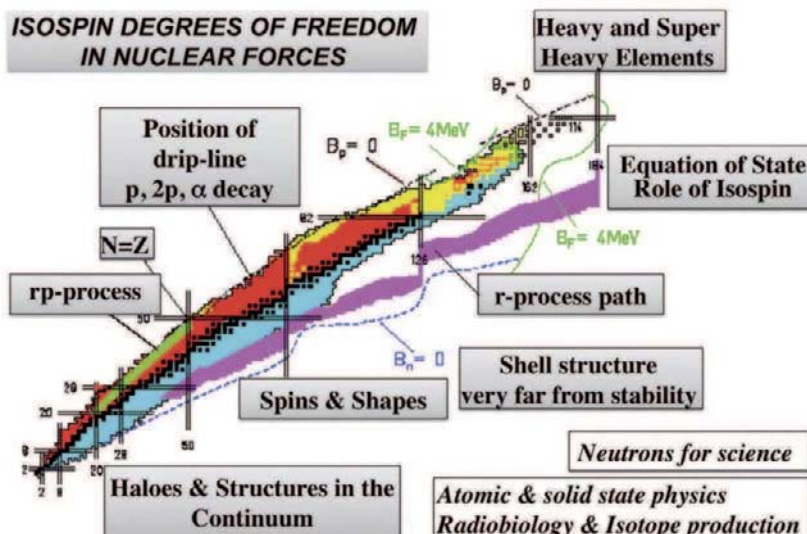


Fig. 1. – Scientific case of the SPIRAL2 facility.

The advanced RIB facilities will produce high-quality beams of exotic nuclei which will allow us to address these and many other questions having also direct links to many branches of modern science.

A major part of the experimental and theoretical research program (fig. 1) at the SPIRAL 2 facility will follow the above-mentioned fundamental motivation of basic nuclear science research, trying to establish a bridge between the nucleon-nucleon interaction inside a nucleus and the underlying quarks and gluons as well as understand the mechanism of interaction between nuclei. This research on the nucleus and on the interactions between its constituents progresses, in particular, using nuclei with unusual neutron-to-proton ratios which open up a considerable field of investigation. By allowing the study of very asymmetric nuclear systems, the nuclei far from stability highlight the phenomena at the origin of the cohesion of the nucleus. SPIRAL 2 thanks to very high intensities of RIB will give access to a whole range of experiments (from elastic scattering to fusion-evaporation reactions), which are inaccessible with modest intensity beams of first-generation RIB facilities. In particular, new exotic shapes and excitation modes and new modes of nuclear decay are expected to be observed. Tests of fundamental symmetries, testing and refinement of the Standard Model of fundamental interactions, and exploration of the magic numbers of protons and neutrons in very exotic nuclei are all enticing avenues of discovery at SPIRAL2.

Many of explosive nucleosynthesis processes involve radioactive nuclei. Due to their very short lifetimes, most of them have not survived long enough to be present on earth. SPIRAL 2 will produce abundantly nuclei lying on or in a close proximity to the r- and rp-process paths, opening up new fields of investigation. In particular, a new insight on

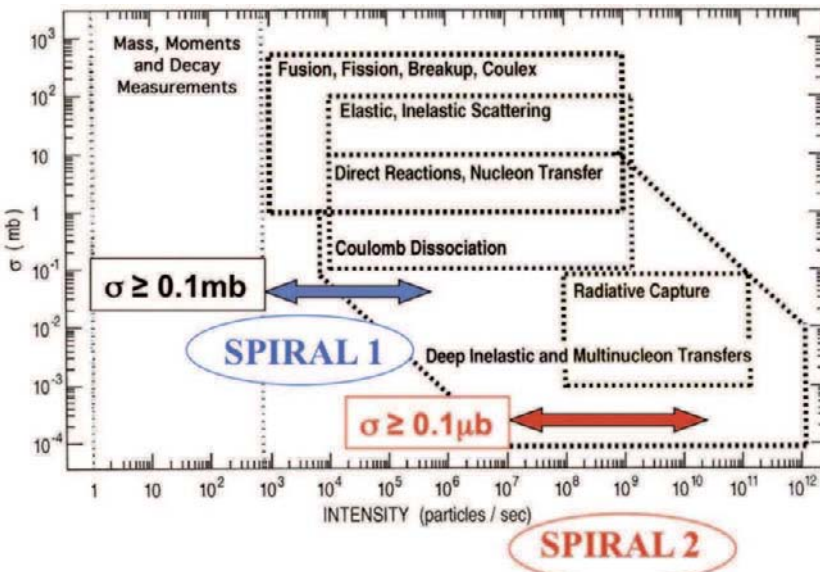


Fig. 2. – The design goal RIB intensities of the SPIRAL 2 facility and the accessible range of nuclear reactions compared to the currently available intensities from SPIRAL 1 (representative for the intensities at the first-generation RIB facilities).

nucleosynthesis might be achieved using direct reactions (d, p), (p, d), etc. These types of reactions are expected to be one of the most powerful tools both for nuclear structure and astrophysics studies at SPIRAL2 (fig. 1 and fig. 2). The facility will match necessary conditions for this kind of measurements, namely high RIB intensities, energy range up to 9 MeV/nucleon for fission fragments and up to 20 MeV/nucleon for neutron-deficient nuclei and a full set of efficient detector systems.

An increase of intensities by 3 to 5 orders of magnitude with respect of those typically available at the first-generation RIB facilities (like SPIRAL1) opens completely new possibilities in nuclear physics. With the RIB intensities exceeding 10^9 particles/s all standard nuclear physics tools like mass, nuclear moments and decay measurements, direct, transfer, Coulomb excitation, break-up, deep-inelastic, radiative capture and fusion-evaporation reactions will be available for experiments with nuclei far from stability. The corresponding cross-sections accessible for detailed spectroscopic studies with high-optical quality ISOL RIB can be as low as 100 nb (to be compared to about $100 \mu b$ today).

The spectacular increase of intensities of RIB expected at SPIRAL2 is shown in fig. 3 on a more quantitative example of neutron-rich beams of Kr isotopes. The SPIRAL2 intensities of post-accelerated beams are expected to surpass by 2-4 orders of magnitude those achievable today (for example at REX IISOLDE facility at CERN). Only with advance of the ultimate-generation RIB facilities like EURISOL a further important gain

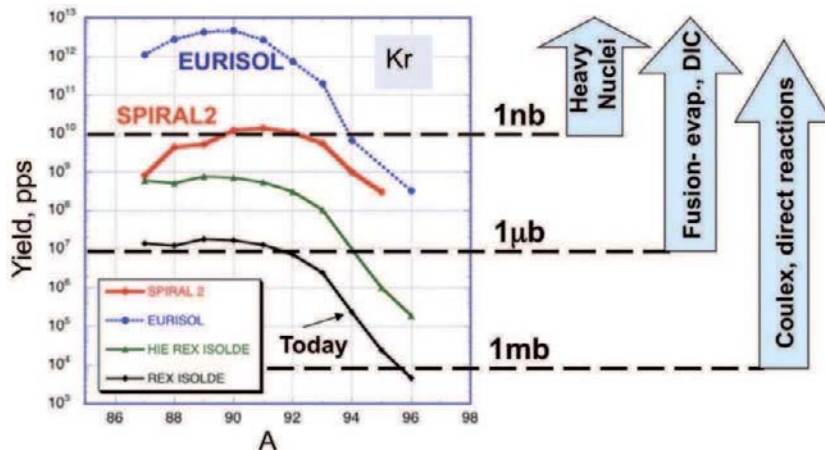


Fig. 3. – Intensities of the post-accelerated beams of Kr isotopes from SPIRAL2 compared to those available at the existing and future (EURISOL) facilities. Typical cross-sections for low energy reactions which may be achieved with different beam intensities are indicated.

in intensities can be realized on a longer-term (15–20 years) perspective. The reachable limits in the production rate can be illustrated on the following example: with intensities close to 10^{10} particles/s for beams of $^{90-92}\text{Kr}$ using a fusion evaporation reaction with a cross-section of 1 nb and a typical 1 mg/cm^2 thick target would lead to a production of 1 evaporation residue per day.

In other terms, the very high intensities of RIB would allow to largely expand a range of isotopes for studies exploring the isospin degrees of freedom like change of deformation, evolution of the reaction cross-section or asymmetry term in the equation of state of nuclear matter. Both neutron-deficient and neutron-rich isotopes forming long isotopic chains (up to 25 neutrons difference) and intensities exceeding 10^5 particles/s will be used for this type of experiments. In fig. 4 examples of these long chains of $^{54-73}\text{Ni}$, $^{74-97}\text{Kr}$ and $^{121-146}\text{Xe}$ produced at SPIRAL 1 (neutron-deficient isotopes), GANIL cyclotrons (high-intensity stable-ion beams) and SPIRAL 2 (neutron-rich beams) facilities are shown.

3. – GANIL, SPIRAL and SPIRAL2 facilities

The GANIL facility [1] (Caen, France) is one of the major RIB and stable-ion beam facilities for nuclear physics, astrophysics and interdisciplinary research in Europe. Since the first beams delivered 25 years ago, the performances of the GANIL accelerator complex, were constantly improved with respect to the beam intensity, energy and available detection systems. In recent years, RIB have been recognized by the international scientific community as one of the most promising avenues for the development of fundamental nuclear physics and astrophysics, as well as for applications of nuclear science. Since the

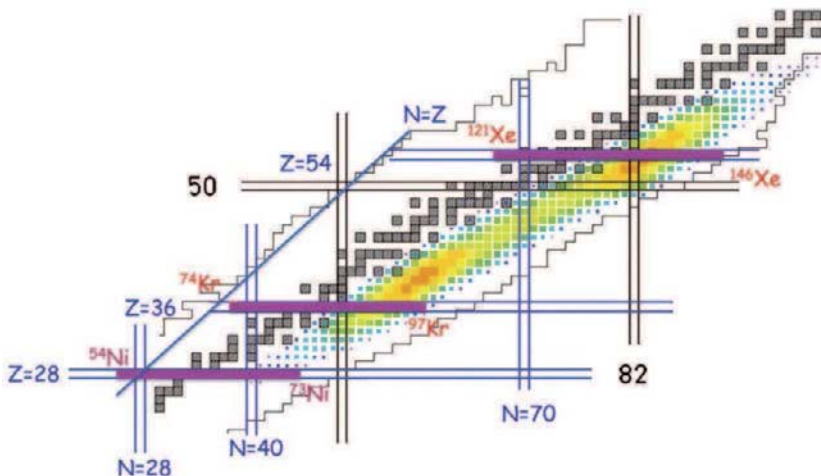


Fig. 4. – Examples of isotopic chains of nickel, krypton and xenon for which the post-accelerated RIB with intensities higher than 10^5 particles/s will be available at the SPIRAL2 facility.

beginning of the experimental program of GANIL, the facility delivered RIB produced in-flight at LISE and SISSI/Alpha fragment separators. More recently, in autumn 2001, the SPIRAL facility allowing for the production and post-acceleration of the ISOL-type RIB entered into operation. The facility, specialized in RIB of rare gases (He, Ne, Ar, Kr but also N, O and F), enlarged importantly the range of experimental possibilities dedicated to study of nuclei far from stability at GANIL. These beams are produced using high-intensity (up to 3 kW) 70–95 MeV/nucleon heavy-ion beams impinging on a universal graphite target. The radioactive atoms diffused from the target are ionized in the ECR ion source and injected to the CIME cyclotron for the post-acceleration to energies ranging from 1 to 25 MeV/nucleon. Today SPIRAL 1 delivers in a routine way high-quality low-energy (keV) and post-accelerated beams of 40 isotopes of 7 elements (fig. 5).

Krypton	69	70	71	72	73	74	75	76	77	78	79	80	81	82	83	84	85	86	...
Argon	30	31	32	33	34	35	36	37	38	39	40	41	42	43	44	45	46	47	...
Neon	16	17	18	19	20	21	22	23	24	25	26	27	28	29	30	31	32		
Fluorine	14	15	16	17	18	19	20	21	22	23	24	25	26	27	28	29			
Oxygen	12	13	14	15	16	17	18	19	20	21	22	23	24	25	26				
Nitrogen	10	11	12	13	14	15	16	17	18	19	20	21	22	23	24				
Helium	3	4	5	6	7	8	9	10											

Stable
7 elements, 40 isotopes

Exotic

Fig. 5. – RIB currently available at the SPIRAL1 facility.

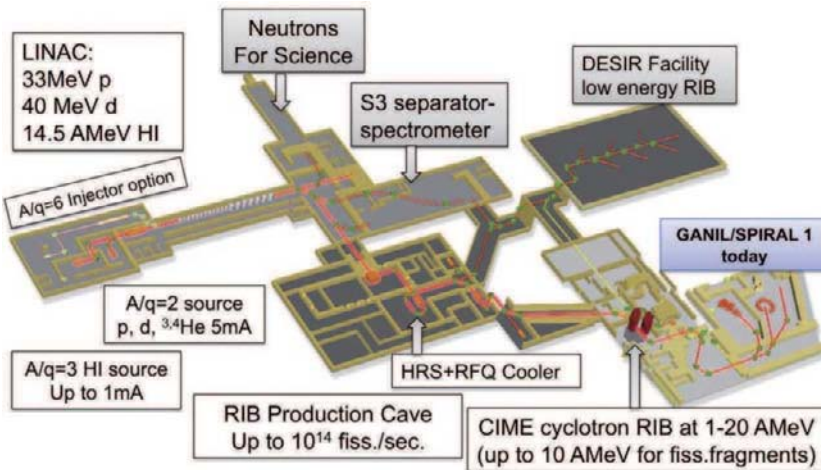


Fig. 6. – A general layout of the SPIRAL2 facility.

Available today intensities and energies of the GANIL stable-ion beams ($Z > 5$) limit the use of high-intensity RIB to relatively light nuclei ($A < 80$). Since the beginning of the SPIRAL project it was proposed to enlarge the range of accelerated ions by production of high-intensity RIB of fission fragments. This idea, after several years of discussions and an important preliminary study phase led, in particular, in the framework of the European RTT Program was concretized in the SPIRAL 2 project [2]. The project is following the European road map for RIB facilities defined by NuPECC [3] (Nuclear Physics European Collaboration Committee—an expert committee of the European Science Foundation), which recommended the construction of two complementary next-generation RIB facilities in Europe. One is based on in-flight fragmentation (IF) as proposed for the FAIR facility at GSI (Darmstadt, Germany) and the other on the isotope-separation on-line (ISOL) method, largely developed at the CERN-ISOLDE facility over the last thirty years (the EURISOL project [4]). Because of the time-line for EURISOL as well as of important unsolved yet technological issues, NuPECC recommends the construction of intermediate-generation facilities that will benefit the EURISOL project in terms of R&D and that will give the community opportunities to perform research and develop applications with RIB. Among the proposed intermediate facilities, SPIRAL2 meets the criteria of European dimension in terms of physics potential, site and size of the investment as it was recognised recently in the ESFRI (European Strategy Forum on Research Infrastructures) roadmap [5]. The SPIRAL 2 facility has entered in its construction phase in 2005 and is supported by the EU FP7 through the Preparatory Phase contract since 2008.

3.1. SPIRAL 2 Facility. – The SPIRAL 2 facility, schematically shown in fig. 6 consists of the superconducting linear accelerator (LINAC) and the associated experimental area (AEL) which include Neutrons For Science (NFS) and Super Separator Spectrometer

(S3) halls, the RIB production building with production cave, a RFQ Cooler and a High Resolution mass Separator (HRS) and the low-energy RIB experimental hall (DESIR). The high-power LINAC will deliver a high-intensity, light-ion beams (up to 40 MeV deuteron beam) as well as a variety of heavy-ion beams with mass-to-charge ratio of 3 and energy up to 14.5 MeV/nucleon. The radioactive ions created using in a variety of target and 1+ ion sources after a charge breeding in the ECR source will be post-accelerated in the existing CIME cyclotron and used in the GANIL experimental halls. The following few sections are dedicated to a short description of the major components of the facility.

3.1.1. SPIRAL 2 Driver Accelerator. The layout of the SPIRAL 2 driver accelerator was frozen in 2006, taking into account the wide variety of beams needed for physics experiments. The biggest challenge is to manage this choice of beams, the high power (200 kW, CW) and the safety issues related to deuteron beam losses.

In the initial phase, two separate injectors are planned:

- the Heavy Ions injector ($q/A = 1/3$): ECR source with its mass analyzer, focusing systems and beam diagnostics
- the Light Ions injector: ECR source (protons and deuterons) with its beam transfer line and diagnostics.

Beams from both injector lines are pre-accelerated with a common RFQ cavity: a 4-vanes copper cavity (88 MHz) composed of 5 sections, 1 meter long each, dissipating 240 kW, with an electrode voltage of 110 kV and output energy of 0.75 AMeV. The Medium Energy Beam line will integrate 3 copper cavities bunchers, focusing and beam diagnostic systems, and a fast chopper for single bunch experiments.

3.1.2. Superconducting LINAC. The SC LINAC is composed of 2 families of 88 MHz SC QWR resonators ($\beta = 0.07$, $\beta = 0.12$). The basic principle of this design was to install the SC resonators in separate cryomodules (1 QWR per cryomodule in the $\beta = 0.07$ section and 2 QWR per cryomodule in the $\beta = 0.12$ section). Between each cryomodule, beam focusing is performed by means of 2 warm quadrupoles with short vacuum/diagnostics boxes in between. Even if the cryogenic losses are higher, compared to other designs implementing 4, 5 or 6 resonators in a cryomodule, it offers several major advantages: flexible beam tuning system with RT Q-poles, space for beam diagnostics at room temperatures and optimized mechanical supports with precise alignment possibilities.

All the QWR resonators are tested before their integration into the cryomodules. The specifications are: accelerating voltage $> 6.5 \text{ MV/m}$, and quality coefficient $Q_0 > 10^9$ at 4.2 K which corresponds to a thermal load of 10 W per resonator. A very challenging goal has been also reached during fabrication procedures: for nearly all resonators, controlled after manufacturing, the frequency was within the $\pm 20 \text{ kHz}$ range, and the beam axis alignment (between inner electrode and beam ports) better than 0.4 mm. Each resonator is driven by a RF power coupler. The nominal CW RF operating power ranges between

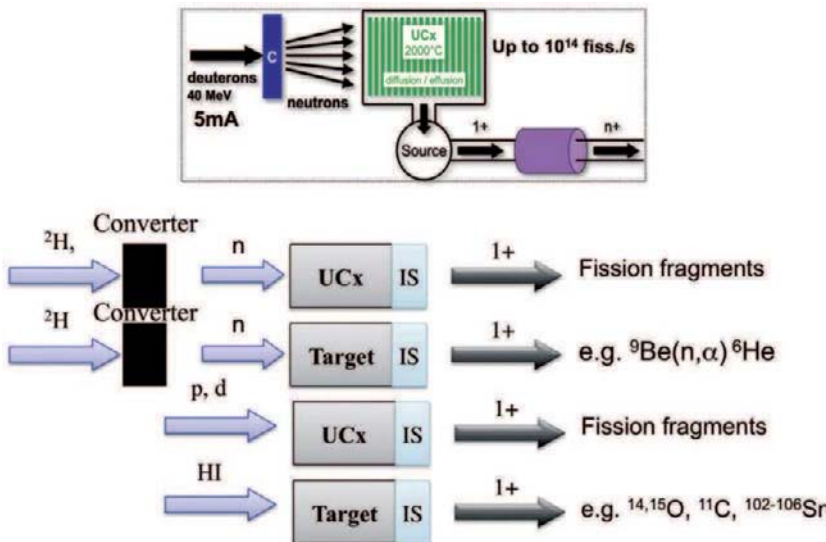


Fig. 7. – Possible RIB production schemes to be used at SPIRAL2. The main RIB production technique leading to intense beams of fission fragments using deuteron beam, graphite converter and high-density uranium carbide target is shown in the upper part of the figure.

5 kW and 15 kW. All the couplers are conditioned and tested at high power (40 kW), before final assembly in the cryomodules.

Most of the essential components of the SPIRAL2 LINAC were already manufactured and are undergoing tests at LPSC Grenoble (heavy-ion injector), Irfu/DSM/CEA Saclay (light-ion injector and low-beta cavities), IPN Orsay (high-beta cavities) and GANIL (elements of beam lines).

3.1.3. Production of Radioactive Ion Beams at SPIRAL 2. The main RIB production scheme of SPIRAL2 is based on the fast-neutron induced fission of uranium target (fig. 7). Using a carbon converter, a 5 mA deuteron beam and a high-density (up to 11 g/cm^3) 2.3 kg uranium carbide target, the fission is expected to reach a rate of up to $10^{14}/\text{s}$. The intensities of the post-accelerated RIB in the mass range from $A = 60$ to $A = 140$ will be of the order of 10^6 to 10^{10} particles/s (pps) surpassing by more than one order of magnitude existing facilities. For example, the intensities should reach 10^9 pps for ^{132}Sn and 10^{10} pps for ^{92}Kr . A direct irradiation of the UC_2 target with beams of protons or $^{3,4}\text{He}$ can be used if higher excitation energy leads to higher production rate for a specific nucleus of interest or if much smaller targets with fast release properties are required.

Thanks to the high-intensity heavy-ion beams provided by the driver the neutron-rich fission RIB will be complemented by beams of nuclei near the proton drip-line, provided by fusion-evaporation or transfer reactions. For example, an in-flight production of up to 8×10^4 atoms of ^{80}Zr per second using a $200 \mu\text{A}$ $^{24}\text{Mg}^{8+}$ beam on a ^{58}Ni target should be possible. Similarly, the heavy- and light-ion beams from LINAC can also be

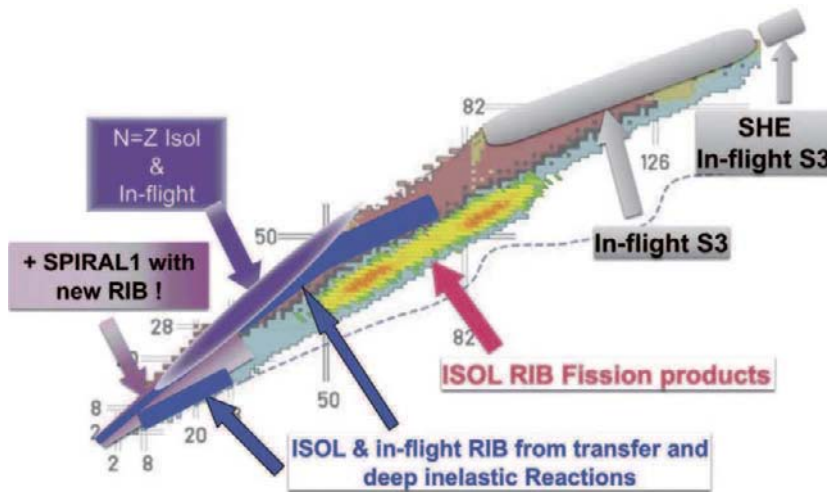


Fig. 8. – RIB and nuclei far from stability accessible with SPIRAL1 and SPIRAL2 produced with in-flight (S3) and ISOL techniques.

used directly on different production targets to produce high-intensity light RIB with the ISOL technique (fig. 7).

Thus the SPIRAL 2 facility will offer a wide range of intense stable and radioactive beams. Both neutron-induced fission and charged-particle-induced fission will be used to produce high-intensity beams of fission fragments. Fusion-evaporation and transfer reactions with high-intensity, stable light- and heavy-ion beams will allow the delivery of neutron-deficient and light radioactive ions. In this case both in-flight production method with the S3 separator as well as ISOL technique can be used. The same reactions may also serve for the production of radioactive samples (targets) of interest for astrophysics or radiobiology. The intense RIBs can be used in turn to study nuclei even further away from the stability line via secondary fusion-evaporation or deep-inelastic reactions. Altogether, the regions of the Chart of the Nuclides that can be reached with the SPIRAL 2 facility, presented in fig. 8, covers a big part of all nuclei far from stability.

At the beginning of operation of SPIRAL2 Phase 2 (see below) the intensities of RIB of fission fragments will be about a factor of 15 lower than the nominal intensities corresponding to the 5×10^{13} fission/s. A careful analysis of the expected production rates, diffusion, ionization and post-acceleration efficiencies led to the estimates of the RIB intensities proposed to the users for the “Day 1” experiments. A full list of the SPIRAL2 RIB can be found in [6]. Examples of these “Day 1” beams for neutron-rich copper, gallium, zinc and krypton isotopes are presented in fig. 9.

The extracted 1+ radioactive ions will be subsequently injected to the 1+/n+ charge breeder (ECR ion source) and post-accelerated to energies of up to 20 MeV/nucleon (up to 7-8 MeV/nucleon for fission fragments) by the existing CIME cyclotron. Thus, using several different production mechanisms and techniques, SPIRAL 2 would allow users to

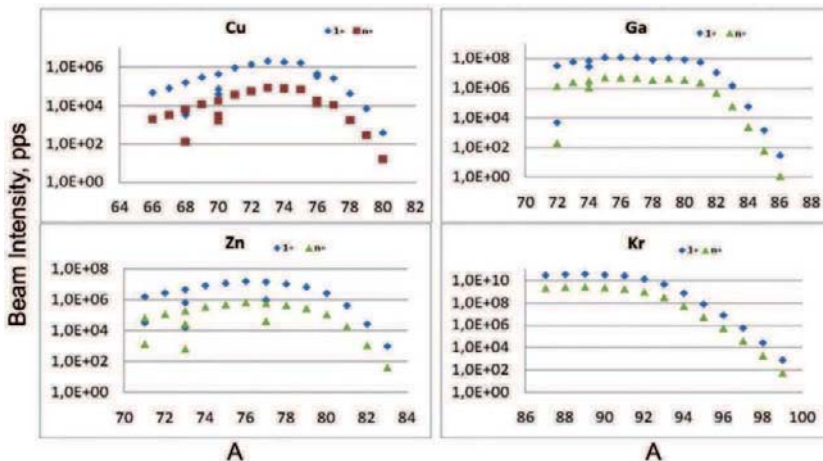


Fig. 9. – Examples of post-accelerated (denoted as n^+) and DESIR (denoted as 1^+) RIB of copper, gallium, zinc and krypton proposed for SPIRAL2 Phase 2 Day 1 experiments. Note: the nominal SPIRAL2 RIB intensities will reach intensities about 15 times higher than those presented in the figure.

perform experiments with a wide range of neutron- and proton-rich nuclei far from the line of stability.

3.1.4. Simultaneous operation of the GANIL/SPIRAL1/SPIRAL2 facility. One of the important features of the future GANIL/SPIRAL1/SPIRAL2 facility will be the possibility to deliver up to five stable or radioactive beams to different users simultaneously in the energy range from keV to several tens of MeV/nucleon. In fig. 10 an example of this kind of parallel operation is shown in which a high-intensity beam from SPIRAL2 LINAC is used to produce a RIB in the SPIRAL2 RIB Production Building. This beam is post-accelerated in the CIME cyclotron and then used in an experiment in the one of the experimental halls of the current GANIL facility. Simultaneously a high-energy (for example 95 MeV/nucleon $^{36}\text{Ar}^{+18}$) beam accelerated by the GANIL sector-separated CSS1 and CSS2 cyclotrons is used in the SPIRAL 1 production cave to produce a second RIB subsequently injected to the low-energy DESIR experimental hall. At the same time, 3 other simultaneous stable-ion beams can be provided for other users at GANIL: first at keV energies at the ARIBE facility, second at the IRRSUD facility using second GANIL injector cyclotron (typically at 1 MeV/nucleon) and third at the SME facility using another charge state of the beam accelerated by the CSS1 cyclotron after the stripping foil placed between CSS1 and CSS2 (for example 12 MeV/nucleon $^{36}\text{Ar}^{+17}$). All in all 5 different energy and/or nature (2 RIB and 3 stable-ion beams) are used by different users. Many other configurations of this type of operation are possible. After the construction of SPIRAL2 Phase 1 the LINAC beams will be delivered for experiments at the NFS and S3 facilities only.

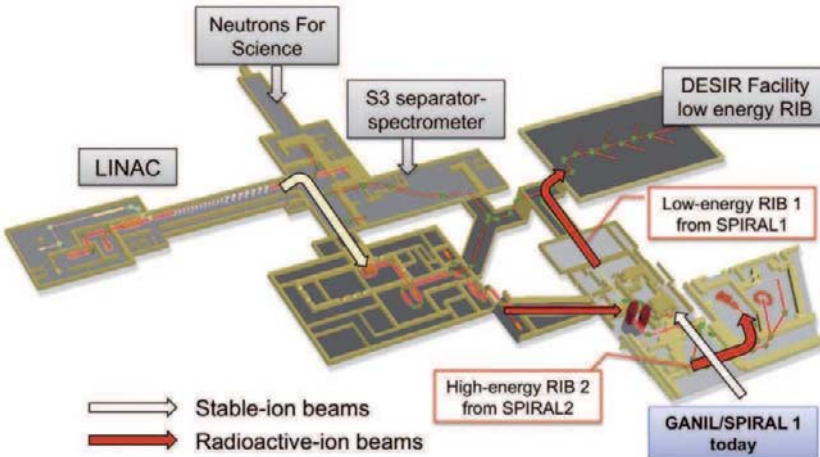


Fig. 10. – An example of operation of the SPIRAL2/SPIRAL1/GANIL facility with two simultaneous RIB delivered for the experiments. One RIB is produced with the high-intensity beam from the SPIRAL2 LINAC in the RIB production building. This RIB is subsequently post-accelerated at the CIME cyclotron and used in an experiment in the existing GANIL experimental area. The second RIB is produced at SPIRAL1 using high-energy primary beam from GANIL cyclotrons. This keV-energy ($1+$ or $n+$) RIB is used in the DESIR experimental hall.

3.1.5. The civil construction of the SPIRAL2 facility. A civil construction of SPIRAL2 is divided into two phases (fig. 11). The first one (LINAC buildings and associated experimental AEL with the NFS and S3 experimental halls,) begun in 2010 with a goal to provide first stable-ion beams in 2012. The second phase (RIB production building and DESIR facility) is currently in the detailed design phase and its construction should start in 2012 aiming at the beginning of operation in 2013-2014.

4. – Experiments with high-intensity stable-ion beams

A complete presentation of the scientific case of the facility, going beyond the scope of this contribution, can be found in the White Book of SPIRAL 2, Letters of Intent and Technical Proposals for SPIRAL 2 (see ref. [6]). In the following paragraphs, several examples of a rich and multipurpose scientific program will be presented. In the following a specific physics case will be presented in relation to different new experimental halls and detection systems.

In the framework of the SPIRAL 2 project two new experimental areas will be constructed. One dedicated to the experiments with high-intensity stable beams delivered by LINAC (Aires Experimentales du LINAC—AEL) and one devoted to research program with low energy RIB proposed recently by the DESIR (Decay, Excitation and Storage of Radioactive Ions) Collaboration.

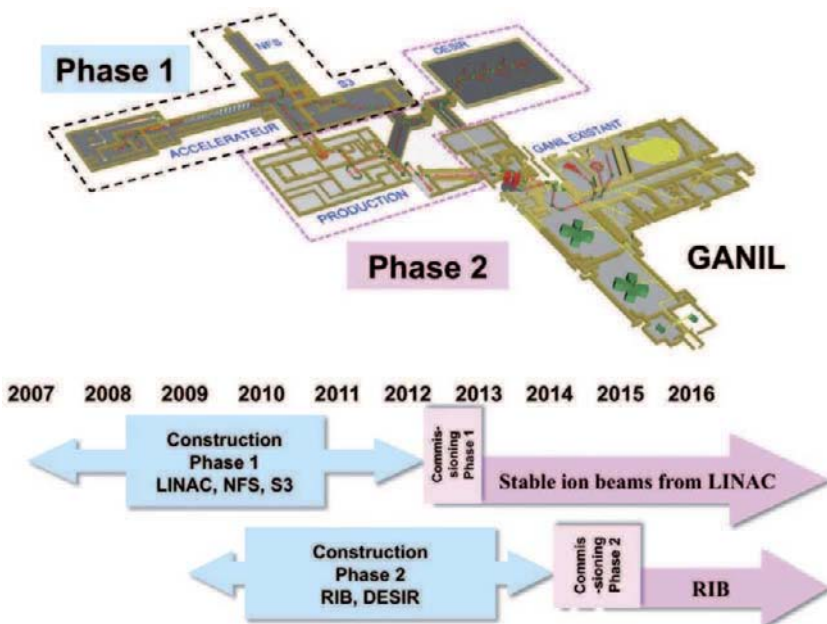


Fig. 11. – Upper part: the construction of the SPIRAL2 facility is divided into two phases. Phase 1 with the LINAC, NFS and S3 experimental halls; phase2: RIB production building and DESIR experimental hall. The timeline corresponding to the two construction phases is presented in the lower part of the figure.

4.1. S3. – One of the experimental halls of AEL will host the NFS facility mentioned above [7]. The second hall will be dedicated to the experiments with Super Spectrometer Separator (S3) [8] and in-flight production of exotic nuclei using LINAC heavy-ion beams.

The S3 physics case and device development is prepared by a large collaboration of more than one hundred physicists, from 30 institutions from 12 countries [8].

The S3 is composed of a two-stage separator. This device is based on a Momentum Achromat followed by a Mass Separator: MAMS. The basic principle of this device is to first suppress primary beam by at least 1:1000 by a pre- separator (momentum achromat) and then do further beam suppression and physical mass channel selection by a mass separator. This device will have the capabilities to fulfill most of the requirements for physics topics described in the following and is well optimized for direct and symmetric kinematics fusion-evaporation reactions and is built on the principles of the Oak Ridge RMS and the Texas A&M MARS separators. The S3 device is designed for several major types of experimental setups. In the following three of them, namely focal plane detectors, gas catcher and detection of particles in the intermediate focal plane (experiments with RIB produced in-flight) are shortly described (see fig. 12 for a schematic representation of these 3 possibilities).

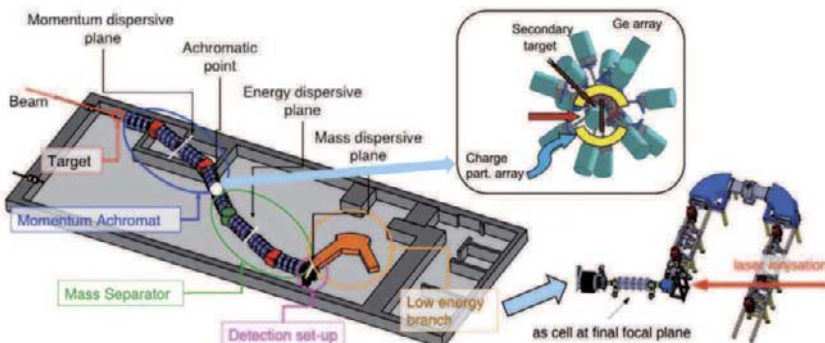


Fig. 12. – A layout of the S3 experimental hall showing examples of three types of experiments possible at the S3 separator spectrometer. The first is using in-flight RIB produced and purified by S3 and detection of reaction products in the final focal plane. The second is using in-flight RIB produced in the first part of S3 and in-beam spectroscopy with EXOGAM array placed in the intermediate focal plane. The third is using gas-cell and high-resolution mass separator placed in the final focus of S3 for the decay spectroscopy of isobarically separated isotopes.

4.1.1. Final focal-plane detectors. Up to five charge states of fusion-evaporation reaction products can be transmitted to the final focal plane of S3 which is of the order of $12 \times 12 \text{ cm}^2$. This implicates a size of an implantation-decay detector or a size of a gas catcher. There will be also possible to reduce the focal-plane size (with poorer mass resolution) for some applications (chemistry, gas trap with laser ionization). The relevant masses will be selected with slits in front of the detection. The S3 focal plane is constituted of several elements: a Time of Flight (ToF), an implantation detector, an electron tunnel and a surrounding gamma-array. This detector set-up is strongly inspired by existing systems like GREAT (University of Jyväskylä) or MUSETT (CEA-Irfu).

4.1.2. Low-energy branch of S3. The low-energy branch of S3 will provide additional selection of the most exotic species that can be produced with the LINAC beams and delivers these isotopes as a 50 keV beam to low-energy experiments located in the S3 hall or the adjacent DESIR experimental area. Taking as an example the ^{100}Sn region, it is clear that isolating at the focal plane of S3 these very rare isotopes will generally require more sophisticated approaches than those used so far. ^{100}Sn will be produced at a rate of a few ions per seconds, separated from the primary beam or other mass isotopes, but will be delivered with about 10^8 ions per second of more abundantly produced mass 100 isobars, all transported by the S3 spectrometer to the focal plane. Existing focal-plane detectors cannot handle such rate and even at lower rates they cannot in general provide useful separation to isolate events connected to ^{100}Sn versus the 10^7 to 10^8 times higher intensity isobars. The approach proposed to handle the high total intensity and provide the required isobar separation is to install a high-intensity gas catcher at the focal plane of the S3 spectrometer, form a high-quality low energy beam from the recoils, and mass separate them with a compact high-resolution isobar separator. This yields a purified low-energy beam of ^{100}Sn , or other isotopes in this area, that can then be transported and studied at will via beta-delayed spectroscopy, mass measurements, or laser spectroscopy.

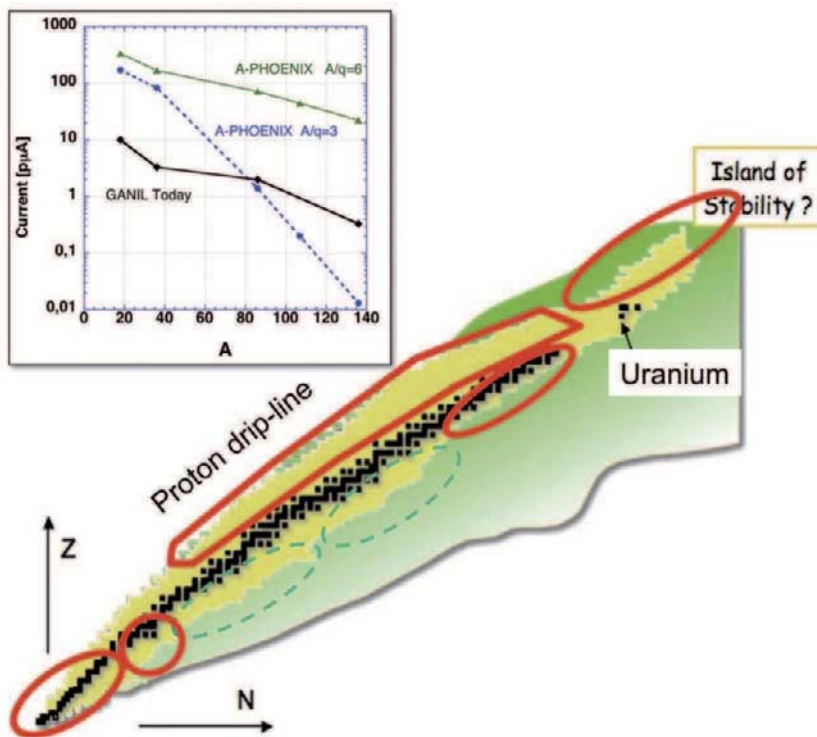


Fig. 13. – Regions of interest at the chart of nuclei accessible for experiments to be performed at S3. Upper part: intensities of stable-ion gaseous beams to be available at the SPIRAL2 LINAC with the $A/q = 3$ and A-Phoenix ECR source (points), with the future $A/q = 6$ and A-Phoenix ECR source (triangles) compared to the beam intensities available today at GANIL (diamonds).

4.1.3. In-flight experiments with S3. Another possibility of experiments at S3 is related to the detection of gamma-rays or charge particles in reactions induced by secondary beams produced and separated in the first part of S3. Thus for example the MUST2 particle detector array surrounding a secondary target placed after momentum achromat section of S3 can be used for transfer reactions. A specific detection system will be foreseen also for Coulex experiments. The compatibility with other detector projects (*i.e.*, PARIS, AGATA, EXOGAM2, MUST2/GASPARD and MAYA/ACTAR) will be ensured for both the intermediate and final focal-plane experiments.

The most important physics topics to be addressed with this top-level equipment and very high stable-ion beams from LINAC are: nuclear haloes and molecules, $N = Z$ nuclei, nuclear structure studied via deep-inelastic collisions as well as physics and chemistry of heavy and superheavy nuclei (fig. 13). The S3 will also provide access to many short-lived isotopes or isotopes of refractory elements which are difficult to produce using ISOL technique. The highest priority for physics of S3 is a delayed decay study of nuclei produced by fusion-evaporation reactions. This topic covers the study of

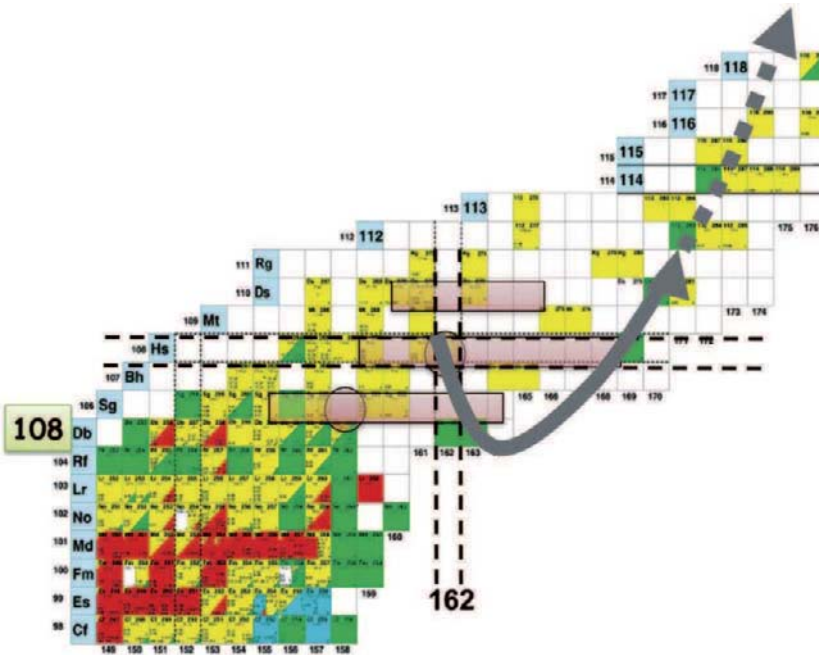


Fig. 14. – An upper-right part of the chart of nuclei. The hashed rectangles correspond to the new isotopes of siborgium, hassium and darmstadtium in the proximity of the neutron number $N = 162$ to be accessible at S3. The arrow indicates a future goal of the S3 facility—production of new elements beyond $Z = 118$.

neutron-deficient nuclei as well as very and super heavy elements. The high production rates will permit detailed studies of nuclei that are today produced only with rates of few per day, either through decay spectroscopy (alpha, proton, electron, gamma...) of ground-state property measurements in ion or atom traps or chemistry apparatus. S3 will be a versatile device, to be used also for studies of light nuclei produced by transfer reactions, or neutron-rich nuclei with deep inelastic scattering and secondary reactions with nuclei produced in the primary target.

4.1.4. Very-heavy nuclei and Superheavy elements (SHE). The high-intensity beams of LINAC will give unprecedented opportunities for the synthesis of new elements, as well as, for detailed studies of the already known elements, in particular it will allow (fig. 14):

- To produce new isotopes from the neutron poor elements produced by cold fusion to the neutron-richer elements of hot fusion, and then obtain some information about their isospin-dependent properties.
- To obtain cross-section measurement systematics to gain insight about the mechanisms of fusion and fission.

- To study chemical properties and, in particular, to elucidate a role of expected relativistic effects on the atomic shell structure of the heaviest elements.
- To get spectroscopic information for elements up to Ds ($Z = 110$) and learn about the evolution of collectivity around the islands of deformation (^{254}No , ^{270}Hs).
- To identify new K-isomers to obtain information about the single-particle states.
- To measure ground-states properties of SHE like their masses, charge radii, etc.

4·1.5. Neutron-deficient nuclei. Fusion evaporation reactions can also produce a wide range of neutron-deficient nuclei with a variety of interesting properties: proton emission, super-allowed beta-decays, shape coexistence, isomers with information on single-particle states and correlations between nucleons. New isotopes with masses in the range 80–200 could be produced. Masses of these nuclei are of interest for the study of the rp-process. Current facilities can fill in some of the gaps in mass measurements, but only a facility like S3 could reach nuclei such as $^{99,100,101}\text{Sn}$, $^{98,99}\text{In}$, $^{95,96}\text{Cd}$. The region around the ^{100}Sn nuclei is of utmost interest, since this nucleus is at the drip line with two closed shells and $N = Z$. It is a benchmark to investigate the states near the Fermi surface and how their wave functions reflect single-particle motion. The high production rates in a combination with the low-energy branch of S3 will open completely new and unique opportunities for this studies.

4·1.6. Neutron-rich nuclei with transfer and deep inelastic reactions. Very high primary beam intensities open also the possibilities of producing neutron rich exotic nuclei, either through the transfer of few nucleons on light nuclei, or with massive transfer for heavier ones. Undoubtedly, the neutron-rich beam intensities produced by SPIRAL2 through U fission will be much higher in all the regions covered by the fission peaks, but it could be possible with S3 to produce nuclei outside these zones, either lighter or heavier. For example multiple nucleon transfer in a $^{136}\text{Xe} + ^{208}\text{Pb}$ reaction can produce neutron-rich nuclei on the ^{208}Pb region and with $^{48}\text{Ca} + ^{208}\text{Pb}$ reaction, neutron-rich nuclei can be significantly produced in the $N = 28$ region. On the light side, the reaction like $^{12}\text{C}(^{13}\text{C}, 2\text{p})^{11}\text{Be}$ can give very high yields (5×10^8 pps) of ^{11}Be , competitive with ISOL-type facilities. The very high intensities on S3 targets will prevent any kind of prompt spectroscopy of these nuclei which is the traditional method to study them. However, as mentioned above, it could be possible to study them in an additional reaction with a secondary target and perform a high cross-section reaction like nucleon transfer or Coulomb excitation.

5. – Experiments with low energy radioactive ion beams

5·1. DESIR. – A completely new experimental hall called DESIR (Decay, excitation and storage of radioactive ions) will be constructed in the framework of the SPIRAL2 project. This hall will be dedicated to experiments with low energy (from 0 to 60 keV)

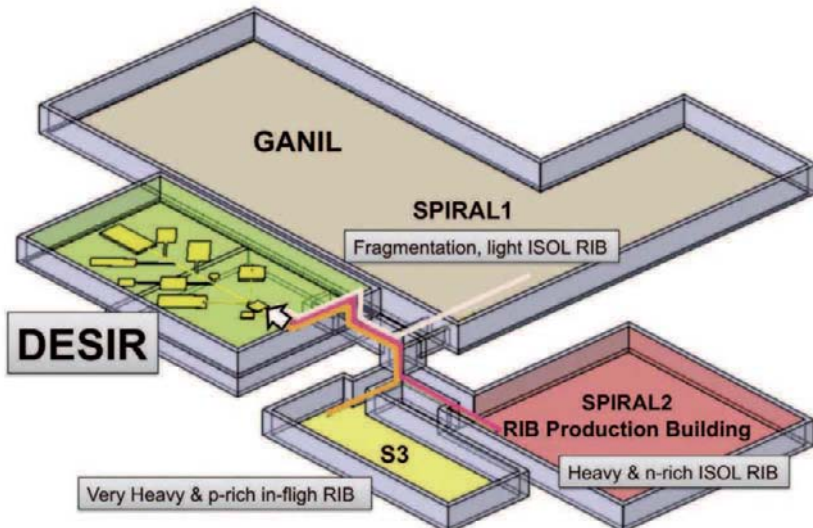


Fig. 15. – A layout showing that nuclei far from stability to be studied at the DESIR facility can be produced at SPIRAL1, SPIRAL2 RIB production building or at S3 facility.

RIB. The physics and the shape of this ambitious facility is developed by a collaboration of more than 100 physicists from 34 institutions from 15 countries [9].

Most of the experiments to be performed at DESIR will determine the fundamental, ground-state properties such as decay mode, half-life, mass, charge radius and shape of very exotic nuclei produced at SPIRAL2. In addition, as shown in fig. 15 DESIR facility can also receive beams from SPIRAL1 and from S3. The fact that DESIR will receive radioactive beams from three different production stations (SPIRAL1, SPIRAL2 and S3) makes it a unique and very versatile facility. The high-intensity and originality of thus produced and studied nuclei far from stability is one of the major advantages of the DESIR facility over others like ISOLDE or TRIUMF.

The DESIR Collaboration proposes the construction of a large experimental hall into which the different beams from the three production sites can be injected and used in world-class experiments. For this purpose, different groups within the DESIR Collaboration have committed to install their equipment, presently under construction in different laboratories across Europe or already used in other laboratories, in the DESIR experimental hall as soon as the hall has been completed. This equipment comprises different ion and atomic traps for high-precision mass measurements, for studies dealing with nucleosynthesis scenarios and the standard model of weak interaction, and for the high-purity preparation of radioactive species for decay studies. The LUMIERE facility, the laser-spectroscopy facility of DESIR, will allow measurements of static properties of the exotic nuclei ground and long-lived isomeric states like their magnetic moment, their quadrupole moment and thus their deformation as well as their spin and parity. The

BESTIOL facility will enable to perform precision measurements in nuclear beta-decay to study fundamental properties like decay modes, half-lives, branching ratios, spins and parities of these exotic nuclei. Finally, the basement of the DESIR facility will contain a highly protected room for high-intensity experiments devoted to material science and industrial applications. The facility layout has been designed in the last two years by the DESIR Collaboration in close collaboration with the SPIRAL2 project management and GANIL. A detailed cost estimate has been made by the DESIR Collaboration and the SPIRAL2 management as well as by the prime contractor in charge of the civil construction of SPIRAL2.

A detailed study of the DESIR facility is presently under way within the framework of the construction Phase 2 of SPIRAL2. This design phase will last until the end of 2011, when construction can begin. After the construction of the infrastructure, *i.e.* the transfer tunnels and the DESIR building (end of 2013), the installation of the beam lines from the production sites to DESIR will commence as well as the installation of the general equipment consisting in a radioprotection monitoring station, stable ion sources coupled to a general-purpose ion buncher for beam preparation, and in experiment facilities (end of 2014). The DESIR facility is expected to go online by 2015.

5.1.1. Physics case of DESIR. The major scientific topics to be addressed at DESIR are: the structure of nuclei near shell closure like in the ^{100}Sn and the ^{132}Sn regions, nuclei near the $N = Z$ line to address nuclear pairing, super-allowed beta-decay, and the astrophysical rp process, properties of nuclei far from stability in the context of the astrophysical r process responsible for the production of a large number of nuclear species in the Universe, heavy and super-heavy elements and the structure of nuclei at the upper end of the periodic table, the study of material properties, work in the framework of the nuclear fuel cycle and much more.

In particular, beta-decay studies can be done with very low beam intensity and therefore are often the first study possible for a new exotic beam. The contribution of beta-decay in the characterization of new nuclei is crucial. Even a simple beta-decay half-life measurement can reveal new phenomena in nuclear structure. As an example, the half-life of ^{11}Li was twice the expected value for p-shell nuclei, suggesting a mixed character of the ground state.

For cases in which the statistics and the purity are high enough so that a full spectroscopic study can be carried out, the probability of β -decay to states of a daughter nucleus provides information on the degree of overlap between the neutron and proton states in the parent and daughter nuclei. When the radioactive decay populates excited states of the daughter nucleus, observation of the radiation associated with their de-excitation yields invaluable spectroscopic information on the energies and characteristics of low-lying excited states. This spectrum of states permits the characterization of the structure of the daughter nucleus concerning its rigidity, deformation and the arrangement of its particles. The identification of new nuclei often opens novel fields of investigation leading to discoveries. Some well-known examples include: nuclei with halos, disappearance of shells, new types of pairing, new regions of deformation. Extremely

neutron-deficient or neutron-rich nuclei are characterized by very high β -decay energies. At the same time, the daughter nuclei have low particle separation energies so that the β -decay may feed excited states that are unbound to emission of nucleons or clusters of nucleons. This mechanism, which occurs for most exotic nuclei, is called β -delayed particle radioactivity. Study of this decay mode already allowed to gain important information on the nuclear structure far from stability. The key point is that if one knows the final state, from the particle spectra one can derive the beta feeding to that state and the associated Fermi or Gamow-Teller (GT) matrix element that give information on the strong interaction within the nucleus. Beta-delayed particle emission has been established for a very long time now and the mechanism governing the decays is quite well understood. In lighter nuclei, the particle emitting states often have an appreciable fraction of the single-particle strength and hence a large width. The distribution of the β -strength in the daughter nucleus determines not only the β half-lives and the rates for β -delayed particle emission and fission but also the shape of the emitted electron/positron and antineutrino/neutrino spectra.

5.1.2. Beta-decay measurements of astrophysical interest. The β -decay studies far off stability are important for astrophysics at least for two reasons: first to infer the abundance of the stable nuclei from the time elapsed at the neutron-rich waiting point nuclei, second to constrain the global duration of the r-process by summing the lifetimes of all isotopic chains to build the heaviest elements in nature like Th, U and Pu. Determinations of half-life and Pn values are especially important at closed shells. The neutron delayed emission smoothens the r abundance curve, as compared to the even-odd staggering observed in the s abundance curve. Short lifetimes would make the building of r-process peaks difficult, but the synthesis of heavier masses easier. At the opposite, long lifetimes would block the process at a given shell closure as the neutron fuel would be exhausted to proceed further. These nuclear structure parameters need to be measured in order to determine whether one r-process could produce the overall mass range of elements or if the abundance curve results from a superposition of several processes. If occurring in the high entropy bubble, the r-process should develop with a short dynamical timescale in order to avoid its suppression by the high neutrino flux of the neutrino-driven wind. Hence, a better knowledge of the β -decay rates at the closed-shells (and especially the evolution of the Gamow-Teller strength $\nu g_{7/2}$ to $\pi g_{9/2}$) and to what extent shells are quenched would enable to deduce if the r-process could occur in such environments. So far the β -decay of ^{130}Cd has shown that the $N = 82$ is probably quenched. In the case of odd nuclei, low-lying excited states could be thermally excited. This could drastically change the lifetime and/or neutron-captures rates of the nuclei involved in the r-process. Therefore energy and spin assignments of low-lying states should also be determined. When the r-process path comes closer to stability, after successive neutron-captures and β -decays at major shell closures, the half-life of the nuclei involved becomes longer. If the neutron flux which prevail in the star is large enough, neutron captures could eventually compete with β -decays. The determination of neutron-capture cross-sections (σn) brings access to the rate of leakage of the r-process towards the next shell closure for a given

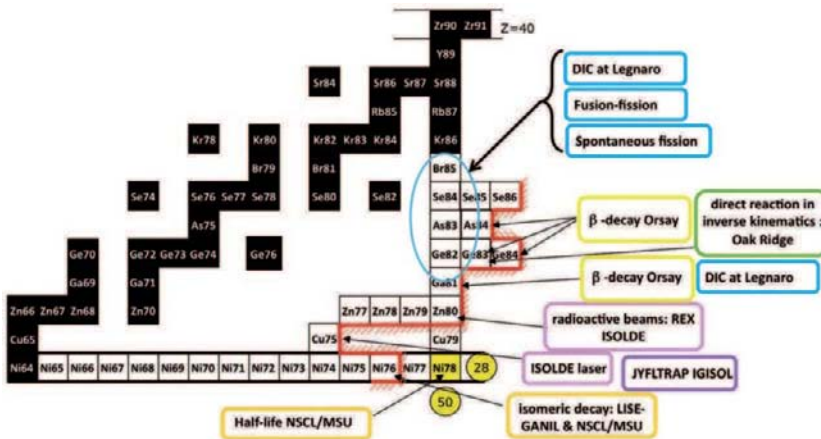


Fig. 16. – Recent experiments on the nuclear structure in the vicinity of ^{78}Ni .

neutron density value. Beta delayed-neutron studies will help to determine the existence of isolated resonance above the neutron-emission threshold in the daughter nucleus, to be used for the determination of neutron capture cross-sections at closed shells.

In the following, an example of β -decay studies in the region of ^{78}Ni which can be performed at DESIR will be shortly presented.

Above ^{78}Ni the natural valence space which opens up corresponds to the filling of the proton fp- $g_{9/2}$ single-particle states and the neutron dgs $N = 4$ shell. This valence space has been extensively studied close to stability, especially with the aim to describe the Zr ($Z = 40$) region and the long known spectacular shape transitions which occur there. In the region from $Z = 28$ to $Z = 40$ and $N = 50$ to $N = 82$, corresponding to very neutron-rich nuclei, only few attempts were made for detailed spectroscopy calculations apart from beyond mean field techniques (restricted to even-even nuclei only). This is partially due to the very limited data available in this largely unknown and experimentally hard to reach region. In particular, the exact neutron single-particle energy sequence and its evolution from stability to $Z = 28$ is still poorly known or understood both from the theoretical and experimental sides. Precise inputs on these evolutions from experiment is necessary and would be extremely valuable in order to perform a correct tuning of the monopole part of the residual interactions used in shell model and start a global description of this mass region. The current status of experiments in this region of the chart of nuclei is summarized in fig. 16. The performed experiments allow to establish that the ground-state spin value of the $N = 51$ odd isotones from ^{83}Ge up to ^{101}Sn is $5/2+$ originating from the occupation of the $\nu 2d_{5/2}$ orbital by the valence neutron. The first $1/2+$ excited state which is known to carry the major part of the $\nu 3s_{1/2}$ strength is seen to decrease continuously from stability towards $Z = 28$. The evolution of the other neutron single-particle states like $\nu 2d^{3/2}$, $\nu 1g_{7/2}$ and $\nu 1h_{11/2}$ remains an open question. The experiments performed at PARRNE, ALTO at IPN Orsay and HRIBF at Oak Ridge

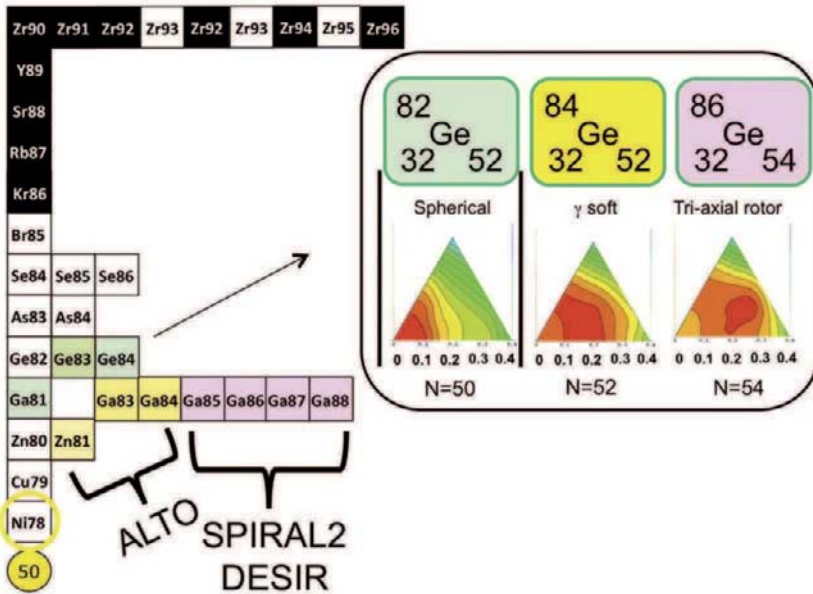


Fig. 17. – A predicted onset of rapidly changing deformation in the even-even neutron-rich germanium isotopes and parent nuclei accessible for the decay-studies at ALTO and SPIRAL2 facilities. The HFB calculation using the Gogny interaction are from O. Perru, thesis Paris-Sud XI (2004) and J. Libert, private communication.

allowed to get the first spectroscopic information in this region. In particular, decays of $^{83,84}\text{Ga}$ and ^{81}Zn , led to propose an existence of a weak coupling structure in the $N = 51$ isotones. A further measurement can be done and, in particular, the predicted in the HFB calculation rapidly changing deformation in the $^{82-86}\text{Ge}$ isotopes (fig. 17) can be studied only with an advent of high production rates of these isotopes at SPIRAL2/DESIR.

6. – Experiments with post-accelerated RIB

Relatively moderate intensities and high cost of radioactive beams impose a use of the most efficient and innovative detection systems such as the magnetic spectrometer VAMOS, the 4II gamma-array EXOGAM and AGATA as well as charged particle detectors like MAYA, MUST 2 and TIARA. Several new concepts of the detection systems (ACTAR, DESIR, FAZIA, GASPARD, PARIS) and a new separator/spectrometer S3 located in dedicated experimental AEL hall were recently proposed (fig. 18). Most of the existing detection systems and the existing experimental area should be adopted to take a full benefit of the high intensity (up to 10^{11} pps) RIB [6].

The following subsections are dedicated to a short description of the above detectors with their respective physics cases.

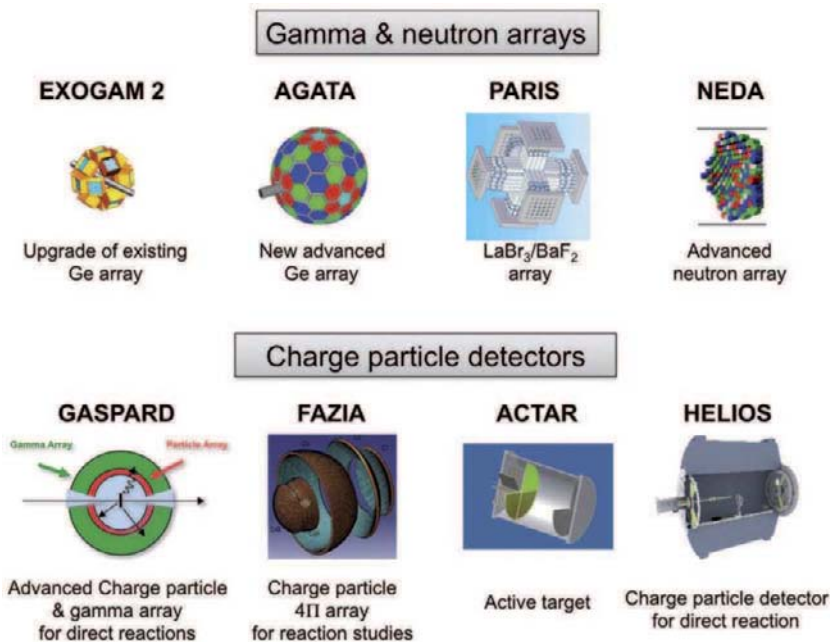


Fig. 18. – New detectors to be used at SPIRAL 2. Upper part: gamma and neutron arrays, lower part charge particles arrays and detectors. The GASPARD array combines a high-efficiency detection of charged particles and gamma-rays.

6.1. EXOGAM 2. – EXOGAM 2 [10] is a project to equip the existing array of sixteen segmented clover HPGe EXOGAM detectors as well as their suppression shield with a highly integrated digital electronics. This will be realized using a new technique in gamma-ray spectroscopy called ADONIS. The main motivations for the new electronics are based on the scientific program of SPIRAL2 and can be summarized by the following requirements:

- much larger throughput (hence efficiency);
- gamma-ray hit localization if possible;
- maintenance issues related to the evolution in technologies of electronic cards.

The 4 year project should lead to the equipment of the all EXOGAM detectors with the new electronics by 2012.

High-resolution gamma-ray spectroscopy is a major tool to understand the structure of atomic nuclei. It is used to explore many different facets of nuclear structure and many different experimental approaches are required to reach this goal. EXOGAM/EXOGAM2 is designed to perform the gamma-ray spectroscopy of exotic nuclei produced by means of reactions induced by radioactive beams from SPIRAL 1 and SPIRAL 2. A feedback

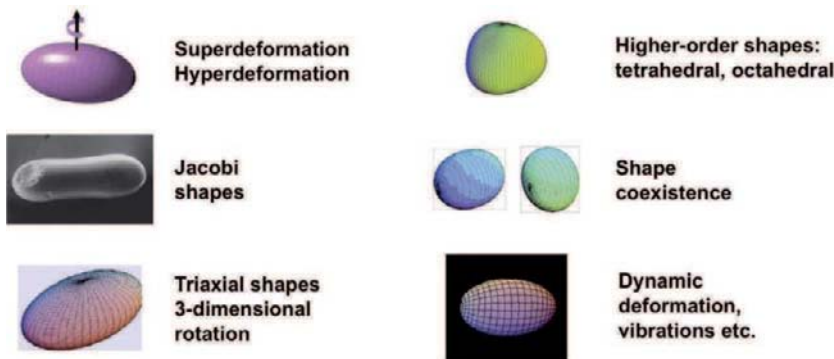


Fig. 19. – A schematic representation of different types of deformation and related phenomena in the rotating nuclei to be studied with high-intensity RIB.

on the use of EXOGAM for the last 5 years indicates that this array is requested in about 40% of the proposals at GANIL and that the array is also frequently used with stable beams at low as well as intermediate energies.

In most of the past experiments, EXOGAM was used in coincidence with an auxiliary detector (the VAMOS spectrometer, the DIAMANT and TIARA charged particle arrays or CD detectors and the Neutron wall). EXOGAM detectors have also been used with LISE spectrometer and eight Clovers have been coupled to the SPEG spectrometer. In the near future, these physics lines of research will be pursued and significantly extended. Indeed in most of the cases the experiments ended up with question marks for two reasons: 1) technical limitations and 2) these first experiments with radioactive beams have just started to reveal what could be done. In the experiments with RIB at SPIRAL2 EXOGAM 2 (as well as AGATA and PARIS) arrays will be used in combination with most of the existing spectrometers, charged particle and neutron arrays.

The physics case for EXOGAM 2 can be roughly classified in the following groups:

- Shapes and shape coexistence in neutron-deficient nuclei (large ground-state deformation in light rare earth nuclei, shape coexistence in Kr isotopes).
- Spectroscopy of $N \sim Z$ nuclei (isospin symmetry breaking in mirror nuclei, single particle excitations around ^{100}Sn , $T = 0$ versus $T = 1$ pairing).
- Shell structure far from stability (spectroscopy of neutron-rich nuclei).
- Nuclear shapes and high-spin spectroscopy (fig. 19).
- Collective modes.
- Nuclear electromagnetic moments.
- Spectroscopy of trans fermium elements.
- Break-up, fusion, elastic and inelastic scattering using RIB.

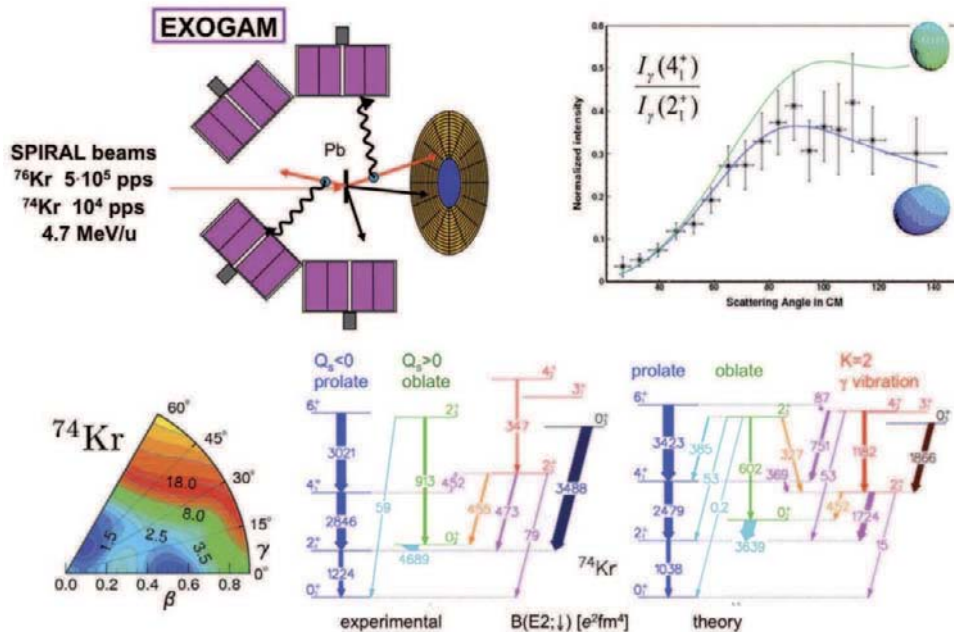


Fig. 20. – An example of the advanced Coulomb excitation experiment with RIB of ^{76}Kr and ^{74}Kr . Upper left: schematic layout of the experimental setup containing EXOGAM germanium array and highly-segmented silicon-strip detectors for the measurement of the recoil scattering angle. Upper right: ratio of the population of the 4^+ and 2^+ states as a function of the scattering angle (points with error bars). Two curves correspond to the prolate (lower curve) and oblate (upper curve) deformation of ^{74}Kr . Lower part: comparison of the experimental and theoretical yrast and non-yrast bands in ^{74}Kr . Clearly different deformations are observed in agreement with the theoretical predictions [11].

The shape of an atomic nucleus is a fundamental property which is governed by a delicate interplay of the macroscopic liquid-drop properties of nuclear matter and microscopic shell effects. Nucleons occupying shape-driving orbitals polarize the nucleus, and the deformed configurations are often stabilized by rotation. Different orbitals can give rise to different types of deformation (prolate, oblate, octupole etc.), resulting in a coexistence of different shapes in the same nucleus. The quadrupole moment, which is accessible experimentally through Coulomb excitation and lifetime measurements, probes the deformation and collective behavior of nuclei. One of the major tools to study the deformation phenomena with RIB is the Coulomb excitation.

A typical experiment of a low-energy Coulomb excitation of exotic nuclei in inverted kinematics with RIB and γ -array as illustrated in fig. 20. In this experiment [11], a shape coexistence in the light krypton isotopes was studied using radioactive ^{74}Kr and ^{76}Kr beams from the SPIRAL 1 facility. The ground-state bands in both isotopes were populated up to the 8^+ state via multi-step Coulomb excitation, and several non-yrast

states were observed. Large sets of matrix elements were extracted for both nuclei from the observed γ -ray yields. Diagonal matrix elements were determined by utilizing the reorientation effect. In both isotopes the spectroscopic quadrupole moments for the ground-state bands and the bands based on excited 0_2^+ states are found to have opposite signs. The experimental data were interpreted within a phenomenological two-band mixing model and model-independent quadrupole invariants are deduced for the relevant 0^+ states using the complete sets of matrix elements and the formalism of quadrupole sum rules. Different deformations are observed for different bands in ^{74}Kr in agreement with the theoretical predictions (see [11] for details).

The same Coulomb excitation technique will be used to explore a huge unexplored experimentally landscape of deformation in very neutron-rich nuclei close to and beyond $N = 50$ and $N = 82$.

6.2. AGATA. – AGATA [12], the first complete 4 Π γ -ray spectrometer solely built from Germanium (Ge) detectors, is based on the novel technique of gamma-ray tracking. AGATA will be an instrument of major importance for nuclear structure studies at the very limits of nuclear stability, capable of measuring γ radiation in a very large energy range (from a few tens of keV up to 10 MeV and more), with the largest possible efficiency and with a very good spectral response. AGATA will be several orders of magnitude more powerful than all current and near-future γ -ray spectrometers. Key parameters of the array are i) a photo-peak efficiency of about 50% at 1 MeV, ii) a position resolution of < 5 mm and iii) a trigger rate of up to 1 MHz. The AGATA Collaboration is intending to use the array at major nuclear physics facilities in Europe like LNL in Legnaro, GSI in Darmstadt and GANIL/SPIRAL1/SPIRAL2 in Caen. The AGATA demonstrator is currently extensively used in experiments at the LNL facility.

The physics case of AGATA at SPIRAL 2 corresponds to a large extent to that presented in the previous section for EXOGAM 2.

6.3. PARIS. – The PARIS [13] array (Photon Array for studies with Radioactive Ion and Stable beams) will provide a high technology for the detection of gamma radiations emitted by exotic nuclei. This 4 Π array of advanced scintillators might be used as a very efficient detector of discrete gamma-rays as well as a gamma calorimeter. The most crucial requirements for the device are the following: The energy resolution shall be of the order of (3-5)% up to photon energies around 40 MeV. The desired accuracy of the entry point location in the (E^*, L) -space demands a resolution of about 5% for the energy sum and below 4 for the γ -ray multiplicity. These numbers imply high efficiency, wide angular coverage and sufficient granularity. High efficiency of the array is essential for all the physics cases due to low cross-sections and/or overwhelming background. In the same line, the angular coverage should be as close as possible to 4 Π . Together with granularity, this feature is even more important if the array is used as a calorimeter. The time-of-flight resolution has to match the sub-nanosecond level in order to remove unwanted background. Scintillator materials of new generation seem to cope with all these requirements. For γ -ray energies above about 2 MeV, relatively low multiplicities

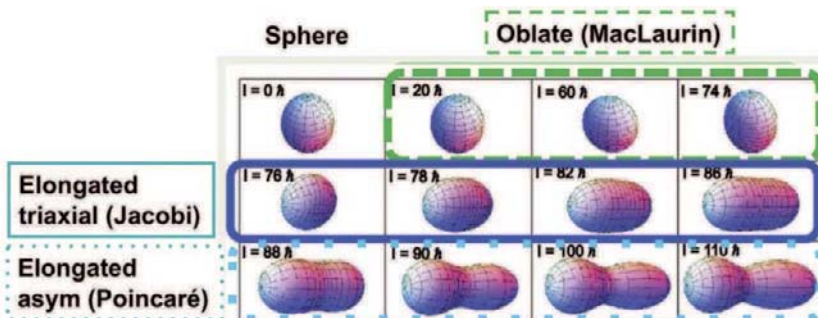


Fig. 21. – Different shape transitions of a fast rotating nucleus as a function of angular momentum.

and fast beams—as is often the case for spectroscopy studies of exotic light neutron-rich nuclei, LaBr_3 scintillators compete with Ge detectors in terms of resolution while being more efficient, what is advantageous for low cross-sections and/or beam intensities. The PARIS prototype detectors (long LaBr_3 crystals and phoswich LaBr_3/CsI or NaI detectors) are currently under tests. These R&D developments and extensive simulation of different possible geometries of the array should lead to a construction of a demonstrator in the coming 2 years.

The very high intensity beams from SPIRAL2 in combination with PARIS and AGATA arrays will allow to study the properties and dynamics of hot exotic nuclei by measuring the high-energy γ -rays associated with the Giant Dipole Resonance (GDR). In particular, intense neutron-rich beams enable fusion-evaporation reactions to be used to populate neutron-rich compound nuclei at very high angular momenta (counterbalanced by the decrease of the fissility). A number of effects may be found in this high angular-momentum regime including the Jacobi or other shape transitions (see fig. 21). The evolution of the GDR strength towards n-rich systems as well as its temperature and spin-dependence will greatly benefit from the future radioactive beams. The extreme N/Z ratios available with SPIRAL2 will significantly deepen our understanding of isospin mixing in heavy $N = Z$ systems. The GDR-decay is also a useful tool for investigating reaction mechanisms. In particular, we are interested in probing the onset of multifragmentation-like phenomena, nuclear viscosity and fusion-quasifission dynamics as well as heavy-ion radiative capture. In some cases, not only the GDR is important but also the multiplicity, sum energy and angular distribution of the emitted γ -rays.

Among the topics mentioned above, PARIS and AGATA detectors will be particularly well suited for the study of intriguing shape evolutions of hot rotating nuclei: Jacobi and Poincaré shape transitions (fig. 21). At sufficiently high temperatures the quantum shell effects in atomic nuclei gradually decrease and eventually vanish and the stability of the corresponding system can be described using the classical notions of the surface tension, that keeps nucleons together, and the competing Coulomb repulsion. However, when the angular momentum of such a system increases, the Coriolis effects become more and more

active so that at a certain critical spin (or the corresponding critical classical rotational frequency) the combined effects of the Coulomb repulsion and centrifugal stretching win the competition with the surface tension and the system becomes quickly unstable. There are two types of instabilities of this kind discussed already in the previous centuries in relation to rotating stellar objects. One of the instabilities that preserve the left-right symmetry is referred to as the Jacobi instability. The name Jacobi shape change is related to the C.G.J. Jacobi predictions for a gravitating rotating object, showing that at a certain angular velocity stellar objects rotating synchronously may change abruptly their shape from a flat ellipsoid with two equal axes, rotating around the short axis, to an elongated triaxial ellipsoid. Other types of transitions, leading to a loss of stability, do break the left-right symmetry. They are referred to as Poincare instability. Such a phenomenon is related to the predictions of H. Poincare for very fast rotating gravitating body, where the elongated triaxial Jacobi shape may change rapidly to a pear shape octupole deformation superposed with other deformations, with increasing rotational velocity. Similar shape transitions are expected to be visible in hot atomic nuclei at very high angular momenta. For example, neutron-rich barium isotopes are among the most suitable nuclei for observing simultaneously both the Jacobi and Poincare shape transitions, their mutual competition, as well as the competition between neutron evaporation and fission. These phenomena are in fact expected to be observed for angular momenta very close to the critical value at which the fission barrier vanishes. The key observable of the shape changes at very high temperatures will be the GDR strength function measured as a function of angular momentum.

6.4. NEDA. – This detector will be an ancillary detector planned to be coupled with a gamma detector array (EXOGAM2, AGATA). It will be used for various nuclear structure studies either on neutron-rich side or neutron-poor side. In addition to a large efficiency and a good neutron-gamma discrimination, NEDA will allow to detect several neutrons simultaneously. Different scintillator materials (like BC537 and BC501A) for individual moduls as well as different geometries of the array (flat (1 Π), spherical (1 Π), staircase (1 Π and 2 Π)) are currently under investigations.

6.5. GASPARD. – GASPARD [14] (GAmma SPectroscopy And paRticle Detection) array will be composed of a 4 Π Silicon array allowing great particle identification capabilities, with a high-efficiency gamma calorimeter (fig. 22). Such combination allows a drastic improvement (factor 10) in excitation energy resolution for bound states as compared to the existing silicon arrays. A gain of a factor 7-8 on the efficiency for detecting coincidence events with respect to the present state-of-the-art ensemble of particle and gamma detection system (MUST2+TIARA+EXOGAM) (fig. 22) will be obtained. The basic concept of the array is to provide the simultaneous detection of recoil particles and γ -rays in a fully integrated and seamless way, with the maximum possible efficiency and solid-angle coverage. Such techniques will gain a large factor in excitation energy resolution compared to particle detection alone and permit the use of thicker targets to increase the available luminosity. For illustration, we recall that using a particle detector

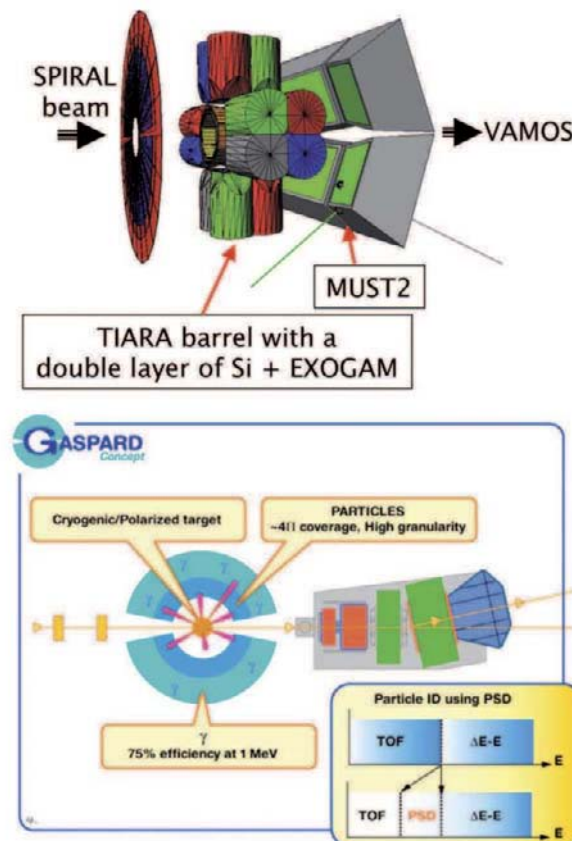


Fig. 22. – The advanced setup used at the GANIL/SPIRAL1 facility for the study of nuclear structure via direct reaction with RIB in inverse kinematics (upper part). A concept of the GASPARD array in combination with the VAMOS spectrometer combining a very high efficiency of gamma-rays and charge particles with a use of cryogenic target (lower part).

such as MUST2, an excitation energy resolution of 300 keV (full width half maximum) is achievable only for certain reactions such as (d, p) and to the condition of using quite thin targets (less than $500 \mu\text{m}/\text{cm}^2$ of CD_2). An improvement by nearly a factor 10 could be obtained for bound states by detecting coincidence gamma-rays using good resolution scintillators such as the newly appeared LaBr_3 crystals which allow ~ 30 keV resolution for 1 MeV gamma-rays. Obviously, this methodology requires a drastic improvement in efficiency for coincidence events with respect to the one provided by the present state-of-the-art ensemble of particle and gamma detection system MUST2+TIARA+EXOGAM (typically 10%). The gamma detection stage must have the best possible efficiency, surpassing that achievable with germanium. GASPARD will offer solid angle coverage close to 4Π for both particles and gamma-rays allowing an efficiency for particle+single gamma coincidence events of 75%. All essential reaction channels will be measured simultane-

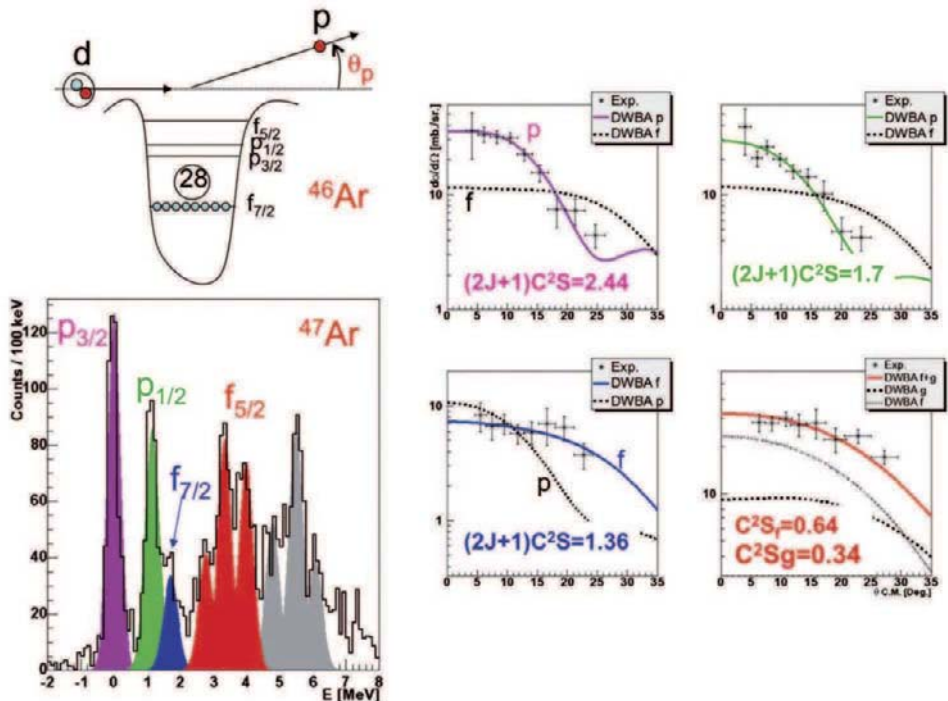


Fig. 23. – An example of the recent nuclear structure studies using (d, p) reaction with the ^{46}Ar beam. Upper left: a principle of the direct reaction measurement. Lower left: the measured proton energy spectrum with the peaks corresponding to the excited p and f orbitals. Right: the measured proton angular distributions and the extracted spectroscopic factors for the $p_{3/2}$, $p_{1/2}$, $f_{7/2}$ and $f_{5/2}$ orbitals, respectively.

ously, together with scattering to both bound and unbound excited states.

An important new feature of the array will be improved particle identification capabilities for low energy light particles (up to $A = 10$). This will allow the use of a more compact device and improve greatly the reaction channel selection, while reducing the need of a spectrograph for the detection of the heavy residue. To achieve this, an option is to implement pulse shape analysis techniques (PSA) with silicon detectors. An R&D program focusing on the PSA with strip silicon detectors is presently being performed in collaboration with physicists of the FAZIA project. The granularity of the gamma detector will be determined by the requirement of balanced contributions between intrinsic and Doppler-induced resolution. The system will be designed such that it will function with both CIME and fragmentation beams. GASPARD will also be designed to couple to ancillary detection systems such as the magnetic spectrometers VAMOS and SPEG. Additional equipment, such as beam tracking detectors as well as cryogenic targets are also in preparation. In particular, the design of the array will integrate a windowless pure $^{1,2}\text{H}$ target such as CHYMENE currently developed by physicists of Irfu/Saclay. Apart

from density increase and background reduction, such a target is appropriate when using high-intensity beams since it minimizes the scattering of beam particles in the forward detectors. GASPARD will also be designed in order to be compatible with the future PARIS and AGATA arrays. Detection of the high energy particles, which is needed for certain reactions, need to be achieved only in limited angle ranges (essentially 5-35 degrees and 60-80 degrees) for which the full energy shall be measured by adding CsI crystals. For the remaining angles the silicon array alone can be used. Recently, a PARIS -GASPARD synergy group has been set up to investigate and implement the synergies between the two projects. This group will investigate the influence of GASPARD Silicon array (detectors, cables, chamber) on the efficiency and resolution for gamma-rays detected by PARIS, and try to find solutions to minimize this effect.

The GASPARD detector will be an ideal tool to study nuclear structure in few-nucleon transfer reactions. Single-neutron transfer reactions such as (d, p) in inverse kinematics at 5–15 MeV/nucleon are an important tool for determining spectroscopic factors. An example of state-of-the-art experiments of this kind is shown in fig. 23. In this study [15], the $N = 28$ shell closure has been investigated via the $^{46}\text{Ar}(d, p)^{47}\text{Ar}$ transfer reaction in inverse kinematics. Energies and spectroscopic factors of the neutron $p_{3/2}$, $p_{1/2}$, and $f_{5/2}$ states in ^{47}Ar were determined and compared to those of the ^{49}Ca isotope. A reduction of the $N = 28$ gap by 330(90) keV and spin-orbit weakening of 10(2)% and 45(10)% for the f and p states, respectively. Such large variations for the f and p spin-orbit splittings could be accounted for by the proton-neutron tensor force and by the density dependence of the spin-orbit interaction, respectively. This contrasts with the picture of the spin-orbit interaction as a surface term only.

Pioneering experiments of this kind with radioactive ion beams of fission fragments have recently been initiated for the reactions $d(^{82}\text{Ga}, p)^{83}\text{Ga}$ and $^9\text{Be}(^{134}\text{Te}, ^8\text{Be})^{135}\text{Te}$ at HRIBF in Oak Ridge. The studies were based on proton detection in the former and γ -ray detection in the latter case, the ^{82}Ga and ^{134}Te beam intensity amounting to 10^4 and 2×10^6 particles/s, respectively. The much higher beam intensities delivered by SPIRAL 2 will allow one to considerably improve the data on spectroscopic factors and to extend them well beyond $N = 82$.

6.6. FAZIA. – The FAZIA [16] project group is composed of more than 10 nuclear physics institutions, which are working in the domain of heavy-ion-induced reactions around and below the Fermi energy (10–100 AMeV). The aim of the project is to build a 4Π array for charged particles, with high granularity and good energy resolution, with A and Z identification capability over the widest possible range. It will use the up-to-date techniques concerning detection, signal processing and data flow, with full digital electronics. The novel pulse shape analysis and detection techniques already developed inside the collaboration, also exploiting a purposely designed digital electronics, are expected to significantly improve the identification capabilities of heavy-ion arrays presently available. The goal is to reach unit-charge identification up to $Z = 70$ and mass identification at the same level up to $A = 50$. Also to that purpose, time of flight will be implemented, with newly developed digital techniques. The expected energy resolution is better than

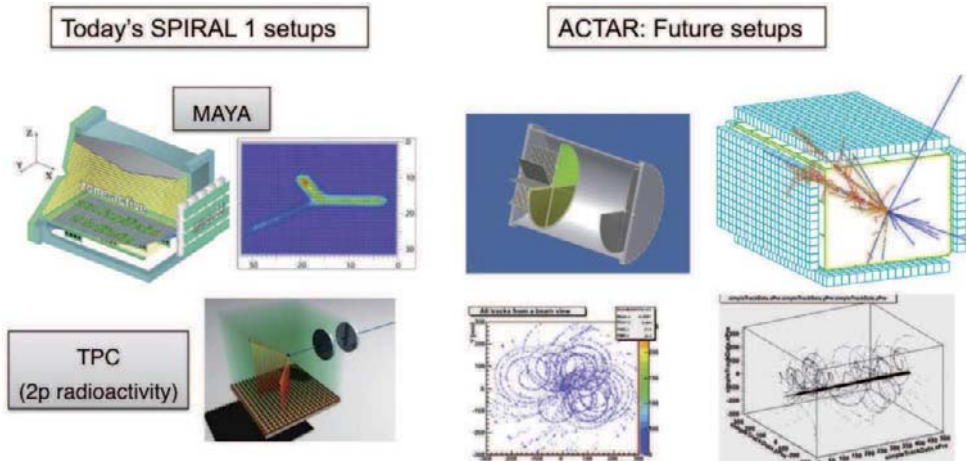


Fig. 24. – Active target (MAYA) and TPC detectors used for RIB-induced reaction and two-proton radioactivity study at GANIL (left). Different geometries and concepts of a new active target detector ACTAR.

one percent in the whole range from few MeV to few GeV. It will be obtained by using Si-Si-Csi telescopes and digital signal processing. The granularity will also be optimized in order to get an angular resolution better than one degree in the laboratory frame (by using silicon-strip detectors for example). Finally, FAZIA will have the maximal coverage of the whole space (at least 90% of 4 π), in order to efficiently perform event-by-event reconstruction of exclusive measurements. Its modularity and portability will also be of paramount importance, since the detector is meant to run in different configurations, possibly with ancillary detectors such as neutron detectors or spectrometers.

The physic case of FAZIA, going beyond the scope of this lecture, is mainly related to the study of the thermodynamics and dynamics of exotic nuclei, exploring the isospin degree of freedom for nuclear matter and its role in the nuclear equation of state, such as for phase transitions or for symmetry energy.

FAZIA is designed to operate at stable and radioactive beams facilities like LNL Legnaro, LNS Catania, GANIL/SPIRAL1/SPIRAL2 and GSI/FAIR in the horizon 2011-2015.

6.7. ACTAR. – ACTAR [17] is a very novel gas detector concept where the gas constitutes both the target and the detection medium. The ACTAR concept (fig. 24) is an advanced version of the MAYA detector [18] developed at GANIL and successfully used in the experiments with RIB in inverse kinematics at GANIL and ISAC II at TRIUMF. Generally, highly inverse reactions will be used where the target gas is p, d, ^3He or ^4He , either pure or mixed with standard detection gases such as isobutane C_4H_{10} . The working principle of the detector is based on the Time Projection Chamber (TPC). The active target should be able to work with beam intensities of up to 10^5 particles/s. Typical cross-sections for the reactions considered are 1–10 mb. With 10^4 particles/s

incident particles, a detector gas pressure of 1 atm, and 100% efficiency, one can expect 20–200 counts/hour. Therefore, within a few days sufficient statistics should be obtained. The lower limit of 10^2 particles/s should give access to a broad range of nuclei very far from stability. The aspects already discussed, such as extremely low energy threshold and the high efficiency, make such a device complementary to more classical detectors such as Si-devices. The research of optimized geometries with simulations of key reactions will be an essential contribution in the study of reactions with low intensity secondary beams. High-quality ASIC electronics should provide a means to a new step forward in the practical realization of such a device.

6.8. HELIOS. – The HELIOS@GANIL Collaboration proposes the development of a HELIOS-like spectrometer [19] for use in conjunction with SPIRAL2 beams. The spectrometer allows for high-resolution studies of nuclear structure via direct reactions induced by short-lived radioactive ion beams. Based on a large superconducting solenoid, outgoing ions are transported in helical orbits to the axis of the device where their energy, position and time of flight are measured. This approach to measuring direct reactions in inverse kinematics offers exceptional Q -value resolution, large acceptance, and simple particle identification. The anticipated range, energy, and intensity of re-accelerated beams from SPIRAL2 are optimal for advancing nuclear structure studies, and a HELIOS-like spectrometer represents an ideal instrument to capitalize on this. A key focus will be to study the structure of neutron-rich nuclei and to map out the evolution of single-particle states over unprecedented ranges of neutron excess.

7. – Conclusions and outlook

The French government approved the construction of SPIRAL 2, a new 200 MEuros RIB facility at GANIL, in 2005. Its construction cost is shared by the French funding agencies CNRS/IN2P3 and CEA/DSM, the regional authorities of Basse-Normandie and international partners. Following recommendations of ESFRI [5], the baseline project as well as new dedicated detectors are supported by the EU FP7 through the Preparatory Phase contract. The construction of the driver accelerator is in progress. The detailed definition of the RIB production building, of the experimental areas and of the dedicated detectors is entering in the final phase. The first beams are expected to be delivered by SPIRAL 2 in 2012. The full GANIL/SPIRAL1/SPIRAL 2 facility will serve a community of about 700–800 users.

The presented lectures provide only a short overview of the very rich and multi-facets scientific objectives and technological challenges of the SPIRAL2 facility. Moreover, the progress of the research in the field of nuclei far from stability is very fast. A regular update of the physics case of the facility is necessary. It is essentially achieved by a regular evaluation of the Letters of Intent and Status Reports of collaborations working on detectors by the Scientific Advisory Committee of SPIRAL2.

Although SPIRAL2 is currently only in the construction phase, future possible upgrades and extensions are already under discussion.

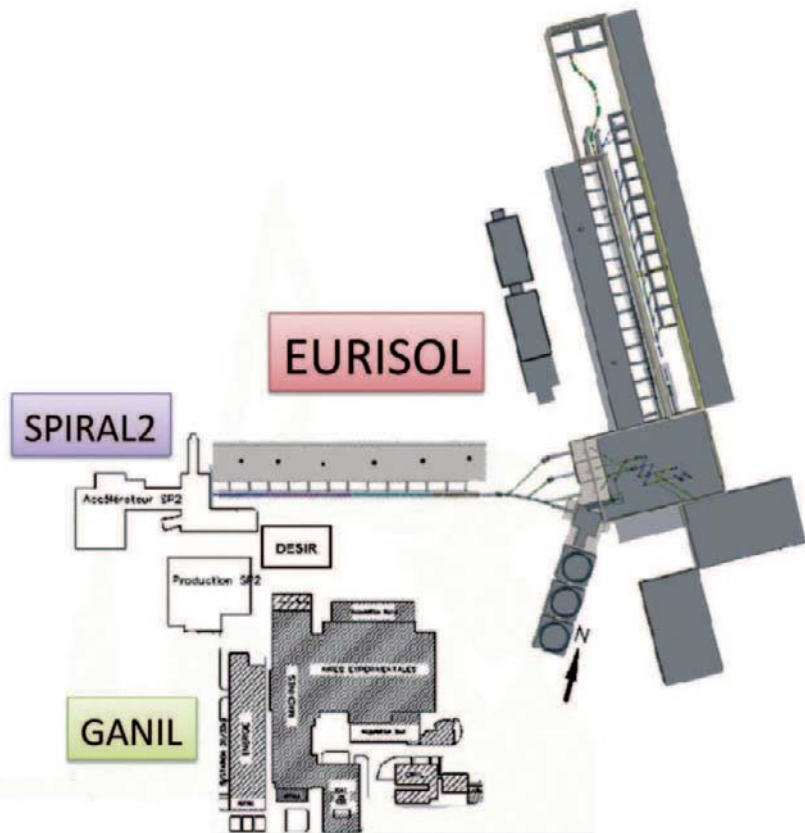


Fig. 25. – A conceptual layout of the EURISOL facility at the site of GANIL. In the displayed configuration the SPIRAL2 LINAC is used as injector of the EURISOL driver accelerator. The layout of the EURISOL experimental halls was adapted from the EURISOL Design Study Report 2010.

During a Conceptual Design Phase the LINAC was the solution chosen for the SPIRAL 2 driver, as it offers better technical options, as well as allowing for a future coordination of GANIL's long-term future in the context of EURISOL. Moreover, the possibility of accelerating both light and heavy ions in the linear accelerator gave a unique and attractive aspect to LINAC allowing for alternative options related to a further extension of the linear accelerator up to intermediate or high (1 GeV for light ions) energies. There are at least two options allowing for a very efficient use of the SPIRAL2 facility as a first step towards EURISOL. The first option implies a use of the SPIRAL2 LINAC as a low-energy part of the EURISOL post-accelerator for RIB. In this case a construction of a new light-ion driver would be necessary to reach the full EURISOL design performances. The second option (fig. 25) assumes that the SPIRAL2 LINAC will serve as a first stage of the EURISOL driver. In this solution a construction of a target area, a new post

accelerator for RIB and the corresponding experimental halls would be necessary. This second option can be constructed in several steps: one of them would consist in a construction of the post-accelerator only which might serve to accelerate the RIB produced by SPIRAL2 to about 150 A MeV . In turn, these beams might be used via fragmentation reactions to reach very efficiently even more neutron-rich nuclei as proposed in the EURISOL Design Study [4].

* * *

This work and the SPIRAL2 Project are supported by the European Union brought the FP7 EU SPIRAL2 Preparatory Phase contract Nr 212692.

REFERENCES

- [1] pro.ganil-spiral2.eu
- [2] pro.ganil-spiral2.eu/spiral2/origin-of-spiral2
- [3] www.nupec.org/index.php?display=lrp2010/main
- [4] www.eurisol.org
- [5] cordis.europa.eu/esfri/publications.htm
- [6] pro.ganil-spiral2.eu/spiral2/what-is-spiral2
- [7] LEDOUX X. *et al.*, pro.ganil-spiral2.eu/spiral2/instrumentation/nfs
- [8] SAVAJOLS H. *et al.*, pro.ganil-spiral2.eu/spiral2/instrumentation/s3/s3-at-ganil
- [9] BLANK B. *et al.*, www.cenbg.in2p3.fr/desir/
- [10] pro.ganil-spiral2.eu/spiral2/instrumentation
- [11] CLMENT E. *et al.*, *Phys. Rev. C*, **75** (2007) 054313.
- [12] www-w2k.gsi.de/agata/
- [13] paris.ifj.edu.pl
- [14] gaspard.in2p3.fr
- [15] GAUDEFROY L. *et al.*, *Phys. Rev. Lett.*, **97** (2006) 092501.
- [16] fazia2.in2p3.fr
- [17] ns.ph.liv.ac.uk/ns-instrum-actar-detector.html
- [18] SAVAJOLS H. *et al.*, *Nucl. Instrum. Methods B*, **266** (2008) 4583.
- [19] www.phy.anl.gov/atlas/helios/index.html

This page intentionally left blank

THE QUARK-GLUON PLASMA AND BEYOND

This page intentionally left blank

Proceedings of the International School of Physics “Enrico Fermi”
Course CLXXVIII “From the Big Bang to the Nucleosynthesis”, edited by A. Bracco and E. Nappi
(IOS, Amsterdam; SIF, Bologna)
DOI 10.3254/978-1-60750-974-5-229

Heavy-ion collisions—Selected topics

F. ANTINORI

INFN, Sezione di Padova - via Marzolo 8, I-35131 Padova, Italy

U. A. WIEDEMANN

Theory Unit, Department of Physics, CERN - CH-1211 Geneva 23, Switzerland

Summary. — We discuss selected topics of the physics of heavy-ion collisions.

1. – Preamble

In July 2010, both of us lectured on the physics of heavy-ion collisions at the International School of Physics “Enrico Fermi” in Varenna, one of us discussing the experimental issues, the other one the theoretical basics and challenges of the field. Those lectures were presented a few months before the start of the LHC heavy-ion programme. Although the properties of the strongly interacting system formed in Pb-Pb collisions at LHC were then unknown, and our lectures were therefore grounded in RHIC phenomenology, the basic foundations of the field, on which we lectured, had been lectured on repeatedly by us and others in the past. When it came to preparing the write-up for the school’s proceedings, we realised that a faithful write-up of our lectures would have been outdated right from the start. Therefore, with the agreement of the school’s directors, we decided to team up to produce the present document, supplementing notes from previous lecture

series (in particular [1]) with experimental and theoretical insights gained from the first LHC heavy-ion run.

2. – Introduction

How do complex, collective phenomena and properties of matter emerge from the fundamental interactions between elementary particles? Heavy-ion physics addresses this question for the theory of strong interactions, Quantum Chromodynamics (QCD), in the regime of extreme energy density.

For idealized situations, such as perfect thermal equilibrium, QCD allows us to calculate the equation of state of strongly interacting matter, the thermodynamic and dissipative properties which govern the propagation of disturbances in that matter, the fate of non-equilibrated structures such as bound states or jets embedded in that matter, the electromagnetic radiation from that matter, etc. An introductory text to heavy-ion physics could start by explaining the calculational techniques and main results of QCD thermodynamics and non-equilibrium dynamics, before focusing on those measurements which are regarded as most suited for a test of QCD at extreme temperature or energy density. A byproduct of such a presentation would be that the text stays close to the historical development of the subject and that it would recall naturally the main motivations for studying nucleus-nucleus collisions.

However, such a presentation would also pose the risk—in particular for the novice in the field—of approaching the rich phenomenology of heavy-ion physics with the unwanted bias of a preconceived theoretical framework. Collective phenomena are not simply there in the data, they need to be established on top of a non-trivial background. And where collective phenomena can be established, they are not necessarily of thermal origin. Moreover, analysis and interpretation of data often require modeling as a bridge between experimental observations and QCD. This multi-step process is at best as reliable as its weakest link. Hence to contribute to research in the field, knowledge about the steps from the first data to a final interpretation appears to be at least as important as the knowledge about the theory of QCD thermodynamics. This motivates our presentation.

The following lectures aim at an introduction to the methods used in heavy-ion physics for establishing collective phenomena and for analysing them in the framework of Quantum Chromodynamics. To the extent possible, our discussion will follow for each class of measurements a three-step logic.

- 1) Establish benchmarks in which collective effects are absent.
- 2) Quantify deviations from these benchmarks.
- 3) Analyse the origin of these deviations.

We introduce different classes of measurements roughly in the order in which they become experimentally accessible in collider experiments. The limited scope of these lectures allows us to touch only a few prominent examples.

3. – Kinematic variables

In this section we shall introduce a few kinematic variables commonly employed in the study of high-energy collisions. We take $c = 1$ and the z -coordinate along the collision axis. The four-momentum of a particle: $p^\mu = (p^0, p^1, p^2, p^3) = (E, \vec{p}) = (E, p_x, p_y, p_z)$ contains the full kinematic information. However, additional variables, derived from the four-momentum, are often used for practical purposes. One such variable is the rapidity y , that we shall now introduce. The relativistic addition of two velocities along the z -axis,

$$(1) \quad \beta = \frac{\beta_1 + \beta_2}{1 + \beta_1 \beta_2},$$

has the same form as the expression for the hyperbolic tangent of a sum:

$$(2) \quad \tanh(y_1 + y_2) = \frac{\tanh(y_1) + \tanh(y_2)}{1 + \tanh(y_1) \tanh(y_2)}.$$

A convenient relativistic extension of the velocity can then be obtained if one introduces a new variable y such that $\beta = \tanh(y)$:

$$(3) \quad y_\beta = y(\beta) = \tanh^{-1}(\beta) = \frac{1}{2} \log \frac{1 + \beta}{1 - \beta}.$$

The rapidity y , which reduces —see (3)— to the velocity β in the non-relativistic limit, has then a simple additive behaviour under a Lorentz transformation along z with a velocity β :

$$(4) \quad y \rightarrow y' = y - y_\beta.$$

In other word, the rapidity y is a relativistic extension of the velocity β , for which, under Lorentz transformation, one can continue to apply the Galilean addition rule also in the relativistic regime. An important corollary is then that rapidity distributions are invariant for a boost along z : $dN(y')/dy' = dN(y)/dy$.

It can be easily verified that

$$(5) \quad y = \frac{1}{2} \log \frac{E + p_z}{E - p_z}.$$

The transverse momentum p_T of a particle is defined as

$$(6) \quad p_T = \sqrt{p_x^2 + p_y^2},$$

and the transverse mass m_T as

$$(7) \quad m_T = \sqrt{m^2 + p_T^2}.$$

Both variables are invariant under Lorentz transformations along the z -axis.

The energy E of a particle can be expressed as

$$(8) \quad E = \sqrt{m_T^2 + p_z^2}.$$

The following useful relations hold:

$$(9) \quad p_z = m_T \sinh(y),$$

$$(10) \quad E = m_T \cosh(y).$$

For high-energy particles, it is possible to approximate the rapidity y by the pseudorapidity η , that only depends on the angle θ of emission of the particle with respect to the z -axis:

$$(11) \quad \eta = -\log \tan(\theta/2) = \frac{1}{2} \log \frac{p + p_z}{p - p_z}.$$

In the ultra-relativistic limit: $p \simeq E$ and therefore $\eta \simeq y$.

The following expressions also hold:

$$(12) \quad p_z = p_T \sinh(\eta),$$

$$(13) \quad p = p_T \cosh(\eta).$$

4. – Invariant cross-sections

The probability for the production of a particle with a certain momentum is often expressed in terms of a differential cross-section. The simple expression for the differential cross-section for production of a particle with momentum (p_x, p_y, p_z) ,

$$(14) \quad \frac{d^3\sigma}{dp_x dp_y dp_z},$$

however, is not Lorentz-invariant, since (taking z along the boost), while dp_x and dp_y are boost invariant, dp_z is not. A Lorentz-invariant expression can be obtained dividing d^3p by the energy E : from (9)

$$(15) \quad dp_z = m_T \cosh(y) dy = E dy,$$

hence, $dp_z/E = dy$ which, as discussed in the previous section, is Lorentz invariant.

An invariant cross-section can then be defined as

$$(16) \quad E \frac{d^3\sigma}{d\vec{p}} = \frac{d^3\sigma}{dp_x dp_y dy}.$$

Using (6) and introducing the azimuthal angle φ ,

$$(17) \quad \varphi = \arctan \frac{p_y}{p_x},$$

the invariant cross-section can be expressed as

$$(18) \quad E \frac{d^3\sigma}{d\vec{p}} = \frac{d^3\sigma}{p_T dp_T d\varphi dy}.$$

Normally, when the distribution does not depend on φ , the azimuthal angle is integrated over, and one of the following, equivalent, expressions is used:

$$(19) \quad E \frac{d^3\sigma}{d\vec{p}} = \frac{1}{2\pi p_T} \frac{d^2\sigma}{dp_T dy} = \frac{1}{\pi} \frac{d^2\sigma}{dp_T^2 dy} = \frac{1}{\pi} \frac{d^2\sigma}{dm_T^2 dy} = \frac{1}{2\pi m_T} \frac{d^2\sigma}{dm_T dy}.$$

5. – Multiplicity distributions

Figure 1 shows the first measurement performed in heavy-ion collisions at the LHC: the number of collisions N_{ev} (“events”) recorded by the ALICE experiment, is plotted as a function of the event multiplicity n in a rather central pseudorapidity interval ($-3.7 < \eta < -1.7$ and $2.8 < \eta < 5.1$). The data were collected during the first Pb-Pb collisions run at the LHC in November 2010, at a collision energy $\sqrt{s_{NN}} = 2.76$ TeV. In contrast to proton-proton collisions, this distribution shows for heavy-ion collisions a prolonged tail towards higher multiplicity. The data are from the first measurement.

We want to establish a benchmark for dN_{ev}/dn , in which collective effects are absent. To this end, we want to determine the multiplicity distribution dN_{ev}/dn under the assumption that particle production in $A + B$ is an incoherent superposition of the collision of an *equivalent* number of nucleon-nucleon collisions. The notion of an “equivalent number” requires a counting rule. In Glauber theory, this counting is based on the number of participants N_{part} , which is the number of nucleons in A and B , which participate in the collision, or it is based on the total number of nucleon-nucleon collisions N_{coll} which occur in the collision of A with B . However, there is no *a priori* reason for not choosing another counting rule, based, for example, on the number of valence quarks rather than nucleons in A and B .

How can we hope to arrive at firm conclusions if the very starting point depends on such an ambiguous choice of what we count? The answer is that the shape of the multiplicity distribution dN_{ev}/dn is rather insensitive to the mechanism of multiparticle production. It is determined largely by purely geometrical information about the overlap of A and B as a function of impact parameter. As a consequence, the shape of dN_{ev}/dn is not useful for determining collective phenomena, but it is a powerful tool for characterizing the geometry of the collision. To determine the latter, it does not matter so much what we count, but it matters that we count. This section gives arguments of why this is so, and it outlines in technical detail how one usually proceeds. And as we shall see

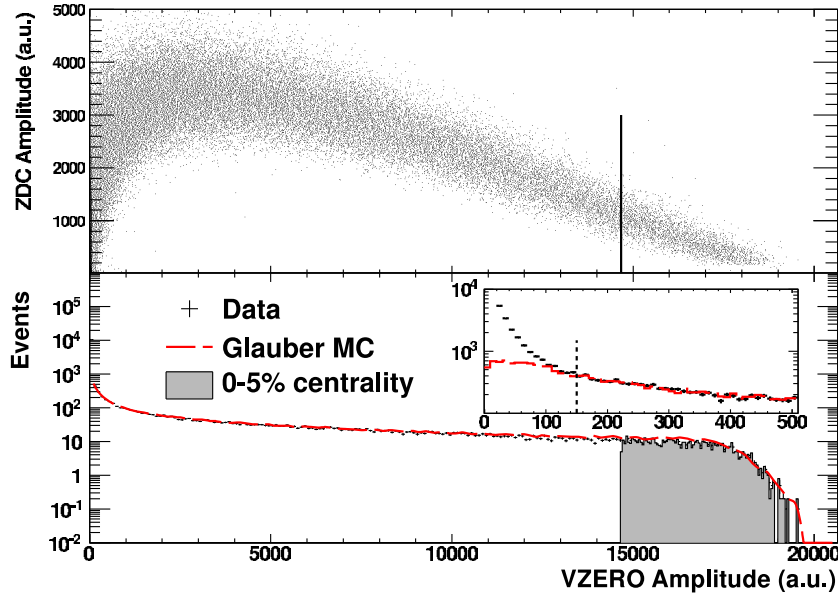


Fig. 1. – One of the first measurements of the LHC heavy-ion program: Upper panel: correlation of the responses in the zero-degree calorimeter ZDC and the VZERO scintillator array in Pb-Pb collisions. The ZDC signal is proportional to the fraction of the initial Pb ion energy that does not partake in the collision (spectators); the VZERO signal is proportional to the number of particles produced in the pseudorapidity range $-3.7 < \eta < -1.7$ and $2.8 < \eta < 5.1$. Lower panel: distribution of the sum of amplitudes in the VZERO scintillator tiles (black histogram); inset shows the low amplitude part of the distribution. The red line shows the fit of the Glauber calculation to the measurement. The fit was performed above the cut indicated in the inset, avoiding the region at low amplitudes dominated by the electromagnetic processes. The shaded area corresponds to the most central 5% of hadronic collisions. Figure taken from [2] (ALICE Collaboration).

in subsequent sections, looking at other measurements as a function of geometrical information about the collision can discriminate collective phenomena from an underlying background.

5.1. Glauber theory. – The distribution of nucleons in a nucleus A is characterized by the nuclear density $\rho_A(\vec{r})$. This density depends on the 3-dimensional radius \vec{r} . We set its norm to unity, $\int d\vec{r} \rho_A(\vec{r}) = 1$. At high centre-of-mass energies, the spherical nucleus is Lorentz-contracted along the beam direction z and what matters is the projection of the nuclear density on the plane of transverse impact parameter b . This transverse density is given by the nuclear profile function

$$(20) \quad T_A(\mathbf{b}) = \int_{-\infty}^{\infty} dz \rho(\mathbf{b}, z).$$

The nucleon-nucleon interaction can be characterized by its inelastic cross-section $\sigma_{nn}^{\text{inel}}$, which we write differential in impact parameter, $\int d\mathbf{r} \sigma(\mathbf{r}) = \sigma_{nn}^{\text{inel}}$. We now discuss nucleon-nucleus (n-A) and nucleus-nucleus (A-B) collisions as incoherent superpositions of nucleon-nucleon collisions.

5.1.1. Nucleon-nucleus (n-A) collisions. For an n-A collision at impact parameter \mathbf{b} , the probability that the projectile nucleon n interacts with the i -th target nucleon at transverse position \mathbf{s}_i^A , $i \in [1, A]$, is

$$(21) \quad p(\mathbf{b}, i) = \int d\mathbf{s}_i^A T_A(\mathbf{s}_i^A) \sigma(\mathbf{b} - \mathbf{s}_i^A) \simeq T_A(\mathbf{b}) \sigma_{nn}^{\text{inel}}.$$

Here, $T_A(\mathbf{b})$ is the number of nucleons at impact parameter \mathbf{b} . We assumed in the second step of (21) that the n-n cross-section is very small compared to the transverse area of the nucleus, and that the differential cross-section can be written as

$$(22) \quad \sigma(\mathbf{b} - \mathbf{s}) \simeq \sigma_{nn}^{\text{inel}} \delta^{(2)}(\mathbf{b} - \mathbf{s}).$$

We shall adopt this approximation throughout our discussion. The one-interaction probability (21) is independent of the index i , $p(\mathbf{b}, i) = p(\mathbf{b})$. It determines the probability $P(n, \mathbf{b})$ that the nucleon undergoes exactly n interactions with nucleons inside A ,

$$(23) \quad P(n, \mathbf{b}) = \binom{A}{n} [1 - p(\mathbf{b})]^{A-n} p(\mathbf{b})^n.$$

From this, one calculates the average number of nucleon-nucleon collisions in an n-A collision at impact parameter \mathbf{b} ,

$$(24) \quad \overline{N}_{\text{coll}}^{nA}(\mathbf{b}) = \sum_{n=0}^A n P(n, \mathbf{b}) = A T_A(\mathbf{b}) \sigma_{nn}^{\text{inel}}.$$

In n-A collisions, the number of collisions is always one less than the number of nucleons participating in the collisions, so

$$(25) \quad \overline{N}_{\text{part}}^{nA}(\mathbf{b}) = 1 + \overline{N}_{\text{coll}}^{nA}(\mathbf{b}).$$

We spell this out since it will be different in A-B collisions. The inelastic n-A cross-section $\sigma_{nA}^{\text{inel}}$ is given by the probability $[1 - P(0, \mathbf{b})]$ that some interaction occurs at impact parameter \mathbf{b} , integrated over the impact parameter,

$$(26) \quad \sigma_{nA}^{\text{inel}} \equiv \int d\mathbf{b} [1 - P_0(\mathbf{b})] \simeq \int d\mathbf{b} \left[1 - \left[1 - T_A(\mathbf{b}) \sigma_{nn}^{\text{inel}} \right]^A \right].$$

In the so-called optical limit, $A \gg 1$, we can exponentiate the integrand,

$$(27) \quad \sigma_A(\mathbf{b}) = \left[1 - \left[1 - T_A(\mathbf{b}) \sigma_{nn}^{\text{inel}} \right]^A \right] \simeq \left[1 - \exp \left[-A T_A(\mathbf{b}) \sigma_{nn}^{\text{inel}} \right] \right].$$

5.1.2. Nucleus-nucleus (A-B) collisions. In an A-B collision at impact parameter \mathbf{b} , a nucleon at transverse position \mathbf{s}^B in nucleus B will undergo on average $\bar{N}_{\text{coll}}^{nA}(\mathbf{b} - \mathbf{s}^B) = A T_A(\mathbf{b} - \mathbf{s}^B) \sigma_{\text{nn}}^{\text{inel}}$ collisions, see eq. (24). So, the average number of nucleon-nucleon collisions in A-B at impact parameter \mathbf{b} is

$$(28) \quad \bar{N}_{\text{coll}}^{AB}(\mathbf{b}) = B \int d\mathbf{s}^B T_B(\mathbf{s}^B) \bar{N}_{\text{coll}}^{nA}(\mathbf{b} - \mathbf{s}^B) = A B T_{AB}(\mathbf{b}) \sigma_{\text{nn}}^{\text{inel}}.$$

Here, we encounter for the first time the nuclear overlap function

$$(29) \quad T_{AB}(\mathbf{b}) \equiv \int d\mathbf{s} T_B(\mathbf{s}) T_A(\mathbf{b} - \mathbf{s}),$$

which plays a central role in describing the transverse geometry of heavy-ion collisions. Other quantities of interest can be calculated by starting with the probability that a nucleon at position \mathbf{s}^B in B participates in the collision. If the nucleons in A are in the configuration $\{\mathbf{s}_i^A\}$, then the probability that the j -th nucleon at position \mathbf{s}_j^B in B interacts with at least one nucleon in A is

$$(30) \quad p(\mathbf{s}_j^B, \{\mathbf{s}_i^A\}) = 1 - \prod_{i=1}^A [1 - \sigma(\mathbf{s}^B - \mathbf{s}_i^A)].$$

The probability for nucleons in an arbitrary configuration $\{\mathbf{s}_i^A\}$ that in the collision of B with A at impact parameter b exactly m nucleons of B participate and $(B-m)$ do not is

$$(31) \quad P_B(m, \mathbf{b}) = \binom{B}{m} \left(\prod_{i=1}^A \prod_{j=1}^B \int d\mathbf{s}_i^A d\mathbf{s}_j^B T_A(\mathbf{s}_i^A) T_B(\mathbf{s}_j^B - \mathbf{b}) \right) \\ \times p(\mathbf{s}_1^B, \{\mathbf{s}_i^A\}) \dots p(\mathbf{s}_m^B, \{\mathbf{s}_i^A\}) [1 - p(\mathbf{s}_{m+1}^B, \{\mathbf{s}_i^A\})] \dots [1 - p(\mathbf{s}_B^B, \{\mathbf{s}_i^A\})].$$

From this, many other quantities of interest can be calculated in a straightforward way (see Question 1 below). For instance, the inelastic cross-section is defined by the probability that something happens at impact parameter \mathbf{b} , integrated over impact parameter

$$(32) \quad \sigma_{AB}^{\text{inel}} \equiv \int d\mathbf{b} [1 - P_B(0, \mathbf{b})] = \int d\mathbf{b} \left[1 - [1 - T_{AB}(\mathbf{b}) \sigma_{\text{nn}}^{\text{inel}}]^{AB} \right].$$

We can invoke the optical limit $AB \gg 1$ to exponentiate the integrand

$$(33) \quad \sigma_{AB}(\mathbf{b}) = [1 - P_B(0, \mathbf{b})] \simeq 1 - \exp [-A B T_{AB}(\mathbf{b}) \sigma_{\text{nn}}^{\text{inel}}].$$

We find that for the inelastic cross-section as well as for the average number of collisions, the nuclear overlap function plays the role which the nuclear profile function played for n-A collisions; more precisely, the expressions for n-A and A-B collisions are related by

the substitution $A T_A \rightarrow A B T_{AB}$. The situation is different for the average number of participants. The average number of nucleons in B participating in an A-B collision at impact parameter b is

$$(34) \quad \frac{1}{1 - P_B(0, \mathbf{b})} \sum_{m=1}^B m P_B(0, \mathbf{b}) = \frac{B \sigma_A(\mathbf{b})}{1 - P_B(0, \mathbf{b})}.$$

Here, the denominator keeps count of the fact that only those encounters of A with B are registered, in which something is happening. The average number of participating nucleons in A and B is obtained by symmetrizing this expression

$$(35) \quad \bar{N}_{\text{part}}^{AB}(\mathbf{b}) = \frac{B \sigma_A(\mathbf{b})}{\sigma_{AB}(\mathbf{b})} + \frac{A \sigma_B(\mathbf{b})}{\sigma_{AB}(\mathbf{b})}.$$

Parametrically, the average number of participants in A-A grows proportional to A , the average number of collisions grows proportional to $A^{4/3}$ (see Question 2 below for a simple example).

To turn the above equations into numbers, we have to specify the nuclear density $\rho(\mathbf{r})$ and the inelastic nucleon-nucleon cross-section σ_{NN} . For the nuclear density of sufficiently large nuclei, $A > 16$, one commonly uses the Woods-Saxon parametrization

$$(36) \quad \rho(\mathbf{r}) = \rho_0 \frac{1}{(1 + \exp[-\frac{r-R}{c}])}, \quad R = 1.07 A^{1/3} \text{ fm}, \quad c = 0.545 \text{ fm}.$$

More precise parametrizations can be found for instance in ref. [3]. The inelastic nucleon-nucleon cross-section is $\sigma_{\text{nn}}^{\text{inel}} \sim 60 \text{ mb}$ at $\sqrt{s} \sim 5 \text{ TeV}$.

Questions:

- 1) Derive eqs. (32) and (34), starting from eq. (31).

Answer: In terms of the shorthand $\bar{p}(\mathbf{b}, \{\mathbf{s}_i^A\}) \equiv \int d\mathbf{s}_j^B T_B(\mathbf{s}_j^B - \mathbf{b}) p(\mathbf{s}_j^B, \{\mathbf{s}_i^A\})$, the probability $P_B(m, \mathbf{b})$ of eq. (31) reads

$$P_B(m, \mathbf{b}) = \left(\prod_{i=1}^A \int d\mathbf{s}_i^A T_A(\mathbf{s}_i^A) \right) \binom{B}{m} \bar{p}(\mathbf{b}, \{\mathbf{s}_i^A\})^m [1 - \bar{p}(\mathbf{b}, \{\mathbf{s}_i^A\})]^{B-m}.$$

Using $\sum_{m=0}^B m \binom{B}{m} \bar{p}^m [1 - \bar{p}]^{B-m} = B \bar{p}$, this leads to

$$\sum_{m=0}^B m P_B(m, \mathbf{b}) = B \left(\prod_{i=1}^A \int d\mathbf{s}_i^A T_A(\mathbf{s}_i^A) \right) \int d\mathbf{s}^B T_B(\mathbf{s}^B - \mathbf{b}) p(\mathbf{s}^B, \{\mathbf{s}_i^A\}).$$

- 2) Consider a cylindrical nucleus of radius R , length $2R$ and nuclear density $\rho(\mathbf{b}, z) = \frac{1}{2\pi R^3} \Theta(R - |\mathbf{b}|) \Theta(2R - z)$. Assume that $R \propto A^{1/3}$, the nuclear number of the cylindrical nucleus A .

Calculate the nuclear profile function of A and the nuclear overlap function for $A + A$.

Determine the average number of participants and the average number of collisions at impact parameter \mathbf{b} . How does $\bar{N}_{\text{part}}(\mathbf{b})$ and $\bar{N}_{\text{coll}}(\mathbf{b})$ scale with A ?

Answer: $T_A(\mathbf{b}) = \frac{1}{\pi R^2} \Theta(R - |\mathbf{b}|)$, $T_{AA}(\mathbf{b}) = \frac{1}{(\pi R^2)^2} S_{AA}(\mathbf{b})$, where $S_{AA}(\mathbf{b}) \equiv R^2 (\beta - \sin \beta)$, $\beta \equiv 2 \arccos \frac{b}{2R}$. It follows that $\bar{N}_{\text{coll}}(\mathbf{b}) = \sigma_{nn} A^2 T_{AA}(b) \sim A^{4/3}$ and $\bar{N}_{\text{part}}(\mathbf{b}) = 2A \int d\mathbf{s} T_A(\mathbf{s}) [1 - [1 - \sigma_{nn} T_A(\mathbf{s} - \mathbf{b})]^A] \simeq \frac{2A}{\pi R^2} S_{AA}(\mathbf{b})$ and so $\bar{N}_{\text{part}}(\mathbf{b}) \sim A$.

5.2. Characterizing the collisions geometry by multiplicity distributions. – Phenomenologically, one finds that soft-particle production in nuclear collisions scales approximately with $\bar{N}_{\text{part}}^{AB}$ over a wide range of centre-of-mass energy [4]. On the other hand, rare hard processes scale with the number of hard partonic collisions, which is proportional to $\bar{N}_{\text{coll}}^{AB}$.

Let us consider a simple model for the average event multiplicity $\bar{n}_{AB}(\mathbf{b})$ produced in a given pseudo-rapidity region in a nucleus-nucleus collision at impact parameter \mathbf{b} . One can take $\bar{n}_{AB}(\mathbf{b})$ proportional to the mean multiplicity \bar{n}_{nn} of a nucleon-nucleon collision at the same centre-of-mass energy. This is consistent with the assumption that $\bar{n}_{AB}(\mathbf{b})$ arises from the incoherent superposition of an equivalent number of n-n collisions. A model parameter $x \in [0, 1]$ allows us to vary the “equivalent number of n-n collisions” between $\bar{N}_{\text{part}}^{AB}(\mathbf{b})$ and $\bar{N}_{\text{coll}}^{AB}(\mathbf{b})$,

$$(37) \quad \bar{n}_{AB}(\mathbf{b}) = \left(\frac{1-x}{2} \bar{N}_{\text{part}}^{AB}(\mathbf{b}) + x \bar{N}_{\text{coll}}^{AB}(\mathbf{b}) \right) \bar{n}_{nn}.$$

The choice $x = 0$, which implies scaling of event multiplicities with the number of participants, is known as the “wounded nucleon model”. It deserves a special name since total event multiplicities scale approximately proportional to $\bar{N}_{\text{part}}^{AB}$ over a wide range of centre-of-mass energy. Varying the model parameter x (within and outside the range favoured by data), we can test the sensitivity of a measurement to details of the mechanism of multi-particle production⁽¹⁾.

If we had a dynamical model of soft-particle production, we could calculate the dispersion d of the mean $\bar{n}_{AB}(\mathbf{b})$. The present set-up does not allow us to do so, and the dispersion d is just another model parameter, which we take to be of order unity. This specifies the probability $P(n, \mathbf{b})$ to find a multiplicity n in a particular collision at impact

⁽¹⁾ In relation (37), the correspondence of \bar{n}_{nn} with the n-n multiplicity at the same energy, although an ingredient of the original wounded nucleon model, is normally not required in Glauber modeling: in practice \bar{n}_{nn} is left as a free parameter determining the maximum value of the A-B multiplicity.

parameter \mathbf{b} , if the average event multiplicity is $\bar{n}_{AB}(\mathbf{b})$,

$$(38) \quad P(n, \mathbf{b}) = \frac{1}{\sqrt{2\pi d \bar{n}_{AB}(\mathbf{b})}} \exp \left[-\frac{(n - \bar{n}_{AB}(\mathbf{b}))^2}{2 d \bar{n}_{AB}(\mathbf{b})} \right].$$

The event multiplicity distribution dN_{ev}/dn is obtained by integrating this probability over the impact parameter

$$(39) \quad \frac{dN_{\text{ev}}}{dn} = \int d\mathbf{b} P(n, \mathbf{b}) \left[1 - (1 - \sigma_{\text{nn}} T_{AB}(\mathbf{b}))^{AB} \right].$$

Here, the last term in the brackets denotes the probability that an inelastic process occurs, see eq. (32). Equation (39) expresses the event multiplicity distribution as a function of the n-n cross-section, the model (37) for the event multiplicity (here defined in terms of $\bar{n}_{AB}(\mathbf{b})$ and its dispersion d), and geometrical information encoded in the nuclear overlap function $T_{AB}(\mathbf{b})$. This information is fully specified by eq. (36) and the subsequent text.

The so-called “analytical” Glauber model or wounded nucleon model is defined by the multiplicity distribution (39) for a pure $\bar{N}_{\text{part}}^{AB}$ -scaling in (37). If one treats the maximal total event multiplicity as a fit parameter, then this analytical Glauber model provides a good description of $\frac{dN_{\text{ev}}}{dn}$ for nucleus-nucleus collisions ranging from AGS energies ($\sqrt{s_{\text{NN}}} > 1 \text{ GeV}$) to LHC energies. For a instance, a comparison of (39) to RHIC data can be found in ref. [6]. “Glauber Monte Carlo” (MC) models differ from the analytical Glauber described here by sampling the nuclear profile functions with MC techniques as distributions of a fixed number A of nucleons. For a sufficiently large number of participants, the difference between “Glauber MC” and “analytical Glauber” becomes negligible for the calculation of $\frac{dN_{\text{ev}}}{dn}$. However, Glauber MCs have the advantage that fluctuations in the shape of the incoming projectile wave function can be included in the modeling. As seen in fig. 2, such fluctuations can lead on an event-by-event basis to spatial anisotropies that would be forbidden by the $T_{AB}(\mathbf{b}) = T_{AB}(-\mathbf{b})$ reflection symmetry of the average nuclear overlap. Possible measurable signatures of such fluctuations are actively investigated currently (for further study, see ref. [5]).

We come now to a crucial observation: A detailed analysis of (39) shows that *the shape of $\frac{dN_{\text{ev}}}{dn}$ depends largely on the geometrical information encoded in $T_{AB}(\mathbf{b})$, and is rather insensitive to assumptions about the microscopic dynamics underlying soft-particle production.* This can be checked by varying the dispersion d or even by changing the value of σ_{nn} . In all these cases, the shape of $\frac{dN_{\text{ev}}}{dn}$ changes only mildly, if one adjusts the maximal multiplicity found in the most central collision by a fit parameter. Establishing this observation is left as an exercise. One can also vary the parameter x which interpolates in (37) between N_{part} - and N_{coll} -scaling. One will find that a significant N_{coll} -contribution tends to a somewhat steeper distribution of $\frac{dN_{\text{ev}}}{dn}$, since it enhances the multiplicity in central events compared to peripheral events. For small values $x < 0.1$, however, also this effect is relatively mild [6].

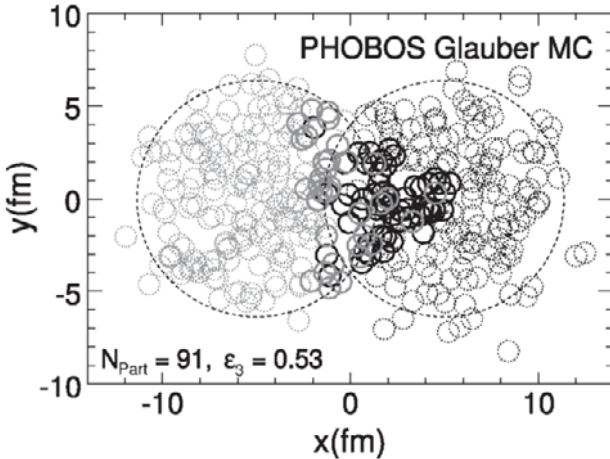


Fig. 2. – Glauber MC simulation of a semi-peripheral collision of two Au-nuclei. Nucleons of the two nuclei are depicted by black and grey circles, respectively. Due to fluctuations in the incoming projectile wave functions, the geometrically active region has in this particular event a triangular shape that is very different from the almond-shaped average nuclear overlap T_{AB} . Figure taken from ref. [5].

5.3. Slicing-up multiplicity distributions. – From the study described above, we conclude that geometrical rather than dynamical information dominates the shape of $\frac{dN_{\text{ev}}}{dn}$. As a consequence, the measurement of $\frac{dN_{\text{ev}}}{dn}$ is not well suited to discriminate between different models of multi-particle production, but it is a powerful tool for characterizing centrality classes. The standard procedure is as follows: the distribution $\frac{dN_{\text{ev}}}{dn}$ is sliced up in segments, 0–5%, indicating, for example, those five per cent of all collected events which have the highest event multiplicity, see the left-hand side of fig. 3. These multiplicity classes $n \in [n_0, n_0 + \Delta n]$ are then related to centrality classes, that is to ranges of impact parameter $b \in [b_0, b_0 + \Delta b]$ of the collision. Because of the dispersion of the event distributions in n and b , an event sample at fixed multiplicity will always contain collisions over a finite range of impact parameter. Centrality and multiplicity are correlated, but the accuracy of an event-by-event determination of the impact parameter is limited by the dispersion. To check how accurately the impact parameter can be determined, one can integrate (39) over a finite range of impact parameter, $b \in [b_0, b_0 + \Delta b]$ and compare the resulting event distribution with the corresponding slice on the left-hand side of fig. 3. This is left as an exercise.

One often characterizes centrality classes by quoting the average number of participants in that centrality class,

$$(40) \quad \langle N_{\text{part}}^{AB} \rangle_{[n_0, n_0 + \Delta n]} \equiv \frac{\int_{n_0}^{n_0 + \Delta n} dn \int d\mathbf{b} P(n, \mathbf{b}) \left[1 - (1 - \sigma_{\text{nn}} T_{AB}(\mathbf{b}))^{AB} \right] N_{\text{part}}(\mathbf{b})}{\int_{n_0}^{n_0 + \Delta n} dn \int d\mathbf{b} P(n, \mathbf{b}) \left[1 - (1 - \sigma_{\text{nn}} T_{AB}(\mathbf{b}))^{AB} \right]}.$$

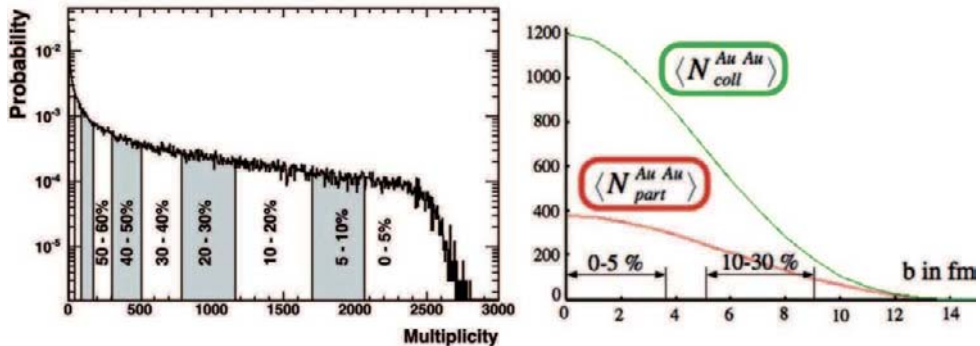


Fig. 3. – Left: a typical event multiplicity distribution of ALICE for uncorrected multiplicity, sliced up in centrality classes. Figure taken from ref. [7]. Right: the correlation of the average number of participants and the average number of collisions in a centrality class to the impact parameter in that centrality class. The range of impact parameter, corresponding to 0–5% and 10–30% centrality is indicated.

A similar average can be defined for the number of collisions. The correlation between this average and the impact parameter of the collision is shown on the right-hand side of fig. 3. We note in particular that selecting the 5% most central events in Au-Au collisions amounts to selecting an event sample with an impact parameter up to $|b| < 3.5$ fm. Since the rate of nucleus-nucleus collisions at impact parameter b is proportional to $b db$, there are more collisions at relatively large impact parameter, and the yield of the most central collisions is geometrically suppressed. So, even data from the most central event class contain collisions at significant finite impact parameter.

At the end of this section, it is appropriate to recall the uncertainties and assumptions entering the characterization of centrality classes. Lacking a dynamical model of soft-hadron production, we have started from the simple ansatz (37) for the average event multiplicity in a centrality class. Within this framework, we have established that the shape of $\frac{dN_{\text{ev}}}{dn}$ is mainly sensitive to the centrality, that is to the impact parameter of the collision, and that it is rather insensitive to details of the model of multiplicity production. We have then tacitly assumed that this holds for all realistic models of multiparticle production; then, $\frac{dN_{\text{ev}}}{dn}$ is a model-independent tool for the measurement of the impact parameter of the collision. Though this assumption is reasonable, it remains an assumption.

In particular, with increasing centre-of-mass energy, it is conceivable that novel mechanisms of multiparticle production contribute significantly to the event multiplicity. So, even if the relation between multiplicity and centrality of nucleus-nucleus collisions is well established at some energy scale, cross-checks at higher centre-of-mass energies are wanted to put the use of Glauber theory for the centrality determination on a firm footing. One experimental cross-check is to measure the energy E_F of those fragments of a nuclear projectile, which stay at projectile rapidity. These fragments should correspond

to those “spectator” nucleons, which did not participate in the collision, and thus

$$(41) \quad E_F = \left(A - \frac{1}{2} N_{\text{part}}(\mathbf{b}) \right) \frac{\sqrt{s_{nn}}}{2}.$$

This correlation between $N_{\text{part}}(\mathbf{b})$, determined experimentally from multiplicity distributions, and E_F is a test of Glauber theory. There are many other tests. At RHIC, for instance, one measured the multiplicity distributions in deuterium-gold (d-Au) collisions under the conditions that i) the proton and neutron in the deuterium both break up, or that ii) the proton interacts with the nucleus while the neutron is detected untouched at forward projectile rapidity. The latter class of p-Au collisions with a spectator neutron selects a more peripheral distribution of impact parameter and comparing the two cases is a sensitive and successful test of Glauber theory (see, for example, fig. 1 in ref. [8]).

Questions:

- 1) Write a short computer program to calculate (39) for the collision of two lead nuclei ($A = 208$).

Check that the output of this program reproduces the shape of fig. 1.

Calculate the integral in (39) restricted to some finite range of impact parameter ($b = 0\text{--}4\text{ fm}$, $4\text{--}6\text{ fm}$, $6\text{--}8\text{ fm}$, etc.) and plot the results. Vary the model parameter x , the value for the dispersion d , the n-n cross-section σ_{nn} . To what extent do variations of these parameters affect the centrality classes ($b = 0\text{--}4\text{ fm}$, $4\text{--}6\text{ fm}$, $6\text{--}8\text{ fm}$, etc.), which you have calculated before?

- 2) Use your computer program to calculate (40) and to reproduced the right-hand side of fig. 3.
- 3) Our discussion of Glauber theory was limited to the case of a spherical nuclear density $\rho_A(\vec{r}) = \rho_A(r)$. There are nuclei which are not spherical but spheroidal, that is with a symmetry axis which is longer than the other two. How would you disentangle an event sample of high centrality, in which this symmetry axis lies parallel to the beam direction, from one in which it is orthogonal to the beam direction? Think about possible confounding factors.

A detailed discussion can be found in ref. [9].

5.4. Constraining dynamical models by multiplicity distributions. – There are many models of multiparticle production in hadronic collisions, but an understanding from first principles is missing. This is so in proton-proton, as well as in nucleus-nucleus collisions, and resulting uncertainties in the extrapolation to higher centre-of-mass energy are comparable. A compilation of models for the event multiplicity in nucleus-nucleus collisions, and how these models compare to data, can be found in refs. [10, 11]. Here, we do not discuss specific models of multiparticle production. We note, however, that multiparticle production in hadronic collisions shows several characteristic features which persist over many orders of magnitude in $\sqrt{s_{NN}}$, see ref. [12].

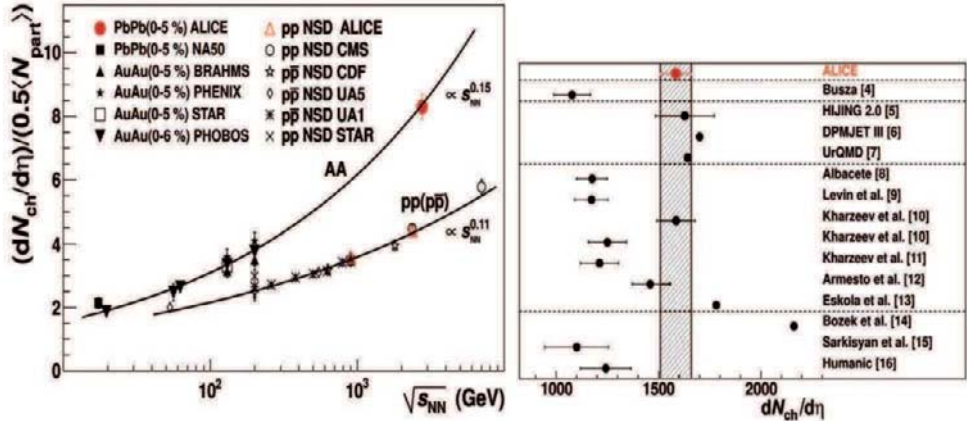


Fig. 4. – Left: the minimum bias charged particle multiplicity distributions, measured over three orders of center-of-mass energy at SPS, RHIC and LHC for nucleus-nucleus collisions, and at the Sp \bar{p} S, Tevatron and LHC for nucleon-nucleon collisions. Right: comparison of the ALICE measurements to a variety of model predictions. Figures taken from ref. [2].

It is interesting in this context to look at the data that ALICE took a few months after these lectures and that are shown in fig. 4. Remarkably, these data show that as a function of $\sqrt{s_{NN}}$, the event multiplicity raises faster in nucleus-nucleus than in nucleon-nucleon collisions. This is a very characteristic dynamical feature that can be expected to constrain models significantly. The comparison of data to model predictions in fig. 4 illustrates further our remarks that an understanding of multi-particle production from first principles is missing and that theoretical uncertainties are comparatively large.

We close this section by introducing an expression widely used to estimate of the energy density attained in a nucleus-nucleus collision. In the final state of a heavy-ion collision, one can measure the average transverse energy $\langle e_T \rangle$ per produced particle, and the total transverse energy produced in the collision per unit rapidity y , $\frac{dE_T}{dy} \propto \frac{dN_{ev}}{dy} \langle e_T \rangle$. The volume in which this energy was contained at an initial time τ_0 , can be obtained by back extrapolating the energy flow along straight lines. For a zero-impact parameter collision between two nuclei of radius R , the total transverse energy is located initially in a transverse area πR^2 , and the system has expanded for a short duration τ_0 in the longitudinal “beam” direction with a speed close to the velocity of light. Bjorken’s estimate of the energy density at time τ_0 is given by the transverse energy contained in this initial volume,

$$(42) \quad \epsilon(\tau_0) = \frac{1}{\pi R^2} \frac{1}{\tau_0} \frac{dE_T}{dy}.$$

The energy density obtained from Bjorken’s estimate is not necessarily equilibrated, it could result equally well from free-streaming particles which do not interact. A value $\tau_0 = 1 \text{ fm}/c$ that is of order $1/\Lambda_{\text{QCD}}$ is typically (and somewhat conventionally) used,

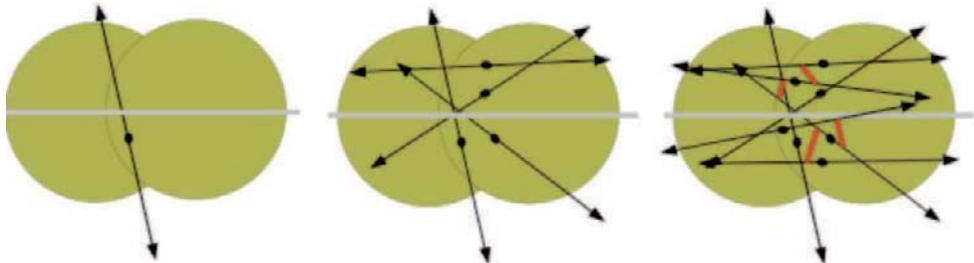


Fig. 5. – Sketch of a nucleus-nucleus collision at finite impact parameter. Black dots denote the location of hard processes in the transverse plane. Left and middle: independent $2 \rightarrow 2$ or $2 \rightarrow n$ processes lead to an azimuthal asymmetry which decreases with multiplicity and which is not correlated to the reaction plan. Right: final-state interactions (characterized by the red segments) have the potential to generate particle correlations with respect to the reaction plane.

corresponding roughly to the formation time, *i.e.* the time it takes for quarks and gluons to be produced in the initial collisions.

6. – Particle production with respect to the reaction plane

In the previous section, we have seen how one can select in nucleus-nucleus collisions an event class characterized by a range of finite impact parameter $b \in [b_{\min}, b_{\max}]$. At finite b , nucleus-nucleus collisions have a reaction plane, which is spanned by the beam axis and the orientation of the impact parameter \mathbf{b} in the transverse plane. In the present section, we shall discuss how to characterize particle production as a function of the azimuthal angle ϕ with respect to the reaction plane.

To get a first idea of why this is interesting, consider the three situations sketched in fig. 5. A single, jet-like $2 \rightarrow 2$ process would produce the largest azimuthal asymmetry, but such incoherent particle production would not be correlated to the reaction plane. Increasing the event multiplicity n_{ev} by superimposing more incoherent processes, the azimuthal asymmetry will reduce statistically as $\propto 1/\sqrt{n_{\text{ev}}}$. Again, this remaining asymmetry is purely statistical; it will point in an arbitrary direction and it will not be correlated to the reaction plane. In contrast, final-state interactions amongst the degrees of freedom produced in the collision are expected to lead to an azimuthal asymmetry which is correlated to the reaction plane. This is so, since the in-medium pathlength of any particle (and thus its probability of interaction) depends on the azimuthal direction ϕ . The correlation of particle production with the reaction plane is interesting, since it gives access to multiparticle final-state interactions and collectivity in the medium.

The picture shown in fig. 5 is nothing but an illustrative sketch. Whether the $2-2$ interactions between particles in the final state is an appropriate picture for understanding nucleus-nucleus collisions, or whether for instance the picture of an evolving fluid is more appropriate, must be established in a data analysis and should not be presupposed by the analysis method employed. The above sketch illustrates, however, that there are in

general two sources of azimuthal asymmetries: those caused by statistical fluctuations, which would be present even in the absence of a reaction plane, for instance if the heavy-ion collision can be viewed as an incoherent superposition of an equivalent number of nucleon-nucleon collisions. And those which are correlated to the reaction plane and which manifest some form of collective behaviour of the matter produced in the section. In this section, we discuss how to disentangle statistical from collective effects.

We consider a single inclusive particle spectrum $f_1(\mathbf{p}) \equiv \frac{dN}{d^3p}$, where the momentum can be written as $\vec{p} = (p_T \cos \phi, p_T \sin \phi, \sqrt{p_T^2 + m^2} \sinh y)$. The azimuthal asymmetry of this spectrum can be characterized fully in terms of the harmonic coefficients

$$(43) \quad v_n \equiv \langle \exp[i n \phi] \rangle = \frac{\int f_1(\mathbf{p}) e^{i n \phi} d^3p}{\int f_1(\mathbf{p}) d^3p}.$$

The coefficients v_n are called n -th-order flow. In general, they can depend on the transverse momentum p_T , the rapidity y , and they can differ for different particle species. In particular, v_1 is referred to as “direct flow” and v_2 as elliptic flow. In the collision of identical nuclei at mid-rapidity, the collision region is symmetric under $\phi \rightarrow -\phi$ and all odd harmonics vanish. In this case, the elliptic flow v_2 is the first non-vanishing coefficient.

6.1. The cumulant method for n -th-order flow. — The coefficients (43) cannot be measured directly, since the orientation of the reaction plane is not known *a priori*. The cumulant method is a systematic approach for relating v_n to measurable quantities, which has been pioneered by [14]. It is based on the analysis of particle correlations. We consider a two-particle inclusive distribution $f(\mathbf{p}_1, \mathbf{p}_2)$ and we perform the harmonic transformation

$$(44) \quad \langle f(\mathbf{p}_1, \mathbf{p}_2) \rangle \equiv \langle \exp[i n (\phi_1 - \phi_2)] \rangle = \frac{\int \exp[i n (\phi_1 - \phi_2)] f(\mathbf{p}_1, \mathbf{p}_2) d^3p_1 d^3p_2}{\int f(\mathbf{p}_1, \mathbf{p}_2) d^3p_1 d^3p_2}.$$

Measuring this particle correlation does not require *a priori* knowledge about the orientation of the reaction plane and it is thus measurable. In general, a two-particle distribution has an uncorrelated part, and a correlated one,

$$(45) \quad f(\mathbf{p}_1, \mathbf{p}_2) = f(\mathbf{p}_1) f(\mathbf{p}_2) + f_c(\mathbf{p}_1, \mathbf{p}_2).$$

The key idea of the cumulant method is to count the correlated part f_c as suppressed by one factor $\sim 1/n_{\text{ev}}$ of the event multiplicity, compared to the leading contribution. For instance, consider the simplified case that $n_{\text{ev}} = 2N$ particles are produced in 2-2 processes, so that any particle is dynamically correlated with exactly one other particle, namely its recoil, and it is uncorrelated with the $2N - 1$ other particles (see fig. 5). In this case, the correlated part is $O(1/n_{\text{ev}})$ -suppressed. An analogous argument holds for other dynamical correlations between particle pairs, for instance dynamical correlations due to resonance decays. Consider n_{ev} pions, some of them stemming from ρ -decays:

each pion will have exactly one resonance decay partner with which it is correlated, and (as long as there is no collective effect which correlates the motion of particles to the global event) it will be uncorrelated with $(n_{\text{ev}} - 1)$ pions. In short, on the right-hand side of eq. (45), the first term retains the information about collectivity, from which the harmonic coefficients v_n in (43) can be calculated. The second term separates two-particle correlations which are typically due to resonance decays or conservation laws and which would fake azimuthal asymmetries not correlated to the reaction plane. Having separated the correlated part in (45), we can write the average (44) as

$$(46) \quad \langle \exp[i n (\phi_1 - \phi_2)] \rangle = v_n v_n + \underbrace{\langle \exp[i n (\phi_1 - \phi_2)] \rangle_c}_{O(1/n_{\text{ev}})} .$$

The correlated part, which is suppressed by $O(1/n_{\text{ev}})$, is often referred to as non-flow correction. It is possible to measure from two-particle correlations (46) the azimuthal asymmetry v_n of a single inclusive hadron spectrum with respect to the reaction plane, if the signal v_n^2 is larger than the non-flow correction, that means

$$(47) \quad v_n \gg 1/\sqrt{n_{\text{ev}}} \quad \text{for two-particle correlations.}$$

What if this condition is not satisfied? One can enhance the sensitivity of the construction by going to the 4th-order cumulant

$$(48) \quad \langle\langle \exp[i n (\phi_1 + \phi_2 - \phi_3 - \phi_4)] \rangle\rangle \equiv \langle \exp[i n (\phi_1 + \phi_2 - \phi_3 - \phi_4)] \rangle - \langle \exp[i n (\phi_1 - \phi_4)] \rangle \langle \exp[i n (\phi_2 - \phi_4)] \rangle - \langle \exp[i n (\phi_1 - \phi_4)] \rangle \langle \exp[i n (\phi_2 - \phi_3)] \rangle .$$

Here, the subtraction terms are chosen such that the leading non-flow corrections cancel. Upon explicit calculation, one finds

$$(49) \quad \langle\langle \exp[i n (\phi_1 + \phi_2 - \phi_3 - \phi_4)] \rangle\rangle = -v_n^4 + O\left(\frac{1}{n_{\text{ev}}^3}\right) + O\left(\frac{v_{2n}^2}{n_{\text{ev}}^2}\right) .$$

In practice, the higher harmonics v_{2n} are much smaller than v_n . Then, to determine the azimuthal asymmetry v_n from (49), we require that the signal

$$(50) \quad v_n \gg 1/n_{\text{ev}}^{3/4} \quad \text{for two-particle correlations.}$$

So, by going to a higher cumulant, we have eliminated 4-particle correlations, which would fake a correlation with the reaction plane in a second-order cumulant analysis, and we have enhanced the sensitivity for discriminating the signal (43) from confounding correlations. One can show that by going to even higher cumulants, one can achieve asymptotically a sensitivity $v_n \gg 1/n_{\text{ev}}$.

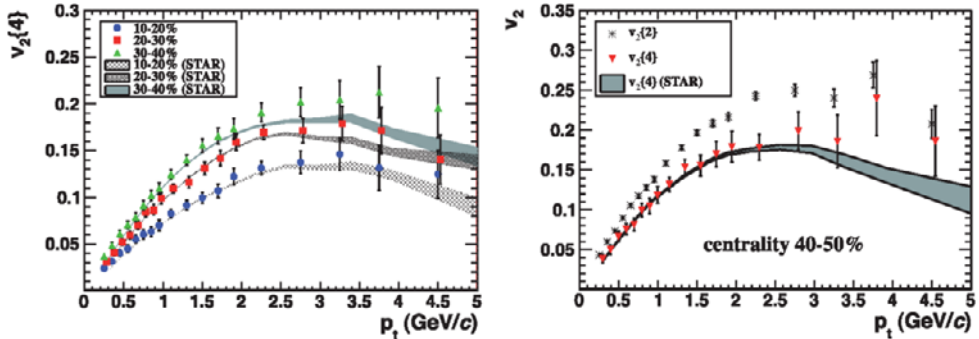


Fig. 6. – Left: transverse-momentum dependence of the elliptic flow v_2 for different centrality bins. Right: the same p_T -differential elliptic flow v_2 for a semi-peripheral event class, reconstructed with 2nd- and 4th-order cumulants. Figures taken from ref. [7] (ALICE Collaboration).

6·2. Elliptic flow at RHIC and at the LHC. – On the left-hand side of fig. 6, we show the transverse-momentum dependence of the elliptic flow v_2 , measured for different centrality classes in Pb-Pb collisions at the LHC and in Au-Au collisions at RHIC. The azimuthal asymmetry v_2 of the final-state single inclusive hadron spectrum is maximal in semi-peripheral collisions, whereas it decreases for more peripheral centrality classes. This is so since v_2 measures a collective phenomenon originating from final-state interactions, and the latter become less important with increasing impact parameter and smaller system size. On the other hand, v_2 decreases towards more central collisions, since the initial geometric asymmetry is decreased. However, while v_2 is constructed such that it should disappear for the idealized case of an event sample at impact parameter $b = 0$, v_2 does not disappear in the sample of the 5% most central collisions. This is so, since even the most central 5% of the total nucleus-nucleus cross-section is an event sample with sizeable average impact parameter, see our discussion in subsect. 5·2.

To appreciate the total size of the v_2 signal, we note that the harmonic coefficients v_n characterize deviations of the single inclusive spectra from azimuthal symmetry as

$$(51) \quad \frac{dN}{d^2\mathbf{p}_t dy} = \frac{1}{2\pi} \frac{dN}{p_T dp_T dy} [1 + 2v_1 \cos(\phi - \Phi_R) + 2v_2 \cos 2(\phi - \Phi_R) + \dots],$$

where Φ_R denotes the azimuth of the reaction plane. In particular, the $\cos 2\phi$ term has the prefactor $2v_2$. So, if v_2 reaches a value of $v_2 \sim 0.2$, then the term in brackets in (51) varies between 0.6 and 1.4. This implies that there are more than twice as many particles emitted in the reaction plane than orthogonal to it. In short, the measured azimuthal asymmetry is large.

We now discuss whether the experimentally measured signal $v_2 \sim 0.2$ is caused by random fluctuations not correlated to the reaction plane, or whether it is indicative of a collective phenomenon. For a simple estimate, we consider the typical case that the events for which v_2 is determined have of the order of $n_{\text{ev}} \sim 100$ final-state particles in

the phase space region which is analysed. Assume that we determine v_2 from 2nd-order cumulants. For the result to be dominated by collective effects, we require according to (47) that $v_n \gg 1/\sqrt{n_{\text{ev}}} \sim 0.1$. For $v_n \sim 0.2$, this condition is not realized. So, we expect that the result of a 2nd-order cumulant analysis of v_2 contains non-negligible non-flow effects. What about a 4th-order cumulant analysis? The signal $v_2 \sim 0.2$ is indeed much larger than $1/n_{\text{ev}}^{3/4} \sim 0.03$, so the inequality (50) holds. As a consequence, we expect that the result of a 4th-order cumulant analysis is stable and that no further non-flow corrections are found if even higher-order cumulants are included in the analysis. This is confirmed in the data analysis, see fig. 6. In short, by disentangling effects from random fluctuations from collective ones, we have established a signal v_2 which is large and which can be attributed to a collective phenomenon.

7. – Hydrodynamic modeling of heavy-ion collisions

In the previous section, we have established for the azimuthal asymmetry v_2 a benchmark in which collective effects are absent and where the signal is due to random fluctuations only. We have then established that the measured value of v_2 is significantly larger than this benchmark, we have disentangled the effect of random fluctuations from the signal of a collective phenomenon by a cumulant analysis, and we have arrived at a value for v_2 which can be attributed to a collective phenomenon.

The question arises to what extent the dynamical origin of this collective phenomenon can be constrained in an interplay of theory and data analysis. What we know is that in nucleus-nucleus collisions at finite impact parameter, the nuclear overlap region of the collision covers initially an almond-shaped, azimuthally asymmetric region in the transverse plane. Upon impact, the distribution of the produced particles is asymmetric in transverse space, but initially it is symmetric in transverse-momentum space. So, the value of v_2 must arise from a mechanism that translates the initial *geometrical* anisotropy into a final-state *momentum-space* anisotropy. This mechanism will be the more efficient, the more the produced degrees of freedom interact with each other after being produced. The maximal signal v_2 may be expected to arise from a hydrodynamical picture of the collision, since any dissipative effect (indicative, for example, of a finite mean-free path between interactions) is expected to reduce v_2 .

So, the first motivation for a modelling of heavy-ion collisions in terms of a fluid is the idea to start from a description which conceivably explores the case of a maximal degree of collectivity. Here we discuss the basis for such model simulations, and how they compare to data on v_2 .

7.1. Tensor decomposition of $T^{\mu\nu}$. – We consider matter in local equilibrium, characterized by its energy momentum tensor $T^{\mu\nu}(x)$ and n charge densities $N_i^\mu(x)$, $i \in [1, n]$. In much of what follows, we do not spell out explicitly the dependence of these thermodynamic fields on the space-time coordinate x . The energy momentum tensor is symmetric

under exchange of Lorentz indices, so we have

$$(52) \quad \text{energy momentum tensor } T^{\mu\nu} \dots 10 \text{ independent functions,}$$

$$(53) \quad \text{conserved charges } N_i^\mu \dots 4n \text{ independent functions.}$$

We introduce now a local flow field $u_\mu(x)$, defined by a normalized vector $u_\mu u^\mu = 1$. The projector on the subspace orthogonal to the flow field is

$$(54) \quad \Delta_{\mu\nu} = g_{\mu\nu} - u_\mu u_\nu.$$

In a tensor decomposition with respect to the flow field, one can disentangle properties which are comoving with the local flow field from those which are leaking out of the comoving rest frame. For the energy momentum tensor, this tensor decomposition reads

$$(55) \quad T^{\mu\nu} = \epsilon u^\mu u^\nu - p \Delta^{\mu\nu} + q^\mu u^\nu + q^\nu u^\mu + \Pi^{\mu\nu}.$$

Here, the different components of $T^{\mu\nu}$ have specific physical interpretations. For instance, the projection

$$(56) \quad \epsilon = u_\mu T^{\mu\nu} u_\nu$$

defines the energy density comoving with the flow field. This can be seen clearly, for instance, by observing that in the frame locally comoving with the fluid, $u_\mu = (1, 0, 0, 0)$, the energy density ϵ is the 00-component of the energy-momentum tensor. Similarly, the isotropic pressure is given by

$$(57) \quad p = -T^{\mu\nu} \Delta_{\mu\nu}/3,$$

which in the locally comoving frame with $u_\mu = (1, 0, 0, 0)$ reduces to the spatial diagonal ii -component of $T^{\mu\nu}$. The heat flow

$$(58) \quad q^\mu = \Delta^{\mu\alpha} T_{\alpha\beta} u^\beta$$

characterizes the energy density which dissipates out of the rest frame locally comoving with the fluid velocity u_μ . The last term of the tensor decomposition (55) is the traceless shear viscous tensor

$$(59) \quad \Pi^{\mu\nu} = \left[\left(\Delta_\alpha^\mu \Delta_\beta^\nu + \Delta_\beta^\mu \Delta_\alpha^\nu \right) / 2 - \Delta^{\mu\nu} \Delta_{\alpha\beta} / 3 \right] T^{\alpha\beta}.$$

The so-called Landau frame is characterized as the frame comoving with the physical 4-velocity of the energy flow. The Landau flow velocity satisfies the implicit equation

$$(60) \quad u_L^\mu \equiv \frac{T_\nu^\mu u_L^\nu}{\sqrt{u_L^\alpha T_\alpha^\beta T_{\beta\gamma} u_L^\gamma}}.$$

In the Landau frame, the heat flow vanishes by construction:

$$(61) \quad q^\mu = 0 \quad \text{in Landau frame.}$$

In the absence of conserved charges, or if one restricts the discussion to cases for which the flow of conserved charges does not differ from the flow of energy, the Landau frame is a natural choice, since it defines the local rest frame of the fluid.

For the conserved charge current $N^\mu(x)$, the corresponding tensor decomposition takes the form

$$(62) \quad N_i^\mu = n_i u^\mu + \bar{n}_i^\mu.$$

Here, n_i is the charge density locally comoving with the flow field.

$$(63) \quad \bar{n}_i^\mu = \Delta_\nu^\mu N_i^\nu$$

is orthogonal to the flow field and characterizes the charge dissipating out of the locally comoving fluid element. For each charge, we can specify the local rest frame comoving with the net charge, characterized by the flow velocity

$$(64) \quad u_E^\mu \equiv \frac{N_i^\mu}{\sqrt{N_i^\mu N_{i\mu}}}.$$

In this so-called Eckard frame, net charge does not flow out of the local rest frame, so $\bar{n}_i^\mu = 0$ by construction. This amounts to replacing the three independent functions $\bar{n}_i^\mu(x)$ by the three independent functions of the Eckard velocity u_E^μ . In what follows, we shall work mainly in the Landau frame.

7.2. Equations of motion for a perfect fluid. – A fluid is called perfect if we can associate to each space-time point x a fluid velocity, such that in the frame comoving with this velocity, the fluid is isotropic at x . So, for each x , there is a fluid rest frame such that $T^{00}(x) = \epsilon(x)$, $T^{ij}(x) = p(x) \delta^{ij}$ and $N_i^\mu(x) = n_i(x) \delta^{\mu 0}$. It follows that in a frame specified by an arbitrary velocity $u_\mu(x)$, the charge currents and energy-momentum tensor of a perfect fluid take the form

$$(65) \quad N_i^\mu = n_i u_\mu,$$

$$(66) \quad T^{\mu\nu} = \epsilon u^\mu u^\nu - p \Delta_{\mu\nu}.$$

This is a tremendous simplification of the general case. The $10+4n$ independent functions entering (52) and (53) are reduced to $5+n$ unknown functions, namely ϵ , p , three independent functions $u^\mu(x)$ and the n functions $n_i(x)$. The conservation laws for the

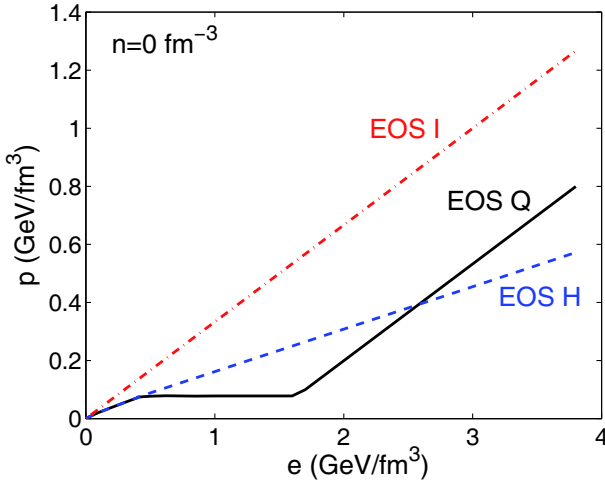


Fig. 7. – Three model equations of state of QCD matter: a hard e.o.s. (EOS I), a soft e.o.s. (EOS H), and an e.o.s. which displays a 1st-order phase transition from a soft “hadronic” e.o.s. at low density to a “hard” partonic e.o.s. at high density. Figure taken from [15].

conserved charges and energy-momentum give $4 + n$ constraints, namely n constraints for the conserved charges and 4 constraints for the energy momentum tensor,

$$(67) \quad \partial_\mu N_i^\mu = 0,$$

$$(68) \quad \partial_\mu T^{\mu\nu} = 0.$$

To fully determine the equations of motion for the $5 + n$ unknowns in (65) and (66), we need one additional constraint. This is provided by the equation of state (e.o.s.), which expresses the pressure p in terms of the energy density, and the charge densities,

$$(69) \quad p = p(\epsilon, n).$$

For a perfect fluid, information about the underlying theory enters only by specifying the equation of state (69). A main characteristic of the equation of state is the velocity of sound

$$(70) \quad c_s^2 = \frac{\partial p}{\partial \epsilon}.$$

An ideal gas has $c_s^2 = 1/3$ and equations of state which come close to this velocity of sound are referred to as “hard”. In a hadron gas, an increase of energy density does not translate as efficiently into a change of pressure, since it leads also to the excitation of higher-lying resonances. As a consequence, a hadron gas is expected to have a much softer equation of state with $c_s^2 \approx 0.15$. Figure 7 shows a set of different equations of

state, used in fluid model simulations of heavy-ion collisions. Realistic model equations of state extrapolate between a soft “hadronic” regime at low density and a hard “partonic” regime at high density.

7.3. Bjorken boost-invariant ideal fluid. – A fluid is called Bjorken boost-invariant, if the longitudinal velocity v_z of the frames locally comoving with the fluid is related to their space-time position like $v_z = z/t$. Here as always, the “longitudinal” coordinate z refers to the direction parallel to the beam. The condition of longitudinal boost-invariance takes a particularly simple form in terms of proper time τ and space-time rapidity η_s ⁽²⁾,

$$(71) \quad t = \tau \cosh \eta_s,$$

$$(72) \quad z = \tau \sinh \eta_s.$$

Now,

$$(73) \quad v_z = \frac{z}{t} = \tanh \eta_s, \quad \text{for Bjorken boost-invariant velocity profile.}$$

A fluid with this velocity distribution will look the same in all longitudinally comoving fluid elements. This distribution is of particular interest in the modelling of heavy-ion collisions, since one expects that at high centre-of-mass energy, the initial conditions of the fluid produced satisfy (73) over a wide range of rapidity. Moreover, one can show that if (73) is satisfied by the initial conditions, then it is preserved by the equation of motion (68). This implies that the longitudinal dynamics is trivial and decouples: one is left with a set of $(2+1)$ -dimensional hydrodynamic equations of motion in the transverse plane, which are computationally less demanding.

To illustrate the consequences of Bjorken boost-invariant flow, we consider here a one-dimensional toy model with equations of motion

$$(74) \quad \partial_t T^{00} + \partial_z T^{z0} = 0,$$

$$(75) \quad \partial_t T^{0z} + \partial_z T^{zz} = 0.$$

Assuming that the energy-momentum tensor is of the ideal form (66), and going to the coordinates (71) and (72), we find

$$(76) \quad \frac{p + \epsilon}{\tau} \cosh \eta_s + \frac{\sinh \eta_s}{\tau} \frac{\partial p}{\partial \eta_s} + \frac{\partial \epsilon}{\partial \tau} \cosh \eta_s = 0,$$

$$(77) \quad \frac{p + \epsilon}{\tau} \sinh \eta_s + \frac{\cosh \eta_s}{\tau} \frac{\partial p}{\partial \eta_s} + \frac{\partial \epsilon}{\partial \tau} \cosh \eta_s = 0.$$

⁽²⁾ Not to be confused with the pseudorapidity η (introduced in sect. 3).

Combining these equations leads to

$$(78) \quad \frac{p + \epsilon}{\tau} + \left. \frac{\partial \epsilon}{\partial \tau} \right|_{\eta_s} = 0,$$

$$(79) \quad \left. \frac{\partial p}{\partial \eta_s} \right|_{\tau} = 0.$$

The equations of motion in η_s and τ decouple. There is no pressure gradient in η_s , and this implies that the initial velocity $v_z = z/t$ remains unchanged throughout the dynamical evolution. The new coordinates (η_s, τ) already take the scaling expansion into account.

The fundamental thermodynamic relation $\epsilon + p = \mu, n + T s$ allows us to relate energy density and pressure to the temperature T , the entropy density s and the chemical potentials μ and charge densities n of the system. In the absence of conserved charges, we have

$$(80) \quad \epsilon + p = T s.$$

The equation of motion (78) can now be rewritten as an evolution equation for the entropy density,

$$(81) \quad \left. \frac{s}{\tau} + \frac{\partial s}{\partial \tau} \right|_{\eta_s} = 0.$$

The solution of this differential equation is

$$(82) \quad s = \frac{\text{const}}{\tau} \quad \text{at constant } \eta_s.$$

Since the one-dimensional volume of the system expands proportional to τ , the total entropy is $S = s \tau = \text{const}$. This is so not only for this toy model but in general: as long as thermodynamic fields do not develop discontinuities, a perfect fluid is a system with isentropic expansion. That means, entropy is not produced during the evolution.

Similarly, we can explore the temperature dependence of the energy density. Writing $d\epsilon = c_s^2 d\epsilon = s dT = \frac{\epsilon + p}{T} dT = (1 + c_s^2) \epsilon \frac{dT}{T}$, we find

$$(83) \quad \frac{d\epsilon}{\epsilon} = \frac{1 + c_s^2}{c_s^2} \frac{dT}{T} \longrightarrow \epsilon \propto T^{1+c_s^{-2}}.$$

For the case of the equation of state of an ideal gas, $\epsilon = 3p$, these expressions reduce to some widely known parametric dependence. The solution of (78) is now $\epsilon \propto \tau^{-4/3}$, the temperature decreases for the case of one-dimensional Bjorken expansion like $T \propto \tau^{-1/3}$, and the energy density (83) is proportional to the 4th power of the temperature.

Despite its simplicity, the features of this $(1+1)$ -dimensional model provide some useful insights into the physics of $(3+1)$ -dimensional fluid simulations. To understand

why this is so, consider a small patch in the transverse plane of a heavy-ion collision which has a boost-invariant velocity profile. As long as the hydrodynamic distributions in the vicinity of this patch show negligible gradients in the transverse direction, the hydrodynamical evolution in the transverse plane is negligible and the main characteristics of the time evolution are captured by the $(1 + 1)$ -dimensional model mentioned above.

7.4. Simulating a Bjorken boost-invariant perfect fluid. – In this section, we discuss fluid dynamic simulations of heavy-ion collisions. We restrict the discussion to the widely studied case of a Bjorken boost-invariant perfect fluid. In this case, the longitudinal dynamics (79) decouples, one is left with a $(2 + 1)$ -dimensional problem. While the fluid dynamic equations of motion do not require model-dependent assumptions, such assumptions enter the initial conditions, the choice of the equation of state and the interfacing of the fluid dynamic simulation with the hadronic final state. We now comment on these aspects in more detail.

For a heavy-ion collision at impact parameter b , the initial transverse geometry is determined by the nuclear overlap function, see sect. 5. Realistic choices of the transverse r -dependence of thermodynamic fields typically base a model ansatz for the energy density or entropy distribution on this geometrical information. For instance, since entropy is conserved under perfect fluid dynamic evolution, it is expected to scale with the final-state multiplicity. This can serve as a motivation for invoking the Glauber model and writing the entropy density distribution in the transverse coordinate \mathbf{r} as a function of the number of participants $N_{\text{part}}(\mathbf{b}, \mathbf{r})$ or the number of collisions $N_{\text{coll}}(\mathbf{b}, \mathbf{r})$, which for a collision at impact parameter \mathbf{b} occur at transverse position \mathbf{r} . A typical ansatz, with the interpolating model parameter x introduced in (37) is

$$(84) \quad s_{\text{init}}(\mathbf{r}) = s(\tau_0, \mathbf{r}, \eta = 0) \propto \left(\frac{1-x}{2} \bar{N}_{\text{part}}^{AB}(\mathbf{b}, \mathbf{r}) + x \bar{N}_{\text{coll}}^{AB}(\mathbf{b}, \mathbf{r}) \right).$$

The normalization of this transverse entropy density distribution at initial time τ_0 is fixed by the final-state multiplicity which determines the total entropy in the final state. The energy density is obtained from this expression by use of the equation of state and the fundamental thermodynamic relation (80). Alternatively, one sometimes starts from an ansatz of the energy density which satisfies the same functional form as (84). In short: there are some uncertainties in specifying the initial energy density distribution, but they are constrained by information about the initial transverse geometry of the collision.

Aside from the initial energy density, a perfect-fluid dynamic simulation requires specification of the initial transverse flow field. Since there is no *a priori* reason why transverse position and momentum should be correlated at initial time τ_0 , the standard assumption is that the transverse flow will arise solely within the fluid dynamic evolution along the spatial density gradients, so that initially $u_\mu(\tau_0) = (1, 0, 0, 0)$ in the entire transverse plane. Figure 8 may illustrate how a non-vanishing transverse flow field builds up during the simulation. A finite impact parameter collision leads initially to an almost elliptic *geometrical* anisotropy of the energy density distribution in the transverse plane.

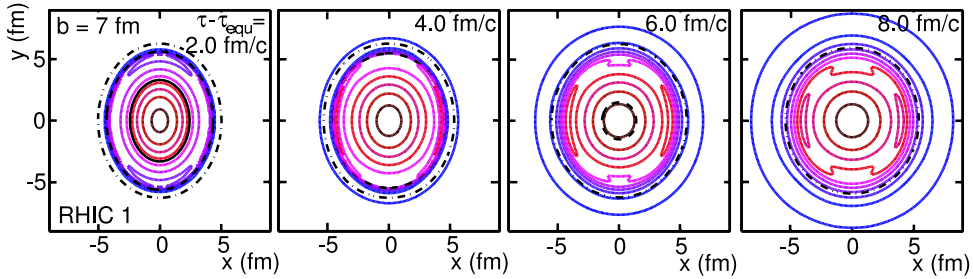


Fig. 8. – Results of a fluid dynamic simulation of a Au+Au collision at impact parameter $b = 7$ fm. The plots show contours of constant energy density in the transverse plane at different times $2, 4, 6$ and 8 fm/ c after initialization of the simulation. Figure taken from ref. [16].

This implies that density gradients are larger in the reaction plane (the x -direction in fig. 8) than orthogonal to it. A stronger density gradient induces a larger increase in flow. As a result, the system is seen to evolve faster within the reaction plane than orthogonal to it. The dynamical evolution translates an initial geometric asymmetry into a final-state momentum asymmetry. (Information about the latter is not given directly in fig. 8, but it is shown in fig. 9. It may also be deduced from the above narrative of the time sequence shown.)

A perfect-fluid dynamical simulation, initialized as mentioned above, describes the expansion of the high-density fluid within the transverse plane. Within a hydrodynamical framework, this evolution can be continued to arbitrarily late times and thus to arbitrar-

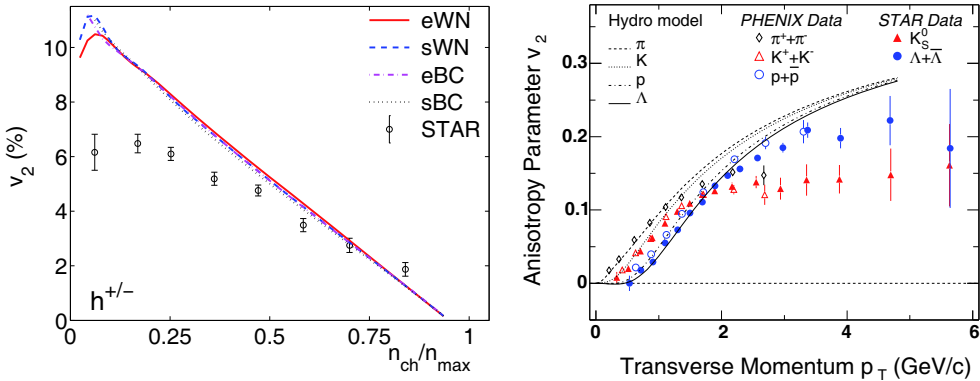


Fig. 9. – Left: transverse-momentum averaged elliptic flow for $\sqrt{s_{NN}} = 130$ GeV Au+Au collisions as a function of collision centrality (n_{ch} is the charged multiplicity at mid-rapidity). The curves are results of fluid dynamical simulations with different choices for the initial energy density profile. Right: the elliptic flow $v_2(p_T)$ as a function of transverse momentum for identified hadrons from minimum bias Au+Au collisions at $\sqrt{s_{NN}} = 200$ GeV, together with curves from fluid dynamical simulations. Figure taken from ref. [17].

ily low densities. However, on physical grounds one expects that below a critical energy density ϵ_c , the microscopic reaction rates in the system are not large enough to maintain local equilibrium. At this stage of the evolution, a fluid dynamic description starts to break down and must be interfaced with another dynamic description. The simplest interface is the so-called sharp Cooper-Frye freeze-out condition. It assumes that if the energy density at the space-time point x reaches the critical value $\epsilon(x) = \epsilon_c$, then this fluid element “freezes out”. This freeze-out condition is realized on a three-dimensional hypersurface $\Sigma(x)$ in 4-dimensional space. The Cooper-Frye freeze-out condition translates the energy density on $\Sigma(x)$ into a corresponding yield of free-streaming hadrons

$$(85) \quad E \frac{dN_i}{d\vec{p}} = \frac{g_i}{(2\pi)^3} \int_{\Sigma} \vec{p} \cdot d\vec{\sigma}(x) f_i(p \cdot u(x), x).$$

The different hadron species i are distributed statistically according to a thermal distribution,

$$(86) \quad f_i(E, x) = \frac{1}{\exp[(E - \mu_i(x))/T(x)] \pm 1}.$$

Here, the local temperature $T(x)$ is the freeze-out temperature on $\Sigma(x)$, and the μ_i are local chemical potentials, relevant for hadrons which carry conserved charges such as baryon number or strangeness. In the single inclusive hadron spectrum (85), these distributions appear boosted with local flow velocity $u_\mu(x)$ at freeze-out. In this way, all hadron species emerge from the same underlying flow field.

In principle, one expects that between a hydrodynamic evolution of a sufficiently dense system, and the free-streaming of particles, there should be a collision phase in which particles have finite mean free path and scatter repeatedly. To what extent such a hadronic rescattering phase cannot be mimicked by interfacing perfect-fluid dynamics with a sharp freeze-out condition is a matter of ongoing debate, which we do not address here. Rather, we close this section by showing in fig. 9 some comparisons of RHIC data with a fluid dynamic simulation, supplemented by sharp Cooper-Frye freeze-out. The magnitude of the p_T -integrated elliptic flow is well reproduced in these collisions for sufficiently large system size, *i.e.* for sufficiently high centrality. For peripheral collisions, however, the azimuthal asymmetry of a fluid dynamic evolution exceeds that in the data. This is often argued to be an indication that the system becomes too small to be describable as a perfect fluid. On the other hand, fluid dynamics reproduces the hadron species dependence of the p_T -differential azimuthal symmetry rather well up to $p_T \lesssim 2$ GeV. This gives strong support to a hydrodynamic picture since the hadron species dependence arises without additional fit parameter as the consequence of emitting hadrons of different masses from the same collective flow field. At high transverse momentum (fig. 9(b)), one sees again deviations of the fluid dynamic simulations from data, but these one may have expected since high- p_T hadrons are likely not fully equilibrated.

7.5. Dissipative corrections to perfect-fluid dynamics. – So far, we have discussed hydrodynamic simulations under the assumption that the fluid is perfect. When is this assumption valid? To identify the relevant quantities for addressing this question, let us consider first a conserved current $j^\mu = \rho u^\mu$. Current conservation leads to

$$(87) \quad \partial_\mu j^\mu = \rho \partial_\mu u^\mu + u^\mu \partial_\mu \rho = 0.$$

Here, $u^\mu \partial_\mu$ is the comoving time derivative, which becomes ∂_t in the rest frame comoving with the fluid velocity. The second combination of partial derivative and velocity field is the expansion scalar

$$(88) \quad \Theta \equiv \partial_\mu u^\mu,$$

which measures locally a spatio-temporal variation of the macroscopic fluid, namely its velocity gradient. Physically, equilibrium (and thus isotropy) is maintained locally in a fluid due to microscopic reactions. If the velocity gradients in the system are too large, then these reaction rate Γ_{rr} cannot catch up any more, dissipative processes become relevant and local isotropy is lost. So, a perfect-fluid assumption is valid if

$$(89) \quad \Gamma_{\text{reaction rate}} \gg \Theta = \partial_\mu u^\mu, \quad \text{for a perfect fluid.}$$

These considerations convey the general idea that dissipative corrections to a perfect fluid can be characterized in a gradient expansion.

If more than the 5 independent functions of the perfect form (65) of the energy momentum tensor are relevant, then the constraints of energy-momentum conservation (68) and equation of state (69) are not sufficient to close the set of equations of motion. To obtain additional constraints, one standard procedure is to invoke the 2nd law of thermodynamics. For a perfect fluid, the entropy flow is $S^\mu = s u^\mu$. We now consider a gradient expansion of S^μ to first order, that is we look for the most general ansatz of the entropy flow. In the Eckart frame, we have to first order the dissipative quantities q^μ , $\Pi^{\mu\nu}$ and $\Pi = p_{\text{eq}} - p$ which denotes the difference between the expected local pressure in case of local equilibrium (defined as $p_{\text{eq}} = p(\epsilon, n)$) and the measured local pressure p which can now deviate from equilibrium. The most general ansatz is

$$(90) \quad S^\mu = s u^\mu + \beta q^\mu,$$

where β is an as yet unknown multiplier. For this ansatz, one can show

$$(91) \quad T \partial_\mu S^\mu = (T\beta - 1) \partial \cdot q + q \cdot (\dot{u} + T \partial \beta) + \Pi^{\mu\nu} \partial_\nu u_\mu + \Pi \Theta \geq 0.$$

It follows from the 2nd law of thermodynamics that the right-hand side of this equation

must be positive for all space-time points. To satisfy this condition, one chooses

$$(92) \quad \beta = 1/T,$$

$$(93) \quad \Pi = \zeta \Theta,$$

$$(94) \quad q^\mu = \kappa T \Delta^{\mu\nu} (\partial_\nu \ln T - \dot{u}_\nu),$$

$$(95) \quad \Pi^{\mu\nu} = 2\eta_{\text{shear}} \left[\frac{1}{2} \left(\Delta_\alpha^\mu \Delta_\beta^\nu + \Delta_\alpha^\nu \Delta_\beta^\mu \right) - \frac{1}{3} \Delta^{\mu\nu} \Delta_{\alpha\beta} \right] \partial^\alpha u^\beta.$$

Here, we have introduced the bulk viscosity ζ , the thermal conductivity κ and the shear viscosity η_{shear} . With these definitions, eq. (91) becomes

$$(96) \quad \partial_\mu S^\mu = \frac{\Pi^2}{\zeta T} - \frac{q \cdot q}{\kappa T^2} \frac{\Pi^{\mu\nu} \Pi_{\mu\nu}}{2\eta_{\text{shear}} T} \geq 0.$$

So, by construction entropy does not decrease at any space-time point. The definitions (92)–(95) provide a set of constraints which ensure the 2nd law of thermodynamics. They define the *a priori* independent functions Π , $\Pi^{\mu\nu}$ and q^μ of the energy momentum tensor in terms of velocity gradients, and they thus close the system of equations of motion. This framework is referred to as relativistic Navier-Stokes hydrodynamics or 1st-order dissipative fluid dynamics, as it includes gradients only up to first order.

A non-vanishing bulk viscosity can arise if internal degrees of freedom are excited in a fluid. In such a case, an increase in energy density is not accompanied instantaneously by the corresponding increase in pressure, but goes for instance into higher excited resonances. In the partonic phase of QCD, such mechanisms are not at work and the bulk viscosity is expected to be negligible. Also, the heat conductivity κ is difficult to determine, since it requires identification of a frame with respect to which heat flows. Any flow of a conserved charge can provide such a frame, so theory has no problems in defining heat conductivity in the Eckart frame of some charge. Experimentally, however, a corresponding operational procedure has not been thought of for heavy-ion collisions. For these reasons, the shear viscosity η_{shear} is the transport coefficient on which the interplay of experiment and theory mainly focuses.

To illustrate the effects of shear viscosity η , we turn again to a simplified model. The model shows Bjorken scaling and has no density or velocity gradients in the transverse plane. So, this is the idealization of a system infinitely extended in the transverse plane. As a consequence, there is no dynamics in the transverse plane, and the system shows for the case of a perfect fluid exactly the dynamics of the $(1+1)$ -dimensional toy model described in eqs. (74)–(82). However, in contrast to a model with only one spatial dimension, shear viscosity does not vanish and one finds

$$(97) \quad \left. \frac{\partial \epsilon}{\partial \tau} \right|_\eta = -\frac{p + \epsilon}{\tau} + \frac{4\eta_{\text{shear}}}{3\tau^2}.$$

It is the last term by which this equation of motion differs from that of a perfect fluid, eq. (81). Using the fundamental thermodynamic relation (80), we find for the entropy

density

$$(98) \quad \frac{d(\tau s)}{d\tau} = \frac{\frac{4}{3}\eta_{\text{shear}}}{\tau T}.$$

We recall that for a perfect fluid with a pure one-dimensional Bjorken expansion, the total entropy is $S \propto \tau s$ and it is conserved, $\frac{d(\tau s)}{d\tau} = 0$, see (82). Dissipative corrections lead to entropy increase in the system. This is seen in our example by the non-vanishing right-hand side of (98), and it is generally so.

We may delineate the region of validity of a perfect-fluid dynamic description by determining to what extent the entropy increase due to viscous effects is negligible. According to (98), we require

$$(99) \quad \frac{\eta_{\text{shear}}}{\tau T} \frac{1}{s} \ll 1, \quad \text{if dissipative corrections are negligible.}$$

If we put into this equation a typical temperature scale $T \sim 200$ MeV and a typical time scale $\tau \sim 1 \text{ fm}/c$, we find $\eta_{\text{shear}}/s \ll 1$. As an aside, we note that the liquid with the lowest shear viscosity over entropy ratio is superfluid helium at 4 K, which has $\eta_{\text{shear}}/s \sim 10$. So, the condition $\eta_{\text{shear}}/s \ll 1$ is a strong constraint on the application of perfect-fluid dynamics in heavy-ion collisions. The fact that perfect-fluid dynamics appears to provide a phenomenologically valid description of the collisions at RHIC is regarded as a strong indication that the QCD matter produced is exceptionally “perfect” in the hydrodynamic sense of the word.

We close by commenting on subjects which despite their relevance cannot be covered in these notes. First, the 1st-order relativistic fluid dynamics description presented here is known to have deficiencies. In particular, it allows for instantaneous acausal propagation, since the spatial gradient on the right-hand side of (92)–(95) translate instantaneously (and thus outside the light cone) into changes of the dissipative components of the energy-momentum tensor. Whether this conceptual problem is a practical problem depends on the size of the velocity gradients. In a 2nd-order relativistic fluid dynamic description, the so-called Israel-Stewart theory, these deficiencies are cured at the price of having to deal with relaxation time constants. Second, we note that the dissipative transport coefficients can be given an exact field-theoretic definition in terms of the Green-Kubo formula. This allows for their calculation from first principles of a quantum field theory, a programme which is vigorously being pursued in perturbative finite-temperature QCD, in lattice QCD and in a family of supersymmetric theories which share common features with QCD and for which transport coefficients can be calculated with the help of string theory techniques.

7.6. Numerical results for dissipative hydrodynamics. – In recent years, the inclusion of viscous corrections has become state of the art in fluid-dynamical simulations of nucleus-nucleus collisions. Figure 10 shows results of one such numerical study. Simulations of ideal fluid dynamics, supplemented with suitable initial conditions, lead to simulated

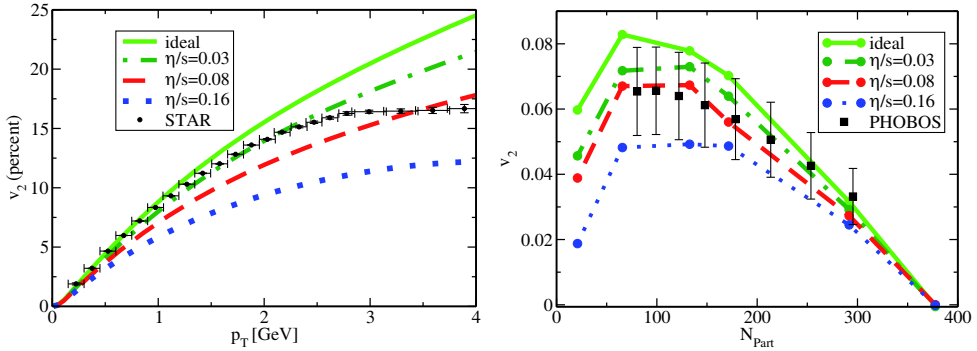


Fig. 10. – Left: transverse-momentum dependence of elliptic flow for $\sqrt{s_{\text{NN}}} = 200$ GeV Au+Au collisions. Data from STAR are compared to fluid dynamic simulations with different values for the ratio of shear viscosity over entropy. Right: the same comparison of data to fluid hydrodynamic simulation for the transverse momentum integrated flow as a function of centrality. Figures taken from ref. [18].

elliptic flow data that show an approximately realistic size, and an approximately realistic p_T - and centrality dependence. However, varying initial conditions within experimental constraints (*e.g.*, by varying the transverse profile of the initial entropy distribution) can modify the size of simulated v_2 data by at least $O(30\%)$. Therefore, the curve labeled “ideal” in fig. 10 should not be regarded as the firm theoretical baseline of a non-viscous fluid dynamic description of elliptic flow data; rather, it is a curve that has a significant dependence on the choice of initial conditions. The one model-independent information in fig. 10 is that, irrespective of details of the initial conditions and the resulting elliptic flow in the absence of viscous corrections, elliptic flow is always seen to be significantly reduced by shear viscous effects. Viscous corrections are so significant, that they lead for values η/s of a few times $\frac{1}{4\pi}$, elliptic flow becomes too small to account for experimental data. This provides strong support for the statement that the data from RHIC and LHC on elliptic flow are consistent with the conjectured lowest bound that shear viscosity over entropy ratio can take in a quantum field theory, $\eta/s = \frac{1}{4\pi}$.

Questions:

1. Check that in the Landau frame, the heat flow q^μ in (58) vanishes.

Answer: In the Landau frame, $q^\mu = \Delta_L^{\mu\alpha} T_{\alpha\beta} u_L^\beta$, where the subscript “L” indicates that the projector is written in terms of the Landau velocity. Now, $T_{\alpha\beta} u_L^\beta \propto u_L^\alpha$ and hence $q^\mu = 0$.

2. The energy momentum tensor (55) has 10 independent functions. In the Landau frame, $q^\mu(x) = 0$. How are the 10 independent functions of $T^{\mu\nu}$ parametrized in this frame?

Answer: $\epsilon(x)$ and $p(x)$ are two independent functions. The tracelessness and orthogonality $u_\mu \Pi^{\mu\nu} = 0$ of the shear viscous tensor implies that there are five

independent functions $\Pi^{\mu\nu}(x)$. In the Landau frame, the remaining three independent functions are not given by the three independent components of q^μ . Rather, the orthogonality condition $q^\mu u_\mu = 0$ implies that there are three independent functions $u^\mu(x)$. So, in the Landau frame, $q^\mu(x) = 0$ everywhere, and the three independent functions $q^\mu(x)$ are replaced by three independent functions $u^\mu(x)$.

3. What is the temperature dependence of entropy density for an ideal fluid?

Answer: Rewrite (80) to obtain $c_s^2 d\epsilon = s dT$. Now calculate $d\epsilon/dT$ from (83) to find $s \propto T^{1/c_s^2}$.

4. Show that (79) holds for a $(3 + 1)$ -dimensional perfect fluid with Bjorken boost-invariant initial condition.

Answer: The lengthy but straightforward calculation can be found in Appendix A of ref. [15].

8. – Hard probes

In heavy-ion collisions at collider energies, there are partonic interactions which occur at high momentum transfer. *A fortiori*, these interactions occur over a small length scale $\Delta x \sim 1/Q$. If this scale is much smaller than the wavelengths of typical excitations in the medium, then one expects on general grounds that the large- Q process is sufficiently pointlike to be unaffected by the medium. However, the partons which enter and leave the hard interaction vertex will propagate through several fermi of dense QCD matter. Thus medium-modification of hard processes can occur via interactions of the partons with the medium in the *incoming* or *outgoing* state. If the hard process can be understood with sufficient precision, then its medium modification can provide information about the medium: the hard process becomes a hard probe.

The picture advocated above assumes that hard processes in heavy-ion collisions can be understood by factorizing the dynamics of the incoming and outgoing partons from that of the hard pointlike partonic interaction. For many hard processes in hadronic (p - p or p - \bar{p}) collisions, we know that such a factorization is realized up to corrections of relative order $\sim 1/Q^2$. For the medium-modifications studied in heavy-ion physics, however, factorization is not proven and it is unlikely to hold in the sense of a $1/Q^2$ -expansion. To what extent factorization is a useful concept for heavy-ion phenomenology remains to be established in a model-dependent interplay with experiment.

8.1. High- p_T single inclusive hadron spectra in nucleus-nucleus collisions. – We shall focus first on one class of hard processes, namely single inclusive hadronic spectra $dN/d^2p_T dy$ close to mid rapidity $y \sim 0$ and for sufficiently high transverse momentum p_T . In the absence of medium effects, the high- p_T particle yield grows proportionally to the number of hard partonic interactions, which is proportional to the number of

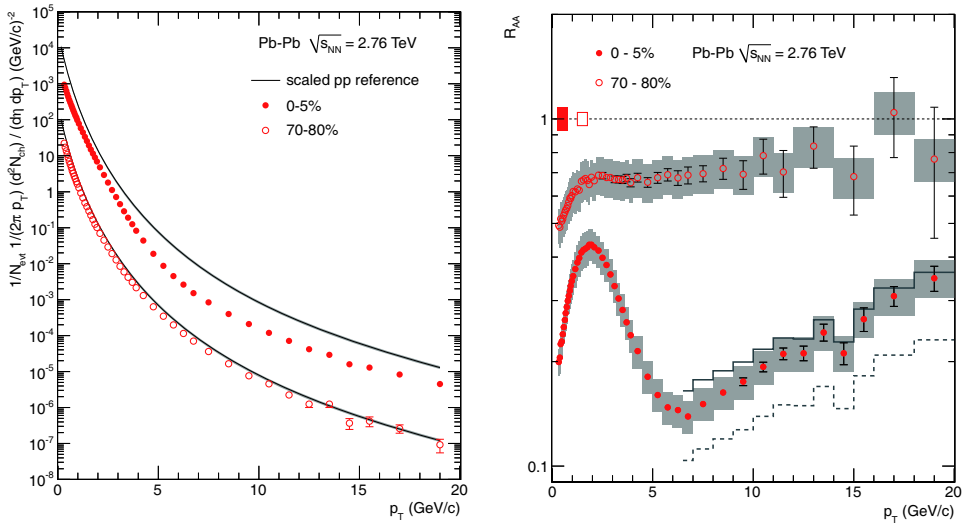


Fig. 11. – Left: transverse-momentum spectra for charged hadrons measured by the ALICE Collaboration in $\sqrt{s_{\text{NN}}} = 2.76$ TeV Pb-Pb collisions at the LHC for the most central and one peripheral centrality class, plotted together with the corresponding binary-scaled p-p reference spectra. Right: the nuclear modification factor equation (101).

nucleon-nucleon collisions,

$$(100) \quad \frac{dN^{A B \rightarrow h}}{d^2p_T dy} = \langle N_{\text{coll}}^{AB} \rangle \frac{dN^{pp \rightarrow h}}{d^2p_T dy}, \quad \text{without medium effects.}$$

Here, the average number $\langle N_{\text{coll}}^{AB} \rangle$ of nucleon-nucleon collisions is determined by a Glauber model calculation, see subsect. 5.1.2. The single inclusive spectrum in a nucleon-nucleon collision is determined either experimentally (*e.g.*, in p+p collisions at RHIC or LHC), or theoretically within the framework of perturbative factorization. To characterize deviations from this benchmark, we introduce the nuclear modification factor

$$(101) \quad R_{AB}^h(p_T, y, \text{centrality}) = \frac{\frac{dN^{A B \rightarrow h}}{d^2p_T dy}}{\langle N_{\text{coll}}^{AB} \rangle \frac{dN^{pp \rightarrow h}}{d^2p_T dy}}.$$

By construction, this factor equals unity in the absence of medium-effects, and it decreases if the medium suppresses the production of hard particles.

The nuclear modification factor R_{AA} for non-identified charged particles at the LHC has been measured by the ALICE Collaboration [19]; it is shown in fig. 11. As a measure of the centrality of the collision, the number of participants is used, see our discussion of fig. 3. The transverse momentum spectra measured for central collisions and for one peripheral centrality class are divided by the binary-scaled p-p reference. For peripheral

nucleus-nucleus collisions, the high- p_T yield of charged hadrons is comparable to that in elementary p-p collisions. With increasing centrality, however, this yield decreases significantly in comparison to the benchmark expectation (100). For the most central collisions, this suppression is approximately 5-fold at RHIC (see figs. 11 and 13), and is even more pronounced at the LHC, reaching a factor 7 at the R_{AA} minimum. In contrast, at RHIC high- p_T photons were found to be unaffected within errors. This is consistent with the picture that the strong medium-induced suppression of high- p_T hadrons is a final-state effect, which does not occur for photons since these do not interact hadronically. Moreover, if one assumes that high- p_T photon spectra remain unmodified, then the nuclear modification factor for photons becomes a test of the assumption that hard processes in heavy-ion collisions scale with the number of binary nucleon-nucleon collisions, which can be determined via a Glauber calculation of $\langle N_{\text{coll}}^{AB} \rangle$.

Figure 11 is only one manifestation of a general phenomenon. In heavy-ion collisions at RHIC, *all* single inclusive hadron spectra were found to be suppressed by comparable large suppression factors. At the LHC, a corresponding detailed analysis will be carried out in the coming years. We first list the generic features found in RHIC data:

- Strong and apparently p_T -independent suppression of R_{AA} at high p_T .

In $\sqrt{s_{\text{NN}}} = 200 \text{ GeV}$, 5–10% central Au-Au collisions at mid-rapidity, one observes a suppression of high- p_T single inclusive hadron yields by a factor ~ 5 , corresponding to $R_{\text{AuAu}}^h(p_T) \simeq 0.2$ for $p_T \sim 5\text{--}15 \text{ GeV}/c$. Within experimental errors, this suppression is p_T -independent for higher transverse momenta in all centrality bins (see, *e.g.*, fig. 13).

- Evidence for final-state effect.

For the most peripheral centrality bin, the nuclear modification factors measured at RHIC are consistent with the absence of medium-effects in both nucleus-nucleus ($R_{AA} \sim 1$) and deuterium-nucleus ($R_{d\text{-Au}} \sim 1$) collisions. With increasing centrality, R_{AA} decreases monotonically. In contrast, no such suppression is seen in d-Au collisions. These and other observations indicate that the suppression occurs on the level of the produced outgoing partons or hadrons, it increases with increasing in-medium pathlength in the final state, and it is absent in d-Au collisions, where the in-medium pathlength is negligible.

- Independence of R_{AA} on hadron identity.

For transverse momenta $p_T \sim 5\text{--}15 \text{ GeV}/c$, all identified hadron spectra show a quantitatively comparable degree of suppression. There is no particle-species dependence of the suppression pattern at high p_T . Since cross-sections for different hadron species differ widely, the species-independence of high- p_T R_{AA} indicates that the mechanism responsible for suppression occurs prior to hadronization.

There are many detailed accounts of these observations in the recent literature, see for instance ref. [13] and references therein. For the purpose of these notes, we merely observe

that the suppression of R_{AA} for hadrons is one of the strongest medium-modifications observed in heavy-ion collisions at RHIC, and that it is a generic phenomenon found in all high- p_T hadron spectra. We also note that the above observations suggest to base a dynamic understanding of this effect on the medium-induced energy loss of high energy final-state partons prior to hadron formation. As a consequence, the standard modeling of single inclusive hadron spectra proceeds by supplementing a pQCD factorized formalism for single inclusive spectra with a medium modification of the produced partons prior to hadronization in the final state. To explain how this medium modification is introduced, we discuss in the next two sections how the propagation of highly energetic partons is modified in the presence of QCD matter.

We conclude this discussion by putting the first LHC measurement, fig. 11, in context with the generic features in RHIC data, listed above. One sees clearly that the ALICE data are consistent both, with the degree of the suppression and with its centrality dependence. In the most central bin, however, the nuclear modification factor measured by ALICE shows characteristic differences if compared to that at RHIC. First, at sufficiently high transverse momentum ($p_T > 7 \text{ GeV}$), the nuclear modification factor shows a monotonous increase that was not visible in the RHIC data. Moreover, a closer look at the LHC Pb-Pb and p-p spectra before taking the ratio (left-hand side of fig. 11) provides insight into the dynamical origin of the peak in R_{AA} at low p_T . In proton-proton collisions, the single inclusive hadron spectrum at LHC energy shows a characteristic power-law dependence in $1/p_T$, as expected from perturbative QCD. In central Pb-Pb collisions, however, ALICE observes a close to exponential slope up to transverse momenta of $p_T \sim 5 \text{ GeV}$, as one would expect for a thermal particle production mechanism. The characteristic shape of R_{AA} for $p_T < 5 \text{ GeV}$ results from dividing an exponential slope by a power-law one and appears to be a manifestation of thermalization up to relatively large transverse momentum.

8.2. Scattering of highly energetic partons in nuclear matter. – The purpose of this subsection is to give for the simplest example a complete derivation of medium-induced gluon radiation of a highly energetic parton traversing a spatially extended target. The case considered is that of an ultra-relativistic quark travelling a long distance through the vacuum (*i.e.* having the time to build up a fully developed perturbative wave function) prior to impinging on the nuclear target. This problem can be formulated and solved, using quantum-mechanical concepts only. Despite its simplicity, it carries many features of a more complete formulation of radiative energy loss, which we discuss in the next subsection. Here, our discussion follows closely ref. [20], where more details can be found.

How can we describe the propagation of a highly energetic parton propagating through dense nuclear matter? At high energy, a spatially extended target appears Lorentz contracted, so the propagation time of a partonic projectile through the target is short, partons propagate independently of each other and their transverse positions do not change during the propagation. For the wave function Ψ_{in} of an incoming hadronic projectile, the relevant degrees of freedom of each of its partonic components are then the position \mathbf{x}_i in transverse space and the colour index α_i in the fundamental, anti-fundamental or

adjoint representation of the colour $SU(N)$ group, corresponding to a quark, anti-quark or gluon in the wave function. We write

$$(102) \quad |\Psi_{\text{in}}\rangle = \sum_{\{\alpha_i, \mathbf{x}_i\}} \psi(\{\alpha_i, \mathbf{x}_i\}) |\{\alpha_i, \mathbf{x}_i\}\rangle.$$

In the eikonal approximation applicable at high projectile energy, the only effect of the propagation is that the wave function of each parton in the projectile acquires an eikonal phase due to the interaction with the target field. These phases are given by Wilson lines along the (straight line) trajectories of the propagating particles

$$(103) \quad W(\mathbf{x}_i) = \mathcal{P} \exp \left[i \int dz^- T^a A_a^+(\mathbf{x}_i, z^-) \right].$$

Here, A^+ is the large component of the target colour field and T^a is the generator of $SU(N)$ in the representation corresponding to a given parton. Equation (103) is the specific form of the phase factor in the lightcone gauge $A^- = 0$ for a projectile moving in the negative z direction, so that the lightcone coordinate $x^+ = (z + t)/\sqrt{2}$ does not change during propagation through the target. The phase factor takes a different form in other gauges or other Lorentz frames, but the final result is gauge invariant and Lorentz covariant, of course. The projectile emerges from the interaction region with the wave function

$$(104) \quad |\Psi_{\text{out}}\rangle = \mathcal{S} |\Psi_{\text{in}}\rangle = \sum_{\{\alpha_i, \mathbf{x}_i\}} \psi(\{\alpha_i, \mathbf{x}_i\}) \prod_i W(\mathbf{x}_i)_{\alpha_i \beta_i} |\{\beta_i, \mathbf{x}_i\}\rangle.$$

The phase factors (103) define the scattering matrix \mathcal{S} .

The physics implemented in the eikonal formalism is the following: the interaction of the projectile wave function with the target field changes the relative phases between components of the wave function and thus “decoheres” the initial state. As a result the final state is different from the initial one, and contains emitted gluons. To see how this works in practice, we consider gluon radiation of a hard quark which propagates at high energy through a nuclear target.

If the quark comes from outside the target, it impinges with a fully developed wave function which contains a cloud of quasi-real gluons. In the first order in perturbation theory, the incoming wave function contains the Fock state $|\alpha\rangle$ of the bare quark, supplemented by the coherent state of quasi-real gluons which build up the Weizsäcker-Williams field $f(\mathbf{x})$,

$$(105) \quad \begin{aligned} |\Psi_{\text{in}}^\alpha\rangle &= |\alpha\rangle + \int d\mathbf{x} d\xi f(\mathbf{x}) T_{\alpha\beta}^b |\beta; b(\mathbf{x}, \xi)\rangle \\ &= \frac{\alpha}{T_{\alpha\beta}^b} \alpha + \frac{\alpha}{T_{\alpha\beta}^b} \text{gluons } b \beta . \end{aligned}$$

Here Lorentz and spin indices are suppressed. In the projectile lightcone gauge $A^- = 0$, the gluon field of the projectile is the Weizsäcker-Williams field

$$(106) \quad A^i(\mathbf{x}) \propto \theta(x^-) f_i(\mathbf{x}), \quad f_i(\mathbf{x}) \propto g \frac{\mathbf{x}_i}{\mathbf{x}^2},$$

where $x^- = 0$ is the lightcone coordinate of the quark in the wave function. The integration over the rapidity of the gluon in the wave function (105) goes over the gluon rapidities smaller than that of the quark. In the leading logarithmic order the wave function does not depend on rapidity and we suppress the rapidity label in the following.

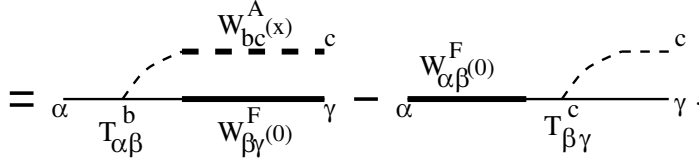
The interaction of the projectile (105) with the target leads to a colour rotation $\alpha_i \rightarrow \beta_i$ of each projectile component i , resulting in an eikonal phase $W(\mathbf{x}_i)_{\alpha_i \beta_i}$. The outgoing wave function reads

$$(107) \quad |\Psi_{\text{out}}^\alpha\rangle = W_{\alpha\gamma}^F(\mathbf{0}) |\gamma\rangle + \int d\mathbf{x} f(\mathbf{x}) T_{\alpha\beta}^b W_{\beta\gamma}^F(\mathbf{0}) W_{bc}^A(\mathbf{x}) |\gamma; c(\mathbf{x})\rangle,$$

where $W^F(\mathbf{0})$ and $W^A(\mathbf{x})$ are the Wilson lines in the fundamental and adjoint representations, respectively, corresponding to the propagating quark at the transverse position $\mathbf{x}_q = \mathbf{0}$ and gluon at $\mathbf{x}_g = \mathbf{x}$.

We want to count the number of gluons in the state (107). If Ψ_{out} lies within the subspace spanned by the incoming states (105), then we have an elastic scattering process in which no gluons are produced. The only gluons in the final state are then gluons of the gluon cloud of the final state quark. So, to select those wave functions, associated with inelastic processes in which gluons are produced, we have to calculate the projection on the subspace orthogonal to the incoming states,

$$(108) \quad |\delta\Psi_\alpha\rangle = |\Psi_{\text{out}}^\alpha\rangle - \sum_\gamma |\Psi_{\text{in}}(\gamma)\rangle \langle \Psi_{\text{in}}(\gamma)| \Psi_{\text{out}}^\alpha\rangle$$



Here, the index γ in the projection operator runs over the quark colour index, so that the second term in (108) projects out the entire Hilbert subspace of incoming states.

The number spectrum of produced gluons is obtained by calculating the number of gluons in the state $\delta\Psi_\alpha$, averaged over the incoming colour index α . After some colour

algebra, one obtains

$$(109) \quad N_{\text{prod}}(\mathbf{k}) = \frac{1}{N} \sum_{\alpha} \langle \delta\Psi_{\alpha} | a_d^{\dagger}(\mathbf{k}) a_d(\mathbf{k}) | \delta\Psi_{\alpha} \rangle \\ = \frac{\alpha_s C_F}{2\pi} \int d\mathbf{x} d\mathbf{y} e^{i\mathbf{k}\cdot(\mathbf{x}-\mathbf{y})} \frac{\mathbf{x}\cdot\mathbf{y}}{\mathbf{x}^2\mathbf{y}^2} \left[1 - \frac{1}{N^2-1} \langle\langle \text{Tr} [W^A{}^{\dagger}(\mathbf{x}) W^A(\mathbf{0})] \rangle\rangle_t \right. \\ - \frac{1}{N^2-1} \langle\langle \text{Tr} [W^A{}^{\dagger}(\mathbf{y}) W^A(\mathbf{0})] \rangle\rangle_t \\ \left. + \frac{1}{N^2-1} \langle\langle \text{Tr} [W^A{}^{\dagger}(\mathbf{y}) W^A(\mathbf{x})] \rangle\rangle_t \right].$$

Here, we have used $f(\mathbf{x}) f(\mathbf{y}) = \frac{\alpha_s}{2\pi} \frac{\mathbf{x}\cdot\mathbf{y}}{\mathbf{x}^2\mathbf{y}^2}$ for the Weizsäcker-Williams field of the quark projectile in configuration space and the symbol $\langle\langle \dots \rangle\rangle_t$ denotes the averaging over the gluon fields of the target.

It is noteworthy that in the radiation spectrum (109), the entire information about the target resides in the target average of two light-like adjoint Wilson lines. Although the presence of quarks leads to the appearance of fundamental Wilson lines in intermediate stages of the calculation, see, *e.g.*, eq. (107), the averaging involved in (109) combines them into adjoint ones with the help of the Fierz identity $W_{ab}^F(\mathbf{x}) = 2 \text{Tr}[T^a W^F{}^{\dagger}(\mathbf{x}) T^b W^F(\mathbf{x})]$.

To arrive at an explicit expression for the target average in (109), one needs to specify the target colour field. A particularly simple model is to assume that A^+ arises from a collection of static scattering centres with scattering potentials $a_a^+(\mathbf{q})$ at positions $(\hat{\mathbf{x}}_n, \hat{z}_n)$. In the high-energy approximation, each scattering centre transfers only transverse momentum to the projectile,

$$(110) \quad A_a^+(\mathbf{x}, z^-) = \sum_n \int \frac{d^2\mathbf{q}}{(2\pi)^2} e^{i(\mathbf{x}-\hat{\mathbf{x}}_n)\cdot\mathbf{q}} a_a^+(\mathbf{q}) \delta(z^- - \hat{z}_n^-).$$

The target average can then be defined as an average over the transverse positions of the static scattering centres. Introducing the longitudinal density of scattering centres, $n(z^-) = \sum_n \delta(z^- - \hat{z}_n^-)$, one has

$$(111) \quad \left\langle \left\langle \int dz^- d\tilde{z}^- A_a^+(\mathbf{x}, z^-) A_a^+(\mathbf{y}, \tilde{z}^-) \right\rangle \right\rangle_t = \int d\xi n(\xi) \frac{C_A}{2} \sigma(\mathbf{x} - \mathbf{y}),$$

$$(112) \quad \sigma(\mathbf{x} - \mathbf{y}) = 2 \int \frac{d^2\mathbf{q}}{(2\pi)^2} |a^+(\mathbf{q})|^2 \left(1 - e^{i\mathbf{q}\cdot(\mathbf{x}-\mathbf{y})} \right).$$

Here, we have introduced the dipole cross-section $\sigma(\mathbf{x} - \mathbf{y})$, which provides in configuration space the full information about the cross-section $|a^+(\mathbf{q})|^2$ of a single scattering centre. The target average of two Wilson lines can then be defined in terms of this dipole

cross-section

$$(113) \quad \frac{1}{N^2 - 1} \langle\langle \text{Tr} [W^{A\dagger}(\mathbf{y}) W^A(\mathbf{x})] \rangle\rangle_t \approx \exp \left[-\frac{C_A}{4C_F} \int d\xi n(\xi) \sigma(\mathbf{x} - \mathbf{y}) \right].$$

8.3. Gluon radiation off quarks produced in the medium. – The purpose of this subsection is to discuss medium-induced gluon radiation off a parton produced in a large momentum transfer process *in the medium*. This problem is significantly more complicated than that discussed in the previous section mainly because of two issues:

- Interference between radiation in the vacuum and medium-induced radiation.

In the absence of a medium, a parton produced in a hard process will radiate its large virtuality Q on a typical timescale $1/Q$ by developing a parton shower. In the rest frame of the medium, this time scale is Lorentz dilated by a factor E_{parton}/M , where the parton mass is $M \sim Q$. Typical radiation times $\sim E_{\text{parton}}/Q^2$ are comparable to the typical in-medium pathlengths in a nucleus-nucleus collision. As a consequence, one expects an interference pattern between the radiation present in the vacuum, and the additional radiation induced due to scattering in the medium.

- Corrections to eikonal approximation are needed.

In the ultra-high-energy (eikonal) approximation, the longitudinal extension of the target is contracted to a delta-function. As a consequence, gluon radiation off a hard parton occurs either before or after the target, but not within the target. This can be seen, *e.g.*, in eq. (108), where the Wilson lines (which stand for interactions between projectile and target) occur in both diagrams only before or after the gluon radiation vertex. In contrast, to take interference effects into account, it is important to locate the gluon emission vertex inside the medium. This requires a formulation which knows about longitudinal distances in the medium. The momentum conjugate to longitudinal distance is the light cone energy p_- . So, to place an emission vertex within the medium, one has to keep track at least of the $1/p_-^+$ corrections to the eikonal formalism.

In the following, we present the main elements of a formulation which goes beyond the eikonal approximation and accounts for interference effects between vacuum and medium-induced radiation. We start by writing down a lightcone Green's function

$$(114) \quad G(\mathbf{r}_{\text{in}}, x_{\text{in}}^-; \mathbf{r}_{\text{out}}, x_{\text{out}}^- | p^-) = \int_{\mathbf{r}(x_{\text{in}}^-) = \mathbf{r}_{\text{in}}}^{\mathbf{r}(x_{\text{out}}^-) = \mathbf{r}_{\text{out}}} \mathcal{D}\mathbf{r}(\xi) \exp \left[i \frac{p_-}{4} \int_{x_{\text{in}}^-}^{x_{\text{out}}^-} x d\xi \dot{\mathbf{r}}^2(\xi) \right] \times W(\mathbf{r}(\xi); x_{\text{in}}^-, x_{\text{out}}^-),$$

$$(115) \quad W(\mathbf{r}; x_{\text{in}}^-, x_{\text{out}}^-) = \mathcal{P} \exp \left[i \int_{x_{\text{in}}^-}^{x_{\text{out}}^-} d\xi A^+(\mathbf{r}(\xi), \xi) \right].$$

Equation (114) is the solution of the Dirac equation for a coloured partonic projectile propagating in a spatially extended colour field A^+ . The solution is exact up to

order $O(1/p^-)$. To this order, it contains a non-eikonal Wilson line (115), which “wiggles” in transverse position along a path $\mathbf{r}(\xi)$. In the limit of ultra-high parton energy, $p^- \rightarrow \infty$, when the finite energy corrections of order $O(1/p^-)$ vanish, this expression reduces to the eikonal Wilson line (103),

$$(116) \quad \lim_{p^- \rightarrow \infty} G(\mathbf{r}_{\text{in}}, x_{\text{in}}^-; \mathbf{r}_{\text{out}}, x_{\text{out}}^- | p^-) = W(\mathbf{r}_{\text{in}}; x_{\text{in}}^-, x_{\text{out}}^-) \delta^{(2)}(\mathbf{r}_{\text{out}} - \mathbf{r}_{\text{in}}).$$

In close analogy to the target averages in the eikonal formalism (see eqs. (111)–(113)), one finds that the target averages over pairs of Green’s functions (114) of energy αp and $(1 - \alpha)p$ leads to a path integral expression

$$(117) \quad \mathcal{K}(\mathbf{r}', z'; \mathbf{r}, z | \mu) = \int \mathcal{D}\mathbf{r} \exp \left[i \int_z^{z'} d\xi \left[\frac{\mu}{2} \dot{\mathbf{r}}^2 + i \frac{1}{2} n(\xi) \sigma(\mathbf{r}) \right] \right].$$

Here, $\mu \equiv \alpha(1 - \alpha)p$. Also, in accordance with the notation used in parton energy loss calculations, we have changed from lightcone coordinates to the longitudinal z , and we have absorbed a factor C_A/C_F in the definition of the dipole cross-section. Keeping these notational changes in mind, one can check that the $\mu \rightarrow \infty$ limit of (117) coincides with the average (113) of two eikonal Wilson lines, as it should.

The inclusive energy distribution of gluon radiation off an in-medium produced parton can be expressed in terms of the Zakharov path integral (117) like

$$(118) \quad \omega \frac{dI}{d\omega} = \frac{\alpha_s C_R}{(2\pi)^2 \omega^2} 2 \operatorname{Re} \int_{\xi_0}^{\infty} dy_l \int_{y_l}^{\infty} d\bar{y}_l \int \mathbf{du} \int_0^{\chi\omega} dk_{\perp} e^{-i\mathbf{k}_{\perp} \cdot \mathbf{u}} e^{-\frac{1}{2} \int_{\bar{y}_l}^{\infty} d\xi n(\xi) \sigma(\mathbf{u})} \\ \times \frac{\partial}{\partial \mathbf{y}} \cdot \frac{\partial}{\partial \mathbf{u}} \int_{\mathbf{y}=0}^{\mathbf{u}=\mathbf{r}(\bar{y}_l)} \mathcal{D}\mathbf{r} \exp \left[i \int_{y_l}^{\bar{y}_l} d\xi \frac{\omega}{2} \left(\dot{\mathbf{r}}^2 - \frac{n(\xi) \sigma(\mathbf{r})}{i \omega} \right) \right].$$

Here, \mathbf{k}_{\perp} denotes the transverse momentum of the emitted gluon. The two-dimensional transverse coordinates \mathbf{u} , \mathbf{y} and \mathbf{r} emerge in the derivation of (118) as distances between the positions of projectile components in the amplitude and complex conjugate amplitude. The longitudinal coordinates y_l , \bar{y}_l integrate over the ordered longitudinal gluon emission points in amplitude and complex conjugate amplitude. The limit $k_{\perp} = |\mathbf{k}_{\perp}| < \chi \omega$ on the transverse phase space restricts gluon emission to a finite opening angle Θ , $\chi = \sin \Theta$. For the full angular integrated quantity, $\chi = 1$.

Equation (118) is a compact expression. Its derivation and full explanation lie outside the scope of these lectures. Here, we limit ourselves to a discussion of the main physics features encoded in (118). We observe first that all information about the medium enters again via the dipole cross-section times density, as in the eikonal formalism (113). While the expression (118) has been derived for a particular model (110) of the target field strength, eq. (113) suggests a more model-independent interpretation: the only medium-dependent information entering the gluon energy distribution (118) is information about

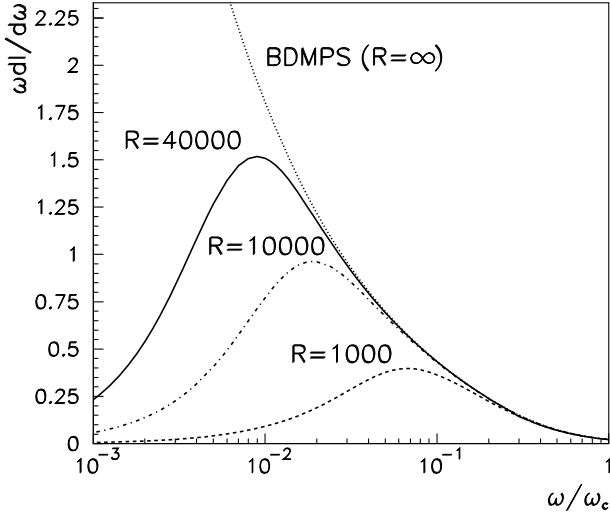


Fig. 12. – The medium-induced gluon energy distribution $\omega \frac{dI}{d\omega}$ as a function of the gluon energy ω in units of $\omega_c = \frac{1}{2}\hat{q}L^2$, and for different values of the kinematic constraint $R = \omega_c L$. Figure taken from ref. [21].

the target expectation value of an adjoint Wilson loop whose long side points in the light-like direction. In fact, what matters mainly is the short transverse distance behaviour of this Wilson loop. At short distances, we can write

$$(119) \quad n(\xi) \sigma(\mathbf{r}) \simeq \frac{1}{2} \hat{q}(\xi) \mathbf{r}^2.$$

Here, $\hat{q}(\xi)$ is referred to as BDMPS (Baier-Dokshitzer-Mueller-Peigné-Schiff) transport coefficient. As first exploited by Zakharov, using (119) in the energy distribution (118) amounts to a saddle point approximation of the path integral. The path integral becomes that of a harmonic oscillator and can be calculated explicitly.

Figure 12 shows a numerical evaluation of the medium-induced gluon energy distribution (118) for a static BDMPS transport coefficient $\hat{q} = \hat{q}(\xi)$ extending over a finite in-medium pathlength L .

Main features of the gluon energy distribution in fig. 12 can be understood in terms of qualitative arguments. We consider a gluon in the hard-parton wave function. This gluon is emitted due to multiple scattering if it picks up sufficient transverse momentum to decohere from the partonic projectile. For this, the average phase φ accumulated by the gluon should be of order one,

$$(120) \quad \varphi = \left\langle \frac{k_\perp^2}{2\omega} \Delta z \right\rangle \sim \frac{\hat{q}L}{2\omega} L = \frac{\omega_c}{\omega}.$$

Thus, for a hard parton traversing a finite path length L in the medium, the scale of the radiated energy distribution is set by the “characteristic gluon frequency”

$$(121) \quad \omega_c = \frac{1}{2} \hat{q} L^2.$$

For an estimate of the shape of the energy distribution, we consider the number N_{coh} of scattering centres which add coherently in the gluon phase (120), $k_\perp^2 \simeq N_{\text{coh}} \langle q_\perp^2 \rangle_{\text{med}}$. Based on expressions for the coherence time of the emitted gluon, $t_{\text{coh}} \simeq \frac{\omega}{k_\perp^2} \simeq \sqrt{\frac{\omega}{\hat{q}}}$ and $N_{\text{coh}} = \frac{t_{\text{coh}}}{\lambda} = \sqrt{\frac{\omega}{\langle q_\perp^2 \rangle_{\text{med}} \lambda}}$, one estimates for the gluon energy spectrum per unit path length

$$(122) \quad \omega \frac{dI}{d\omega dz} \simeq \frac{1}{N_{\text{coh}}} \omega \frac{dI^{1\text{ scatt}}}{d\omega dz} \simeq \frac{\alpha_s}{t_{\text{coh}}} \simeq \alpha_s \sqrt{\frac{\hat{q}}{\omega}}.$$

This $1/\sqrt{\omega}$ -energy dependence of the medium-induced non-Abelian gluon energy spectrum is expected for sufficiently small $\omega < \omega_c$. It is confirmed in fig. 12 if one neglects (as for the above estimate) kinematical constraint in transverse phase space, which cut off the energy distribution in the infrared. For the ω -integrated average parton energy loss, one finds analytically from (118)

$$(123) \quad \langle \Delta E \rangle_{R \rightarrow \infty} = \lim_{R \rightarrow \infty} \int_0^\infty d\omega \omega \frac{dI}{d\omega} = \frac{\alpha_s C_R}{2} \omega_c \propto \hat{q} L^2.$$

The same parametric dependence $\propto \hat{q} L^2$ can be found from the above pocket estimates, if one integrates the differential distribution (122) over an in-medium path length L and over the gluon energy ω up to ω_c , above which (122) breaks down since the phase φ is smaller than unity. So, the pocket estimate (122) provides the correct small- ω behaviour as well as the correct dependence of the average energy loss on density and in-medium path length. In particular, the L^2 -dependence was first derived by BDMPS.

8.4. Comparing parton energy loss calculations to data on R_{AA} . — Models including radiative parton energy loss have been shown to reproduce the main qualitative and quantitative features of high- p_T hadron spectra at RHIC. In the simplest case, one uses the standard pQCD factorized formalism for the calculation of single inclusive hadron spectra in p-p. This defines the denominator of the nuclear modification factor (101). For the calculation of the same spectrum in nucleus-nucleus collisions, one then specifies a model in which the transverse momentum of the outgoing partons is degraded as a function of the in-medium path length and of properties of the medium (such as its local density). For instance, the BDMPS parton energy loss discussed in the previous section leads to a model description, in which this final-state parton energy loss depends on the BDMPS quenching parameter \hat{q} and the geometry of the collision. Figure 13 shows but one example that models of radiative parton energy loss can reproduce main features in the data if the only model parameter \hat{q} is chosen appropriately.

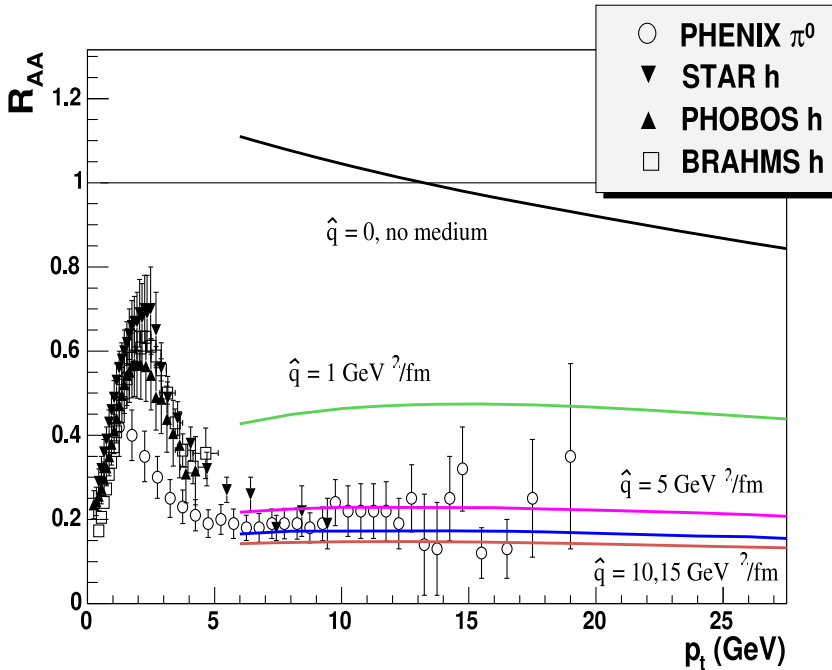


Fig. 13. – The nuclear modification factor $R_{AA}(p_T)$ for charged hadrons and neutral pions in central Au+Au collisions at 200 A GeV, together with curves from a model of radiative parton energy loss [22] for different quenching parameter \hat{q} .

A sector where there is currently significant tension between data and theoretical predictions is that of heavy flavour quenching. In the BDMPS formalism, energy loss effects are expected to be smaller for heavy flavour particles than for their light flavour counterparts [23], due to the suppression of small angle gluon radiation for massive partons and to the colour coupling being smaller for quarks than for gluons⁽³⁾. Experimentally, on the other hand, heavy flavours seem to be quenched at a similar level as light flavours. An example is shown in fig. 14, where the nuclear modification factor for non-photonic electrons (a sample of electrons from which the contribution from conversions and Dalitz decays has been subtracted, and that is therefore expected to be dominated by heavy-flavour electrons) is plotted *versus* p_T for d-Au and Au-Au collisions at RHIC [24]. For Au-Au collisions at transverse momenta above 5 GeV/c the R_{AA} of non-photonic electrons reaches values around 0.2, comparable with those measured for light hadrons. The predictions from various theoretical models are also shown in the figure. The theoretical uncertainties, not indicated in these model curves, are significant, and taking them into

⁽³⁾ Heavy flavour hadrons originate mainly in quark jets, while light hadrons originate from a p_T -dependent mixture of quark and gluon jets.

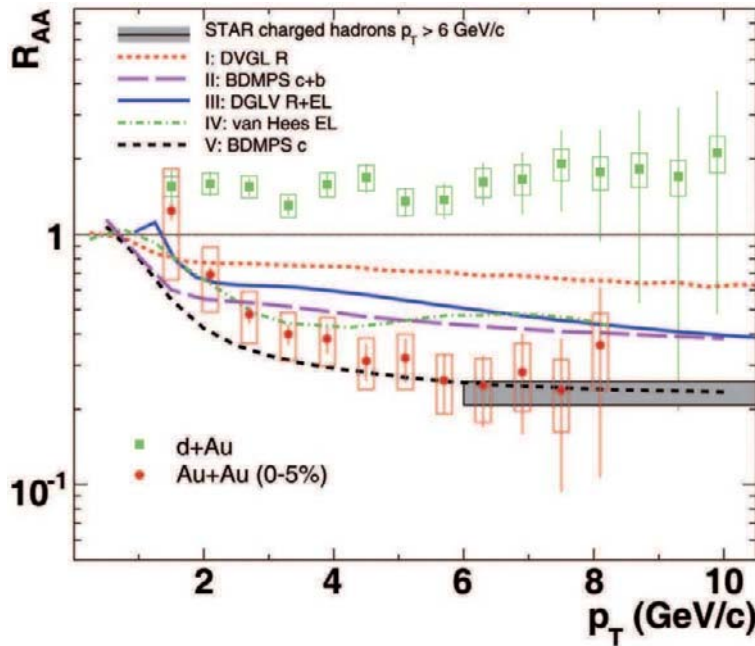


Fig. 14. – The nuclear modification factor, R_{AA} , measured by the STAR Collaboration for d-Au and Au-Au collisions at $\sqrt{s_{NN}} = 200$ GeV, compared with theoretical predictions [24].

account, it has been argued that one cannot state inconsistency of the data with radiative BDMPS parton energy loss [25]. However, fig. 14 shows that there is a significant tension between theory and data: All the theoretical curves lie above the data for R_{AA} , except for one: a BDMPS calculation in which the contribution from electrons coming from beauty decays is neglected, and the full electron sample is assumed to originate in charm decays (in medium energy loss is expected to be larger for c quarks than for b quarks, due to the mass-dependence of the effect). Indeed, the relative amounts of the charm and beauty contributions to the electron spectra at RHIC are poorly constrained theoretically, and the limited heavy flavour capabilities of the RHIC detectors do not allow a direct experimental separation of the two components. In addition, non-photonic electrons, by themselves, provide a much less direct measurement of heavy-flavour production than the reconstruction of heavy flavour decay vertices. The above discussion illustrates the importance of direct heavy flavour capabilities in the heavy-ion experiments. ALICE, ATLAS and CMS are equipped with high granularity vertex detectors, that will enable separate, direct measurements of the charm and beauty quenchings. This, in turn, will provide firm quantitative constraints on the colour charge and mass dependence of parton energy loss in the QCD medium formed in heavy-ion collisions.

We note that calculations of medium-induced radiative energy loss have been performed mainly close to the eikonal limit, where the projectile energy E is much larger

than the energy of the radiated gluons ω , that is much larger than the transverse gluon energy \mathbf{k} , that is assumed to be much larger than typical momentum scales presented by the medium,

$$(124) \quad E \gg \omega \gg |\mathbf{k}| \gg \Lambda_{\text{QCD}}, T.$$

In the phenomenological praxis, all these assumptions become questionable: significant contributions to radiative energy loss can arise from highly energetic gluons $\omega \simeq O(E)$ and from large angle radiation $|\mathbf{k}| \simeq O(\omega)$. Also, medium-induced gluon radiation will typically include a collinear contribution $|k| \simeq O(\Lambda_{\text{QCD}})$. In addition to a refined theoretical treatment of radiative parton energy loss, going beyond the strong approximation (124) implies that additional contributions to parton energy loss can become important. In particular, collisional energy loss proceeds via elastic scattering on constituents of the medium. Since elastic cross-sections are dominated by small-angle scatterings and grow weakly with center of mass energy, the collisional energy loss mechanism is expected to be suppressed parametrically by a power $1/E$ compared to radiative parton energy loss. It has been argued, however, that collisional mechanisms may contribute significantly in the kinematic range accessible at RHIC. In models in which radiative and collisional mechanisms are super-imposed incoherently, collisional mechanisms can contribute in particular to a stronger medium-induced suppression of heavy flavored hadrons and their decay products [26].

A full-fledged critical review of the state of the art in such data comparison lies beyond the scope of these lecture notes. It would have to include a detailed discussion of alternative descriptions of parton energy loss, additional nuclear effects (such as initial state p_T -broadening), trigger biases in different measurements, issues of nuclear geometry and expansion of the collision region, etc. All these issues are problems of current research. For a recent review, see ref. [27].

8.5. From single inclusive hadron suppression to reconstructed jet quenching. – The signatures for “jet quenching” discussed in these notes so far, were not jets but single inclusive hadron spectra. To account for the observed suppression in R_{AA} , however, we invoked a microscopic dynamics that must affect the entire parton shower, and not only its leading hadronic fragment. It is a longstanding theoretical challenge to extend the current formulation of jet quenching models to the medium-modification of “true”, fully reconstructed jets. In recent years, there has been significant progress in this direction, mainly due to the development of jet finding algorithms that work in the high multiplicity environment of heavy ion collisions [28], and with the development of a first generation of Monte Carlo tools that produce jet-quenched multi-particle final states (see ref. [27] for an overview). Reconstructed jet measurements in heavy-ion collisions are also a formidable experimental challenge, on which there has been significant effort at RHIC, and where the much higher center-of-mass energies at the LHC provide now qualitatively novel opportunities. In our lectures in Varenna, we had emphasized these opportunities by showing several model studies.

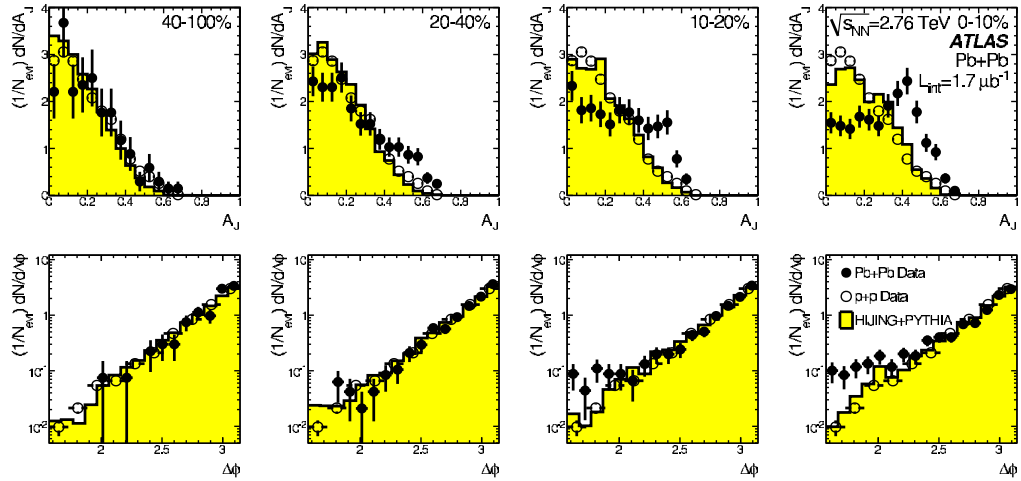


Fig. 15. – ATLAS measurement of the dijet asymmetry distribution in Pb+Pb collisions at the LHC. Top: dijet asymmetry distributions for data (points) and unquenched HIJING with superimposed PYTHIA dijets (solid yellow histograms), as a function of collision centrality (left to right from peripheral to central events). Proton-proton data from $\sqrt{s} = 7$ TeV, analyzed with the same jet selection, is shown as open circles. Bottom: distribution of $\Delta\phi$, the azimuthal angle between the two jets, for data and HIJING+PYTHIA, also as a function of centrality. Figure taken from [29].

Recently, the ATLAS [29] and CMS [30] Collaborations presented first measurements of a strongly enhanced dijet asymmetry in nucleus-nucleus collisions at RHIC. This is the first reconstructed jet observable measured at the LHC. For two jets of energy E_{T1} , E_{T2} , recoiling against each other at an azimuthal angle $|\phi_1 - \phi_2| > \pi/2$, the dijet asymmetry A_J is defined via the ratio

$$(125) \quad A_J \equiv \frac{E_{T1} - E_{T2}}{E_{T1} + E_{T2}}.$$

Here, E_{T1} is the energy of the most energetic jet in the sample. A detailed discussion of the many physics effects that enter a discussion of the A_J -distribution in p-p collisions is beyond the scope of this subsection. We note only that the measurements of jets depends, of course, on the jet definition, and that significant dijet-asymmetries in p-p collisions result, *e.g.*, from 3- and more jet events, in which the most energetic jet is balanced by more than one jet. The striking effect seen at LHC (see fig. 15) is that the rate of asymmetric dijet events increases with increasing collision centrality, while the azimuthal distribution of dijets remains almost unchanged. This is indicative of a strong medium modification of the jet fragmentation that originates from the soft jet fragments (and not, *e.g.*, from an enhanced three-jet rate). For a qualitative explanation of why this is so, we refer to ref. [31].

This subsection is but a teaser, alerting the reader that many of the open questions discussed in our lectures in Varenna start now to be addressed by experimental data from the LHC.

Use your chance to work on such questions!

Questions:

- Calculate explicitly the projection $|\delta\Psi_\alpha\rangle$ in (108) of the wave function $|\Psi_{\text{out}}^\alpha\rangle$ (107) on the subspace orthogonal to the incoming states.

Answer: The result has the structure given diagrammatically in (108). Details about the derivation can be found in ref. [20].

- From the explicit expression for $|\delta\Psi_\alpha\rangle$ in (108) derive the number of produced gluons (109).

REFERENCES

- [1] WIEDEMANN U. A., *Heavy-ion collisions: Selected topics*, CERN Yellow Report, CERN-2008-007.
- [2] AAMODT K. *et al.* (THE ALICE COLLABORATION), *Phys. Rev. Lett.*, **105** (2010) 252301 [arXiv:1011.3916 [nucl-ex]].
- [3] DE JAGER C. W., DE VRIES H. and DE VRIES C., *At. Data Nucl. Data Tables*, **14** (1974) 479.
- [4] BIALAS A., BLESZYNKI M. and CZYZ W., *Nucl. Phys. B*, **111** (1976) 461.
- [5] ALVER B. and ROLAND G., *Phys. Rev. C*, **81** (2010) 054905; **82** (2010) 039903 (Erratum) [arXiv:1003.0194 [nucl-th]].
- [6] KHARZEEV D. and NARDI M., *Phys. Lett. B*, **507** (2001) 121 [arXiv:nucl-th/0012025].
- [7] AAMODT K. *et al.* (THE ALICE COLLABORATION), arXiv:1011.3914 [nucl-ex].
- [8] ADAMS J. *et al.* (STAR COLLABORATION), *Phys. Rev. Lett.*, **91** (2003) 072304 [arXiv:nucl-ex/0306024].
- [9] KUHLMAN A. J. and HEINZ U. W., *Phys. Rev. C*, **72** (2005) 037901 [arXiv:nucl-th/0506088].
- [10] ARMESTO N. and PAJARES C., *Int. J. Mod. Phys. A*, **15** (2000) 2019 [arXiv:hep-ph/0002163].
- [11] ESKOLA K. J., *Nucl. Phys. A*, **698** (2002) 78 [arXiv:hep-ph/0104058].
- [12] BUSZA W., *Acta Phys. Polon. B*, **35** (2004) 2873 [arXiv:nucl-ex/0410035].
- [13] BORGHINI N. and WIEDEMANN U. A., arXiv:0707.0564 [hep-ph].
- [14] BORGHINI N., DINH P. M. and OLLITRAULT J. Y., *Phys. Rev. C*, **63** (2001) 054906 [arXiv:nucl-th/0007063].
- [15] KOLB P. F., SOLLFRANK J. and HEINZ U. W., *Phys. Rev. C*, **62** (2000) 054909 [arXiv:hep-ph/0006129].
- [16] KOLB P. F. and HEINZ U. W., arXiv:nucl-th/0305084.
- [17] HEINZ U. W., arXiv:nucl-th/0512051.
- [18] ROMATSCHKE P. and ROMATSCHKE U., *Phys. Rev. Lett.*, **99** (2007) 172301 [arXiv:0706.1522 [nucl-th]].
- [19] AAMODT K. *et al.* (ALICE COLLABORATION), *Phys. Lett. B*, **696** (2011) 30 [arXiv:1012.1004 [nucl-ex]].
- [20] KOVNER A. and WIEDEMANN U. A., arXiv:hep-ph/0304151.
- [21] SALGADO C. A. and WIEDEMANN U. A., *Phys. Rev. D*, **68** (2003) 014008 [arXiv:hep-ph/0302184].
- [22] ESKOLA K. J., HONKANEN H., SALGADO C. A. and WIEDEMANN U. A., *Nucl. Phys. A*, **747** (2005) 511 [arXiv:hep-ph/0406319].

- [23] DOKSHITZER Y. L. and KHARZEEV D. E., *Phys. Lett. B*, **519** (2001) 199 [arXiv:hep-ph/0106202].
- [24] ABELEV B. I. *et al.* (STAR COLLABORATION), *Phys. Rev. Lett.*, **98** (2007) 192301.
- [25] ARMESTO N., CACCIARI M., DAINESE A., SALGADO C. A. and WIEDEMANN U. A., *Phys. Lett. B*, **637** (2006) 362 [arXiv:hep-ph/0511257].
- [26] WICKS S., HOROWITZ W., DJORDJEVIC M. and GYULASSY M., *Nucl. Phys. A*, **784** (2007) 426 [arXiv:nucl-th/0512076].
- [27] WIEDEMANN U. A., arXiv:0908.2306 [hep-ph].
- [28] CACCIARI M., ROJO J., SALAM G. P. and SOYEZ G., *Eur. Phys. J. C*, **71** (2011) 1539 [arXiv:1010.1759 [hep-ph]].
- [29] AAD G. *et al.* (ATLAS COLLABORATION), arXiv:1011.6182 [hep-ex].
- [30] CHATRCHYAN S. *et al.* (CMS COLLABORATION), arXiv:1102.1957 [nucl-ex].
- [31] CASALDERREY-SOLANA J., MILHANO J. G. and WIEDEMANN U. A., *J. Phys. G*, **38** (2011) 035006 [arXiv:1012.0745 [hep-ph]].

This page intentionally left blank

Open-charm analysis for energy loss studies with ALICE at LHC

C. BIANCHIN(*) for the ALICE COLLABORATION

*Dipartimento di Fisica, Università di Padova and INFN, Sezione di Padova
Via Marzolo 8, 35131 Padova, Italy*

Summary. — In high-energy Pb-Pb collisions at LHC, a deconfined QCD medium is expected to be produced. The open charm and beauty mesons are a powerful probe to investigate the medium properties and its effects on particle production since they experience all the deconfined phase. The ALICE experiment is well suited to perform open-charm analysis thanks to the excellent tracking system, its high-resolution secondary vertex reconstruction capabilities and particle identification performance. In this proceeding the status of the analysis of p-p collisions at $\sqrt{s} = 7$ TeV and the perspectives for Pb-Pb measurements will be presented.

1. – Introduction

The main task of the ALICE experiment [1-4] at LHC is to study high-energy heavy-ion collisions where the Quark Gluon Plasma (QGP) is expected to be formed. The heavy quarks are a powerful tool to investigate this high-density and strongly interacting state of matter because they are produced early in the interaction and experience all the lifetime of the hot matter. Heavy quarks are in fact produced in a time scale of

(*) E-mail: chiara.bianchin@pd.infn.it

$\hbar/(2m_Qc^2)$ mostly through gluon-gluon fusion; this corresponds to about $0.08 \text{ fm}/c$ for the charm quark while the formation time of the QGP is estimated to be $1 \text{ fm}/c$.

The heavy-flavoured mesons bring the information of energy loss suffered by the heavy quark due to the interaction with the medium and they can be crucial in explaining how this energy loss occurs. In fact, the energy loss has been observed at RHIC but is not completely understood so far. One of the main sources is radiative in-medium energy loss which depends on the mass and the colour charge of the particle. The radiation is suppressed at small angles for massive partons because of the “dead cone effect” [5] and is larger for gluons, which have stronger colour charge with respect to quarks. Therefore, one should observe a pattern of decreasing energy loss when going from the mostly gluon-originated light-flavour hadrons (h^\pm or π^0) to the D and then B mesons. Other medium effects such as collisional energy loss [6] and in-medium fragmentation [7] may be relevant and are expected to depend on the parton mass.

The observable used by the experiments to highlight the medium and nuclear effects is the *nuclear modification factor* R_{AA} defined as follows:

$$(1) \quad R_{AA}(p_T) = \frac{d^2N_{AA}/dp_T dy}{N_{\text{coll}} \times d^2N_{pp}/dp_T dy},$$

where $d^2N_{AA(pp)}/dp_T dy$ is the p_t -differential yield in nucleus-nucleus (p-p) collisions and N_{coll} represents the number of binary collisions. If A-A collisions were a simple superposition of independent nucleus-nucleus collisions this ratio should not show any deviation from unity. The RHIC experiments have measured a significant deviation from 1 both for light hadrons and for heavy-flavour hadrons, measured via non-photonic electrons. These, however, only provide a rather indirect measurement, since RHIC experiments are not equipped with a vertex detector and cannot select displaced vertices. The QGP formation is not the only effect which can cause a deviation from unity, therefore initial-state effects such as modification of parton distribution functions must be studied separately with p-A collisions. Moreover, besides constituting a benchmark for Pb-Pb results, p-p collisions are also interesting *per se* since the charm cross-section has never been measured at the energies LHC will reach. This will allow a test of pQCD calculations.

2. – ALICE performance

The ALICE experiment is composed of a central barrel of detectors at mid-rapidity and a muon spectrometer at forward rapidity. In the analyses presented in this paper a subset of the central barrel detector is used, namely the Inner Tracking System (ITS), the Time Projection Chamber (TPC) and the Time-Of-Flight detector (TOF) and the V0 scintillator for triggering. The ALICE barrel is embedded in a magnetic field of 0.5 T oriented along the beam axis (z). The expected p_t resolution for tracks reconstructed in the TPC and in the ITS is $\sim 1\% (p_t \lesssim 10 \text{ GeV}/c)$, the primary vertex resolution is expected to be $\sim 10 \mu\text{m}$ (in Pb-Pb) and the expected resolution on the minimum $r\phi$ distance of the prolonged track with respect to the primary vertex (impact parameter) is $\sim 60 \mu\text{m}$ for

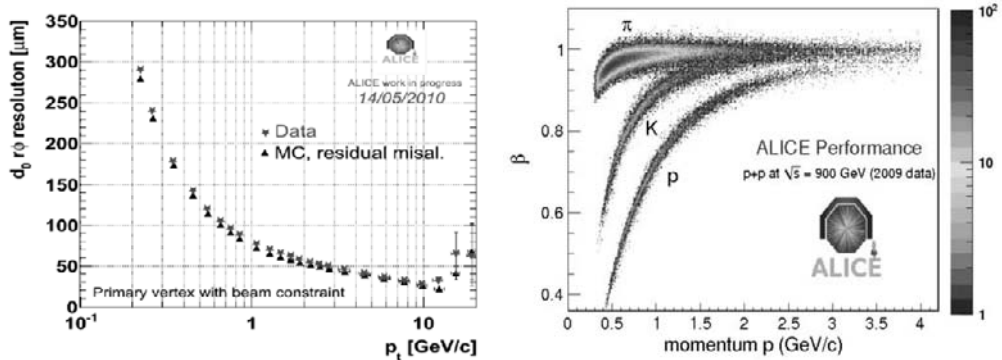


Fig. 1. – Left panel: impact parameter resolution in p-p collisions compared to MC simulation with residual misalignment. Right panel: β as a function of momentum with the TOF detector from p-p collisions at $\sqrt{s} = 0.9$ TeV.

$p_t \simeq 1$ GeV/c. More details about the detector can be found in the references [1-3]. Such performance allows the ALICE experiment to separate secondary vertices at few hundreds of μm and thus to perform heavy-flavour meson analysis reconstructing hadronic decays with $c\tau$ in the $100\,\mu\text{m}$ range. Several analyses are in preparation, such as $D^0 \rightarrow K^-\pi^+$, $D^+ \rightarrow K^-\pi^+\pi^+$, $D^{*+} \rightarrow D^0\pi^+$, $D_s^+ \rightarrow K^+K^-\pi^+$, $D^0 \rightarrow K^-\pi^+\pi^-\pi^+$ and $\Lambda_c^+ \rightarrow K^-\pi^+p$.

In this analysis, particle identification is provided by the TPC and the TOF in different ranges of momentum: the TPC information is used in $0.2 \lesssim p \lesssim 1$ GeV/c and the TOF in the range $0.2 \lesssim p \lesssim 2$ GeV/c.

The impact parameter resolution measured in p-p collisions at $\sqrt{s} = 7$ TeV compared with MC with residual misalignment is reported in the left panel of fig. 1 while in the right panel the velocity (β) measured by TOF as a function of momentum in p-p collisions at $\sqrt{s} = 0.9$ TeV is shown.

2.1. Expected performance for $D^0 \rightarrow K\pi$ analysis in p-p. – The precision of ALICE measurements will allow a sensitive test of the pQCD predictions to be performed as shown in fig. 2 left panel. In this plot, the differential cross-section for a sample of 10^9 p-p events at $\sqrt{s} = 14$ TeV corresponding to the statistics of one year of data at the nominal energy (simulation) is compared to MNR [8] and FONLL [9] calculations. In the right panel, the expected systematic and statistical errors (for different statistics scenarios) at the present $\sqrt{s} = 7$ TeV are compared to the model uncertainty and show that in one year of data taking (10^9 minimum bias events) ALICE will be able to provide a significant comparison with theoretical predictions in $1 \lesssim p_t < 15$ GeV/c.

Figure 3 (left panel) shows the expected performance for the $R_{AA}^{D^0}$ with predictions that assume various medium densities (related to the transport coefficient \hat{q}), and charm mass hypotheses and use the EKS98 parametrization [10] for shadowing. While the R_{AA} highlights the energy loss dependence on the medium properties, the $R_{B/D}^e$ (fig. 3, right panel), the ratio of the nuclear modification factor of B and D mesons using their electron spectra, allows the variation with the mass of the parton to be studied.

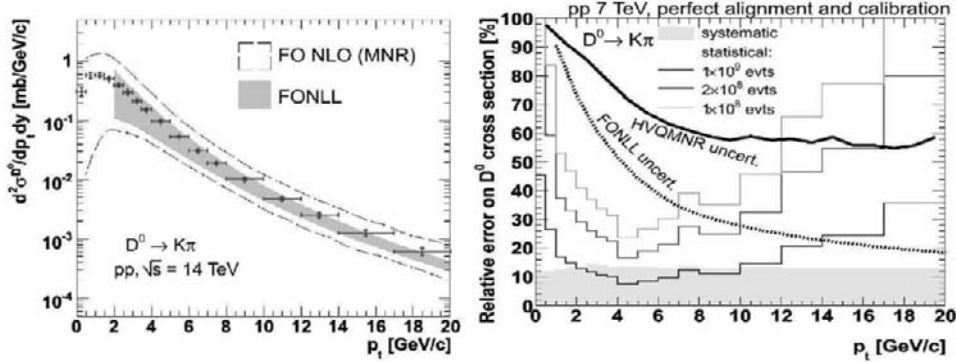


Fig. 2. – Monte Carlo studies: in the left panel the differential cross-section for D^0 in p-p collisions at $\sqrt{s} = 14$ TeV compared to models. In the right panel the relative error estimated with different statistics for p-p collisions at $\sqrt{s} = 7$ TeV compared to models uncertainty.

3. – Status of the analysis of p-p collisions at $\sqrt{s} = 7$ TeV

The cross-section for each D meson can be written as

$$(2) \quad \begin{aligned} \frac{d^2\sigma^{D^0}(p_t, y)}{dy dp_t} \Big|_{y=0} &\approx \frac{1}{2} \frac{1}{2y_{\max}} \frac{f_D \cdot N_{\text{sel}}^{\text{reco}}(p_t)|_{|y| < y_{\max}}}{\varepsilon \cdot BR \cdot \mathcal{L}_{\text{INT}}} \\ &= \frac{1}{2} \frac{1}{2y_{\max}} \frac{f_D \cdot N_{\text{sel}}^{\text{reco}}(p_t)|_{|y| < y_{\max}}}{\varepsilon \cdot BR \cdot N_{\text{inel}}^{\text{tot}}} \sigma_{\text{inel}}^{\text{tot}}, \end{aligned}$$

where $y_{\max} \sim 1$ and the main components to be determined are the raw yield ($N_{\text{sel}}^{\text{reco}}(p_t)$), the efficiency corrections (ε) and the fraction of prompt charm (f_D). Therefore the main steps to measure the D cross-section are: a) topological criteria to select displaced secondary vertices using the significance maximization; b) subtraction of remaining back-

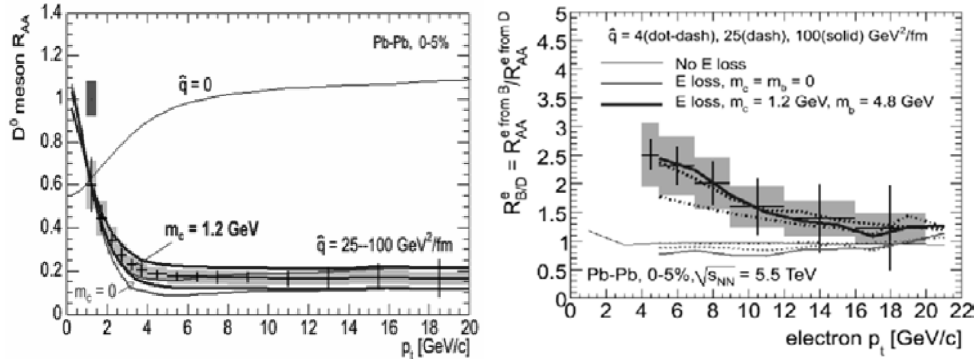


Fig. 3. – Monte Carlo studies: left panel shows the $R_{AA}^{D^0}$ as a function of p_t ; right panel the ratio $R_{B/D}^e$ (see text for the definition) as a function of p_t .

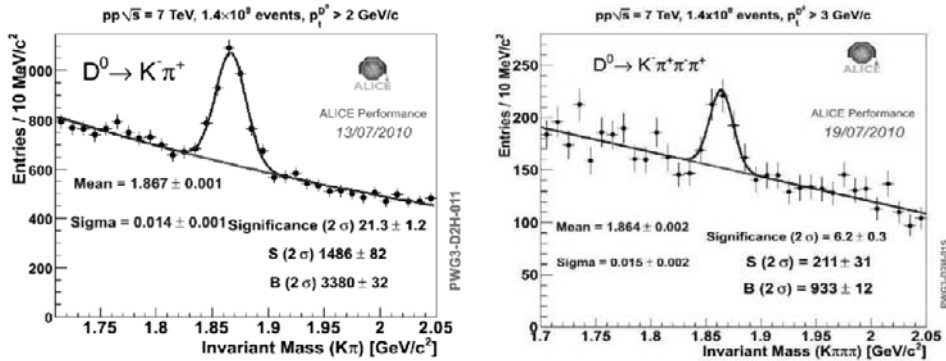


Fig. 4. – Left panel: $D^0 \rightarrow K^- \pi^+$ invariant mass distribution ($p_t > 2$ GeV/c). Right panel: $D^0 \rightarrow K^- \pi^+ \pi^- \pi^+$ invariant mass distribution ($p_t > 3$ GeV/c).

ground and extraction of the raw yield with an invariant mass analysis; c) correction for feed-down from B; d) correction for efficiencies; e) D cross-section normalization.

The topological cuts applied to extract the signal a) exploit the transverse distance of the decaying particles from the primary vertex (impact parameter) and the direction of the reconstructed momenta with respect to the D meson flight line. The particle identification provided by TOF and TPC is used to select kaons in order to reduce the combinatorial background.

The data sample used is formed by about $1.4 \cdot 10^8$ minimum bias events triggered with the V0 scintillator and the ITS detector. So far significant signals have been observed for D^0 (in 2 and 4 prongs), D^+ , D^* and D_s reconstructed in their hadronic channel. The signals for each channel are extracted in some p_t bins and the invariant mass spectra for

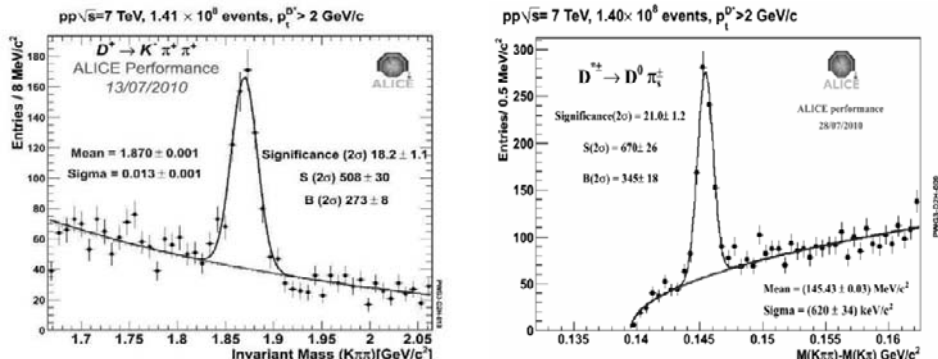


Fig. 5. – Left panel: $D^+ \rightarrow K^- \pi^+ \pi^+$ invariant mass distribution ($p_t > 2$ GeV/c). Right panel: $\Delta M = m_{D^*} - m_{D^0}$ distribution ($p_t > 2$ GeV/c).

$D^0 \rightarrow K\pi$, $D^0 \rightarrow K\pi\pi\pi$, $D^* \rightarrow D^0\pi$ and $D^+ \rightarrow K\pi\pi$ are reported in figs. 4 and 5. The D^0 in 4 prongs will be a good term of comparison for the results obtained with the 2 prongs channel and the ratios between mesons yield will be measured. The D^* channel is also used for D-jet angular correlation study to estimate the fraction of charm coming from gluon splitting exploiting the different emission angle (≈ 0) with respect to pair creation ($\approx \pi$). The first studies with a simple cone algorithm for jet reconstruction show a small signal, but more detailed analysis has to be performed.

4. – Conclusions

The ALICE experiment is well suited to study the energy loss with heavy flavour in Pb-Pb collisions and to test pQCD predictions in p-p, thanks to precise vertex reconstruction, tracking down to low p_t and particle identification. The detector performance is already close to the design targets and the first signals of D^0 , D^+ , D^* and D_s have been observed with a sample of about $1.4 \cdot 10^8$ minimum bias events at $\sqrt{s} = 7$ TeV. The analysis to obtain the cross-section for transverse momenta from about 1 to 15 GeV/c is in progress and this measurement will be a reference for the study of the R_{AA} and the charm suppression in Pb-Pb collisions which are foreseen for November 2010.

REFERENCES

- [1] The ALICE experiment at CERN LHC, *JINST*, **0803** (2008) S08002.
- [2] CARMINATI F. *et al.* (ALICE COLLABORATION), *J. Phys. G: Nucl. Part. Phys.*, **30** (2004) 1517.
- [3] ALME J. *et al.*, *Nucl. Instrum. Methods A*, **622** (2010) 316.
- [4] ALICE COLLABORATION *et al.*, *J. Phys. G: Nucl. Part. Phys.*, **32** (2006) 1295.
- [5] DOKSHITZER YU. L. and KHARZEEV D. E., *Phys. Lett. B*, **519** (2001) 199; arXiv:hep-ph/0106202.
- [6] DJORDJEVIC M., *Phys. Rev. C*, **74** (2006) 064907.
- [7] SHARMA R., VITEV I. and ZHANG B-W, *Phys. Rev. C*, **80** (2009) 054902, arXiv:0904.0032v2 [hep-ph].
- [8] MANGANO M. L., NASON P. and RIDOLFI G., *Nucl. Phys. B*, **373** (1992) 295.
- [9] CACCIARI M. *et al.*, *JHEP*, **0407** (2004) 033.
- [10] ESKOLA K. J. *et al.*, *Eur. Phys. J. C*, **9** (1999) 61.

Dark matter: A window to New Physics at the electroweak scale

A. MASIERO(*)

*Dipartimento di Fisica “G. Galilei”, Università di Padova
INFN, Sezione di Padova - Padova, Italy*

Summary. — The coming decade will have a main goal for particle physics: discovery and understanding of the alleged new physics beyond the Standard Model (SM) which has to be present at the TeV scale if it is to provide the needed ultraviolet completion of the SM for the stabilisation of its electroweak breaking energy scale. In these lectures I discuss why the dark matter issue represents the best hope we have to shed light on such TeV new physics among the various items (neutrino masses, cosmic matter-antimatter asymmetry, inflation, dark energy) of the astroparticle road to new physics. In particular, I will emphasize the complementary role of the LHC physics and the dark matter searches in our thirty-year old quest for low-energy supersymmetry signals.

1. – Introduction

The electroweak standard model (SM) is by now more than fourty years old and it enjoys a full maturity with an extraordinary success in reproducing the many electroweak tests which have been going on since its birth. Not only have its characteristic gauge

(*) E-mail: masiero@pd.infn.it

bosons, W and Z, been discovered and also has the top quark been found in the mass range expected by the electroweak radiative corrections, but the SM has been able to account for an impressively long and very accurate series of measurements. Indeed, in particular at LEP, some of the electroweak observables have been tested with precisions better than the per mille level without finding any discrepancy with the SM predictions. We can safely state that LEP has fully established the validity of the SM as a quantum field theory. At the same time, the SM has successfully passed another very challenging class of exams, namely it has so far accounted for all the very suppressed or forbidden processes where flavour changing neutral currents (FCNC) are present.

Hence, we can firmly state that no matter which physics should lie beyond the SM, necessarily such new physics has to reproduce the SM with great accuracy at energies of $O(100\text{ GeV})$. This represents a major breakthrough in our exciting progress towards a unified picture of fundamental interactions.

And, yet, in spite of all this glamorous success of the SM in reproducing the impressive set of experimental electroweak results, we are deeply convinced of the existence of new physics beyond this model. We see two main classes of motivations pushing us beyond the SM.

First, we have theoretical reasons to believe that the SM is not the whole story. The SM does not truly unify the elementary interactions (if nothing else, gravity is left out of the game), it does not provide a rationale for the structured pattern of fermion masses and mixings (flavor problem) and it exhibits the gauge hierarchy problem in the scalar sector (namely, the scalar Higgs mass is not protected by any symmetry and, hence, it would tend to acquire large values of the order of the energy scale at which new physics sets in). Together with these theoretical complaints comes a set of “observational” reasons pushing us beyond the SM: neutrino masses, dark matter (DM), dark energy (DE), the cosmic matter-antimatter asymmetry (baryogenesis) and the need for an inflationary epoch. The reason why they qualify as possible evidences of New Physics (NP) beyond the SM is simple: considering the whole spectrum of particles and their interactions within the SM context, there is *no* possibility to account for massive neutrinos, for the existence of DM particle candidates, for a dynamical mechanism to give rise to a cosmic matter-antimatter asymmetry starting from a symmetrical situation and, finally, the Higgs scalar potential of the SM is not suitable to produce an adequate inflationary epoch in the very early stages of evolution of our Universe. I left out of this “cahier de doleances”, the dark energy issue. It is certainly true that within the SM we do not find any plausible explanation for it, which in my view is somewhat linked to the famous unsolved “cosmological constant problem”, but I think that it is unfair to blame the SM for such failure: this is a more general problem which, maybe, concerns our understanding, or better our ignorance, about a correct quantum description of gravity, in particular of its infrared behaviour.

Therefore, in particle physics the discovery and subsequent understanding of the NP beyond the SM is a priority. Most of us are convinced that such NP should be linked to the electroweak symmetry breaking, hence it should set in at an energy scale close to the 100–1000 GeV benchmark we mentioned above as the border of our actual knowledge

of fundamental interactions so far. The reason of this conviction rests upon the crucial point (technically known as the “gauge hierarchy problem”) that we need a mechanism to stabilize the energy scale at which the electroweak symmetry breaking occurs, *i.e.* the TeV scale. The LHC which is now operating at CERN is the accelerator machine having all the potentialities to get access to such low-energy NP.

The status of our present understanding of cosmology can play an important role in driving the investigation beyond the SM, understanding the nature of NP. Undoubtedly, the major breakthrough in physics in these last two decades has been represented by the amazing changes we went through in the way we see the Universe and its major, fundamental constituents. In a few years, thanks to a breathtaking progress in observational cosmology, we have been driven to a new Standard Model of Cosmology, the so-called “ Λ CDM” model. This is characterized by a critically dense Universe where ordinary matter (baryons) constitute only 5% (at most) of the entire energy density. The remaining 95% is in exotic forms, which still demand to be theoretically understood and experimentally revealed. This overwhelming part of the Universe is usually divided into two components: DM and DE with a ratio roughly one to three between DM and DE. While DM represents a form of energy which gravitationally clusterizes (namely, through gravitation it is constrained within the galactic clusters and superclusters), DE denotes a form of unclusterized energy which is thought to be smoothly spread allover the whole Universe. Moreover, even considering only the baryonic component, a new puzzle emerges, namely that of the overwhelming dominance of baryons over anti-baryons in the present Universe.

The (rather strangely looking) picture of the Universe summarized above addresses profound and severe questions to particle physics. What are the sources of DM and DE? Are they related? How can we experimentally reveal them? Can present observations find an explanation within General Relativity (GR) or do they ask for an extension of it? How was the asymmetry between matter and anti-matter produced?

Finding an answer to (some of) these questions in the particle physics context implies that we envisage NP beyond the SM of particle physics. As a matter of fact, as I mentioned above, within the SM there is neither an adequate DM candidate nor any theoretical clue to understand the nature of DE. Moreover, there is no way to generate a cosmic matter-antimatter asymmetry starting from a symmetric initial condition. In other words, today we witness a serious clash between the SM of particle physics and the “ Λ CDM” model, whose solution calls for NP and represents one of the greatest challenges in modern science.

It would be a stunning breakthrough if at the LHC, together with the first signals of a (possibly unexpected) TeV NP, we could also collect the first hints to a deeper comprehension of the most fundamental constituents of the whole Universe.

From a cosmological point of view, the most promising candidate for DM was recognized to be a weakly interacting massive particle (WIMP) with a mass in the tens or hundreds of GeV. On the other hand, theoretical research in particle physics lead to the discovery that extensions of the SM introducing new physics at the electroweak scale were offering, as a “bonus”, interesting WIMP candidates (for instance, the lightest

supersymmetric (SUSY) particle (LSP) in SUSY extensions of the SM or the lightest Kaluza-Klein (LKK) mode in theories with extra-dimensions). In view of the amazing coincidence between particle physics and cosmology parameters making the WIMP so interesting from the DM point of view, we think that it is nowadays compelling to explore all the possible, rich aspects of the interplay between LHC and DM searches from the WIMP perspective.

Differently from DM, DE is unlikely to call for a particle candidate. Indeed, the accelerated expansion of the Universe demands DE to exhibit a negative pressure, while particle flow lead to a non-negative pressure. The Einstein cosmological constant can presently account for the data. An interesting alternative is that DE, instead of being a quantity which remains constant, has its own evolution in time, *i.e.* we have a Dynamical DE (DDE). The prototype of such a proposal is provided by a scalar field with a suitable potential whose energy density keeps varying with time. One of the main goals of next generation experiments on DE is just to ascertain a possible dynamics in DE evolution. This means that we should be able to get information on the accelerated expansion of the Universe at different redshifts establishing whether DE has to be attributed to a cosmological constant or to an evolving DDE.

Both the constant and the dynamical interpretations of DE share the problem of the extreme tuning of the energy scale associated to DE (of the millielectronvolt order) with respect to common particle physics scales. Together with it, we have a series of maybe equally profound problems, which can be gathered under the name of “coincidence” questions. Why DM and baryons have comparable densities? Why also DE has a comparable density and has it just in the present cosmic epoch? Motivated in part by the attempt to address these questions, the possibility of an interaction between DDE and DM and/or baryons has also attracted great interest. In particular, it was realized that, even in the absence of a direct DM-DE interaction, the presence of DE could have a major impact on the nature and present abundance of DM. Indeed, the scalar field responsible for the DDE could lead to significant departures from the standard cosmological evolution based on General Relativity (GR), in particular at its the early stages. The most remarkable examples are provided by DDE models based on scalar-tensor (ST) theories of gravity, or by the so-called “kination” scenarios, in which the kinetic energy of the DDE scalar field dominates over the radiation energy density for a period in the early Universe. In particular, in the ST case, it was shown that, even taking into account all the increasingly severe constraints on departures from GR (from Big bang Nucleosynthesis (BBN), Cosmic Microwave Background Radiation (CMBR) and the solar system tests), the expansion rate in the decisive moment when the WIMP DM decouples from the thermal bath could have been strongly different from the standard one. This can radically change the predicted abundances of the different DM candidates in a particular model, bringing about phenomenological implications of utmost relevance.

Within the SM, both the amount of *CP* and the nature of the electroweak phase transition preclude any possibility to have an efficient dynamical mechanism to originate a cosmic matter-antimatter asymmetry. When proceeding beyond the SM, a very interesting mechanism has been suggested: baryogenesis through leptogenesis. In this

case, use is made of the CP -violating out-of-equilibrium decay of the (heavy) right-handed neutrino entering the so-called “see-saw” mechanism which is based on a large Majorana mass for the right-handed neutrino.

Leptogenesis makes it possible to link two apparently unrelated observations: the matter-antimatter asymmetry of the Universe in cosmology and neutrino masses and mixing in particle physics. It is intriguing that the measured values are in agreement in a non-trivial way, with some interesting bounds on the involved parameters. In this context it becomes very attractive to try to tie together leptogenesis, violation of lepton number and lepton flavor violation (LFV).

In this lecture I will briefly review:

- The main features of the Standard Model (SM) such as its spectrum, the Lagrangian and its symmetries, the Higgs mechanism, the successes and shortcomings of the SM.
- Two major particle physics candidates for DM: massive (light) neutrinos and the lightest supersymmetric (SUSY) particle in SUSY extensions of the SM with R parity (to be defined later on). Light neutrinos and the lightest sparticle are “canonical” examples of the hot and cold DM, respectively. This choice does not mean that these are the only interesting particle physics candidates for DM. For instance axions are still of great interest as CDM candidates and their experimental search is proceeding at full steam.
- I will revisit the DM issue in the context of cosmological scenarios where the expansion rate of the Universe can (even drastically) differ from the standard one at temperatures higher than the MeV scale, *i.e.* before nucleosynthesis starts.

This lecture is meant to be an introduction to some DM issues for readers who are not familiar with the subject and, in particular, who need an introduction to the particle physics aspects of the DM problem. No discussion on the searches of DM will be presented in this lecture.

2. – The Standard Model of particle physics

In particle physics the fundamental interactions are described by the Glashow-Weinberg-Salam Standard Theory (GSW) for the electroweak interactions [1] (for a review see [2]) and QCD for the strong one. GWS and QCD are gauge theories based respectively on the gauge groups $SU(2)_L \times U(1)_Y$ and $SU(3)_c$ where L refers to left, Y to hypercharge and c to colour. We recall that a gauge theory is invariant under a local symmetry and requires the existence of vector gauge fields living in the adjoint representation of the group. Therefore in our case we have:

- i) 3 gauge fields $W_\mu^1, W_\mu^2, W_\mu^3$ for $SU(2)_L$;
- ii) 1 gauge field B_μ for $U(1)_Y$;
- iii) 8 gauge bosons λ_μ^a for $SU(3)_c$.

TABLE I. – *The fermionic spectrum of the SM.*

Fermions	Generations			$SU(2)_L \otimes U(1)_Y$
	I	II	III	
$E_{bL} \equiv \begin{pmatrix} \nu_b \\ e_b^- \end{pmatrix}_L$	$\begin{pmatrix} \nu_e \\ e^- \end{pmatrix}_L$	$\begin{pmatrix} \nu_\mu \\ \mu^- \end{pmatrix}_L$	$\begin{pmatrix} \nu_\tau \\ \tau^- \end{pmatrix}_L$	(2, -1)
e_{bR}	e_R^-	μ_R^-	τ_R^-	(1, -2)
$Q_{bL} \equiv \begin{pmatrix} u_b \\ d_b \end{pmatrix}_L$	$\begin{pmatrix} u \\ d \end{pmatrix}_L$	$\begin{pmatrix} c \\ s \end{pmatrix}_L$	$\begin{pmatrix} t \\ b \end{pmatrix}_L$	(2, 1/3)
u_{bR}	u_R	c_R	t_R	(1, 4/3)
d_{bR}	d_R	s_R	b_R	(1, -2/3)

The SM fermions live in the irreducible representations of the gauge group and are reported in table I: the indices L and R indicate, respectively, the left and right fields, $b = 1, 2, 3$ the generation, the colour is not shown.

The Lagrangian of the SM is dictated by the invariance under the Lorentz group and the gauge group and the request of renormalizability. It is given by the sum of the kinetic fermionic part $\mathcal{L}_{\text{K mat}}$ and the gauge one $\mathcal{L}_{\text{K gau}}$: $\mathcal{L} = \mathcal{L}_{\text{K mat}} + \mathcal{L}_{\text{K gau}}$. The fermionic part reads for one generation:

$$(1) \quad \mathcal{L}_{\text{K mat}} = i\bar{Q}_L \gamma^\mu \left(\partial_\mu + igW_\mu^a T_a + i\frac{g'}{6}B_\mu \right) Q_L + i\bar{d}_R \gamma^\mu \left(\partial_\mu - i\frac{g'}{3}B_\mu \right) d_R \\ + i\bar{u}_R \gamma^\mu \left(\partial_\mu + i\frac{2g'}{3}B_\mu \right) u_R + i\bar{E}_L \gamma^\mu \left(\partial_\mu + igW_\mu^a T_a - i\frac{g'}{2}B_\mu \right) E_L \\ + i\bar{e}_R \gamma^\mu \left(\partial_\mu - ig'B_\mu \right) e_R,$$

where the matrices $T_a = \sigma_a/2$, σ_a are the Pauli matrices, g and g' are the coupling constants of the groups $SU(2)_L$ and $U(1)_Y$, respectively. The Dirac matrices γ^μ are defined as usual. The colour and generation indices are not specified. This Lagrangian $\mathcal{L}_{\text{K mat}}$ is invariant under two global accidental symmetries, the leptonic number and the baryonic one: the fermions belonging to the fields E_{bL} and e_{bR} are called leptons and transform under the leptonic symmetry $U(1)_L$ while the ones belonging to Q_{bL} , u_{bR} and d_{bR} baryons and transform under $U(1)_B$.

The Lagrangian for the gauge fields reads

$$(2) \quad \mathcal{L}_{\text{K gau}} = -\frac{1}{4} \left(\partial_\mu W_\nu^a - \partial_\nu W_\mu^a + \epsilon^{abc} W_\mu^b W_\nu^c \right) \left(\partial^\mu W^{\nu a} - \partial^\nu W^{\mu a} + \epsilon^{ab'c'} W_\nu^{b'} W_\mu^{c'} \right) \\ - \frac{1}{4} \left(\partial_\mu B_\nu - \partial_\nu B_\mu \right) \left(\partial^\mu B^\nu - \partial^\nu B^\mu \right).$$

2.1. The Higgs mechanism and vector boson masses. – The gauge symmetry protects the gauge bosons from having a mass. Unfortunately the weak interactions require massive gauge bosons in order to explain the experimental behaviour. However adding a direct mass term for gauge bosons breaks explicitly the gauge symmetry and spoils renormalizability. To preserve such nice feature of gauge theories, it is necessary to break spontaneously the symmetry. This is achieved through the Higgs mechanism. We introduce in the spectrum a scalar field H , which transforms as a doublet under $SU(2)_L$, carries hypercharge while is colourless. The Higgs doublet has got the following potential V_{Higgs} , kinetic terms \mathcal{L}_{K_H} and Yukawa couplings with the fermions \mathcal{L}_{Hf} :

$$(3) \quad V_{\text{Higgs}} = -\mu^2 H^\dagger H + \lambda(H^\dagger H)^2,$$

$$\begin{aligned} \mathcal{L}_{K_H} &= - \left(\partial_\mu H + igW_\mu^a T_a H + i\frac{g'}{2} B_\mu H \right)^\dagger \left(\partial_\mu H + igW_\mu^a T_a H + i\frac{g'}{2} B_\mu H \right), \\ \mathcal{L}_{Hf} &= - \sum_{b,c}^{\text{gener.}} \left(\lambda_{bc}^d \bar{Q}_{Lb} H D_{Rc} + \lambda_{bc}^u \bar{Q}_{Lb} \tilde{H} U_{Rc} + \lambda_{bc}^e \bar{E}_{Lb} H E_{Rc} \right) + \text{h.c.}, \end{aligned}$$

where the parameters μ e λ are real constants, λ_{bc}^d , λ_{bc}^u and λ_{bc}^e are 3×3 matrices on the generation space. \tilde{H} indicates the charge conjugated of H : $\tilde{H}^a = \epsilon^{ab} H_b^\dagger$.

While the Lagrangian is invariant under the gauge symmetry the vacuum is not and the neutral component of the doublet H develops a vacuum expectation value (vev):

$$(4) \quad \langle H^0 \rangle = \begin{pmatrix} 0 \\ v \end{pmatrix}.$$

This breaks the symmetry $SU(2)_L \otimes U(1)_Y$ down to $U(1)_{EM}$. We recall that when a global symmetry is spontaneously broken, in the theory appears a massless Goldstone boson; if the symmetry is local (gauge) these Goldstone bosons become the longitudinal components of the vector bosons (it is said that they are eaten up by the gauge bosons). The gauge bosons relative to the broken symmetry acquire a mass as shown in $\mathcal{L}_{M\text{gauge}}$:

$$(5) \quad \mathcal{L}_{M\text{gauge}} = -\frac{1}{2} \frac{v^2}{4} [g^2(W_\mu^1)^2 + g^2(W_\mu^2)^2 + (-gW_\mu^3 + g'B_\mu)^2].$$

Therefore there are three massive vectors W_μ^\pm and Z_μ^0 :

$$(6) \quad W_\mu^\pm = \frac{1}{\sqrt{2}} (W_\mu^1 \mp iW_\mu^2),$$

$$(7) \quad Z_\mu^0 = \frac{1}{\sqrt{g^2 + g'^2}} (gW_\mu^3 - g'B_\mu),$$

whose masses are given by

$$(8) \quad m_W = g \frac{v}{2},$$

$$(9) \quad m_Z = \sqrt{(g^2 + g'^2)} \frac{v}{2},$$

while the gauge boson $A_\mu \equiv \frac{1}{\sqrt{g^2+g'^2}}(gW_\mu^3 + g'B_\mu)$, relative to $U(1)_{EM}$, remains massless as imposed by the gauge symmetry. Such mechanism is called Higgs mechanism and preserves renormalizability.

2.2. Fermion masses. – Fermions are spinors with respect to the Lorentz group $SU(2) \otimes SU(2)$. Weyl spinors are two component spinors which transform under the Lorentz group as

$$(10) \quad \chi_L \quad \text{as} \quad \left(\frac{1}{2}, 0 \right),$$

$$(11) \quad \eta_R \quad \text{as} \quad \left(0, \frac{1}{2} \right)$$

and therefore are said to be left-handed and right-handed, respectively.

A fermion mass term must be invariant under the Lorentz group. We have two possibilities:

- 1) a Majorana mass term couples just one spinor with itself:

$$(12) \quad \chi^\alpha \chi^\beta \epsilon_{\alpha\beta} \quad \text{or} \quad \eta^{\dot{\alpha}} \eta^{\dot{\beta}} \epsilon_{\dot{\alpha}\dot{\beta}}.$$

It is not invariant under any local or global symmetry under which the field transforms not trivially;

- 2) a Dirac mass term involves two different spinors χ_L and η_R :

$$(13) \quad \chi^\alpha \bar{\eta}^\beta \epsilon_{\alpha\beta} \quad \text{or} \quad \bar{\chi}^{\dot{\alpha}} \eta^{\dot{\beta}} \epsilon_{\dot{\alpha}\dot{\beta}}.$$

It can be present even if the fields carry quantum numbers.

In the Standard Model Majorana masses are forbidden by the gauge symmetry in fact we have that for example:

$$\begin{aligned} e_L e_L &\Rightarrow Q \neq 0, \\ \nu_L \nu_L &\Rightarrow SU(2)_L \neq \end{aligned}$$

and $SU(2)_L$ forbids Dirac mass terms:

$$(14) \quad \overline{e_L} e_R \Rightarrow SU(2)_L \neq .$$

Therefore no direct mass term can be present for fermions in the SM.

However when the gauge symmetry breaks spontaneously the Yukawa couplings provide Dirac mass terms to fermions which read

$$(15) \quad \mathcal{L}_{M\text{ mat}} = +\frac{1}{\sqrt{2}}\lambda^e v\bar{e}_L e_R + \frac{1}{\sqrt{2}}\lambda^u v\bar{u}_L u_R + \frac{1}{\sqrt{2}}\lambda^d v\bar{d}_L d_R + \text{h.c.}$$

with masses

$$(16) \quad \begin{aligned} m_e &= \frac{1}{\sqrt{2}} \lambda_e v, \\ m_u &= \frac{1}{\sqrt{2}} \lambda_u v, \\ m_d &= \frac{1}{\sqrt{2}} \lambda_d v. \end{aligned}$$

We notice that neutrinos are massless and so remain at any order in perturbation theory:

- i) lacking of the right component they cannot have a Dirac mass term;
- ii) belonging to a $SU(2)_L$ doublet, they cannot have a Majorana mass term.

However from experimental data we can infer that neutrinos are massive and that their mass is very small compared to the other mass scales in the SM. The SM cannot provide such mass to neutrinos and hence this constitutes a proof of the existence of Physics beyond the SM. The problem of ν masses will be addressed in more detail later on.

2.3. Successes and difficulties of the SM. – It is remarkable that the relatively simple structure of the SM succeeds to pass the innumerable experimental tests ranging from the high energy frontier (high-energy accelerator physics) to the high intensity frontier (high-precision electroweak physics and flavor physics). However, we see good reasons to expect the existence of Physics beyond the SM. From a theoretical point of view the SM cannot give an explanation of the existence of three families, of the hierarchy present among their masses, of the fine tuning of some of its parameters, of the lacking of unification of the three fundamental interactions (considering the behaviour of the coupling constants, we see that they tend to unify at a scale $M_X \sim 10^{15}$ GeV where a unified simple group might arise), of the hierarchy problem of the scalar masses which tend to become as large as the highest mass scale in the theory. From an experimental point of view, the non-vanishing neutrino masses are a proof of Physics beyond the SM. Also cosmo-particle physics gives strong hints in favor of Physics beyond the SM: in particular baryogenesis cannot find a satisfactory explanation in the SM, inflation is not predicted by SM and finally we have the DM problem.

3. – The dark matter problem: experimental evidence

Let us define Ω (for a review see [3] and [4]) as the ratio between the density ρ and the critical density $\rho_{\text{crit}} = \frac{3H_0^2}{8\pi G} = 1.88 h_0^2 \times 10^{-29} \text{ g cm}^{-3}$ where H_0 is the Hubble constant, G the gravitational constant:

$$(17) \quad \Omega = \frac{\rho}{\rho_{\text{crit}}} .$$

The Ω_{lum} due to the contribution of the luminous matter (stars, emitting clouds of gases) is given by

$$(18) \quad \Omega_{\text{lum}} \leq 0.01.$$

First evidences of dark matter come from observations of galactic rotation curves (circular orbital velocity *vs.* radial distance from the galactic center) using stars and clouds of neutral hydrogen. These curves show an increasing profile for little values of the radial distance r while for bigger ones it becomes flat, finally decreasing again. According to Newtonian mechanics this behaviour can be explained if the enclosed mass rises linearly with galactocentric distance. However, the light falls off more rapidly and therefore we are forced to assume that the main part of matter in galaxies is made of non-shining matter or dark matter (DM) which extends for a much bigger region than the luminous one. The limit on Ω_{galactic} which can be inferred from the study of these curves is

$$(19) \quad \Omega_{\text{galactic}} \geq 0.1.$$

The simplest idea is to suppose that the DM is due to baryonic objects which do not shine. However both Big-Bang nucleosynthesis (BBN) and very precise determinations of the acoustic peaks in Cosmic Background Radiation (CBR) (WMAP results) point out that Ω_B cannot exceed 5%, hence making it impossible to account for the whole amount of DM.

1/3 of the BBN baryon density is given by stars, cold gas and warm gas present in galaxies. The other 2/3 are probably in hot intergalactic gas, warm gas in galaxies and dark stars such as low-mass objects which do not shine (brown dwarfs and planets) or the result of stellar evolution (neutron stars, black holes, white dwarfs). These last ones are called MACHOS (MAssive Compact Halo Objects) and can be detected in our galaxy through microlensing.

From cluster observations, from the evolution of the abundance of clusters and measurements of the power spectrum of large-scale structures and from the WMAP data on CBR, we obtain a very significant and puzzling result: the energy density of DM accounts for roughly one fourth of the critical energy density.

Hence the major part of dark matter is non-baryonic. The crucial point is that the SM does not possess any candidate for such non-baryonic relics of the Early Universe. Hence the demand for non baryonic DM implies the existence of new Physics beyond the SM.

Non-baryonic DM divides into two classes (see [3] and [4]): cold DM (CDM) (examples: neutral heavy particles called WIMPS (Weakly Interacting Massive Particles) or very light ones as axions) and hot DM (HDM) (example: the light neutrinos of the SM). What discriminates between these two kinds of DM is the ratio between the mass of the particle and the temperature at which such particle decouples. For instance, consider a light neutrino with a mass below the eV. Weak interactions have rates which drop below

the expansion rate of the Universe when the temperature of the primordial plasma is in the MeV range. Hence, at their freeze-out, the neutrinos are ultra-relativistic and, indeed, it will take a very long time before they derelativize, *i.e.* before the Universe temperature drops below their tiny mass. This is a typical example of HDM. Let us turn to a CDM candidate. This is the case, for instance, of a particle which interacts weakly and has a mass of $O(100\text{ Gev})$. As we will see below, such a WIMP typically freezes out (*i.e.* its interactions start having rates smaller than the Universe expansion rate) when the temperature is few GeVs, *i.e.* the WIMP is certainly non-relativistic at the moment of the freeze-out. The above definition of HDM and CDM in relation to the property of the DM particle to be relativistic or non-relativistic at its freeze-out temperature is certainly convenient because of its clarity, however it slightly oversimplifies the most general situation. Indeed, there are cases where the mass of the DM candidate is of no relevance: for instance, axions are thought to be extremely light, yet they are CDM and not HDM candidates since the energy related to axions is linked to their oscillation energy. The most precise definition of HDM and CDM considers the moment their density fluctuations enters the horizon (the interested reader can consult some cosmology textbook, for instance [3], for a more detailed discussion of this point).

4. – Lepton number violation and neutrinos as HDM candidates

The first candidate for DM we will review are neutrinos which can account for HDM: particles that were relativistic at their decoupling from the thermal bath when their rate of interaction became smaller than the expansion rate and they freeze out (or, to be more precise, at the time galaxy formation starts at $T \sim 300\text{ eV}$). The SM has no candidate for HDM, however it is now well established from experimental data that neutrinos are massive and very light. Therefore they can account for HDM. We briefly discuss their characteristics.

4.1. Neutrino masses in the SM and beyond. – The SM cannot account for neutrino masses: we cannot construct either a Dirac mass term as there is only a left-handed neutrino and no right-handed component, or a Majorana mass term because such mass would violate the lepton number and the gauge symmetry.

To overcome this problem, many possibilities have been suggested:

- within the SM spectrum we can form an $SU(2)_L$ singlet with ν_L using a triplet formed by the scalar bilinear HH as $\nu_L \nu_L HH$. When the Higgs field H develops a vev this term gives rise to a Majorana mass term. However, the operator containing the two fermionic lepton doublets and the two Higgs doublets has canonical dimension $3/2 + 3/2 + 1 + 1 = 5$ and, hence, it is a non-renormalizable operator which cannot be written in the (density) Lagrangian of the SM which includes only operators of dimension less or equal to four. This operator can be written in the Lagrangian of the SM once we consider such a model not a fundamental theory, but, rather, the low-energy limit (effective theory) of a more fundamental description of particle physics setting in at an energy scale much above the typical electroweak scale.

- We can introduce a new Higgs triplet Δ and produce a Majorana mass term as in the previous case when Δ acquires a vacuum expectation value.
- However, the most economical way to extend the SM is to introduce a right-handed component N_R , singlet under the gauge group, which couples with the left-handed neutrinos. The lepton number L can be either conserved or violated. In the former option neutrinos acquire a “regular” Dirac mass like for all the other charged fermions of the SM. The left- and right-handed components of the neutrino combine together to give rise to a massive four-component Dirac fermion. The problem is that the extreme lightness of neutrinos (in particular of the electron neutrino) requires an exceedingly small neutrino Yukawa coupling of $O(10^{-11})$ or so. Although quite economical, we do not consider this option particularly satisfactory.

The other possibility is to link the presence of neutrino masses to the violation of L . In this case one introduces a new mass scale, in addition to the electroweak Fermi scale, in the problem. Indeed, lepton number can be violated at a very high or a very low mass scale. The former choice represents, in our view, the most satisfactory way to have massive neutrinos with a very small mass. The idea (see-saw mechanism [5]) is to introduce a right-handed neutrino in the fermion mass spectrum with a Majorana mass M much larger than M_W . Indeed, being the right-handed neutrino a singlet under the electroweak symmetry group, its mass is not chirally protected. The simultaneous presence of a very large chirally unprotected Majorana mass for the right-handed component together with a “regular” Dirac mass term (which can be at most of $O(100 \text{ GeV})$) gives rise to two Majorana eigenstates with masses very far apart.

The Lagrangian for neutrino masses is given by

$$(20) \quad \mathcal{L}_{\text{mass}} = -\frac{1}{2}(\bar{\nu}_L \bar{N}_L^c) \begin{pmatrix} 0 & m_D \\ m_D & M \end{pmatrix} \begin{pmatrix} \nu_R^c \\ N_R \end{pmatrix} + \text{h.c.},$$

where ν_R^c is the CP -conjugated of ν_L and N_L^c of N_R . It holds that $m_D \ll M$. Diagonalizing the mass matrix we find two Majorana eigenstates n_1 and n_2 with masses very far apart:

$$m_1 \simeq \frac{m_D^2}{M}, \quad m_2 \simeq M.$$

The light eigenstate n_1 is mainly in the ν_L direction and is the neutrino that we “observe” experimentally while the heavy one n_2 is in the N_R one. The key-point is that the smallness of its mass (in comparison with all the other fermion masses in the SM) finds a “natural” explanation in the appearance of a new, large mass scale where L is violated explicitly (by two units) in the right-handed neutrino mass term.

4.2. Thermal history of neutrinos. – Let us consider a stable massive neutrino (of mass less than 1 MeV) (see for example [3]). If its mass is less than 10^{-4} eV it is still

relativistic today and its contribution to Ω_M is negligible. In the opposite case it is non-relativistic and its contribution to the energy density of the Universe is simply given by its number density times its mass. The number density is determined by the temperature at which the neutrino decouples and, hence, by the strength of the weak interactions. Neutrinos decouple when their mean free path exceeds the horizon size or equivalently $\Gamma < H$. Using natural units ($c = \hbar = 1$), we have that

$$(21) \quad \Gamma \sim \sigma_\nu n_{e^\pm} \sim G_F^2 T^5$$

and

$$(22) \quad H \sim \frac{T^2}{M_{\text{Pl}}},$$

so that

$$(23) \quad T_{\nu d} \sim M_{\text{Pl}}^{-1/3} G_F^{-2/3} \sim 1 \text{ MeV},$$

where G_F is the Fermi constant, T denotes the temperature, M_{Pl} is the Planck mass. Since this decoupling temperature $T_{\nu d}$ is higher than the electron mass, then the relic neutrinos are slightly colder than the relic photons which are “heated” by the energy released in the electron-positron annihilation. The neutrino number density turns out to be linked to the number density of relic photons n_γ by the relation

$$(24) \quad n_\nu = \frac{3}{22} g_\nu n_\gamma,$$

where $g_\nu = 2$ or 4 according to the Majorana or the Dirac nature of the neutrino, respectively.

Then one readily obtains the ν contribution to Ω_M :

$$(25) \quad \Omega_\nu = 0.01 \times m_\nu (\text{eV}) h_0^{-2} \frac{g_\nu}{2} \left(\frac{T_0}{2.7} \right)^3.$$

Imposing $\Omega_\nu h_0^2$ to be less than one (which comes from the lower bound on the lifetime of the Universe), one obtains the famous upper bound of $200(g_\nu)^{-1}$ eV on the sum of the masses of the light and stable neutrinos:

$$(26) \quad \sum_i m_{\nu_i} \leq 200(g_\nu)^{-1} \text{ eV}.$$

Clearly from eq. (25) one easily sees that it is enough to have one neutrino with a mass in the 1–20 eV range to obtain Ω_ν in the 0.1–1 range of interest for the DM problem.

However, the data on neutrino oscillations point to neutrino masses definitely smaller than 1 eV; to be more precise, this is certainly true if we consider schemes where neutrinos

possess hierarchical masses (with a direct or inverse hierarchy). In the case of degenerate neutrino masses, one could barely consider neutrinos to be in the eV region. However, as we are going to see below, the data on the large-scale structures disfavor neutrinos with masses larger than 1 eV; indeed, such cosmological data provide the best bound we have so far on the sum of the masses of the stable, light neutrinos.

4.3. HDM and structure formation. – Hence massive neutrinos with mass in the eV range are very natural candidates to contribute an Ω_M larger than 0.1. The actual problem for neutrinos as viable DM candidates concerns their role in the process of large-scale structure formation. The crucial feature of HDM is the erasure of small fluctuations by free streaming: neutrinos stream relativistically for quite a long time till their temperature drops to $T \sim m_\nu$. Therefore a neutrino fluctuation in order to be preserved must be larger than the distance d_ν travelled by neutrinos during such interval. The mass contained in that space volume is of the order of the supercluster masses:

$$(27) \quad M_{J,\nu} \sim d_\nu^3 m_\nu n_\nu (T = m_\nu) \sim 10^{15} M_\odot,$$

where n_ν is the number density of the relic neutrinos, M_\odot is the solar mass. Therefore the first structures to form are superclusters and smaller structures as galaxies arise from fragmentation in a typical top-down scenario. Unfortunately in these schemes one obtains too many structures at superlarge scales. Hence schemes of pure HDM are strongly disfavoured by the demand of a viable mechanism for large-structure formation.

As I said above, not only are such cosmological data ruling out the light neutrinos as being the main source of DM, but also they constitute the most powerful way we have at our disposal to put an upper bound on their masses. Including the WMAP and the large-scale structure data we infer that the sum of the light, stable neutrinos has to be less than 1 eV; indeed, if one includes all possible restrictions coming from the LSS data, such bound becomes even more restrictive, in the 0.2 eV range [6]. I emphasize that this is indeed a very impressive result: it does not constrain single neutrino masses, but, rather, the whole sum of the three neutrino masses, hence providing crucial information that we could not (and probably will not be able to) gather from particle physics experiments.

5. – Low-energy SUSY and DM

Another kind of DM, widely studied, called cold DM (CDM) is made of particles which were non-relativistic at their decoupling. Natural candidates for such DM are Weakly Interacting Massive Particles (WIMPs), which are very heavy if compared to neutrinos. The SM does not have non-baryonic neutral particles which can account for CDM and therefore we need to consider extensions of the SM as supersymmetric SM in which there are heavy neutral particles remnants of annihilations such as neutralinos (for a review see [7]).

5.1. Neutralinos as the LSP in SUSY models. – One of the major shortcomings of the SM concerns the protection of the scalar masses once the SM is embedded into some

underlying theory (and at least at the Planck scale such new physics should set in to incorporate gravity into the game). Since there is no typical symmetry protecting scalar masses (while for fermions there is the chiral symmetry and for gauge bosons there are gauge symmetries), the clever idea which was introduced in the early 80's to prevent scalar masses to get too large values was to have a supersymmetry (SUSY) unbroken down to the weak scale. Since fermion masses are chirally protected and as long as SUSY is unbroken there must be degeneracy between the fermion and scalar components of a SUSY multiplet, then having a low-energy SUSY it is possible to have an “induced protection” on scalar masses (for reviews, see [8]). What is crucial is the qualification of the supersymmetric extension of the SM as a “*low-energy*” symmetry: this means that SUSY has to remain a good symmetry of Nature down to an energy scale of the order of the scale at which the electroweak symmetry of the SM breaks down. I emphasize that this is certainly a non-trivial requirement we impose on the SUSY extensions of the SM. Indeed, it appears not so daring to assume that at some stage SUSY should be present at the fundamental level. After all, SUSY is the largest possible symmetry to be compatible with a consistent quantum field theory and in its local version, *i.e.* supergravity, it allows for the presence of gravity among the other fundamental interactions paving the way to the consistent gravity quantization within the superstring formulation. However, all these exciting properties of SUSY at a fundamental level of description of the natural laws should not be confused with the role of SUSY as a low-energy symmetry that we are advocating to cope with the gauge hierarchy puzzle. In superstring theories one could expect SUSY to be broken at some superlarge energy scale, maybe the scale at which the extra dimensions turn out to be compactified. Such a scale could be threateningly close to the Planck scale. If that is the fate of SUSY, then we should conclude that there is no relation at all between the presence of SUSY in Nature and our “phenomenological” effort to stabilize the electroweak breaking at the appropriate low-energy level. In short, the SUSY protection of the Higgs mass is efficient up to the scale at which SUSY is broken. If we intend to have a Higgs boson at the M_W scale, then SUSY has to be broken at an energy scale comparable to the M_W scale, namely 15 or 16 orders of magnitude below the Planck scale!

Such low-energy nature of SUSY entails an immediate consequence of paramount phenomenological relevance: since the mass splitting in any supermultiplet can be at most of the order of the energy scale of the SUSY breaking, the SUSY partners of the ordinary particles must have masses of the order of the electroweak scale, *i.e.* they have to lie in the hundreds of GeV or few TeVs energy ballpark.

However the mere supersymmetrization of the SM faces an immediate problem. The most general Lagrangian contains terms which violate baryon and lepton numbers producing a too fast proton decay. Indeed, the induced four-fermion operators causing proton decay would be mediated by SUSY particles which, from what we saw above, have a mass in the TeV range. If a four-fermion proton decay mediated by superheavy boson of mass of $O(10^{16}$ GeV) turns out to barely respect the present bound on the proton lifetime $O(10^{34})$ years, obviously in the case of a TeV mass mediator it would lead to a practically instantaneous proton decay. To prevent this catastrophic result, we have

to add some symmetry which forbids all or part of these dangerous terms with L or B violations. The most familiar solution is the imposition of a discrete symmetry, called R matter parity, which forbids all these dangerous terms. It reads over the fields contained in the theory:

$$(28) \quad R = (-1)^{3(B-L)+2S}.$$

B , L and S denote the baryon, lepton and spin quantum numbers of the field under consideration. R is a multiplicative quantum number reading -1 over the SUSY particles and $+1$ over the ordinary particles. Clearly in models with R parity the lightest SUSY particle can never decay. This is the famous LSP (lightest SUSY particle) candidate for CDM.

Notice that proton decay does not call directly for R parity. Indeed this decay entails the violation of both B and L . Hence, to prevent a fast proton decay one may impose a discrete symmetry which forbids all the B -violating terms in the SUSY Lagrangian, while allowing for terms with L violation (the vice versa is also viable). Models with such alternative discrete symmetries are called SUSY models with broken R parity. In such models the stability of the LSP is no longer present and the LSP cannot be a candidate for stable CDM.

5.2. Neutralinos in the Minimal Supersymmetric Standard Model. – If we extend the SM in the minimal way, adding for each SM particle a supersymmetric partner with the same quantum numbers, we obtain the so-called Minimal Supersymmetric Standard Model (MSSM). In this context the neutralinos are the eigenvectors of the mass matrix of the four neutral fermions partners of the W_3 , B , H_1^0 and H_2^0 called, respectively, wino \tilde{W}_3 , bino \tilde{B} , higgsinos \tilde{H}_1^0 and \tilde{H}_2^0 . There are four parameters entering the mass matrix, M_1 , M_2 , μ and $\tan\beta$:

$$(29) \quad M = \begin{pmatrix} M_2 & 0 & m_Z \cos\theta_W \cos\beta & -m_Z \cos\theta_W \sin\beta \\ 0 & M_1 & -m_Z \sin\theta_W \cos\beta & m_Z \sin\theta_W \sin\beta \\ m_Z \cos\theta_W \cos\beta & -m_Z \sin\theta_W \cos\beta & 0 & -\mu \\ -m_Z \cos\theta_W \sin\beta & m_Z \sin\theta_W \sin\beta & -\mu & 0 \end{pmatrix},$$

where $m_Z = 91.19 \pm 0.002$ GeV is the mass of the Z boson, θ_W is the weak mixing angle, $\tan\beta \equiv v_2/v_1$ with v_1 , v_2 vevs of the scalar fields H_1^0 and H_2^0 , respectively.

In general M_1 and M_2 are two independent parameters, but if one assumes that a grand-unification scale takes place, then at grand unification $M_1 = M_2 = M_3$, where M_3 is the gluino mass at that scale. Then at the M_W scale one obtains

$$(30) \quad M_1 = \frac{5}{3} \tan^2 \theta_W M_2 \simeq \frac{M_2}{2},$$

$$(31) \quad M_2 = \frac{g_2^2}{g_3^2} m_{\tilde{g}} \simeq m_{\tilde{g}}/3,$$

where g_2 and g_3 are the $SU(2)$ and $SU(3)$ gauge coupling constants, respectively and $m_{\tilde{g}}$ is the gluino mass.

The relation (30) between M_1 and M_2 reduces to three the number of independent parameters which determine the lightest neutralino composition and mass: $\tan\beta$, μ and M_2 . The neutralino eigenstates are denoted usually by $\tilde{\chi}_i^0$, $\tilde{\chi}_1^0$ being the lightest one.

If $|\mu| > M_1, M_2$ then $\tilde{\chi}_1^0$ is mainly a gaugino and in particular a bino if $M_1 > m_Z$, if $M_1, M_2 > |\mu|$ then $\tilde{\chi}_1^0$ is mainly a higgsino. The corresponding phenomenology is drastically different leading to different predictions for CDM.

For fixed values of $\tan\beta$ one can study the neutralino spectrum in the (μ, M_2) -plane. The major experimental inputs to exclude regions in this plane are the request that the lightest chargino be heavier than $m_Z/2$ and the limits on the invisible width of the Z hence limiting the possible decays $Z \rightarrow \tilde{\chi}_1^0 \tilde{\chi}_1^0$, $\tilde{\chi}_1^0 \tilde{\chi}_2^0$. Moreover if the GUT assumption is made, then the relation (30) between M_2 and $m_{\tilde{g}}$ implies a severe bound on M_2 from the experimental lower bound on $m_{\tilde{g}}$ of Tevatron. The theoretical demand that the electroweak symmetry be broken radiatively, *i.e.* due to the renormalization effects on the Higgs masses when going from the superlarge scale of supergravity breaking down to M_W , further constrains the available (μ, M_2) region. The first important outcome of this analysis is that the lightest neutralino mass exhibits a lower bound of roughly 30 GeV. The actual bound on the mass of the lightest neutralino $\tilde{\chi}_1^0$ from LEP2 is

$$(32) \quad m_{\tilde{\chi}_1^0} \geq 40 \text{ GeV}$$

for any value of $\tan\beta$. This bound becomes stronger if we put further constraints on the MSSM, like, for instance, in the Constrained MSSM (CMSSM) where we have only four independent SUSY-parameters plus the sign of the μ parameter.

It should be reminded that all the above bounds on the lightest neutralino take into account a situation where some unification of the gaugino masses occurs, hence making it possible to limit the mass parameter M_1 through the severe experimental bounds on M_2 as derived from LEP physics. If one removes such unification condition of the gaugino masses, then it is possible to have neutralinos as light as few GeVs [9].

5.3. Thermal history of neutralinos and Ω_{CDM} . – Let us focus now on the role played by $\tilde{\chi}_1^0$ as a source of CDM. The lightest neutralino $\tilde{\chi}_1^0$ is kept in thermal equilibrium through its electroweak interactions not only for $T > m_{\tilde{\chi}_1^0}$, but even when T is below $m_{\tilde{\chi}_1^0}$. However for $T < m_{\tilde{\chi}_1^0}$ the number of $\tilde{\chi}_1^0$ s rapidly decreases because of the appearance of the typical Boltzmann suppression factor $\exp[-m_{\tilde{\chi}_1^0}/T]$. When T is roughly $m_{\tilde{\chi}_1^0}/20$ the number of $\tilde{\chi}_1^0$ diminished so much that they do not interact any longer, *i.e.* they decouple. Hence the contribution to Ω_{CDM} of $\tilde{\chi}_1^0$ is determined by two parameters: $m_{\tilde{\chi}_1^0}$ and the temperature at which $\tilde{\chi}_1^0$ decouples ($T_{\chi d}$) which fixes the number of surviving $\tilde{\chi}_1^0$ s. As for the determination of $T_{\chi d}$ itself, one has to compute the $\tilde{\chi}_1^0$ annihilation rate and compare it with the cosmic expansion rate.

Several annihilation channels are possible with the exchange of different SUSY or ordinary particles, f , H , Z , etc. Obviously the relative importance of the channels depends on the composition of $\tilde{\chi}_1^0$.

In the minimal SUSY standard model there are five new parameters in addition to those already present in the non-SUSY case. Imposing the electroweak radiative breaking

further reduces this number to four. Finally, in simple supergravity realizations the soft parameters A and B are related. Hence we end up with only three new, independent parameters. One can use the constraint that the relic $\tilde{\chi}_1^0$ abundance provides a correct Ω_{CDM} to restrict the allowed area in this 3-dimensional space. Or, at least, one can eliminate points of this space which would lead to $\Omega_{\tilde{\chi}_1^0} > 1$, hence overclosing the Universe.

There exists a vast literature on the subject of SUSY WIMPs and accelerator physics. To review such material is beyond the scope of my lecture. I refer the interested reader to the thorough and broad review of Jungman *et al.* [7] and the original papers therein quoted for a general discussion of SUSY in the MSSM and to the works in [10] for an updated analysis.

Finally a comment on models without R parity. From the point of view of DM, the major implication is that in this context the LSP is no longer a viable CDM candidate since it decays. There are very special circumstances under which this decay may be so slow that the LSP can still constitute a CDM candidate.

6. – Changing the expansion rate in the past

In a standard flat FRW universe described by GR, the expansion rate of the universe, $H_{\text{GR}} \equiv \dot{a}/a$, is set by the total energy density, $\tilde{\rho}_{\text{tot}}$, according to the Friedmann law

$$(33) \quad H_{\text{GR}}^2 = \frac{1}{3M_{\text{Pl}}^2} \tilde{\rho}_{\text{tot}},$$

where M_{Pl} is the Planck mass, related to the Newton constant by $M_{\text{Pl}} = (8\pi G)^{-1/2}$. If the total energy density is dominated by relativistic degrees of freedom, the expansion rate is related to the temperature through the relation

$$(34) \quad H_{\text{GR}} \simeq 1.66 g_*^{1/2} \frac{T^2}{M_{\text{Pl}}},$$

with g_* the effective number of relativistic degrees of freedom.

We will modify the above H - T relation by considering a modification of GR in which an effective Planck mass, different from M_{Pl} appears in (34). This can be realized in a fully covariant way in ST theories. We will consider the class of ST theories which can be defined by the following action [11]:

$$(35) \quad S = S_g + \sum_i S_i,$$

where S_g is the gravitational part, given by the sum of the Einstein-Hilbert and the scalar field actions,

$$(36) \quad S_g = \frac{M_*^2}{2} \int d^4x \sqrt{-g} \left[R + g^{\mu\nu} \partial_\mu \varphi \partial_\nu \varphi - \frac{2}{M_*^2} V(\varphi) \right],$$

where $V(\varphi)$ can be either a true potential or a (Einstein frame) cosmological constant, $V(\varphi) = V_0$. The S_i 's are the actions for separate “matter” sectors

$$(37) \quad S_i = S_i \left[\Psi_i, A_i^2(\varphi) g_{\mu\nu} \right],$$

with Ψ_i indicating a generic field of the i -th matter sector, coupled to the metric $A_i^2(\varphi) g_{\mu\nu}$. The actions S_i are constructed starting from the Minkowski actions of Quantum Field Theory, for instance the SM or the MSSM ones, by substituting the flat metric $\eta_{\mu\nu}$ everywhere with $A_i^2(\varphi) g_{\mu\nu}$.

The emergence of such a structure, with different conformal factors A_i^2 for the various sectors can be motivated in extra-dimensional models, assuming that the two sectors live in different portions of the extra-dimensional space.

We consider a flat FRW space-time

$$ds^2 = dt^2 - a^2(t) dl^2,$$

where the matter energy-momentum tensors, $T_{\mu\nu}^i \equiv 2(-g)^{-1/2} \delta S_i / \delta g^{\mu\nu}$ admit the perfect-fluid representation

$$(38) \quad T_{\mu\nu}^i = (\rho_i + p_i) u_\mu u_\nu - p_i g_{\mu\nu},$$

with $g_{\mu\nu} u^\mu u^\nu = 1$.

The cosmological equations then take the form

$$(39) \quad \frac{\ddot{a}}{a} = -\frac{1}{6M_*^2} \left[\sum_i (\rho_i + 3 p_i) + 2M_*^2 \dot{\varphi}^2 - 2V \right],$$

$$(40) \quad \left(\frac{\dot{a}}{a} \right)^2 = \frac{1}{3M_*^2} \left[\sum_i \rho_i + \frac{M_*^2}{2} \dot{\varphi}^2 + V \right],$$

$$(41) \quad \ddot{\varphi} + 3 \frac{\dot{a}}{a} \dot{\varphi} = -\frac{1}{M_*^2} \left[\sum_i \alpha_i (\rho_i - 3p_i) + \frac{\partial V}{\partial \varphi} \right],$$

where the coupling functions α_i are given by

$$(42) \quad \alpha_i \equiv \frac{d \log A_i}{d \varphi}.$$

The Bianchi identity holds for each matter sector separately, and reads

$$(43) \quad d(\rho_i a^3) + p_i da^3 = (\rho_i - 3 p_i) a^3 d \log A_i(\varphi),$$

implying that the energy densities scale as

$$(44) \quad \rho_i \sim A_i(\varphi)^{1-3w_i} a^{-3(1+w_i)},$$

with $w_i \equiv p_i/\rho_i$ the equation of state associated to the i -th energy density (assuming w_i is constant).

6.1. GR as a fixed point. – To start, consider the case of a single matter sector, S_M . In order to compare the ST case with the GR one of eqs. (33), (34), it is convenient to Weyl-transform to the so-called Jordan Frame (JF), where the energy-momentum tensor is covariantly conserved. The transformation amounts to a rescaling of the metric according to

$$(45) \quad \tilde{g}_{\mu\nu} = A_M^2(\varphi) g_{\mu\nu},$$

keeping the comoving spatial coordinates and the conformal time $d\eta = dt/a$ fixed. The JF matter energy-momentum tensor, $\tilde{T}_{\mu\nu}^M \equiv 2(-\tilde{g})^{-1/2} \delta S_M / \delta \tilde{g}^{\mu\nu}$, is related to that in eq. (38) by $\tilde{T}_{\mu\nu}^M = A_M^{-2} T_{\mu\nu}^M$, so that energy density and pressure transform as

$$(46) \quad \tilde{\rho}_M = A_M^{-4} \rho_M, \quad \tilde{p}_M = A_M^{-4} p_M,$$

while the cosmic time transforms as $d\tilde{t} = A_M dt$. One can easily verify that the above-defined quantities satisfy the usual Bianchi identity, that is eq. (43) with vanishing RHS, and that, as a consequence, $\tilde{\rho}_M \sim \tilde{a}^{-3(1+w_M)}$. The expansion rate, $H_{\text{ST}} \equiv d \log \tilde{a} / d\tilde{t}$, is given by

$$(47) \quad H_{\text{ST}} = \frac{1 + \alpha_M(\varphi) \varphi'}{A_M(\varphi)} \frac{\dot{a}}{a},$$

where we have defined α_M according to eq. (42), and $(\cdot)' \equiv d(\cdot)/d \log a$. Using (47) and (46) in (40), we obtain the Friedmann equation in the ST theory,

$$(48) \quad H_{\text{ST}}^2 = \frac{A_M^2(\varphi)}{3M_*^2} \frac{(1 + \alpha_M(\varphi) \varphi')^2}{1 - (\varphi')^2/6} \left[\tilde{\rho}_M + \tilde{V} \right],$$

where $\tilde{V} \equiv A_M^{-4} V$. Comparing to eq. (33), we see that apart from the extra contribution to $\tilde{\rho}_{\text{tot}}$ from the scalar field potential, the ST Friedmann equation differs from the standard one of GR by the presence of an effective, field-dependent Planck mass,

$$(49) \quad \frac{1}{3M_{\text{Pl}}^2} \rightarrow \frac{A_M^2(\varphi)}{3M_*^2} \frac{(1 + \alpha_M(\varphi) \varphi')^2}{1 - (\varphi')^2/6} \simeq \frac{A_M^2(\varphi)}{3M_*^2},$$

where the last equality holds with very good approximations for all the choices of A_i functions considered in the present paper.

If the conformal factor $A_M^2(\varphi)$ is constant, then the full action $S_g + S_M$ is just that of GR (with $M_{\text{Pl}} = M_*/A_M$) plus a minimally coupled scalar field. Therefore, the coupling function α_M , defined according to eq. (42), measures the “distance” from GR of the ST theory, $\alpha_M = 0$ being the GR limit. Changing A_M , and, therefore, changing the

effective Planck mass, opens the way to a modification of the standard relation between H and $\tilde{\rho}$, or T . In order to study the evolution of $A_M(\varphi)$, one should come back to eq. (41). Considering an initial epoch deeply inside radiation domination, we can neglect the contribution from the potential on the RHS. The other contribution, the trace of the energy-momentum tensor ($\rho_M - 3p_M$) is zero for fully relativistic components but turns on to positive values each time the temperature drops below the mass threshold of a particle in the thermal bath. Assuming a mass spectrum—*e.g.*, that of the SM, or of the MSSM—one finds that this effect is effective enough to drive the scalar field evolution even in the radiation domination era [12].

The key point to notice is that if there is a field value, φ_0 , such that $\alpha_M(\varphi_0) = 0$, this is a *fixed point* of the field evolution. Moreover, if α'_M is positive (negative) the fixed point is attractive (repulsive). Since $\alpha_M = 0$ corresponds to the GR limit, we see that GR is a—possibly attractive—fixed point configuration.

The impact on the DM relic abundance of a scenario based on this mechanism of attraction towards GR was considered in [12, 13].

7. – Implications for dark matter in the CMSSM

A modification of the Hubble rate at early times has impact on the formation of dark matter as a thermal relic, if the particle freeze-out occurs during the period of modification of the expansion rate. ST cosmologies with a Hubble rate increased with respect to the GR case have been discussed in refs. [12-14], where the effect on the decoupling of a cold relic was discussed and bounds on the amount of increase of the Hubble rate prior to Big Bang Nucleosynthesis have been derived from the indirect detection signals of dark matter in our Galaxy. For cosmological models with an enhanced Hubble rate, the decoupling is anticipated, and the required amount of cold dark matter is obtained for larger annihilation cross-sections: this, in turn, translates into larger indirect detection rates, which depend directly on the annihilation process. In refs. [13, 14] we discussed how low-energy antiprotons and gamma-rays fluxes from the galactic center can pose limits on the admissible enhancement of the pre-BBN Hubble rate. We showed that these limits may be severe: for dark matter particles lighter than about a few hundred GeV antiprotons set the most important limits, which are quite strong for dark matter masses below 100 GeV. For heavier particles, gamma-rays are more instrumental in determining significant bounds. Such bounds are relevant if one entertains the hypothesis that an enhanced DM annihilation rate may be at the origin of the recently observed positron excess by the PAMELA space experiment [15].

In the case of the cosmological models which predict a reduced Hubble rate, the situation is opposite: a smaller expansion rate implies that the cold relic particle remains in equilibrium for a longer time in the early Universe, and, as a consequence, its relic abundance turns out to be smaller than the one obtained in GR. In this case, the required amount of dark matter is obtained for smaller annihilation cross-sections, and therefore indirect detection signals are depressed as compared to the standard GR case: as a

consequence, no relevant bounds on the pre-BBN expansion rate can be set. On the other hand, for those particle physics models which typically predict large values for the relic abundance of the dark matter candidate, this class of ST cosmologies may have an important impact in the selection of the regions in parameter space which are cosmologically allowed.

A typical and noticeable case where the relic abundance constraint is very strong is offered by minimal SUGRA models. A reduction of the expansion rate will have a crucial impact on the allowed regions in parameter space, which are therefore enlarged. The potential reach of accelerators like the Large Hadron Collider (LHC) or the International Linear Collider (ILC) on the search of supersymmetry may therefore be affected by this broadening of the allowed parameter space, especially for the interesting situation of looking for supersymmetric configurations able to fully explain the dark matter problem.

8. – Conclusion

At the end of these lectures there is a main message concerning DM and new physics at the TeV scale that I tried to convey since the Introduction and throughout the main body of this contribution to the proceedings of the School: out of the four main “observational” motivations pushing us to go beyond the SM physics (neutrino masses, dark matter, baryogenesis and inflation), the DM issue constitutes the most promising candidate to represent the bridge towards a “low-energy” NP, namely a new physics showing up at the TeV scale. The see-saw mechanism for neutrino masses, most baryogenetic or leptogenetic mechanisms responsible for a dynamical origin of the cosmic matter-antimatter asymmetry and almost all inflationary models invoke the presence of some form of NP at very high energy scales. Unfortunately, these latter scales are unaccessible not only to present, but even to foreseeable future experimental exploration. On the contrary the attractive class of WIMP candidates for DM is likely to be linked to NP at the electroweak scale. Indeed, the most complete realization of TeV NP coping with the gauge hierarchy problem, namely the low-energy SUSY extension of the SM, entails the presence of a WIMP candidate, its lightest SUSY particle, at least once the discrete R -parity symmetry is enforced to prevent a too fast proton decay. Also theories which tackle the Higgs mass issue by means of an extension of the usual four-dimensional space-time through the introduction of extra dimensions are likely to have their lightest Kaluza-Klein mode as a viable WIMP candidate. We see that the two main roads pointing to a NP supplementing the SM at the TeV scale, namely the “theoretical” motivation of the gauge hierarchy and the “observational” motivation of accounting for the presence of DM, conspire together to provide us a most exciting prospect for the decade to come. Throughout high-energy physics (mainly LHC) and DM searches we could be able to provide a fundamental milestone to finally answer one of the most dramatic questions which have ever accompanied human history even before the advent of modern science: what is the Universe made of?

* * *

It is a great pleasure to thank my collaborators G. BERTONE, R. CATENA, M. FORNASA, N. FORNENGO, L. PIERI, M. PATO, M. PIETRONI, M. SCHELKE and M. TAOSO for sharing with me their views, hopes and worries about various aspects of the “dark side” of the Universe.

REFERENCES

- [1] SALAM A., in *Elementary Particle Theory*, edited by SVARTHOLM N. (Stockholm, Sweden) 1967; WEINBERG S., *Phys. Rev. Lett.*, **19** (1967) 1264; GLASHOW S. L., *Nucl. Phys.*, **22** (1961) 579.
- [2] PESKIN M. E. and SCHROEDER D. V., *An Introduction to Quantum Field Theory* (Addison-Wesley P.C., Reading, Mass) 1995.
- [3] For an introduction to the DM problem, see, for instance: KOLB R. and TURNER S., in *The Early Universe* (Addison-Wesley, New York, N.Y.) 1990; *Dark Matter*, edited by SREDNICKI M. (North-Holland, Amsterdam) 1989; PRIMACK J., SECKEL D. and SADOULET B., *Annu. Rev. Nucl. Part. Sci.*, **38** (1988) 751.
- [4] For a recent review, see BERTONE G., HOOPER D. and SILK J., *Phys. Rep.*, **405** (2005) 279; see also: TAOSO M., BERTONE G. and MASIERO A., *JCAP*, **0803** (2008) 022.
- [5] MINKOWSKI P., *Phys. Lett. B*, **67** (1977) 421; GELL-MANN M., RAMOND P. and SLANSKY R., in *Supergravity*, edited by VAN NIEUWENHUIZEN P. and FREEDMAN D. (North Holland) 1979, p. 315; YANAGIDA T., in *Proceedings of the Workshop on the Unified Theory and the Baryon Number in the Universe*, edited by SAWADA O. and SUGAMOTO A., KEK Report No. 79-18, Tsukuba (1979), p. 95; MOHAPATRA R. N. and SENJANOVIC G., *Phys. Rev. Lett.*, **44** (1980) 912; SCHECHTER J. and VALLE J. W. F., *Phys. Rev. D*, **25** (1982) 774.
- [6] See, for instance, FOGLI G. L., LISI E., MARRONE A., MELCHIORRI A., PALAZZO A., SERRA P., SILK J. and SLOSAR A., *Phys. Rev. D*, **75** (2007) 053001.
- [7] JUNGMAN G., KAMIONKOWSKI M. and GRIEST K., *Phys. Rep.*, **267** (1996) 1, and references therein.
- [8] For reviews, see NILLES H. P., *Phys. Rep. C*, **110** (1984) 1; HABER H. and KANE G., *Phys. Rep. C*, **117** (1985) 1; MARTIN S. P., *A Supersymmetry Primer*, in *Perspectives on Supersymmetry II*, edited by KANE G., e-Print: hep-ph/9709356.
- [9] FORNENGO N., BOTTINO A., DONATO F. and SCOPEL S., *Nucl. Phys. Proc. Suppl.*, **138** (2005) 28.
- [10] For instance, see HOOPER D., in *TASI 2008 Lectures on DM*, arXiv:0901.4090 [hep-ph] and references therein; ELLIS J. and OLIVE K., in *Particle Dark Matter: Observations, Models and Searches*, edited by BERTONE G., Chapt. 8, pp. 142-163, e-Print: arXiv:1001.3651 [astro-ph.CO].
- [11] CATENA R., PIETRONI M. and SCARABELLO L., *Phys. Rev. D*, **70** (2004) 103526.
- [12] CATENA R., FORNENGO N., MASIERO A., PIETRONI M. and ROSATI F., *Phys. Rev. D*, **70** (2004) 063519.
- [13] SCHELKE M., CATENA R., FORNENGO N., MASIERO A. and PIETRONI M., *Phys. Rev. D*, **74** (2006) 083505.
- [14] DONATO F., FORNENGO N. and SCHELKE M., *JCAP*, **0703** (2007) 021.
- [15] CATENA R., FORNENGO N., PATO M., PIERI L. and MASIERO A., *Phys. Rev. D*, **81** (2010) 123522.

This page intentionally left blank

Primordial nucleosynthesis in the presence of sterile neutrinos

L. GARCÍA(*), J. TEJEIRO and L. CASTAÑEDA

Observatorio Astronómico Nacional, Universidad Nacional de Colombia - Bogotá, Colombia

Summary. — The primordial nucleosynthesis process has been studied in cosmology since the forties, when Alpher, Bethe and Gamov described the reactions that could take place in the expanding universe represented by FRW metric. From this moment, the computations of light nuclei abundances have been improved with numerical techniques but also with astrophysical developments. However, it is imperative to upgrade the calculated abundances. In this work, we consider the influence of sterile neutrinos, as a contribution of dark matter in radiation domination and their effects in the Hubble factor H , through relativistic degrees of freedom, to compute the relative abundances of primordial nuclei that were produced in cosmological nucleosynthesis by solving the Boltzmann equation. In addition, we make a comparison between our results and the WMAP values for ^2H , ^3He , ^4He and ^7Li abundances.

1. – Introduction

While the Standard Model of cosmology has been developing since the thirties by Friedmann, Roberson, Walker and Lemaitre in order to describe the Universe at large scale, in nuclear physics, there were hard efforts to understand the nuclei formation process, the particles which constitute them and their interactions.

Otherwise, Gamov *et al.* [1,2] were trying to find out the chemical elements that could be formed at the early stages of the Universe, taking into account the chain of reactions

(*) E-mail: lagarciape@unal.edu.co

that could take place, the fundamental interactions and the expansion of the Universe. Gamov concluded that only the first 5 elements must have formed in this scenario, due to the Coulomb barrier and the lack of nuclei with high binding energy with atomic number between 5 to 8.

These results were confirmed by Wagoner in 1974 [3], using a numerical code that solves the Boltzmann equation for the present reactions in primordial nucleosynthesis (neutron decay, formation of deuteron, ^3He , ^4He and ^7Li ; other nuclei could be formed, but their abundances would be many orders of magnitude below the named elements) from $0.1\text{s} < t < 3\text{ min}$.

From this moment, the progress in the understanding of the early universe has been impelled by theoretical advances in cosmology [4], as well as in high energy physics, which has included fundamental details of Big Bang Nucleosynthesis (BBN) [5], the refinement of measurement techniques of the primordial abundances at high redshifts and computational development.

In addition, the study of the spectrum CMB and its anisotropies allows to know with a high level of accuracy cosmological parameters and to compare them with the corresponding values found with BBN. Indeed, the analysis with several techniques including CMB and BBN constrain the parameters of the cosmological model.

Nowadays, primordial nucleosynthesis is one of the most important probes for the Standard Model of cosmology and it represents a powerful way to test fundamental physics [6]. For this reason, in this work we study BBN including sterile neutrinos (a suitable candidate for being dark matter) in radiation domination, which modifies the Hubble parameter and thus, the Boltzmann equation. In this way, it is possible to explain the discrepancies between the theoretical calculations for light nuclei relative abundances and the observed values.

2. – Sterile neutrinos

There are many candidates for cold dark matter which come from models beyond the Standard Model of particle physics, such that: axions, gravitinos, neutralinos, sterile neutrinos, etc.

However, the sterile neutrinos are one of the most interesting candidates for cosmologists, but also for astrophysicists [7] owing to the fact that they do not interact via any fundamental interaction, except gravity. It means that they must be massive, so they would be described as cold dark matter candidates, in agreement with current cosmological models. Nevertheless, the mechanisms that generate their mass, as their mass range and their species number, depend strongly on the model.

Sterile neutrinos are fermions with spin $s = \frac{1}{2}$ and mixed flavour states of active neutrinos, so they can be described as

- right-helicity states and Majorana mass; their associated masses are $10\text{ MeV} \ll m_{\nu_s} \ll 150\text{ MeV}$ [8] (many orders of magnitude up to ordinary neutrinos masses). If they were Majorana fermions, they would be their own antiparticle, $\nu_s = \bar{\nu}_s$.

- Pseudo-Dirac neutrinos, so much lighter than Majorana neutrinos (keV masses), and with an associated antiparticle for each species.

In order to incorporate them successfully in the model and not affect the intrinsic processes that take place in radiation-dominated era, it is necessary to impose some conditions, such as their masses be larger than active neutrinos masses $m_{\nu_s} \gg m_{\nu_o}$. This statement is immediately satisfied by both descriptions. Furthermore, $0 < \Delta N_\nu < 3$, where ΔN_ν is the number of sterile neutrino species. This is required because works carried out by Steigman, Dolgov, Kirilova and Barger suggest that more than 3 species give ${}^4\text{He}$ abundances higher than the observed value. Finally, we must ensure that this kind of neutrinos must decouple from cosmological plasma earlier or at least at the same time as active neutrinos *freeze-out*, to be considered as dark matter.

3. – Hubble factor and cosmological time

The relativistic energy density contribution of sterile neutrinos [9,10] can be quantified using the factor ζ^2 such that

$$(1) \quad \rho_{\text{rad}} \Rightarrow \rho'_{\text{rad}} = \zeta^2 \rho_{\text{rad}}, \quad \text{where} \quad \rho'_{\text{rad}} = \rho_{\text{rad}} + \rho_x, \quad \rho_x = \Delta N_\nu \rho_\nu.$$

In the previous electron-positron annihilation the factor ζ takes the value

$$(2a) \quad \zeta^2 = \frac{\rho'}{\rho} = \frac{g'_{\text{eff}}}{g_{\text{eff}}} = \frac{2 + \frac{7}{8}(4 + 6 + 2\Delta N_\nu)}{2 + \frac{7}{8}(4 + 6)} = \frac{\frac{43}{4} + \frac{7}{4}\Delta N_\nu}{\frac{43}{4}} = 1 + \frac{7}{43}\Delta N_\nu,$$

$$(2b) \quad \zeta = (1 + 0.163\Delta N_\nu)^{1/2},$$

after this process

$$(3a) \quad \zeta^2 = \frac{\rho'}{\rho} = \frac{g'_{\text{eff}}}{g_{\text{eff}}} = \frac{2 + \frac{7}{8}(6 + 2\Delta N_\nu (\frac{4}{11})^{4/3})}{2 + \frac{7}{8}(6) (\frac{4}{11})^{4/3}} = 1 + \frac{\frac{7}{4}\Delta N_\nu (\frac{4}{11})^{4/3}}{2 + \frac{21}{4}\Delta N_\nu},$$

$$(3b) \quad \zeta = (1 + 0.135\Delta N_\nu)^{1/2},$$

are obtained where the factor 2 corresponds to the contribution of each sterile neutrino and its antiparticle and $(\frac{4}{11})^{1/3}$ is the relative temperature between neutrinos and photons caused by the transfer of entropy coming from electron-positron pair to particles coupled to the plasma (photons).

It is well known that the temperature scales as $T \propto a^{-1}$ during the Universe evolution. During radiation domination the scale factor a scales as $a \sim t^{1/2}$, therefore eq. (1) implies the following relation for the cosmological time:

$$(4) \quad t \Rightarrow t' = \zeta^{-1}t.$$

TABLE I. – *Hubble factor for $T = Q = 1.293 \text{ MeV}$ including sterile neutrinos.*

ΔN_ν	$H(x = 1)(\text{s}^{-1})$
0	1.132
1	1.221
2	1.304
3	1.382

Given Friedmann's equation

$$(5a) \quad H^2 = \frac{8\pi G}{3} \rho'_{\text{rad}} = \frac{4\pi^3 G}{45} T^4 g'_{\text{eff}},$$

$$(5b) \quad H = \left(\frac{4\pi^3 G}{45} \right)^{1/2} \left(\frac{43}{4} + \frac{7}{4} \Delta N_\nu \right)^{1/2} T^2.$$

Using the dimensionless variable $x = \frac{Q}{T}$ ($Q = 1.293 \text{ MeV}$, the neutron to proton mass difference) and $G^{-1/2} = m_{\text{pl}}$, one obtains

$$(6a) \quad H(x, \Delta N_\nu) = \left(\frac{4\pi^3}{45} \right)^{1/2} \frac{Q^2}{m_{\text{pl}}} \left(\frac{43}{4} + \frac{7}{4} \Delta N_\nu \right)^{1/2} x^{-2},$$

$$(6b) \quad H(x, \Delta N_\nu) = 0.3454 \text{ s}^{-1} \left(\frac{43}{4} + \frac{7}{4} \Delta N_\nu \right)^{1/2} x^{-2}.$$

The results of table I summarize the effects over the Hubble factor by increasing the number of neutrinos, whereas table II shows that cosmological time decreases with increasing number of sterile neutrinos. Furthermore, an expression for t is found in terms

TABLE II. – *Cosmological time during radiation domination—after active neutrinos decoupling—including sterile neutrinos.*

ΔN_ν	$\left(\frac{0.1 \text{ MeV}}{T} \right)^2 t(\text{s})$
0	132.0
1	122.4
2	114.6
3	108.2

of the number of species of non-active neutrinos

$$(7) \quad t = 432.79 \text{ s} \left(\frac{0.1 \text{ MeV}}{T} \right)^2 \left(\frac{43}{4} + \frac{7}{4} \Delta N_\nu \right)^{-1/2}.$$

The relative abundance for light nuclei produced in cosmological nucleosynthesis is obtained by solving the Boltzmann equation with the assumption of nuclear statistical equilibrium (chemical and thermal equilibrium, but kinematic evolution)

$$(8) \quad \frac{dX_n}{dt} = \lambda_{np}((1 - X_n)e^{-Q/T} - X_n),$$

where X_n is the neutron's abundance for $x \rightarrow \infty$ and λ_{np} is the weak decay rate $n \Rightarrow p$ that contributes according to the following decays:

$$(9) \quad \nu + n \leftrightarrow e + p, \quad n + \bar{e} \leftrightarrow \nu + p, \quad n \leftrightarrow e + p + \bar{\nu}.$$

Equation (8) can be written as (using $x = \frac{Q}{T}$)

$$(10) \quad \frac{dX_n}{dx} = \frac{\lambda_{np}x}{H(x=1)}(X_n - (1 - X_n)e^{-x}),$$

$\lambda_{np} = \frac{255}{\tau_n x^5}(x^2 + 6x + 12)$ [11]. The challenge is to find a solution of the differential equation in terms of ΔN_ν

$$(11) \quad \frac{dX_n}{dx} = \frac{255}{\tau_n H(x=1)x^4}(X_n - (1 - X_n)e^{-x})(x^2 + 6x + 12).$$

TABLE III. – *Calculated abundances for light nuclei compared with WMAP results* [13].

ΔN_ν	$D/H \times 10^{-5}$	${}^3\text{He}/H \times 10^{-5}$	Y_p	${}^7\text{Li}/H \times 10^{-10}$
0	2.650	1.046	0.241	1.27
1	2.716	1.062	0.253	1.26
2	2.794	1.094	0.264	1.28
3	2.818	1.161	0.274	1.36
[13]	2.75	1.05	0.2484	4.41
	± 0.24	± 0.06	± 0.0004	± 0.30

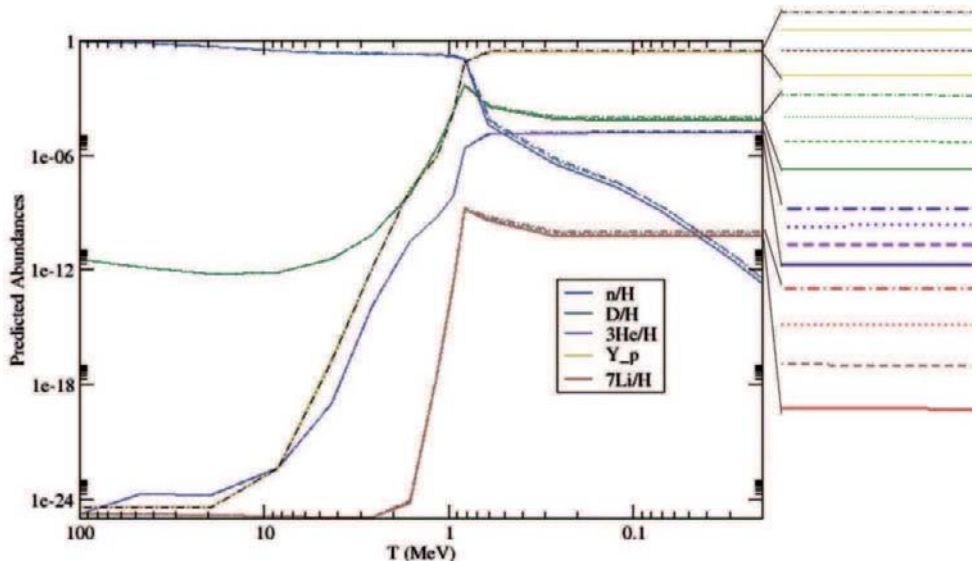


Fig. 1. – The solid lines represent the Standard Model predictions. The dashed, dotted and dash-dotted lines represent 1, 2 and 3 sterile neutrinos, respectively.

4. – Computed abundances with sterile neutrinos

Solving eq. (11) it is possible to resolve numerically the chains which produce the cosmological nuclei. It was done with the public code provided by Wagoner and Kawano [12] varying the number of sterile neutrinos from 0 to 3 for $100 < T < 0.01$ MeV.

It was allowed to have abundances up to 10^{-25} and the contributions of curvature or cosmological constant were ignored. Moreover, chemical potentials that could degenerate the model were neglected, thus $\mu_{\nu_i} = 0.0$, $\tau_n = 885.7$ s and $g = 1.0$ were used.

Figure 1 shows the behaviour of the abundance curves with respect to the plasma temperature. On the other hand, fig. 2 shows the variation of the abundances against the cosmological parameter η_B . The calculated abundances for light nuclei are compared with the WMAP results [13] and are given in table III.

It is noticed that it is necessary to increase the number of iterations (small temperature intervals) in order to enhance the resolution of the curves, especially for ^7Li , whose evolution depends strongly on the reactions that compete in its creation. Also, there is a consistency problem between the values obtained by CMB techniques and astrophysical methods.

Despite that, the shape of the curves is the expected one. In fact, examining these plots we can conclude that the introduction of sterile neutrino in the model is justified, because the abundances predictions are improved notably, with the exception of ^3He whose relative abundance is almost unaltered.

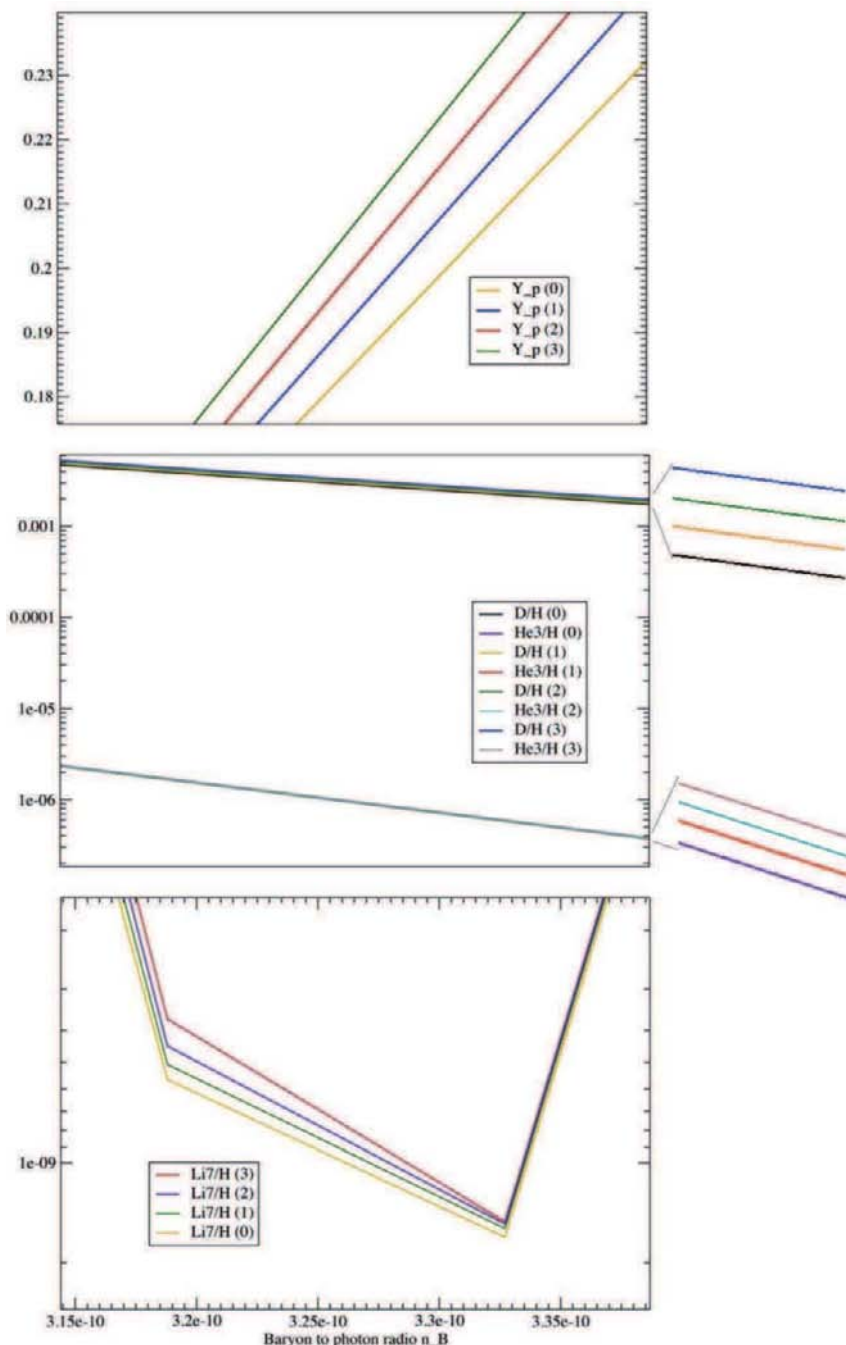


Fig. 2. – Relative abundances *vs.* η_B varying the number of sterile neutrinos from 0 to 3.

5. – Conclusions

- Sterile neutrinos are excellent candidates to cold dark matter, and they adjust to BBN if they satisfy some conditions described above. Moreover one needs to study in depth the details of the model which describes them, in order to define their masses, their decoupling period and also, the number of species.
- Including this kind of particle in primordial nucleosynthesis gives very good results for light-nuclei computed abundances, with the exception of ^7Li . However, it is important to remark that this isotope has a strong dependence on the cosmological inputs, but also on cross-sections of reactions that take place before its synthesis.
- The results can be improved if other parameters that we have fixed, as τ_n , g , etc., are considered to be varied. In addition, it is also possible to take into account radiative corrections in the chains of nuclear reactions. In this way, it is viable to estimate values for some cosmological parameters as η_B or Ω_B .

* * *

This work is supported and developed by the Observatorio Astronómico Nacional under the auspices of Universidad Nacional de Colombia.

REFERENCES

- [1] ALPHER R., BETHE H. and GAMOV G., *Phys. Rev.*, **73** (1978) 803.
- [2] GAMOV G., *Phys. Rev.*, **70** (1946) 572.
- [3] WAGONER R. V., *International Astronomical Union*, **63** (1974) 195.
- [4] STEIGMAN G., SCHRAMM D. N., OLIVE K., TURNER M. S. and YANG J., *Astrophys. J.*, **281** (1984) 493.
- [5] SERPICO P. D., ESPOSITO S., IOCCO F., MANGANO G., MIELE G. and PISANTI O., *Nuclear Reaction Network for Primordial Nucleosynthesis: a detailed analysis of rates uncertainties and light nuclei yields*, Preprint in [arXiv: <http://lanl.arxiv.org/abs/0408.076v2>].
- [6] SANKAR S., *Big-Bang Nucleosynthesis*, Preprint in [arXiv: <http://lanl.arxiv.org/abs/0406663v1>].
- [7] DE VEGA H., FALVELLA M. and SANCHEZ N., *HIGHLIGHTS and CONCLUSIONS of the Chalonge 14th Paris Cosmology Colloquium 2010: “The Standard Model of the Universe: Theory and Observations”*, Preprint in [arXiv: <http://lanl.arxiv.org/abs/1009.3494v2>].
- [8] DOLGOV A. D., HANSEN S. H., RAFFELT G. and SEMIKOV D. V., *Nucl. Phys. B*, **590** (2000) 562.
- [9] STEIGMAN G., SCHRAMM D. N. and GUNN J. E., *Phys. Lett. B*, **66** (1977) 202.
- [10] DODELSON S., *Modern Cosmology* (Academic Press) 2003.
- [11] BERNSTEIN J., *Kinetic Theory in the Expanding Universe* (Cambridge University Press) 1988.
- [12] KAWANO L., *Let’s go: The Early Universe II*, Fermilab preprint FERMILAB-PUB-92/04-A (1992).
- [13] MOLARO P., *Primordial Light Element Abundances*, Preprint in [arXiv: <http://lanl.arxiv.org/abs/0708.3922v1>].

LOW-ENERGY REACTIONS FOR ASTROPHYSICS

This page intentionally left blank

Proceedings of the International School of Physics “Enrico Fermi”
Course CLXXVIII “From the Big Bang to the Nucleosynthesis”, edited by A. Bracco and E. Nappi
(IOS, Amsterdam; SIF, Bologna)
DOI 10.3254/978-1-60750-974-5-319

The LUNA experiment at LNGS

A. GUGLIELMETTI for the LUNA COLLABORATION

*Università degli studi di Milano, Dipartimento di Fisica and INFN, Sezione di Milano
Milano, Italy*

Summary. — At astrophysically relevant temperatures, nuclear cross-sections are extremely small and experimental measurements in a laboratory at the Earth’s surface are hampered by the cosmic background. The LUNA Collaboration has exploited the unique features of the rock cover offered by the LNGS underground laboratory in terms of background reduction, to study very important H-burning reactions at astrophysically relevant energies. After a general introduction on the LUNA experiment, the most important results and their astrophysical consequences will be reviewed. On-going and future measurements will also be presented.

1. – Introduction

It is well known [1] that stars generate energy and produce elements by means of thermonuclear fusion reactions which start from the most abundant and lightest element, hydrogen, and gradually synthesize heavier elements. Hydrogen burning can proceed either through the p-p chain or through the more efficient CNO cycle or even through the NeNa and MgAl cycles in stars more evolved and hotter than our Sun. The net result is the transformation of 4 protons into a ${}^4\text{He}$ nucleus with an energy release of about 27 MeV. The fusion of hydrogen into helium occurs during the longer part of the star’s life (main sequence) and is responsible for the prodigious luminosity of the star itself. All these fusion reactions occur in stars in a very well-defined energy range, the so-called

Gamow peak, which is the result of the convolution between the energetic distribution of nuclei in stars at a given temperature and the energetic dependence of the reaction cross-section. The first, given by the Maxwell-Boltzmann distribution, has a maximum for $E = kT$ (where T is the star temperature and k the Maxwell-Boltzmann constant) and then decreases exponentially for increasing energy while the second, given by the tunneling probability through a Coulomb barrier, decreases exponentially for decreasing energy. In particular the reaction cross-section for charged particles can be written as

$$(1) \quad \sigma(E) = \frac{S(E)}{E} e^{-2\pi\eta},$$

where $S(E)$ is the astrophysical factor which contains the pure nuclear behavior of the cross-section and η is the Sommerfeld parameter given by

$$(2) \quad \eta = (31.29/2\pi) Z_1 Z_2 \sqrt{\frac{\mu}{E}},$$

Z_1 and Z_2 being the charges of the interacting nuclei, μ the reduced mass and E the interaction energy expressed in keV in the centre-of-mass reference system. As an example, in our Sun, whose temperature is 1.5×10^7 K, the maximum of the Maxwell-Boltzmann distribution occurs at about 1 keV, the Coulomb barrier for most of the reactions of both p-p chain and CNO cycle is between 0.5 and 2 MeV and the Gamow peak for the same reactions is below 30 keV. At such low energy, the cross-section is extremely low, down to the femtobarn level in “the worst” cases, due to the already mentioned exponential decrease of the cross-section with decreasing energy. Therefore, direct measurements are mostly hampered by the cosmic background in a laboratory at the Earth’s surface where the signal-to-background ratio would be too small. The usual approach is to extrapolate the observed energy dependence of the cross-section at high energies down to the low and significant energy region leading to substantial uncertainties. In particular a possible narrow resonance in the unmeasured region, the tail of a broad or sub-threshold resonance or even a change in the reaction mechanism can completely modify the reaction rate.

2. – Why underground: the LUNA project

The LUNA (Laboratory for Underground Nuclear Astrophysics) Collaboration has exploited the silent environment of the underground laboratory under the Gran Sasso Mountain in Italy (LNGS) to overcome this difficulty by performing direct measurements at the relevant energies. The rock cover of about 1400 m (3800 m water equivalent) reduces the muon component of the cosmic background of a factor 10^6 , the neutron component of a factor 10^3 and the gamma component of a factor 10 with respect to the Earth’s surface. As a result, the gamma background above 3 MeV in an HPGe detector placed underground at LNGS is reduced by a factor 2500 with respect to the same detector placed over-ground. Moreover, for lower energy gammas where the background is dominated by environmental radioactivity, the effect of passive shielding is enhanced

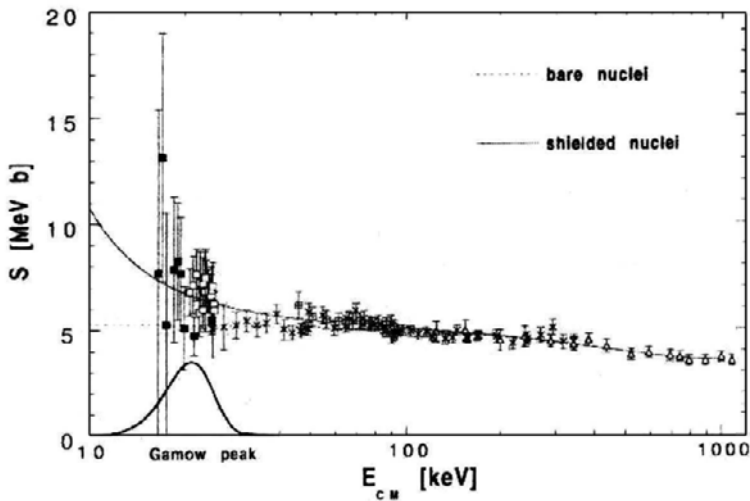


Fig. 1. – Astrophysical factor for the ${}^3\text{He} + {}^3\text{He}$ reaction measured by the LUNA Collaboration at the Gamow peak energy. No resonance was found in the Sun energetically interesting region.

by going underground. Indeed, in a laboratory on the Earth's surface, a passive shielding can be built around the detector but the shield efficiency cannot be increased by making it thicker with the addition of further material since cosmic muons interact with it creating background signals in the detector itself. This problem is of course dramatically reduced in an underground laboratory being the muon flux much lower. The LUNA Collaboration has installed two accelerators underground: a compact 50 kV "home-made" machine [2] and a commercial 400 kV one [3]. Common features of the two are the intense current production, the long-term stability and the precise energy determination. The first two features are essential to maximize the reaction rate, while the third is important in view of the exponential energy dependence of the cross-section.

3. – Results

With the first 50 kV machine the LUNA Collaboration studied two key reactions of the p-p chain: ${}^3\text{He}({}^3\text{He}, 2\text{p}){}^4\text{He}$ and ${}^2\text{H}(\text{p}, \gamma){}^3\text{He}$ at the relevant Gamow peak energies by using gas targets and very efficient particle or gamma detectors. The first reaction plays a big role in the proton-proton chain strongly affecting the calculated solar neutrino luminosity. A resonance at the thermal energy of the Sun was suggested long ago [4] to explain the observed ${}^8\text{B}$ solar neutrino flux: it would have possibly decreased the relative contribution of the alternative reaction ${}^3\text{He}({}^4\text{He}, \gamma){}^7\text{Be}$ which generates the branch responsible for ${}^7\text{Be}$ and ${}^8\text{B}$ neutrino production in the Sun. The LUNA result [5] shown in fig. 1 inferred the absence of resonances up to the lower limit of the Solar Gamow peak thus excluding the old possible explanation of the solar neutrino puzzle now ruled out by the recent discovery of neutrino oscillations [6]. This reaction was measured almost

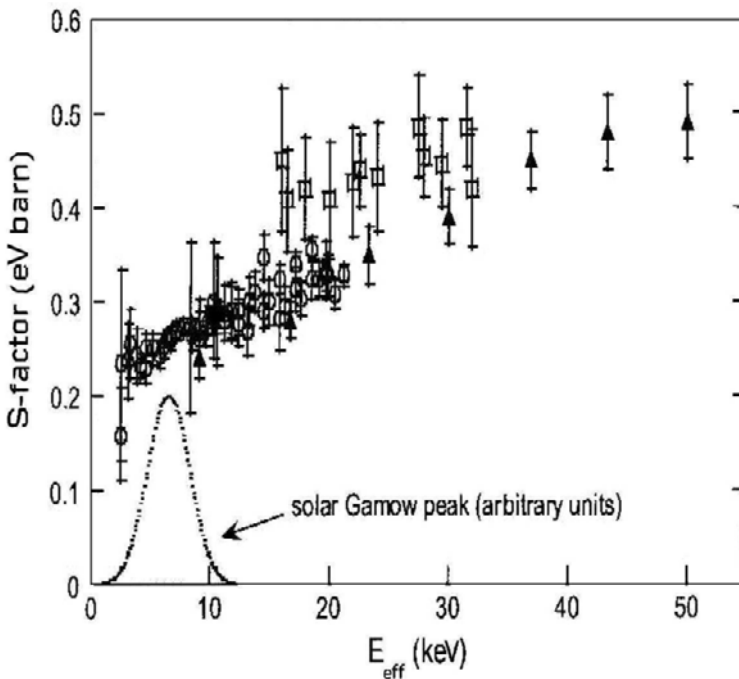


Fig. 2. – Astrophysical factor for the $^2\text{H}(\text{p}, \gamma)^3\text{He}$ reaction: The LUNA Collaboration results are shown as open circles.

within the whole solar Gamow peak (15–27 keV) and its cross-section varies by more than two orders of magnitude in the measured energy range. At the lowest energy of 16.5 keV its value is only 0.02 pb corresponding to a count rate of 2 events/month, rather low even for the “silent” experiment of underground physics.

The $^2\text{H}(\text{p}, \gamma)^3\text{He}$ reaction is fundamental for regulating the life of a proto star before the main sequence is reached. This reaction allows the burning of primordial deuterium by conversion into ^3He with a net energy release: in such a way the gravitational contraction of the protostar is slowed down and its lifetime made longer. The observational properties of the protostar are freezed until the original deuterium is fully consumed. This reaction is also fundamental in the Big-Bang Nucleosynthesis (BBN): because of the photodisintegration of deuterium, the formation of ^3He is delayed until the temperature drops to approximately 8×10^8 K. Knowledge of the cross-section at low energies is required. The measured astrophysical factor [7] is shown in fig. 2 together with older results. Also in this case the interesting energy ranges, *i.e.* the solar Gamow peak, the Gamow peak for a protostar and the BBN region were reached.

The first reaction studied with the 400 kV accelerator was $^{14}\text{N}(\text{p}, \gamma)^{15}\text{O}$, the bottleneck of the CNO cycle controlling the cycle’s energy production-rate. This reaction provides the ^{13}N and ^{15}O solar neutrino flux, which depends almost linearly on it, and

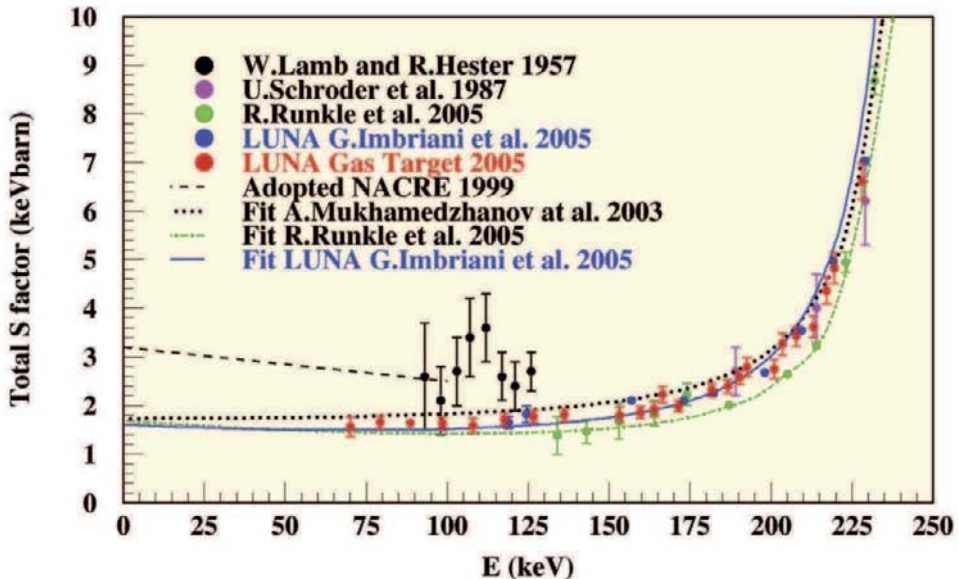


Fig. 3. – Astrophysical factor for the $^{14}\text{N}(\text{p}, \gamma)^{15}\text{O}$ reaction: LUNA results are shown together with previous literature data and theoretical extrapolations.

determines the age of globular clusters, the oldest systems in the Galaxy. As a matter of fact, during most of its life, a low-mass star burns hydrogen in the center via the p-p chain. However, when the central H mass fraction reduces down to 0.1, the nuclear energy produced by the H-burning becomes not sufficient and the stellar core must contract to extract some energy from its gravitational field. Then, the central temperature (and the density) increases and the H-burning switches from the p-p chain to the more efficient CNO burning. Thus the escape from the main sequence is powered by the onset of the CNO burning whose bottleneck is the $^{14}\text{N}(\text{p}, \gamma)^{15}\text{O}$ reaction. In particular, a rate modification of this reaction changes the luminosity of the turn-off point in the Hertzsprung-Russell diagram of a globular cluster. The luminosity of this point gives then the age of the cluster: the higher the cross-section is, the younger is the age, for a given turn-off luminosity. Two different apparatus were used to study this reaction: a solid target coupled with an HPGe detector in the energy region from 140 to 400 keV [8, 9] to measure single gamma transitions and the angular distribution and a gas target with a very efficient 4π BGO detector down to 70 keV [10] to obtain the total astrophysical factor at the lowest measurable energy. Figure 3 shows the results for the astrophysical factor obtained at LUNA, previous literature data and theoretical extrapolations. The LUNA results obtained with the two techniques are in very nice agreement between each others in the overlapping energy region and determine a value of the astrophysical factor lower by a factor 2 with respect to that given in the NACRE compilation [11]. The astrophysical consequences are significant: the CNO neutrino yield in the Sun is

decreased by about a factor 2 and the age of the Globular Clusters is increased by 0.7–1 Gy [12] up to 14 billion years with respect to current estimates. This last result reflects in an increase of the lower limit on the age of the Universe.

Then the ${}^3\text{He}({}^4\text{He}, \gamma){}^7\text{Be}$ reaction was measured. This is the onset of the ${}^7\text{Be}$ and ${}^8\text{B}$ branches of the p-p chain from which the ${}^7\text{Be}$ and ${}^8\text{B}$ neutrinos are generated. Solar neutrino fluxes depend on both astrophysical and nuclear physics inputs: in the case of ${}^7\text{Be}$ and ${}^8\text{B}$ neutrinos, one of the most important parameters is the cross-section of the ${}^3\text{He}({}^4\text{He}, \gamma){}^7\text{Be}$ reaction. After the successful measurements of the ${}^8\text{B}$ neutrino flux with a 3.5% uncertainty performed by SNO [13] and SuperKamiokande [14] and in view of a similar result on the ${}^7\text{Be}$ neutrino flux from the Borexino experiment [15], a comparable uncertainty on the ${}^3\text{He}({}^4\text{He}, \gamma){}^7\text{Be}$ cross-section was demanded. Only under these circumstances, the neutrinos would give reliable information on the interior of the Sun and on its physical and chemical properties. Moreover, the ${}^3\text{He}({}^4\text{He}, \gamma){}^7\text{Be}$ reaction is fundamental for the big-bang nucleosynthesis being the main source for ${}^7\text{Li}$ production. The predicted abundance of such isotope is a factor 2-3 higher than the observed one. Even if it is unlikely that the explanation of this discrepancy could come from the ${}^3\text{He}({}^4\text{He}, \gamma){}^7\text{Be}$ cross-section, a better knowledge of its value represented the necessary basis for the search of alternative solutions to the ${}^7\text{Li}$ problem. In the last forty years, the ${}^3\text{He}({}^4\text{He}, \gamma){}^7\text{Be}$ reaction was measured using two different approaches: either the detection of direct α -capture γ -rays (prompt γ method) or the detection of the ${}^7\text{Be}$ radioactivity through the electron capture of ${}^7\text{Be}$ into ${}^7\text{Li}$ and its subsequent de-excitation from the first excited to the ground state (activation method). Results obtained with the two techniques showed, on average, a discrepancy of about 15% which was the origin of the large uncertainty on the ${}^3\text{He}({}^4\text{He}, \gamma){}^7\text{Be}$ cross-section [16]. To solve this problem, the LUNA Collaboration performed an experiment with both techniques at the same time and with a careful eye on reducing the systematical uncertainties. A re-circulating ${}^3\text{He}$ extended windowless gas target was coupled to a 137% HPGe detector in close view of the interaction chamber. The ${}^4\text{He}$ intense beam of the LUNA 400 kV machine was focused on a removable copper beam-stop which served both as the end cap of a calorimeter (to measure the beam current) and as a catcher for the ${}^7\text{Be}$ nuclei allowing for a delayed off-line measurement of their activity. Being the Q -value of the reaction about 1.5 MeV, the prompt γ -rays are in the region of natural background: a massive shielding (0.3 m^3) was therefore built around the target chamber and the HPGe detector. This consisted in several layers of lead bricks and an inner layer of Oxygen Free High Conductivity (OFHC) copper bricks. Moreover, the target chamber and the calorimeter were constructed using OFHC copper and no welding materials were used. All this system was enclosed in an anti-radon envelope consisting in a Plexiglas box flushed with N_2 gas to avoid ${}^{222}\text{Rn}$ accumulation. As already underlined, the efficiency of the shielding was increased by the underground location and a background suppression of five orders of magnitude was obtained for γ -rays below 2 MeV with respect to a background spectrum measured underground with no shielding [17]. The typical α -beam current was high (about $250 \mu\text{A}$), thus causing a reduction of the target density due to the so-called beam-heating effect. This was measured through the detection of the beam particles elastically

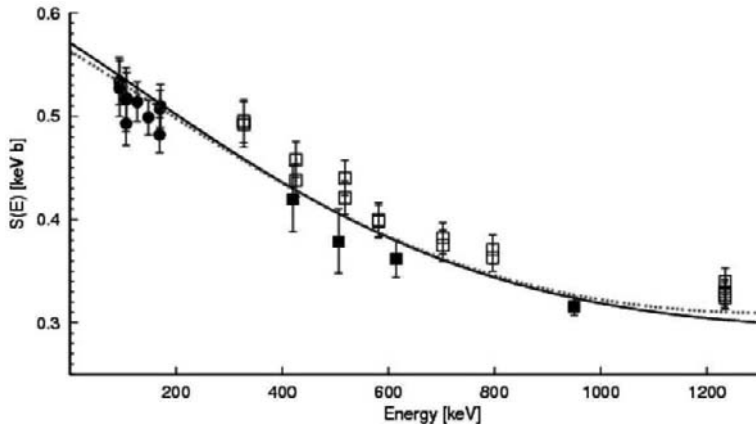


Fig. 4. – Astrophysical S -factor for the ${}^3\text{He}({}^4\text{He}, \gamma){}^7\text{Be}$ reaction obtained from recent experiments. The filled squares are from ref. [23], the open squares from ref. [24] while the filled circles are the LUNA data [21, 22]. The solid and dotted curves are the theoretical predictions by [25] and [26], respectively, obtained considering the weighted average of $S(0)$ of the different experiments (see text).

scattered on the target atoms [18]. Moreover, in order to reduce the systematic error coming from the uncertainty on the angular distribution, a lead collimator was positioned inside the target chamber to collect mostly γ -rays emitted at 55° , where the contribution of the second Legendre polynomial vanishes. After each run, the calorimeter cap was dismounted and its activity counted off-line with a 125% HPGe detector, shielded by 15 cm of lead and 10 cm of copper on each side and placed in the low-activity laboratory of LNGS [19]. The experiment was divided into two phases: in the former the cross-section was measured at $E = 127$ and $E = 148$ keV (CM reference frame) with the activation technique only [20], in the latter both techniques were used to measure the cross-section at $E = 93, 106$ and 170 keV [21, 22]. A comparison of the results obtained with the two techniques was therefore possible and reduced significantly the systematic uncertainties. Moreover, the cross-sections measured with the two methods were consistent at the level of 4% [21, 22]. While the LUNA data partly covered the energy window interesting for BBN (80–400 keV), an extrapolation is still needed for reaching the solar Gamow peak at 22 keV. The most recent results [23, 24] and the LUNA data [21, 22] for the astrophysical S -factor as a function of the center-of-mass energy are shown in fig. 4, together with the theoretical

$$S(0) = 0.567 \pm 0.018 \pm 0.004 \text{ keV} \cdot b,$$

where the last error accounts for the uncertainty on the adopted theoretical model. The most recent results [23, 24] and the LUNA data [21, 22] for the astrophysical S -factor as a function of the center-of-mass energy are shown in fig. 4, together with the theoretical

extrapolations [25, 26] of the $S(0)$ value. The goal of the 3% uncertainty was therefore reached but a unique set of data exploring the entire interesting energy range is still highly desirable to precisely determine the S -factor energy dependence.

After 2006, the “non-solar” phase of the experiment started, mainly devoted to the study of (p,γ) reactions on nitrogen, oxygen, neon, sodium and magnesium isotopes, belonging to CNO, NeNa and MgAl cycles of hydrogen burning. These cycles become important for second-generation stars whose central temperatures and masses are higher than our Sun and whose evolution stage is such that the necessary seeds for those reactions are already present. Due to the higher Coulomb barriers, these cycles are relatively unimportant for energy generation while being essential for the nucleosynthesis of elements with mass number higher than 20. The $^{25}\text{Mg}(p,\gamma)^{26}\text{Al}$ reaction is the slowest of the Mg-Al cycle. The β^+ decay of ^{26}Al ($T_{1/2} = 7 \times 10^5$ y) populates the 1.8 MeV excited state of ^{26}Mg which then decays to the ground state by γ -emission. Observations from satellites [27, 28] have determined an amount of ^{26}Al in our galaxy of about 6 solar masses through the detection of this γ -ray line. Moreover, the presence of ^{26}Al in the interstellar medium has been determined from the observation of ^{26}Mg isotopic enrichment (extinct ^{26}Al) in carbonaceous meteorites [29], again detecting the 1.8 MeV line. While the former observation gives evidence that ^{26}Al nucleosynthesis is still active on a large scale, the latter suggests that ^{26}Al was produced not later than 4.6 billion years ago (time of the condensation of the solar-system material). ^{26}Al is mainly produced via the $^{25}\text{Mg}(p,\gamma)^{26}\text{Al}$ reaction which is active in the hydrogen burning shell of off-main sequence stars of any mass and in the carbon burning regions of massive stars. Therefore different astrophysical environments are responsible for ^{26}Al nucleosynthesis and the reaction cross-section should be precisely studied in a wide energy range since each environment is characterized by a temperature range corresponding to an energy window. In particular the reaction is dominated by narrow resonances, giving rise to a rather complex decay scheme of γ -ray cascades. Before LUNA, the strengths of these resonances were experimentally studied only down to 190 keV, in some cases with huge discrepancies among results obtained with different techniques; see for instance [30]. Indeed, the reaction can be studied by detecting the prompt gammas or by counting the ^{26}Al nuclei with accelerator mass spectroscopy (AMS). At LUNA several resonances were investigated with different and complementary techniques: an HPGe low-efficiency and high-resolution detector was used for the higher energy resonances (304 and 190 keV), a low-resolution but high-efficiency BGO detector was used also for the lower energy ones (130 and 93 keV) and the AMS technique was used for the 304 keV resonance using the CIRCE facility of Caserta (Italy) [31] on the LUNA proton-irradiated Mg targets. The 304 keV resonance was measured with the three techniques in order to understand possible systematic uncertainties and compare with previous results. A huge effort was devoted to the study of the target stoichiometry since this is a critical parameter for determining the reaction rate. Both natural Mg targets (of well-known isotopic composition) and enriched ^{25}Mg targets were used. The former for determining the resonance strengths of relatively high energy resonances of (p,γ) reactions on $^{24,25,26}\text{Mg}$ isotopes, while the latter only for the $^{25}\text{Mg}(p,\gamma)^{26}\text{Al}$ reaction. The results obtained with the nat-

ural targets give a normalization of those obtained with the enriched targets, also for lower energies resonances. For the higher energy resonances, the following results were obtained [32]: for the 304 keV resonance of $^{25}\text{Mg}(\text{p},\gamma)^{26}\text{Al}$ reaction, measured with three different techniques (HPGe, BGO and AMS), a very good agreement was found among the different approaches for the resonance strength. By comparing the LUNA result with literature data, a strong disagreement is found only with the result of Arazi *et al.* [30] obtained with the AMS technique. The evaluation of NACRE [11] combined with the LUNA result yields an improved uncertainty of 4%. For the 214 keV resonance of the $^{24}\text{Mg}(\text{p},\gamma)^{25}\text{Al}$ reaction, the LUNA resonance strength is lower by more than 10% with respect to Powell *et al.* [33]. However, a strong direct capture component dominates the resonance contribution and a re-analysis of the reaction at astrophysical energies by using a *R*-matrix formalism with improved γ -width knowledge is worthwhile. For the $^{26}\text{Mg}(\text{p},\gamma)^{27}\text{Al}$ 326 keV resonance, an apparent discrepancy in the literature [11] was solved and the resonance strength was measured with a high accuracy. For the 190 and 93 keV resonances of the $^{25}\text{Mg}(\text{p},\gamma)^{26}\text{Al}$ reaction the data analysis is on-going: a preliminary evaluation gives for the strength of the 190 keV resonance a similar outcome to the one described for the 304 keV one.

4. – On-going measurements

In the last two years, the LUNA Collaboration has been engaged in the study of the $^{15}\text{N}(\text{p},\gamma)^{16}\text{O}$ reaction and in the preparation of the $^2\text{H}(\alpha,\gamma)^6\text{Li}$ and $^{17}\text{O}(\text{p},\gamma)^{18}\text{F}$ measurements.

Proton capture on ^{15}N gives rise to ^{16}O which can then decay either alpha to ^{12}C or gamma to the ground state of ^{16}O itself. This introduces a reaction branch linking the first CNO (or CN) cycle with the second CNO (or NO cycle). The amount of this branching ratio has always been a matter of debate since both reactions are characterized by strong low-energy resonances. The reaction rate is dominated by two broad low-energy resonances at 338 keV and 1028 keV and the associated interference terms. In addition, it is expected to have a strong non-resonant direct capture component which may contribute significantly to the reaction cross-sections at stellar energies. Before the LUNA measurements, the astrophysical *S*-factor of this reaction was known only down to interaction energies of 155 keV with large uncertainties. Moreover, a discrepancy existed between the *S*-factor extrapolated at zero energy (*S*(0)) from the different data sets existing in the literature [34–36]. The LUNA Collaboration has undertaken different approaches to investigate this reaction and clarify the situation on the *S*(0) value. In a first effort, a re-analysis of the data acquired during a past measurement of the $^{14}\text{N}(\text{p},\gamma)^{15}\text{O}$ reaction with a high-efficiency BGO detector was performed, exploiting the fact that the gas target was composed of natural nitrogen (0.3% ^{15}N). The data covered only a limited energy range (90–230 keV) and were affected by large uncertainties at low energy [37]. Then a systematic study using enriched ^{15}N solid-target and HpGe detectors started, in collaboration with the University of Notre Dame (USA). In this phase, a wide energy range (100–2000 keV) was covered by measuring the reaction at three different

facilities (LUNA and two accelerators at the University of Notre Dame). This allowed a large overlap with previous measurements and a sound basis for a precise R -matrix fit [38]. In the most recent experiment, a low-resolution but high-efficiency BGO detector was used in combination with enriched solid targets. This allowed to reach lower energies than previously achieved (77 keV) and to reduce the statistical uncertainties. Titanium nitride targets enriched in ^{15}N (nominal value about 98%) produced using the reactive sputtering technique were used. Two sets of targets were prepared: one in the FZ-Karlsruhe and the other in the Laboratori Nazionali di Legnaro. Since the target properties (stoichiometry and isotopic ratio) are directly related to the measured yield, two ancillary measurements were performed to determine these characteristics:

- high- Z Elastic Recoil Detection (ERD) performed in Munich;
- resonance scan profiles performed at the FZD in Dresden.

For each bombarded target, the stoichiometry was determined by the ERD measurements and the ^{14}N content by the height of the plateau of the resonance scans performed on the $E_R = 278$ keV resonance of the $^{14}\text{N}(\text{p}, \gamma)^{15}\text{O}$ reaction. Knowing the stoichiometry, the amount of ^{15}N in the targets was reconstructed since ^{14}N and ^{15}N are the only nitrogen isotopes. In Dresden, in order to evaluate the nitrogen profile along the target thickness, the resonance profiles of the $E_R = 430$ keV resonance of the $^{15}\text{N}(\text{p}, \alpha\gamma)^{12}\text{C}$ reaction were measured. This is a narrow resonance that produces a γ -ray of 4.4 MeV. The nitrogen profiles have been measured both in an area irradiated by the LUNA beam and in one not irradiated. In this way, the effect of the target deterioration due to the beam irradiation by the LUNA beam was corrected. To maximize the efficiency, a 4π -BGO summing crystal detector was used. Its efficiency was evaluated with a GEANT4 code. This was tested in a previous experiment [37] and compared with the experimental results of radioactive sources (^{137}Cs , ^{60}Co and ^{22}Na) and the $E_R = 163$ keV resonance of the $^{11}\text{B}(\text{p}, \gamma)^{12}\text{C}$ reaction. In the region of interest for the $^{15}\text{N}(\text{p}, \gamma)^{16}\text{O}$ reaction (~ 12 MeV in the γ -spectrum), the efficiency was estimated to be 68%. The natural background was negligible for all energies and the beam induced background, due to the $^{11}\text{B}(\text{p}, \gamma)^{12}\text{C}$ reaction, was taken into account by adding a 3% systematic uncertainty. The data analysis was performed with two different techniques yielding consistent results. A publication is in preparation.

The $^2\text{H}(\alpha, \gamma)^6\text{Li}$ reaction is fundamental in the Big-Bang Nucleosynthesis (BBN) and determines the amount of primordial ^6Li in the Universe. Recently, ^6Li isotope has been detected in a number of metal poor stars [39, 40] and its quantity has been found to be higher than expected from BBN by 2-3 orders of magnitude [41]. Direct measurements of this reaction have been performed only down to 1 MeV and around the 711 keV resonance [42, 43] while the region of interest for BBN is between 30 and 400 keV. The reaction can be measured at LUNA up to 130 keV (about 400 keV in the laboratory reference system) with the present machine while going to higher energies and eventually overlap with previous direct measurements would require a different, higher voltage,

machine. A set-up very similar to the one already used for the ${}^3\text{He}({}^4\text{He}, \gamma){}^7\text{Be}$ reaction [22] could in principle be used since the Q -value of these two reactions are very similar. Therefore, a measurement with an intense α beam impinging on a windowless gas target filled with ${}^2\text{H}$ with a high efficiency and very well shielded HPGe detector in close view of the target was planned. However, for this reaction, a side effect exists and has to be dealt with. This consists in the Rutherford scattering of the alpha beam on the deuterium target atoms which can then undergo both ${}^2\text{H}({}^2\text{H}, n){}^3\text{He}$ and ${}^2\text{H}({}^2\text{H}, p){}^3\text{H}$ reactions. While the latter do not disturb the measurement, the former produce neutrons ($E_n(\text{max}) = 3.4 \text{ MeV}$) which can in principle constitute a problem for the underground laboratory. Moreover, the ${}^2\text{H}({}^2\text{H}, n){}^3\text{He}$ reaction can induce $(n, n' \gamma)$ reactions, generating a considerable beam-induced background in the γ -ray spectrum and, in particular, in the energy region around 1.6 MeV where the capture transition to the ground state of ${}^6\text{Li}$ is expected. The concurring ${}^2\text{H}({}^2\text{H}, p){}^3\text{H}$ process can be used to evaluate the neutron production of the ${}^2\text{H}({}^2\text{H}, n){}^3\text{He}$ reaction: the cross-sections of both reactions are well known and from the measured proton rate one can derive the neutron rate. In March 2009 a test was performed in order to evaluate those numbers which previously were analytically calculated. A silicon detector was installed inside the target chamber to reveal the 3 MeV protons of the ${}^2\text{H}({}^2\text{H}, p){}^3\text{H}$ reaction. The efficiency of the set-up was evaluated with a Monte Carlo simulation. The neutrons inferred from the protons were in agreement with calculations and scale as the square of the gas pressure as expected. Moreover, an HPGe detector was used to detect the 693 keV line due to the $(n, n' \gamma)$ reactions on the Ge atoms of the detector itself. This provided an alternative and independent method to monitor the neutron flux, in agreement with the other one. Meanwhile, an optimized set-up was developed in order to reduce the target volume and increase the detection efficiency. This allows to decrease the side effect constituted by the ${}^2\text{H}({}^2\text{H}, n){}^3\text{He}$ reaction decreasing the free path of the scattered ${}^2\text{H}$ nuclei while keeping the expected signal the same. The apparatus was tested with a ${}^4\text{He}$ beam and a ${}^2\text{H}$ gas target and turned out to be well suited to measure the cross-section of the ${}^2\text{H}(\alpha, \gamma){}^6\text{Li}$ reaction in the energy region of interest. The background in the HPGe detector was evaluated thus allowing a calculation of the statistical evidence (ratio of the signal S and its uncertainty σ) of the measurement. This was done assuming (arbitrarily) the signal predicted on the basis of Mukhamedzhanov *et al.* [44] results. A target pressure of 1 mbar and a beam current of $200 \mu\text{A}$ would allow to reach a discovery potential at the level of an astrophysical S -factor of $6 \times 10^{-7} \text{ keV} \cdot b$ in about 6 months of measurement (50% duty cycle), thus allowing to establish if the observed ${}^6\text{Li}$ abundance is due to primordial nucleosynthesis or it is necessary to invoke new mechanisms, such as non-standard processes (decays/annihilations of supersymmetrical particles) during the big bang and/or post-primordial production in cosmic-ray spallation. The data taking started in October 2010.

The ${}^{17}\text{O}(p, \gamma){}^{18}\text{F}$ and ${}^{17}\text{O}(p, \alpha){}^{14}\text{N}$ reactions belong to the CNO cycles. Their reaction rates govern the ${}^{17}\text{O}$ and ${}^{18}\text{F}$ nucleosynthesis in different stellar sites like red giants, AGB stars, massive stars and classical novae. Each environment is characterized by

a different temperature range corresponding to a different energy window. As a whole, the reaction rate should be known from 18 to 390 keV proton beam energy in the laboratory system. A pioneering work [45] in the energy range 0.3–1.9 MeV measured the direct capture (DC) contribution. However the ^{18}F level scheme is quite complex and two low energy resonances at 70 and 193 keV are expected to strongly influence the reaction rate. The 193 keV resonance was extensively studied in recent years by two experimental groups [46, 47] and [48]: the obtained resonance strengths are in disagreement by more than one standard deviation. Additionally, a re-analysis of the DC component obtained by [45] was performed [47] taking into account the contribution of the broad resonances at 590 and 716 keV. This resulted in completely different energy dependence with respect to [45]. The 70 keV resonance was measured only through the alpha channel, $^{17}\text{O}(\text{p}, \alpha)^{14}\text{N}$ [49]. At LUNA the DC contribution of the $^{17}\text{O}(\text{p}, \gamma)^{18}\text{F}$ can be measured from 90 to 400 keV. Moreover, the 70 keV resonance can be studied both in the α and in the γ channel. The measurement will be divided into three phases. In the first, a low-efficiency but high-resolution HPGe detector will be used and a detailed study of the γ cascades will be possible. This phase will be complemented with a concurrent measurement of the α channel in four Si detectors. In the second phase a high-efficiency but low-resolution 4π BGO summing crystal will be used and the lowest energy region will become accessible. Finally in the third phase a complementary study of the 590 and 716 keV resonances will be performed in a laboratory at the Earth's surface. In all cases, solid enriched targets are foreseen. These will be produced in the LNGS chemistry laboratory by anodic oxidization of tantalum backings in an electrolyte composed of isotopically enriched water. Preliminary tests have been performed using water enriched in ^{18}O , which is much less expensive than ^{17}O . Targets with different isotopic abundances and thicknesses were produced. The stability of the targets under beam bombardment was studied by measuring the profile of the 151 keV resonance in the $^{18}\text{O}(\text{p}, \gamma)^{19}\text{F}$ reaction. This gave encouraging results demonstrating that the target production mechanism is under control. The measurement is foreseen to start at the beginning of 2011.

The actual LUNA Collaboration program also foresees the measurement of (p, γ) reactions on ^{18}O , ^{22}Ne and ^{23}Na . This will presumably be completed in the next 3–4 years.

5. – The future: LUNA MV project

In 2007, the LUNA Collaboration submitted a Letter of Intent (LoI) to the LNGS Scientific Committee which contained an experimental program mainly devoted to helium-burning reactions. In particular the $^{12}\text{C}(\alpha, \gamma)^{16}\text{O}$ reaction, “Holy Grail” of nuclear astrophysics, the (α, n) reactions on ^{13}C and ^{22}Ne which provide the neutron source for the s-process (a process responsible for the synthesis of about half of all heavy elements beyond Fe) and other (α, γ) reactions on ^{14}N , ^{15}N and ^{18}O relevant for the He-burning stage of stellar evolution are foreseen. These reactions are relevant at higher temperatures (larger energies) than reactions belonging to the hydrogen-burning studied so far at LUNA thus requiring a higher voltage machine, like a closed, single-ended positive-ion

accelerator with a maximum terminal voltage of 3.5 MV. After the submission of the LoI, an intense interaction between the LUNA Collaboration on one side and the LNGS Scientific Committee and the LNGS management on the other side started. Two more documents (LoI addendum and LoI update) were submitted by the LUNA Collaboration to the LNGS Scientific Committee. A dedicated committee of scientists covering different expertises in the field of nuclear astrophysics, neutron shielding, accelerators, safety and radioprotection was formed. This produced a very positive report on the LUNA MV project, strongly recommending its realization at LNGS. The so-called “interferometric node” at LNGS was identified as the best possible place to install the accelerator underground due to its size and distance from the other LNGS experiments. For this solution a few more technical problems have still to be addressed among which the presence of another experiment *in situ* and the water uptake inlet for the Teramo aqueduct. A detailed technical feasibility study of the LUNA MV project will be performed starting from 2011.

REFERENCES

- [1] ROLFS C. and RODNEY W., *Cauldrons in the Cosmos* (University of Chicago Press, Chicago) 1988.
- [2] GREIFE U. *et al.*, *Nucl. Instrum. Methods A*, **350** (1994) 327.
- [3] FORMICOLA A. *et al.*, *Nucl. Instrum. Methods A*, **507** (2003) 609.
- [4] FOWLER B. A., *Nature*, **238** (1972) 24.
- [5] BONETTI R. *et al.*, *Phys. Rev. Lett.*, **82** (1999) 5205.
- [6] AHMAD Q. R. *et al.*, *Phys. Rev. Lett.*, **89** (2002) 11301.
- [7] CASELLA C. *et al.*, *Nucl. Phys. A*, **706** (2002) 203.
- [8] FORMICOLA A. *et al.*, *Phys. Lett. B*, **591** (2004) 61.
- [9] IMBRIANI G. *et al.*, *Eur. Phys. J. A*, **25** (2005) 455.
- [10] LEMUT A. *et al.*, *Phys. Lett. B*, **634** (2006) 483.
- [11] ANGULO C. *et al.*, *Nucl. Phys. A*, **656** (1999) 3.
- [12] IMBRIANI G. *et al.*, *Astron. Astrophys.*, **420** (2004) 625.
- [13] AHARMIN B. *et al.*, *Phys. Rev. C*, **75** (2007) 045502.
- [14] HOSAKA J. G. *et al.*, *Phys. Rev. D*, **73** (2006) 112010.
- [15] ARPESELLA C. *et al.*, *Phys. Lett. B*, **658** (2008) 101.
- [16] ADELBERGER E. *et al.*, *Rev. Mod. Phys.*, **70** (1998) 055502.
- [17] CACIOLLI A. *et al.*, *Eur. Phys. J. A*, **39** (2009) 179.
- [18] MARTA M. *et al.*, *Nucl. Instrum. Methods*, **569** (2006) 729.
- [19] ARPESELLA C. *et al.*, *Appl. Radiat. Isot.*, **47** (1996) 991.
- [20] BEMMERER D. *et al.*, *Phys. Rev. Lett.*, **97** (2006) 122502.
- [21] CONFORTOLA F. *et al.*, *Phys. Rev. C*, **75** (2007) 065803.
- [22] COSTANTINI H. *et al.*, *Nucl. Phys. A*, **814** (2008) 144.
- [23] SINGH B. N. *et al.*, *Phys. Rev. Lett.*, **93** (2004) 262503.
- [24] BROWN T. A. D. *et al.*, *Phys. Rev. C*, **76** (2007) 055801.
- [25] DESCOUVEMONT P. *et al.*, *At. Data Nucl. Data Tables A*, **88** (2004) 203.
- [26] KAJINO T. *et al.*, *Astrophys. J.*, **319** (1987) 531.
- [27] KNODLSEDER J. *et al.*, *Astron. Astrophys.*, **345** (1999) 813.
- [28] WINKLER C. *et al.*, *Astron. Astrophys.*, **4115** (2003) L1.

- [29] WASSERBURG G. J., *Protostars and Planets II*, edited by BLACK D. C. and MATTHEWS M. S. (University of Arizona Press, Tucson) 1985, p. 703.
- [30] ARAZI A. *et al.*, *Phys. Rev. C*, **74** (2006) 025802.
- [31] TERRASI F. *et al.*, *Nucl. Instrum. Methods B*, **259** (2007) 14.
- [32] LIMATA B. *et al.*, *Phys. Rev. C*, **82** (2010) 015801.
- [33] POWELL D. C. *et al.*, *Nucl. Phys. A*, **660** (1999) 349.
- [34] HEBBARD D. F. *et al.*, *Nucl. Phys.*, **15** (1960) 289.
- [35] ROLFS C. and RODNEY W., *Nucl. Phys. A*, **235** (1974) 450.
- [36] MUKHAMEDZANOV A. *et al.*, *Phys. Rev. C*, **78** (2008) 015804.
- [37] BEMMERER D. *et al.*, *J. Phys. G*, **36** (2009) 045202.
- [38] LE BLANC P. J. *et al.*, *Phys. Rev. C*, **82** (2010) 055804.
- [39] SMITH V. *et al.*, *Astrophys. J.*, **408** (1993) 262.
- [40] SMITH V. *et al.*, *Astrophys. J.*, **644** (2006) 229.
- [41] COC A. *et al.*, *Astrophys. J.*, **600** (2004) 544.
- [42] ROBERTSON R. G. H. *et al.*, *Phys. Rev. Lett.*, **47** (1981) 1967.
- [43] MOHR P. *et al.*, *Phys. Rev. C*, **47** (1994) 1543.
- [44] MUKHAMEDZANOV A. *et al.*, *Phys. Rev. C*, **52** (1995) 3483.
- [45] ROLFS C. *et al.*, *Nucl. Phys. A*, **217** (1973) 29.
- [46] FOX C. *et al.*, *Phys. Rev. Lett.*, **93** (2004) 081102.
- [47] FOX C. *et al.*, *Phys. Rev. C*, **71** (2005) 055801.
- [48] CHAFA A. *et al.*, *Phys. Rev. C*, **75** (2007) 035810.
- [49] BLACKMON J. C. *et al.*, *Phys. Rev. Lett.*, **741** (1995) 2642.

Proceedings of the International School of Physics “Enrico Fermi”
Course CLXXVIII “From the Big Bang to the Nucleosynthesis”, edited by A. Bracco and E. Nappi
(IOS, Amsterdam; SIF, Bologna)
DOI 10.3254/978-1-60750-974-5-333

Nuclear astrophysics results with the Trojan Horse Method

C. SPITALERI

Dipartimento di Fisica ed Astronomia, Università di Catania - Catania, Italy
INFN-LNS - Catania, Italy

Summary. — Because of the Coulomb barrier, reaction cross-sections in astrophysics cannot be accessed directly at the relevant Gamow energies, unless very favorable conditions are met. Theoretical extrapolations of available data are then needed to derive the astrophysical $S(0)$ -factor. Various indirect techniques have been used in order to obtain additional information on the parameters entering these extrapolations. The Trojan Horse Method is an indirect method which might help to bypass some of the problems typically encountered in direct measurements, namely the presence of the Coulomb barrier and electron screening between the interacting nuclei.

1. – Introduction

In the last decades, impressive improvements in astrophysical observations and in computational models of stellar structure and evolution have made it possible for the first time to significantly improve our understanding of energy generation and nucleosynthesis processes that take place in a variety of astrophysical sites, from quiescent stars like our Sun to explosive phenomena like novae, X-ray bursts, and supernovae.

Nuclear reactions in such environments remain a key ingredient for detailed description of stellar evolution and for the explanation of the abundance of the elements in the Universe. Ideally, laboratory measurements of key astrophysical reactions should be carried out at the energy of astrophysical interest, referred to as the Gamow energy region (E_G), which depends on the temperature of the stellar plasma at which a given reaction takes place as well as on the charge of the interacting nuclei. Therefore the knowledge, with good accuracy, of nuclear reaction cross-sections and rates at interaction energies E_G are required. In order to obtain the accurate measurement of thermonuclear fusion reaction rates great experimental efforts have been devoted to extend the knowledge of nuclear reaction cross-sections $\sigma(E)$ down to E_G [1-4].

For charged-particle-induced reactions the cross-section $\sigma(E)$ drops exponentially with decreasing the center-of-mass energy due to the hindrance of the Coulomb barrier ($E_{C.b.}$). As a consequence, exponential measurements become increasingly more challenging and extrapolation from data at higher energies are needed. In general, this extrapolation is performed on the so-called astrophysical $S(E)$ -factor, that is, a smoother function of energy, defined by the relationship

$$(1) \quad \sigma_b(E) = \frac{1}{E} S_b(E) \exp[-2\pi\eta],$$

where η , defined as $\eta = Z_1 Z_2 / (hv)$, is the Sommerfeld parameter which depend on the charge numbers Z_1 , Z_2 of the colliding nuclei and their relative velocity v in the entrance channel; E is the center-of-mass energy of the interacting particles, $\exp[2\pi\eta]$ is the inverse of the Gamow factor, which removes the dominant energy dependence of the bare nucleus cross-section $\sigma_b(E)$ due to the barrier penetrability. This definition assume that the $E_{C.b.}$ is that associated to the cross-section $\sigma_b(E)$ for bare nucleus.

Direct experimental studies of astrophysical fusion reactions are thus complicated by a number of factors. First, the characteristic small cross-sections translate into poor signal-to-noise ratios in the experimental detection system. Ideally, underground measurements with high beam currents and large solid-angle, high-efficiency detectors are needed to optimize the signal-to-noise ratio by: a) greatly reducing the background and b) maximizing the reaction yield. So far, only a few reactions have been studied underground at relevant Gamow energy region. In all other cases, extrapolations of reaction cross-sections are carried out from data taken at higher energies with the help of some theoretical formalism (e.g., R -matrix) where applicable. Yet, such extrapolations may be unreliable if contributions from resonances near the Gamow peak and/or from the tails of sub-threshold states are unknown.

Secondly, the measured cross-section must be corrected for the effect of the electron screening [5] arising from the presence of electrons in the target atoms and, possibly, in the (partly) ionized projectiles. The presence of these electrons contributes to an enhancement of the measured cross-section compared to that between bare nuclei. A similar screening effect is also present in stellar plasmas, where fully ionized atoms are surrounded by a “sea” of electrons at the so-called Debye-Hueckel radius, which in turn

depends on conditions of plasma temperature and density and may vary during stellar evolution. Since the electron screening measured in the laboratory differs from the one in the plasma, it is important that the measured cross-sections for nuclear reactions of astrophysical interest be the bare ones, so that plasma screening corrections can be subsequently applied [6]. Because of these intrinsic limitations in the *direct* experimental study of nuclear reactions for astrophysics, alternative methods for determining bare-nuclei cross-sections are needed. In this context several indirect methods such as Coulomb Dissociation [7], Asintotic Normalization Coefficients [8, 9], the Trojan Horse Method (THM) have been developed in the last twenty years [10-17].

2. – Basic theory

The THM is a powerful technique which selects the quasi-free (QF) contribution of an appropriate three-body reaction $a + B \rightarrow C + D + S$ reaction, performed at energies well above the Coulomb barrier to extract a charged particle two-body cross-section $B + x \rightarrow C + D$ in quasi-free (QF) kinematics [10, 11] at astrophysical energies free from Coulomb suppression [18].

Particularly the THM has been successfully applied to the bare nucleus cross-sections measurements of reactions between charged particles (see refs. [19-40] in table I) at sub-Coulomb energies. A recent application of the THM is addressed to the possibility to study neutron-induced reactions on radioactive nuclei. This was already tested with stable beams [40, 41].

In this paper, the THM will be presented within the Plane Wave Impulse Approximation approach (PWIA) framework and it will applied to non-resonant reactions with dominant $l = 0$ partial wave contribution. The motivations for such a simplified approach in the application of the THM will be discussed. In particular some of the basic critical points of the simplified approximation and the phenomenological approach are presented. More sophisticated theoretical formulations can be found in refs. [10, 11, 14-16]. The key ideas on which the method is based are presented in the following sections. Briefly, the THM is based on a quasi-free break-up reaction mechanism (fig. 1), whereby the reaction of astrophysical interest $x + B \rightarrow C + D$ can be studied through the $A + B \rightarrow C + D$ process. The quasi-free $B(A, CD)S$ reaction between the nucleus A and the nucleus B , can be described by a Feynman diagram (fig. 1), where only the first term of the Feynman series is retained [42]. In the Impulse Approximation (IA) the three-body reaction $A + B \rightarrow C + D + S$ is considered to be well represented by this simple Feynman diagram (fig. 1), while other graphs (triangle graphs) indicating re-scattering between the reaction products, are neglected. Under these hypotheses, the incident particle B is considered to interact only with a part (x -cluster) of the target nucleus B , while the other part (S -cluster) is considered as a spectator to the $B(x, C)D$ virtual reaction.

In the IA approach the three-body reaction cross-section is proportional to the cross-section of the binary reaction [43]. Following the simpler Plane Wave Impulse Approximation (PWIA) (it is enough to describe, in a simple way, this process), the three-body reaction can be factorized into two terms corresponding to the vertices of fig. 1 and is

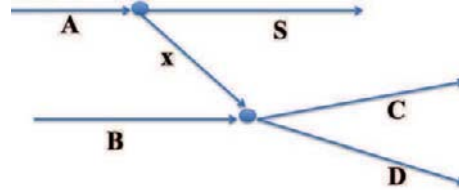


Fig. 1. – Feynman diagram representing the quasi-free $A(B, CD)S$ reaction.

given by [44]

$$(2) \quad \frac{d^3\sigma}{d\Omega_C d\Omega_D dE_C} = (KF) \cdot |\phi(p_{xS})|^2 \cdot \left[\frac{d\sigma}{d\Omega} \right]^{\text{HOES}},$$

TABLE I. – *Two-body reactions studied via the Trojan Horse Method Direct.*

Indirect reaction	Direct reaction	E_{A-B} (MeV)	Q_2 (MeV)	THM-Nucl (x -cluster)	References
1) ${}^2\text{H}({}^7\text{Li}, \alpha\alpha)\text{n}$	${}^1\text{H}({}^7\text{Li}, \alpha){}^4\text{He}$	19–22	15.12	${}^2\text{H}$ (p)	[13, 21, 22]
2) ${}^3\text{He}({}^7\text{Li}, \alpha\alpha)\text{d}$	${}^1\text{H}({}^7\text{Li}, \alpha){}^4\text{He}$	33	11.85	${}^3\text{He}$ (p)	[23]
3) ${}^2\text{H}({}^6\text{Li}, \alpha{}^3\text{He})\text{n}$	${}^1\text{H}({}^6\text{Li}, \alpha){}^3\text{He}$	22–34	1.79	${}^2\text{H}$ (p)	[24, 25]
4) ${}^6\text{Li}({}^6\text{Li}, \alpha\alpha){}^4\text{He}$	${}^2\text{H}({}^6\text{Li}, \alpha){}^4\text{He}$	5	22.37	${}^6\text{Li}$ (d)	[12, 26, 27]
5) ${}^2\text{H}({}^9\text{Be}, \alpha{}^6\text{Li})\text{n}$	${}^1\text{H}({}^9\text{Be}, \alpha){}^6\text{Li}$	22	−0.10	${}^2\text{H}$ (p)	[28]
6) ${}^2\text{H}({}^{10}\text{B}, \alpha{}^7\text{Be})\text{n}$	${}^1\text{H}({}^{10}\text{B}, \alpha){}^7\text{Be}$	27	6.30	${}^2\text{H}$ (p)	[29]
7) ${}^2\text{H}({}^{11}\text{B}, \alpha_0{}^8\text{Be})\text{n}$	${}^1\text{H}({}^{11}\text{B}, \alpha){}^8\text{Be}$	27	6.30	${}^2\text{H}$ (p)	[30, 31]
8) ${}^2\text{H}({}^{15}\text{N}, \alpha{}^{12}\text{C})\text{n}$	${}^1\text{H}({}^{15}\text{N}, \alpha){}^{12}\text{C}$	60	2.740	${}^2\text{H}$ (p)	[32, 33]
9) ${}^2\text{H}({}^{18}\text{O}, \alpha{}^{15}\text{N})\text{n}$	${}^1\text{H}({}^{18}\text{O}, \alpha){}^{15}\text{N}$	54	1.76	${}^2\text{H}$ (p)	[34, 35]
10) ${}^2\text{H}({}^{17}\text{O}, \alpha{}^{14}\text{N})\text{n}$	${}^1\text{H}({}^{17}\text{O}, \alpha){}^{14}\text{N}$	41	−1.03	${}^2\text{H}$ (p)	[36]
11) ${}^6\text{Li}({}^3\text{He}, \text{p}{}^4\text{He}){}^4\text{He}$	${}^2\text{H}({}^3\text{He}, \text{p}){}^4\text{He}$	5–6	16.88	${}^6\text{Li}$ (d)	[37]
12) ${}^2\text{H}({}^6\text{Li}, \text{p}{}^3\text{H}){}^4\text{He}$	${}^2\text{H}(\text{d}, \text{p}){}^3\text{H}$	14	2.59	${}^6\text{Li}$ (d)	[38]
13) ${}^6\text{Li}({}^{12}\text{C}, \alpha{}^{12}\text{C}){}^2\text{H}$	${}^4\text{He}({}^{12}\text{C}, {}^{12}\text{C}){}^4\text{He}$	20, 16	0	${}^6\text{Li}$ (α)	[39]
14) ${}^2\text{H}({}^6\text{Li}, \text{t}{}^4\text{He}){}^1\text{H}$	$\text{n}({}^6\text{Li}, \text{t}){}^4\text{He}$	14	2.22	${}^2\text{H}$ (n)	[40, 41]
15) ${}^2\text{H}(\text{p}, \text{pp})\text{n}$	${}^1\text{H}(\text{p}, \text{p}){}^1\text{H}$	5–6	2.22	${}^2\text{H}$ (p)	[18]

where $[\frac{d\sigma}{d\Omega}]^{\text{HOES}}$ is the half-off-energy-shell differential cross-section for the binary $B(x, C)D$ reaction at the center-of-mass energy E given in post-collision prescription (PCP) by the relation [45]

$$(3) \quad E = E_{CD} - Q_{2b},$$

where Q_{2b} is the binary $x + B \rightarrow C + D$ reaction's Q -value and E_{CD} is the relative energy in the exit channel, KF is a kinematical factor containing the final-state phase space factor and is a function of the masses, momenta, and angles of the outgoing particles [49]. Since in the applications to the THM the two clusters x - S in the nucleus A are most likely in s -state, the expected momentum distribution has a maximum at $p_{xS} = 0$.

Early experiments to investigate the QF reaction mechanism at energies close to the Coulomb barrier have been performed within an INFN Catania-IRB Zagreb Collaboration since 1976 [20,24]. In particular, excitation functions of two-body reactions extracted by means of the QF three-body cross-sections were obtained and found to be in overall good agreement with existing direct data [20, 24]. The further extension of this type of studies to ultra-low energies of astrophysical interest was later stimulated by the idea proposed by Baur in 1986 [10] that a given two-body reaction of interest may be studied by an appropriate three-body one, provided a suitable nucleus is used as the Trojan Horse. Since then, the Catania group has pioneered and further improved the application of the THM to the study of astrophysical reactions. The many successfully investigated cases are presented in table I. Examples of some of these reactions are presented in the following sections.

Despite being based on a relatively simple idea, the method involves a non-trivial theoretical description [10,11,14-16] and requires the careful selection of the experimental conditions to guarantee that the appropriate reaction mechanism is selected (see for instance [30]). In particular, the QF mechanism must be identified and distinguished from other reaction processes feeding the same exit channel such as, for example, sequential decay and/or direct break-up. Kinematical conditions, satisfying the requirement that cluster S remain a spectator to the $x + B \rightarrow C + D$ reaction, imply that its momentum distribution within the Trojan horse nucleus A remains unchanged after the interaction has taken place. This can be accomplished by detecting the reaction products C and D in coincidence at *quasi-free angles*, *i.e.* angles at which the QF contribution is maximized. For example, in a nucleus where spectator S has a momentum distribution peaked around zero, the DFA will be those at which S is left with zero momentum and thus energy.

2.1. Energy prescriptions. – Beam energies have been carefully chosen to optimize the kinematical conditions for the presence of quasi-free mechanism under the assumptions of the IA. The beam energy is chosen in such a way to overcome the Coulomb barrier $(E_C)^{AB}$ in the entry channel $A + B$. Thus, particle x is brought inside the nuclear interaction zone to induce the relevant reaction $x + B \rightarrow C + D$. The QF kinematical conditions must be chosen in such a way that the relative energy E_{x-B} can span the astrophysical region of interest below the Coulomb barrier $(E_C)^{x-B}$ [10]. This is possible

because the initial projectile velocity is compensated for by the binding energy of particle x inside A ([13,30] and references therein). Thus, the x - B relative energy of the fragments can be very low. In symbols, we have

$$(4) \quad E = E_{x-B} - B_{xS} = E_{QF}$$

with E_{x-B} the projectile energy in the two-body center-of-mass system and B_{xS} the x - S binding energy.

2.2. PWIA: applicability conditions. – It is very important to have the same criterion with the aid of which we may establish experimentally the correctness of the pole approximation in each specific case. The applicability of the pole approximation is limited to the small momentum p_S . Namely, the region where the pole diagram is expected to be predominant in the reaction mechanism [42] is given by

$$(5) \quad 0 \leq p_S \leq k_{xS},$$

with p_S the momentum of the cluster x when it interacts with the particle B in the half-off energy shell (HOES), and k_{xS} the momentum in the on-energy shell (OES) defined by the relation $k_{xS} = \sqrt{2\mu_{xS}B_{xS}}$ where μ_S is the reduced mass and B_{xS} is the binding energy of the system xS , respectively, and Q_{xS} is the Q -value for the virtual decay.

2.3. Experimental momentum distribution

2.3.1. PWIA. An alternative application of QF reactions is the measurements of the x - S momentum distribution. If the cross-section is known, the momentum distribution $|\phi(p_S)|^2$ can be obtained from the QF yield with the energy sharing method or by measuring an angular correlation (see for instance [30] and references therein).

The momentum distribution $|\phi(p_S)|^2$ is obtained, in the energy sharing approach, by selecting a narrow relative energy windows ΔE and a center-of-mass angular range $\Delta\theta_{cm}$.

This is done by considering the relative energy spectrum E_{CD} vs. p_S . The two-dimensional spectrum is shown in fig. 2 for the case of the ${}^2H({}^{11}B, {}^8Be)\alpha_0$ n reaction [30]. If the factorization of eq. (3) is applicable, dividing the quasi-free coincidence yield (Y) by the kinematic factor, a quantity which is proportional to the product of the momentum distribution by the $x + B \rightarrow C + D$ a two-body cross section is obtained. In a restricted relative energy ΔE and center-of-mass angular range, the differential binary cross-section can be considered almost constant and

$$(6) \quad |\phi(p_S)_{exp}|^2 \propto \frac{Y}{KF}.$$

In fig. 3 the experimental momentum distribution for the proton inside deuteron for the ${}^2H({}^{11}B, \alpha_0 {}^8Be)n$ reaction at $E_{{}^{11}B} = 27$ MeV is reported. The squared Hulthen function (dashed line) in momentum space, superimposed onto the data, reproduces quite well

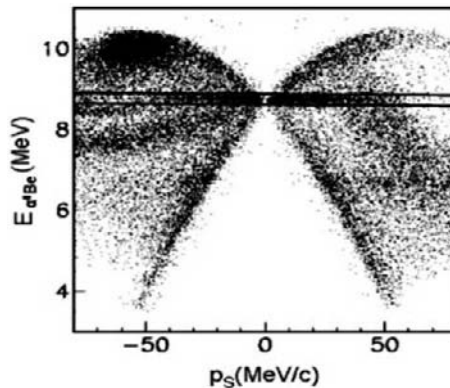


Fig. 2. – $E_{\alpha^0 Be}$ relative energy as a function of the spectator momentum p_s extracted from the ${}^2H({}^{11}B, \alpha_0 {}^8Be)n$ reaction [30].

the shape of experimental data. The theoretical FWHM is in good agreement with the experimental one [30].

The momentum distribution calculated in the PWIA and DWIA might differ both in their absolute value and their shape [46]. For instance, at high incident energies (more than about 100 MeV for $(p, p \alpha)$, $(p, p d)$ and $(\alpha, 2\alpha)$ reactions) the two calculations have essentially the same shape at least for values of the spectator cluster momenta smaller than about 60 MeV/c. At lower energies, absorption and distortion effects become more important, so that the validity of the PWIA is less and less justified (see for instance [48] and references therein). In general the following considerations apply:

- i) At low relative momenta, the shapes of the DWIA and PWIA distributions coincide. However, while PWIA introduces unphysical zeros in the momentum distribution, the DWIA represents a more realistic approach [46, 47].

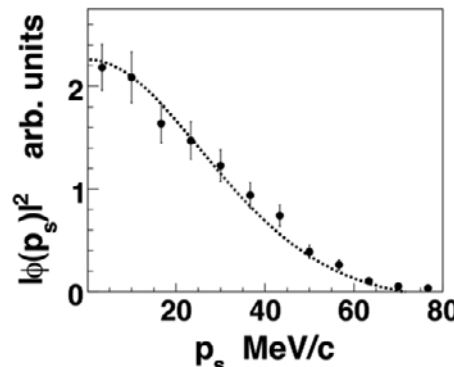


Fig. 3. – Deuteron experimental momentum distribution (full dots) extracted from the ${}^2H({}^{11}B, \alpha_0 {}^8Be)n$ reaction compared with the theoretical one (dotted line) [30].

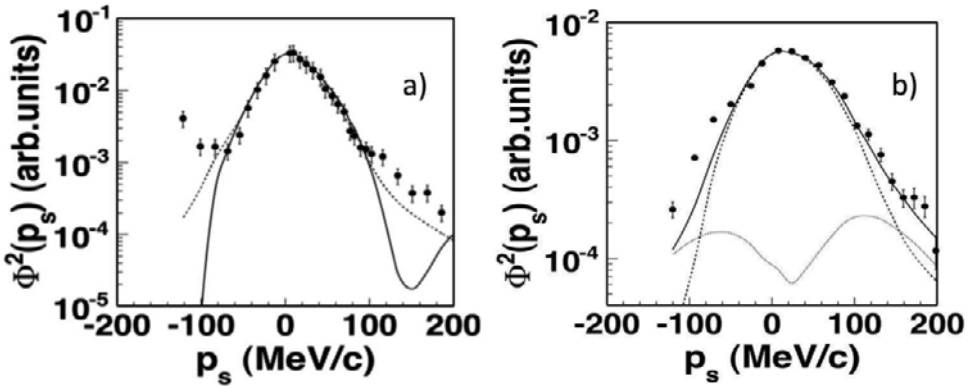


Fig. 4. – Momentum distribution of cluster α inside the ${}^6\text{Li}(p, p\alpha){}^2\text{H}$ reaction (a), and of cluster α inside the ${}^9\text{Be}(p, p\alpha){}^5\text{He}$ reaction (b). Normalizations are done equalizing the maximum value of the theoretical distributions to the maximum values of the experimental data. The full (dashed) curve is the DWIA (PWIA) distribution [47].

- ii) In DWIA treatment the absolute value of the momentum distribution undergoes a dramatic decrease due to wave absorption effects, which are not taken into account in PWIA.

An important point to be stressed is that in the THM only events with a spectator momentum close to the QF condition, cut-off of few tens of MeV/ c (see for details table II) are taken into account. In the case:

- i) the essential features of the $|\phi(\mathbf{p}_s)|^2$ are the same in both procedures within the experimental uncertainties;
- ii) the differences in the absolute values can be recovered by normalization to the experimental data.

In the case of non-resonant reactions at low incident energies but with high Q -value, the standard procedure is totally reliable. Conversely, in reactions with both low incident energies and Q -values distortions might intervene introducing more marked differences between the PWIA and DWIA momentum distributions. They are responsible for a drastic change of the width (FWHM) in the spectator momentum distribution [50-52]. The line in fig. 4 shows the trend of the experimental momentum distribution widths for the data available in the literature as a function of the transferred momentum q_t [52]. In table II, a number of experimental cases is shown. In particular, in the case of the ${}^{11}\text{B} + \text{d}$ reaction at incident energy of 27 MeV and transferred momentum of 370 MeV/ c , the value of the experimental [FWHM] is 58 MeV/ c . Thus, it matches its asymptotic value of 58 MeV/ c (fig. 5). In some experimental works it was necessary to reduce the theoretical FWHM in order to reproduce the experimental distribution.

TABLE II. – *Three-body QF reactions studied: k_S -limit of pole approximation applicability and the selected Δp_S ranges in the QF experiments.*

Indirect Reaction	E_{A-B} (MeV)	μ_{xS}	k_S (MeV/c)	Δp_S MeV/c	Ref.
1) $^2\text{H}(^7\text{Li}, \alpha\alpha)\text{n}$	20	0.5	45	0–40	[13, 20, 22]
2) $^3\text{He}(^7\text{Li}, \alpha\alpha)\text{d}$	33	0.67	83	0–30	[23]
3) $^2\text{H}(^6\text{Li}, \alpha^3\text{He})\text{n}$	14. 25	0.5	45	0–30	[24, 25]
4) $^6\text{Li}(^6\text{Li}, \alpha\alpha)^4\text{He}$	5	1.5	61	0–35	[26]
5) $^2\text{H}(^9\text{Be}, \alpha^6\text{Li})\text{n}$	22	0.5	45	0–20	[28]
6) $^2\text{H}(^{11}\text{B}, \alpha_0^8\text{Be})\text{n}$	27	1.5	45	0–40	[30, 31]
7) $^2\text{H}(^{15}\text{N}, \alpha^{12}\text{C})\text{n}$	60	0.5	45	0–40	[32, 33]
8) $^2\text{H}(^{18}\text{O}, \alpha^{15}\text{N})\text{n}$	54	0.5	45	0–40	[34, 35]
9) $^2\text{H}(^{17}\text{O}, \alpha^{14}\text{N})\text{n}$	41	0.5	83	0–30	[36]
10) $^6\text{Li}(^3\text{He}, \text{p}^4\text{He})^4\text{He}$	5–6	0.67	61	0–20	[37]
11) $^2\text{H}(^6\text{Li}, \text{p}^3\text{H})^4\text{He}$	14	2.59	61	0–10	[38]
12) $^6\text{Li}(^{12}\text{C}, \alpha^{12}\text{C})^2\text{H}$	20.16	0	61	0–10	[39]
13) $^2\text{H}(^6\text{Li}, \text{t}^4\text{He})^1\text{H}$	14	1.5	45	0–20	[40]
14) $^2\text{H}(\text{p}, \text{pp})\text{n}$	5–6	1.5	45	0–20	[18]

2.3.2. DWBA. As already mentioned, in the analysis of THM applications the PWIA is usually adopted since it fairly describes the experimental data. Anyway, to check the validity of the PWIA approach and to reproduce those data where distortions cannot be neglected, the more realistic Distorted Wave Born Approximation (DWBA) should be employed. The experimental data (fig. 6) [34, 36] show that, even in the DWBA if we limit our event selection to the region close to the maximum of the momentum distribution, DWBA and PWIA approaches give the same results. We will consider data of the $^{18}\text{O}(\text{p}, \alpha)^{15}\text{N}$ reaction studied using a deuteron as TH nucleus [34] (see fig. 6(a)). The p-n momentum distribution $^{18}\text{O}(\text{p}, \alpha)^{15}\text{Ns}$ shown in fig. 6(a) as a dashed line. The solid line reproduces the experimental behaviour for $p_S \leq 50 \text{ MeV}/c$ while for larger momenta it departs from the experimental data. The normalization factor is obtained by scaling the calculated distribution to the experimental one [34]. The DWBA calculation is instead given by a short dashed line in the same fig. 6(a). It has been performed by means of the FRESCO computer code, taking the optical model potential parameters from Perey

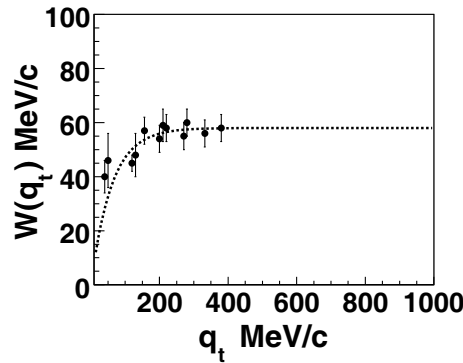


Fig. 5. – Width [FWHM] for the momentum distribution of the proton inside the deuteron as a function of the transferred momentum q_t . The line superimposed to the data represents an empirical fit described in ref. [52] and references therein.

and Perey [53]. In the range from 0 to 50 MeV/c, the difference between PWIA and DWBA momentum distributions is negligibly small, about 4%, in comparison with other uncertainties.

Same considerations stand for the $^{17}\text{O}(\text{p}, \alpha)^{14}\text{N}$ reaction (fig. 6(b)) [36]. These results strengthen the importance and reliability of the PWIA approach.

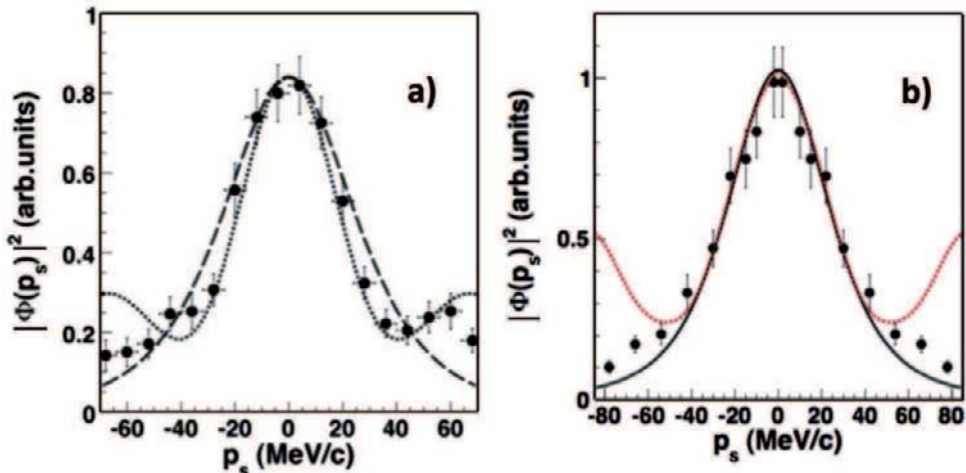


Fig. 6. – Experimental momentum distribution (full dots) compared with theoretical ones, given by the square of the Hulthen wave function in momentum space (long dashed line) and DWBA momentum distribution evaluated by means of the FRESCO code (short dashed line). Normalization was left as a fitting parameter: (a) $^{18}\text{O}(\text{d}, \alpha)^{15}\text{N}$ reaction [34]; (b) $^{17}\text{O}(\text{p}, \alpha)^{14}\text{N}$ reaction [36].

3. – Data analysis

In general the experiments are characterized by relatively simple experimental setup. The main requirement is high energy and angular resolutions. Usually the detection set-up consists of two or more couples of coincidence telescopes arranged at the opposite side of the beam direction at quite forward angles, the experiments being usually performed in inverse kinematics. These kinematics calculations, in general, show the strong dependence of the E_{xB} uncertainty on the angular resolution of both projectiles. That is why in our experiments an angular resolution of the order of 0.1° - 0.5° is required.

A number of steps are involved in the data analysis before the two-body cross-section of astrophysical relevance can be extracted. These steps include:

- 1) selection of the “Trojan horse” nucleus;
- 2) identification of events due to the three-body reaction of interest $A+B \rightarrow C+D+S$;
- 3) selection of the QF reaction mechanism;
- 4) extraction of the HOES two-body cross-section from the measured three-body in arbitrary units;
- 5) correction for the penetration probability of the HOES cross-section below the Coulomb barrier E^{xB} ;
- 6) normalization procedure to obtain the bare nucleus cross-section $\sigma_b(E)$ in absolute units;
- 7) checks on the selection of events through validity tests;
- 8) extraction of the electron screening potential when ultra-low energy measurements are available.

3.1. Selection of the Trojan horse nucleus. – Since the (p, α) reactions play a key role in many stellar nucleosynthesis paths, a number of indirect investigations with the THM has been focused on this kind of processes. These measurements are usually performed in inverse kinematics with a *deuteron-target* as *virtual-proton* target. The choice of a deuteron as TH-nucleus is suggested by a number of reasons: it has a unique simple “cluster” structure (proton plus neutron); its wave function is well known; its binding energy is low; the cluster spectator is not charged; the inter-cluster xS motion takes place at $l = 0$, thus the momentum distribution has a maximum for $p_S = 0 \text{ MeV}/c$. In table III a list of other TH-nuclei is reported with the corresponding virtual x participant. It is clear that different choices of TH-nuclei are available to get the same virtual x . We note from table III that, for example, a virtual participant proton can be hidden either inside a deuteron ${}^2\text{H} = (\text{p} + \text{n})$ with $\text{n} = \text{spectator}$ (binding energy $B_{\text{p}-\text{n}} = 2.25 \text{ MeV}$) or inside ${}^3\text{He} = (\text{p} + \text{d})$ with $\text{d} = \text{spectator}$ ($B_{\text{p}-\text{d}} = 5.49 \text{ MeV}$).

TABLE III. – *Main feature of the candidates Trojan Horse Nuclei.*

	TH nucleus	xS cluster	Momentum l -relative	Binding energy (MeV)
1)	^2H	p-n	0	2.22
2)	^3H	d-n	0	6.26
3)	^2He	d-p	0	5.49
4)	^6Li	d- α	0	1.47
5)	^7Li	t- α	1	2.47
6)	^7Be	^3He - α	1	1.58
7)	^{16}O	α - ^{12}C	0	7.16
8)	^{20}Ne	α - ^{16}O	0	4.73

The choice of best particle A (TH-nucleus) in the $A + B \rightarrow C + D + S$ three-body reaction to study the $x + B \rightarrow C + D$ two-body reaction is mainly linked to

- i) the binding energy of the x - S cluster system in the TH-nucleus;
- ii) the appropriate incident energy of the projectile;
- iii) the Q -value of $A + B \rightarrow C + D + S$ three-body reaction;
- iv) the energy range of the excitation function for the two body relevant reaction to be investigate;
- v) the different contributing reaction mechanisms with the three particles C , D and S in the final state (sequential decay and direct breakup).

Another very important point to emphasize is that all TH-nuclei (^2H , ^6Li , ^3He , ^{16}O) used so far in the performed experiments (table III) are always characterized by an $l = 0$ orbital angular momentum for the inter-cluster xS motion. In this condition the momentum distribution shows a peak at $k_S = 0$. This choice is linked not only to the reduction of experimental difficulties when selecting the QF mechanism but also to theoretical considerations for the applicability of the pole approximation [42]. Indeed, the extension to measurements with TH nuclei having $l = 1$ is desirable since it would allow for the investigation the excitation functions of nuclear reactions induced by virtual tritium and ^3He that can be obtained from the cluster systems $^7\text{Li} = t-\alpha$ and $^7\text{Be} = \alpha-^3\text{He}$, respectively (see table III).

3.2. QF data selection: study of momentum distribution in angular correlation. – A way to discriminate between SD and QF events is through an angular correlation analysis of the data. Coincidence data are projected onto the C (or D) energy axis E_C (or E_D) at a fixed angle for one of the two particles and different angles for the other

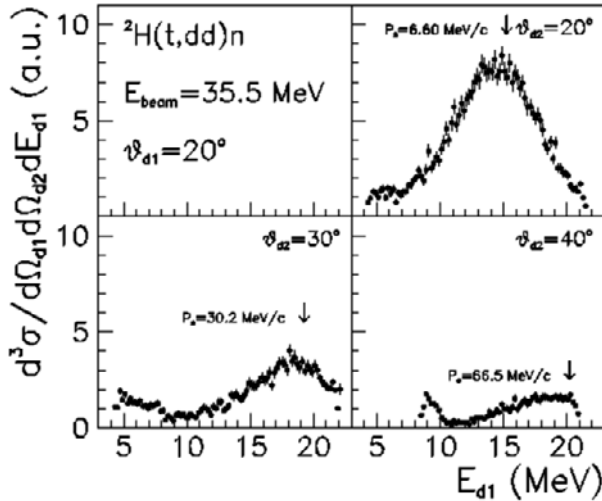


Fig. 7. – Typical angular correlation spectra for the $^2\text{H}(^3\text{H}, \text{d d})\text{n}$ reaction at a beam energy of 35.5 MeV. Coincidence data are projected onto $E_{d1} = 20^\circ$ [55].

particle. Figure 7 shows examples of the angular correlation analysis for the $^2\text{H}(^3\text{H}, \text{d d})\text{n}$ reaction at a beam energy of 35.5 MeV for a deuteron angle $\theta_{d1} = 20^\circ$ and angles for the other deuteron $\theta_{d2} = 20^\circ$ to 40° . Since the momentum distribution of the p-n system in the nucleus ^2H has a maximum for $(p_S)^{\min} = 0$, the feature expected for a quasi-free reaction is a coincidence yield attaining a maximum when $(p_S)^{\min}$ approaches zero MeV/c [54, 55]. The $(\theta_{d1}, \theta_{d2})$ angles corresponding to this condition represent the so-called quasi-free angles. In the spectra of fig. 7, three typical features appear:

- a broad peak around $(p_S)^{\min}$ is observed (marked with an arrow);
- this peak does not correspond to the excited states of the ${}^4\text{He}$ or ${}^3\text{H}$ intermediate systems (see references for more details);
- the magnitude of the cross-section of the broad peak is stronger at $(p_S)^{\min} = 0 \text{ MeV}/c$, and decreases while moving away from zero.

Figure 8 shows the experimental yield componed with the theoretical momentum distribution (see figure caption). This represents a first necessary check for the existence of the quasi-free mechanism. In general, the presence of SD contribution can make this test much more complicate.

3.3. Extraction of the two-body cross-section from the measured three-body reaction. – If the experimental momentum distribution $|\phi(p_S)|^2$ is measured, one can, in principle, extract the half-off-energy-shell cross-section by measuring the three-body reaction and calculating KF. In particular, in the analysis, this product $(KF)|\phi(p_S)|^2$ is provided by

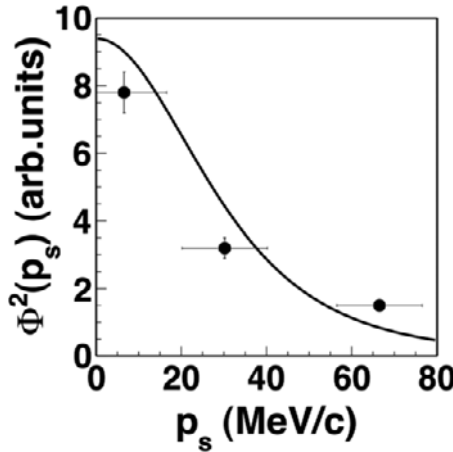


Fig. 8. – ${}^2\text{H}({}^3\text{H}, \text{dd})\text{n}$ reaction. Experimental yield distribution (full dots), integrated on as a function of the undetected particle momentum p_s , projected in the p_s range and compared with the theoretical momentum distribution given in terms of a Hulthen function (full line) [55].

a Monte Carlo calculation:

$$(7) \quad \left[\frac{d\sigma}{d\Omega} \right]^{\text{HOES}} \propto \left[\frac{Yd}{[(KF)|\phi(\mathbf{p}_S)|^2]} \right].$$

We stress that this relation is valid as far as the pole approximation is applicable. To get the absolute value, the cross-section can be normalized to the binary reaction in an energy range ΔE above the Coulomb barrier.

In the THM applications, the reaction $x + B \rightarrow C + D$ is induced inside the short range of the B nuclear field. Thus, the HOES cross-section corresponds to the nuclear contribution to the cross-section. For this reason, the penetration probability of the Coulomb barrier has to be introduced in order to compare the THM cross-section with the direct data from the literature in the energy region below the Coulomb barrier.

4. – Validity tests of pole approximation

Equation (1), for the pole graph represented in fig. 1, has the remarkable characteristic that the reaction amplitude is factorized, *i.e.* it can be written as the product of two amplitudes and a propagator, and depends only on three variables instead of five in the general case [42]. These characteristics makes it possible to express the differential cross-section of the reaction through that of the virtual process in the right-hand vertex (the $x + B \rightarrow C + D$ reaction). In the PWIA as well as in the DWIA the three-body reaction cross-section is proportional to the cross-section of the virtual two-body reaction (eq. (1)). Thus, the factorization test can be used.

Different tests of the pole approximation mechanism have been proposed at low energies. As already mentioned, the analysis of the experimental results for three-body reactions is complicated by the presence of other reaction mechanisms, constituting a background for QF data. Because of the uncertainties that can be introduced by the presence of this background in the applicability of the IA, a series of experiments were carried out to provide some critical tests of pole approximation or of the IA. We present hereafter some tests allowing us to test the validity of the pole approximation.

They apply to the behavior of the $\sigma(\theta_{\text{cm}}, E_{\text{cm}})$: both excitation function $\sigma(E_{\text{cm}})$ and angular distributions $\sigma(\theta_{\text{cm}})$ of the binary reaction $A+x \rightarrow C+D$ must be compared with the corresponding two-body $\sigma(E_{\text{cm}})^{\text{HOES}}$ excitation function and angular distributions $\sigma(\theta_{\text{cm}})^{\text{HOES}}$, respectively (see [30] and references therein).

4.1. Comparison of excitation functions

4.1.1. A1) $\sigma(E)$ above the Coulomb barrier. If the energy $E_{xB} = E$ is higher than the Coulomb barrier $(E_C)^{xB}$ between the particles in the entrance channel of the $x + B \rightarrow C + D$ reaction, a necessary condition for the pole approximation is

$$(8) \quad \sigma(E_{\text{cm}})^{\text{HOES}} \propto \sigma(E_{\text{cm}})^{\text{OES}}.$$

4.1.2. A2) $\sigma(E)$ below the Coulomb barrier. If E_{xB} of the relative motion is smaller than the Coulomb barrier $(E_C)^{xB}$, to compare the results with those from direct measurements it is necessary to correct the HOES cross-section for the penetration function P_l through the Coulomb barrier; a necessary condition for the validity of the pole approximation is that the cross-section of the two-body $\sigma(E_{\text{cm}})^{\text{TH}}$ reaction is proportional to the binary direct reaction $\sigma(E_{\text{cm}})^{\text{OES}}$:

$$(9) \quad \sigma(E_{\text{cm}})^{\text{TH}} = \sigma(E_{\text{cm}})^{\text{HOES}} P_l(k_{xB} r_{xB}) \propto \sigma(E_{\text{cm}})^{\text{OES}},$$

where the penetration probability of the Coulomb barrier is defined by the equation

$$(10) \quad P_l(k_{xB} r_{xB}) = \frac{k_{xB} r_{xB}}{F_l^2(k_{xB} r_{xB}) + G_l^2(k_{xB} r_{xB})},$$

with F_l and G_l the regular and irregular Coulomb wave functions, k_{xB} and r_{xB} the x - B relative wave number and interaction radius, respectively.

4.1.3. A3) above and below the Coulomb barrier. In some cases, it is possible to accomplish the A1) and A2) prescriptions at the same time. Figure 9 shows the behaviour of the excitation function of the TH ${}^6\text{Li}(p, {}^3\text{He}){}^4\text{He}$ reaction, above and below the Coulomb barrier, extracted from the QF contribution to the ${}^2\text{H}({}^7\text{Li}, \alpha {}^3\text{He})\text{n}$ experiment [25] compared to the excitation function measured in the two-body binary reaction [58]. Experimental TH data are shown as full dots. Open symbols are direct data as given in [25]. The result of the validity test is positive. The overall agreement is quite good above and below the Coulomb barrier.

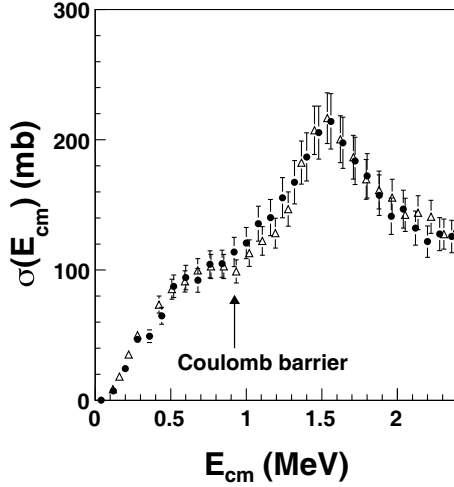


Fig. 9. – Indirect p- ${}^6\text{Li}$ excitation function (full circles) [25] compared with the direct data from ref. [58] (open triangles).

4.2. Comparison of the angular distributions: above and below the Coulomb barrier.

– As a second test a comparison between the indirectly extracted angular distributions and the direct behavior is performed. The relevant angle to get the indirect angular distributions can be calculated according to ref. [56] for the spectator in the target,

$$(11) \quad \theta_{\text{cm}} = \arccos \frac{(\mathbf{v}_B - \mathbf{v}_x) \cdot (\mathbf{v}_C - \mathbf{v}_D)}{|\mathbf{v}_B - \mathbf{v}_x| |\mathbf{v}_C - \mathbf{v}_D|}$$

and for spectator in the projectile by

$$(12) \quad \theta_{\text{cm}} = \arccos \frac{(\mathbf{p}_{xS}) \cdot (\mathbf{v}_C - \mathbf{v}_D)}{|\mathbf{p}_{xS}| |\mathbf{v}_C - \mathbf{v}_D|}.$$

A necessary condition for the pole approximation is that the total cross-section of the two-body reaction $\sigma(\theta_{\text{cm}})^{\text{HOES}}$ is proportional to that of the binary direct reaction $\sigma(\theta_{\text{cm}})^{\text{OES}}$

$$(13) \quad \sigma(\theta_{\text{cm}})^{\text{HOES}} \propto \sigma(\theta_{\text{cm}})^{\text{OES}}.$$

This applies both above and below E^{CB} . Indeed, the effect of P_l ($k_{xB} r_{xB}$) on the angular distributions, which is calculated for a given E_{cm} , is only the introduction of an overall scaling factor.

5. – Results

The THM provides an independent bare nucleus cross-section measurement, $\sigma_b(E)$ (or equivalently the bare nucleus astrophysical factor $S_b(E)$). Thus, it is possible to

extract information on the electron screening potential [22] by comparing $S_b(E)$ with the astrophysical factor $S_s(E)$ obtained from shielded nucleus. Once the two-body cross-section has been extracted, the THM astrophysical S -factor can be obtained according to

$$(14) \quad [S_b(E)]^{\text{THM}} = E \cdot [\sigma_b(E)]^{\text{THM}} \cdot \exp[-2\pi\eta].$$

Thus, the energy dependence of $[S_b(E)]^{\text{THM}}$ should show the same trend of that derived by the direct measurements $[S_b(E)]$, except in the ultra-low energy range ΔE_{ES} where the two data sets should differ due to the effects of electron screening:

$$(15) \quad [S_b(E)]^{\text{THM}} \propto [S_b(E)],$$

where ($E > \Delta E_{ES}$). If needed, the value for the electron screening potential U_e can then be obtained by comparing the two data sets. As already mentioned, the THM does not allow us to extract the absolute value of the astrophysical S -factor. However, the absolute scale for $[S_b(E)]^{\text{THM}}$ can be obtained by

- normalisation of the THM data to the direct ones at energies E^* where the electron screening effects are negligible:

$$(16) \quad N_{\text{abs.value}} = \frac{[S_b(E^*)]^{\text{OES}}}{[S_b(E^*)]^{\text{THM}}} ;$$

- in case of resonances, the normalization is performed equalizing the areas of the same resonance in both THM and direct data.

6. – Astrophysics applications: The light element depletion problem

The abundances of light elements, such as lithium, beryllium and boron, play a key role in a number of astrophysical problems yet to be completely solved, such as the big-bang nucleosynthesis and the light nuclei depletion. Both production and destruction mechanisms must be studied and their cross-sections should be measured at the energies of astrophysical interest. The (p, α) reactions are crucial for the light element destruction in a stellar environment ($E_{\text{cm}} = 1\text{--}50\text{ keV}$) and the cross-sections (or reaction rates) of these reactions are necessary inputs for the astrophysical models of light element abundances in the Universe. In this context, great efforts have been devoted to the study, both directly and via THM, of relevant reactions, such as ${}^7\text{Li}(p, \alpha){}^4\text{He}$ [13, 21, 22], ${}^6\text{Li}(p, \alpha){}^3\text{He}$ [25], ${}^6\text{Li}(d, \alpha){}^4\text{He}$ [12, 26, 27], ${}^9\text{Be}(p, \alpha){}^6\text{Li}$ [28], ${}^{10}\text{B}(p, \alpha){}^7\text{Be}$ [29], ${}^{11}\text{B}(p, \alpha){}^8\text{Be}$ [30] at astrophysical energies.

For some of them, for instance the lithium isotopes, it has also been possible to extract the electron screening potentials U_e^{THM} which were found to be in agreement with the direct U_e^{DIR} estimates but with much smaller uncertainties. In the following sections we will describe the results in details.

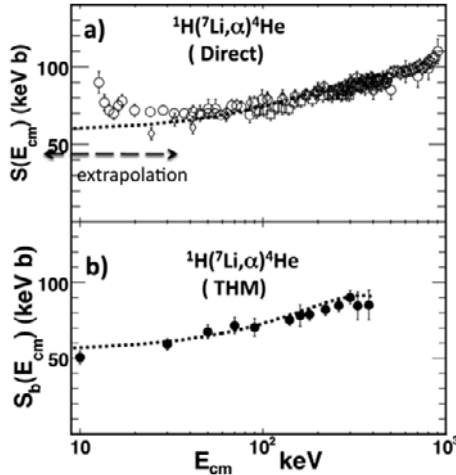


Fig. 10. – $S(E)$ astrophysical factor: (a) the solid line is the results of a polynomial fit to the direct data [58]. (b) THM bare nucleus $S_b(E)$ factor for the ${}^7\text{Li}(\text{p}, \alpha){}^4\text{He}$ (black dots) [22]. The line is the results of a polynomial fit to the THM data [21, 22].

6.1. The ${}^7\text{Li}(\text{p}, \alpha){}^4\text{He}$ reaction. – The cross-section $\sigma(E)$ of the ${}^7\text{Li}(\text{p}, \alpha){}^4\text{He}$ reaction has been measured in a wide energy range, $E_{cm} = 15$ keV to $E_{cm} > 10$ MeV, but above the energy range of interest for astrophysics (see ref. [13] and references therein). The directly measured $S(E)$ -factor is enhanced at sub-Coulomb energies ($E_{cm} \leq 100$ keV) by the electron clouds surrounding the interacting nuclides. An extrapolation procedure based on a polynomial expansion was used to obtain information on $S_b(0)$. Both direct data (open symbols) and extrapolation (dotted line) are reported in fig. 10(a).

To bypass these extrapolations, the bare nucleus $S(E)$ factor $S_b(E)$ was extracted applying the THM to the ${}^2\text{H}({}^7\text{Li}, \alpha\alpha)\text{n}$ three-body reaction. The ${}^7\text{Li}$ beam incident energy was 19–21 MeV. In the data analysis the simpler PWIA formalism was used. The data [22] were also analyzed by using the improved Modified Plane Wave Born Approximation (MPWBA) [15] method. The extracted $S_b(E)$ is reported in fig. 10(b) together with a new parameterization based on R -matrix calculations [22] with a quoted $S(0)$ of 55 keV b. The astrophysical factor value $[S_b(0)]^{\text{THM}}$ is in agreement with the astrophysical factor $S_b(0)$ -extrapolation from high-energy direct data [57, 58] and with the value suggested by R -matrix fit [59]. The NACRE compilation [60] and the recent analysis in [61] give a value slightly higher than the one obtained via THM.

The electron screening potential U_e turns out to be $U_e = 330 \pm 40$ eV [22], in agreement with the determination of $U_e = 300 \pm 160$ eV (molecular) from extrapolation [58]; this has to be compared with the adiabatic limit (U_e)^{adiab} = 186 eV.

6.2. The ${}^6\text{Li}(\text{p}, \alpha){}^3\text{He}$ reaction. – As in the previous case, the ${}^6\text{Li}(\text{p}, \alpha){}^3\text{He}$ reaction cross-section is enhanced at sub-Coulomb energies ($E_{cm} < 100$ keV) by the electron clouds surrounding the interacting nuclides [5, 6]. An extrapolation procedure is necessary

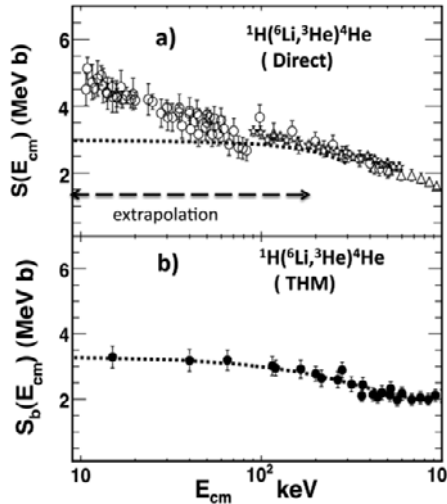


Fig. 11. – (a) $S(E)$ astrophysical-factor direct data for the ${}^6\text{Li}(\text{p}, \alpha){}^3\text{He}$ [62-65]. The solid line is the results of a polynomial fit to the direct data. (b) THM bare nucleus $S(E)$ factor for the ${}^6\text{Li}(\text{p}, \alpha){}^3\text{He}$. The solid line is the results of a polynomial fit to THM data.

to obtain information at the Gamow energy. Direct data are reported in fig. 11(a), with the polynomial expansion to perform the extrapolation. The THM was thus applied to determine $S_b(E)$ [25]. The cross-section of $d({}^6\text{Li}, \alpha{}^3\text{He})n$ three-body reaction was performed at 25 MeV of $E_{^6\text{Li}}$ beam-energy. The experiment clearly revealed the presence of the quasi-free mechanism proceeding through a virtual two-body reaction between the incident ${}^6\text{Li}$ and the proton in ${}^2\text{H}$.

The quasi-free two-body cross-section was compared with the direct data showing a quite good overall agreement in the E_{cm} (${}^6\text{Li}$ -p relative energy) range 0.12–2.4 MeV, with a distinct contribution from the resonant behaviour associated with the 7.2 MeV (5/2-) state of ${}^7\text{Be}$ [25]. A further study of the three-body reaction was performed at 14 MeV of beam energy in order to populate the very low energy part of the ${}^6\text{Li}$ -p bare nucleus $S(E)$ -factor spectrum, down to the Gamow peak [25]. The bare nucleus $S(E)$ -factor was extracted in the energy range $E_{\text{cm}} = 0.01$ to 1.2 MeV, and normalized to direct data taken from [62] in the energy range $E_{\text{cm}} = 0.8$ to 1.2 MeV. The normalized low-energy THM data are reported in fig. 11(b) as full circles. The full line in the same figure represents the result of a second-order polynomial fit to the THM data providing a $S(0)$ value of $[S_b(0)]^{\text{THM}} = 3.0 \pm 0.3$ MeV b. The zero-energy astrophysical factor extracted via THM $[S_b(0)]^{\text{THM}}$ is consistent with the fits to direct measurements [58, 62-65] and with that reported in the NACRE compilation [60]. These results lead to unchanged astrophysical implications [66].

The astrophysical factor $[S_b(0)]^{\text{THM}}$ is not in agreement with R -matrix calculations [59, 67]. According to the direct estimate, the electron screening potential $[U_e]^{\text{THM}}$ is not in agreement with the adiabatic limit, which yield $U_e = 186$ eV as in the previous case.

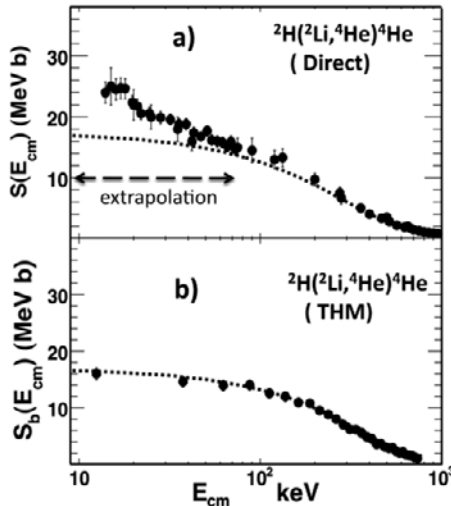


Fig. 12. – (a) $S(E)$ astrophysical-factor direct data for the ${}^6\text{Li}(\text{d}, \alpha){}^4\text{He}$ [57, 58]. The solid line is the results of a polynomial fit to the direct data. (b) THM bare nucleus $S(E)$ factor for the ${}^6\text{Li}(\text{d}, \alpha){}^4\text{He}$. The solid line is the results of a polynomial fit to THM data [26].

6.3. The ${}^6\text{Li}(\text{d}, \alpha){}^4\text{He}$ reaction. – In the same context, the ${}^6\text{Li}(\text{d}, \alpha){}^4\text{He}$ reaction cross-section has been measured via the THM applied to the ${}^6\text{Li}({}^6\text{Li}, \alpha\alpha){}^4\text{He}$ three-body reaction. After the standard THM analysis, the bare nucleus $S(E)$ -factor was extracted in the energy range $E_{\text{cm}} = 10\text{--}700\text{ keV}$ and normalized to direct data taken from [58] (see fig. 12) in the energy range $E_{\text{cm}} = 600$ to 700 keV . The normalized THM data are reported in fig. 12(b) as black dots. The dashed line in the same figure represents the theoretical trend, which was obtained in [25]. The measurement at astrophysical energies was then repeated by means of the THM as is extensively reported in [26]. The indirect measurement yielded $S(0) = 16.9 \pm 0.5\text{ keV b}$. The result is consistent with the direct estimate of $S_b(E) = 17.4\text{ MeV b}$ [58]. The electron screening potential turns out to be $U_e = 320 \pm 50\text{ eV}$, in agreement with the direct determinations of $U_e = 380 \pm 250\text{ eV}$ and $U_e = 330 \pm 120\text{ eV}$ [58] but far from the adiabatic limit, as in the previous cases.

The systematic discrepancy between experimental data and adiabatic approximation is evident in all the cases discussed above. This discrepancy has been attributed to the different chemical structure of the target [66]. However, additional experimental and theoretical investigations are needed to better understand this problem. In any case, the isotopic independence of the electron screening effect, which was already investigated in other works [58], is confirmed.

Inserting the new THM data in the astrophysical codes, no relevant change in reaction rate as well as in the subsequent stellar evolution and primordial nucleosynthesis is found [66, 68]. The lithium depletion problem is therefore not linked to a wrong evaluation of the ${}^{6,7}\text{Li}(\text{p}, \alpha){}^{3,4}\text{He}$ ${}^6\text{Li}(\text{d}, \alpha){}^4\text{He}$ cross-sections but has its origins on a non-satisfactory evaluation of stellar processes, *e.g.*, convection and/or other non-standard mixing mechanisms.

7. – Conclusions

The present paper reports on the basic features of the THM. Some of the main tests for checking the correct selection of the events related to the QF reaction mechanisms, necessary for the application of the THM, were discussed. Applications to reactions induced by protons in the lithium isotopes at energies close to the Gamow peak were shown. From these results the possibility of extracting, without extrapolation, the bare nucleus cross-section at ultra-low energies as well as information on the electron screening potential was clearly shown.

REFERENCES

- [1] BURGIGE E. M., BURBIGE G., FOWLER W. A. and HOYLE H., *Rev. Mod. Phys.*, **29** (1957) 547.
- [2] FOWLER W. A., *Rev. Mod. Phys.*, **56** (1984) 149.
- [3] ROLFS C. and RODNEY W. S., *Caldrons in the Cosmos* (University of Chicago Press, Chicago) 1988.
- [4] ROLFS C., *Prog. Part. Nucl. Phys.*, **153** (2001) 23.
- [5] ASSENBAUM H., LANGANKE K. L. and ROLFS C., *Z. Phys. A*, **327** (1987) 461.
- [6] STRIEDER F. *et al.*, *Naturwiss.*, **88** (2001) 461.
- [7] BAUR G., BERTULANI C. and REBEL H., *Nucl. Phys. A*, **458** (1986) 188.
- [8] MUKAMEDZHANOV A. M. *et al.*, *Phys. Rev. C*, **56** (1997) 1302.
- [9] MUKAMEDZHANOV A. M. and TRIBBLE R. E., *Phys. Rev. C*, **59** (1999) 3418.
- [10] BAUR G., *Phys. Lett. B*, **178** (1986) 135.
- [11] SPITALERI C., *Problem of Fundamental Modern Physics, II*, edited by CHERUBINI R., DALPIAZ P. and MINETTI B. (World Scientific) 1990.
- [12] CHERUBINI S. *et al.*, *Astrophys. J.*, **457** (1996) 855.
- [13] SPITALERI C. *et al.*, *Phys. Rev. C*, **60** (1999) 055802.
- [14] SPITALERI C., *Nucl. Phys. A*, **719** (2003) 99c.
- [15] TYPEL S. and WOLTER H. H., *Few Body Syst.*, **29** (2000) 7.
- [16] TYPEL S. and BAUR G., *Ann. Phys. (N.Y.)*, **305** (2003) 228.
- [17] MUKAMEDZHANOV A. M. *et al.*, *J. Phys. G, Nucl. Part. Phys.*, **35** (2008) 014016.
- [18] TUMINO A. *et al.*, *Phys. Rev. Lett.*, **98** (2007) 252502.
- [19] LATTUADA M. *et al.*, *Nucl. Phys. A*, **458** (1985) 493.
- [20] ZADRO M. *et al.*, *Phys. Rev. C*, **40** (1989) 181.
- [21] ALIOTTA M. *et al.*, *Eur. Phys. J. A*, **9** (2000) 435.
- [22] LATTUADA M. *et al.*, *Astrophys. J.*, **562** (2001) 1076.
- [23] TUMINO A. *et al.*, *Eur. Phys. J. A*, Direct (Doi:10.11114/epja/i2006-08-038-1 (2006)).
- [24] CALVI G. *et al.*, *Phys. Rev. C*, **41** (1990) 1848.
- [25] TUMINO A. *et al.*, *Phys. Rev. C*, **67** (2003) 065803.
- [26] SPITALERI C. *et al.*, *Phys. Rev. C*, **63** (2001) 005801.
- [27] MUSUMARRA A. *et al.*, *Phys. Rev. C*, **64** (2001) 068801.
- [28] WEN Q. *et al.*, *Phys. Rev. C*, **78** (2008) 035805.
- [29] ROMANO S. *et al.*, *Eur. Phys. A*, Direct (Doi:10.11114/epja/i2006-08-034-1 (2006)).
- [30] SPITALERI C. *et al.*, *Phys. Rev. C*, **69** (2004) 055806.
- [31] LAMIA L. *et al.*, *Nuovo Cimento*, **31** (2009) 423.
- [32] LA COGNATA M. *et al.*, *Phys. Rev. C*, **76** (2007) 065804.
- [33] LA COGNATA M. *et al.*, *Phys. Rev. C*, **80** (2009) 012801.

- [34] LA COGNATA M. *et al.*, *Phys. Rev. Lett.*, **10** (2008) 152501.
- [35] LA COGNATA M. *et al.*, *Phys. Rev. C*, **82** (2010) 032801.
- [36] SERGI M. L. *et al.*, *Phys. Rev. C*, **82** (2010) 032801.
- [37] LA COGNATA M. *et al.*, *Phys. Rev. C*, **72** (2005) 065802.
- [38] RINOLLO A. *et al.*, *Nucl. Phys. A*, **758** (2005) 146c.
- [39] SPITALERI C. *et al.*, *Eur. Phys. J. A*, **7** (2000) 181.
- [40] TUMINO A. *et al.*, *Eur. Phys. J. A*, **25** (2005) 649.
- [41] GULINO M. *et al.*, *J. Phys. G, Nucl. Part. Phys.*, **37** (2010) 125109.
- [42] SHAPIRO I. S., KOLYBASOV V. M. and AUGUST J. P., *Nucl. Phys.*, **61** (1965) 353.
- [43] CHEW G. F. and WICK G. C., *Phys. Rev.*, **85** (1952) 636.
- [44] JACOB G. and MARIS TH. A., *Rev. Mod. Phys.*, **38** (1966) 121.
- [45] GROSSIODOR J. Y. *et al.*, *Phys. Rev. Lett.*, **32** (1974) 177.
- [46] CHANT N. S. and ROOS P. G., *Phys. Rev. C*, **15** (1977) 57.
- [47] ROOS P. G. *et al.*, *Phys. Rev. C*, **15** (1977) 69.
- [48] BARBARINO S. *et al.*, *Nuovo Cimento*, **53** (1979) 327.
- [49] FALICA P. G. *et al.*, *Lett. Nuovo Cimento*, **22** (1978) 547.
- [50] BARBARINO S. *et al.*, *Phys. Rev. C*, **21** (1980) 1104.
- [51] PIZZONE R. G. *et al.*, *Phys. Rev. C*, **71** (2005) 058801.
- [52] PIZZONE R. G. *et al.*, *Phys. Rev. C*, **80** (2009) 025807.
- [53] PEREY C. M. and PEREY F. G., *At. Data Nucl. Data Tables*, **17** (1976) 353.
- [54] BLAGUS S. *et al.*, *Z. Phys. A*, **337** (1990) 325.
- [55] LA COGNATA M. *et al.*, *Few Body Syst.*, **44** (2008) 1.
- [56] SLAUS I. *et al.*, *Phys. Rev. C*, **8** (1974) 444.
- [57] ROLFS C. and KAVENAGH R. W., *Nucl. Phys. A*, **455** (1986) 179.
- [58] ENGSTLER S. *et al.*, *Phys. Nucl. A*, **342** (1992) 471.
- [59] BARKER F. C., *Phys. Rev. C*, **62** (2000) 044607.
- [60] ANGULO C. *et al.*, *Nucl. Phys. A*, **656** (1999) 3.
- [61] CYBURT H. C., *Phys. Rev. D*, **70** (2004) 023505.
- [62] ELWYN A. J. *et al.*, *Phys. Rev. C*, **20** (1979) 1984.
- [63] GEMEINHARDT W., KAMKE D. and VON RHONECK C., *Z. Phys.*, **197** (1966) 58.
- [64] SPINKA H., TOMBRELLO T. and WINKLER H., *Nucl. Phys. A*, **164** (1971) 1.
- [65] MARION J. B., WEBER G. and MOZER F. S., *Phys. Rev.*, **104** (1977) 1402.
- [66] PIZZONE R. G. *et al.*, *Astron. Astrophys.*, **438** (2005) 779.
- [67] BARKER F. C., *Nucl. Phys. A*, **707** (2002) 277.
- [68] PIZZONE R. G. *et al.*, *Astron. Astrophys.*, **398** (2003) 423.

Neutron capture measurements at the CERN neutron time-of-flight facility: Nuclear astrophysics aspects

P. M. MILAZZO

INFN, Sezione di Trieste - Trieste, Italy

Summary. — Nuclear astrophysics, advanced nuclear technology and nuclear structure physics present many cases that require neutron capture reaction data with high precision. In particular, focusing on nuclear astrophysics, refined data are needed for stellar nucleosynthesis, investigation of stellar physical conditions and applications to evaluations of the age of the Universe. New neutron capture measurements were performed at the pulsed neutron time-of-flight (n_TOF) facility at CERN, where the white neutron energy spectrum ranges from thermal to hundreds of MeV, covering the full energy range of interest for nuclear astrophysics. Moreover, the high instantaneous neutron flux, and the favourable background conditions in the experimental area make this facility unique for high-resolution time-of-flight measurements of neutron-induced reaction cross-sections. The n_TOF Collaboration is presently operating two different experimental set-ups. The first consists of two low-neutron sensitivity C_6D_6 detectors with the analysis relying on the pulse height weighting technique. In addition, a total absorption calorimeter, consisting of 40 BaF_2 crystals covering the whole solid angle, was used. A review of the astrophysical program made at the n_TOF facility, results on selected stable and unstable samples and implications are presented.

1. – Introduction

The origin of the elements is an important topic to understand the evolution of the Universe. Hydrogen and helium, and small amounts of lithium, were formed in the period between about 100 seconds and 20 minutes after the big bang [1]. This period of primordial nucleosynthesis was followed by galactic condensation and the formations of the stars. All elements heavier than lithium have been formed in stars, and the elements heavier than iron have been formed via neutron capture processes in the stars.

Stellar nucleosynthesis has first been extensively reviewed in the reference work [2] and more recently in [3, 4]. The isotopes up to ^{56}Fe can be synthesized by fusion reactions during the different stages of the evolution of a star. It is nowadays well established that neutron capture processes in red giant stars and supernovae are responsible for the formation of nearly all isotopes with higher masses [3]. This was first recognized by the discovery of technetium in red giant stars [5].

The neutron capture mechanisms are known as s- and r-processes, where “s” stands for slow and “r” for rapid referring to the time scale of the β -decay. The neutron source inside the red giant stars are mainly the $^{22}\text{Ne}(\alpha, n)^{25}\text{Mg}$ and $^{13}\text{C}(\alpha, n)^{16}\text{O}$ reactions. The s- and r-processes are responsible for the production of the stable and neutron rich isotopes, respectively. A thorough knowledge of the s-process, for which much more experimental data are available, constrains the possibilities of the r-process. A competing mechanism is the p-process, referring to photodisintegration reaction like (γ, n) , (γ, p) and (γ, α) , they influence the abundances from the proton rich side.

If the compound nucleus, formed after a neutron capture event, is unstable against the β -decay, it may decay before it captures a second neutron. This is what happens in the s-process which is the main process of synthesis in the red giant stars, where thousands of years may pass between two successive neutron captures on a nucleus. In this way many of the isotopes from ^{56}Fe to ^{209}Bi are formed. Heavier nuclei than Bi are unstable and cannot be formed by neutron capture anymore. The s-process path follows closely the valley of stability in the chart of the nuclei and ends at ^{209}Bi .

In the r-process the neutron capture process is much faster and occurs on much shorter time scales. The time between consecutive neutron captures is the order of seconds. In order to achieve the according extremely high neutron fluxes, the astrophysical site for the r-process is believed to be of explosive nature, like in a supernova, or in the presence of very high neutron densities as in the case of merging neutron stars.

Approximately one half of the abundances in the mass region $A \geq 56$ can be assigned to each of the two processes.

Neutron capture cross-sections are a key ingredient in the development of stellar models using the calculation of nuclear abundances in stellar environments. At the branching points along the nucleosynthesis paths uncertainties in the cross-sections can propagate into large differences in the production of higher mass nuclei within a given model.

The accuracy at the level of a few percent is mandatory for studying the details of nucleosynthesis processes.

2. – The n_TOF facility

A new neutron time-of-flight facility is operating at CERN from May 2002 [6]. Neutrons are produced by spallation reactions induced by a pulsed, 6 ns wide, $20\text{ GeV}/c$ proton beam with up to 7×10^{12} protons per pulse, impinging on a $80 \times 80 \times 60\text{ cm}^3$ lead target, yielding about 300 neutrons per incident proton. A 5 cm water slab surrounding the lead target serves as a coolant and at the same time as a moderator of the initially fast neutron spectrum, providing a wide energy spectrum from 25 meV to about 1 GeV with a nearly $1/E$ isolethargic flux dependence up to 1 MeV. A vacuum neutron beam line leads to the experimental area at 185 m from the lead target [7].

The neutron beam is obtained by means of two collimators, consisting of layers of iron and borated polyethylene. The iron serves to stop fast neutrons, while the hydrogen in polyethylene moderates the neutrons and ^{10}B captures the slower neutrons. One collimator has an inner diameter of 11 cm, an outer diameter of 50 cm and is placed at 135 m from the lead target. The second collimator is located near the experimental area at a distance of 175 m: it has an outer diameter of 40 cm and an inner diameter of 1.8 cm (capture measurements). This collimation results in a nearly symmetric Gaussian-shaped beam profile at the sample position with a standard deviation of about 0.77 cm. The spatial distribution has been accurately measured as a function of neutron energy.

In order to remove residual charged particles going along the neutron beam line, a 1.5 T sweeping magnet has been placed at a distance of 145 m of the spallation target. A previously observed background due to negative muon capture has been drastically reduced by means of a 3 m thick iron shielding located just after the sweeping magnet. The experimental area where the samples and detectors are mounted for capture and fission experiments ranges from 182 to 190 m. The neutron beam line is extended for an additional 12 m beyond the experimental area to minimize the background from back-scattered neutrons.

The neutron kinetic energy is determined by the time of flight. This is possible since the proton beam is pulsed. The impact of the proton beam on the lead target is closely related to the creation time of neutrons of all energies. The detection of a reaction product of a neutron-induced reaction in the experimental area provides the time the neutron has taken to travel the distance from the spallation target to the experimental area. The velocity and hence the kinetic energy of the neutron can be deduced from the flight time and the flight distance. The repetition period of the proton pulses is at least 2.4 s, which is low enough to cover the energy range down to subthermal energies and to prevent overlapping of slow neutrons in subsequent cycles.

A pulsed white neutron source is characterized by the energy distribution of its neutron flux, both time-averaged and per time-of-flight bunch, but also by its energy resolution. The energy distribution of the neutron flux at the sample position at 185 m for a standard time-of-flight bunch of 7×10^{12} protons is shown in fig. 1. The data are based on a measurement performed with a ^{235}U loaded parallel-plate fission ionization chamber from the Physikalisch Technische Bundesanstalt in Braunschweig [8], and below 1 keV

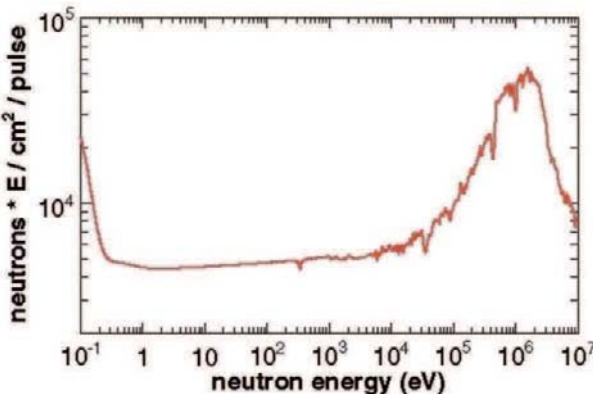


Fig. 1. – The neutron flux as a function of the neutron energy.

from a ⁶Li-based in beam neutron flux monitor [9]. The ⁶Li-based flux detector is always present during the measurements.

The flux per bunch governs the signal-to-noise ratio. In capture experiments a high flux per bunch results in a favorable ratio of γ -rays from (n, γ) reactions to γ -rays from radioactivity. In order to obtain the average flux, which is relevant for the duration of the experiment, one just multiplies the instantaneous flux with the repetition rate of the proton beam. At higher neutron energies the reaction cross-sections do not show the resonance structure anymore and have a smooth behavior. Therefore an approximate knowledge of the energy resolution is sufficient. At lower energies in the resolved resonance region however the cross-section can vary several orders of magnitude over a few eV. The full distribution of the energy resolution, which is often non-Gaussian, is needed to determine accurately the description of the resonances. The resolution in energy for a measured flight time can conveniently be expressed in terms of a spread in the effective flight distance. The distribution of this equivalent distance is an appropriate quantity to evaluate the resolution as a function of the neutron energy [10].

3. – The experimental setup

Two different detectors have been used in the neutron capture measurements.

The first one consists in a pair of an in-house developed deuterated benzene C₆D₆ γ -ray detectors contained in a cylindrical low-mass carbon fiber housing.

Special care was devoted to reduce the neutron sensitivity of the experimental setup to the smallest possible level. This was achieved by detailed Monte Carlo simulations of all detector components and with a reduction of materials around the scintillator cells. In this way, an optimized detector was developed for accurate measurements of the resonance-dominated (n, γ) cross-sections of light and neutron magic isotopes [11].

The detectors were placed perpendicular to the neutron beam at a distance of about 3 cm from the beam axis. The background due to in-beam γ -rays was reduced by placing

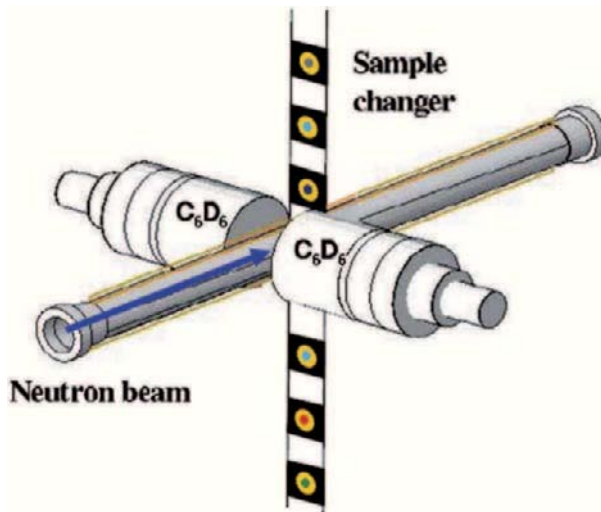


Fig. 2. – Schematic view of the experimental setup with liquid-scintillator detectors and the sample changer.

the detectors 9.2 cm upstream of the sample position. Moreover, the low neutron capture cross-sections of both carbon and deuterium assure a low contribution from sample scattered neutrons to the background.

Given that this detector does not measure the full γ -ray cascade following neutron capture, it requires the use of weighting functions to reconstruct the neutron capture yield [12]. Although detection efficiency for a single detector is only about 3% for a 1 MeV γ -ray, due to the γ -ray multiplicity after neutron capture, the efficiency to detect a capture event is roughly 20% for the set of two detectors. The samples were kept in position by a carbon fiber sample changer.

The light output of the detectors was calibrated at 662, 1173, and 1332 keV by means of ¹³⁷Cs and ⁶⁰Co reference sources. An additional calibration point at 6.13 MeV was obtained by means of a composite ²³⁸Pu/¹³C source. The calibration was repeated in regular intervals to verify the stability of the detectors and of the data acquisition system.

A sketch of this experimental setup is shown in fig. 2

A second neutron capture detector consists of a 4π 100% efficiency total absorption capture detector, made up of 40 BaF₂ crystals contained in ¹⁰B loaded carbon fiber capsules, coupled to XP4512B photomultipliers equipped with for this purpose designed voltage dividers. Samples are surrounded by a C₁₂H₂₀O⁴(⁶Li)₂ neutron absorber which moderates and absorbs sample scattered neutrons. The ensemble is placed in the center of the calorimeter. Since this detector is used to select the total γ -ray cascade from neutron capture, it can distinguish γ -rays originating from other processes [13].

For the capture measurements the reaction yields are normalized either to the cross-section of ¹⁹⁷Au (n, γ), which is a standard in the energy region above 200 keV,

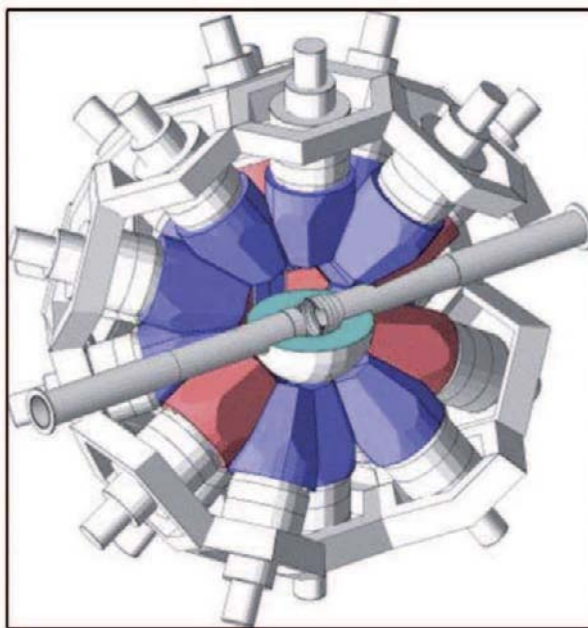


Fig. 3. – Schematic view of the 4π calorimeter experimental setup.

or to a low-energy saturated resonance in a ^{197}Au reference sample or in the sample to be measured itself.

A sketch of this experimental setup is shown in fig. 3.

4. – The neutron capture measurements

The cross-sections of neutron-induced reactions can show variations of several orders of magnitude on an energy scale of only a few eV. The origin of these resonances is related to the excitation of nuclear states in the compound nuclear system formed by the neutron and the target nucleus, at excitation energies lying above the neutron binding energy of typically several MeV. At these high excitation energies for nuclei of medium and heavy mass the nuclear system is extremely complex and no nuclear model is capable of predicting the position and other properties of these excited states. Cross-sections can therefore only be accessed by measurements.

A compilation of experimentally observed resonance data can be found in nuclear data libraries, where data are stored as a set of physical properties for each nuclear level excited by the incident neutron, which are energy, spin, parity and partial widths. These data allow the reconstruction of the resonance cross-sections, capture, scattering and total, at any given target temperature.

The quantity determined in a neutron capture experiment is the capture yield, *i.e.* the fraction of incident neutrons undergoing (n, γ) interaction on a defined sample. The

capture yield is directly linked to the capture and total cross-sections. The data analysis was then based on an accurate measurement of the capture yield.

Once extracted the experimental capture yields, the analysis of the resonances was done by means of the multi-level analysis code SAMMY [14]. The resonance parameters obtained by SAMMY analyses are the resonance energy E_R , the radiative width Γ_γ , the neutron width Γ_n , spin and parity. It is then possible to extract the capture kernel K

$$K = g \frac{\Gamma_n \cdot \Gamma_\gamma}{(\Gamma_n + \Gamma_\gamma)},$$

where

$$g = \frac{(2J+1)}{(2I_n+1)(2I_0+1)}$$

is the statistical spin factor determined by the resonance spin, J , the spin of the incident neutron, $I_n = 1/2$, and the spin of the target nucleus, $I_0 = 0$.

Capture kernels are directly linked to the calculation of capture cross-sections.

5. – Measurements of astrophysical interest

The astrophysics experimental campaign at n_TOF was focussed on neutron magic nuclei, which act as a bottleneck for the flow of s-process, nuclei with $A \leq 120$, branching points isotopes and isotopes of special interest as the Os important for nuclear cosmochronology.

Capture measurements with the C₆D₆ detectors concerned ^{24,25,26}Mg, ⁵⁶Fe, ^{90,91,92,93,94,96}Zr [15-17], ¹³⁹La [18], ¹⁵¹Sm [19, 20], ^{186,187,188}Os [21, 22], ¹⁹⁷Au [23], ^{204,206,207,208}Pb [24-26], ²⁰⁹Bi [27], and ²³²Th [28]. The BaF₂ 4π calorimeter has been used for measurements of ¹⁹⁷Au, ^{233,234}U, ²³⁷Np, ²⁴⁰Pu and ²⁴³Am. Several of these measurements are still under analysis, while for others final data have been published.

Table I summarises the motivations of measurements of different isotopes.

5.1. The ^{90,91,92,93,94,96}Zr(n, γ), ¹³⁹La reactions. – The neutron capture measurement of these isotopes has a particular relevance in the nuclear astrophysics; since the Zr belongs to the first s-process peak in the solar abundance distribution at $N = 50$ while the La belongs to the second s-process peak at $N = 82$. The ⁹⁰Zr and the ¹³⁹La are neutron magic and are characterized, like the ^{91,92,93,94}Zr, by a low neutron capture cross-section and are predominately of s-process origin. The most neutron-rich Zr stable isotope, ⁹⁶Zr, is traditionally considered to be an r-only isotope with a small s-process admixture. Its abundance is considered to be a strong indicator in the efficiency of the ²²Ne neutron source during the He shell burning episodes of thermally pulsing asymptotic giant branch stars. The ¹³⁹La acts as a bottleneck between the abundant light n-capture element of the first s-process peak and the heavy elements from Sm up to Pb and Bi, it is very important for interpreting the element abundance patterns in very old, metal poor stars. Since the La abundance is completely represented by ¹³⁹La it can be used to distinguish

TABLE I. – *Neutron capture cross-sections measurements performed at n_TOF.*

$^{24,25,26}\text{Mg}$	Isotopic abundance in stellar grains. Importance of the $^{22}\text{Ne}(\alpha, \text{n})^{25}\text{Mg}$ for the s-process neutron balance.
$^{90,91,92,93,94,96}\text{Zr}$	s-process branching at $A = 95$. Sensitivity to neutron flux during the s-process.
^{139}La	Bottleneck in the s-process flow. $N = 82$ neutron shell closure.
^{151}Sm	s-process branching at $A = 151$.
$^{186,187,188}\text{Os}$	Nuclear cosmochronology.
^{197}Au	Standard and cross-section normalization.
$^{204,206,207,208}\text{Pb}$	End of the s-process.
^{209}Bi	

the s-process components from the products of explosive r-process nucleosynthesis, the s/r ratio is of utmost importance for the galactical chemical evolution.

The major motivation of these measurements was to reduce the uncertainties to a few percent, as required to improve the stellar s-process model.

In fig. 4 is reported the comparison of the Maxwellian Averaged Cross-Section (MACS) calculated with n_TOF data with other experimental results.

The capture cross-section of the ^{139}La in terms of resonance parameter was measured in a large energy range from 0.6 eV up to 9 keV, these results show sizeable differences with respect to the previous experimental data and allow to extract the related nuclear quantities with improved accuracy.

5.2. The ^{151}Sm reaction. – The ^{151}Sm is a branching point in the s-process path, in particular, this branching is sensitive to the temperature at which the s-process is taking place. The accurate determination of the neutron capture cross-section of this isotope can thus provide crucial information on the thermodynamics condition of the AGB stars.

The result obtained at n_TOF represents the firm estimate of the capture rate for the first time based on experimental values. This allowed to obtain two important conclusions with respect to the s-process nucleosynthesis in this mass region: 1) the classical model, based on the phenomenological study of the s-process fails to produce consistent result of the branching at ^{151}Sm and ^{147}Pm , 2) the p-process contribution to the production of ^{152}Gd can amount up 30% of the solar-system observed abundance.

5.3. The $^{186,187,188}\text{Os}(\text{n}, \gamma)$ reactions. – The time duration of the nucleosynthesis of the heavy elements produced by neutron capture processes can be used to set limits on the age of the universe [29], among several cosmic clock based on the abundances of long-lived radioactive isotopes the $^{187}\text{Os}/^{187}\text{Re}$ is one of the more interesting.

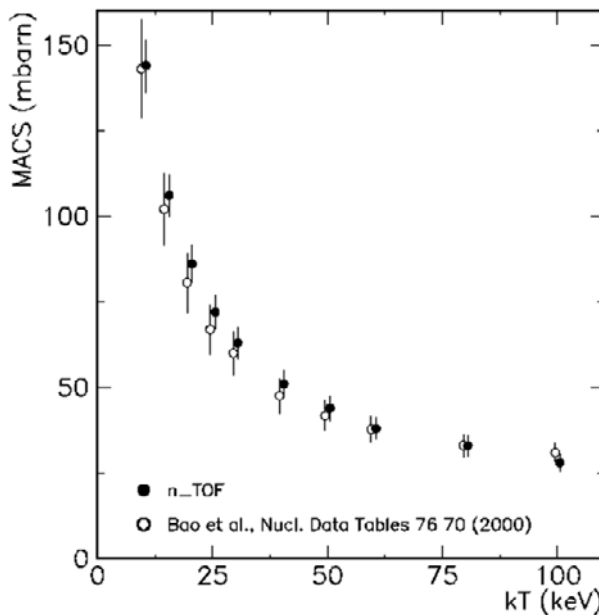


Fig. 4. – ^{91}Zr Maxwellian Averaged Cross-Sections (MACS) calculated at different thermal energy, with n_TOF data and with evaluation studies.

The clock is based on the extremely long half-life of ^{187}Re ($\tau_{1/2} = 43.3\text{ Gy}$) decay to ^{187}Os and on the fact that ^{186}Os and ^{187}Os are shielded against direct r-process production. Then, thanks to the well-established s-process abundances of the ^{186}Os and ^{187}Os , the Re/Os clock can be characterized by the enhancement in the abundance of ^{187}Os due to ^{187}Re β -decay to ^{187}Os . The uncertainty on the capture cross-section ratio ($\sigma^{186}\text{Os}/\sigma^{187}\text{Os}$) propagates into an age (t_0) uncertainty of the order of $\Delta(\sigma^{186}\text{Os}/\sigma^{187}\text{Os}) \approx 10\% \rightarrow \Delta t_0 \approx 3\text{ Gy}$.

The results show that the cross-sections for all Os isotopes are available in the entire range of astrophysical interest with typical uncertainties of 5%. The data clearly show, for the first time, the competition of the inelastic channel for the ^{186}Os . A final statement concerning the Re/Os clock could be given only after a firm estimation of the inelastic scattering cross-section. Presently, the data seem to indicate an older age of the Universe than the one obtained with other methods, but it may be due to the very crude model used so far.

6. – Conclusions

With the description of the cross-section measurement campaign activities at CERN n_TOF, we have shown how the characteristics of a neutron spallation source can be favorably used for neutron cross-section measurements of interest in nuclear astrophysics.

The challenge related to the neutron capture cross-section measurements have been met, the n_TOF cross-sections are available in the energy range of astrophysical interest with an uncertainty less than 5%.

REFERENCES

- [1] ALPHER R. A., BETHE H. A. and GAMOW G., *Phys. Rev.*, **73** (1948) 803.
- [2] BURBIDGE E. M., BURBIDGE G. R., FOWLER W. A. and HOYLE F., *Rev. Mod. Phys.*, **29** (1957) 547.
- [3] WALLERSTEIN G. *et al.*, *Rev. Mod. Phys.*, **69** (1997) 995.
- [4] ARNOULD M. and TAKAHASHI K., *Rev. Prog. Phys.*, **62** (1999) 395.
- [5] MERRILL A. P. W., *Science*, **115** (1952) 484.
- [6] RUBBIA C. *et al.*, Tech. Rep. CERN/LHC (1998) 98-02.
- [7] ABBONDANNO U. *et al.*, Tech. Rep. CERN/SL (2002) 053 ECT.
- [8] BORCEA C. *et al.*, *Nucl. Instrum. Methods Phys. Res. A*, **513** (2003) 524.
- [9] MARRONE S. *et al.*, *Nucl. Instrum. Methods Phys. Res. A*, **517** (2004) 389.
- [10] COCEVA C. *et al.*, *Nucl. Instrum. Methods Phys. Res. A*, **489** (2002) 346.
- [11] PLAG R. *et al.*, *Nucl. Instrum. Methods Phys. Res. A*, **496** (2003) 425.
- [12] BORELLA A. *et al.*, *Nucl. Instrum. Methods Phys. Res. A*, **577** (2007) 626.
- [13] GUERRERO C. *et al.*, *Nucl. Instrum. Methods Phys. Res. A*, **608** (2009) 424.
- [14] LARSON N. M., Report ORNL, TM-9179 (2006) R7.
- [15] TAGLIENTE G. *et al.*, *Phys. Rev. C*, **77** (2008) 035802.
- [16] TAGLIENTE G. *et al.*, *Phys. Rev. C*, **78** (2008) 045804.
- [17] TAGLIENTE G. *et al.*, *Phys. Rev. C*, **81** (2010) 055801.
- [18] TERLIZZI R. *et al.*, *Phys. Rev. C*, **75** (2007) 035807.
- [19] ABBONDANNO U. *et al.*, *Phys. Rev. Lett.*, **93** (2004) 161103.
- [20] MARRONE S. *et al.*, *Phys. Rev. C*, **73** (2006) 034604.
- [21] MOSCONI M. *et al.*, *Phys. Rev. C*, **82** (2010) 015802.
- [22] FUJII K. *et al.*, *Phys. Rev. C*, **82** (2010) 015804.
- [23] MASSIMI C. *et al.*, *Phys. Rev. C*, **81** (2010) 044616.
- [24] DOMINGO-PARDO C. *et al.*, *Phys. Rev. C*, **74** (2006) 055802.
- [25] DOMINGO-PARDO C. *et al.*, *Phys. Rev. C*, **75** (2007) 015806.
- [26] DOMINGO-PARDO C. *et al.*, *Phys. Rev. C*, **76** (2007) 045805.
- [27] DOMINGO-PARDO C. *et al.*, *Phys. Rev. C*, **74** (2006) 025807.
- [28] AERTS G. *et al.*, *Phys. Rev. C*, **73** (2006) 054610.
- [29] CLAYTON D. D. *et al.*, *Astrophys. J.*, **139** (1964) 637.

NUCLEAR STRUCTURE FOR ASTROPHYSICS

This page intentionally left blank

Isomeric states in neutron-rich lead isotopes populated by fragmentation of ^{238}U at 1 GeV A

G. BENZONI

INFN, Sezione di Milano - Via Celoria 16, 20133, Milano

Summary. — Neutron-rich nuclei beyond $N = 126$ in the lead region were populated by fragmenting a ^{238}U beam at 1 GeV A on a Be target and then separated by the Fragment Separator at GSI. Their isomeric and beta-decays were observed, enabling the study of the shell structure of neutron-rich nuclei around $Z = 82$ shell closure. Preliminary results of the analysis are hereby reported.

1. – Introduction

The region of neutron-rich lead isotopes is of particular interest to trace the evolution of single-particle levels and the residual proton-neutron interaction beyond the doubly magic ^{208}Pb . While ^{208}Pb is well understood in terms of shell model, experimental data on heavier isotopes are very scarce and it is far from clear to what extent the shell model holds.

While extensive research has been pursued in past years on proton-rich isotopes, information on the neutron-rich side is scarce. Additionally the evolution of proton shell structure beyond ^{208}Pb is crucial for the stabilization of superheavy elements. Attempts to populate this region of the chart of nuclides with $Z > 80$ have been made in the past using deep inelastic reactions induced on both ^{208}Pb and ^{238}U targets [1], but the charge

equilibration process tends to drive the reaction towards the production of stable nuclei. While the relatively long expected lifetimes would make these nuclei adequate candidates to be produced with the ISOL method, few successful experiments have been performed so far using the pulsed release technique for contaminant suppression [2]. These latter experiments populated Bi and Fr isotopes but could only study their β -decay.

The β -decay of neutron-rich nuclei around $Z = 82$ is of particular interest for astrophysical purposes: it is well established that the r-process path lies very far away from accessible nuclei, therefore astrophysical models have to extrapolate extensively in order to predict production rates in stellar environments. Nowadays these models differ substantially one from the other and, even for modestly neutron-rich nuclei, predictions of lifetimes and production rates can vary orders of magnitude [3].

The region of neutron-rich isotopes around Pb offers favourable conditions for the formation of isomeric states due to the presence of high- j orbitals which reside close to the proton and neutron Fermi surface. The location of isomeric states provides a useful empirical calibration of shell model residual interaction between specific high- j orbitals. In addition, the neutron separation energy is predicted to reduce to a few MeV for heavy nuclei with $N = 126$, potentially creating conditions for weakly bound isomeric states.

In the past, this region of the chart of nuclides has been populated by cold fragmentation reactions [4]. The cited experiment, owing to technical difficulties, such as low primary beam intensity and low detection efficiency, could give structure information only up to ^{212}Pb . The experiment described in this paper was proposed with the aim of extending our knowledge towards more neutron-rich Pb isotopes. The predicted existence of isomeric states is used as an experimental tag to study the shell structure of these nuclei. The exploitation of an active stopper will also allow the study of the β -decay of the populated species.

2. – Experimental details

The nuclei of interest were produced by means of fragmentation of a relativistic ^{238}U beam at $1\text{ GeV}/u$, provided by the UNILAC-SIS GSI accelerator complex, on a $2\text{ g}/\text{cm}^2$ Be target. The resulting fragments were transmitted and separated using the FFragment Separator (FRS) [5].

The FRS consists of two double-dipoles stages intervened by a variable-thickness and variable-profile degrader. The FRS separates the nuclei by means of the $B\rho-\Delta E-B\rho$ scheme, and can be operated both in achromatic and monochromatic modes. Standard FRS detectors consist in position-sensitive TPC detectors placed in the intermediate and final focal planes, for trajectory reconstruction, two positon-sensitive fast scintillator detectors for TOF measurement, and two ionization chambers to measure the charge of the nuclei.

The nuclei of interest are transported to the final focal plane where the Stopped-beam RISING set up [6] is placed: it consists of a ball of 105 HPGe detectors grouped in Clusters of 7 elements each. The surrounding BGO anti-Compton shields were removed in order to place the detectors as close as possible to the stopper therefore increasing the

efficiency of the array. Each individual detector had two parallel preamplifier outputs, sent to two different acquisition branches. One is sent to 105 channels in Digital Gamma Finder (DGF-4C) modules [7]. The individual DGF channel triggers were validated by a master trigger signal generated from the plastic scintillator placed in the final focal plane (SCI41). This signal was sent to a DGF channel in each crate locating the DGF modules, in order to provide an internal check of the synchronization of the DGF clocks and also to provide a time-difference measurement of a delayed γ -ray via the DGF γ -time signal. The clock frequency of the DGF modules corresponds to 25 ns/channel. The maximum coincidence gate that can be achieved using these modules is 400 μ s. The second output from the germanium preamplifiers is sent to an analogue timing branch composed of a standard TFA-CFD-TDC timing circuit. The output of the CFD is again sent to two separate TDC modules, one named “short range” (1 μ s full range with a 0.31 ns/channel step), and the other named “long range”, up to 800 μ s with a 0.73 ns/channel.

In the present experiment an active stopper consisting of $9.5 \times 5 \text{ cm}^2$ 1 mm thick DSSSD, arranged in three rows of three elements each, was used to allow the study of the β -decay of the nuclei of interest [8]. Each detector consists of 16 front strips and 16 back strips, each with a width of 3 mm, thus providing 256 pixels to encode x and y positions. The Si detectors are used to identify both implantation and β -decay events. This poses stringent requirements on the electronics since it has to deal with signals generated by electrons with few MeV energy and heavy isotopes with energies in GeV range. MESYTEC MPR-32 logarithmic preamplifiers, which are linear up to 1–2 MeV and then have a logarithmic response in the implantation regime, were employed. While they are not suited to measure the entire energy loss they are indeed useful to disentangle the two different signals without saturating the modules. Two scintillator detectors were placed one in front and the other behind the Si array to serve as trigger and veto detectors for the implantation.

The scintillator detector placed in the final focal plane is also used as trigger for the implantation events, while an OR of the Si detectors was chosen as trigger for the β -decay events. An Al degrader with variable thickness is placed right before the Si stoppers in order to ensure the implantation of the nuclei in the Si detectors. Additionally the FRS was operated in monochromatic mode in order to optimise the implantation of the nuclei of interest in the Si.

The experiment, which lasted 6 days, consisted in the measurement of three different FRS settings: the first one, centring around ^{205}Pb was used to check the Z and A/Q calibration, thanks to the presence of known isomeric states in ^{205}Pb and neighbouring nuclei. Afterwards the FRS dipoles were set to transmit ^{215}Pb and then ^{217}Pb in the central trajectory to reach exotic species.

3. – Identification of nuclear species

The main difficulties in studying nuclei around neutron-rich Pb isotopes are threefold: primarily we have charge states of the primary beam with a similar A/Q ratio that can be transmitted up to the intermediate focal plane causing an overload of the detectors;

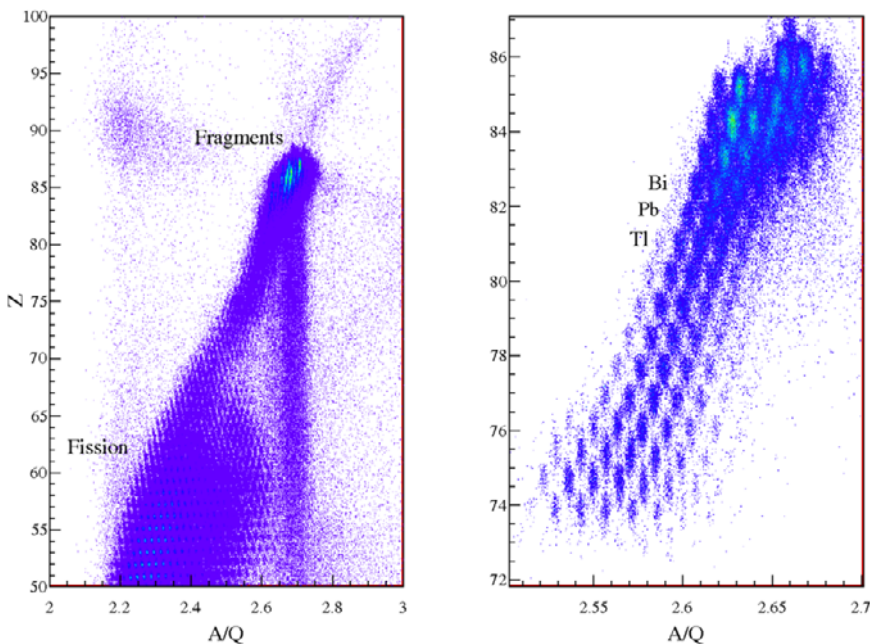


Fig. 1. – Left panel: Z vs. A/Q identification plot including all acquired events with no specific cleaning conditions. High- Z products and fission fragments are clearly visible in the picture. Right panel: same plot as in the left panel but with the selection of ions that did not change their charge state while traversing the S2 degrader (see fig. 2). A good resolution in both Z and A/Q is achieved.

secondarily the fragmentation reaction produces high- Z nuclei around Th and Ac with cross-sections larger than the nuclei of interest, being closer to the primary beam; and finally, one also has to deal with the production of several fission fragments due to the fission of ^{238}U . Several solutions have been applied in order to avoid these problems. An additional Al degrader (the so-called S1 degrader), 2.4 g/cm^2 thick, was placed after the first dipole to help rejecting heavy elements and charge states of the primary beam by changing their velocity. Narrow slits around the primary target helped focussing the reaction products forward, therefore selecting preferably fragmentation over fission reaction products, the latter having an almost isotropic distribution.

The calculated transmission of the FRS for the heavy nuclei addressed in this experiment is around 40%. In order to maximize this transmission, the velocity of the fragments should be kept as high as possible. Therefore the degrader in the intermediate focal plane was set to be the thinnest possible (700 mg/cm^2). Having a high recoil velocity also helps maintaining a good Z resolution in the MUSIC chambers.

Even using the aforesaid solutions the identification of the nuclei produced in the reaction is complicated (see fig. 1). The use of a thick production target and of a thick S1

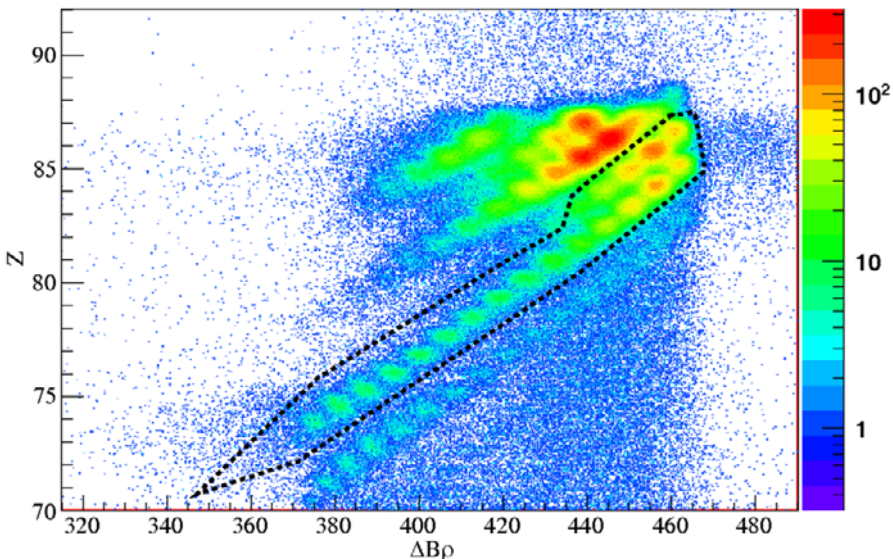


Fig. 2. – $\Delta B\rho$ vs. Z plot showing different locii corresponding to nuclei that changed their charge state between second and third FRS stage. The nuclei that did not change their charge state are indicated by a contour line.

degrader has the drawback of inducing changes in the charge state of the nuclei. This is a severe effect: predictions by the GLOBAL code [9] show that almost 40% of the nuclei pick up an electron when transversing these materials. This effect helps complicating the identification plot since nuclei that are in a different charge state fall in the same position in a Z vs. A/Q plot.

With the current set-up it is not possible to identify the charge state of the nuclei. The degrader at the central focal plane of the FRS was then used as a passive energy-loss device for charge state separation. The difference in magnetic rigidity between the first and second stage of the fragment separator can be used to estimate the energy loss of the ion through the degrader. This information, together with the energy loss of the ions as measured at the final focal plane using MUSIC detectors, allows an unambiguous charge state discrimination. This technique is of particular interest in case of heavy, neutron-rich nuclei [10]. By plotting the quantity $\Delta B\rho$ against Z we obtain the picture in fig. 2. Here different locii can be identified, corresponding to a modification of the charge state (by pick up or loss of electrons). A selection of nuclei that did not change their charge state between the first and second stage of the FRS helps clearing the ID plot and recognizing main structures in the spectrum. Such gate is shown in fig. 2 by a dotted line.

A number of isotopes for each nuclear species ranging from Hg ($Z = 80$) to Bi ($Z = 83$) were populated and implanted in each of the setting with the yields reported in table I.

TABLE I. – *Production and implantation yields for isotopes populated in the $^{215-217}\text{Pb}$ setting.*

Nucleus	^{215}Pb setting		^{217}Pb setting	
	Produced ions	% Implanted ions	Produced	% Implanted
^{206}Hg	570	89	120	73
^{207}Hg	1800	92	200	70
^{208}Hg	2300	92	600	87
^{209}Hg	1400	93	800	92
^{210}Hg	600	91	550	90
^{209}Tl	500	95	150	83
^{210}Tl	1900	93	400	75
^{211}Tl	3000	89	1100	89
^{212}Tl	2300	87	1400	85
^{213}Tl	1000	81	1000	86
^{212}Pb	400	88	300	80
^{213}Pb	2400	85	900	81
^{214}Pb	4700	84	2500	85
^{215}Pb	3400	78	2800	81
^{216}Pb	1400	72	1500	79
^{215}Bi	700	82	500	75
^{216}Bi	4500	74	2700	80
^{217}Bi	9500	70	7000	77
^{218}Bi	6600	52	7400	63
^{219}Bi	2700	35	3800	47

The condition for an ion to be implanted is that signal, for at least one Si pixel, has been registered in a defined range of energy.

4. – Isomeric decay

The use of a highly segmented γ spectrometer as the RISING Cluster ball is very useful in this kind of experiments where nuclei move at high relativistic energies (above 100 MeV/u), and are brought to a complete stop by degrading their energy in Al. This process creates a large background due to bremsstrahlung which blinds several crystals, reducing the efficiency for the measurement of isomeric decays in the same event. The high granularity of the RISING array is intended to overcome this problem. The multiplicity of this prompt-flash radiation varies with the atomic charge of the implanted nuclei, and is of the order of 10-15 crystals in standard cases [12].

In addition to a decrease in the efficiency, the presence of this prompt-flash radiation also causes problems in the time determination of isomeric decay. This is due to the time width of this prompt flash component, which can be estimated to be around 30 ns.

In order to identify each nuclear species we exploited the presence of isomeric states by constructing E_γ vs. T_γ matrices like the one in fig. 3, where isomeric states are clearly

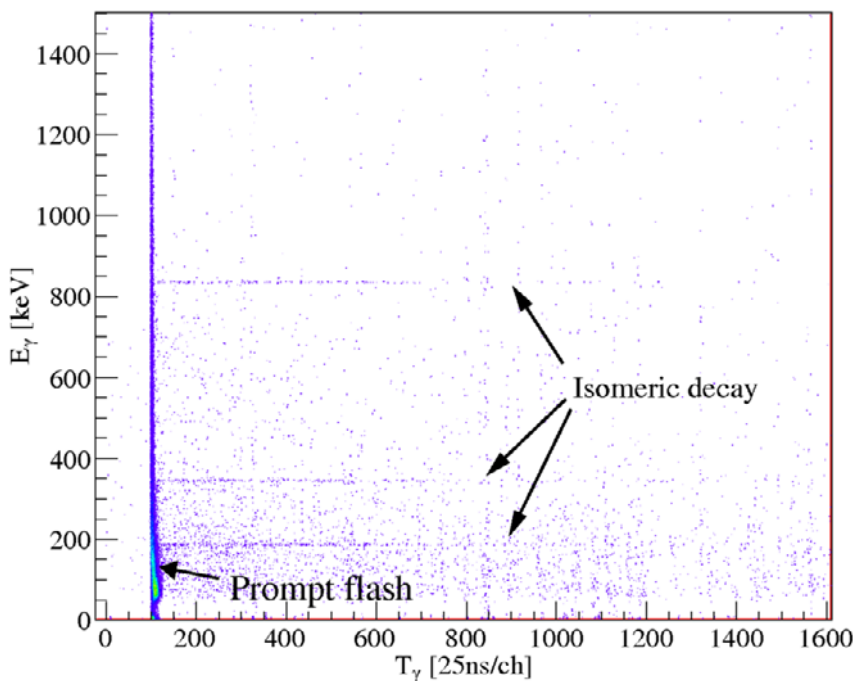


Fig. 3. – E_γ vs. T_γ for a given nucleus. Horizontal lines, indicated by arrows, correspond to the de-excitation of a long-living isomeric state. The intense prompt-flash peak is also indicated.

recognizable since they stand out as lines extending to longer times. The projection of such a matrix on the energy axis, cutting out the contribution of prompt decay due to bremsstrahlung, reveals clearly the energy of transitions that de-excite the isomer.

In this early stage of data analysis we concentrated our attention on the Pb isotopic chain, which was the primary goal of the experiment. As mentioned before Pb isotopes ranging from 212 to 218 were successfully populated and implanted.

An 8^+ seniority isomer is expected to be present in each of these nuclei. As expected we collected a very similar spectrum for each of the even isotopes, $^{212-214-216}\text{Pb}$. The γ line directly de-exciting the isomer, corresponding to the $8^+ \rightarrow 6^+$ transition, is never visible in the spectrum since it lies at very low energies, below the electronic threshold for the HPGe detectors. No isomer could be observed in ^{218}Pb , presumably owing to the shortening of the lifetime, expected for this isotope.

If we compare the ^{212}Pb spectrum (fig. 4) to the one measured by Pfutzner [4], the present experiment remeasured and confirmed the energies of the transitions deexciting the 8^+ isomer. An additional line, corresponding to the $2^+ \rightarrow 0^+$ transition, is measured for the first time. The extracted lifetime is also consistent with previous estimates.

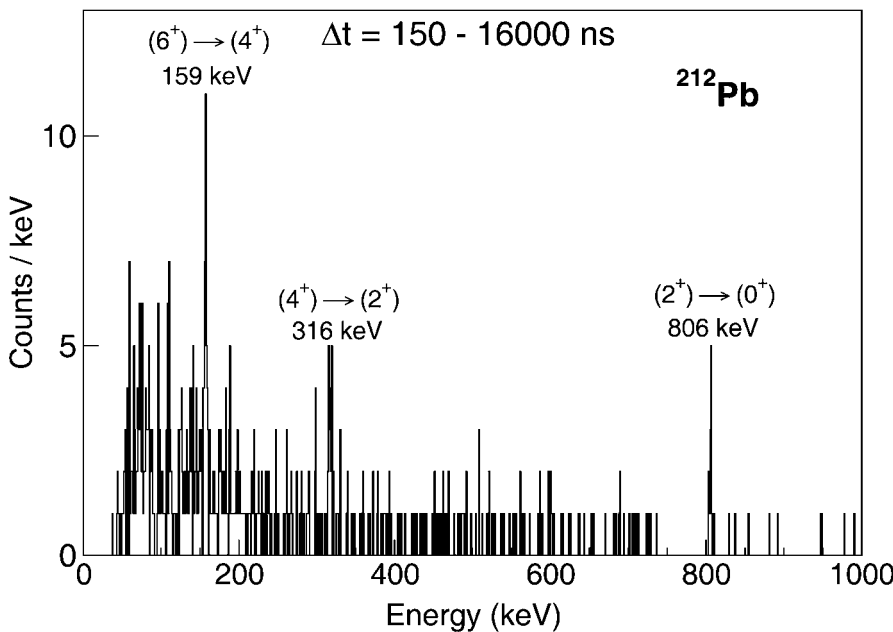


Fig. 4. – γ spectrum of the de-excitation of the 8^+ isomer in ^{212}Pb . Three main lines are visible in the spectrum.

5. – Conclusion and perspectives

This paper reported on a recent experiment aimed at populating isomeric states in heavy nuclei around doubly magic ^{208}Pb . The nuclei of interest were produced by relativistic fragmentation of ^{238}U beam and transported and separated by the GSI FRS separator. At the final focal plane the nuclei are brought to rest and their decay, both isomeric and β -decay, are analysed by the RISING active stopper setup.

Information on isomeric states in the Pb chain ranging from 212 to 218 has been extracted.

The on-going analysis aims at establishing the existence of other isomeric states in all the implanted chains of isotopes, in particular in Bi, Tl and Hg. Large-scale shell model calculations based on the Kuo-Herling interaction [13] are being set up in order to describe the structure of all these nuclei. The comparison will not only take into account the transition energies, but also $B(E2)$ will be estimated starting from the lifetime of the measured isomeric states.

Another important aspect that is being taken care of is the β -decay of the most exotic species. Correlation spectra between implanted ions and subsequent β events are being constructed. Owing to the predicted long lifetimes for the populated species (see [3]) and the high count rate, the evaluation of the background is a delicate issue that is now under close examination.

* * *

The excellent work of the GSI accelerator staff is acknowledged. The collaboration of this experiment includes: N. AL-DAHAN, J. ALCANTARA NUÑEZ, A. ALGORA, N. ALKHOMASHI, P. R. P. ALLEGRO, Y. AYYAD, J. BENLLIURE, P. BOUTACHKOV, M. BOWRY, A. BRACCO, A. M. BRUCE, M. BUNCE, E. CASAREJOS, F. C. L. CRESPI, F. CAMERA, A. CORSI, L. CORTES, A. M. DENIS BACELAR, A. DEO, Zs. DOMBRADI, C. DOMINGO-PRADO, M. DONCEL, K. EPPINGER, F. FARINON, G. F. FARRELLY, A. GADEA, H. GEISSEL, J. GERL, N. GOEL, M. GORSKA, A. GOTTARDO, J. GREBOSZ, E. GREGOR, T. HABERMAN, R. HOISCHEN R. JANIK, S. KLUPP, I. KOJOUHAROV, N. KURZ, S. LEONI, S. LUNARDI, S. MANDAL, R. MENEGAZZO, D. MENGONI, B. MILLION, D. R. NAPOLI, F. NAQVI, R. NICOLINI, C. NOCIFORO, M. PFÜTZNER, S. PIETRI, T. PISSULLA, Zs. PODOLYAK, A. PROCHAZKA, W. PROKOPOWICZ, F. RECCHIA, M. W. REED, P. H. REGAN, R. V. RIBAS, D. RUDOLPH, E. SAHIN, H. SCHAFFNER, A. SHARMA, B. SITAR, D. SIWAL, K. STEGER, P. STRMEN, T. P. D. SWAN, I. SZARKA, J. J. VALIENTE-DOBÓN, P. M. WALKER, H. WEICK, O. WIELAND and H.-J. WOLLERSHEIM.

REFERENCES

- [1] BRODA R., *J. Phys. G: Nucl. Part. Phys.*, **32** (2006) R151.
- [2] DE WITTE H. *et al.*, *Phys. Rev. C*, **69** (2004) 044305.
- [3] BORZOV I. N., *Phys. Rev. C*, **67** (2003) 025802.
- [4] PFÜTZNER M. *et al.*, *Phys. Lett. B*, **444** (1998) 32.
- [5] GEISSEL H. *et al.*, *Nucl. Instrum. Methods B*, **70** (1992) 286.
- [6] PIETRI S. *et al.*, *Acta Phys. Pol. B*, **38** (2007) 1255.
- [7] http://www.xia.comDGF-4C_Download.html.
- [8] KUMAR R. *et al.*, *Nucl. Instrum. Methods A*, **598** (2009) 754.
- [9] SCHEIDENBERGER C. *et al.*, *Nucl. Instrum. Methods B*, **142** (1998) 441.
- [10] AUDOUIN L. *et al.*, *Nucl. Instrum. Methods Phys. Res. A*, **381** (1996) 462.
- [11] DETISTOV P. *et al.*, *Acta Phys. Pol. B*, **38** (2007) 1287.
- [12] PIETRI S. *et al.*, *Eur. Phys. J. ST*, **150** (2007) 319.
- [13] WARBURTON E. K. and BROWN A., *Phys. Rev. C*, **43** (1991) 602.

This page intentionally left blank

Proceedings of the International School of Physics “Enrico Fermi”
Course CLXXVIII “From the Big Bang to the Nucleosynthesis”, edited by A. Bracco and E. Nappi
(IOS, Amsterdam; SIF, Bologna)
DOI 10.3254/978-1-60750-974-5-377

Neutron spectroscopic factors

JENNY LEE

*National Superconducting Cyclotron Laboratory and Department of Physics and Astronomy
Michigan State University - East Lansing, MI 48824, USA*

RIKEN, Nishina Center - 2-1 Hirosawa, Wako, Saitama 351-0198, Japan

M. B. TSANG

*National Superconducting Cyclotron Laboratory and Department of Physics and Astronomy
Michigan State University - East Lansing, MI 48824, USA*

Joint Institute of Nuclear Astrophysics, MSU - East Lansing, MI 48824, USA

Summary. — Spectroscopic factors are fundamental quantities in nuclear physics. They have been extensively used in understanding the single-particle properties of nuclear structures and astrophysical network calculations. Neutron spectroscopic factors of 88 ground state and 565 excited states for $Z = 3\text{--}28$ stable nuclei from (d, p) and (p, d) transfer reactions have been extracted using a systematic approach with minimum assumptions. This extensive set of data suggests that the extracted spectroscopic factors are in good agreement with the predictions of the large-basis shell-model predictions. We have extended the analysis to the experimental data obtained from inverse neutron transfer reaction of proton-rich ^{34}Ar and neutron-rich ^{46}Ar . The experimental results show little reduction of the ground-state neutron spectroscopic factor of the proton-rich nucleus ^{34}Ar compared to that of ^{46}Ar . The results suggest that correlations, which generally reduce such spectroscopic factors, do not depend strongly on the neutron-proton asymmetry of the nucleus in this isotopic region as was reported in knockout reactions. The present results are consistent with results from systematic studies of transfer reactions and the dispersive-optical model analysis, but are inconsistent with the trends observed in knockout reaction measurements.

1. – Introduction

Transfer reaction is a powerful probe to study the single-particle structure in a nucleus. The single-particle nature is governed by the nucleon-nucleon (N - N) correlations which modify the nuclear wave functions from the independent particle mean-field model. These correlations manifest themselves indirectly through the reduction in the occupancy of a single-particle state which is quantified by the spectroscopic factor (SF).

Mathematically, spectroscopic factor is defined by a matrix element between the initial state in the entrance channel and the final state in the exit channels [1,2]. For an $A(d,p)B$ one-nucleon transfer reaction, for example, this matrix element evaluates the degree to which the wave function of the final nucleus B can be described by the initial nucleus A plus a neutron in a specific single-particle orbit. For the one-step transfer reaction in the Distorted-Wave Born Approximation (DWBA), the experimental spectroscopic factor is the ratio of the experimental cross-sections to the cross-sections calculated within a reaction model. The overlap integral between the wave functions of one state in nucleus A and another state in nucleus B for transfer between these states gives the theoretical counterpart [1, 2]. Measurements of spectroscopic factors therefore provide quantitative information about the single-particle structure of nuclei, and connect the experimental results to theoretical nuclear structure in the shell model calculations.

In the past half-century, transfer reaction has been used as an experimental tool to obtain abundant spectroscopic information for stable nuclei. With the recent revived interest in transfer reactions stemming from the availability of radioactive beams with high luminosity, it is essential to review and understand the existing theoretical reaction models of transfer reactions, and develop a systematic framework to study the structures from stable to exotic nuclei. In this article, the methodology to extract consistent spectroscopic factors systematically using published angular distributions of (p,d) and (d,p) transfer reactions is introduced in sect. 2. Based on this framework, a survey of deduced ground-state and excited-state spectroscopic factors of $Z = 3\text{--}28$ stable nuclei is described in sect. 3, which provides checks for the descriptions of nucleon correlations in the current nuclear structure calculations. Section 4 presents the extension of transfer reaction measurements to the exotic Ar isotopes and discusses the asymmetry dependence of nucleon correlations based on the relative spectroscopic factor.

2. – Extraction of spectroscopic factors from transfer reactions

Transfer reactions provide most of the spectroscopic factor information for stable nuclei in the past half century. However, it is not unusual to find published spectroscopic factors for a particular nucleus that fluctuate by a factor of two as shown in the left panel of fig. 1.

In this case, ^{41}Ca should be a well-understood nucleus as composed of a neutron outside the closed ^{40}Ca core and the ground-state neutron spectroscopic factor should be one. Instead, many different spectroscopic factors values were extracted from $^{40}\text{Ca}(d,p)^{41}\text{Ca}$ reactions. Similarly, one can often find that published spectroscopic factor values for

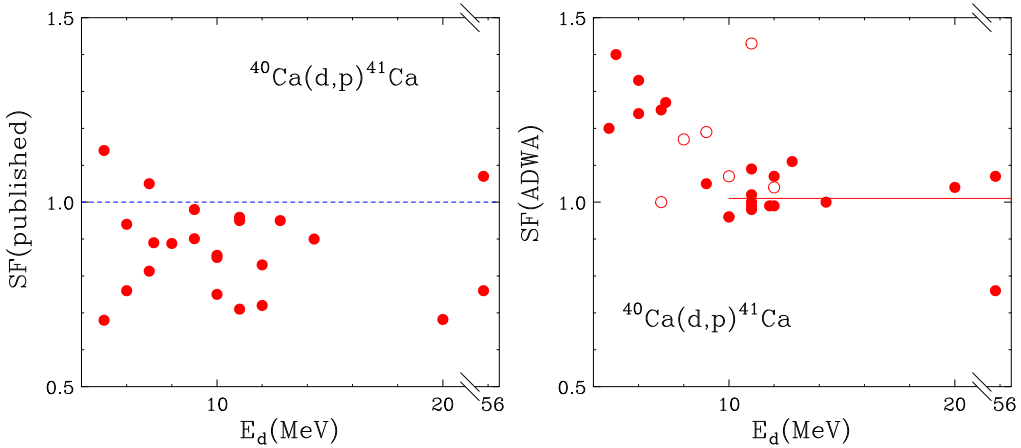


Fig. 1. – Left: fluctuations in the published ground-state spectroscopic factors of ^{41}Ca extracted from $^{40}\text{Ca}(d,p)^{41}\text{Ca}$ reactions. The blue dashed line is the shell model prediction. (Right) Extracted ground-state spectroscopic factors of ^{41}Ca using the systematic approach described in this work. The red solid line is the averaged value of spectroscopic factors for $E_d > 10 \text{ MeV}$.

the same reaction by different authors agree within uncertainties, even though the data used to extract them are not in agreement [3]. Many of the difficulties in the past extractions of spectroscopic factors have been associated with ambiguities in the optical model parameterizations which are used in the DWBA model to construct the distorted waves of incoming and outgoing reaction channels. Geometries of the bound-state radial wave functions of the transferred particle are strongly correlated to the magnitudes of the spectroscopic factors [1, 2]. In addition, the deuteron breakup effects have been found to be important in the calculated angular distributions and deduced spectroscopic factors [4]. These inconsistencies in spectroscopic factor extractions hinder the use of transfer reactions from studying evolution of nuclear structures, such as the shell evolution along the isotopic or isotonic chains. Therefore it is crucial to develop a systematic approach to extract consistent and reliable relative spectroscopic factors from transfer reactions.

A consistent three-body analysis of neutron transfer reaction data involving minimal assumptions has been developed for (p, d) and (d, p) transfer reactions [5, 6]. The methodology uses Adiabatic Distorted-Wave Approximation (ADWA), an extension of DWBA theory with the Johnson-Soper (JS) adiabatic approximation to the neutron, proton, and target three-body system [4] taking into account the deuteron break-up. To avoid the ambiguity in optical potentials obtained from individual best fits to elastic scattering data, Chapel-Hill 89 global nucleon-nucleus optical potentials [7] are used and these neutron and proton potentials are folded to obtain the deuteron optical potential. Nonlocality corrections with range parameters of 0.85 fm and 0.54 fm for the proton and deuteron channels, respectively, are assumed [8]. The deuteron finite-range corrections are calculated

using the local energy approximation and the strength ($D_0^2 = 150006.25 \text{ fm}^3$) and range ($\beta = 0.7457 \text{ fm}$) parameters of the Reid soft-core 3S_1 - 3D_1 neutron-proton interaction [9]. For simplicity, a central neutron potential of Woods-Saxon shape with fixed radius ($r_0 = 1.25 \text{ fm}$) and diffuseness ($a_0 = 0.65 \text{ fm}$) parameters is assumed and the depth of potential is adjusted to reproduce the experimental binding energy. We use the University of Surrey version of TWOFNR [10], a direct reaction model code, to calculate the angular distributions [3, 5, 6].

We reanalyze the data sets of $^{40}\text{Ca}(d,p)^{41}\text{Ca}$ using the systematic ADWA analysis approach. Consistent spectroscopic factors of ^{41}Ca are obtained as shown in the right panel of fig. 1. The increase of spectroscopic factors at $E_d < 10 \text{ MeV}$ is attributed to the resonance structures in the elastic scattering of the deuterons [11], which is not taken into account in the present reaction model. Between 10 to 56 MeV, we find that the mean spectroscopic factor, 1.01 ± 0.06 shown by the solid line, describes the data at all energies within experimental errors. Same methodology was applied to extract ground-state and excited-state SF values for lithium to nickel isotopes from extensive measured (d,p) and (p,d) angular distributions as presented in sect. 3. The comprehensive studies demonstrate the usefulness of the systematic method with minimum assumption in extracting consistent and reliable SF values from transfer reactions.

3. – Survey of spectroscopic factors from transfer reactions for stable nuclei

Eighty-eight ground-state and 565 excited-state neutron spectroscopic factors have been extracted using the systematic analysis as discussed in sect. 2. In the simplest shell model, the pairing interaction couples pairs of neutrons to spin zero similar to the Cooper pairs in a superconductor. Group of paired nucleons with magic numbers form a core. The nucleons outside the core are called valence nucleons which interact independently of each other and with the mean field of the core. In this description of Independent Particle Model (IPM), one can obtain a simple relationship between the number of valence nucleons (n) and the spectroscopic factors [3] for nuclei with even number of valence neutrons (n) exceed those of the neighboring odd n nuclei

$$(1) \quad \text{SF} = n \quad \text{for } n = \text{even}; \quad \text{SF} = 1 - \frac{n-1}{2j+1} \quad \text{for } n = \text{odd}.$$

The left panel of fig. 2 compares the experimentally extracted ground-state SF's for nuclei with predictions from the independent particle model plus pairing. Open symbols represent odd- Z elements and the closed symbols represent even- Z elements. The line indicates perfect agreement. Most extracted values are less than the predictions of the IPM-plus-maximal-pairing as represented by eq. (1). This is expected because the IPM neglects many important correlations between the nucleons in orbits near the Fermi energy as well as nucleon-core and short-range corrections [12].

It is well known that if one diagonalizes the residual interaction within a Large-Basis Shell-Model, LB-SM [13] that involves the mixing of several different orbitals in the shell model basis close to the Fermi energy, one can obtain a better description of the nucleus.

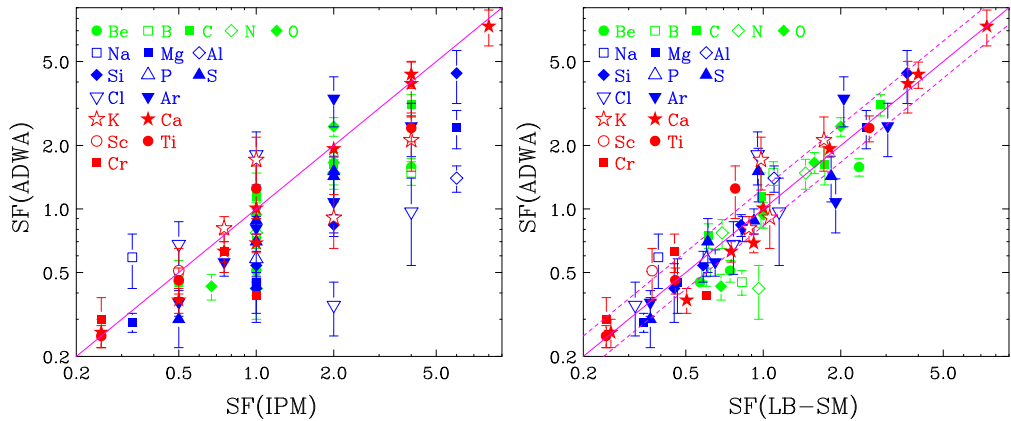


Fig. 2. – Comparison of experimental spectroscopic factors to predictions from the independent particle model of eq. (1) (left panel) and Large-Basis-Shell-Model (LB-SM) (right panel). Open and closed symbols denote elements with odd and even Z , respectively. The solid lines indicate perfect agreement. For reference, the two dashed lines in the right panel indicate $\pm 20\%$ of the solid line.

Using Oxbash code with the PPN, SPSDPF, SDPN, SD, and FPPN model space and the corresponding CKPPN, WBP, WPN, W, and FPBPPN interactions [13,14] as input, the ground-state neutron SF's for 74 nuclei have been calculated with uncertainties of about 10–20% [12]. Their predicted values are compared to the data in the right panel of fig. 2. In contrast to the IPM-plus-pairing calculations, the agreement between data and LB-SM predictions are within 20% for most cases, as indicated by the two dashed lines. This shows that the correlations between nucleons in orbits near the Fermi energy included in the LB-SM calculation are the most important one to consider [12].

The excited-state SF values are of particular interest because they are needed in astrophysical network calculations. Based on the same methodology, we have extracted 565 neutron spectroscopic factors of *sd*- and *fp*-shell nuclei. We are able to compare 125 of the extracted spectroscopic factors to values predicted by LB-SM calculations and evaluate the accuracies of spectroscopic factors predicted by different interactions [15].

Two interactions, USDA and USDB, have been obtained to describe *sd* shell nuclei with an inert ^{16}O core [16]. Figure 3 (left) shows the comparison of experimental excited states spectroscopic factors, SF(ADWA), to predictions from large-basis shell-model calculations, SF(LB-SM). The ends of the horizontal error bars indicate the range of values predicted by USDA and USDB interactions. Symbols indicate the averaged values. The solid line represents perfect agreement between data and theory. The dashed lines correspond to $\pm 30\%$ deviations (expected experimental uncertainties) from the solid line. There are three states ($3.908 \text{ MeV} (5/2^+)$ state in ^{25}Mg , $7.692 \text{ MeV} (3/2^+)$ and $8.290 \text{ MeV} (5/2^+)$ states in ^{29}Si), with very small calculated spectroscopic factors (< 0.005), outside the range of the established systematics. Small calculated SFs originate from large cancellations of contributions from different components of the wave functions, which are

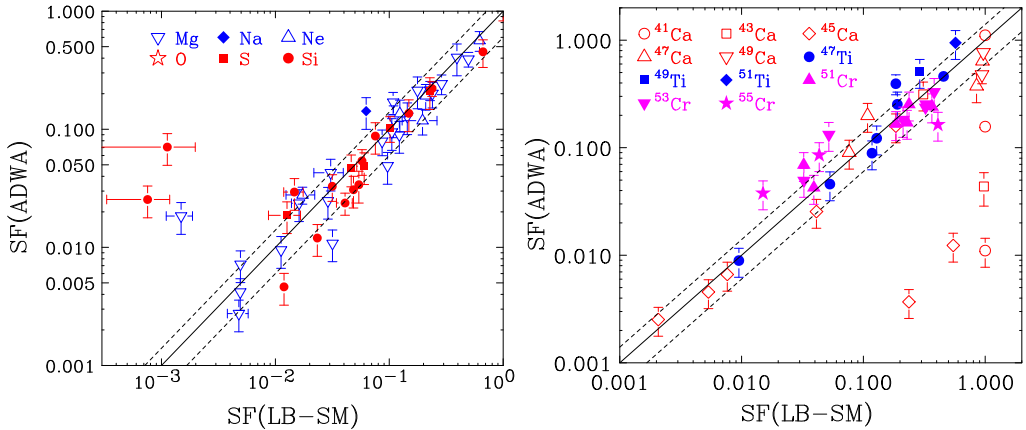


Fig. 3. – Comparison of experimental spectroscopic factors to predictions from the LB-SM for the *sd*-shell nuclei (left panel) and for Ca, Ti and Cr isotopes (right panel). The solid lines indicate perfect agreement. For reference, the two dashed lines in the right panel indicate $\pm 30\%$ of the solid line (see text).

hard to control even in the best shell-model calculation. Indeed, the calculated values using USDA and USDB interactions differ from each other by more than a factor of 2 and underpredict the experimental values by more than a factor of 10. Clearly, these cases would be important to examine further both experimentally and theoretically as the capability of predicting very small (< 0.005) spectroscopic factors of *sd* shell nuclei is important for astrophysical applications.

Beyond the *sd* shell nuclei, regions of interest will be around the $N = 20, 28$ and $Z = 20, 28$ magic shell closures. The right panel of fig. 3 compares both experimental ground-state and excited-state spectroscopic factors, SF(ADWA), to predictions from large-basis shell-model for the ^{41,43,45,47,49}Ca, ^{47,49,51}Ti and ^{51,53,55}Cr isotopes, SF(LB-SM). Complete basis with the interaction GXPF1A is used in the theoretical calculations [17, 18]. The solid line indicates perfect agreement between data and predictions. Dashed lines represent $\pm 30\%$ deviations from the solid line. The calculated and measured SFs near the boundaries of the *fp* shell-model space can disagree by factors of hundreds. The largest discrepancies when using the modern GXPF1A interaction [17, 18] occur for the 2.462 MeV ($p_{3/2}$) and 6.870 MeV ($f_{5/2}$) states in ⁴¹Ca, the 2.944 MeV ($p_{3/2}$) state in ⁴³Ca and the 4.312 MeV ($p_{1/2}$) and 4.468 MeV ($p_{1/2}$) states in ⁴⁵Ca, most of which have theoretical predicted spectroscopic factors near unity. This is consistent with the observation that for nuclei near the closed shell, the LB-SM calculations give similar predictions as the Independent Particle Model (IPM). Because of proximity of these nuclei to the *sd* shell, their excited-state wave functions have strong contributions from particle-hole excitations that lie outside the *fp* model space [19]. It is rather difficult at the present time to include hole excitations of the *sd* shell core as reliable effective interactions will be required for the larger *sd-fp* shell Hilbert space. In contrast, the excited states of midshell nuclei, such as Ti and Cr, do not have this problem.

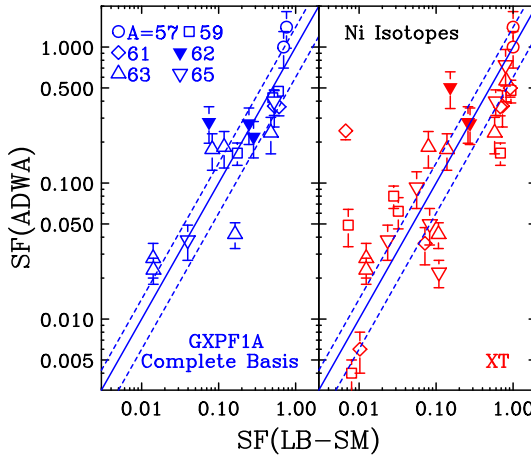


Fig. 4. – Comparison of the experimental SF values, SF(ADWA) and the shell-model calculations with the GXPF1A interaction in the pf model space (left panel) and the JJ4PNA interaction in gfp model space (right panel). The solid line indicates perfect agreement between data and predictions. Dashed lines represent $\pm 30\%$ deviations from the solid line.

For Ni isotopes, subsets of the extracted spectroscopic factors are compared to predictions of large-basis shell models in the full pf model space using the GXPF1A effective interaction [17, 18], and the $(f_{5/2}, p_{3/2}, p_{1/2}, g_{9/2})$ model space using the JJ4PNA interaction [20] as shown in fig. 4. Only excited states at energy level below 3.5 MeV are shown. The extracted spectroscopic factors cluster around the shell model values, but the agreement of the spectroscopic factors between data and calculations is not better than a factor of two. Since the experimental uncertainties are in the order of 20–30%, the data can be used to evaluate newer interactions in the pf and $(f_{5/2}, p_{3/2}, p_{1/2}, g_{9/2})$ model spaces. The results indicate improvement of interactions in this model space is needed [21].

A priori, transfer reactions do not yield absolute spectroscopic factors as the analysis depends on other input parameters such as the geometry of the neutron bound-state wave function as well as the optical potentials used in the reaction model. However, if the analysis utilizes a consistent set of parameters, the relative spectroscopic factors can be determined reliably. Relative SF values are sufficient to study the evolution of nuclear structure; while the absolute normalization in SF magnitude is only required to determine how much correlation removes the single-particle strengths from the Hilbert space in which the shell model states are degenerated.

Since the shell model includes the effects of correlations within the model space, but not those outside the model space, the shell model spectroscopic factors represent the upper limit. Reduction of the spectroscopic factors is one signature of the correlations experienced by the nucleons. This is evidenced in the smaller SF values predicted by the large-basis shell-model compared to those predicted by the Independent Particle Model.

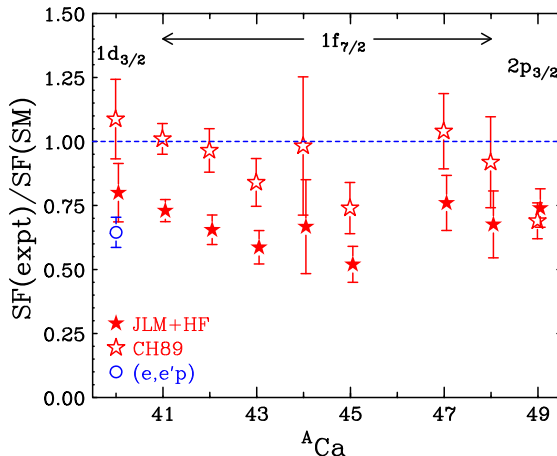


Fig. 5. – Ratios of the experimentally deduced spectroscopic factors to those of the shell-model SF(SM) for the calcium isotopic chain. The open and closed symbols are SF values extracted using CH89 and JLM+HF approach, respectively.

Constant quenching ($\sim 30\text{--}40\%$) of the proton SF values are observed in the studies of $(e, e'p)$ reactions for nuclei near the closed shell compared to the independent particle model (IPM) expectations [22]. For nuclei near the closed shell, the LB-SM calculations give similar predictions as the IPM model. The suppression of the proton spectroscopic factors extracted in the $(e, e'p)$ study has been attributed to the insufficient treatment of nucleon-nucleon correlations including both short- and long-range correlations in the current shell models [23].

To study the suppression of the spectroscopic factors in transfer reactions over a range of nuclei, we use the microscopic potentials with constraints based on physics input. We use the Jeukenne, Lejeune and Mahaux (JLM) nucleon optical interactions [24] and constraint the density of the potential as well as the transferred neutron orbital rms radii with the Hartree-Fock (HF) calculations [25]. With the JLM+HF method, an overall $\sim 30\%$ suppression in SF values for most nuclei is obtained [26]. Figure 5 shows the SF values deduced using CH89 and JLM+HF method for Ca isotopes to illustrate the consistent SF reductions in transfer reaction analysis. The open circle in the same figure denotes the result from $^{40}\text{Ca}(e, e'p)$ measurement.

4. – Transfer reaction measurements for exotic Ar isotopes

Based on the consistent ADWA framework, the comprehensive analyses of transfer reaction data shown in sect. 2 suggest that the reduction factors R_s , defined as the ratio of the experimental spectroscopic factor to prediction, are independent of the neutron binding energy for stable nuclei within statistical errors [15, 26]. The reduction factor quantifies the percentage of correlation absent in the shell model descriptions. To understand

the regions of extreme N/Z , measurements of (p, d) neutron transfer reactions involving proton-rich ^{34}Ar and neutron-rich ^{46}Ar beams were performed. These measurements were done in inverse kinematics to extract the experimental neutron SFs for ^{34}Ar and ^{46}Ar . The difference between neutron and proton separation energy ($\Delta S = Sn - Sp$), which characterizes the asymmetry dependence of relative shift for neutron and proton Fermi surface, is 12.41 MeV and -10.03 MeV for ^{34}Ar and ^{46}Ar , respectively. In previous global studies the maximum ΔS is 7.31 MeV with a few measurements at ΔS smaller than -10 MeV. This significantly expands the separation energy difference of isotopes. The ^{34}Ar results would highlight the correlations effects in the proton-rich regime [27].

In the present experiments, the deuteron angular distributions from $p(^{34}\text{Ar}, d)^{33}\text{Ar}$ and $p(^{46}\text{Ar}, d)^{45}\text{Ar}$ transfer reactions were measured using radioactive secondary beams of ^{34}Ar and ^{46}Ar at 33 MeV/nucleon at the National Superconducting Cyclotron Laboratory at Michigan State University [28]. The $p(^{36}\text{Ar}, d)^{35}\text{Ar}$ reaction was also measured using a degraded ^{36}Ar primary beam at 33 MeV/nucleon for comparison with published normal kinematics data [29]. These beams were transported and focused on CH_2 targets with areal densities of 7.10 mg/cm^2 for $^{34,36}\text{Ar}$ and 2.29 mg/cm^2 for ^{46}Ar reactions. Deuterons were detected in the High-Resolution Array (HiRA) [30] in coincidence with the recoil residues detected in the S800 focal plane [31,32]. An array of 16 HiRA telescopes [30] was placed at 35 cm from the target where they subtended polar angles of $6^\circ \leq \theta_{\text{lab}} \leq 45^\circ$. Each telescope contained $65 \mu\text{m}$ thick ΔE and $1500 \mu\text{m}$ thick E silicon strip detectors, backed by 3.9 cm thick CsI(Tl) crystals. The strips in these telescopes effectively subdivided each telescope into 1024 $2 \text{ mm} \times 2 \text{ mm}$ pixels. Detailed descriptions of experimental setup can be found in ref. [33].

Deuterons were identified in HiRA with standard energy loss techniques using the energy deposited in the ΔE and E silicon strip and CsI detectors. Reaction residues were identified in the S800 spectrometer using the energy loss and the time-of-flight (TOF) information of the focal plane detectors [31,32]. Figure 6 (a-c) show the Q value spectra determined event by event of deuterons that stop in the thick Si detector for $p(^{34,36,46}\text{Ar}, d)^{33,35,45}\text{Ar}$. The observed resolutions of 500, 470 and 410 keV FWHM for the transitions to the ground states of $^{33,35,45}\text{Ar}$ respectively agree with the expectation from GEANT4 [34] simulations taking into account the finite beam spot size, the energy resolution of the Si detectors, energy loss and angular straggling in the target. Measurements using a 1.7 mg/cm^2 carbon target reveal that the background is negligible when both deuteron and the heavy recoil are detected. The absolute normalization of the cross-section was achieved to within 10% by directly counting the beam particles with a Micro-Channel Plate detector [35,36] placed $\sim 10 \text{ cm}$ upstream of the target which also provide the start TOF signal for particles detected by the S800 spectrometer.

Figures 6(d), 6(e) and 6(f) show the differential cross-sections for the ground-state transition of $p(^{34}\text{Ar}, d)^{33}\text{Ar}$, $p(^{36}\text{Ar}, d)^{35}\text{Ar}$, and $p(^{46}\text{Ar}, d)^{45}\text{Ar}$, respectively. The solid circles in the lower panels denote the data from present measurements and the open squares in fig. 6(e) denote $^{36}\text{Ar}(p, d)^{35}\text{Ar}$ data in normal kinematics with 33.6 MeV proton beam [29]. The agreement between the two experiments is very good [33]. For $p(^{46}\text{Ar}, d)^{45}\text{Ar}$ reaction, the ground state ($f_{7/2}$) and the first excited state (542 keV, $p_{3/2}$)

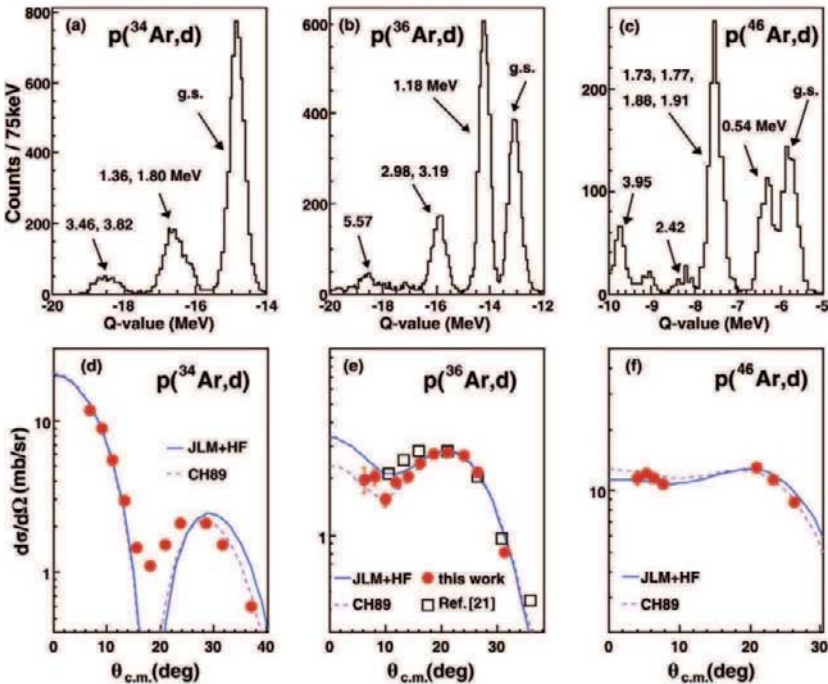


Fig. 6. – Q -value spectrum ((a)–(c), top panels) and ground-state deuteron angular distributions ((d)–(f), bottom panels) of $p(^{34,36,46}\text{Ar}, d)^{33,35,46}\text{Ar}$. The open squares in panel (e) are data from previous normal kinematics experiments [21]. The solid and dashed lines represent the calculations using JLM+HF and CH89 approach, respectively [27].

cannot be resolved for center-of-mass angles larger than 8° . Fortunately, the angular distributions of the ground state ($l = 3$) and first excited state ($l = 1$) are very different. Specifically, the angular distribution for the excited state exhibits a deep minimum near $\theta_{\text{c.m.}} = 20\text{--}27^\circ$, close to a factor of 100 smaller than that of ground state, therefore, the cross-sections for the ground state could be unambiguously extracted [33].

The dashed curves in figs. 6(d-f) show the ADWA calculations using the CH89 potential with the conventional neutron bound-state Woods-Saxon potential parameter, $r_0 = 1.25$ and $a_0 = 0.65$ fm. The solid lines in figs. 6(d-f) show the ADWA calculations using the JLM microscopic potential and the bound-state neutron potential, which have been constrained by Hartree-Fock calculations. Both calculations reproduce the shape of experimental angular distributions. Normalizing the ADWA model calculations to the data gives the SF values. Similar to previous analysis, SF(JLM+HF) values are about 30% smaller than the SF(CH89) values. The ground-state neutron SF's for ^{34}Ar and ^{36}Ar were calculated in the sd -shell model space using USDB effective interaction [16]. The ground-state neutron SF for ^{46}Ar was calculated in the sd - pf model space using the interaction developed by Nummela *et al.* [37].

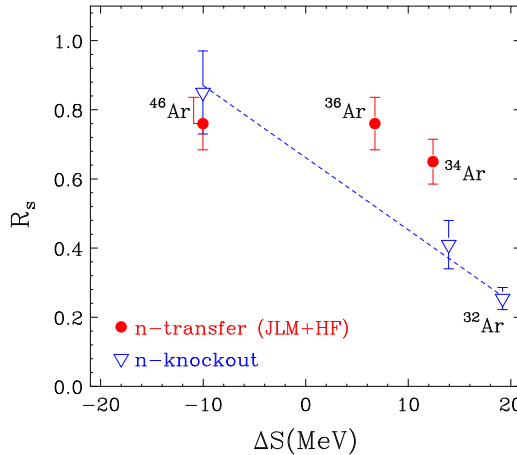


Fig. 7. – R_s are plotted as a function of the difference in the neutron and proton separation energies, ΔS , as open circles ($R_s(\text{CH89}) = \text{SF}(\text{CH89})/\text{SF}(\text{LB-SM})$) and closed circles ($R_s(\text{JLM + HF}) = \text{SF}(\text{JLM + HF})/\text{SF}(\text{LB-SM})$).

The weak dependence of reduction factors on the asymmetry of the three Ar isotopes is similar to the trends obtained from the recent dispersive-optical-model analysis of elastic-scattering and bound-level data for $^{40-49}\text{Ca}$ isotopes [38]. In contrast, a much larger systematic suppression in SFs has been reported for the knockout reactions [39], when the removed nucleon has a large separation energy or asymmetry. As shown by the open triangles in fig. 7, the neutron R_s extracted from knockout reactions for ^{34}Ar is approximately a factor of two smaller than that for ^{46}Ar [39]. Even larger reductions have been observed for neutron knockout from ^{32}Ar [39], a nucleus for which transfer data is not available. This suggests that there is a systematic difference between the conclusions drawn from these two probes for the spectroscopic factors of strongly bound particles. Thus a re-examination of the reaction theory description of transfer reactions and knockout reactions including the input parameters used in these analyses may be needed.

5. – Conclusions

Utilizing global optical-model potentials and consistent sets of parameters systematically, the long-standing inconsistency and ambiguities in the nucleon-nucleus potentials as well as single-particle parameters can be resolved. As a result, relative spectroscopic factors can be determined over a wide range of nuclei. The survey of neutron spectroscopic factors provides important benchmarks for the neutron-transfer reaction studies and an independent mean to test the residual interactions and Hilbert spaces used in the current nuclear structure calculations.

To extend the studies to exotic region, we have extracted the neutron ground-state spectroscopic factors of proton-rich ^{34}Ar and neutron-rich ^{46}Ar and stable ^{36}Ar nuclei

using (p, d) transfer reactions with radioactive beams in inverse kinematics. Consistent with previous systematic studies with stable nuclei, the reduction factors for symmetric ^{36}Ar and neutron-rich ^{46}Ar are similar. The weak dependence of reduction factors on the asymmetry of the three Ar isotopes is similar to the trends obtained from the recent dispersive-optical-model analysis of elastic-scattering data for $^{40-49}\text{Ca}$ isotopes.

* * *

This work was supported by the National Science Foundation under Grant Numbers PHY-060007, and PHY-0822648. This proceeding is an adaptation of the PhD thesis of JENNY LEE [33].

REFERENCES

- [1] AUSTERN N., *Direct Nuclear Reaction Theories* (John Wiley & Sons, New York) 1970.
- [2] GLENDENNING NORMAN K., *Direct Nuclear Reactions* (World Scientific Publishing) 2004.
- [3] LEE JENNY, TSANG M. B. and LYNCH W. G., *Phys. Rev. C*, **75** (2007) 064320 and references therein.
- [4] JOHNSON R. C. and SOPER P. J. R., *Phys. Rev. C*, **1** (1970) 976.
- [5] LIU X. D. *et al.*, *Phys. Rev. C*, **69** (2004) 064313.
- [6] LIU X. D., PhD thesis, Michigan State University (2005) http://groups.nscl.msu.edu/nscl_library/Thesis/Liu,%20Xiaodong.pdf.
- [7] VARNER R. L. *et al.*, *Phys. Rep.*, **201** (1991) 57.
- [8] PEREY F. G., *Nuclear Spectroscopy and Reactions*, edited by CERNY J. (Academic, New York) 1974.
- [9] KNUTSON L. D., THOMSON J. A. and MEYER H. O., *Nucl. Phys. A*, **241** (1975) 36.
- [10] IGARASHI M. *et al.*, Computer Program TWOFNR (Surrey University version).
- [11] OHLSSEN G. G. and SHAMU R. E., *Nucl. Phys.*, **45** (1963) 523.
- [12] TSANG M. B., LEE JENNY and LYNCH W. G., *Phys. Rev. Lett.*, **95** (2005) 222501.
- [13] BROWN B. A., *Prog. Part. Nucl. Phys.*, **47** (2001) 517.
- [14] BROWN B. A. *et al.*, Computer program, <http://www.nscl.msu.edu/~brown/resources/oxbash-august-2004.pdf>.
- [15] TSANG M. B., LEE JENNY, SU S. C., DAI J. Y., HOROI M., LIU H., LYNCH W. G. and WARREN S., *Phys. Rev. Lett.*, **102** (2009) 062501.
- [16] BROWN B. A. and RICHTER W. A., *Phys. Rev. C*, **74** (2006) 034315.
- [17] HONMA M., OTSUKA T., BROWN B. A. and MIZUSAKI T., *Phys. Rev. C*, **69** (2004) 034335.
- [18] HONMA M., OTSUKA T., BROWN B. A. and MIZUSAKI T., *Eur. Phys. J. A*, **25**, Suppl. 1 (2005) 499.
- [19] HONMA M., OTSUKA T., BROWN B. A. and MIZUSAKI T., *Phys. Rev. C*, **65** (2002) 061301(R).
- [20] LISETSKIY A. *et al.*, *Phys. Rev. C*, **70** (2004) 044314.
- [21] LEE JENNY *et al.*, *Phys. Rev. C*, **79** (2009) 054611.
- [22] KRAMER G. J., BLOK H. P. and LAPIK'AS L., *Nucl. Phys. A*, **679** (2001) 267, and references therein.
- [23] DICKOFF W. H. and BARBIERI C., *Prog. Part. Nucl. Phys.*, **52** (2004) 377.
- [24] JEUKENNE J.-P. *et al.*, *Phys. Rev. C*, **1** (1970) 976.
- [25] BROWN B. A., *Phys. Rev. C*, **58** (1998) 220.
- [26] LEE JENNY *et al.*, *Phys. Rev. C*, **73** (2006) 044608.

- [27] LEE JENNY *et al.*, *Phys. Rev. Lett.*, **104** (2010) 112701.
- [28] MORRISSEY D. J. *et al.*, *Nucl. Instrum. Methods Phys. Res. B*, **204** (2003) 90.
- [29] KOZUB R. L., *Phys. Rev.*, **172** (1968) 1078.
- [30] WALLACE M. S. *et al.*, *Nucl. Instrum. Methods Phys. Res. A*, **583** (2007) 302.
- [31] YURKON J. *et al.*, *Nucl. Instrum. Methods Phys. Res. A*, **422** (1999) 291.
- [32] BAZIN D. *et al.*, *Nucl. Instrum. Methods Phys. Res. B*, **204** (2003) 629.
- [33] CHING HUI and LEE JENNY, PhD thesis, Michigan State University (2010) http://groups.nscl.msu.edu/nscl_library/Thesis/Lee,%20Hui%20Ching.pdf.
- [34] AGOSTINELLI S. *et al.*, *Nucl. Instrum. Methods Phys. Res. A*, **506** (2003) 250.
- [35] SHAPIRA D. *et al.*, *Nucl. Instrum. Methods Phys. Res. A*, **449** (2000) 396.
- [36] SHAPIRA D. *et al.*, *Nucl. Instrum. Methods Phys. Res. A*, **454** (2000) 409.
- [37] SIGNORACCI A. and BROWN B. A., *Phys. Rev. Lett.*, **99** (2007) 099201.
- [38] CHARITY R. J. *et al.*, *Phys. Rev. C*, **76** (2007) 044314.
- [39] GADE A. *et al.*, *Phys. Rev. C*, **77** (2008) 044306 and reference therein.

This page intentionally left blank

Proceedings of the International School of Physics “Enrico Fermi”
Course CLXXVIII “From the Big Bang to the Nucleosynthesis”, edited by A. Bracco and E. Nappi
(IOS, Amsterdam; SIF, Bologna)
DOI 10.3254/978-1-60750-974-5-391

Measurement of isospin mixing in hot ^{80}Zr compound nucleus

A. CORSI, A. BRACCO, F. CAMERA, F. C. L. CRESPI, A. GIAZ, S. LEONI,
R. NICOLINI and V. VANDONE

Dipartimento di Fisica, Università di Milano and INFN, Sezione di Milano - Milano, Italy

O. WIELAND, G. BENZONI, N. BLASI, S. BRAMBILLA and B. MILLION

INFN, Sezione di Milano - Milano, Italy

S. BARLINI, L. BARDELLI, M. BINI, G. CASINI, A. NANNINI, G. PASQUALI
and G. POGGI

Dipartimento di Fisica, Università di Firenze and INFN, Sezione di Firenze - Firenze, Italy

V. L. KRAVCHUK, M. CINAUSERO, M. DEGERLIER, F. GRAMEGNA and T. MARCHI

INFN, Laboratori Nazionali di Legnaro - Legnaro, Italy

D. MONTANARI

Dipartimento di Fisica, Università di Padova and INFN, Sezione di Padova - Padova, Italy

G. BAIocco, M. BRUNO, M. D’AGOSTINO, L. MORELLI and G. VANNINI

Dipartimento di Fisica, Università di Bologna and INFN, Sezione di Bologna - Bologna, Italy

M. CIEMALA, M. KMIECIK, A. MAJ, K. MAZUREK, W. MECZYNSKI and S. MYALSKI

The Henryk Niewodniczański Institute of Nuclear Physics PAN - Krakow, Poland

Summary. — Isospin mixing induced by Coulomb interaction has been measured in the compound nucleus $^{80}\text{Zr}^*$ with $Z = N = 40$ at $T \sim 2$ MeV produced in a fusion-evaporation reaction. The observable sensitive to the isospin purity of the compound nucleus is the giant dipole resonance γ decay. The Coulomb spreading width of the $I = I_0 + 1$ state and the degree of isospin mixing of the compound nucleus has been obtained via statistical model analysis of the measured γ spectrum.

1. – Isospin mixing in nuclei

In the isospin formalism, neutrons and protons are assumed to be different states of the nucleon with values $1/2$ and $-1/2$ of the projection I_z of the isospin operator I . According to this definition, the projection of isospin operator for a nucleus can be written as

$$(1) \quad I_z = (N - Z)/2.$$

Isospin symmetry is largely preserved by the nuclear interactions and the main violations of isospin symmetry are due to the Coulomb interaction [1]. The effect of isospin symmetry violation is that, strictly speaking, isospin is not a good quantum number for the nucleus. In most cases this effect can be neglected or is small enough to be treated in a perturbative way.

The nuclear force prefers the states with the lowest possible isospin I_0 consistent with the given I_z , that is $I_0 = I_z$, corresponding to completely aligned isospin. This rule holds well for all even-even and odd-mass nuclei and it breaks down only in several odd-odd self-conjugate nuclei like ^{34}Cl , ^{42}Si , ^{42}Sc and ^{46}V , where $I = 0$ and $I = 1$ states are almost degenerate [2].

The isospin mixing can be described as a polarization induced by the Coulomb interaction which has the effect of populating states with $I > I_0$. In first-order perturbation theory the admixture of $I = I_0 + 1$ states into $I = I_0$ states can be written as

$$(2) \quad \alpha^2 = \sum_{I=I_0+1} \frac{|\langle I = I_0 + 1 | H_c | I = I_0 \rangle|^2}{(E_{I=I_0+1} - E_{I=I_0})^2},$$

where H_c is the isovector part of the Coulomb potential. Since the Coulomb potential preserves angular momentum J and parity π , it can couple only states with the same J^π and, more efficiently, with similar spatial wave function.

The results of theoretical calculations on ^{80}Zr are collected in table I:

Taking into account only the non-analytic methods, the results listed in table I range from 2.5% to 4.5% as obtained in the most recent non-perturbative calculation. Indeed

TABLE I. – Several theoretical calculations of $\alpha_{I_0+1}^2$ are quoted from the references listed in the last column in chronological order. The abbreviation HF stands for Hartree-Fock, EDF for Energy Density Functionals, TDA for Tamm-Dancoff approximation. In the third column are listed the different parameterizations of Skyrme interaction used in non-analytic approaches.

$\alpha_{I_0+1}^2$ (%)	Method	Interaction	Ref.
1	analytic		[3]
3.6	HF+TDA	SG2	[4]
3.1	HF+TDA	SIII	[4]
3	HF spherical	SIII	[5]
2.5	HF deformed	SIII	[5]
3.9	HF	SIII	[6]
2.21	analytic		[6]
4.5	EDF	SLy4	[7]

the dependence of the results on the method used as well as the lack of experimental data for nuclei with $Z > 32$ [8, 9] calls for new measurements.

At higher excitation energy, the levels come closer and also develop a finite width Γ . This fact can be still accounted for in first-order perturbation theory introducing a complex energy.

$$(3) \quad \alpha^2 = \sum_{I=I_0+1} \left| \frac{\langle I = I_0 + 1 | H_c | I = I_0 \rangle}{(E_{I=I_0+1} + i\Gamma_{I=I_0+1}/2) - (E_{I=I_0} + i\Gamma_{I=I_0}/2)} \right|^2.$$

The maximum of α^2 is expected to occur when the level spacing became similar to the width of the states [10]. At high excitation energy, as the ones reached by the compound nucleus (CN) populated in heavy-ion fusion reactions, the compound decay width $\Gamma_{\text{CN}}^\uparrow$ increases and the lifetime decreases according to the Heisenberg rule. Wilkinson first suggested that the hot CN may decay before isospin mixing has been achieved, producing a restoration of isospin symmetry at high temperature [11].

Harney, Richter and Weidenmüller have developed a formalism to describe isospin mixing between two classes of states $|I_<\rangle = |I_0, I_z\rangle$ and $|I_>\rangle = |I_0 + 1, I_z\rangle$ of the hot CN [12]. By analogy with other symmetry-breaking mechanisms, they describe the isospin mixing of states $|I_<\rangle$ into states $|I_>\rangle$ in terms of a spreading width Γ^\downarrow defining the timescale of symmetry breaking induced by the Coulomb interaction H_c :

$$(4) \quad \Gamma_>^\downarrow = 2\pi |\langle I_> | H_c | I_< \rangle|^2 \rho(I_<).$$

$\Gamma_>^\downarrow$ is physically equivalent to the spreading width of the isobaric analog state (IAS) and changes only slowly (if at all) with CN excitation energy. $\Gamma_<^\downarrow$ can be defined exchanging

TABLE II. – *The CN decay width $\Gamma_{\text{CN}}^\uparrow$ (MeV) and Coulomb mixing width Γ_c^\downarrow followed by the corresponding lifetime τ and τ_{mixing} for the CN⁸⁰Zr calculated within the Statistical Model. The values are given for ⁸⁰Zr* CN at $T = 2.1$ MeV and for two nuclei populated along its decay cascade. The corresponding average nuclear temperatures of the CN (T) are listed in the first column.*

T (MeV)	$\Gamma_{\text{CN}}^\uparrow$ (keV)	τ (s)	Γ^\downarrow (keV)	τ_{mixing} (s)
2.1	230	$2.8 \cdot 10^{-21}$	10	$6.4 \cdot 10^{-20}$
1.9	150	$4.4 \cdot 10^{-21}$	10	$6.4 \cdot 10^{-20}$
1.8	130	$4.9 \cdot 10^{-21}$	10	$6.4 \cdot 10^{-20}$

$>$ and $<$ and is linked to $\Gamma_>^\downarrow$ by the detailed balance once level density ρ is defined both for $|I_<\rangle$ and $|I_>\rangle$ states:

$$(5) \quad \Gamma_<^\downarrow = \frac{\rho(I_>)}{\rho(I_<)} \Gamma_>^\downarrow.$$

Within the S -matrix formalism, the fraction $\alpha_<^2$ of states $|I_<\rangle$ that mix to states $|I_>\rangle$ can be written in terms of the Coulomb spreading width $\Gamma_{<,>}^\downarrow$ and CN decay width $\Gamma_{<,>}^\uparrow$ as

$$(6) \quad \alpha_<^2 = \frac{\Gamma_{>}/\Gamma_<} {1 + \Gamma_{<}/\Gamma_<^\uparrow + \Gamma_{>}/\Gamma_>^\uparrow}.$$

Similarly, the fraction $\alpha_>^2$ of states $|I_>\rangle$ that mix to states $|I_<\rangle$ is

$$(7) \quad \alpha_>^2 = \frac{\Gamma_{>}/\Gamma_>} {1 + \Gamma_{>}/\Gamma_>^\uparrow + \Gamma_{<}/\Gamma_<^\uparrow}.$$

The restoration of isospin symmetry due to the finite lifetime of the CN is accounted for by the competition between CN decay width $\Gamma_{\text{CN}}^\uparrow$ and Coulomb spreading width Γ^\downarrow . These widths are associated to a lifetime via Heisenberg rule. Typical values are listed in table II for the decay of ⁸⁰Zr*.

2. – Measurement of isospin symmetry via Giant Dipole Resonance

The Giant Dipole Resonance (GDR) statistically populated on hot compound nuclei decays via particles or E1- γ emission. In the long-wavelength approximation ($\lambda \gg$ nuclear dimension, with $\lambda \sim 100$ fm for $E_\gamma = 15$ MeV and the radius of an $A = 80$ nucleus ~ 5 fm) E1 transitions are isovector and therefore follow the selection rules for isovector transitions which prescribe $I_{\text{final}} = I_{\text{initial}} \pm 1$, in self-conjugate (*i.e.* with $N = Z$) nuclei. Therefore, γ decay in self-conjugate nuclei mediated by the isovector Giant Dipole Resonance (GDR) is forbidden from an $I_{\text{initial}} = 0$ to an $I_{\text{final}} = 0$ state and takes places only due to the admixture of components with $I > 0$, which can γ decay to $I = 0$ states.

TABLE III. – For each reaction, E_{beam} is the energy of the incoming beam, CN is the compound nucleus produced, $I_z = (N - Z)/2$ the third component of isospin quantum number, E^* the excitation energy, $\langle J \rangle$ the average angular momentum of the CN and T the average nuclear temperature of the CN. The average is performed within the Statistical Model calculation adopting the PHOSWICH-gated CN spin-population cross-section.

Reaction	E_{beam} (MeV)	CN	I_z	E^* (MeV)	$\langle J \rangle (\hbar)$	T (MeV)
$^{37}\text{Cl} + ^{44}\text{Ca}$	153	^{81}Rb	7/2	83	38	2.2
$^{40}\text{Ca} + ^{40}\text{Ca}$	200	^{80}Zr	0	83	42	2.1

The degree of mixing of the initial CN can be evaluated in the framework of Statistical Model. A description of the statistical decay of the hot CN is implemented in the computer code CASCADE developed by Pühlhofer [13]. Harakeh [14] and, subsequently, Behr [15] have implemented a version of CASCADE code including the isospin formalism, which has been used in this analysis (see subsect. 4·2).

3. – Description of the experiment

The experiment was performed at Laboratori Nazionali di Legnaro (Italy) with beams delivered by the TANDEM-ALPI accelerator complex.

The used detection apparatus included the HECTOR array of 8 large-volume BaF₂ scintillators for high energy γ -ray detection [16], the GARFIELD setup of 96 ΔE - E telescopes for light-charged particles identification [17] and 32 PHOSWICH triple-stage scintillators from FIASCO array used to select fusion-evaporation reactions [18]. Both GARFIELD and PHOSWICH detectors are equipped with fast digital sampling electronics for the analysis of the electric signals [19, 20].

The acquisition system was triggered by the PHOSWICH detectors (covering an angle between 5° and 13° degrees with respect to the beam axis). The bias in the phase-space population of the detected residues induced by their geometrical efficiency has been taken into account as described in sect. 4.

The reactions measured are listed in table III.

Both the reactions produce a compound nucleus of mass ~ 80 at $E^* = 83$ MeV but with different I_z . In both reactions, N/Z of projectile and target nucleus are very similar and no dynamical dipole contribution [21] is expected in the measured γ spectra.

As explained in sect. 2, the GDR γ decay from $^{80}\text{Zr}^*$ is an observable sensitive to the degree of mixing in the compound nucleus. Conversely, since the GDR γ decay of the $I_z = 7/2$ compound nucleus ^{81}Rb is not forbidden, it can be used as a reference to tune the GDR and Statistical Model parameters. In fact, the last ones are sensitive to the bulk properties of the nucleus (mass and shape) and to its excitation energy and temperature, that are very similar for the two measured systems. The last assumption will be verified in subsect. 4·1 by comparing the slope of light charged particles spectra.

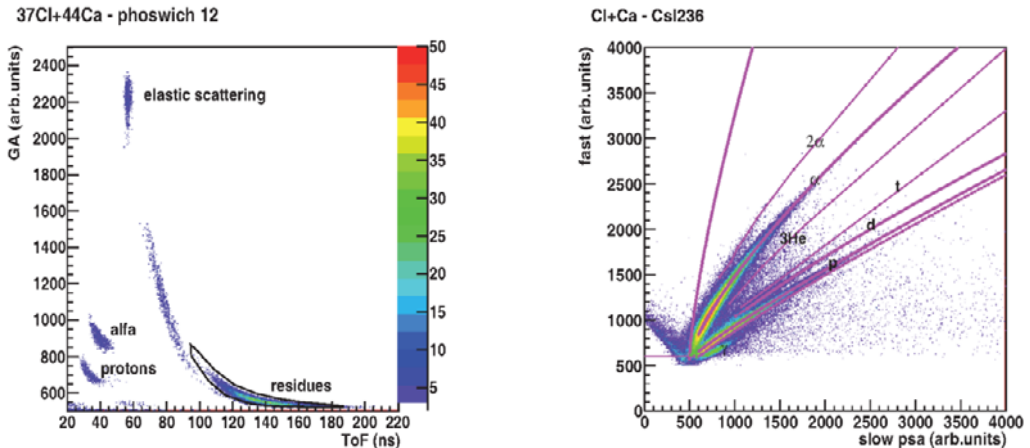


Fig. 1. – Left panel: light output of the first scintillator layer (GA) *vs.* time of flight in one of the PHOSWICH detectors. Elastically scattered beam, light charged particles and fusion-evaporation residues have been identified as specified by the labels. The graphical cut encircling the fusion-evaporation residues is the one used to select the fusion-evaporation channel. Right panel: fast *vs.* slow psa matrix, with slow psa = $3.5 \times$ (slow – 4 \times fast), of one of the CsI detectors of GARFIELD array. The identification lines are drawn on the top of the ridges corresponding to different isotopes.

4. – Data analysis

4.1. Data reduction. – The events of interest in this analysis are the ones detected in coincidence with a fusion-evaporation residue in PHOSWICH detectors. The identification of fusion-evaporation residues in one of the PHOSWICH detectors is shown in the left panel of fig. 1.

Light charged particles spectra have been detected by PHOSWICH and GARFIELD arrays, but only the last one yields the information on their energy. Light charged particles identification has been performed with pulse-shape analysis of the light output of CsI detector which constitute the *E* stage of GARFIELD telescopes. The isotopic identification is shown in the fast *vs.* slow matrix in the right panel of fig. 1.

The energy spectra of light charged particles are shown in fig. 2. It can be noticed that the slope of the spectra, that is sensitive to the effective temperature of the decay, is the same for the two reactions. This observation confirms the validity of our method consisting in using ^{81}Rb as a reference system for ^{80}Zr as far as statistical model parameters are concerned.

4.2. Statistical model analysis. – The γ spectrum measured in coincidence with fusion-evaporation residues (plotted with dots in fig. 3) has been analyzed with the version of CASCADE statistical model code which includes the appropriate isospin physics in CN population and decay [14, 15]. The used population cross-section as a function of angular momentum was not the standard one but it was the one obtained taking into account the

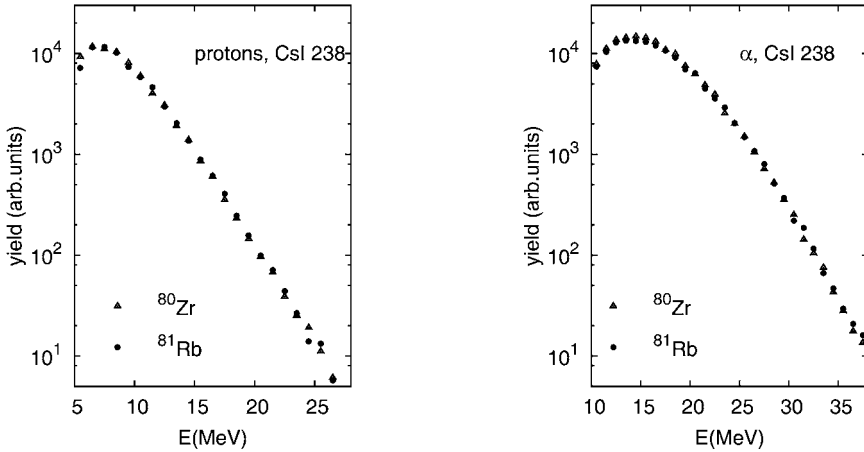


Fig. 2. – Proton (left) and α (right) energy spectra from one CsI detector of GARFIELD array. In each panel, the emission from ^{80}Zr (hollow triangles) is compared with the one from ^{81}Rb (filled dots).

phase-space selection induced by the PHOSWICH geometrical acceptance. The analysis was performed with a recursive fitting procedure based on χ^2 minimization technique. The analysis of the reference system ^{81}Rb has allowed to extract GDR parameters to be used for the system ^{80}Zr . In a second step, the Coulomb spreading width Γ^\downarrow , that

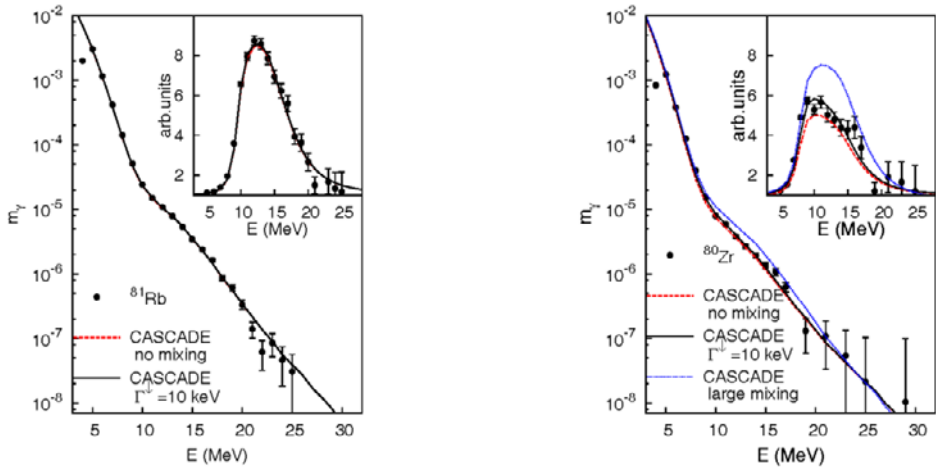


Fig. 3. – Measured γ -multiplicity spectra (filled dots) for ^{81}Rb (left panel) and ^{80}Zr (right panel) compared with best-fitting statistical model calculation [13-15]. The insets display the spectra (both measured and from CASCADE calculation) divided by a spectrum without GDR in order to better emphasize the GDR peak shape. The long-dashed curves are obtained without mixing, *i.e.* $\Gamma_\downarrow = 0$, the continuous curve with the best fitting $\Gamma_\downarrow = 10$ keV, while the short-dotted curve (plotted only for ^{80}Zr) with a very large mixing.

TABLE IV. – Best-fitting parameters obtained from the statistical model analysis [14,15], together with their statistical error: centroid, E_{GDR} (MeV), width Γ and strength S of GDR (obtained from ^{81}Rb analysis) and Coulomb spreading width $\Gamma_>^\downarrow$ (obtained from ^{80}Zr analysis).

E_{GDR} (MeV)	Γ (MeV)	S	$\Gamma_>^\downarrow$ (keV)
16.2 ± 0.17	10.8 ± 0.2	0.9 ± 0.035	10 ± 3

is a free parameter in this version of CASCADE, has been tuned to obtain the best-fitting curve (continuous line in fig. 3, right panel) for the γ decay of ^{80}Zr . Finally, we have verified that the set of best-fitting parameters listed in table IV still reproduces the γ -decay spectrum of ^{81}Rb .

As a further check, we have also tried to reproduce the γ -decay spectrum of ^{80}Zr without enabling isospin mixing. This is possible only using a much smaller width $\Gamma = 9.7$ MeV, that does not allow any more to reproduce the γ -decay spectrum of ^{81}Rb . Therefore both decay spectra can be reproduced simultaneously (*i.e.* with the same set of GDR parameters) only introducing isospin mixing.

5. – Results and conclusions

This analysis has allowed to obtain the GDR parameters for mass ~ 80 compound nuclei at $E^* = 83$ MeV. Furthermore, the hindrance of GDR γ decay in the self-conjugate nucleus ^{80}Zr has allowed to evaluate the degree of isospin mixing achieved by the compound nucleus. Within the statistical model, a set of CN with different angular momenta J and temperatures T is initially populated and the isospin mixing parameter is calculated separately for each J . It is common in the literature to express the degree of mixing as a weighted average of the γ yield. This procedure in our case yields an average isospin mixing parameter $\alpha_<^2 = 0.05 \pm 0.01$.

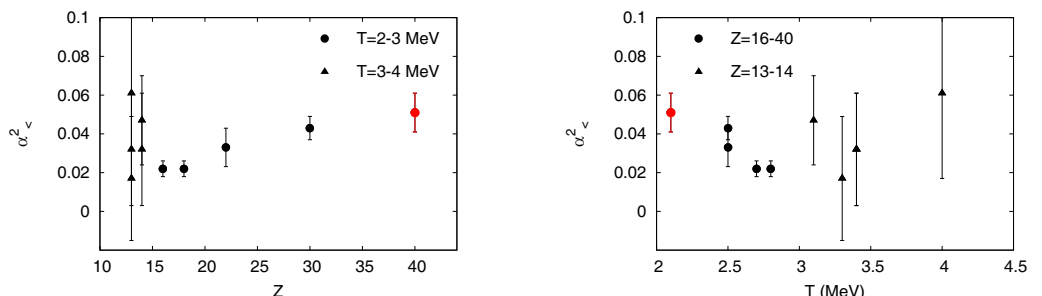


Fig. 4. – (Colour on-line) Systematics of $\alpha_<^2$ measured via GDR decay of the hot CN with $Z = 13\text{--}14$ and $T = 3\text{--}4$ MeV (triangles) [15] and with $Z = 16\text{--}40$ and $T = 2\text{--}3$ MeV (dots) [8, 22, 23]. The result obtained from the analysis described in subsect. 4.2 belongs to the second group and is plotted with a red square. The left panel displays the dependence of $\alpha_<^2$ on atomic number Z , the right panel the dependence on nuclear temperature T .

The existing systematics on $\alpha_{<}^2$ obtained from the analysis of CN decay with the same procedure is presented in fig. 4 [8, 15, 22, 23]. One can see that, if the comparison is limited to the systems with $Z = 16\text{--}40$ and $T = 2\text{--}3\text{ MeV}$, the expected increase of $\alpha_{<}^2$ with increasing Z and decrease with increasing temperature is found.

Since the data in fig. 4 have been measured at finite temperature, the corresponding value of $\alpha_{<}^2$ and its trend cannot be directly compared with the calculations performed for the nuclear ground state. Therefore, further investigations are required in order to compare the results obtained within this procedure (that indeed works only for the decay of hot CN) with the ones resulting from calculations in the nuclear ground state (see table I).

* * *

This work has been supported by the INFN and partially by the Polish Ministry of Science and Higher Education (Grants No. N N202 309135).

REFERENCES

- [1] AUERBACH N., HÜFNER J., KERMAN A. K. and SHAKIN C. M., *Phys. Rev. Lett.*, **23** (1969) 484.
- [2] SOPER J. M., *Isospin in Nuclear Physics. Isospin Purity of Low-Lying Nuclear States*. (North-Holland Publishing Company) 1969.
- [3] BOHR A. and MOTTELSON B., *Nuclear Structure I* (W.A. Benjamin, Inc., New York) 1969.
- [4] HAMAMOTO I. and SAGAWA H., *Phys. Rev. C*, **48** (1993) R960.
- [5] DOBACZEWSKI J. and HAMAMOTO I., *Phys. Lett. B*, **345** (1995) 181.
- [6] COLÒ G., NAGARAJAN M. A., VAN ISACKER P. and VITTURI A., *Phys. Rev. C*, **52** (1995) R1175.
- [7] SATULA W., DOBACZEWSKI J., NAZAREWICZ W. and RAFALSKI M., *Phys. Rev. Lett.*, **103** (2009) 012502.
- [8] KICIŃSKA-HABIOR M., *Nucl. Phys. A*, **36** (2005) 1133.
- [9] FARNEA E., DE ANGELIS G., GADEA A., BIZZETI P. G., DEWALD A., EBERTH J., ALGORÀ A., AXIOTIS M., BAZZACCO D., BIZZETI-SONA A. M., BRANDOLINI F., COLÒ G., GELLETLY W., KACI M. A., KINTZ N., KLUG T., KRÖLL T., LENZI S. M., LUNARDI S., MARGINEAN N., MARTINEZ T., MENEGAZZO R., NAPOLI D. R., NYBERG J., PAVAN P., PODOLYÁK Z., PETRACHE C. M., QUINTANA B., RUBIO B., SPOLAORE P., STEINHARDT T., TAIN J. L., THELEN O., UR C. A., VENTURELLI R. and WEISZFLOG, M., *Phys. Lett. B*, **551** (2003) 56.
- [10] BEHR J. A., *Giant Dipole Radiation and Isospin Purity in Highly Excited Compound Nuclei*. PhD thesis, University of Washington (1991).
- [11] WILKINSON D. H., *Phil. Mag.*, **1** (1956) 379.
- [12] HARNEY H. L., RICHTER A. and WEIDENMÜLLER H. A., *Rew. Mod. Phys.*, **58** (1986) 607.
- [13] PÜHLHOFER F., *Nucl. Phys. A*, **280** (1977) 267.
- [14] HARAKEH M. N., DOWELL D. H., FELDMAN G., GARMAN E. F., LOVEMAN R., OSBORNE J. L. and SNOVER K. A., *Phys. Lett. B*, **176** (1986) 297.
- [15] BEHR J. A., SNOVER K. A., GOSSETT C. A., KICIŃSKA-HABIOR M., GUNDLACH J. H., DREBI Z. M., KAPLAN M. S. and WELLS D. P., *Phys. Rev. Lett.*, **70** (1993) 3201.

- [16] WIELAND O., BRACCO A., CAMERA F., BENZONI G., BLASI N., BRAMBILLA S., CRESPI F., GIUSSANI A., LEONI S., MASON P., MILLION B., MORONI A., BARLINI S., KRAVCHUK V. L., GRAMEGNA F., LANCHAIS A., MASTINU P., MAJ A., BREKIESZ M., KMIECIK M., BRUNO M., GERACI E., VANNINI G., CASINI G., CHIARI M., NANNINI A. and ORDINE A., *Phys. Rev. Lett.*, **97** (2006) 012501.
- [17] GRAMEGNA F., ABBONDANNO U., ANDREANO A., BASSINI R., BONUTTI F., BRUNO M., CASINI G., D'AGOSTINO M., MANZIN G., MARGAGLIOTTI G. V., MASTINU P. F., MILAZZO P. M., MORONI A., SQUARCINI M., TONETTO F., VANNINI G. and VANNUCCI L., *Nucl. Instrum. Methods Phys. Res. A*, **389** (1997) 474.
- [18] BINI M., CASINI G., OLMI A., POGGI G., STEFANINI A. A., BARDELLI L., BARTOLI A., BIDINI L., COPPI C., CARMINE P. D., MANGIAROTTI A., MAURENZIG P. R., PASQUALI G., PIANTELLI S., POGGI S., TACCETTI N. and VANZI E., *Nucl. Instrum. Methods Phys. Res. A*, **515** (2003) 497.
- [19] BARDELLI L., POGGI G., BINI M. and PASQUALI G., *Nucl. Instrum. Methods Phys. Res. A*, **572** (2007) 882.
- [20] PASQUALI G., CIARANFI R., BARDELLI L., BINI M., BOIANO A., GIANNELLI F., ORDINE A. and POGGI G., *Nucl. Instrum. Methods Phys. Res. A*, **570** (2007) 126.
- [21] CORSI A., WIELAND O., KRAVCHUK V. L., BRACCO A., CAMERA F., BENZONI G., BLASI N., BRAMBILLA S., CRESPI F. C. L., GIUSSANI A., LEONI S., MILLION B., MONTANARI D., MORONI A., GRAMEGNA F., LANCHAIS A., MASTINU P., BREKIESZ M., KMIECIK M., MAJ A., BRUNO M., D'AGOSTINO M., GERACI E., VANNINI G., BARLINI S., CASINI G., CHIARI M., NANNINI A., ORDINE A., DI TORO M., RIZZO C., COLONNA M. and BARAN V., *Phys. Lett. B*, **679** (2009) 197.
- [22] WÓJCIK E., KICIŃSKA-HABIOR M., KIJĘWSKA O., KOWALCZYK M., KISIELIŃSKI M. and CHOIŃSKI J., *Acta. Phys. Pol. B*, **37** (2006) 207.
- [23] WÓJCIK E., KICIŃSKA-HABIOR M., KIJĘWSKA O., KOWALCZYK M., KISIELIŃSKI M. and CHOIŃSKI J., *Acta. Phys. Pol. B*, **38** (2007) 1496.

POSTERS

This page intentionally left blank

Proceedings of the International School of Physics “Enrico Fermi”
Course CLXXVIII “From the Big Bang to the Nucleosynthesis”, edited by A. Bracco and E. Nappi
(IOS, Amsterdam; SIF, Bologna)
DOI 10.3254/978-1-60750-974-5-403

Identification of hadrons at high momentum with the HMPID detector in the ALICE experiment at the LHC

F. BARILE on behalf of the ALICE COLLABORATION

*Dipartimento Interateneo di Fisica “M. Merlin” and INFN, Sezione di Bari
via E. Orabona 4, 70126 Bari, Italy*

Summary. — The LHC physics programme envisages to collide lead ions with the aim to recreate the conditions just after the Big Bang under laboratory conditions. ALICE features an experimental layout optimized to study this physics topic. The ALICE-HMPID detector has been designed to identify charged hadrons (π , K, p) in the momentum range $1 \leq p \leq 5 \text{ GeV}/c$. Preliminary HMPID results from p-p collisions at $\sqrt{s} = 7 \text{ TeV}$ will be presented.

1. – Introduction

ALICE (A Large Ion Collider Experiment) [1, 2] is devoted to the study of heavy-ion collisions at LHC energies. In particular, great care has been devoted to design a high-quality particle identification system in the central region exploiting the combination of several sub-detectors: the Inner Tracking System (ITS), the Time-Projection-Chamber (TPC), the Transition-Radiation-Detector (TRD), and the Time-Of-Flight (TOF). The central system is complemented by three small-area detectors: the High-Momentum-Particle-Identification-Detector (HMPID), the PHoton-Specrometer (PHOS) and the electromagnetic calorimeter (EMCal).

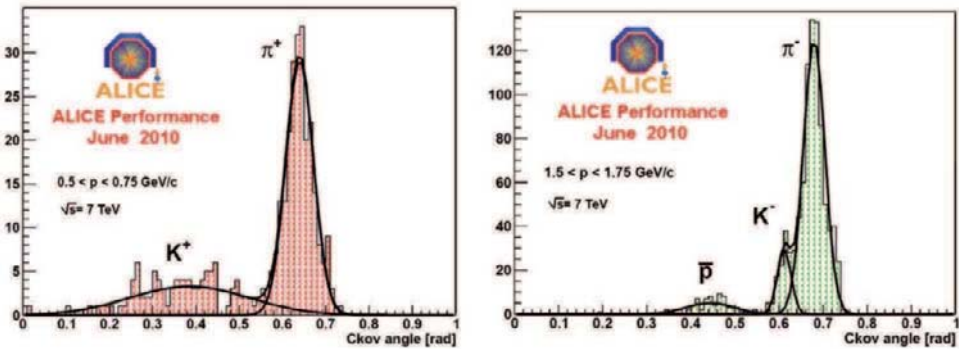


Fig. 1. – Left: Cherenkov angle distributions for π^+ , K^+ at $0.5 \leq p \leq 0.75 \text{ GeV}/c$ ($\sqrt{s} = 7 \text{ TeV}$, $B = 0.5 \text{ T}$). Right: Cherenkov angle distributions for π^- , K^- and \bar{p} at $1.5 \leq p \leq 1.75 \text{ GeV}/c$ ($\sqrt{s} = 7 \text{ TeV}$, $B = 0.5 \text{ T}$).

2. – The ALICE-HMPID detector

The ALICE-HMPID [3] performs track-by-track charged-particle identification by means of measurement of Cherenkov angles, exploiting the momentum information provided by the tracking devices. The HMPID enhances the PID capability of the ALICE experiment by enabling identification of particles beyond the momentum interval attainable through energy loss (in ITS and TPC) and Time-Of-Flight measurements (in TOF). The detector was optimized to extend the useful range for π/K and K/p discrim-

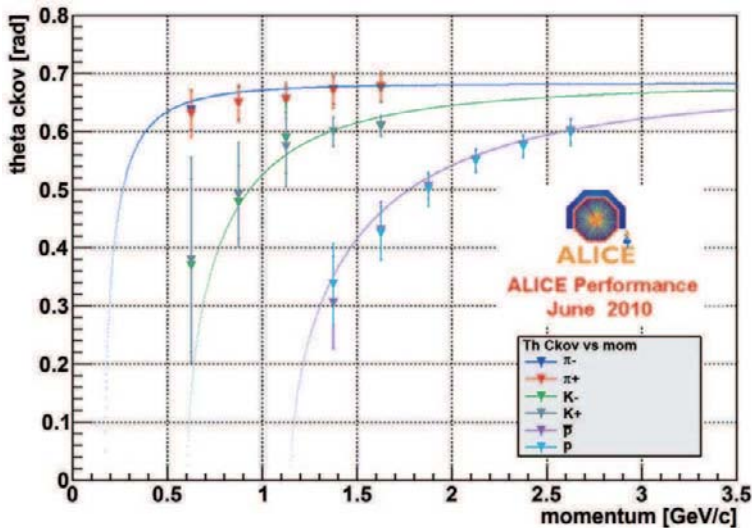


Fig. 2. – Cherenkov angle as a function of the track momentum ($0.5 \leq p \leq 2.75 \text{ GeV}/c$).

ination, on a track-by-track basis, up to 3 and 5 GeV/c , respectively. The HMPID is based on proximity-focusing Ring Imaging Cherenkov (RICH) counters and consists of seven modules of about $1.5 \times 1.5 \text{ m}^2$ each, mounted in an independent support cradle. The radiator, which defines the momentum range covered by the HMPID, is a 15 mm thick layer of low chromaticity C_6F_{14} (perfluorohexane) liquid with an index of refraction of $n = 1.2989$ at 175 nm corresponding to $\beta_{\min} = 0.77$ (*i.e.* a momentum threshold $p_{\text{th}} = 1.21m$, where m is the particle mass). The photon detection is provided by a multiwire chamber coupled with a pad-segmented CsI photocatode (CsI Q.E. $\approx 25\%$ at 175 nm, pad size $0.8 \times 0.84 \text{ cm}^2$).

3. – Analysis and results

ALICE has recorded data during the first LHC pp runs at $\sqrt{s} = 7 \text{ TeV}$ in March 2010 ($B = 0.5 \text{ T}$). The HMPID detector has successfully collected enough statistics to allow the detector alignment and the evaluation of the calibration parameters needed to estimate its performance. The analysis has been restricted to the momentum range $0.5 \leq p \leq 2.75 \text{ GeV}/c$, due to the small statistics available at larger momenta. The Cherenkov angle distributions for nine sub-range of $0.25 \text{ GeV}/c$ have been extracted. Figure 1 shows two examples of the Cherenkov angle distributions for $0.5 \leq p \leq 0.75 \text{ GeV}/c$ (particles) and $1.5 \leq p \leq 1.75 \text{ GeV}/c$ (antiparticles). The number of particles under single Gaussian and the mean value (with relative errors) have been evaluated. In fig. 2 the Cherenkov angle as function of the track momentum measured by the tracking devices is shown. The points correspond to the mean values of the Cherenkov angle distributions (fig. 1). The theoretical curves (solid lines) fit well the experimental points for π , K, p.

4. – Conclusion

The first results from the HMPID detector are presented. In the first p-p collisions at $\sqrt{s} = 7 \text{ TeV}$ and $B = 0.5 \text{ T}$ the Cherenkov angle distributions and the Cherenkov angle as a function of the track momentum ($0.5 \leq p \leq 2.75 \text{ GeV}/c$) have been evaluated. The HMPID detector is ready to contribute to the ALICE physics programme.

REFERENCES

- [1] ALICE COLLABORATION, Physics Performance Report, Vol. I, *J. Phys. G: Nucl. Part. Phys.*, **30** (2004) 1517.
- [2] ALICE COLLABORATION, Physics Performance Report, Vol. II, *J. Phys. G: Nucl. Part. Phys.*, **32** (2006) 1295.
- [3] CERN/LHCC 9819, ALICE TDR 1, 14 August 1998.

This page intentionally left blank

Proceedings of the International School of Physics “Enrico Fermi”
Course CLXXVIII “From the Big Bang to the Nucleosynthesis”, edited by A. Bracco and E. Nappi
(IOS, Amsterdam; SIF, Bologna)
DOI 10.3254/978-1-60750-974-5-407

New studies of the dynamical dipole in asymmetric heavy-ion reactions: A probe of the nuclear equation of state

A. GIAZ, A. CORSI, F. CAMERA, A. BRACCO, F. C. L. CRESPI, S. LEONI,
R. NICOLINI and V. VANDONE

Dipartimento di Fisica, Università di Milano and INFN, Sezione di Milano - Milano, Italy

G. BENZONI, N. BLASI, S. BRAMBILLA, B. MILLION and O. WIELAND
INFN, Sezione di Milano, Milano, Italy

T. MARCHI, V. L. KRAVCHUK, M. CINAUSERO, M. DEGELIER,
F. GRAMEGNA and V. RIZZI

INFN, Laboratori Nazionali di Legnaro - Legnaro, Italy

P. BEDNARCYK, M. CIEMALA, M. KMIECIK, A. MAJ,
K. MAZUREK and W. MECZYNSKI

The Henryk Niewodniczański Institute of Nuclear Physics, PAN - Krakow, Poland

G. BAIOCCHI, M. BRUNO, M. D’AGOSTINO, L. MORELLI and G. VANNINI

Dipartimento di Fisica, Università di Bologna and INFN, Sezione di Bologna - Bologna, Italy

S. BARLINI, L. BARDELLI, M. BINI, S. CARBONI, G. CASINI, M. CHIARI, A. NANNINI,
G. PASQUALI, S. PIANTELLI and G. POGGI

Dipartimento di Fisica, Università di Firenze and INFN, Sezione di Firenze - Firenze, Italy

A. ORDINE

INFN, Sezione di Napoli - Napoli, Italy

R. ALBA, C. MAIOLINO and D. SANTONOCITO

INFN, Laboratori Nazionali del Sud - Catania, Italy

M. COLONNA, M. DI TORO and C. RIZZO

*Dipartimento di Fisica e Astronomia dell’Università di Catania
and INFN Laboratori Nazionali del Sud - Catania, Italy*

D. MONTANARI

INFN, Sezione di Padova - Padova, Italy

Summary. — In heavy-ion nuclear reactions the process leading to complete fusion is expected to produce pre-equilibrium γ -ray emission, called dynamical dipole (DD), when particular conditions are met. Indeed, when there is an N/Z asymmetry between projectile and target, charge equilibration takes place with a collective dipole oscillation associated to a γ -ray emission. The existing experimental data concerning this pre-equilibrium γ -ray emission are still rather scarce and mainly concentrated in the $A \simeq 132$ mass region. It is important to point out that the model, used to compare the data, critically depends on the nuclear equation of state with its symmetry term. The very preliminary results concerning the measurement of the DD γ -ray emission in the fusion reaction ^{16}O ($E_{\text{lab}} = 192$ MeV) + ^{116}Sn at 12 MeV/u will be presented. The experiment aims at the measurement of the total emission yield of the DD at 12 MeV/u where the predicted theoretical yield does not completely reproduce the experimental data. The experiment has been performed at the INFN Legnaro Laboratories using the GARFIELD-HECTOR array.

1. – Introduction

The dynamical-dipole emission mechanism is associated to the charge equilibration process in fusing system. As a matter of fact, in heavy-ion fusion reactions, energy and angular momentum are quickly distributed among all single-particle degrees of freedom while charge equilibration takes place on a longer timescale.

In the case of charge asymmetric entrance channels one expects, at the time of the compound nucleus (CN) formation, a pre-equilibrium photon emission from the dipole oscillation due to the isospin transfer dynamics.

It has been shown that, in general, the strength of the dynamical dipole mainly depends on the beam energy and on the asymmetry in N/Z value between projectile and target. Experimentally, it was observed for $A = 132$ that dynamical-dipole emission increases with beam energy up to ≈ 10 MeV/u, then the yield decreases [1-3]. This behavior was interpreted as due to the onset of fast charge equilibration mechanisms like prompt neutron emission [4] which reduces the N/Z asymmetry.

The approach which has successfully described the dynamical-dipole γ -ray emission uses the dynamical evolution of the dipole in the framework of Boltzam-Nordheim-Vlasov (BNV) model and employs the bremsstrahlung expression for the calculation of the photon emission yield.

The understanding of this mechanism is relevant in the study of exotic nuclear matter especially in view of the future availability of intense radioactive beams that are expected to give a boost to this kind of measurements.

The experiment is part of an experimental campaign focused to the measurement of the total DD emission yield for the same fusion reaction but at different beam energy

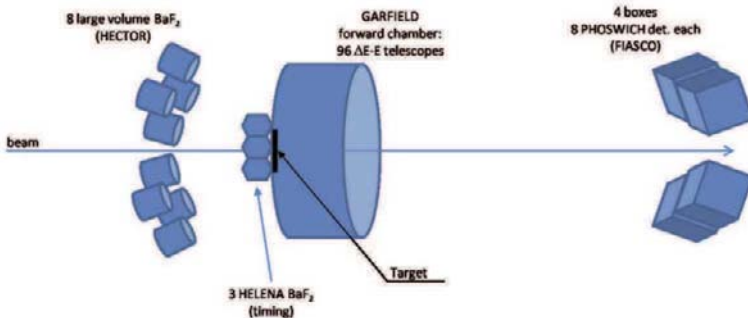


Fig. 1. – A sketch of the experimental setup.

(8, 12, 15.6 MeV/u). The experiment was performed at the INFN Legnaro laboratories using the HECTOR-GARFIELD apparatus [5,6]. Data at 8.0 and 15.6 MeV/u have been already discussed in [7]. In this paper we present the preliminary results on 12 MeV/u reaction.

In this measurement, part of the HELENA array (which was fully refurbished for its use in the AGATA demonstrator campaign) was used to provide a time reference and for the measurement of pre-equilibrium fast neutron.

2. – Experimental setup

The experimental setup was composed by different detection systems in order to provide correlated information on γ -rays and particle emission in coincidence with the evaporation residue. The setup is illustrated in fig. 1. In particular, the forward chamber of the GARFIELD apparatus is dedicated to the measurement of light charged particles (LCP) emitted during the different steps of the fusion-evaporation process.

GARFIELD is an array of micro-strip gas chamber-CsI(Tl) scintillator telescopes for the identification and measurement of light charged particles and fragments. It covers an angular range from $\theta = 29^\circ$ to $\theta = 82^\circ$ and 2π in ϕ . It is divided in 24 sectors each one containing 8 ΔE - E telescopes. The ΔE signal is given by the gaseous micro-strip detectors which collect and amplify the primary electrons produced along the ionization track of the incident particle [8]. The chamber is filled with CF_4 gas at a pressure of 48 mbar and the electrical drift field is kept uniform by a field cage to a value of $\simeq 1.2 \text{ V/cm/Torr}$. The main advantage of using micro-strip gas chambers is the low threshold for Z identification from protons up to highly ionizing heavy ions. The residual energy signal is provided by CsI(Tl) scintillators which are also lodged in the gas volume.

The FIASCO [9] array consists of four boxes placed in the very forward direction (5° – 13°) to be used as an evaporation residue trigger and as a proton/alpha multiplicity counter. Each box contains eight phoswich detectors made of three layer scintillators. The first two stages are, respectively, a thin $200 \mu\text{m}$ and a 5 mm plastic material, while the last one is a 50 mm CsI(Tl). The light produced in the three ranges is collected by a common photomultiplier. GARFIELD and FIASCO detectors use fully digitized elec-

tronics [10, 11] that allows on-line pulse shape analysis of both GARFIELD CsI(Tl) and FIASCO multilayer scintillators. This allows to perform LCP pulse shape identification in GARFIELD and evaporation residue accurate selection in FIASCO.

Eight large-volume BaF₂ scintillators from HECTOR array are used for the measurement of the high-energy γ -rays [5, 12].

Two additional groups of small ($3'' \times 3''$) BaF₂ scintillators from the HELENA array have been used. The first group was placed close to the target to provide a time reference to be compared with the one obtained from the pulsed beam radiofrequency (RF), while the second one was mounted in the forward direction for the measurement of pre-equilibrium neutrons. HECTOR and HELENA arrays use analog neutron-gamma discrimination modules, fully integrated GARFIELD digital general acquisition framework.

To detect the dynamical-dipole γ emission it is necessary to select the fusion-evaporation reaction from the other channels and the measurement of the pre-equilibrium energy loss will be deduced from the light charged particles. For this reason the main triggers of the experiment include the logic OR of the HECTOR array, the logic OR of the FIASCO and the logic OR of GARFIELD. Furthermore to have a precise measurement of the DD contribute it is necessary to have all the possible coincidences between high-energy γ -rays, evaporation residues, LCP and neutrons, so in the main trigger some logic AND between the different arrays are introduced (AND of FIASCO and HECTOR, AND of FIASCO and GARFIELD, AND of FIASCO and forward HELENA).

3. – Preliminary results

The analysis of the data has been focused to produce the high energy γ -ray spectrum emitted in the fusion evaporation process (see the data in fig. 2). From a preliminary analysis we have estimated ≈ 20000 coincidence events between high-energy γ -rays (10–20 MeV) and one evaporation residue.

A preliminary comparison with Statistical Model shows evidence of an excess yield between 10–20 MeV (see fig. 2 and fig. 3) which is attributed to dynamical-dipole emission. The extra yield has been compared with the previous results obtained at 8 MeV/u and 15.6 MeV/u (see [7]). The measured data display the same rise and fall behavior (see fig. 3) observed in [2] but with a smaller amplitude.

The measured pre-equilibrium contribution has been compared to the theoretical predictions from BNV-model calculations [4]. The different nuclear equation-of-state parametrizations used in calculation do not seem to produce a good agreement with measured data.

This difference between the expected and measured DD total γ -ray yield calls for further investigation, *e.g.*, performing new theoretical calculations with different parameterization of N-N cross-section and a more detailed description of the pre-equilibrium particle emission. The angular distribution of γ -rays measured in the backward hemisphere (covered by HECTOR detectors) will be extracted from data at 12 MeV/u and the comparison with the one obtained within theoretical model will provide a much deeper detailed check of the model.

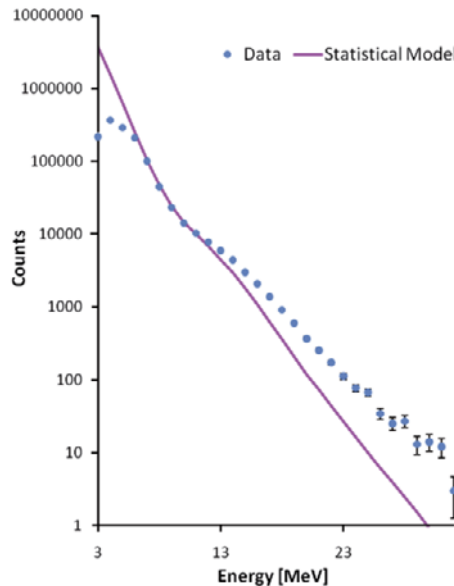


Fig. 2. – The comparison between the BaF₂ energy spectrum and prediction by the statistical model. An excess of counts between 10–20 MeV is visible. The two spectra have been normalized at 7 MeV.

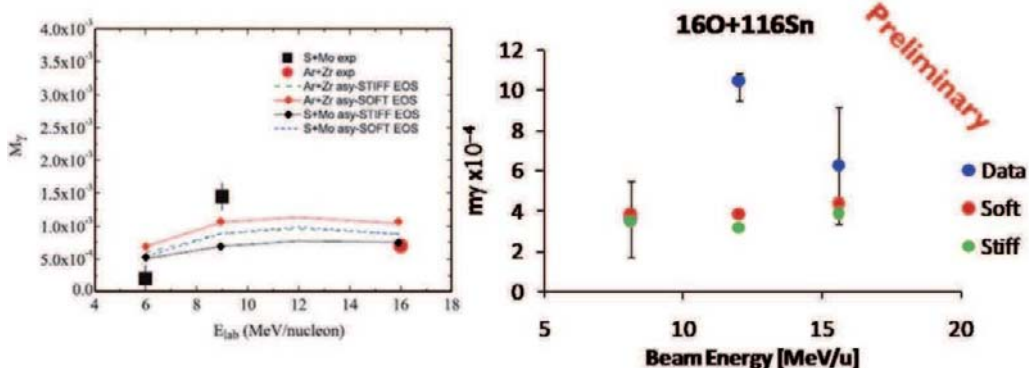


Fig. 3. – The DD γ -emission yield measured in mass region $A \simeq 132$ for beam energy ranging from 6 to 15 MeV/u. Left panel: data reported in ref. [2]. Right panel: data points at 8 and 15.6 MeV/u are from [7]. The point at 12 MeV/u is still a preliminary result.

REFERENCES

- [1] PIERROUTSAKOU D. *et al.*, *Phys. Rev. C*, **71** (2005) 056405.
- [2] PIERROUTSAKOU D. *et al.*, *Phys. Rev. C*, **80** (2009) 024612.
- [3] MARTIN B. *et al.*, *Phys. Lett. B*, **664** (2008) 47.
- [4] BARAN V. *et al.*, *Phys. Rev. Lett.*, **87** (2001) 18.
- [5] KMIĘCIK M. *et al.*, *Phys. Rev. C*, **70** (2004) 064317.
- [6] GRAMEGNA F. *et al.*, *Nuclear Science Symposium Conference Record, IEEE*, **2** (2004) 1132.
- [7] CORSI A. *et al.*, *Phys. Rev. Lett.*, **679** (2009) 197.
- [8] GRAMEGNA F. *et al.*, *Nucl. Instrum. Methods A*, **389** (1997) 474.
- [9] BINI M. *et al.*, *Nucl. Instrum. Methods A*, **515** (2003) 497.
- [10] BARDELLI L. *et al.*, *Nucl. Instrum. Methods A*, **572** (2007) 882.
- [11] BARDELLI L. *et al.*, *Nucl. Instrum. Methods A*, **570** (2007) 127.
- [12] WIELAND O. *et al.*, *Phys. Rev. Lett.*, **97** (2006) 012501.

A pair spectrometer for E0 transitions measurements

L. GUERRO

Divisione di Fisica, Scuole di Scienze e Tecnologie, Università di Camerino

Via Madonna delle Carceri, I-62032 Camerino, Italy

INFN, Sezione di Perugia - Via Pascoli, I-06123 Perugia, Italy

Summary. — E0 transitions in radiative capture reactions between light nuclei may become important at very low energy and, thus, play an important role in nuclear astrophysics. At higher energy their contributions may be shadowed by more intense transitions. Therefore the experimental study of E0 transitions requires a specific detection setup, able to uniquely identify events where an electron-positron pair is detected and to measure their total kinetic energy. A compact pair spectrometer based on three silicon diodes forming a $\Delta E-E$ telescope has been designed to be installed in the jet target chamber of the recoil mass separator ERNA at the CIRCE laboratories of Caserta. The detector design and its expected performances are described and future experiments are discussed.

1. – E0 transitions

The possibility that the components related to E0 transitions contribute to the total cross-section in radiative capture reactions was never taken into account, basically for the lack of experimental data. Theoretical calculations have been made in the case of some reactions (${}^3\text{He} + {}^4\text{He}$, ${}^4\text{He} + {}^{12}\text{C}$), which seem not to favour these transitions in those cases [1, 2]. It must be said, however, that only through these transitions alpha

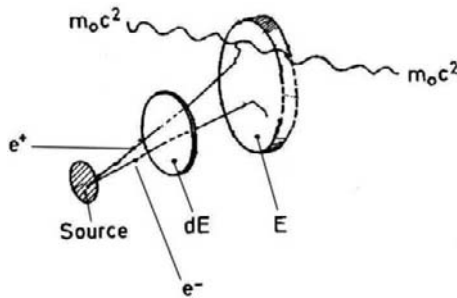


Fig. 1. – Schematic view of the pair spectrometer.

captures on even-even nuclei may proceed in *s*-wave: in light systems at low energy, the centrifugal barrier contributes significantly to the total barrier and the penetrability in *s*-wave is much higher than in the case of higher angular momentum. The ERNA Collaboration will focus on the study of two cases, where E0 transitions may play an important role: the $^{12}\text{C}(\alpha, \gamma)^{16}\text{O}$ and $^{16}\text{O}(\alpha, \gamma)^{20}\text{Ne}$ reactions.

1.1. Pair creation by internal conversion. – In order to develop a new detection system, it is necessary to know energy and angular correlation about the e^+e^- pair emission. The correlation function for the zero-pole transition in the Born approximation is [3]

$$(1) \quad P(\Theta, E_+)/N_0 = p_+p_-(E_+E_- - 1 + p_+p_- \cos \Theta)d\Omega_+d\Omega_-dE_+,$$

where p_{\pm} , E_{\pm} are the momenta and energies of electron and positron and Θ is the angle between their directions. This formula shows that there is no preferred direction for the resultant momentum of pairs from a monopole decay. Using eq. (1) it is possible to show that for a high-energy pair transition in a nuclide of low atomic number, the energy distribution is given by [4]

$$(2) \quad N(E)dE \propto E^2(E_0 - E)^2dE,$$

where $N(E)dE$ is the number of electrons (positrons) emitted with kinetic energy between E and $E + dE$ and $E_0 = E_T - 2m_e c^2$, where E_T is the nuclear transition energy. If the transition is, in addition, a $0^+ \rightarrow 0^+$ decay, the angular correlation is given by [4]

$$(3) \quad W(\Theta) = 1 + \cos \Theta.$$

2. – The pair spectrometer

A schematic layout of the setup is shown in fig. 1. The system consists of two silicon detectors operating in a twofold coincidence, that gives the total kinetic energy of the positron-electron pair when both particles are emitted into this solid angle. For the design of the apparatus the following aspects have to be considered: the ΔE -counter

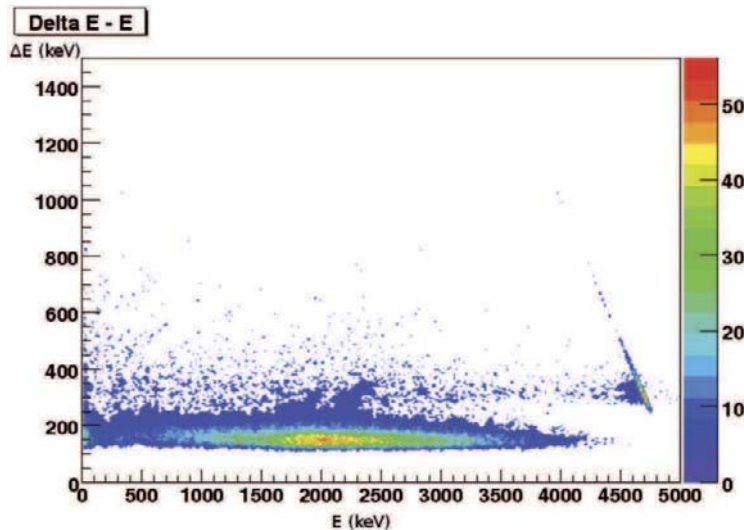


Fig. 2. – ΔE - E matrix; the pair conversion peak is the blue spot one on the right side.

should be kept thin (about $500\text{ }\mu\text{m}$), then the electrons suffer only a small energy loss and reach the E-detector with high counting probability; for electrons with energies greater than 500 keV , the specific energy loss is nearly independent of energy and amounts to $0.35\text{--}0.40\text{ keV per }\mu\text{m silicon}$. Thus those events which involve the passage of two particles through the counter can be pulse-height selected, in such a way that only the pairs will be measured.

2.1. Monte Carlo simulation of the detector performances. – A reliable calculation of the efficiency of the detector is needed in order both to extrapolate the duration of the measurement and to aid in the design and construction of the detector. The flow of the computer program for the Monte Carlo calculation has been done with Geant4. First, the geometry of the detector has been simulated and the test chamber in order to consider the effects of the particles impinging on its walls. Second, the direction and the energy of the positron and electron are generated by sampling eqs. (2) and (3). We shot a total of $2 \cdot 10^6$ pair creation events, obtaining the ΔE - E matrix shown in the density plot in fig. 2. The geometrical efficiency extrapolated from the simulation is 1.3% while the pair efficiency is 0.12%, which in our case corresponds to nearly 2500 pair events detected. This efficiency gives a too low statistics and hence a long time for the measurement. We shall take in consideration the possibility of measuring the single e^+ or e^- , using the continuous spectrum of electrons and positrons with the energy distribution function of eq. (2), reaching an efficiency up to 2% and 3% according to the position of the E layer.

3. – Conclusions

A spectrometer of the designed described above has been developed for application in nuclear astrophysics cross-section measurements. First tests with a $^{90}\text{Y} + ^{90}\text{Sr}$ electron source will be performed in order to determine the resolution and the efficiency of the detectors. A second test to understand the in-beam pair detection capabilities of the spectrometer will be performed at the CIRCE Laboratories in Caserta with the $^{19}\text{F}(\text{p}, \alpha)^{16}\text{O}$ reaction, which has a well-known pair emission cross-section [5]. The last step is to apply this technique to the $^{12}\text{C}(\alpha, \gamma)^{16}\text{O}$ reaction, to have an extrapolation of the cross section at stellar energies.

* * *

This work has been supported by INFN - Sezione di Perugia (ERNA funds), Italy.

REFERENCES

- [1] SNOVER K. A. and HURD A. E., *Phys. Rev. C*, **67** (2003) 055801.
- [2] BAUR G. and SNOVER K. A., *Phys. Rev. C*, **75** (2007) 058801.
- [3] OPPENHEIMER J. R., *Phys. Rev.*, **60** (1941) 164.
- [4] FREEMAN W. S. *et al.*, *Nucl. Instrum. Methods*, **204** (1983) 445.
- [5] RANKEN W. A., BONNER T. W. and MCCRARY J. H., *Phys. Rev.*, **109** (1958) 1646.

Proceedings of the International School of Physics “Enrico Fermi”
Course CLXXVIII “From the Big Bang to the Nucleosynthesis”, edited by A. Bracco and E. Nappi
(IOS, Amsterdam; SIF, Bologna)
DOI 10.3254/978-1-60750-974-5-417

Study of high-lying states in ^{208}Pb with the AGATA Demonstrator

R. NICOLINI, A. BRACCO, S. LEONI, F. CAMERA, F. BIROCCHI, A. CORSI,
F. C. L. CRESPI, A. GIAZ, L. PELLEGRI, S. RIBOLDI and V. VANDONE
Università degli Studi, Milano, Italy
INFN, Sezione di Milano - via Celoria 16, 20133 Milano, Italy

A. CAMPLANI
Università degli Studi, Milano, Italy

G. BENZONI, N. BLASI, C. BOIANO, S. BRAMBILLA, B. MILLION and O. WIELAND
INFN, Sezione di Milano - via Celoria 16, 20133 Milano, Italy

D. BAZZACCO, E. FARNEA, A. GOTTARDO, C. MICHELAGNOLI,
D. MONTANARI and C. UR
Università di Padova and INFN, Sezione di Padova - Padova, Italy

D. MENGONI
Università di Padova and INFN, Sezione di Padova - Padova, Italy
School of Engineering and Science, University of the West of Scotland - Paisley, Scotland, UK

G. DE ANGELIS, P. MOLINI, D. R. NAPOLI, F. RECCHIA,
E. SAHIN and J. J. VALIENTE-DOBON
INFN, Laboratori Nazionali di Legnaro - Legnaro, Italy

A. GADEA
INFN, Laboratori Nazionali di Legnaro - Legnaro, Italy
IFIC - Valencia, Spain

A. MAJ, M. CIEMALA and M. KMIECIK
The Henryk Niewodniczański Institute of Nuclear Physics, PAN - 31-342, Kraków, Poland

R. KEMPLEY
University of Surrey - Guildford, UK

A. BÜRGER
University of Oslo - Norway

P. REITER
Institut für Kernphysik, Universität zu Köln - Germany

Summary. — An experiment aiming at the study of the gamma decay from the Giant Resonance region in the nuclei ^{208}Pb , ^{90}Zr has recently been performed with the AGATA Demonstrator coupled to an array of large-volume scintillators ($\text{LaBr}_3\text{:Ce}$, BaF_2) to increase the overall gamma detection efficiency. The ^{208}Pb and ^{90}Zr nuclei were excited with inelastic scattering of ^{17}O at the incident energy of 20 MeV/u. The ejectiles were detected in a pair of silicon E - ΔE telescopes placed at forward angles. Preliminary results concerning the first partial analysis of the measurement with the ^{208}Pb target are here presented.

1. – Introduction

Giant resonances are fundamental high-frequency modes of excitation of nuclei, and have been studied over the years since they provide useful information on nuclear structure and on the effective nucleon-nucleon interaction [1]. They can be excited employing different probes, including heavy ions [2]. In particular, the inelastic scattering of ^{17}O has been successfully used to populate the Giant Quadrupole Resonance in ^{208}Pb , making it possible to study its gamma decay and its coupling to low-lying collective states [3]. More recently, detailed studies at very high resolution [4-8] have provided evidence for fine structures below and above particle threshold. These structures are expected to carry relevant information on the microscopic nature of the giant resonance modes. A tool expected to provide a better understanding of the fine structure of giant resonances is the gamma decay, which is very sensitive to the multipolarity of the resonance and to its coupling to specific states.

Motivated by this interest an experiment with the AGATA Demonstrator was performed using inelastic scattering of ^{17}O at bombarding energy of 20 MeV/u. This beam energy is optimal for the excitation of the giant quadrupole resonance [2]. The beam current was limited to about 0.5 pnA in order to cope with the high count rate in the detectors. Most of the data were obtained with two different targets, one of ^{208}Pb 2 mg/cm² thick and the other of ^{90}Zr 2.6 mg/cm² thick.

2. – Experimental setup and data analysis

The scattered ^{17}O ions were detected by two segmented silicon E - ΔE telescopes [9] (cooled to -20°C), made of detectors 1000 μm and 200 μm thick. Each detector had an active area of $20 \times 50 \text{ mm}^2$ divided in 60 pads of $4 \times 4 \text{ mm}^2$, half of which were read out and acquired. The telescopes, mounted symmetrically with respect to the beam axis, were placed at 12° for the ^{208}Pb reaction and at 8° for the ^{90}Zr reaction. It was not possible to place the detectors at smaller angles due to the excessive count rate that they would suffer from the elastic scattering channel.

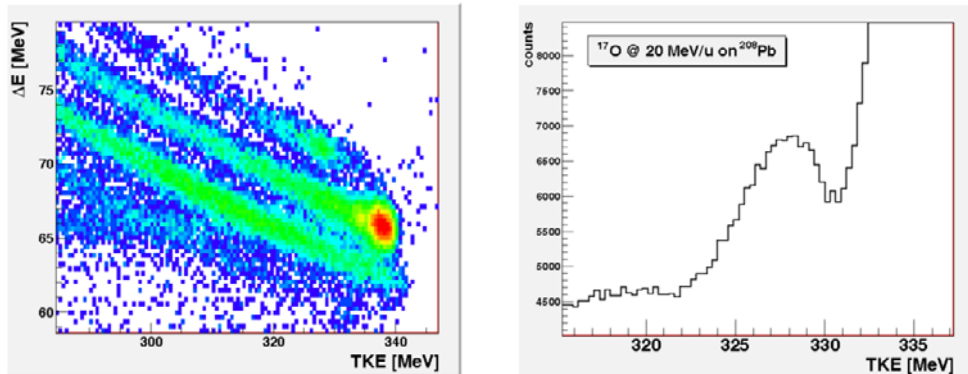


Fig. 1. – Left panel: TKE- ΔE matrix obtained in the Si telescopes. Right panel: kinetic energy spectrum of ^{17}O .

The Total Kinetic Energy (TKE) of the ion was obtained by summing the E and ΔE detectors signal, pixel by pixel. The ΔE -TKE correlation is given in fig. 1, left, top panel, showing a good separation of the O isotopes. A portion of the energy spectrum of the inelastically scattered ^{17}O is shown in the bottom panel of fig. 2; the large bump centered around the energy of 329 MeV ($E^* \sim 11$ MeV) is known to be dominated by the Giant Quadrupole Resonance [3].

The AGATA Demonstrator used to measure the gamma decay is the first phase of the AGATA gamma-ray spectrometer, a new generation HPGe detector array using the techniques of pulse shape analysis and tracking [10]. For the present experiment, the setup consisted of 3 triple-clusters, for a total of 9 crystals of HPGe.

The gamma decay was also measured with an array consisting of different scintillator detectors, $\text{LaBr}_3:\text{Ce}$ and BaF_2 . The $\text{LaBr}_3:\text{Ce}$ scintillators have the best energy resolution among all scintillators used for gamma spectroscopy, as well as an excellent time resolution. Three cylindrical $\text{LaBr}_3:\text{Ce}$ scintillators were mounted around the AGATA Demonstrator, one $3'' \times 3''$ and two $3.5'' \times 8''$. Most of the remaining solid angle available was covered by 3 clusters of BaF_2 detectors from the Helena array.

The first step of the data reduction consisted in the selection of the events in which an inelastically scattered ^{17}O ion was detected in the Si telescopes. The energy spectrum of γ -rays obtained with this condition with the AGATA Demonstrator is shown (in green) in fig. 2 together with the spectrum obtained without any gating condition (in red). It is evident that this condition enhances the intensity of the ^{208}Pb γ -ray transitions at 2615 keV (3^-) and at 4085 keV (2^+).

The second step of the analysis was to correlate the excitation energy of the target and the total gamma-ray energy measured in coincidence with the scattering event. For example, the blue spectrum in fig. 2 is obtained by requiring an excitation energy between 2 and 5 MeV. This spectrum, when compared to the others (all are normalized to the total number of counts), clearly shows a further enhancement of the peaks due to

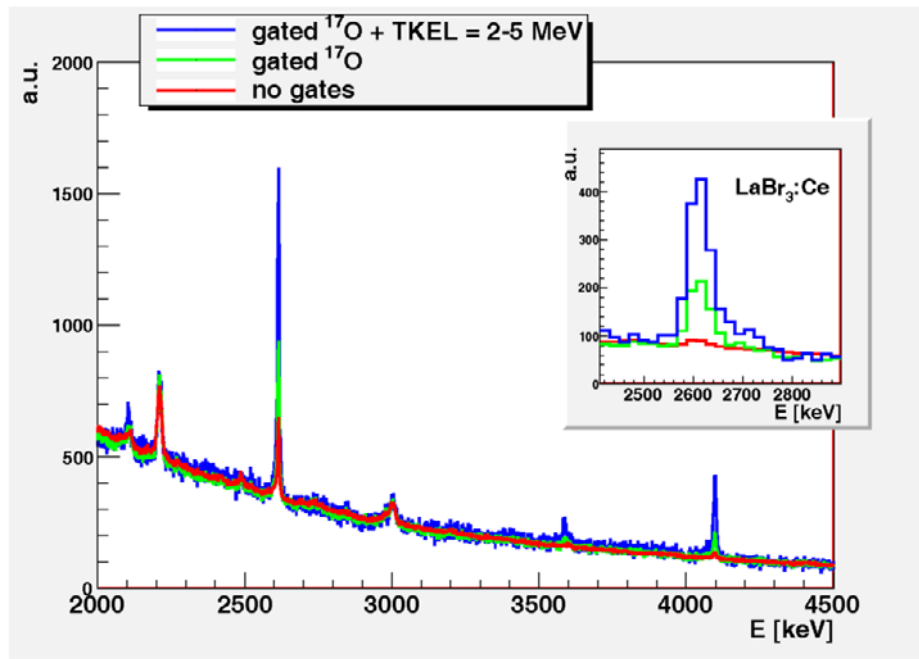


Fig. 2. – Gamma-ray energy spectra measured with the AGATA Demonstrator under various gating conditions, as described in the legend, and normalized to the total number of counts. The inset shows the energy spectrum around the 2615 keV line measured with one crystal of LaBr₃:Ce under the same gating conditions.

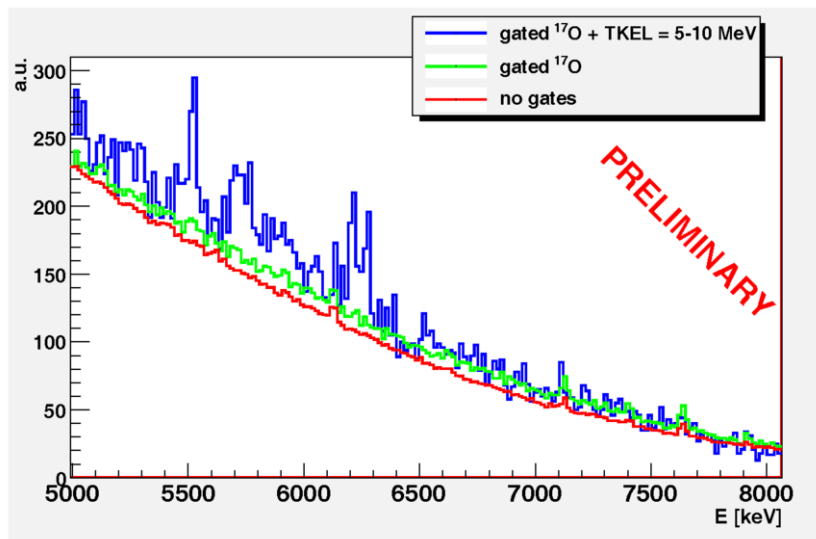


Fig. 3. – Gamma-ray energy spectra measured with the AGATA Demonstrator under various gating conditions, as described in the legend. All the spectra have been normalized so that they have the same area over the 0–15 MeV range.

gamma transitions in ^{208}Pb with respect to the background. The inset in fig. 2 shows the 2615 keV transition measured with a crystal of $\text{LaBr}_3:\text{Ce}$ under the same gating conditions described above.

After having checked that the data gated by lower values of excitation energy have the expected behavior it is interesting to see the decay corresponding to excitation energies between 5 and 10 MeV, region in which “pygmy” structures have been identified with (γ, γ') experiments [4]. In this spectrum, in blue in fig. 3, some peaks are clearly visible, possibly associated with pygmy structures in ^{208}Pb . In particular, the peak at 6.26 MeV and the peak at 5.52 MeV have already been identified by (γ, γ') experiments, while the other peak at ~ 6.20 MeV is not yet identified; the structures at ~ 5.7 MeV could be related to the first escape peak of the doublet. The scintillator spectra under the same gating conditions confirm the presence of these structures, seen also in a test experiment performed at LBL with a smaller detection efficiency [11]. Further investigations are of course needed, in particular taking into account the response function of the detectors.

3. – Conclusions

Some preliminary results of an experiment on gamma decay from the inelastic scattering of ^{17}O at the energy of 20 MeV/u on a ^{208}Pb target have been presented. This first part of the analysis was intended to check the performances of the setup and to reproduce some expected results. However, already with what obtained so far one can foresee some interesting results on the population of the pygmy resonance. Further analyses will be carried out in order to take into account the response function of the detectors and to refine the correlation between gamma-ray energy and excitation energy measured in the Si telescopes. Altogether, with the planned work we expect to make another step toward a better understanding of the underlying structure of giant resonances.

REFERENCES

- [1] BORTIGNON P. F., BRACCO A. and BROGLIA R. A., *Giant Resonances, nuclear structure at finite temperature, Contemporary Concepts in Physics* (Harwood Academic Publishers) 1998.
- [2] BERTRAND F. E. et al., *Nucl. Phys. A*, **482** (1988) 287C.
- [3] BEENE J. R. et al., *Phys. Rev. C*, **39** (1989) 1308.
- [4] RYEZAYEVA N. et al., *Phys. Rev. Lett.*, **89** (2002) 272502.
- [5] HARTMANN T. et al., *Phys. Rev. Lett.*, **93** (2004) 192501.
- [6] ENDERS J. et al., *Nucl. Phys. A*, **741** (2004) 3.
- [7] SAVRAN D. et al., *Phys. Rev. Lett.*, **97** (2006) 172502.
- [8] RICHTER A., *Prog. Part. Nucl. Phys.*, **55** (2005) 387.
- [9] MENGONI D., PhD thesis (2007) TRACE project.
- [10] BAZZACCO D., *Nucl. Phys. A*, **746** (2004) 248C.
- [11] DELEPLANQUE M. A. et al., Berkeley National Laboratories Nuclear Science Divison Annual Report (2005).

This page intentionally left blank

Proceedings of the International School of Physics “Enrico Fermi”
Course CLXXVIII “From the Big Bang to the Nucleosynthesis”, edited by A. Bracco and E. Nappi
(IOS, Amsterdam; SIF, Bologna)
DOI 10.3254/978-1-60750-974-5-423

Recent developments in gamma-ray spectroscopy with new scintillators, LaBr₃(Ce), to investigate nuclear structure at high excitation and far from stability

L. PELLEGRI, F. BIROCCHI, A. BRACCO, F. CAMERA, A. CORSI, F. C. L. CRESPI,
A. GIAZ, S. LEONI, R. NICOLINI, S. RIBOLDI and V. VANDONE

Università and INFN, Sezione di Milano - Via Celoria 16, 20133, Milano, Italy

G. BENZONI, N. BLASI, S. BRAMBILLA, C. BOIANO, B. MILLION and O. WIELAND
INFN, Sezione di Milano - Via Celoria 16, 20133, Milano, Italy

D. MONTANARI

Università di Padova and INFN, Sezione di Padova - Padova, Italy

Summary. — Lanthanum bromide scintillators are among the new most promising detectors for nuclear spectroscopy experiments. Their relevant performances in terms of energy resolution, time resolution and high density make them a suitable alternative even with respect to germanium-based solid-state detectors, which, on the other side, are more expensive and difficult to operate. However, the huge amount of optical photons emitted in burst by cerium-doped lanthanum bromide scintillators poses severe constraints on the specifications of photomultipliers, namely they must operate at very large instantaneous current values with minimum saturation of output pulse signals. We analyse the effects of output signal saturation in photomultiplier tubes as a function of the power supply high voltage level and the amount of energy released in the scintillator crystal and propose a simple model to characterize this very complex phenomenon. According to the proposed model, a preliminary first-order correction has been extracted. This technique reduces the non-linear response of a LaBr₃(Ce) scintillator by almost an order of magnitude for γ -rays of 9 MeV.

1. – Introduction

In the last few years, the lanthanum bromide scintillators are attracting the nuclear spectroscopy scientific community because of their “almost ideal” scintillation properties. Recent studies have shown that LaBr₃(Ce) material gives optimal energy resolution for scintillators (2.7% at 662 keV), an excellent time resolution (≈ 300 ps), good efficiency and a negligible variation of light output within the temperature range -20 to $+60$ °C [1, 2]. The availability of LaBr₃(Ce) crystals in volumes larger than 1000cc could make lanthanum bromide scintillators a possible alternative to HPGe detectors for γ -ray measurements. In fact, if compared with HPGe, these crystals provide an excellent trade-off between efficiency and energy resolution, with, in addition, sub-nanosecond timing [3]. In particular the new lanthanum bromide scintillators are optimal for experiments focused on the measurement of the collective properties of nuclei and nuclei near the drip-lines. In these cases the ideal detector must have high detection efficiency, for high energy gamma rays, a good timing resolution in order to suppress the background and a good energy resolution. However, because of the inherently high light yield of the new lanthanum bromide scintillators, even with low-gain photomultipliers (PMTs) considerable saturation effects may be revealed for high energy interacting radiation and such non-linearity affects time and energy spectra. Therefore it is extremely important to account and correct for these effects.

2. – Methods

In case standard analog electronics is used for energy spectroscopy, PMT signal saturation directly translates into a mismatch between the amount of estimated and the effective energy released in the scintillator crystal. This underestimation, often referred to as a PMT “non-linearity” issue, may produce noticeable effects even in specifically optimized experimental set-ups. In particular, these resulting effects should be accounted for and corrected in nuclear physics experiments, like Giant Dipole Resonance (GDR) and Giant Quadrupole Resounrance (GQR) gamma decay measurements, which require a wide energy range.

In order to better understand and overcome this relevant PMTs issue, we set-up a digital acquisition system based on a digital oscilloscope (Lecroy WaveRunner). Signals acquired by the free-running ADCs inside the scope (5 GHz, 8 bits) have been stored on a personal computer running a specifically developed “Matlab” application. The PMT has been optically connected to a cerium-doped lanthanum bromide scintillator (LaBr₃(Ce)), 3" \times 3" in size [4].

3. – Application

We analyzed the effects of output signal saturation in photomultiplier tubes coupled to large-volume LaBr₃(Ce) as a function of the power supply high voltage level and the amount of energy released in the scintillator crystal and we proposed a simple model to characterize this very complex phenomenon.

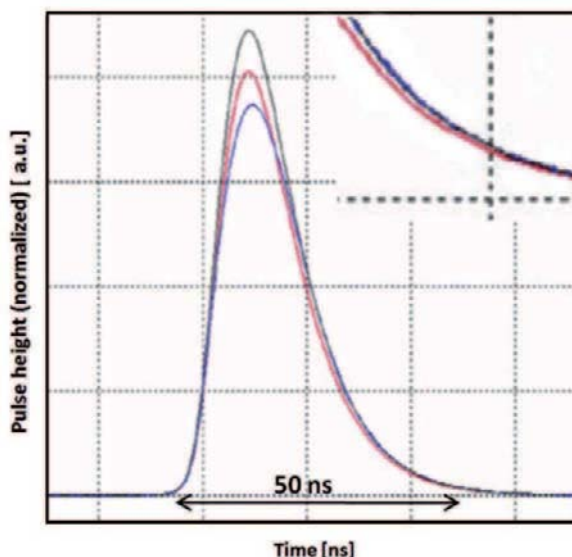


Fig. 1. – Reference pulse for 356 keV (red line); reference pulse for 8990 keV (saturated, blue line); reference pulse for 8990 keV (saturation corrected, black line). This first-order correction has been applied by manually fitting the unsaturated pulse (red line) to the lower parts of the saturated pulse (blue line).

As the amount of signal distortion depends on the amplitude of the PMT anode output current, which in turn is related to i) the amount of energy deposited in the scintillator crystal and ii) the PMT multiplying gain as a function of the high voltage power supply, we assumed that no saturation effects would be present on the digitized

Full Energy Peak [keV]	Energy estimation by amplifier + MCA [MCA channels]	Energy under-estimation error	First-order correction factor m	Energy estimation corrected [MCA channels]	Energy estimation residual error
356	253	≈ 0%	--	--	≈ 0%
661	472	≈ 0%	1.00	472	≈ 0%
1173	790	≈ 0%	1.00	790	≈ 0%
1332	889	≈ 0%	1.00	889	≈ 0%
2223	1434	0.64%	1.01	1448	-0.36%
4440	2738	2.97%	1.04	2820	-1.03%
8998	5171	8.60%	1.097	5636	-1.1%

Fig. 2. – Correction of the energy estimation provided by a completely independent analog spectroscopy system.

“356 keV” reference pulse; moreover, we assumed that in case of higher energies, the shape of the corresponding reference pulses would not be noticeably distorted in their lower regions. In order to preliminarily validate the basic assumptions of the model, we extracted the normalization factor which make the initial and final part of the measured pulse to overlap the 356 keV pulse which is our reference in shape (see fig. 1).

Once calculated the correction factors m for all the energy peaks, we consequently adjusted the raw energy estimations, for energies up to 9 MeV, provided by a completely independent analog spectroscopy system, hence reducing the maximum error associated to the PMT output signal saturation by almost an order of magnitude (see fig. 2).

In summary, we studied the saturation effects of PMTs, coupled to a lanthanum bromide scintillator ($\text{LaBr}_3(\text{Ce})$), on time and energy spectra for high energy gamma-rays interacting radiation. In order to analyze the PMT output signal saturation we set-up a digital acquisition system based on a digital oscilloscope (Lecroy WaveRunner). We described a simple model to characterize this very complex phenomenon and we reduced the maximum energy estimation error, due to the PMT non-linearity, by almost an order of magnitude. The relevant aspect of this work is that the proposed model can be applied to different crystals, in particular to the other crystals used in the lanthanum bromide scintillators array. In addition the proposed model can be applied not on-line but off-line in laboratory.

REFERENCES

- [1] NICOLINI R. *et al.*, *Nucl. Instrum. Methods A*, **582** (2007) 554.
- [2] CRESPI F. C. L. *et al.*, *Nucl. Instrum. Methods A*, **602** (2009) 520.
- [3] CAMERA F. *et al.*, NSS IEEE Poster Presentation (2009).
- [4] PELLEGRI L., Tesi di Laurea Magistrale, Università degli Studi di Milano (2010).

Proceedings of the International School of Physics “Enrico Fermi”
Course CLXXVIII “From the Big Bang to the Nucleosynthesis”, edited by A. Bracco and E. Nappi
(IOS, Amsterdam; SIF, Bologna)
DOI 10.3254/978-1-60750-974-5-427

Order-to-chaos transition in warm rotating ^{174}W nuclei

V. VANDONE, S. LEONI, A. BRACCO, S. BOTTONI, F. CAMERA, A. CORSI,
F. C. L. CRESPI, A. GIAZ and R. NICOLINI

*Università degli Studi di Milano and INFN, Sezione di Milano
Via Celoria 16, 20133, Milano, Italy*

G. BENZONI, N. BLASI, C. BOIANO, S. BRAMBILLA,
B. MILLION and O. WIELAND

INFN, Sezione di Milano - Via Celoria 16, 20133, Milano, Italy

D. BORTOLATO, E. CALORE, A. GOTTARDO, D. R. NAPOLI,
E. SAHIN and J. J. VALIENTE DOBON

INFN, Laboratori Nazionali di Legnaro - Legnaro, Italy

D. BAZZACCO, M. BELLATO, E. FARNEA, S. LUNARDI, D. MENGONI,
C. MICHELAGNOLI, D. MONTANARI, F. RECCHIA and C. A. UR

Università di Padova and INFN, Sezione di Padova - Padova, Italy

A. GADEA and T. HÜYÜK

IFIC - Valencia, Spain

N. CIEPLICKA, A. MAJ and M. KMIECIK

The Niewodniczanski Institute of Nuclear Physics, PAN - Krakow, Poland

A. ATAC, S. AKKOYUN and A. KASKAS

Department of Physics, Faculty of Science, Ankara University - Ankara, Turkey

S. KETENCI

Department of Physics, Nidge University - Nidge, Turkey

J. NYBERG and P. A. SÖDERSTRÖM

Department of Physics and Astronomy, Uppsala University - Sweden

Summary. — The transition between order and chaos is studied in the warm rotating nucleus ^{174}W by gamma-spectroscopy, focusing on the conservation of selection rules of the K quantum number with the excitation energy. The ^{174}W nucleus was populated at high spins by the fusion-evaporation reaction of ^{50}Ti (at 217 MeV) on a ^{128}Te backed target. The experiment was performed in Legnaro National Laboratory using the AGATA Demonstrator HPGe-array (AD) coupled with an array of 27 BaF_2 scintillator detectors. High-energy γ -rays measured in the AD and in the scintillators array will be also analyzed to study the Giant Dipole Resonance (GDR) in the compound nucleus ^{178}W . The discrimination between n and γ in the AD detectors will be employed, following a procedure recently developed by Monte Carlo simulations and using digital Pulse Shape Analysis timing techniques.

1. – Introduction

The transition between order and chaos in a quantum-mechanical system is a fascinating subject that is currently investigated in different research fields, ranging from nuclear to atomic, molecular and solid-state physics. Close to the yrast line (at temperature $T \sim 0$), the nucleus behaves as an ordered system with well-defined quantum numbers and associated selection rules. Moving toward higher excitation energy, energy levels start to interact giving rise to a gradual loss of selection rules. As a consequence, quantum numbers lose their meaning with temperature. The extreme regime is the chaotic region of the compound nucleus, where only energy, spin and parity are well defined for each energy level. A useful probe to study the weakening of the selection rules with temperature is the K -quantum number, *i.e.* the projection of the total angular momentum on the symmetry axis. Close to the yrast line K is a well-defined quantum number, and low- K and high- K γ -decay flows are well distinguished. As the internal energy increases, a statistical K -mixing process takes place, due to the high density of states. Therefore, by studying the γ -decay flow in the large region between the cold regime close to the yrast line and the chaotic compound nucleus, information on the order-to-chaos transition can be obtained [1]. So far, the only studied case in this respect is the ^{163}Er nucleus [2], for which a first indication of a gradual transition between order and chaos was observed around 2.5 MeV of excitation energy. This calls for additional experimental investigation and an interesting physics case is represented by the ^{174}W nucleus [3], here discussed. In particular, ^{174}W is characterized by the existence of low- K ($\sim 3\text{--}4$) and high- K ($\sim 8\text{--}12$) rotational bands extending up to spin $39\hbar$, with two high- K bands ($K = 8$ and $K = 12$) built on isomeric states with lifetime larger than 120 ns.

In this paper we present preliminary results from an experiment performed in July 2010 at Legnaro National Laboratory of INFN, using the first phase of the Advanced GAMMA Tracking Array (AGATA) [4], coupled to a multiplicity filter of BaF₂ scintillators.

2. – The experiment

The ^{174}W nucleus was populated by the fusion-evaporation reaction of ^{50}Ti (at 217 MeV) on a ^{128}Te target (1 mg/cm² thick backed by 50 mg/cm² of $^{\text{nat}}\text{Pb}$). The reaction is expected to reach spins as high as $\sim 60\hbar$ and energy of ~ 4 MeV above the yrast line, therefore providing a good population of the warm rotational regime. The experimental setup consisted of four triple clusters of the AGATA HPGe-array placed at 16 cm from the target (with an absolute efficiency of $\sim 5\%$ at 1.3 MeV), coupled with an array of 27 BaF₂ scintillator detectors, covering $\sim 25\%$ of the total solid angle. To probe the gradual weakening of selection rules of the K -quantum number γ - γ matrices gated by low- K and high- K structures will be constructed and analyzed by statistical fluctuation techniques [5]. This will allow to estimate the number of low- K and high- K bands and their correlations, as a function of excitation energy. In particular, the selection of low- K and high- K transitions will require the use of both prompt and delayed γ coincidences with respect to a time reference given by the HELENA array. Furthermore, the scintillator array will help focusing on the high-multiplicity and high-energy part of the γ -cascades, where the full transition into the chaotic regime is expected to

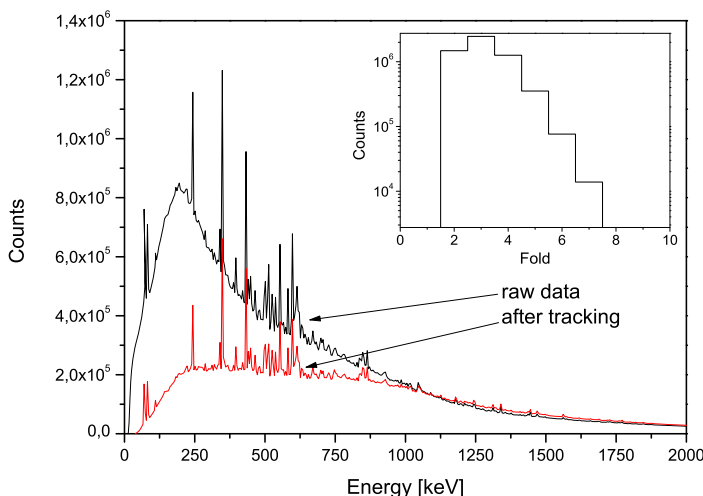


Fig. 1. – Comparison between γ -ray spectra, one before and the other after the γ -ray tracking procedure. The strong peaks correspond to the γ -transitions of the yrast line of ^{174}W . The inset shows the Ge fold distribution, as obtained after tracking.

take place. Since we have used a backed target, the lifetime of the excited rotational bands will be also measured, as a test of the deformation stability with temperature. As a by-product of the experiment, we plan to investigate the dependence of the width of the Giant Dipole Resonance (GDR) built on the compound nucleus ^{178}W , as a function of the angular momentum. This will be done by studying the high-energy γ -rays measured with both the HELENA array and the AD. This study plays an important role in the understanding of the different damping mechanisms of the GDR at finite temperature [6]. A crucial point of this analysis will be the discrimination between neutron and γ , which we plan to perform following a method recently developed by Monte Carlo Calculations for the AGATA tracking array [7]. In this connection, we will also investigate the possibility of improving the HPGe time resolution of the AGATA detectors applying an algorithm based on pulse shape analysis techniques, which for standard coaxial HPGe detectors has given an improvement of $\sim 50\%$ [8].

The experiment was performed with an average current of 1 pA (in order to prevent target damage), requiring as trigger conditions either four-fold events in AGATA or three-fold events in AGATA in coincidence with at least one event in HELENA. Typical count-rates were ~ 1.5 kHz for AGATA and ~ 1 kHz for the scintillator array. In approximately one-week experiment the total amount of collected data was roughly 40 TB. In fig. 1 we show a comparison between a γ -ray spectrum constructed using only the core electrode signals (raw data) and the energy spectrum obtained after applying the tracking procedure [4]. One can notice the large reduction of low-energy background events, resulting in a significant improvement of the peak-to-background ratio. The inset of the figure shows the Ge fold distribution (after tracking), which is found to be peaked around 3, an essential requirement for building γ - γ gated matrices.

REFERENCES

- [1] BRACCO A. *et al.*, *Rep. Prog. Phys.*, **65** (2002) 299.
- [2] BENZONI G. *et al.*, *Phys. Lett. B*, **72** (2005) 034307.
- [3] TANDEL S. K. *et al.*, *Phys. Rev. C*, **73** (2006) 044306; **77** (2008) 024313.
- [4] BAZZACCO D., *Nucl. Phys. A*, **746** (2004) 248c.
- [5] DØSSING T. *et al.*, *Phys. Rep.*, **268** (1996) 1.
- [6] BRACCO A. *et al.*, *Nucl. Phys. A*, **599** (1996) 83c.
- [7] ATAC A. *et al.*, *Nucl. Instrum. Methods A*, **607** (2009) 554.
- [8] CRESPI F. C. L. *et al.*, *Nucl. Instrum. Methods A*, **620** (2010) 299.

International School of Physics “Enrico Fermi”

Villa Monastero, Varenna

Course CLXXVIII

19 – 24 July 2010

“From the Big Bang to the Nucleosynthesis”

Directors

Angela BRACCO
Dipartimento di Fisica
Università di Milano
and INFN, Sezione di Milano
Via Celoria 16
20133 Milano
Italy
tel.: ++39 02 50317252
fax: ++39 02 50317487
angela.bracco@mi.infn.it

Eugenio NAPPI
INFN, Sezione di Bari
Via G. Amendola 173
70124 Bari
Italy
tel.: ++39 080 5583411
fax: ++39 080 5534938
eugenio.nappi@ba.infn.it

Scientific Secretary

Bénédicte MILLION
INFN, Sezione di Milano
Via Celoria 16
20133 Milano
Italy
tel.: ++39 02 50317292
fax: ++39 02 50317487
benedicte.million@mi.infn.it

Lecturers

Federico ANTINORI
INFN, Sezione di Padova
Via Marzolo, 8
35131 Padova
Italy
tel.: ++39 049 8275937
fax: ++39 049 8277166
federico.antinori@pd.infn.it

Thomas AUMANN
GSI
Planckstraße 1
64291 Darmstadt
Germany
tel. ++49 6159710
fax: ++49 6159712785
t.aumann@gsi.de

Marcello BALDO
INFN, Sezione di Catania
Via S. Sofia 64
95123 Catania
Italy
tel.: ++39 095 3785311
fax: ++39 095 337938
baldo@ct.infn.it

Peter BUTLER
 Department of Physics
 University of Liverpool
 Oliver Lodge Laboratory
 Liverpool L69 7ZE
 UK
 tel.: ++44 151 794 3443
 fax: ++44 151 794 3348
 peter.butler@liverpool.ac.uk

William LYNCH
 Department of Physics and Astronomy
 and National Superconducting Cyclotron
 Laboratory (NSCL)
 Michigan State University
 East Lansing, MI 48824-1321
 USA
 tel.: ++1 517 333 6319
 fax: ++1 517 353 5967
 lynch@nscl.msu.edu

Muhsin N. HARAKEH
 KVI (Kernfysisch Versneller Instituut)
 Zernikelaan 25
 9747 AA Groningen
 The Netherlands
 tel.: ++31 50 363 3600
 Fax: ++31 50 363 4003
 m.n.harakeh@kvi.nl

Antonio MASIERO
 Dipartimento di Fisica
 Università di Padova
 and INFN, Sezione di Padova
 Via Marzolo 8
 35131 Padova
 Italy
 tel.: ++39 049 8277127
 fax: ++39 049 8277166
 antonio.masiero@pd.infn.it

Karlheinz LANGANKE
 GSI
 Planckstraße 1
 64291 Darmstadt
 Germany
 tel.: ++49 6159 71 2747
 fax: ++49 6159 71 2990
 k.langanke@gsi.de

Tohru MOTOBAYASHI
 RIKEN - Nishina Center
 2-1 Hirosawa, Wako
 Saitama 351-0198
 Japan
 tel.: ++81 48 467 9452
 MOTOBAYA@RIKEN.JP

Marek LEWITOWICZ
 Grand Accélérateur National
 d'Ions Lourds
 Bd Henri Becquerel
 BP 55027
 14076 Caen 05
 France
 tel.: ++33 231 454647
 fax: ++33 231 454665
 lewitowicz@ganil.fr

Urs WIEDEMANN
 CERN
 TH Department
 CH-1211 Genève 23
 Switzerland
 tel.: ++41 22 7672753
 fax: ++41 22 7676555
 urs.wiedemann@cern.ch

Seminar Speakers

Giovanna BENZONI
 Dipartimento di Fisica
 Università di Milano
 and INFN, Sezione di Milano
 Via Celoria 16
 20133 Milano
 Italy
Giovanna.benzoni@mi.infn.it

Alessadra GUGLIELMETTI
 Dipartimento di Fisica
 Università di Milano
 and INFN, Sezione Milano
 Via Celoria 16
 20133 Milano
 Italy
Alessandra.guglielmetti@mi.infn.it

Paolo Maria MILAZZO
 INFN Sezione di Trieste
 c/o Dipartimento di Fisica,
 Università di Trieste
 Via A. Valerio 2
 34127 Trieste
 Italy
 tel.: ++39 040 5583088
 fax: ++39 040 5583350
paolo.milazzo@ts.infn.it

Betty TSANG
 Joint Institute of Nuclear Astrophysics
 and National Superconducting
 Cyclotron Laboratory (NSCL)
 Michigan State University
 East Lansing, MI 48824-1321
 USA
 tel.: ++1 517 333 6386
 fax: ++1 517 353 5967
btsang@nscl.msu.edu

Students

Andrea AGOSTINELLI
 Università di Bologna
 INFN, Sezione di Bologna
 Via Irnerio 46
 40126 Bologna
 Italy
 tel.: ++39 339 6201483
andrea.agostinelli@hotmail.it

Francesco BARILE
 Dipartimento Interateneo di Fisica
 Università di Bari
 and INFN, Sezione di Bari
 Via Amendola 173
 70126 Bari
 Italy
 tel.: ++39 080 5442531
 fax: ++39 080 5442470
francesco.barile@ba.infn.it

Francesca BELLINI
 Università di Bologna
 INFN, Sezione di Bologna
 Via Irnerio 46
 40126 Bologna
 Italy
 tel.: ++39 051 2091152
bellini@bo.infn.it

Susanna BERTELLI
 INFN, Sezione di Ferrara
 Polo Scientifico Tacnologico
 Via Saragat 1
 44100 Ferrara
 Italy
bertelli@fe.infn.it

Livio BIANCHI
 Università di Torino
 and INFN, Sezione di Torino
 Via Pietro Giuria 1
 10125 Torino
 Italy
1bianchi@to.infn.it

Stefano CARBONI
 Dipartimento di Fisica
 Università di Firenze
 and INFN, Sezione di Firenze
 Via Sansoni 1
 50019 Sesto Fiorentino (FI)
 Italy
carboni@fi.infn.it

Chiara BIANCHIN
 Università di Padova
 and INFN, Sezione di Padova
 Via Marzolo 8
 35131 Padova
 Italy
 tel.: ++41 22 7678378
chiara.bianchin@cern.ch

Anna CORSI
 Università di Milano
 and INFN, Sezione di Milano
 Via Celoria 16
 20133 Milano
 Italy
 tel.: ++39 02 50317295
anna.corsi@mi.infn.it

Jitka BRABCOVÁ
 Faculty of Nuclear Sciences
 and Physical Engineering (FNSPE)
 Czech Technical University (CTU)
 Behová 7
 Prague 1 11519
 Czech Republic
 tel.: ++420 721538578
jit.brabcova@seznam.cz

Daniele DE GRUTTOLA
 Università di Salerno
 Via Ponte Don Melillo
 84084 Fisciano (SA)
 Italy
 tel.: ++39 089 969346
degruttola@sa.infn.it

Ion BURDUCEA
 Horia Hulubei National Institute
 of Physics and Nuclear Engineering
 IFIN HH
 Str. Atomistilor 407
 P.O. box MG-6
 Bucharest - Magurele
 Romania
 tel.: ++4021 4042345 / 4522867
 fax: ++4021 4574440
ionburducea@yahoo.com

Fay FILMER
 Oliver Lodge laboratory
 Department of Physics
 University of Liverpool
 Oxford Street
 Liverpool, Merseyside L697ZE
 UK
 tel.: ++44 151 7943381
 fax: ++44 151 7943348
ff@ns.ph.liv.ac.uk

Fiorella Maria Celeste FIONDA
Dipartimento di Fisica "M. Merlin"
Università di Bari
and INFN, Sezione di Bari
Via Orabona 4
70126 Bari
Italy
tel.: ++39 080 15443187
fax: ++39 080 5442470
fiorella.fionda@ba.infn.it

Liam GAFFNEY
Oliver Lodge Laboratory
Department of Physics
University of Liverpool
Oxford Street
Liverpool, Merseyside L697ZE
UK
tel.: ++44 151 7943381
fax: ++44 151 7943358
lg@ns.ph.liv.ac.uk

Luz Angela Garcia PEÑALOZA
Universidad Nacional de Colombia
sede Bogotá
Observatorio Astronómico Nacional
Apartado Aéreo 2584
Bogotá
Colombia
tel.: ++57 14422460 / 13165000
fax: ++57 13165383
luzangelagarcia22@gmail.com

Farnaz Ghazi MORADI
Department of Physics - KTH
Alba Nova University Center
SE-10691 Stockholm
Sweden
tel.: ++46 085 5378199
farnazg@kth.se

Agnese GIAZ
INFN, Sezione di Milano
Via Celoria 16
20133 Milano
Italy
tel.: ++39 02 50317217
agnese.giaz@gmail.com

Leonardo GUERRO
Dipartimento di Fisica
Università di Camerino
Via Madonna delle Carceri 9
62032 Camerino (MC)
Italy
tel.: ++39 073 7402518
fax: ++39 073 7402853
leonardo.guerro@unicam.it

Jasna KRIVICIC
Dipartimento di Astronomia
Università di Padova
Vicolo dell'Osservatorio 3
35122 Padova
Italy
tel.: ++39 328 0538450
jasna.krivicic@unipd.it

Daniele MADAFFARI
Dipartimento di Fisica
Università di Perugia
Via A. Pascoli, snc
06123 Perugia
Italy
tel.: ++39 075 5852788
fax: ++39 075 44666
danaffari@gmail.com

Tommaso MARCHI
 INFN, Laboratori Nazionali di Legnaro
 Viale dell'Università 2
 35020 Legnaro (PD)
 Italy
 tel.: ++39 049 8068390
 fax: ++39 049 641925
tommaso.marchi@lnl.infn.it

Luna PELLEGRI
 INFN, Sezione di Milano
 Via Celoria 16
 20133 Milano
 Italy
 tel.: ++39 02 50317217
 fax: ++39 02 50317487
luna.pellegrini@gmail.com

Caterina MICHELAGNOLI
 Dipartimento di Fisica "G. Galilei"
 Università di Padova
 and INFN, Sezione di Padova
 Via Marzolo 8
 35131 Padova
 Italy
 tel.: ++39 049 8277176
cmichela@pd.infn.it

Daniele PIGATO
 Politecnico di Torino
 Corso Duca degli Abruzzi 24
 10129 Torino
 Italy
 tel.: ++39 015 542170
dnlpgt@tin.it

Alina MOVSESYAN
 GSI
 Planckstrasse 1
 D-64291 Darmstadt
 Germany
 tel.: ++49 615 9712435
a.movsesyan@gsi.de

Roberta SPARTÀ
 INFN, Laboratori Nazionali del Sud
 and Dipartimento di Fisica
 Università di Catania
 Via Santa Sofia 62
 95123 Catania
 Italy
 tel.: ++39 339 2854835
rsparta@lns.infn.it

Roberto NICOLINI
 Dipartimento di Fisica
 Università di Milano
 Via Celoria 16
 20133 Milano
 Italy
 tel.: ++39 02 50317295
roberto.nicolini@unimi.it

Mihai STRATICIUC
 Horia Hulubei National Institute
 of Physics and Nuclear Engineering
 IFIN HH
 Str. Atomistilor n. 407
 P.O. box MG-6
 Bucharest - Magurele
 Romania
 tel.: ++4021 4042345 / ++4074 4656024
 fax: ++4021 4574440
mstrat@nipne.ro

Uzma TABASSAM
INFN Sezione di Perugia
and Dipartimento di Fisica
Università di Camerino
Via Madonna delle Carceri 9
62032 Camerino (MC)
Italy
tel.: ++39 0737 402518
fax: ++39 0737 402853
uzma.tabassam@unicam.it

Cristina TERREVOLOI
Dipartimento di Fisica "M. Merlin"
and INFN, Sezione di Bari
Via Orabona 4
70126 Bari
Italy
tel.: ++39 080 5443180
fax: ++39 080 5442470
cristina.terrevoli@ba.infn.it

Oscar TRIPPELLA
Dipartimento di Fisica
Università di Perugia
Via A. Pascoli snc
06123 Perugia
Italy
tel.: ++39 075 5852788
fax: ++39 075 44666
oscartrippella@hotmail.it

Valeria VANDONE
INFN, Sezione di Milano
Via Celoria 16
20133 Milano
Italy
tel.: ++39 02 50317217
fax: ++39 02 50317487
Valeria.vandone@mi.infn.it

Observers

Philip M. GORE
629 Country Club Ln
Nashville, TN 37205
USA
tel.: +1 615 3566470
p.m.gore.phys@earthlink.net

Elizabeth F. JONES
629 Country Club Ln
Nashville, TN 37205
USA
tel.: +1 615 3568848
e.f.jones.phys@earthlink.net

Luigi VANNUCCI
INFN, Laboratori Nazionali di Legnaro
Viale dell'Università 2
35020 Legnaro (PD)
Italy
tel.: ++39 049 8068311
fax: ++39 049 641925
vannucci@lnl.infn.it

This page intentionally left blank

**PROCEEDINGS OF THE INTERNATIONAL
SCHOOL OF PHYSICS
“ENRICO FERMI”**

Course I (1953)

Questioni relative alla rivelazione delle particelle elementari, con particolare riguardo alla radiazione cosmica

edited by G. PUPPI

Course II (1954)

Questioni relative alla rivelazione delle particelle elementari, e alle loro interazioni con particolare riguardo alle particelle artificialmente prodotte ed accelerate

edited by G. PUPPI

Course III (1955)

Questioni di struttura nucleare e dei processi nucleari alle basse energie

edited by C. SALVETTI

Course IV (1956)

Proprietà magnetiche della materia

edited by L. GIULOTTO

Course V (1957)

Fisica dello stato solido

edited by F. FUMI

Course VI (1958)

Fisica del plasma e relative applicazioni astrofisiche

edited by G. RIGHINI

Course VII (1958)

Teoria della informazione

edited by E. R. CAIANIELLO

Course VIII (1958)

Problemi matematici della teoria quantistica delle particelle e dei campi

edited by A. BORSELLINO

Course IX (1958)

Fisica dei pioni

edited by B. TOUSCHEK

Course X (1959)

Thermodynamics of Irreversible Processes

edited by S. R. DE GROOT

Course XI (1959)

Weak Interactions

edited by L. A. RADICATI

Course XII (1959)

Solar Radioastronomy

edited by G. RIGHINI

Course XIII (1959)

Physics of Plasma: Experiments and Techniques

edited by H. ALFVÉN

Course XIV (1960)

Ergodic Theories

edited by P. CALDIROLA

Course XV (1960)

Nuclear Spectroscopy

edited by G. RACAH

Course XVI (1960)

Physicomathematical Aspects of Biology

edited by N. RASHEVSKY

Course XVII (1960)

Topics of Radiofrequency Spectroscopy

edited by A. GOZZINI

Course XVIII (1960)

Physics of Solids (Radiation Damage in Solids)

edited by D. S. BILLINGTON

Course XIX (1961)

Cosmic Rays, Solar Particles and Space Research

edited by B. PETERS

Course XX (1961)

Evidence for Gravitational Theories

edited by C. MØLLER

Course XXI (1961)

Liquid Helium

edited by G. CARERI

Course XXII (1961)

Semiconductors

edited by R. A. SMITH

Course XXIII (1961)

Nuclear Physics

edited by V. F. WEISSKOPF

- Course XXIV (1962)
Space Exploration and the Solar System
edited by B. ROSSI
- Course XXV (1962)
Advanced Plasma Theory
edited by M. N. ROSENBLUTH
- Course XXVI (1962)
Selected Topics on Elementary Particle Physics
edited by M. CONVERSI
- Course XXVII (1962)
Dispersion and Absorption of Sound by Molecular Processes
edited by D. SETTE
- Course XXVIII (1962)
Star Evolution
edited by L. GRATTON
- Course XXIX (1963)
Dispersion Relations and their Connection with Casualty
edited by E. P. WIGNER
- Course XXX (1963)
Radiation Dosimetry
edited by F. W. SPIERS and G. W. REED
- Course XXXI (1963)
Quantum Electronics and Coherent Light
edited by C. H. TOWNES and P. A. MILES
- Course XXXII (1964)
Weak Interactions and High-Energy Neutrino Physics
edited by T. D. LEE
- Course XXXIII (1964)
Strong Interactions
edited by L. W. ALVAREZ
- Course XXXIV (1965)
The Optical Properties of Solids
edited by J. TAUC
- Course XXXV (1965)
High-Energy Astrophysics
edited by L. GRATTON
- Course XXXVI (1965)
Many-body Description of Nuclear Structure and Reactions
edited by C. L. BLOCH
- Course XXXVII (1966)
Theory of Magnetism in Transition Metals
edited by W. MARSHALL
- Course XXXVIII (1966)
Interaction of High-Energy Particles with Nuclei
edited by T. E. O. ERICSON
- Course XXXIX (1966)
Plasma Astrophysics
edited by P. A. STURROCK
- Course XL (1967)
Nuclear Structure and Nuclear Reactions
edited by M. JEAN and R. A. RICCI
- Course XLI (1967)
Selected Topics in Particle Physics
edited by J. STEINBERGER
- Course XLII (1967)
Quantum Optics
edited by R. J. GLAUBER
- Course XLIII (1968)
Processing of Optical Data by Organisms and by Machines
edited by W. REICHARDT
- Course XLIV (1968)
Molecular Beams and Reaction Kinetics
edited by CH. SCHLIER
- Course XLV (1968)
Local Quantum Theory
edited by R. JOST
- Course XLVI (1969)
Physics with Intersecting Storage Rings
edited by B. TOUSCHEK
- Course XLVII (1969)
General Relativity and Cosmology
edited by R. K. SACHS
- Course XLVIII (1969)
Physics of High Energy Density
edited by P. CALDIROLA and H. KNOEPFEL
- Course IL (1970)
Foundations of Quantum Mechanics
edited by B. D'ESPAGNAT
- Course L (1970)
Mantle and Core in Planetary Physics
edited by J. COULOMB and M. CAPUTO
- Course LI (1970)
Critical Phenomena
edited by M. S. GREEN
- Course LII (1971)
Atomic Structure and Properties of Solids
edited by E. BURSTEIN

- Course LIII (1971)
Developments and Borderlines of Nuclear Physics
 edited by H. MORINAGA
- Course LIV (1971)
Developments in High-Energy Physics
 edited by R. R. GATTO
- Course LV (1972)
Lattice Dynamics and Intermolecular Forces
 edited by S. CALIFANO
- Course LVI (1972)
Experimental Gravitation
 edited by B. BERTOTTI
- Course LVII (1972)
History of 20th Century Physics
 edited by C. WEINER
- Course LVIII (1973)
Dynamics Aspects of Surface Physics
 edited by F. O. GOODMAN
- Course LIX (1973)
Local Properties at Phase Transitions
 edited by K. A. MÜLLER and A. RIGAMONTI
- Course LX (1973)
C-Algebras and their Applications to Statistical Mechanics and Quantum Field Theory*
 edited by D. KASTLER
- Course LXI (1974)
Atomic Structure and Mechanical Properties of Metals
 edited by G. CAGLIOTI
- Course LXII (1974)
Nuclear Spectroscopy and Nuclear Reactions with Heavy Ions
 edited by H. FARAGGI and R. A. RICCI
- Course LXIII (1974)
New Directions in Physical Acoustics
 edited by D. SETTE
- Course LXIV (1975)
Nonlinear Spectroscopy
 edited by N. BLOEMBERGEN
- Course LXV (1975)
Physics and Astrophysics of Neutron Stars and Black Hole
 edited by R. GIACCONI and R. RUFFINI
- Course LXVI (1975)
Health and Medical Physics
 edited by J. BAARLI
- Course LXVII (1976)
Isolated Gravitating Systems in General Relativity
 edited by J. EHlers
- Course LXVIII (1976)
Metrology and Fundamental Constants
 edited by A. FERRO MILONE, P. GIACOMO and S. LESCHIUTTA
- Course LXIX (1976)
Elementary Modes of Excitation in Nuclei
 edited by A. BOHR and R. A. BROGLIA
- Course LXX (1977)
Physics of Magnetic Garnets
 edited by A. PAOLETTI
- Course LXXI (1977)
Weak Interactions
 edited by M. BALDO CEOLIN
- Course LXXII (1977)
Problems in the Foundations of Physics
 edited by G. TORALDO DI FRANCIA
- Course LXXIII (1978)
Early Solar System Processes and the Present Solar System
 edited by D. LAL
- Course LXXIV (1978)
Development of High-Power Lasers and their Applications
 edited by C. PELLEGRINI
- Course LXXV (1978)
Intermolecular Spectroscopy and Dynamical Properties of Dense Systems
 edited by J. VAN KRANENDONK
- Course LXXVI (1979)
Medical Physics
 edited by J. R. GREENING
- Course LXXVII (1979)
Nuclear Structure and Heavy-Ion Collisions
 edited by R. A. BROGLIA, R. A. RICCI and C. H. DASSO
- Course LXXVIII (1979)
Physics of the Earth's Interior
 edited by A. M. DZIEWONSKI and E. BOSCHI
- Course LXXIX (1980)
From Nuclei to Particles
 edited by A. MOLINARI
- Course LXXX (1980)
Topics in Ocean Physics
 edited by A. R. OSBORNE and P. MALANOTTE RIZZOLI

- Course LXXXI (1980)
Theory of Fundamental Interactions
edited by G. COSTA and R. R. GATTO
- Course LXXXII (1981)
Mechanical and Thermal Behaviour of Metallic Materials
edited by G. CAGLIOTI and A. FERRO MILONE
- Course LXXXIII (1981)
Positrons in Solid-State Physics
edited by W. BRANDT and A. DUPASQUIER
- Course LXXXIV (1981)
Data Acquisition in High-Energy Physics
edited by G. BOLOGNA and M. VINCCELLI
- Course LXXXV (1982)
Earthquakes: Observation, Theory and Interpretation
edited by H. KANAMORI and E. BOSCHI
- Course LXXXVI (1982)
Gamow Cosmology
edited by F. MELCHIORRI and R. RUFFINI
- Course LXXXVII (1982)
Nuclear Structure and Heavy-Ion Dynamics
edited by L. MORETTO and R. A. RICCI
- Course LXXXVIII (1983)
Turbulence and Predictability in Geophysical Fluid Dynamics and Climate Dynamics
edited by M. GHIL, R. BENZI and G. PARISI
- Course LXXXIX (1983)
Highlights of Condensed Matter Theory
edited by F. BASSANI, F. FUMI and M. P. TOSI
- Course XC (1983)
Physics of Amphiphiles: Micelles, Vesicles and Microemulsions
edited by V. DEGIORGIO and M. CORTI
- Course XCI (1984)
From Nuclei to Stars
edited by A. MOLINARI and R. A. RICCI
- Course XCII (1984)
Elementary Particles
edited by N. CABIBBO
- Course XCIII (1984)
Frontiers in Physical Acoustics
edited by D. SETTE
- Course XCIV (1984)
Theory of Reliability
edited by A. SERRA and R. E. BARLOW
- Course XCV (1985)
Solar-Terrestrial Relationship and the Earth Environment in the Last Millennia
edited by G. CINI CASTAGNOLI
- Course XCVI (1985)
Excited-State Spectroscopy in Solids
edited by U. M. GRASSANO and N. TERZI
- Course XCVII (1985)
Molecular-Dynamics Simulations of Statistical-Mechanical Systems
edited by G. CICCOTTI and W. G. HOOVER
- Course XCVIII (1985)
The Evolution of Small Bodies in the Solar System
edited by M. FULCHIGNONI and Ľ. KRESĀK
- Course XCIX (1986)
Synergetics and Dynamic Instabilities
edited by G. CAGLIOTI and H. HAKEN
- Course C (1986)
The Physics of NMR Spectroscopy in Biology and Medicine
edited by B. MARAVIGLIA
- Course CI (1986)
Evolution of Interstellar Dust and Related Topics
edited by A. BONETTI and J. M. GREENBERG
- Course CII (1986)
Accelerated Life Testing and Experts' Opinions in Reliability
edited by C. A. CLAROTTI and D. V. LINDLEY
- Course CIII (1987)
Trends in Nuclear Physics
edited by P. KIENLE, R. A. RICCI and A. RUBBINO
- Course CIV (1987)
Frontiers and Borderlines in Many-Particle Physics
edited by R. A. BROGLIA and J. R. SCHRIEFFER
- Course CV (1987)
Confrontation between Theories and Observations in Cosmology: Present Status and Future Programmes
edited by J. AUDOUZE and F. MELCHIORRI
- Course CVI (1988)
Current Trends in the Physics of Materials
edited by G. F. CHIAROTTI, F. FUMI and M. TOSI

Course CVII (1988)

*The Chemical Physics of Atomic
and Molecular Clusters*
edited by G. SCOLES

Course CVIII (1988)

*Photoemission and Absorption
Spectroscopy of Solids and Interfaces
with Synchrotron Radiation*
edited by M. CAMPAGNA and R. ROSEI

Course CIX (1988)

Nonlinear Topics in Ocean Physics
edited by A. R. OSBORNE

Course CX (1989)

*Metrology at the Frontiers of Physics
and Technology*
edited by L. CROVINI and T. J. QUINN

Course CXI (1989)

Solid-State Astrophysics
edited by E. BUSSOLETTI and G. STRAZZULLA

Course CXII (1989)

*Nuclear Collisions from the Mean-Field
into the Fragmentation Regime*
edited by C. DETRAZ and P. KIENLE

Course CXIII (1989)

*High-Pressure Equation of State:
Theory and Applications*
edited by S. ELIEZER and R. A. RICCI

Course CXIV (1990)

*Industrial and Technological Applications
of Neutrons*
edited by M. FONTANA and F. RUSTICHELLI

Course CXV (1990)

*The Use of EOS for Studies
of Atmospheric Physics*
edited by J. C. GILLE and G. VISCONTI

Course CXVI (1990)

*Status and Perspectives of Nuclear
Energy: Fission and Fusion*
edited by R. A. RICCI, C. SALVETTI
and E. SINDONI

Course CXVII (1991)

*Semiconductor Superlattices
and Interfaces*
edited by A. STELLA

Course CXVIII (1991)

Laser Manipulation of Atoms and Ions
edited by E. ARIMONDO, W. D. PHILLIPS
and F. STRUMIA

Course CXIX (1991)

Quantum Chaos
edited by G. CASATI, I. GUARNERI
and U. SMILANSKY

Course CXX (1992)

Frontiers in Laser Spectroscopy
edited by T. W. HÄNSCH and M. INGUSCIO

Course CXXI (1992)

Perspectives in Many-Particle Physics
edited by R. A. BROGLIA, J. R. SCHRIEFFER
and P. F. BORTIGNON

Course CXXII (1992)

Galaxy Formation
edited by J. SILK and N. VITTORIO

Course CXXIII (1992)

Nuclear Magnetic Double Resonance
edited by B. MARAVIGLIA

Course CXXIV (1993)

Diagnostic Tools in Atmospheric Physics
edited by G. FIOCCO and G. VISCONTI

Course CXXV (1993)

Positron Spectroscopy of Solids
edited by A. DUPASQUIER and A. P. MILLS jr.

Course CXXVI (1993)

*Nonlinear Optical Materials: Principles
and Applications*
edited by V. DEGIORGIO and C. FLYTZANIS

Course CXXVII (1994)

*Quantum Groups and their Applications
in Physics*
edited by L. CASTELLANI and J. WESS

Course CXXVIII (1994)

*Biomedical Applications of Synchrotron
Radiation*
edited by E. BURATTINI and A. BALERNA

Course CXXIX¹ (1994)

*Observation, Prediction and Simulation
of Phase Transitions in Complex Fluids*
edited by M. BAUS, L. F. RULL
and J. P. RYCKAERT

Course CXXX (1995)

Selected Topics in Nonperturbative QCD
edited by A. DI GIACOMO and D. DIAKONOV

Course CXXXI (1995)

*Coherent and Collective Interactions
of Particles and Radiation Beams*
edited by A. ASPECT, W. BARLETTA
and R. BONIFACIO

¹This course belongs to the NATO ASI Series C, Vol. 460 (Kluwer Academic Publishers).

Course CXXXII (1995)

Dark Matter in the Universe

edited by S. BONOMETTO and J. PRIMACK

Course CXXXIII (1996)

Past and Present Variability of the Solar-Terrestrial System: Measurement, Data Analysis and Theoretical Models

edited by G. CINI CASTAGNOLI

and A. PROVENZALE

Course CXXXIV (1996)

The Physics of Complex Systems

edited by F. MALLAMACE and H. E. STANLEY

Course CXXXV (1996)

The Physics of Diamond

edited by A. PAOLETTI and A. TUCCARONE

Course CXXXVI (1997)

Models and Phenomenology

for Conventional and High-Temperature Superconductivity

edited by G. IADONISI, J. R. SCHRIEFFER and M. L. CHIOFALO

Course CXXXVII (1997)

Heavy Flavour Physics: a Probe of Nature's Grand Design

edited by I. BIGI and L. MORONI

Course CXXXVIII (1997)

Unfolding the Matter of Nuclei

edited by A. MOLINARI and R. A. RICCI

Course CXXXIX (1998)

Magnetic Resonance and Brain Function: Approaches from Physics

edited by B. MARAVIGLIA

Course CXL (1998)

Bose-Einstein Condensation in Atomic Gases

edited by M. INGUSCIO, S. STRINGARI and C. E. WIEMAN

Course CXLI (1998)

Silicon-Based Microphotonics: from Basics to Applications

edited by O. BISI, S. U. CAMPISANO, L. PAVESI and F. PRIULO

Course CXLII (1999)

Plasmas in the Universe

edited by B. COPPI, A. FERRARI and E. SINDONI

Course CXLIII (1999)

New Directions in Quantum Chaos

edited by G. CASATI, I. GUARNERI and U. SMILANSKY

Course CXLIV (2000)

Nanometer Scale Science and Technology

edited by M. ALLEGRENI, N. GARCÍA and O. MARTI

Course CXLV (2000)

Protein Folding, Evolution and Design

edited by R. A. BROGLIA, E. I. SHAKHNOVICH and G. TIANA

Course CXLVI (2000)

Recent Advances in Metrology and Fundamental Constants

edited by T. J. QUINN, S. LESCHIUTTA and P. TAVELLA

Course CXLVII (2001)

High Pressure Phenomena

edited by R. J. HEMLEY, G. L. CHIAROTTI, M. BERNASCONI and L. ULIVI

Course CXLVIII (2001)

Experimental Quantum Computation and Information

edited by F. DE MARTINI and C. MONROE

Course CXLIX (2001)

Organic Nanostructures: Science and Applications

edited by V. M. AGRANOVICH and G. C. LA ROCCA

Course CL (2002)

Electron and Photon Confinement in Semiconductor Nanostructures

edited by B. DEVEAUD-PLÉDRAN, A. QUATTROPANI and P. SCHWENDIMANN

Course CLI (2002)

Quantum Phenomena in Mesoscopic Systems

edited by B. ALTSHULER, A. TAGLIACOZZO and V. TOGNETTI

Course CLII (2002)

Neutrino Physics

edited by E. BELLOTTI, Y. DECLAIRS and P. STROLIN

Course CLIII (2002)

From Nuclei and their Constituents to Stars

edited by A. MOLINARI, L. RICCATTI, W. M. ALBERICO and M. MORANDO

Course CLIV (2003)

Physics Methods in Archaeometry

edited by M. MARTINI, M. MILAZZO and M. PIACENTINI

Course CLV (2003)

The Physics of Complex Systems (New Advances and Perspectives)

edited by F. MALLAMACE and H. E. STANLEY

Course CLVI (2003)

Research on Physics Education

edited by E.F. REDISH and M. VICENTINI

Course CLVII (2003)

The Electron Liquid Model in Condensed Matter Physics

edited by G. F. GIULIANI and G. VIGNALE

Course CLVIII (2004)

Hadron Physics

edited by T. BRESSANI, U. WIEDNER
and A. FILIPPI

Course CLIX (2004)

Background Microwave Radiation and Intracluster Cosmology

edited by F. MELCHIORRI and Y. REPHAELEI

Course CLX (2004)

From Nanostructures to Nanosensing Applications

edited by A. D'AMICO, G. BALESTRINO
and A. PAOLETTI

Course CLXI (2005)

Polarons in Bulk Materials and Systems with Reduced Dimensionality

edited by G. IADONISI, J. RANNINGER
and G. DE FILIPPIS

Course CLXII (2005)

Quantum Computers, Algorithms and Chaos

edited by G. CASATI, D. L. SHEPELYANSKY,
P. ZOLLER and G. BENENTI

Course CLXIII (2005)

CP Violation: From Quarks to Leptons

edited by M. GIORGI, I. MANNELLI,
A. I. SANDA, F. COSTANTINI
and M. S. SOZZI

Course CLXIV (2006)

Ultra-Cold Fermi Gases

edited by M. INGUSCIO, W. KETTERLE
and C. SALOMON

Course CLXV (2006)

Protein Folding and Drug Design

edited by R. A. BROGLIA, L. SERRANO
and G. TIANA

Course CLXVI (2006)

Metrology and Fundamental Constants

edited by T. W. HÄNSCH, S. LESCHIUTTA,
A. J. WALLARD and M. L. RASTELLO

Course CLXVII (2007)

Strangeness and Spin in Fundamental Physics

edited by M. ANSELMINO, T. BRESSANI,
A. FELICIELLO and PH. G. RATCLIFFE

Course CLXVIII (2007)

Atom Optics and Space Physics

edited by E. ARIMONDO, W. ERTMER,
W. P. SCHLEICH and E. M. RASEL

Course CLXIX (2007)

Nuclear Structure far from Stability: New Physics and New Technology

edited by A. COVELLO, F. IACHELLO,
R. A. RICCI and G. MAINO

Course CLXX (2008)

Measurements of Neutrino Mass

edited by F. FERRONI, F. VISSANI
and C. BROFFERIO

Course CLXXI (2008)

Quantum Coherence in Solid State Physics

edited by B. DEVEAUD-PLÉDRAN,
A. QUATTROPANI and P. SCHWENDIMANN

Course CLXXII (2008)

Astrophysics of Galaxy Clusters

edited by A. CAVALIERE and Y. REPHAELEI

Course CLXXIII (2009)

Nano Optics and Atomics:

Transport of Light and Matter Waves

edited by R. KAISER, D. S. WIERSMA
and L. FALLANI

Course CLXXIV (2009)

Physics with Many Positrons

edited by R. S. BRUSA, A. DUPASQUIER
and A. P. MILLS jr.

Course CLXXV (2009)

Radiation and Particle Detectors

edited by S. BERTOLUCCI, U. BOTTIGLI
and P. OLIVA

This page intentionally left blank